



**Forschungszentrum Karlsruhe**  
Technik und Umwelt

**Wissenschaftliche Berichte**  
FZKA 5581

# **Development of Self-Cooled Liquid Metal Breeder Blankets**

compiled by:

**S. Malang, M. S. Tillack**

Contributors:

**L. Barleon, S. Baumgärtner, H. U. Borgstedt,  
L. Bühler, G. Bürkle, F. Dammel, H. Feuerstein,  
U. Fischer, K. Gabel, H. Gerhardt, H. Glasbrenner,  
T. Heider, T. Jordan, K. Kleefeldt, H. Kleykamp,  
R. Lindau, A. Möslang, P. Norajitra, G. Reimann,  
J. Reimann, H. Riesch-Oppermann,  
H.-J. Ritzhaupt-Kleissl, K. Schleisiek, G. Schmitz,  
H. Schnauder, R. Stieglitz, B. Tellini,  
H. Tsige-Tamirat**

**Projekt Kernfusion**

**November 1995**



**FORSCHUNGSZENTRUM KARLSRUHE**  
Technik und Umwelt  
Wissenschaftliche Berichte  
FZKA 5581

# **Development of Self-Cooled Liquid Metal Breeder Blankets**

compiled by: *S. Malang and M.S. Tillack\**

*Contributors: L. Barleon, S. Baumgärtner, H.U. Borgstedt, L. Bühler,  
G. Bürkle, F. Dammel, H. Feuerstein, U. Fischer, K. Gabel, H. Gerhardt,  
H. Glasbrenner, T. Heider, T. Jordan, K. Kleefeldt, H. Kleykamp,  
R. Lindau, A. Möslang, P. Norajitra, G. Reimann, J. Reimann,  
H. Riesch-Oppermann, H.-J. Ritzhaupt-Kleissl, K. Schleisiek,  
G. Schmitz, H. Schnauder, R. Stieglitz, B. Tellini, H. Tsige-Tamirat*

**Projekt Kernfusion**

\* on assignment from the University of California, San Diego

**Forschungszentrum Karlsruhe GmbH, Karlsruhe**  
**1995**

1997

1997

1997

1997

Als Manuskript gedruckt  
Für diesen Bericht behalten wir uns alle Rechte vor

Forschungszentrum Karlsruhe GmbH  
Postfach 3640, 76021 Karlsruhe

ISSN 0947-8620

## **Abstract**

The development of liquid metal breeder blankets for fusion reactors has been performed in the Forschungszentrum Karlsruhe as a part of the European fusion blanket development program with the aim to select the two most promising concepts in 1995 for further development. In this report are described the designs of self-cooled blankets together with the results of the accompanying R&D program of the years 1992-1995.

The program includes design studies as well as theoretical and experimental work in the fields of neutronics, magneto-hydrodynamics, thermohydraulics, mechanical stresses, compatibility and purification of lead-lithium, tritium extraction and control, safety, reliability, electrical insulating coatings, and fabrication technologies for blanket segments.

*This work has been performed in the framework of the nuclear fusion project of the Kernforschungszentrum Karlsruhe and is supported by the European Union within the European Fusion Technology Program.*

## **Entwicklung von selbstgekühlten Flüssigmetall-Brutblankets Zusammenfassung**

Die Entwicklung von Flüssigmetall-Blankets für Fusionsreaktoren erfolgte im Forschungszentrum Karlsruhe als Teil des Europäischen Blanketentwicklungsprogrammes mit dem Ziel, in 1995 die zwei aussichtsreichsten Konzepte zur weiteren Entwicklung auszuwählen. Beschrieben sind in dem Bericht Entwürfe von selbstgekühlten Blankets zusammen mit den Ergebnissen des zugehörigen F+E-Programmes der Jahre 1992-1995.

Das Programm umfaßt neben Entwurfsstudien theoretische und experimentelle Arbeiten auf den Gebieten Neutronik, Magnetohydrodynamik, Thermohydraulik, mechanische Spannungen, Verträglichkeit und Reinigung von Blei-Lithium, Tritium-Extraktion und -Permeation, Sicherheit, Zuverlässigkeit, Isolationschichten, und Fabrikationstechnologien für Blanketsegmente.

*Die vorliegende Arbeit wurde im Rahmen des Projektes Kernfusion des Forschungszentrums Karlsruhe durchgeführt und ist ein von der Europäischen Union geförderter Beitrag im Rahmen des Fusionstechnologieprogramms.*

The first part of the document discusses the importance of maintaining accurate records of all transactions. It emphasizes that every entry should be supported by a valid receipt or invoice. This ensures transparency and allows for easy verification of the data. The second part of the document outlines the procedures for handling discrepancies. It states that any differences between the recorded amounts and the actual amounts should be investigated immediately. The third part of the document provides a detailed breakdown of the financial data for the period covered. It includes a table showing the various categories of income and expenses, along with their respective amounts. The final part of the document concludes with a summary of the overall financial performance and a recommendation for future actions.

The following table provides a detailed breakdown of the financial data for the period covered. It includes a table showing the various categories of income and expenses, along with their respective amounts. The data is presented in a clear and concise manner, allowing for easy comparison and analysis. The table is organized into columns representing different categories and rows representing different time periods. This format facilitates the identification of trends and patterns in the data. The information provided in this table is essential for understanding the financial health of the organization and for making informed decisions about its future operations.

The data presented in the table above shows a steady increase in income over the period, while expenses remain relatively stable. This indicates a positive financial trend for the organization. However, it is important to note that there are still areas where costs can be reduced, such as in the area of marketing and administrative expenses. By implementing cost-saving measures in these areas, the organization can further improve its financial performance and ensure long-term sustainability.

In conclusion, the financial data for the period covered shows a strong performance overall. The organization has successfully managed its resources and achieved its financial goals. The detailed breakdown provided in the table allows for a thorough understanding of the organization's financial position and highlights areas for improvement. It is recommended that the organization continue to monitor its financial performance closely and take proactive steps to address any potential risks or challenges.

The following table provides a detailed breakdown of the financial data for the period covered. It includes a table showing the various categories of income and expenses, along with their respective amounts. The data is presented in a clear and concise manner, allowing for easy comparison and analysis. The table is organized into columns representing different categories and rows representing different time periods. This format facilitates the identification of trends and patterns in the data. The information provided in this table is essential for understanding the financial health of the organization and for making informed decisions about its future operations.

The data presented in the table above shows a steady increase in income over the period, while expenses remain relatively stable. This indicates a positive financial trend for the organization. However, it is important to note that there are still areas where costs can be reduced, such as in the area of marketing and administrative expenses. By implementing cost-saving measures in these areas, the organization can further improve its financial performance and ensure long-term sustainability.

In conclusion, the financial data for the period covered shows a strong performance overall. The organization has successfully managed its resources and achieved its financial goals. The detailed breakdown provided in the table allows for a thorough understanding of the organization's financial position and highlights areas for improvement. It is recommended that the organization continue to monitor its financial performance closely and take proactive steps to address any potential risks or challenges.

The following table provides a detailed breakdown of the financial data for the period covered. It includes a table showing the various categories of income and expenses, along with their respective amounts. The data is presented in a clear and concise manner, allowing for easy comparison and analysis. The table is organized into columns representing different categories and rows representing different time periods. This format facilitates the identification of trends and patterns in the data. The information provided in this table is essential for understanding the financial health of the organization and for making informed decisions about its future operations.

## Table of Contents

<b>1.</b>	<b>Introduction</b>	<b>1</b>
<b>2.</b>	<b>Liquid Metal Breeder Blanket Concepts</b>	<b>9</b>
2.1	Self-cooled blanket with First Wall cooling in toroidal direction	10
2.2	Self-cooled Blanket with Helium-cooled First Wall (Dual Coolant Concept)	14
2.3	Self-cooled blanket with First Wall cooling in poloidal direction	21
2.4	Helium-cooled liquid metal blanket for ITER	23
2.4.1	Introduction	23
2.4.2	Blanket design	26
2.4.3	Blanket performance assessment	30
2.4.4	Modifications in the concepts	35
<b>3.</b>	<b>Fabrication Technology of Blanket Segments</b>	<b>39</b>
3.1	Diffusion welding	39
3.2	Bending of FW box	42
3.3	Electron beam welding	43
3.3.1	Results of EB welding investigations	44
3.3.2	Modelling of the EB welding process; reliability analysis	48
3.4	Insulating coatings	49
3.4.1	Coating process options	49
3.4.2	Aluminization tests	50
3.4.3	Oxidation	51
3.4.4	Self-healing	52
3.4.5	Summary and future prospects	53
3.5	Flow Channel Inserts	53
3.5.1	Objectives	53
3.5.2	Material selection and layer morphology	54
3.5.3	Bonding and testing of the bonding strength	55
3.5.4	Conclusions	57

<b>4. Neutronics</b>	<b>59</b>
4.1 Neutronic characteristics of the blanket	59
4.2 Computational procedure and blanket modelling	60
4.3 Tritium breeding	64
4.4 Nuclear power generation	65
4.5 Activation and afterheat calculations	67
4.5.1 Afterheat generation	69
4.5.2 Activation product inventories	71
4.6 Shielding analysis	80
<b>5. Magnetohydrodynamics (MHD) of Liquid Metal Flow</b>	<b>87</b>
5.1 Introduction	87
5.2 Overview of MHD phenomena and solution methods	89
5.2.1 Discussion of MHD design issues	89
5.2.2 Governing equations	95
5.2.3 MHD phenomena	97
5.3 Solution methods	99
5.3.1 Direct numerical simulation	99
5.3.2 Asymptotic solution	101
5.4 Experimental methods	103
5.4.1 The MEKKA facility	106
5.4.2 Measuring techniques	106
5.4.2.1 Integral quantities	106
5.4.2.2 Local quantities	107
5.4.3 Data acquisition system	109
5.5 Results on MHD-flows in hydraulic elements	111
5.5.1 Flows in single ducts with constant cross section perpendicular to B	111
5.5.1.1 Fully developed flows	111
5.5.1.2 Nonhomogeneous magnetic field	115
5.5.2 Single ducts with changing flow direction or cross section in the plane perpendicular to B	116
5.5.3 Single ducts with changing flow direction or cross section in the plane of B (3D geometries)	120
5.5.3.1 Expansions and contractions	120
5.5.3.2 The 90°-bend with one leg parallel to B	121
5.5.3.3 U-bend flows	125

5.5.4	Combining and distributing flows in manifolds	131
5.5.4.1	Manifolds in the plane perpendicular to B	131
5.5.4.2	Manifolds in the plane of B	137
5.5.5	Liquid metal flow interaction in multi-channel ducts	142
5.5.5.1	Multi-channel flow in straight ducts	142
5.5.5.2	Multi-bend flow	144
5.5.5.3	Pressure drop reduction in multi-bend flows	151
5.5.6	Methods for pressure drop reduction	152
5.5.6.1	Flow channel inserts	152
5.5.6.2	Direct insulating coatings	155
5.6	Heat transfer for laminar MHD flows	158
5.6.1	Governing equations and boundary conditions	158
5.6.2	Heat transfer in fully developed channel flow	159
5.6.3	Heat transfer in ducts of arbitrary geometry	160
5.6.4	Heat transfer in a complex blanket element	163
5.7	Heat transfer and MHD turbulence experiments	164
5.7.1	Flow measurements of MHD turbulence in an electrically insulated duct (GALINKA)	164
5.7.2	MHD/Heat transfer in an electrically insulated duct	166
5.7.3	MHD/Heat transfer in a duct with thin conducting Hartmann walls	171
5.8	Computation of blanket pressure drop	173
<b>6.</b>	<b>Thermomechanics</b>	<b>183</b>
6.1	Cooling system thermal-hydraulics	183
6.2	Thermal and stress analysis	190
6.2.1	Thermal analysis	190
6.2.2	Stress analysis	193
<b>7.</b>	<b>Tritium Extraction and Recovery</b>	<b>199</b>
7.1	Tritium extraction with NaK cold trap	199
7.1.1	Principal considerations	199
7.1.2	Overview of hydrogen removal by cold trapping	201
7.1.3	Experimental investigations	206
7.1.4	Theoretical work	209
7.1.5	Results for hydrogen removal	212

7.1.5.1	Mesh-packed cold traps .....	212
7.1.5.2	Rotational Cold Trap (RTC) .....	219
7.1.6	Results for hydrogen recovery .....	223
7.1.7	Layout of the Tritium Extraction System (TES) for PbLi .....	226
7.2	Tritium extraction from Pb-17Li with solid getters .....	231
7.2.1	Possible getter materials .....	232
7.2.2	Experiments .....	232
7.2.3	Results .....	234
7.2.4	Other observations .....	236
7.2.5	Evaluation of the getter process .....	236
7.2.6	Summary .....	237
<b>8.</b>	<b>Pb-17Li Physical Chemistry .....</b>	<b>241</b>
8.1	Corrosion of the structural material in flowing Pb-17Li .....	242
8.2	Compatibility of metals and alloys in static Pb-17Li .....	244
8.3	Removal of corrosion products .....	247
8.3.1	Formation of corrosion products .....	247
8.3.2	Experiments .....	248
8.3.3	Results .....	249
8.4	Aerosols and activation products .....	254
8.4.1	Experiments .....	254
8.4.2	Evaporation of lithium + lead, aerosols .....	255
8.4.3	Behavior of Po-210 .....	257
8.4.4	Behavior of bismuth .....	260
8.4.5	Summary .....	260
8.5	Behavior of lithium replenishment .....	261
8.5.1	Gravitational segregation .....	262
8.5.2	Thermal gradient segregation .....	263
8.5.3	Replenishment of lithium .....	264
8.5.4	Summary .....	266
<b>9.</b>	<b>Ancillary Loop System .....</b>	<b>269</b>
9.1	Steam generator design .....	269
9.2	Circulation pump .....	270
9.3	Power conversion system .....	270
9.4	Subdivision of the primary systems .....	273

<b>10. Testing of Electrical Insulators</b> .....	<b>275</b>
10.1 Tests in Pb-17Li .....	275
10.2 Results of irradiation tests with alumina in the FZK cyclotron facility .....	279
10.3 Irradiation in the HFR-Petten .....	284
<b>11.0 Safety and Environmental Impact</b> .....	<b>289</b>
11.1 Blanket materials and toxic materials inventory .....	290
11.1.1 Volumes and volume fractions in the blanket segment .....	290
11.1.2 Coolant inventories .....	292
11.1.2.1 Inventories in piping .....	294
11.1.2.2 Inventories in components .....	296
11.1.2.3 Summary of coolant inventories .....	296
11.1.3 Toxic inventories .....	296
11.1.3.1 Tritium inventory .....	297
11.1.3.2 Activation products inventory .....	300
11.2 Energy sources for mobilisation .....	303
11.2.1 Energy liberated during plasma disruptions .....	303
11.2.2 Energy due to delayed plasma shutdown .....	304
11.2.3 Decay heat .....	304
11.2.4 Work potential of helium coolant .....	305
11.2.5 Exothermic chemical reactions .....	307
11.2.5.1 Pb-17Li-water reactions .....	307
11.2.5.2 Pb-17Li-air reactions .....	309
11.2.5.3 Pb-17Li-nitrogen reactions .....	309
11.2.5.4 Pb-17Li-concrete reactions .....	310
11.3 Fault tolerance .....	310
11.3.1 Behavior during electromagnetic transients .....	310
11.3.2 LOCA temperature transients .....	312
11.3.2.1 LOCA in a First Wall helium subsystem .....	312
11.3.2.2 LOCA in the Pb-17Li circuit .....	313
11.3.2.3 LOCA in the NaK circuit .....	314
11.4 Tritium and activation products release .....	315
11.4.1 Release during normal operation .....	315
11.4.2 Tritium release in accidental situations .....	315
11.4.3 Activation products release for a Pb-17Li LOCA .....	317
11.5 Waste generation and management .....	321

<b>12. Reliability and Availability</b> .....	<b>325</b>
12.1 Introduction .....	325
12.2 Methodology .....	326
12.2.1 Basic events .....	326
12.2.2 Failure rates and repair times .....	327
12.3 Evaluation results .....	327
12.3.1 External cooling system evaluation .....	327
12.3.2 Blanket segment evaluation .....	335
12.4 Conclusions .....	339
<b>13. Conclusions</b> .....	<b>343</b>

## 1. Introduction

Tritium breeding blankets in a fusion power reactor have a decisive influence on the safety, environmental impact and cost of fusion power. The development and testing of such blankets requires an expensive long-term programme, and therefore must be restricted to a small number of attractive concepts. Most important are tests in a fusion environment, which are one of the main goals of the International Thermonuclear Experimental Reactor (ITER). The blanket development programme therefore must be consistent with the time scale of the ITER programme, with a planned start of operation in the year 2005.

The European Union (EU) has been engaged since 1989 in a programme to develop tritium breeding blankets for application in a power reactor with the goal to select the two most promising concepts in 1995. There are four concepts under development, which are described in [1-1, 1-2, 1-3, 1-4]. Two of these blanket concepts rely on the use of lithium ceramics as breeder material, helium as coolant and beryllium as neutron multiplier. An eutectic lead lithium alloy (Pb-17Li) is used as breeder material in the other two concepts, cooled either by water or by circulating the liquid breeder material itself to external heat exchangers.

A common basis for DEMO blankets has been specified by the Test blanket Advisory Group (TAG) [1-5]. Some of the key performance-related parameters are shown in Table 1-1. More details concerning the DEMO specifications are given in [1-2].

Pure lithium or lithium-lead alloys are attractive breeder materials in fusion power reactor blankets, since they are immune to irradiation damage and offer tritium self-sufficiency without the need for additional Be neutron multiplier. The high thermal conductivity of liquid metals facilitates robust and rather simple designs, especially if the liquid metal serves as both breeder and coolant.

The R&D work related to such a self-cooled blanket concept for the period 1989-1991 is described in [1-6]. The work was continued, and the new results are described in this report. The two reports together form a complete summary of the results for the period 1989-1995.

Several design concepts have been examined, and are described in Chapter 2. These include:

**Table 1-1 Selected DEMO specifications**

Fusion power	2200 MW
Average neutron wall loading	2.2 MW/m <sup>2</sup>
Average surface heat flux	0.4 MW/m <sup>2</sup>
Plasma operating mode	continuous
Tritium breeding requirement	self-sufficient with 10 ports 3 m high x 1 m wide
Impurity control	double-null divertor
First wall protection	none
Number of TF coils	16
Toroidal magnetic field on axis	6 T
Number of segments	32 inboard, 48 outboard
Blanket/shield thickness	1.18 m inboard, 1.86 m outboard
Structural material	MANET
Lifetime, displacement damage	20000 full-power hours, 70 dpa
Disruption current decay *	20 MA to zero in 20 ms
Thermal efficiency **	≥ 30%

\* segments may become inoperative, but must be removeable by standard exchange procedures

\*\* ratio of electricity produced to the sum of neutron and surface heat fluxes

1. A self-cooled design with toroidal first wall coolant paths
2. A self-cooled design with simple poloidal flow paths and a separate He coolant in the first wall (the Dual Coolant blanket)
3. A self-cooled design with simple poloidal flow paths and an advanced method for first wall heat removal using turbulent heat transport
4. A convertible blanket for ITER employing Pb shielding material to be replaced by Pb-17Li stagnant breeder, with He cooling of the first wall and breeding zones.

The Dual Coolant blanket concept was chosen as the reference solution. The need for some form of electrical insulation between the coolant and the load-bearing structures is acknowledged for all liquid metal cooled DEMO blankets. The reference solution of direct insulating coatings was chosen, with a laminated insert - the so-called "flow-channel insert" - as a backup solution.

Chapters 3 through 12 describe the results of R&D carried out on topics identified as important issues for self-cooled liquid metal blankets. The focus of the R&D was to help guide the design process and to place the greatest emphasis on issues which contribute the most to discriminate between design concepts for the purpose of design selection. Figure 1-1 summarizes the logic for the overall DEMO blanket development effort. The key issues and R&D results are summarized briefly below.

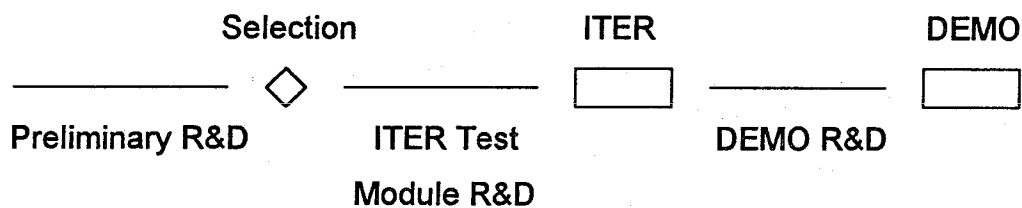


Figure 1-1 Strategy for DEMO blanket R&D

### Fabrication Technology

The blanket structures have been designed to minimize the probability of coolant leakage or performance degradation which might lead to the need for plant shutdown. Reliable methods for fabrication are essential to meet those goals. The key technologies for these blanket concepts include the joining of the first wall by diffusion and E-beam welding, box bending, and the fabrication of the MHD insulation - either insulating coatings or flow channel inserts (FCI's). The principal fabrication and assembly steps have been demonstrated. Prototypes have been bonded, inspected and leak tested, as described in detail in Chapter 3.

### Neutronics

Neutronics calculations were performed to provide inputs to thermomechanical calculations and safety evaluations. This includes tritium production rates, activation inventories, afterheat, and shielding. Tritium self-sufficiency is a requirement for all blankets; it is easily achieved with the Dual Coolant concept. Low shielding effectiveness of He and Pb-17Li coolants is a concern. However, simple measures - even without optimization - can be applied to solve these problems. Po production is a particular concern for safety; errors in the UKACT1 data library were

found, leading to the conclusion that Po inventories will be 5 - 10 times lower than previously predicted, and may no longer be considered the dominant radioisotope.

### **Magnetohydrodynamics**

One of the most important concerns for liquid metal blankets is magnetohydrodynamic (MHD) effects and their influence on thermal hydraulics and corrosion. Concerns over MHD effects arise not only due to the limits placed on blanket operating parameters, but also due to potentially large uncertainties. In the 1980's, the level of understanding of MHD phenomena in liquid metal blankets was very primitive, primarily based on simple empirical correlations and heuristic arguments. The lack of fundamental understanding of the behavior of the fluid in complex fusion-relevant geometries was a critical issue for this class of blankets.

Due to the efforts associated with the work described here, as well as increased efforts on self-cooled liquid metal blankets worldwide, the state of our understanding and predictive capabilities for MHD flow and heat transfer has grown enormously. Data and three-dimensional numerical solutions have been obtained for all of the essential geometric elements of blankets under laminar flow conditions, including bends, cross-section changes, multiple-duct arrays and manifolds. A general purpose "core flow" computer code has been developed and extensively validated against experimental data, further increasing confidence in our ability to accurately predict thermal-hydraulic behavior of blankets. Recent experiments on 2-dimensional MHD turbulence provide strong encouragement that improved heat transfer will allow advanced concepts with liquid metals used as a first wall coolant in simple poloidal ducts.

### **Thermomechanics**

Detailed 3D calculations of the thermal and stress fields were performed on the reference Dual Coolant blanket. The results were compared with allowable temperature limits and with stress levels specified in the ASME code. Allowing for a small increase in the shield operating temperature, the present design meets all requirements.

## **Tritium extraction and recovery**

The requirements on the blanket tritium removal and recovery system are low tritium inventory in the total blanket system and acceptable levels of tritium permeation through the steam generator into the water loop. The reference technique uses permeation from the primary Pb-17Li loop into a NaK-filled gap in the double-walled steam generator. The key performance issues relate to the removal rates in the cold trap located in the NaK loop and the cold trap recovery rate. Both mesh-packed and rotational cold traps were demonstrated by operating with short and long loading times, including measurements of deposition and recovery rates. An alternative technique using a metal getter was also explored by measuring H transport in Pb-17Li and deposition and recovery of H in vanadium getters in the loops.

## **Pb-17Li physical chemistry**

The eutectic Pb-17Li is a unique alloy system proposed specifically for fusion applications fairly recently; many of its properties were poorly known when the concept was proposed, leading to speculations of several serious issues involving corrosion of the structural alloy, transport of corrosion and activation products, impurity control, and segregation and replenishment of the eutectic. These issues all have been addressed through a programme of analysis and experiments described in Chapter 8.

Corrosion experiments indicate that Pb-17Li is compatible with MANET up to 470°C. With insulating layers between the steel and Pb-17Li, the corrosion rate was drastically reduced below the limit of detection. Some of the more important new results involve the chemistry of Po and Bi. New experimental evidence suggests that Po forms the compound PbPo, which has an evaporation rate orders of magnitude lower than pure Po, thereby dramatically reducing its potential release rate. Bi is found to form the compound  $\text{Li}_3\text{Bi}$ , which can be cold trapped. This, together with observations of Bi transport to cover gas interfaces (as with corrosion products) suggests that low impurity levels (below 10 wppm) can be obtained in the coolant.

## **Ancillary loop systems**

The ancillary loops include 4 He systems (2 inboard and 2 outboard) and 3 Pb-17Li systems (1 inboard and 2 outboard). Redundancy has been built into each of the 7 systems, such that any single loop can fail without forcing the plant to shut down. This provides a decisive advantage in availability, but increases the capacity, and therefore cost, considerably. The double-wall steam generator is the only novel component used in the ancillary systems; special attention has been given to its design.

## **Electrical insulators**

Electrical insulators are a critical feature of self-cooled liquid metal blankets. Adequate heat removal, which is one of the most basic functions of the blanket, requires that the insulating properties are not excessively degraded in the fusion environment. Tests have been performed to characterize the compatibility of  $\text{Al}_2\text{O}_3$  (as fabricated according to the technique described in Chapter 3) with flowing Pb-17Li in the PICOLO loop for 1000-10000 hours. Initial results indicate no degradation of the coating.

The effect of irradiation on the resistivity of the coating is also an important concern. Experiments to study both reversible (RIC) and irreversible (RIED) effects have been performed in the FZK Dual Beam facility and are planned in the HFR Petten reactor. These experimental efforts are described in Chapter 10.

## **Safety**

Safety aspects of the Dual Coolant blanket were analyzed, and are described in Chapter 11. The major safety-related attributes considered were:

1. Inventories of tritium and activation products
2. Energy sources for mobilization of hazardous materials
3. Fault tolerance against thermal and electromagnetic transients
4. Accident release rates and maximum doses at the site boundary
5. Waste generation and management

## Reliability

The system availability of the Dual Coolant blanket has been analyzed in order to obtain preliminary quantitative estimates. To accomplish this, the system was divided into two subsystems: the blanket segments and the external systems. Since the external cooling circuits are composed primarily of components using established technology, the component failure rates can be estimated relatively easily. However, no experience is available for the blanket segments, in which case the failure rates have been determined "synthetically". Basic events which may lead to segment failure have been defined and their causes broken down into tractable "reliability indicators" such as number and length of welds, number and dimensions of bends, etc. Data for these reliability indicators are obtained by transfer from other technologies, combined with assumptions based on expert opinion to establish a common reliability data base.

The results of the evaluation have been used for comparative evaluations with the other DEMO blanket candidates. They are also useful for identifying the main contributors to unavailability, and thus the most important areas of research and development which could lead to higher availability.

## References

- [1-1] M. Dalle Donne (ed.), European DEMO BOT Solid Breeder Blankets, KfK 5429, Nov. 1994.
- [1-2] S. Malang, K. Schlesiak (ed.), Dual Coolant Blanket Concept, KfK 5424, Nov. 1994.
- [1-3] L. Giancarli (ed.), Water-Cooled Pb-17Li DEMO Blanket Line, DMT 94/538 (SERMA/LCA/1678), Dec. 1994.
- [1-4] M. Eid (ed.), Helium-Cooled Ceramic Breeder in Tube Blanket Line, DMT 94/576 SERMA/1682 (RI-RCT 94/2), Dec. 1994.
- [1-5] E. Proust, L. Anzidei, G. Casini, M. Dalle Donne, L. Giancarli, S. Malang, Breeding Blanket for DEMO, Fusion Engineering and Design 22 (1993), 19-33.
- [1-6] S. Malang, J. Reimann, H. Sebening (ed.), DEMO-relevant Test Blanket for NET/ITER, Part 1: Self-Cooled Liquid Metal Breeder Blanket, Vol. 1 and 2, KfK 4907 and 4908 (1991).



## 2. Liquid Metal Breeder Blanket Concepts

The research and development work at the Forschungszentrum Karlsruhe in the area of liquid metal breeders has concentrated on self-cooled blanket concepts. The use of the same liquid metal both as breeder and coolant enables the simplest blanket design, characterized by a small number of ducts and welds, with the potential for high reliability. The main challenge in designing such self-cooled blankets is to deal with the strong influence of the magnetic field on the liquid metal flow. Cooling of the first wall (FW) can be a special problem, since the velocities required for sufficient heat removal can cause a high pressure drop and, as a consequence, high mechanical stresses.

There are different possibilities to facilitate this problem. For bulk heat removal, all of the solutions are based on the use of an electrical insulator between the flowing liquid metal and the load-bearing walls. For FW cooling, several approaches were examined. One approach is to arrange the FW cooling channels in the toroidal direction, i.e. parallel to the main magnetic field. This concept has been investigated extensively and is described in Section 2.1.

A completely different approach is to cool the first wall not with liquid metal, but with helium. The majority of the power deposited in the blanket is by bulk heating. This power is removed using liquid metal in simple, straight poloidal cooling ducts. The robust He-cooled first wall box provides a double containment barrier for the liquid metal. This Dual Coolant concept became the proposed reference solution for DEMO, and is described in Section 2.2.

In addition to the development of these two concepts, small exploratory work has been initiated to investigate the possibility to increase heat transfer by a special kind of magnetic hydrodynamic turbulence. Such a heat transfer enhancement could make more advanced blanket concepts feasible, as discussed in Section 2.3.

The possibility to use helium as coolant in a separately cooled liquid metal blanket has been investigated at the Forschungszentrum Karlsruhe as an alternative solution for a so-called convertible blanket for use in ITER [2-1]. The idea behind such convertible blankets is to start the operation with non-breeding shielding blankets and convert them later into tritium breeding blankets by replacing not the entire segment, but the liquid metal filling only. A helium-

cooled concept based on the use of sodium-potassium (NaK) or a non-breeding Pb-alloy during the operation as shielding blanket, to be replaced by Pb-17Li, is described in Section 2.4.

## **2.1 Self-cooled Blanket with First Wall Cooling in Toroidal Direction**

Such a blanket concept had been proposed in the US-Blanket Comparison and Selection Study [2-2] where it was ranked as a leading concept for commercial Tokamak power reactors. This concept was based on the use of lithium as breeder material and vanadium as structural material. The high temperature strength of vanadium, the excellent heat transport properties of lithium and the good compatibility between the two materials enabled a blanket design without employing an electrical insulator inside the blanket segments. The magnetohydrodynamic (MHD) pressure drop was minimized by flowing the coolant in the FW cooling channels in parallel to the main magnetic field and by adjusting the wall thickness of the poloidal ducts to the internal pressure (that means decreasing in flow direction from inlet to outlet).

The same flow scheme has been utilized in a breeding blanket concept for NET [2-3] and in an European concept for a self cooled DEMO reactor blanket [2-4]. Both of these concepts are based on the use of the eutectic lead-lithium alloy Pb-17Li as breeder/coolant and on electrically decoupling the flowing liquid metal from the load bearing walls by so-called Flow Channel Inserts (FCI) [2-5] in which a thin ceramic layer is sandwiched between two steel sheets.

Tritium breeding was increased by the use of beryllium as neutron multiplier, enabling breeding blankets to be located only in the outboard region of the torus. Self-cooled liquid metal blankets at the inboard region are more difficult to design due to the higher magnetic field strength and the more limited space there. For this case, the inboard blanket is a water-cooled steel shield.

The new DEMO reactor specification as released by the Test Blanket Advisory Group (TAG) in March 1990 allows the inboard blanket segment to be split into upper and lower halves with separate coolant supply from the top (upper half) and bottom (lower half) leading to acceptable low MHD pressure drop. This was the reference solution for a self-cooled DEMO blanket and is described in [1-6]. A

brief description of this concept is repeated here, since a large fraction of the MHD research (see Chapter 5) was dedicated to this concept.

There are 48 outboard segments, with both inlet and outlet coolant tubes arranged at the top end of the segments. At the inboard side the torus is divided into 32 segments. The inboard segments are split into upper and lower halves. At the upper half the coolant inlet and outlet tubes are connected to the top end of the segment, at the lower half to the bottom end. This arrangement can be seen in Fig. 2.1-1 which shows a vertical cross section of the torus.

The arrangement of inlet and outlet tubes at the same end of a segment requires a double pass of the coolant through the segment. The flow path is identical for the outboard segments and the upper half of the inboard segments. Coolant enters the blanket at the top end, flows downward in the rear channels, turns 180° at the bottom end and flows upward. This flow perpendicular to the magnetic field does not allow velocities high enough for sufficient first wall cooling. Therefore, the full coolant flow in the upward direction is diverted into the relatively small toroidal channels (parallel to the main magnetic field) of the blanket front region. This coolant diversion is achieved by a slight inclination of the walls in the return ducts. The liquid metal flows with relatively high velocity in the toroidal channels between the plasma facing first wall and the second wall. Passing two meander-shaped cooling channels in the toroidal direction, the coolant is heated up further before it flows back in the return channels to the exit at the top end of the blanket.

This flow path used in the front part of the blanket can be seen in Fig. 2.1-2 which shows a cross-section of an outboard segment.

Compared to a single toroidal channel for first wall cooling, the arrangement of meander-shaped channels leads to a mechanically stiff region in the front of the segment and to lower liquid metal temperatures in the first wall cooling channel because this liquid metal is coming from a zone characterized by a low power density due to the steep gradient in volumetric heat generation.

The first wall separating the toroidal cooling channels from the plasma chamber is considered to be the most critical part of the blanket segment. It is thermally loaded by a rather high heat flux caused by radiation and a particle flux at the plasma facing surface. To avoid excessive thermal stresses, the wall thickness must

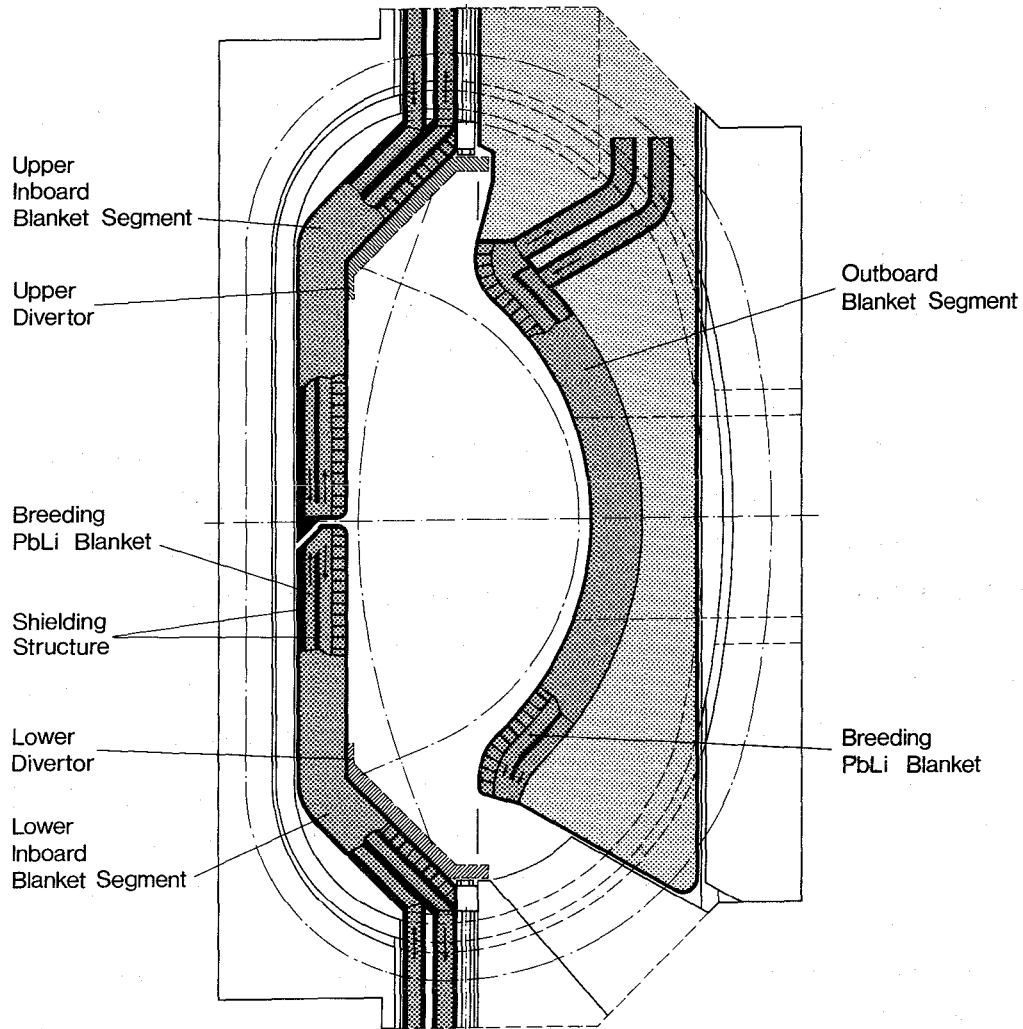


Fig. 2.1-1 Arrangement of self-cooled breeding blankets in DEMO

not exceed 6 mm. The strength of the first wall is increased by giving it a corrugated shape with webs welded in between to support it.

In the blanket segment, the coolant flows with velocities between 0.5 m/s (in the inlet channels perpendicular to the magnetic field) and 2 m/s (along the first wall, parallel to the magnetic field). In spite of this optimum flow and velocity distribution, failure to decouple electrically the load-carrying walls from the liquid metal would result in excessively high MHD pressure drops due to the voltage induced by the magnetic field.

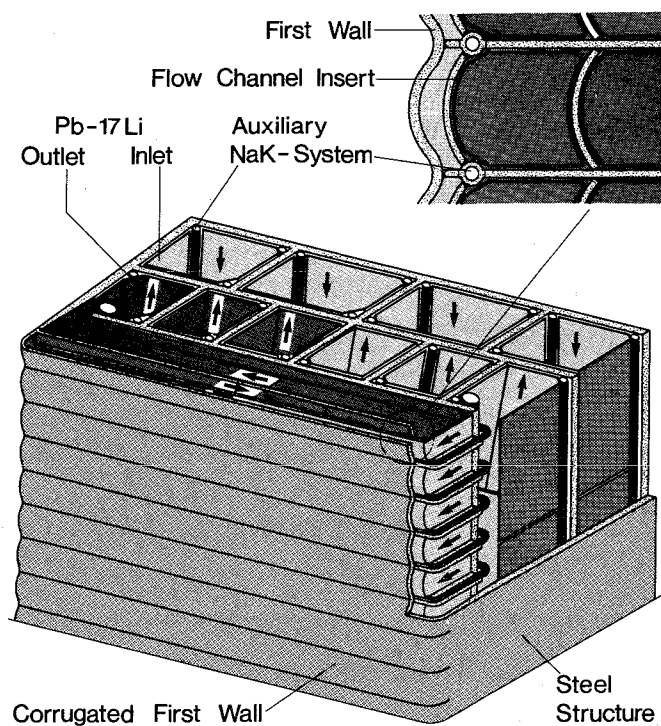


Fig. 2.1-2 Cross-section of a self-cooled blanket segment

In the blanket design, all coolant channels except the first wall cooling channel are equipped with flow channel inserts (FCIs) shown in Fig. 2.1-3.

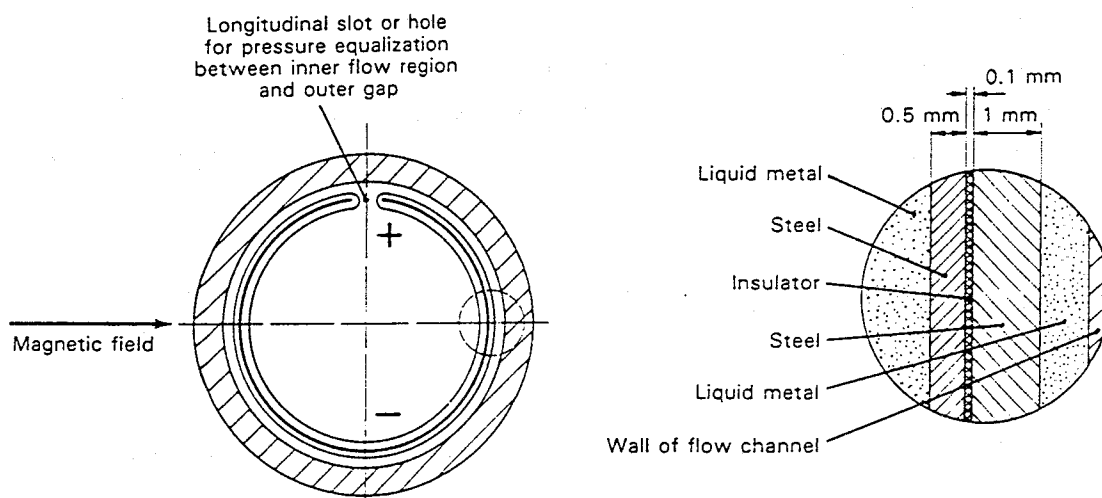


Fig. 2.1-3 Principle of flow channel inserts

Mechanical stresses in the FCI become insignificant when a longitudinal slot or holes are made for pressure equalization between the inner flow region and the outer gap. The voltage induced in the liquid metal flowing through the FCI is short-circuited only over the inner liner. Even the longitudinal slot does not give the voltage an additional short-circuit path. The FCI covers the total surface of all flow channels perpendicular to the magnetic field or only parts of it. The thickness of the inner liner can be reduced to a minimum value necessary for sufficient corrosion resistance (0.2 ÷ 0.5 mm) in order to minimize the MHD pressure drop. The flow in the toroidal channels is basically parallel to the main magnetic field and requires therefore no FCIs.

## 2.2 Self-cooled Blanket with Helium-cooled First Wall (Dual Coolant Concept)

The MHD investigations described in Chapter 5 proved the feasibility of the blanket concept with changing flow directions (poloidal → radial → toroidal → radial → poloidal) (see Sect. 2.1). But nevertheless, the Dual Coolant concept has been selected as reference concept of self-cooled liquid breeder blankets for the following reasons (see [1-2]):

- a) First wall cooling with liquid metal flowing in the toroidal direction requires rather complicated liquid metal ducts with difficult flow control.
- b) A single wall between the liquid metal breeder and the plasma implies the risk of a liquid metal spill into the plasma chamber in case of leaks.
- c) More than one cooling system is required even in an entirely self-cooled blanket in order to ensure afterheat removal in case of malfunctions in a liquid metal loop.

These problems are avoided if the FW is cooled with helium, and the breeding zone by circulating the liquid metal breeder.

The Dual Coolant concept was developed according to the following design principles:

- Top priority on safety and reliability. The liquid breeder is contained in a strong segment box which provides two barriers between the liquid metal and vacuum vessel. The design is leak-tolerant: a single failure of any weld does not require immediate shut-down and blanket exchange. Redundant

internal cooling systems ensure reliable afterheat removal in case of a loss of coolant event, and redundant external cooling systems allow continued operation in case of any single failure.

- Simplicity in design and fabrication. Large liquid metal ducts are used, in which the number and length of welds is small and tolerance requirements on manufacturing moderate. The manifold system for the He first wall coolant is an integral part of the blanket structure.
- Minimum waste generation. The breeder material can be reused after blanket replacement. In addition, the shield in the back portion of the blanket is removable, and also can be reused. Only the MANET structural box needs replacement.

The main disadvantage of this Dual Coolant concept compared to the previously studied version of a self-cooled lead-lithium blanket concept is the use of two completely different cooling systems. The two coolants - lead-lithium and helium - require completely different methods and components for heat and tritium extraction which increases the development cost, the space requirements and the operating complexity.

The overall geometry of the blanket segments is identical to the one described in the previous section. A vertical cross-section of the torus with the arrangement of the blanket segments and the access lines is shown in Fig. 2.2-1. Splitting of the inboard segment reduces in half the mass flow and the duct length, respectively, leading to a reduction of the MHD pressure drop by roughly a factor of four at the expense of doubling the number of supply lines. The resulting pressure drop for a divided inboard segment is smaller than for an undivided outboard segment. Therefore, this solution has been selected as the reference design. Undivided inboard segments, however, would be feasible too, since the MHD pressure drop is decisively reduced by insulating coatings in all liquid metal ducts.

The torus is divided in the toroidal direction into 16 sectors. Each sector contains 3 outboard and 2 inboard segments which are exchanged through a common port at the top of the torus. All access lines for the 3 outboard segments and the upper halves of the inboard segments enter the vacuum chamber through this port. Only the lower halves of the two inboard segments are served from the bottom together with the lower divertor plates.

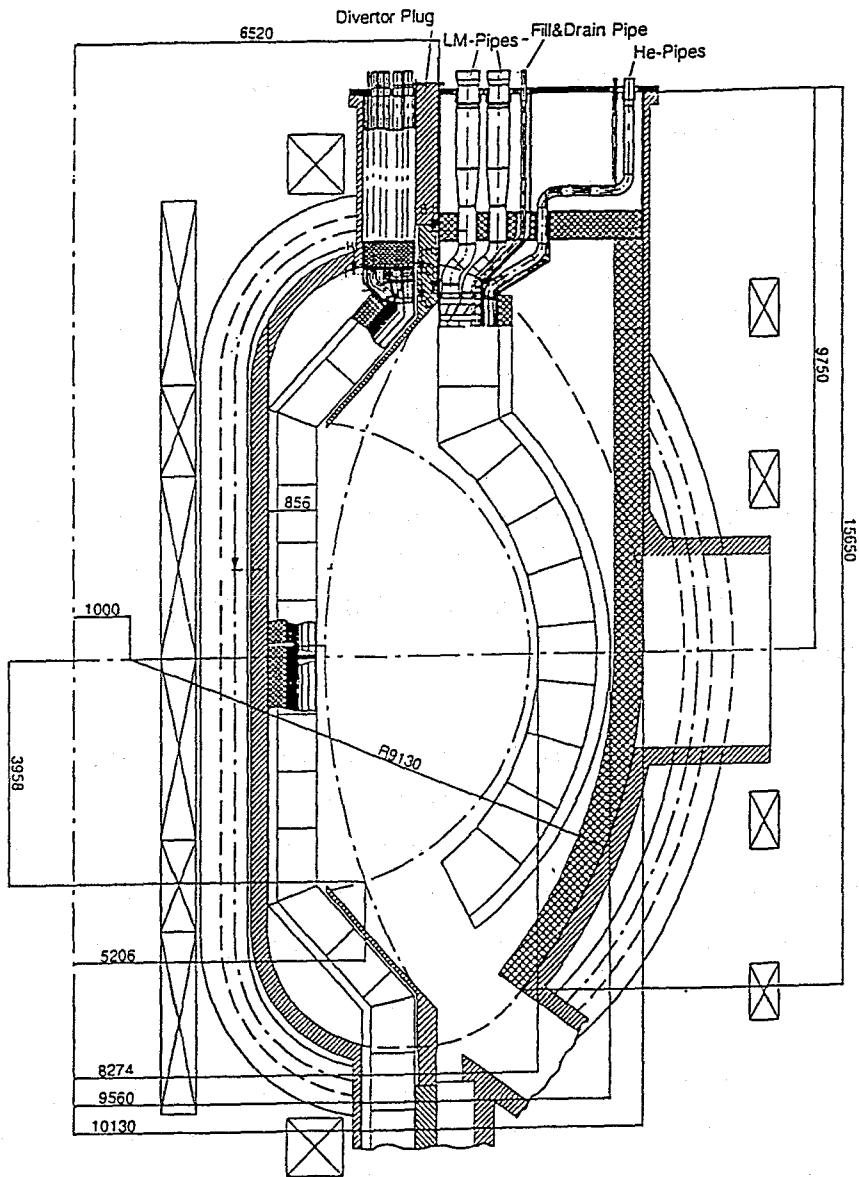
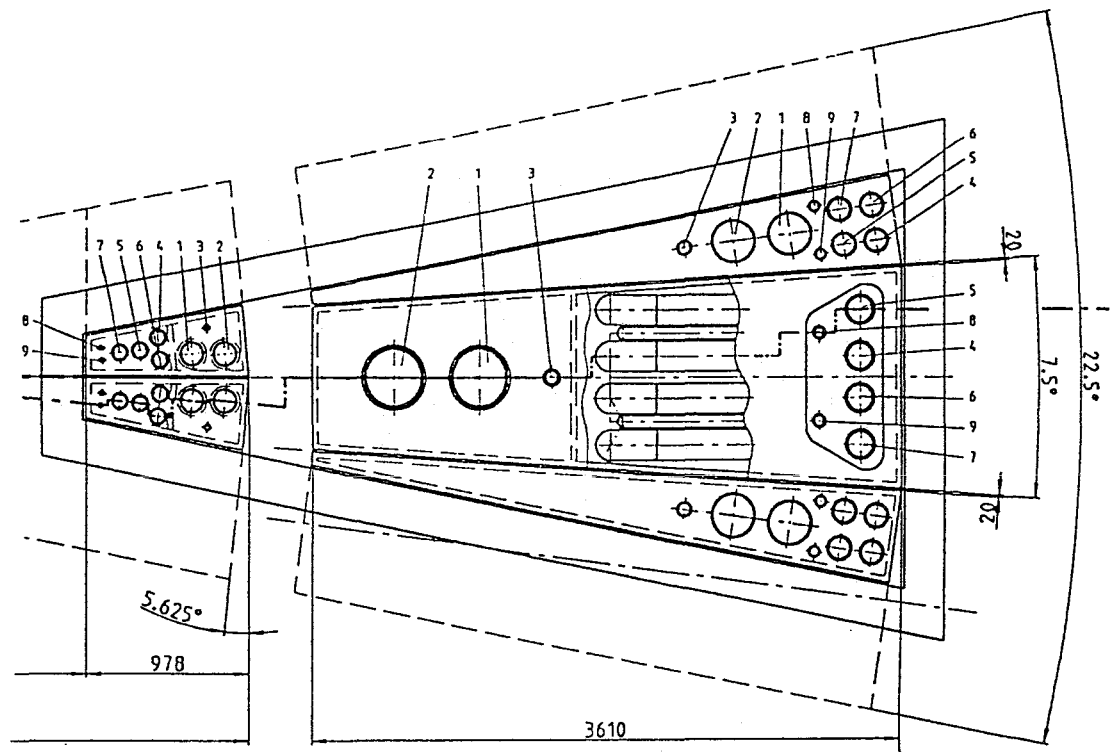


Fig. 2.2-1 Cross-sections of the DEMO reactor with Dual Coolant Blanket

Each blanket segment is connected to one liquid-metal loop and to two completely separated helium cooling loops. The arrangement of the cooling lines for liquid metal and helium in the region of the port is shown in Fig. 2.2-2.

Figure 2.2-3 shows a perspective view of an outboard segment. The concept is characterized by a U-shaped first wall with helium cooling channels in radial/toroidal direction. This FW forms together with the helium manifolds at the back side of the segment a box containing the liquid metal breeder. There is a grid of steel plates inside this box creating large liquid metal ducts and, as an additional function, reinforcing the FW box.



- |     |                               |   |                  |
|-----|-------------------------------|---|------------------|
| 1   | liquid metal inlet            | 4 | helium I inlet   |
| 2   | liquid metal outlet           | 5 | helium I outlet  |
| 3   | liquid metal filling/draining | 6 | helium II inlet  |
| 8,9 | leak detection                | 7 | helium II outlet |

Fig. 2.2-2 Top view of the flange covering blanket exchange port

The Pb-17Li enters the blanket at the top, flows downwards in three rows of parallel channels at the rear side, turns around at the bottom by 180°, and flows upwards in the first row. This allows the velocity in each row to be adjusted according to the local heat generation rate. Compared to an entirely self-cooled concept, the liquid metal ducts are larger and the required liquid metal velocity is smaller since only the internally generated heat has to be removed by liquid metal cooling. Nevertheless, electrical insulation is required between the load-carrying walls and the flowing liquid metal. This could be achieved either by the use of flow-channel inserts or by coating the duct walls with an insulating layer. The second method is the proposed solution although the feasibility has not yet been demonstrated.

Helium cooling of the FW is divided into two completely independent systems. The cooling channels are alternatively connected to one of the systems in order to

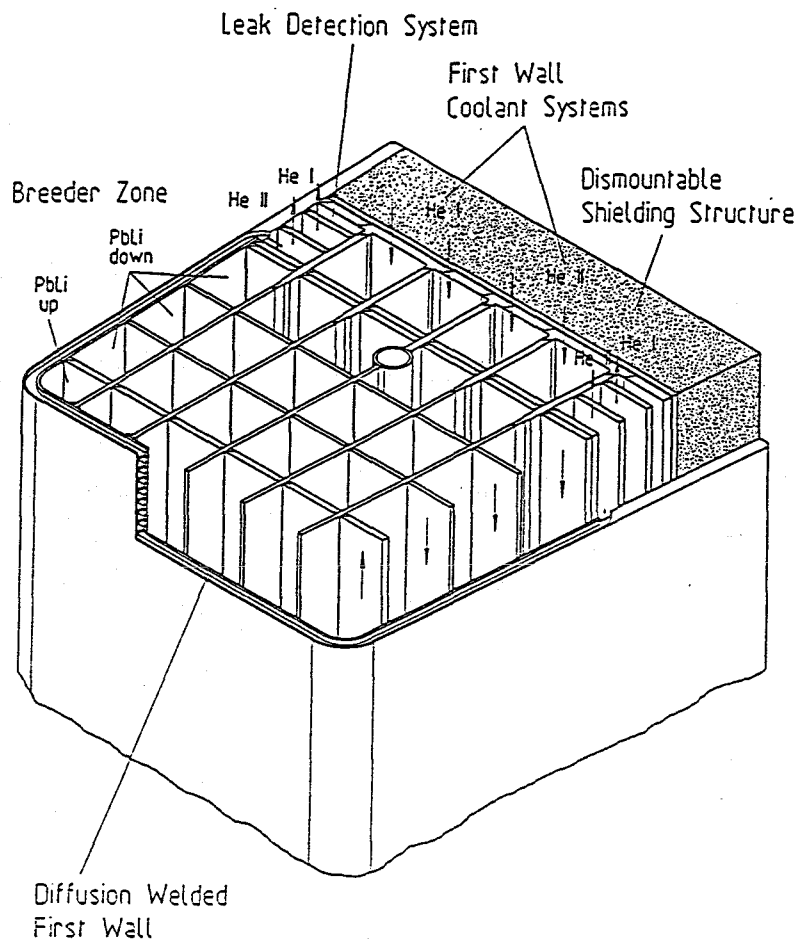
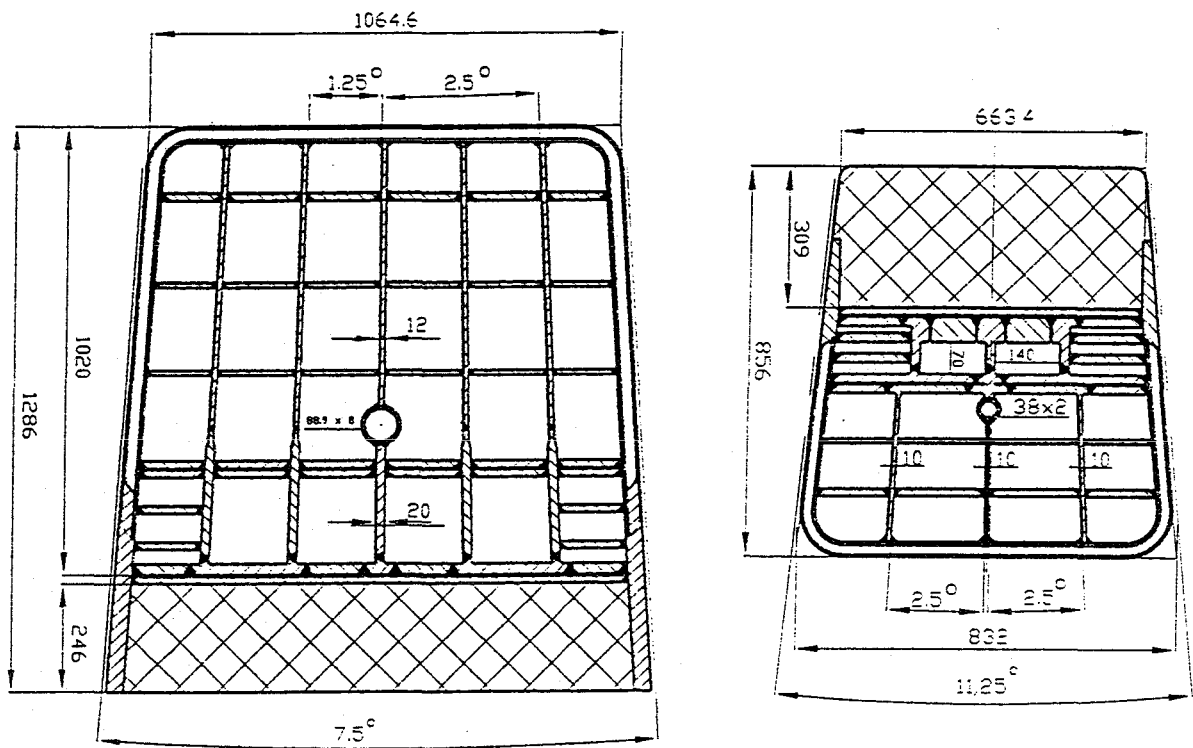


Fig. 2.2-3 Perspective view of an outboard segment

minimize FW temperature increase in case of a Loss-Of-Coolant Accident (LOCA) in one of the circuits.

The selected design of the FW cooling system is characterized by the following features:

- a) Integrated manifolds. The helium manifolds are an integral part of the segment box as shown in Figures 2.2-3 and 2.2-4. No separate welds for each cooling channel with all the implications in regard to manufacturing and reliability are required.
- b) Multiple passes of the coolant through the FW. The total helium mass flow passes 4 times through the FW in the outboard and inboard segment. This allows for relatively large coolant channels leading to a very stiff segment box and results in a small temperature rise for each pass.



a) outboard

b) inboard

Fig. 2.2-4 Horizontal cross section of blanket segments

- c) Reduction of the number of parallel channels per pass with increasing distance from the blanket inlet. This increases the helium velocity and consequently, the heat transfer coefficients in blanket regions with higher helium temperatures.
- d) Alternating flow direction in the FW cooling channels. The helium of the two cooling loops flows in opposite direction through the FW cooling channels. This leads to a symmetric temperature field in the segment box with lower thermal stresses.
- e) Heat transfer at the FW enhanced by surface roughening. The envisaged manufacturing method allows artificial surface roughening at the FW in order to enhance the heat transfer at the wall with the high heat flux. Since only one of four walls in a channel is roughened, the increase in pressure

drop is marginal. This method results in lower structural temperature and smaller temperature variations in the segment box.

Fig. 2.2-5 shows the internal geometry of the first wall, including the connections made between FW sections during fabrication.

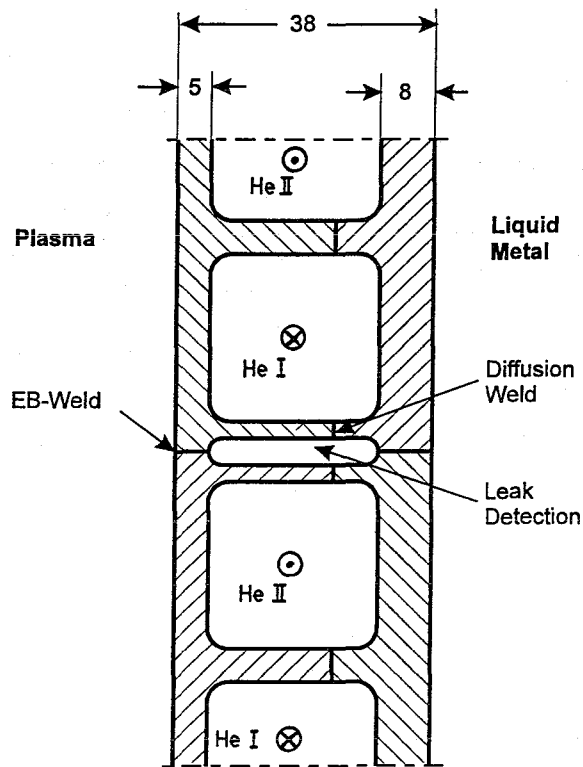


Fig. 2.2-5 FW cooling channels and connection between FW sections

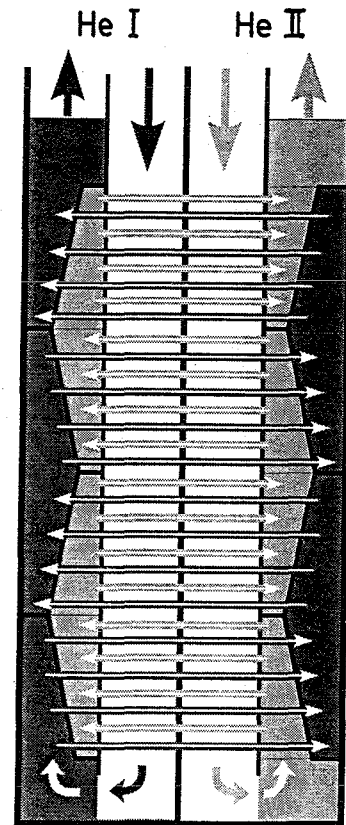


Fig. 2.2-6 Helium flow in FW and manifolds

The helium flow in the manifold and the distribution to the cooling channels are shown in Fig. 2.2-6. Helium enters the segment in two parallel channels at the top, flows downward at the rear side of the segment and turns around at the bottom by 180°. The manifolds in upward direction are divided into two parallel ducts with varying cross-sections to account for the variation of the helium flow. The results of this geometry are the desired flow scheme in the FW channels and a roughly constant velocity in the manifolds.

An important design issue of breeding blankets for a power reactor is shielding of the superconducting magnets. The blankets have to reduce both neutron and gamma fluxes by a large amount since the additional shielding components including the vacuum vessel cannot be replaced during the entire reactor

lifetime. It is clear that the blanket (in a commercial power plant) has to be replaced 5 to 10 times during this time due to the neutron damage of the first wall. The neutron damage in the blanket, however, decreases exponentially in the radial direction and would allow the blanket to be split into a front part, to be replaced and disposed of quite frequently, and a rear part, which could be a reusable component. Hence, the design presented attempts to minimize the waste generation by designing the shielding zone as a dismantlable component with separate cooling. The neutron flux in this region is low enough to allow reuse over the entire reactor life-time. This shield containing roughly twice as much steel as the front part has the additional benefit of providing a strong mechanical support for the blanket structure.

### **2.3 Selfcooled Blanket with First Wall Cooling in Poloidal Direction**

This is a blanket concept in which the front cooling channels are oriented in the poloidal direction. The coolant is fed from the top via a manifold to the rear channels, flows downward, is turned at the bottom of the blanket module by a hairpin bend, and flows upward in the front channels. A schematic view of such a concept is shown in Fig. 2.3-1. The downflow velocity in the rear channels can be kept low due to the low volumetric heat source in this part of the blanket module. The velocity in the front channels has to be much higher in order to avoid an unacceptable heating rate of the first wall. In Chapter 5.2.1 the corresponding correlations to calculate the needed velocity are given.

Such a blanket concept has been investigated during the ARIES program [2-6] and in a design proposal for a breeding blanket for ITER [2-7]. In both concepts liquid lithium as coolant and as breeder material and a vanadium alloy with an electrically insulating V-Ti-N coating on the V-Ti alloy surface are considered.

A study conducted at FZK based on Pb-17Li as liquid metal, ferritic steel as structural material and using the Flow Channel Insert (FCI) technique showed that under DEMO-blanket conditions the MHD pressure drop would exceed the upper limit even if the blanket would be divided in two parts with separate in- and outlets at the top and the bottom of the reactor [2-8, 2-9]. Using a perfect insulating coating on the duct walls, as proposed for the Dual Coolant blanket concept, the pressure drop could be decreased far below the upper limits.

As shown in Chapter 5.1 for thin conducting walls, an improvement of the heat transfer from the first wall to the circulating liquid metal in the front channels would allow a reduction of the velocity of the coolant and by this the governing pressure in the front channel. If the heat transfer - expressed as an improved heat conductivity of the liquid metal - would be increased by a factor of about 3, even a poloidal flow concept with thin conducting walls (FCI's) and Pb-17Li would be possible for a blanket divided poloidally into two halves.

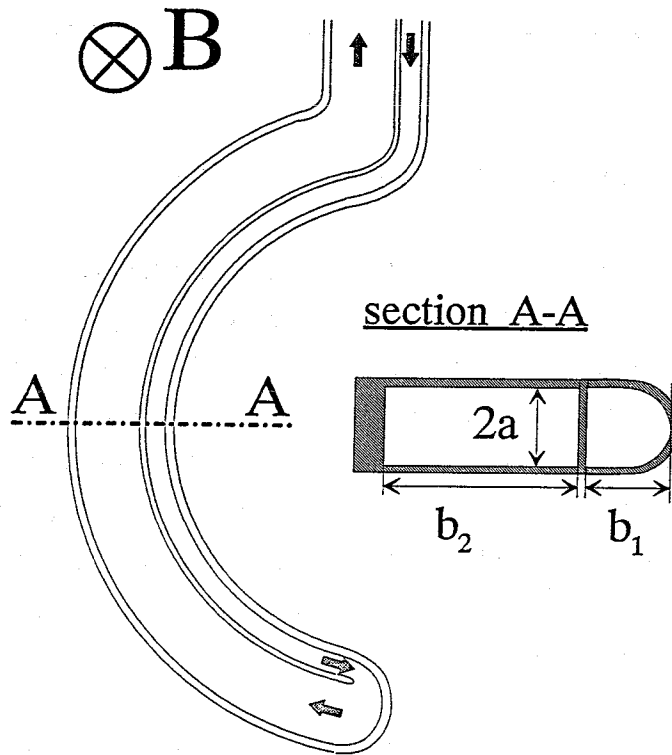


Fig. 2.3-1 Self-cooled liquid metal blanket poloidal flow concept (schematic)

In designing the front coolant channels of a self-cooled liquid metal cooled blanket with poloidal flow, a generic conflict results. From the mechanical strength point of view, a corrugated or even a half circular shaped front wall as proposed in [2-7] would be advantageous. But in the case of fully electrically insulated channels, this would lead to a velocity distribution with zero velocity at the meridian of the front channel as shown in Fig. 5.6-2c.

Additionally, two-dimensional turbulence with the vortex axis parallel to the magnetic field would be suppressed, at least near the first wall. Both effects de-

crease the heat transfer so that the mean velocity for insulated channels of this shape has to be increased, which results in an increased pressure drop.

From the MHD point of view, a flat first wall aligned with the main toroidal field is preferable because a flat velocity profile is expected in the case of fully electrically insulated channels or a M-shaped profile with velocity jets at the first and second wall (see Section 5.5.2) in the case of thin conducting walls (e.g. FCI's), the latter acting as a turbulence promotor.

Therefore, taking advantage of these MHD-effects which increase the heat transfer and allow one to reduce the MHD pressure drop, and by this also the pressure in the cooling channels and the mechanical load, a rectangular shaped cross section of the front duct is recommended.

Summarizing, one could conclude that taking advantage of all the above mentioned effects like the M-shaped velocity profile in rectangular thin walled channels combined with the hereby or additionally promoted MHD-turbulence, a self-cooled liquid metal poloidal flow concept should be possible even with Pb-17Li as liquid metal and with the FCI-technique if the blanket module is divided in two parts reducing the heated length of the front chanel by a factor two.

## **2.4 Helium-cooled Liquid Metal Blanket for ITER**

### **2.4.1 Introduction**

A "convertible" blanket (CB) was proposed which is based on the idea to switch from the shielding configuration of the ITER Basic Performance Phase (BPP) to the breeding configuration of the Enhanced Performance Phase (EPP) by exchanging the liquid metal without replacing the blanket structure. The benefit consists in the saved time (2 - 3 years) and the corresponding costs required for the fabrication and replacement of 120 blanket segments. Additionally, part of the technology used for the CB is similar to that required for DEMO blankets. Therefore, the use of the CB could provide DEMO-relevant experience.

As a response to the very ambitious CB design proposed by the ITER Joint Central Team at the beginning of 1993, the European Home Team asked the associations participating in the DEMO Blanket Programme to elaborate an alternative CB Concept for a reactor with an average neutron wall load of 1 MW/m<sup>2</sup> (for further

specifications, see Table 2.4-1). This concept is based on austenitic steel structures using water or helium cooling and relying on the use of non-breeding liquid Pb alloy for the BPP, replaced for the EPP by the liquid breeder material Pb-17Li. Liquid metal cooling (self-cooling) was not considered because the leadtime for qualifying the required insulations under irradiation was considered to be incompatible with the ITER-EDA time schedule.

Table 2.4-1 Main selected ITER specifications

Fusion power (nominal)	1500 MW
Neutron wall loading	1.0 MW/m <sup>2</sup>
Power excursions (100 exc. for 10 s)	2500 MW
Maximal surface heat flux on FW (nominal)	0.25 MW/m <sup>2</sup>
Plasma major/minor radius	775/280 cm
Plasma elongation	1.6
Outboard breeder zone thickness	60 cm
Inboard breeder zone thickness	40 cm
Number of inboard/top/outboard segments	48/48/72

The CB concept has been elaborated in 1993 over a period of two months through a collaborative work of CEA and KfK as leading associations, and the participation of ENEA [2-10, 2-11]. The design incorporates essential characteristics of the European Blanket Concepts for a DEMO reactor [2-12, 2-13, 2-14]. A poloidal cross-section of the considered ITER reactor is shown in Fig. 2.4-1. The total blanket consists of 72 outboard segments, 48 inboard and 48 topboard. Both CB versions are based on the following design characteristics:

- double welds with leak control in between
- first wall (FW) direct cooling using toroidal channels
- stiff segment box
- liquid metal pool with poloidal cooling tubes

The detailed design differs for the two coolant options due to different coolant characteristics and preferred manufacturing technologies. The water-cooled CB was presented in detail elsewhere [2-15]; in this report, the helium-cooled CB will be outlined in more detail. Since this concept is not one of the DEMO designs, the analysis is not included in the remaining chapters; therefore, a short summary of performance and R&D issues is presented here.

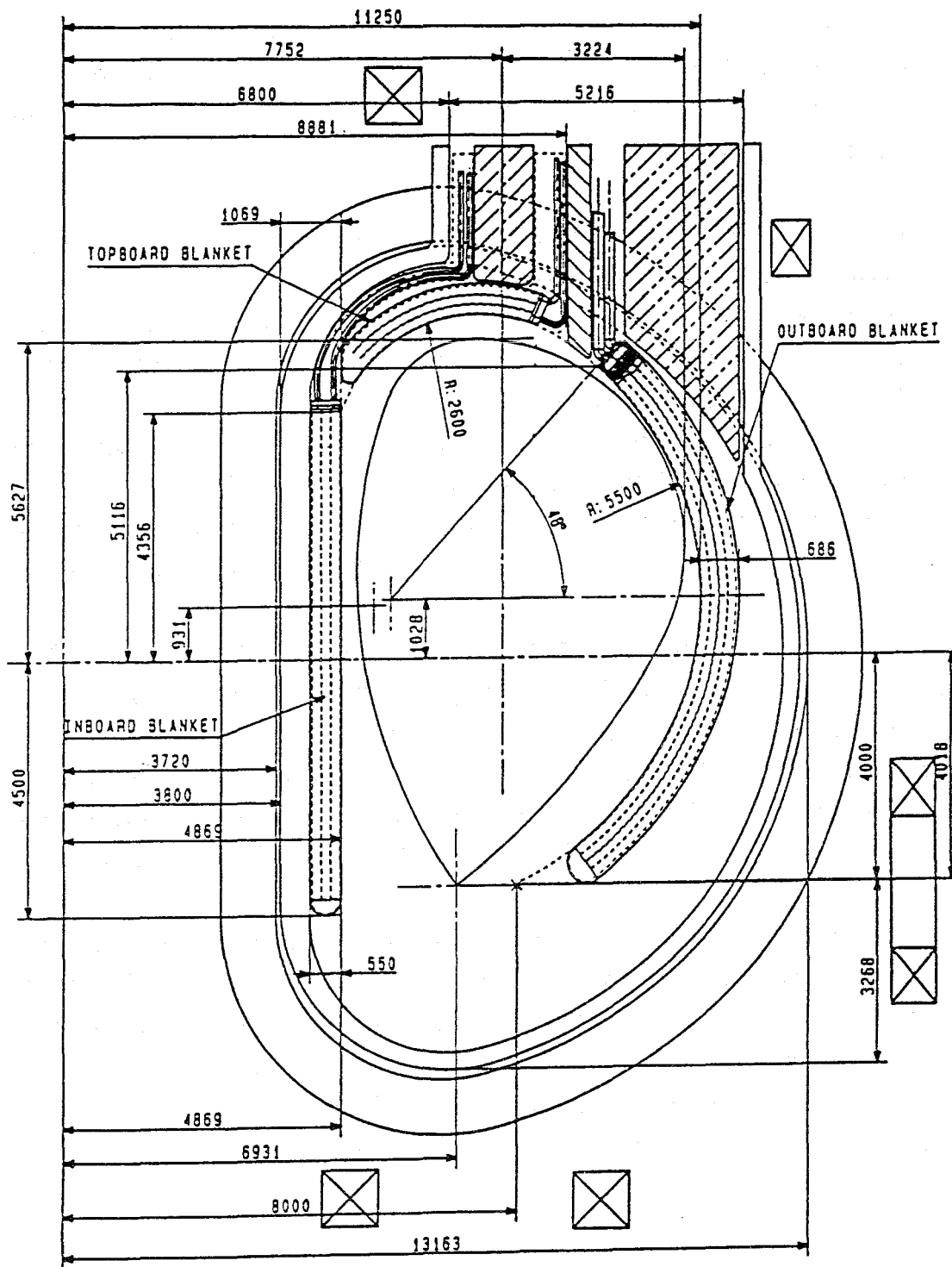


Fig. 2.4-1 Considered ITER torus cross-section

## 2.4.2 Blanket design

The design of the helium-cooled CB is very similar to the design of the DEMO-relevant Dual Coolant Blanket [2-13, 2-16] described in Section 2.2. It differs mainly by using helium-cooled tubes in the liquid metal pool (Fig. 2.4-2) instead of circulating the liquid metal to an external heat exchanger. Again the following design rules are applied:

- double containment of the liquid metal to the plasma side with a monitoring space between the two welds,
- single walls allowed between plasma and helium but not single welds,
- each weld is allowed to leak without requiring an immediate shutdown of the machine and a blanket exchange,
- liquid metal ducts designed for the full gas pressure to avoid damage propagation in the case of gas leaks without fast pressure relief,
- malfunction of the FW cooling loop with a delayed plasma shutdown does not lead to temperature rises in the blankets requiring an exchange.

Figure 2.4-2 shows a cross-section of the outboard blanket and details of the FW structure. This structure consists of two grooved plates, containing the toroidal coolant channels which are diffusion-welded and then bent to the U-shape. The combination of this FW structure, thick back plate and grid of reinforcing steel plates results in a stiff blanket segment box which withstands high pressures. The supply helium ducts for the FW channels are also a part of this grid structure.

Two independent helium loops are used for the FW cooling. The coolants enter the blanket segment at the top sides, flow downwards in two parallel channels at the rear side and are diverted at the bottom ends to the manifolds at the outer sides of the segment. The helium flows in multiple passes through the FW channels and leaves the blanket at the blanket top (for details see [2-16]). Characteristic values of the thermohydraulic layout are given in Table 2.4-2.

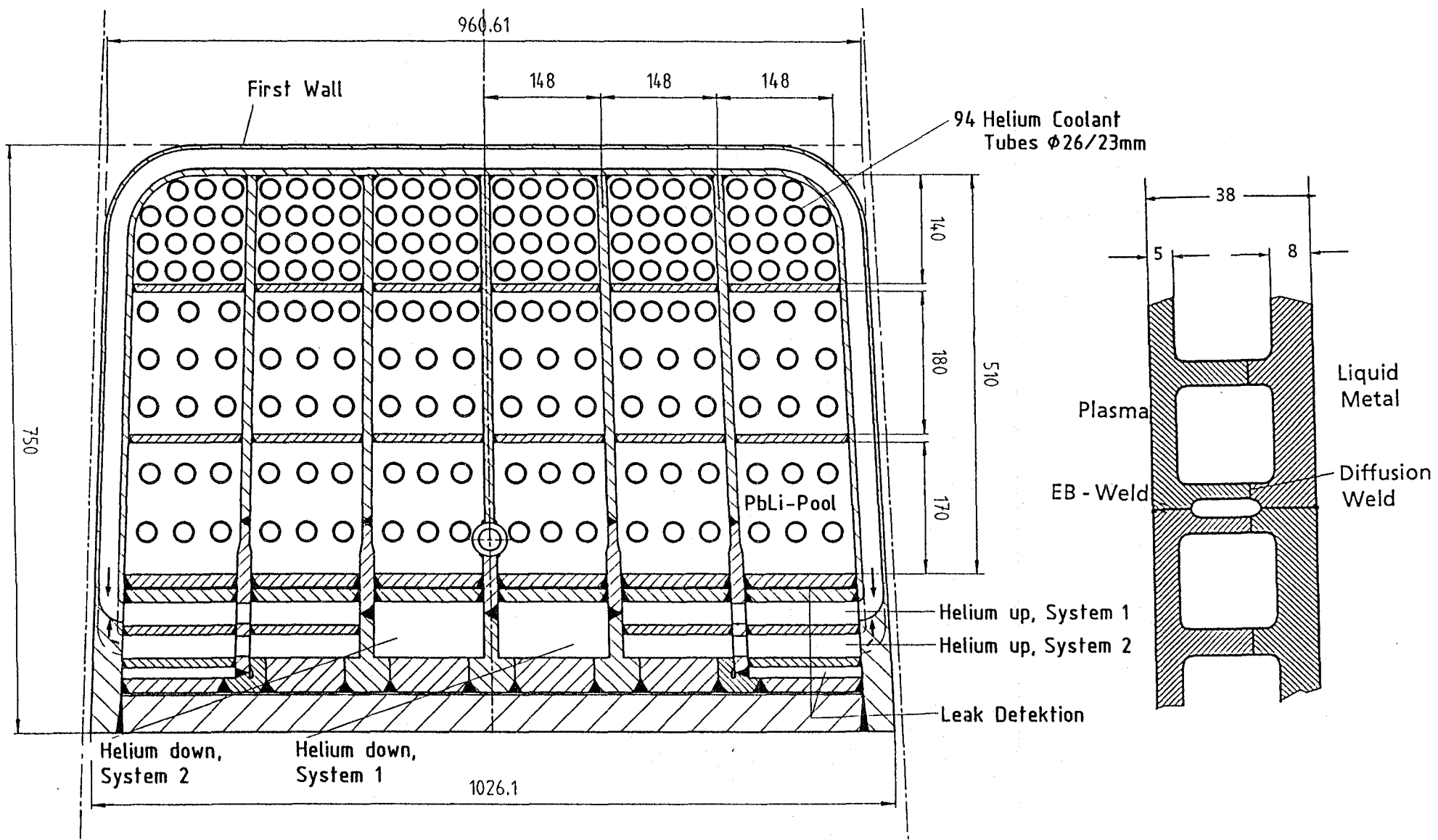


Fig. 2.4-2 Outboard blanket and details of FW structure

Table 2.4-2 EPP design point

	First Wall Cooling		Liquid Metal Pool	
	outboard	inboard	outboard	inboard
helium mass flow rate (kg/s)	10.9	7.7	12.83	6.63
inlet/outlet temperature (°C)	250/330	250/330	250/400	250/400
helium pressure (MPa)	10	10	8	10
duct dimensions (mm)	25 x 25	20 x 25		
pipe diameter $d_a/d_i$			26/23	26/23
number of passes	8	8		
number of pipes			96	48
max. helium velocity (m/s)	49	47	50	41
pressure drop (MPa)	0.14	0.11	0.22	0.18

About 70 % of the generated power is removed by the poloidal cooling system consisting of hairpin-type single-walled tubes connected to the headers at the blanket top, as shown in Fig. 2.4-3.

The helium flows downwards in the front part and returns in the rear part. The distribution of the tubes in the blanket cross-section is adjusted to the power distribution obtained from neutron transport calculations.

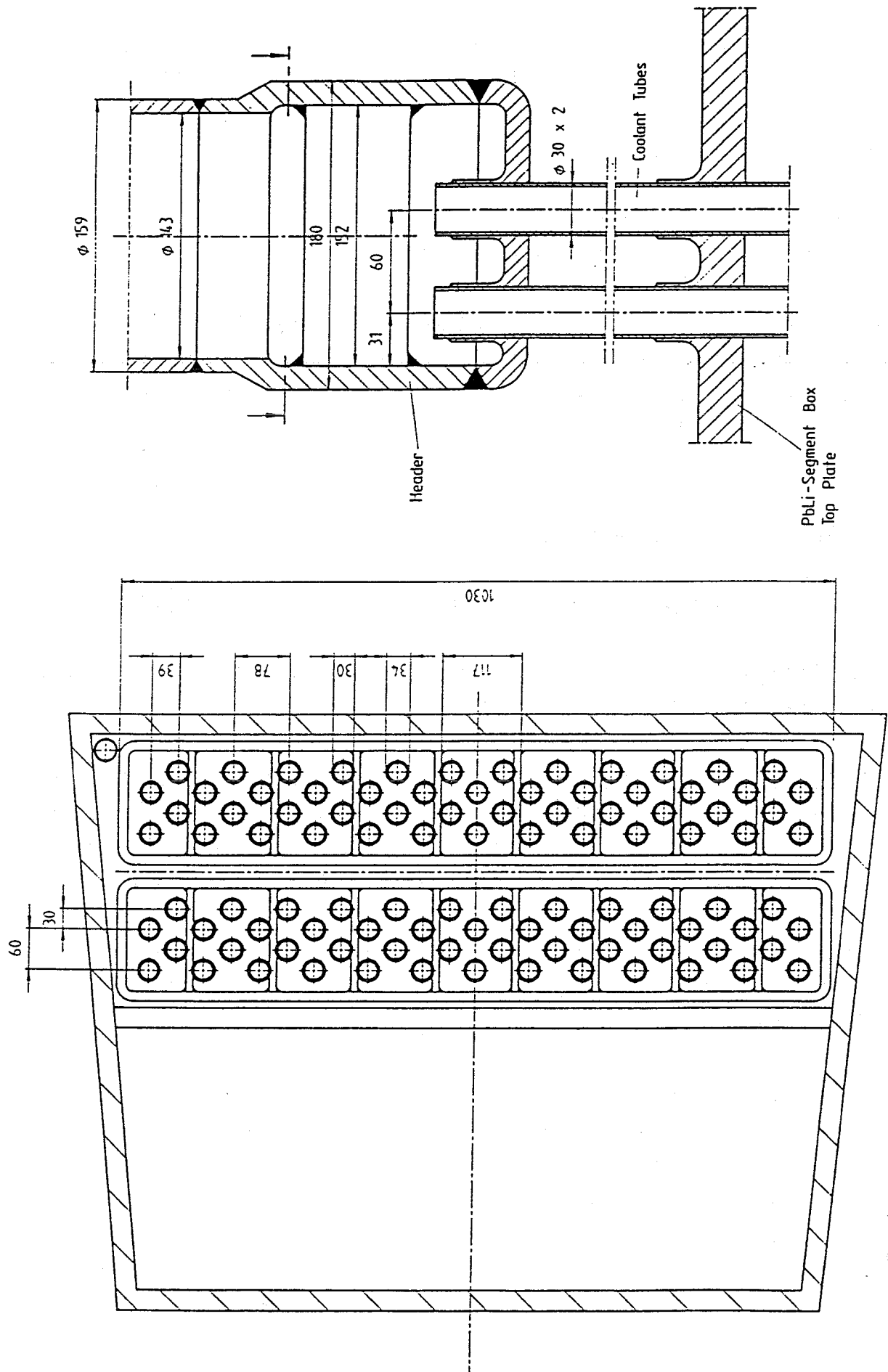


Fig. 2.4-3 Poloidal headers for inboard blanket

Figure 2.4-4 shows for nominal power the temperature distribution close to the FW in the different blanket planes. The highest FW temperature (441°C) occurs in the top plane. The maximum interface temperature (355°C) exists in the blanket bottom plane; both values are below the maximum acceptable values.

The temperature distributions were the basis for stress analyses which resulted in a maximum acceptable system pressure of 10 MPa.

The limited thermo-mechanical analyses showed that there is a considerable margin for design improvement which could be used e.g. to reduce the cross-section of the helium tubes (increase of breeding ratio) or to increase the safety margin for off-normal operation.

### 2.4.3 Blanket performance assessment

Specific features and performances of the CB are discussed in the following:

Tritium Breeding: Neutronic 3D calculations predict a TBR of 0.96 which is larger than the required ITER value (TBR = 0.7).

Tritium Removal and Control: Tritium is removed outside the vacuum vessel with a helium purged bubble column, as developed for the water-cooled Pb-Li blanket [2-17]. For this purpose, the liquid metal inventory is circulated 10 times a day resulting in a MHD pressure drop for uncoated tubings of less than 0.2 MPa.

Tritium permeation losses, however, become unacceptably high for uncoated tubings ( $\approx 10$  g/d). Therefore, tritium permeation barriers must be provided, leading to even lower pressure drop.

Velocity profiles are dramatically affected by the presence of a strong magnetic field, even for the very low flow rates required for breeder circulation. Figure 2.4-5 shows velocity distributions found between the tubes (H-zones) and those found close to the second wall (S-zone), as calculated using the Core Flow Approximation [2-18]. High velocity jets near walls are expected to affect tritium permeation behavior, although the nature and importance of this effect have not been quantified.



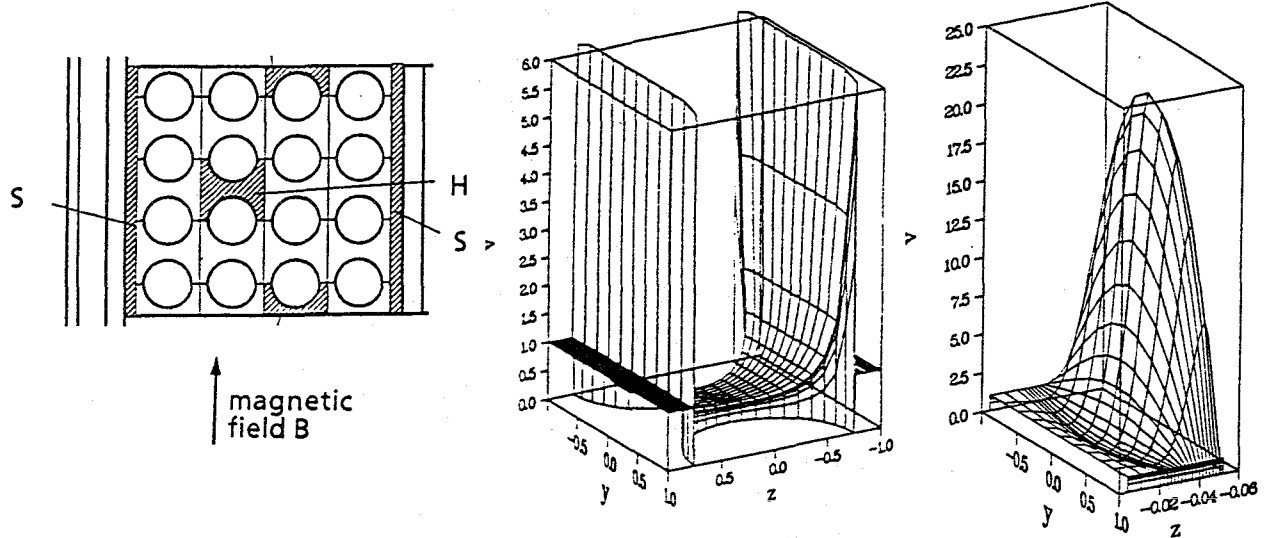


Fig. 2.4-5 Subregions considered for MHD analysis and characteristic velocity distributions

**Response to Power Excursions:** It has been assumed that ITER blankets must have the capability to accommodate 100 power excursions at 170 % nominal power ( $P_n$ ) for 10 s. A peak temperature of 486°C in the top plane of the FW was calculated. This temperature increase is connected with a reduction of admissible stress of only about 2 %, i.e., the loss in material strength is negligible. The contribution of 100 excursions to the total fatigue damage can be neglected.

**Plasma Disruption:** In order to reduce significantly the forces on the blanket segments during plasma disruptions, the ITER Joint Central Team proposed to connect electrically the FWs of the blanket segments. By this means, eddy currents in the blanket box (which give rise to Lorentz forces) should be reduced. Calculations with the CARIDDI code [2-19] showed that the box currents are reduced by a factor of about 2.5 for connected FWs ("continuous" FW) compared to the electrically separated blankets, see Fig. 2.4-6. This reduction and the different time behaviour will result in much more expressed reductions of the stresses within the blanket. These reductions could amount to one or two orders of magnitude, so that disruption loads are no longer a feasibility issue. An interesting result is that internal insulators do not effect this behaviour.

**LOCA Conditions:** First analyses of failure of one of the FW coolant systems predicted a maximum temperature of 510°C after 12 s. The stress analysis for these conditions has not yet been carried out but it is expected that the transient will not cause severe damage to the blanket.

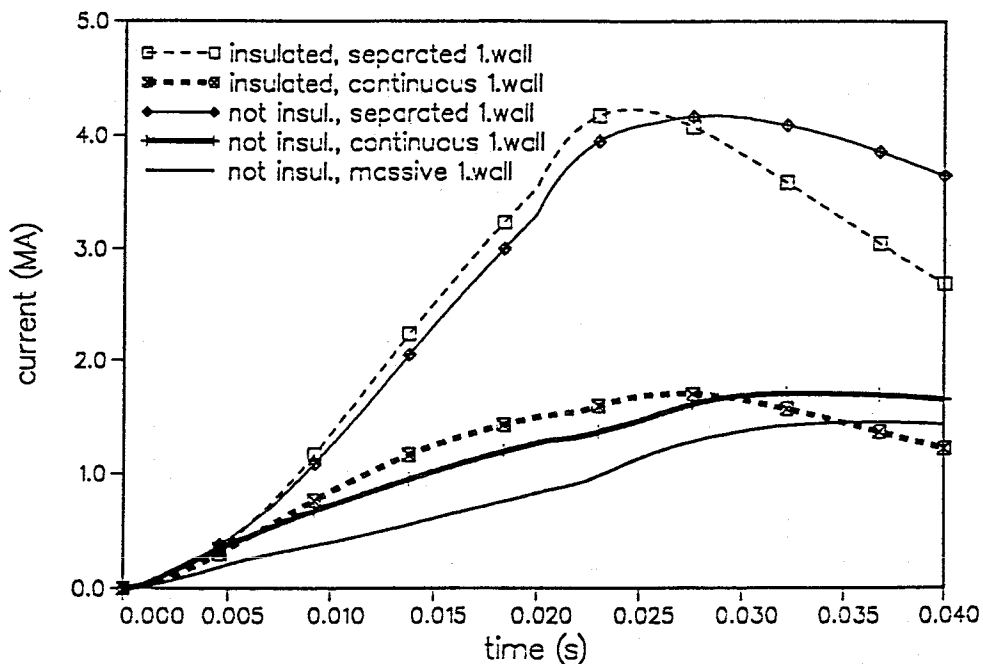


Fig. 2.4-6 Electric currents in the liquid metal blanket box

**Reliability:** The principle of double containment or double welds is applied to reach a high degree of failure tolerance. Single failures neither require immediate blanket segment exchange nor lead to severe damage of other components. A reliability analysis on the influences of weld number, shape, process and controllability must be performed.

**Blanket Lifetime:** Important factors are the mechanical and thermal loads, corrosion processes and the radiation damage. These loads resulting from pressures and temperature differences have been assessed; the admissible values for tensile strength and long-term creep strength are not exceeded. The integral fatigue damage resulting from  $10^5$  power cycles and 100 excursions is far below the admissible limits. Corrosion will not be a problem if temperature and impurity limitations are respected. Hence, the blanket lifetime seems to be determined by radiation-induced damage of the structural material. The conclusion of a preliminary assessment of this influence is that the utilisation of 316L(N) at fluences up to 1 MWy/a seems to be feasible, with the need of further experimental verifications and of incorporating the irradiation damage effects in the safety margins.

**Shielding Efficiency:** The shielding efficiency of the helium-cooled CB is rather low. However, the vacuum vessel can be designed for a high shielding performance by rather simple measures, such as using layers of water. 3D calculations with the MCNP-code [2-20] for a vacuum vessel with a thickness of 50 cm and

5 layers of water showed (Fig. 2.4-7) that the neutron flux density decreases steeply across the outer vacuum vessel reaching a low level nearly independent of the used liquid metal. Figure 2.4-8 shows the distribution of the corresponding power production. For a non-breeding Pb-alloy a higher power production is calculated in the steel structure and the vacuum vessel.

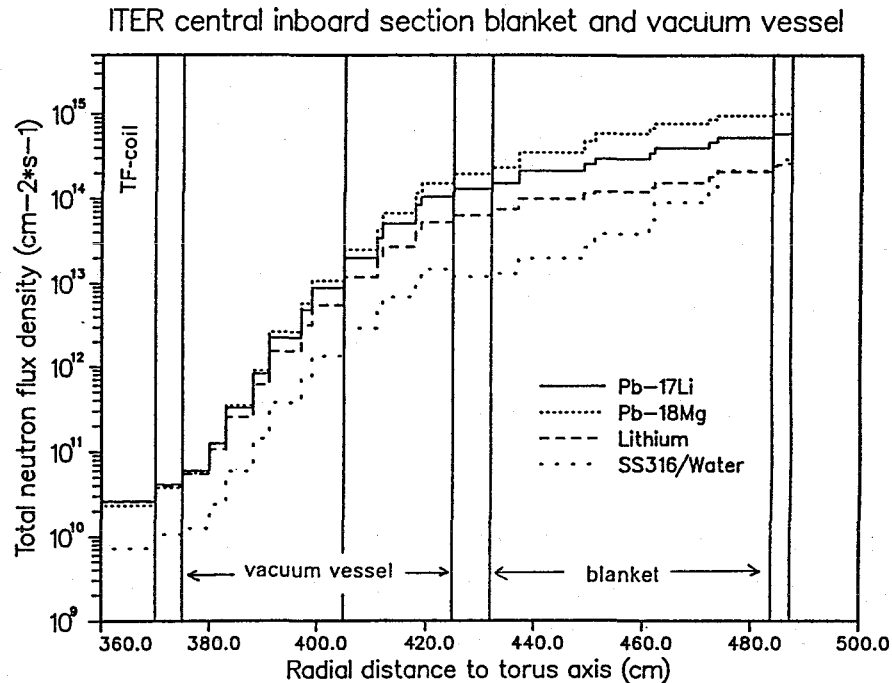


Fig. 2.4-7 Radial distribution of the total neutron flux density along the ITER inboard blanket

Specific Features of the BPP: Pb-Mg and Pb-Bi are the prime candidates for the BPP. Pb-Bi is attractive because of the low melting point of 125°C which allows one to reduce both coolant pressure and blanket temperature (although nuclear heating in the FW structure increases by about 40 %). These reductions improve blanket reliability and expand the safety margins. The main drawback of Pb-Bi is the production of 210 Po. The production rate is strongly dependent on the BPP operation scenario. Specific safety studies are required. For Pb-18 Mg the activation characteristics are only slightly worse than those of Pb-17Li. The higher melting point (250°C compared to 235°C for Pb-17Li) and the higher nuclear heating in the FW structure must be taken into account in a more detailed design.

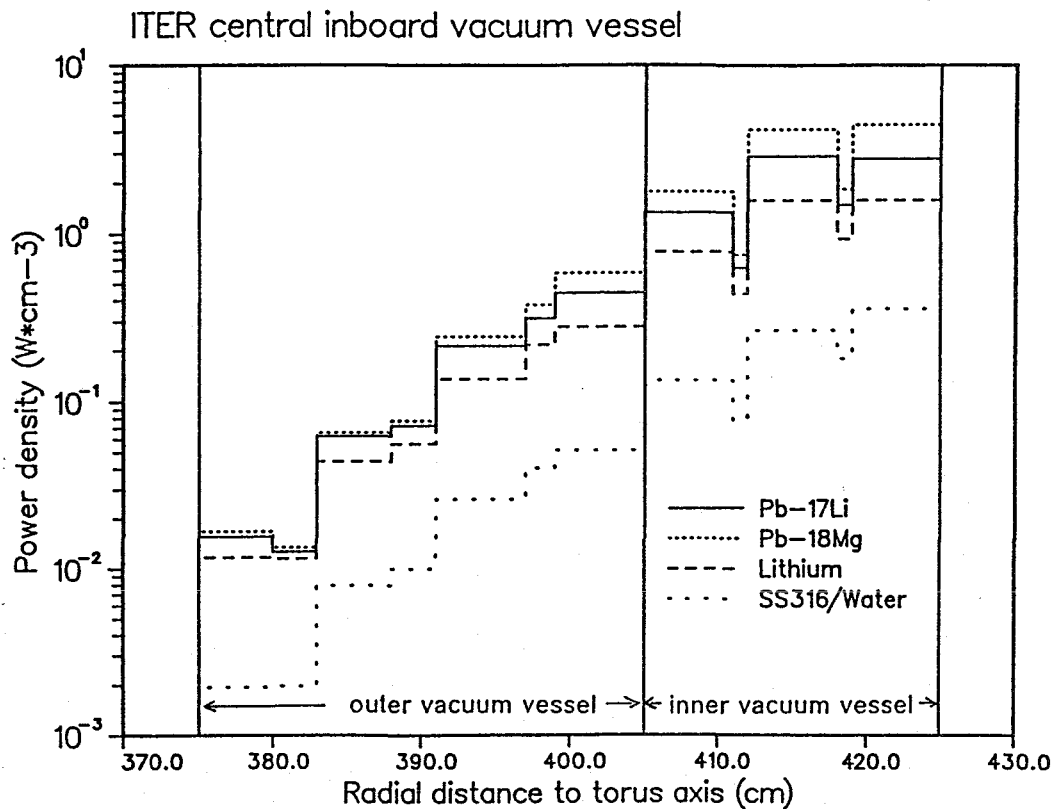


Fig. 2.4-8 Radial distribution of the total power density along the ITER inboard blanket

#### 2.4.4 Modifications in the concepts

**Ferritic/Martensitic Steel as Structural Material:** The use of ferritic/martensitic steel could extend the operational range to much higher reactor values (average neutron wall load  $\approx 2 \text{ MW/m}^2$ , neutron fluence  $\approx 5 \text{ MW a/m}^2$ ) if the increase of the DBTT under neutron irradiation is no longer an essential drawback. Using ferritic/martensitic steels, the temperatures in the helium-cooled CB can be increased (without increasing the coolant pressure) which alleviates the problem of being sufficiently above the DBTT. An assessment of the current and planned R&D work indicates that the corresponding database could be provided in the required ITER time schedule.

**Use of Electrical Insulations:** If insulating coatings could be qualified up to the end of the ITER/EDA, the design of the CB could be easily modified to self-cooling of the breeding zone, making this version very similar to the Dual Coolant Concept [2-16].

**Different FW Design:** Besides the FW design presented above, other options were considered during the collaborative work on ITER CB blankets [2-10, 2-11]. A dif-

ferent design was preferred for the water-cooled CB [2-15]. Depending on the progress in fabrication each of the design options could be used for each coolant.

## REFERENCES

- [2-1] J. Reimann et al., Convertible liquid metal blankets for ITER with Pb-17Li as breeding material, *Fusion Eng. and Design* 27 (1995) 353-362.
- [2-2] D.L. Smith et al., Blanket Comparison and Selection Study (Final Report), ANL, ANL/FPP-84-1. Vols. 1,2, and 3 (Sept. 1984).
- [2-3] S. Malang et al., Self-cooled Liquid metal Blanket concept, *Fusion Technol.*, 14 (Nov. 1988), pp. 1343-1356.
- [2-4] S. Malang et al., Self-Cooled Blanket Concept Using Pb-17Li as Liquid Breeder and Coolant, *Fusion Engng. Des.* 14 (1991), pp. 373-399.
- [2-5] S. Malang, V. Casal, K. Arheidt, U. Fischer, W. Link, K. Rust: Liquid metal cooled blanket concept for NET, *Fusion Technology; Proc. of the 14th Symp. on Fus. Techn. Avignon, F, September 8-12, 1986; Oxford (u.a.): Pergamon Press 1986, Vol. 1, S. 1273-80.*
- [2-6] Najmabadi, F.; Conn, R.W. et al.; The ARIES-II and ARIES-IV Second Stability Tokamak Reactors; *Fusion Techn.* Vol. 21, May 1992, pp. 1721-1728.
- [2-7] Hua, Th.Q.; Gohar, Y.; MHD Pressure Drop and Thermal Hydraulic Analysis for the ITER Breeding Blanket Design. *Fusion Engineering and Design* 27 (1995) 696.
- [2-8] Barleon, L., 1990, private communication.
- [2-9] John, H., Malang, S., Sebening, H. (editors) 1991, DEMO-relevant test blankets for NET/ITER, FZK report, KfK 4908.
- [2-10] J. Reimann, L. Giancarli, S. Malang, L. Petrizzi, E. Proust, J.F. Salavy, K. Schleisiek, "Convertible Liquid Metal Blankets for ITER with Pb-17Li as Breeding Material, Third International Symposium on Fusion Nuclear Technology, Los Angeles, California, USA, June 27-July, 1994.
- [2-11] L. Giancarli, E. Proust, J. Reimann, K. Schleisiek, "Alternative Convertible Blanket for ITER", SERMA/BP/1527, 1993.
- [2-12] E. Proust, L. Anzidei, G. Casini, M. Dalle Donne, L. Giancarli, S. Malang, "Breeding Blankets for DEMO", *Fus. Eng. & Design* 22, 1993, pp. 19-33.
- [2-13] S. Malang, E. Bojarsky, L. Bühler, H. Deckers, U. Fischer, P. Norajitra, J. Reiser, "Dual Coolant Liquid Metal Breeder Blanket", *Fusion Technology* 1992, pp. 1424-1428.
- [2-14] L. Giancarli, Y. Severi, L. Baraer, P. Leroy, J. Mercier, E. Proust, J. Quintric-Bossy. "Water-cooled lithium-lead blanket design studies for DEMO reactor: definition and recent developments of the box-shaped concept", *Fusion Technology* 21, 1992, 2081.
- [2-15] L. Giancarli, E. Proust, L. Baraer, B. Bielak, J. Quintric-Bossy, X. Raepsaet, J.F. Salavy, L. Sdedano, Y. Severi, J. Szczepanski. "The EC Conceptual Design Proposal of a Water-cooled Convertible Blanket for ITER", 15th Symp. *Fus. Eng., Hyannis (USA), Oct. 11-15, 1993.*

- [2-16] S. Malang, K. Schleisiek (eds). "Dual Coolant Blanket Concept", KfK 5424, Nov. 1994.
- [2-17] L. Giancarli (ed) "Water-cooled Pb-17Li DEMO Blanket"; Report DMT 94/538, 1994
- [2-18] L. Bühler, " Liquid metal flow in arbitrary thin-walled channels under a strong transverse variable magnetic field", Fusion Eng. Des. 17(1991) 215-220.
- [2-19] L. V. Boccaccini, "Electromagnetic forces and stresses caused by a plasma disruption in the Karlsruhe solid breeder blanket", Proc. of the Workshop on Electromagnetic Forces and Related Effects on Blankets and other Structures Surrounding the Plasma Torus, Karlsruhe, Oct. 20-21, 1992, pp. 158-173.
- [2-20] J.F. Briesmeister (Ed.); MCNP-A General Monte Carlo Code for Neutron and Photon Transport, Version 3A, Report La-7396m, Rev. 2, Sept. 1986.



### **3. Fabrication Technology of Blanket Segments**

The development of technologies needed for the fabrication of blanket segments has been started, partly in collaboration with industry companies and other research organizations. The status and the principal results obtained so far are summarized below.

Figures 2.2-3 through 2.2-5 show the final configuration of the blanket segments for the Dual Coolant concept. The principal fabrication and assembly steps are:

1. mill grooves for first wall coolant channels
2. diffusion weld front and rear first wall plates together
3. bend first wall plates into U-shape
4. machine poloidal faces and leak detection channels of U-shaped sections
5. E-beam weld U-shaped sections together poloidally
6. Weld upper tube plate and bottom manifold cover
7. insert and weld internal plates forming Pb-Li channels
8. assemble and weld He manifolds
9. weld transfer piping and top flange
10. apply MHD insulation (coatings or FCI)

Heat treatment, inspection, pressure and leak tests are performed at several steps in the process, as described later.

The most critical fabrication steps for this blanket concept includes the joining of the first wall and the fabrication of the MHD insulation - either insulating coatings or flow channel inserts (FCI's). Sections 3.1-3.3 describe tests to demonstrate the feasibility of diffusion welding, first wall bending, and E-beam welding of the blanket segments. Section 3.4 describes the application of an  $Al_2O_3$  coating on MANET; and Section 3.5 describes the fabrication of the FCI - a laminated structure of  $Al_2O_3$  or  $Al_2O_3/TiO_2$  sandwiched inside a thin ferritic steel sheath.

#### **3.1 Diffusion Welding**

The self-cooled blanket with helium-cooled first wall (Dual Coolant Concept) provides for a blanket box with integrated cooling channels. It is intended to join the plates forming the box by diffusion welding (bonding). By this technique, structural plates with milled cooling channels are pressed against each other over the full face in vacuum under mechanical pressure and at temperatures of approx. 1000 °C. The bonding occurs in two stages. In the first stage (molding in), plastic

deformation of the surfaces creates intimate contact between the two pieces. In the second stage, material diffusion occurs at the interfaces, which causes the jointing of the two plates. In order to test this technique, the Institut für Kern-technik und Energiewandlung (KE), Stuttgart, performed bonding tests on behalf of the Karlsruhe Research Center [3-1]. In a first test series, the jointing parameters needed to produce a flawless solid composite were determined and optimized on small specimens, 80 x 80 mm in size, with milled cooling and inspection channels, by variation of the relevant parameters of surface preparation and bonding.

Following thermal treatment of the specimens, the tests were evaluated by examining the helium tightness of the channel structures at 10 bar internal pressure, by metallographic examination of the binding zone, and by examination of strength in a bending test with bonded material and - for comparison - on specimens made of the base material. All specimens were pressure-tight. The best bonding results were achieved with specimens having finely ground surfaces and at bonding temperatures of 980 °C and 1050 °C, respectively. The bonding pressure was 30 MPa and 18 MPa, respectively, and then 7 MPa, for one hour each. It appeared from the bending tests that the strength was nearly the same as that of the base material. Fig. 3.1-1 shows the micrograph of a specimen with finely ground faces to be joined.

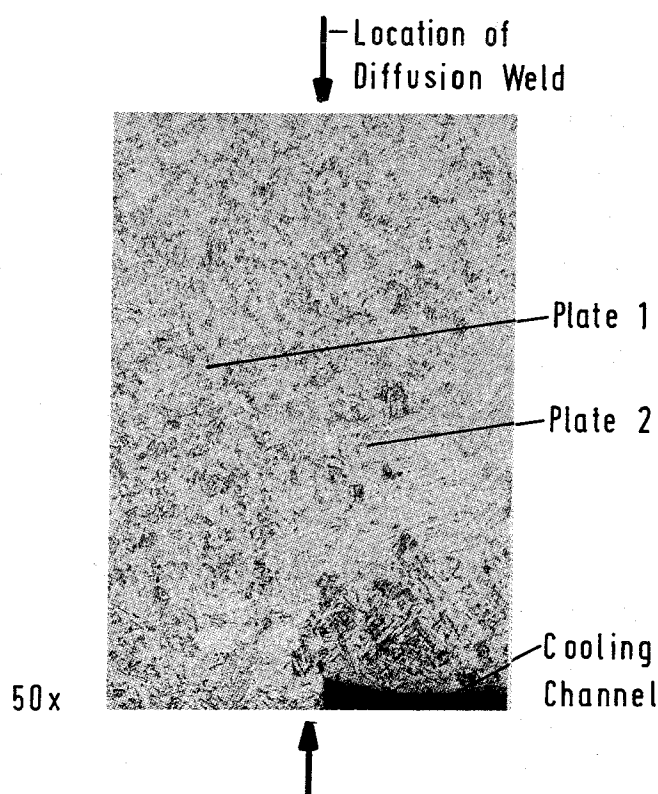


Fig. 3.1-1 Micrograph of a diffusion-bonded specimen

The positions of the faces of the two plates to be joined have been marked by arrows. The structure has been found to be regular with fine grains within the bonded zone and beyond into the base material.

In a subsequent test step three plates with prototype cooling structures (Fig. 3.1-2) were bonded using the optimized jointing parameters. The contact pressures required for molding in were adapted to the modified bonding surface; they were 22 MPa for 70 minutes and then 15 MPa for 50 minutes.

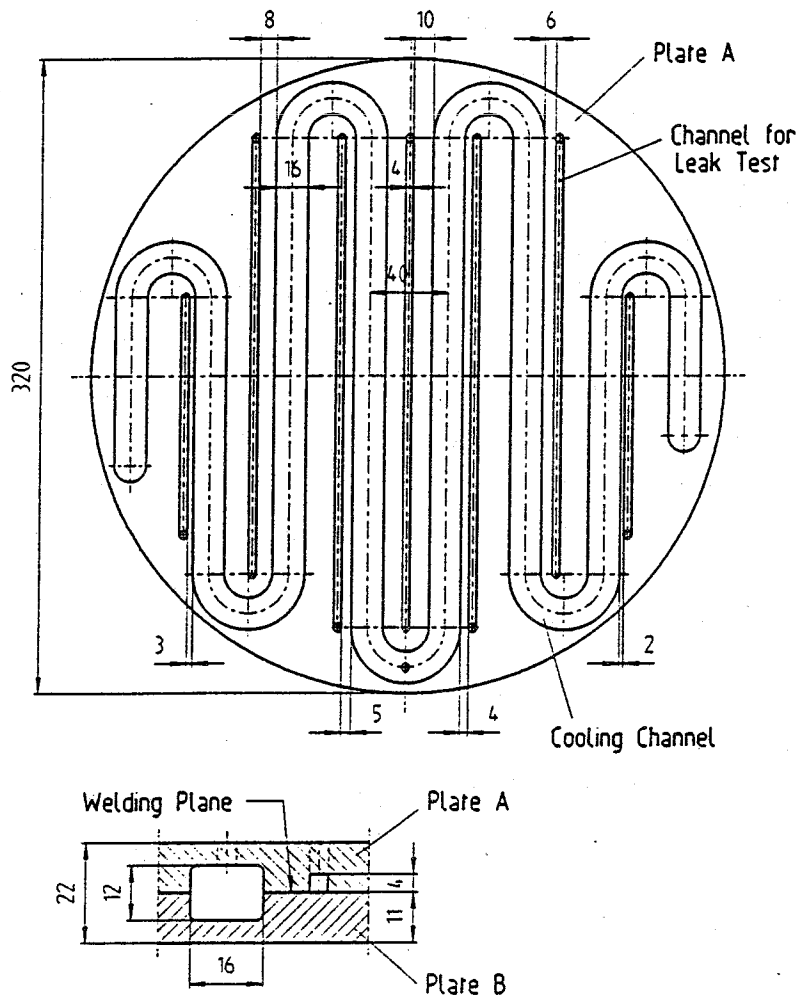


Fig. 3.1-2 MANET 2 plates for diffusion bonding tests

Examination of the quality of bonding by metallographic examination, strength examinations in bending and tensile tests yielded flawless bonding of the test plates over the full face. The tensile tests made evident the strength of the base material. The meander shaped cooling channels milled in were subjected to an internal pressure of up to 150 bar with helium and remained pressure-tight towards the inspection channels running in parallel at 2 mm distance, down to the

detection limit of the leak test instrument. The prototype plates were subjected to additional non-destructive testing by ultrasonic scanning. Also this test provided evidence of flawless bonding of the plate pairs over the entire bonded zone.

No material-specific problems emerged in the diffusion bonding tests; MANET could be bonded well. It appeared in the tests that by this technique, large-surface plates with integrated cooling channel structure can be made whose bonding is vacuum-tight with high strength. As regards structures with a particularly unfavorable height to width ratio of the webs separating the cooling channels, the jointing parameters, especially the contact pressures needed for molding in, must be carefully adapted.

Vacuum diffusion bonding facilities featuring a similar performance would have to be designed for manufacture of structural components having reactor dimensions. The vacuum facilities offer the best prerequisite for optimum bonding by providing a constant vacuum during the bonding operation and monitoring by instruments the force/deformation track. Other conceivable means of manufacturing such structural components would be bonding in open benchtop hot presses with modified heater systems using vacuum cases as well as welding in HIP facilities using compression dies and an adapted encapsulating technique.

### **3.2 Bending of FW Box**

To obtain the U-shape of the blanket box the diffusion bonded FW plates with integrated cooling channels have to be bended with angles of about  $96^\circ$  for the inboard and  $86^\circ$  for the outboard blanket segments. To investigate this fabrication step, a study was carried out to exhibit the methods and parameters of the bending process (temperature, filling material, bending machine), and to elaborate an experimental program [3-2].

For the envisaged FW thickness and bending radii, elongations of the outside fibre of about 13 % have been estimated. This should be bearable for the MANET because deformation tests with a similar martensitic steel 1.4914 have shown that much higher elongations are possible without ruptures or local constrictions [3-3].

Bending at room temperature seems to be feasible and also cheaper than bending at high temperature (500-700 °C) because of the lower technical expense for the bending process. Furthermore, the values for the uniform elongation de-

crease with rising temperature. This enhances the problem of non-uniform thickness reduction of the elongated side of the FW. The only advantage of bending at elevated temperature is the reduction of the required bending forces.

To increase the accuracy of the FW geometry (especially the stability of the webs between the cooling channels) the channels can be filled with special filling material during the bending procedure, e.g. an eutectic Sn-Bi alloy.

As a result of the preliminary bending study it can be stated that no major problems are expected in the bending process. Nevertheless, bending tests with representative FW plates have been started in May 1995.

To ascertain specific bending parameters like the location of the neutral plane, the maximum and local deformation, and the geometry variations during bending, the tests will be accompanied by FEM calculations. This will support the extrapolation of the test results to other geometries without additional tests. To reduce the stress in the region of the diffusion weld, this welding will be positioned in the calculated neutral plane of the double plate.

### **3.3 Electron Beam Welding**

Joining of materials using electron beam (EB) welding has several attractive properties. The heat input into the material is comparatively low, and very precise fabrication is possible. Also, nondestructive (ultrasonic) investigation of EB welds is not so difficult as with other welding procedures. This makes EB welding an attractive process for different parts of the blanket and first wall in a DEMO fusion reactor, irrespective of the final design and decision on coolant and breeding medium. The following investigations are focused on the Dual Coolant blanket concept as a reference concept but can easily be generalized to meet the specific needs of other design concepts.

In the Dual Coolant blanket concept (see 2.2), EB welding is used to join the U-shaped first wall (FW) sections which make up a blanket segment. According to the safety and reliability criteria which admit no single welds between plasma and liquid metal breeder, EB double welds are proposed for this purpose. The gap between the two welds additionally serves as part of a leak detection system. Joining of the double weld in a single pass is essential for the fabrication process. Also it is required that inspection is feasible in order to ensure proper quality of the welds.

### **3.3.1 Results of EB Welding Investigations**

A development and qualification program has been carried out with ferritic/martensitic steel which includes the investigation of the manufacturing of the weld geometry as well as the feasibility of nondestructive inspection of the welds.

A task has been set up with the help of an industrial manufacturer (Siemens/KWU) in which the feasibility of a double weld with leak detection slot of the required dimensions could be demonstrated [3-4]. The task consisted in the general qualification of the welding procedure using simple weld geometries (5 specimens) and was extended to meet specific geometric boundary conditions by using two specimens with cooling channels. This was to confirm that the welding procedure is not influenced by the presence of cooling channels in the joined sections. An additional purpose of the task was to confirm the possibility of nondestructive testing under geometric constraints. Finally, with respect to a reliability assessment of the welds, a combined nondestructive/destructive investigation program is needed to reveal the geometry of typical welding flaws as well as the uncertainties of the nondestructive investigation procedure. These results serve as input quantities for a future probabilistic assessment of welding reliability.

The main results at the current state of the investigations can be summarized as follows:

- It was demonstrated that EB welding is feasible to obtain a double weld with the required geometry (see Fig. 2.2-5).
- The leak detection slot between the two parts of the double weld remains open after welding and it is thus possible to use single pass welding, which is an essential requirement with regard to the assembly of the blanket.
- Nondestructive (ultrasonic) investigation is feasible. Geometric constraints can affect the sensitivity of US inspection. It is possible to detect gross flaws, e.g. flaws that result in improper condition of the weld (which could be demonstrated during test weldings), while the ability of detecting very small flaws (~0.2 mm), especially in the vicinity of the leak detection channel, and pores is difficult. These points are still under investigation.

- For additional ultrasonic investigations, a 1 cm thick strip containing the complete weld was cut out of the specimen. The strip was investigated by an ultrasonic probe with orthogonal incidence. Resolution of US results showed that US in this case can replace part of the metallographic investigations.
- Metallographic investigation was performed with the only one of the specimens where US investigation and surface crack test revealed significant indentations in the weld. Fig. 3.3-1 shows the plan of the metallographic sections along the double weld specimen. Sections along the weld are labelled beginning with L. Sections perpendicular to the weld have labels beginning with Q. For better understanding, a side view of the weld is given in the rightmost part of Fig. 3.3-1. A proper quality of the weld geometry could be found at sections Q7/Q8 and at sections Q1/Q2 (see Fig. 3.3-2). At sections Q3/Q4, however, metallographic results showed improper quality of the weld. Fig. 3.3-3 shows the section Q4 at the left side of the leak detection slot and Q3 at the right side. It can be seen that the electron beam did not meet the junction of the welded parts. This behaviour is attributed by the manufacturer to a deflection of the electronic beam which is due to insufficient demagnetization of the specimen before welding. Metallography also showed (at somewhat higher magnification) that there is some lack of fusion at the root of the leak detection gap (size:  $\approx 0.1-0.2$  mm) at the sections Q2 and Q4. These indications were not regarded as faults in the weld. The sections L5 and L6 showed some isolated pores with sizes of  $\approx 50$   $\mu\text{m}$ .

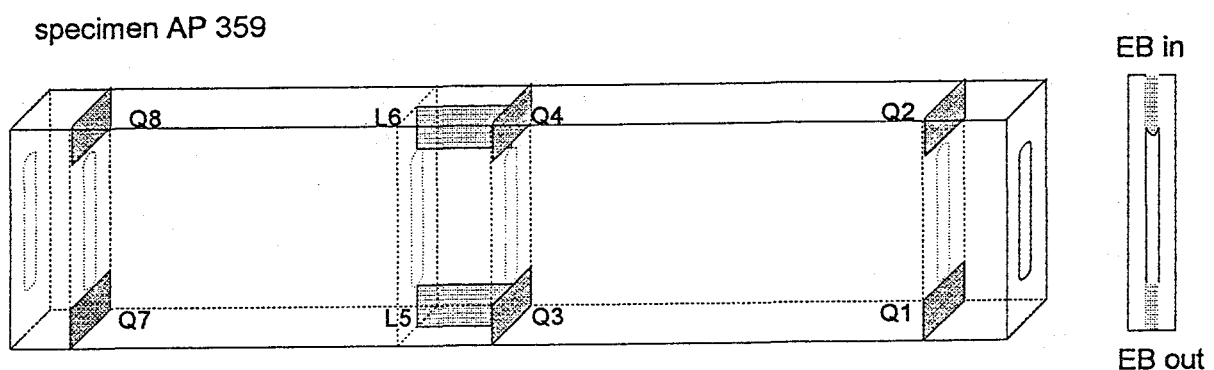
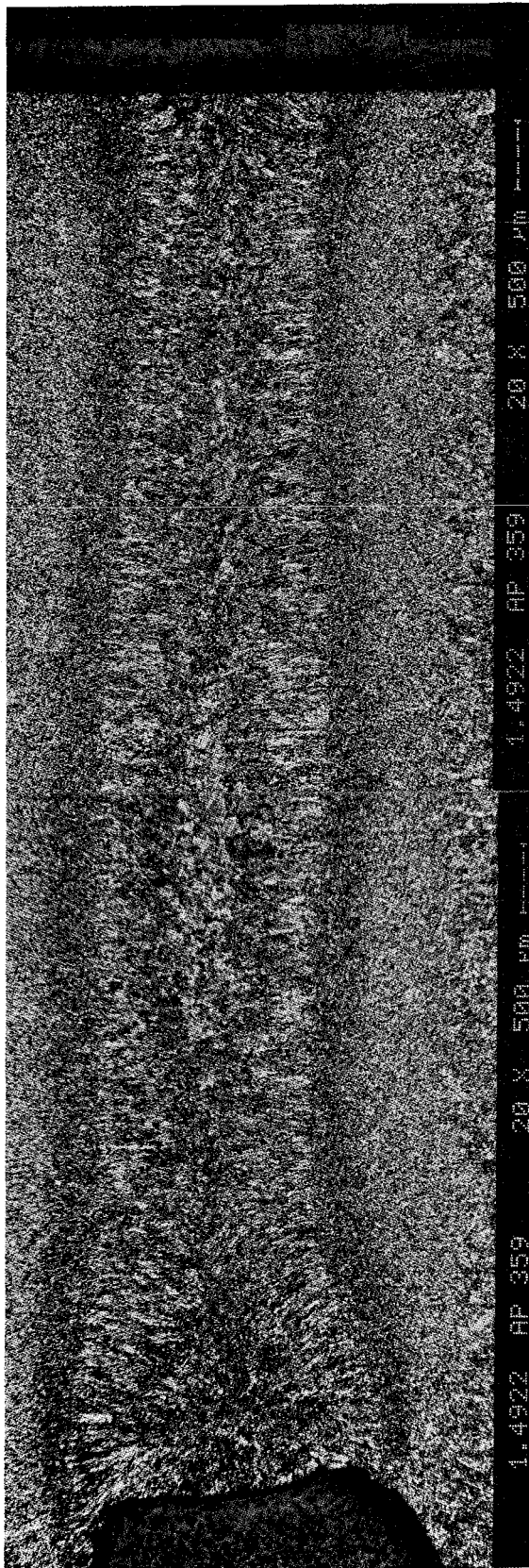


Fig. 3.3-1 Plan of metallographic sections of the double weld specimen (left) and side view of the weld (right)

Q1



Q2

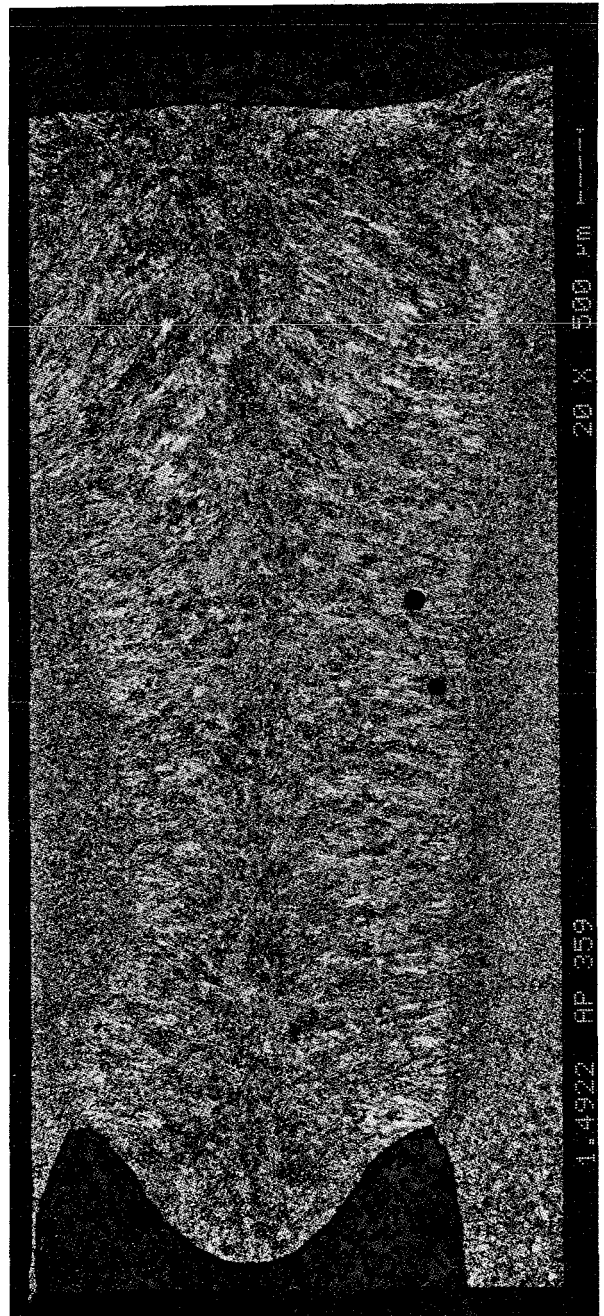
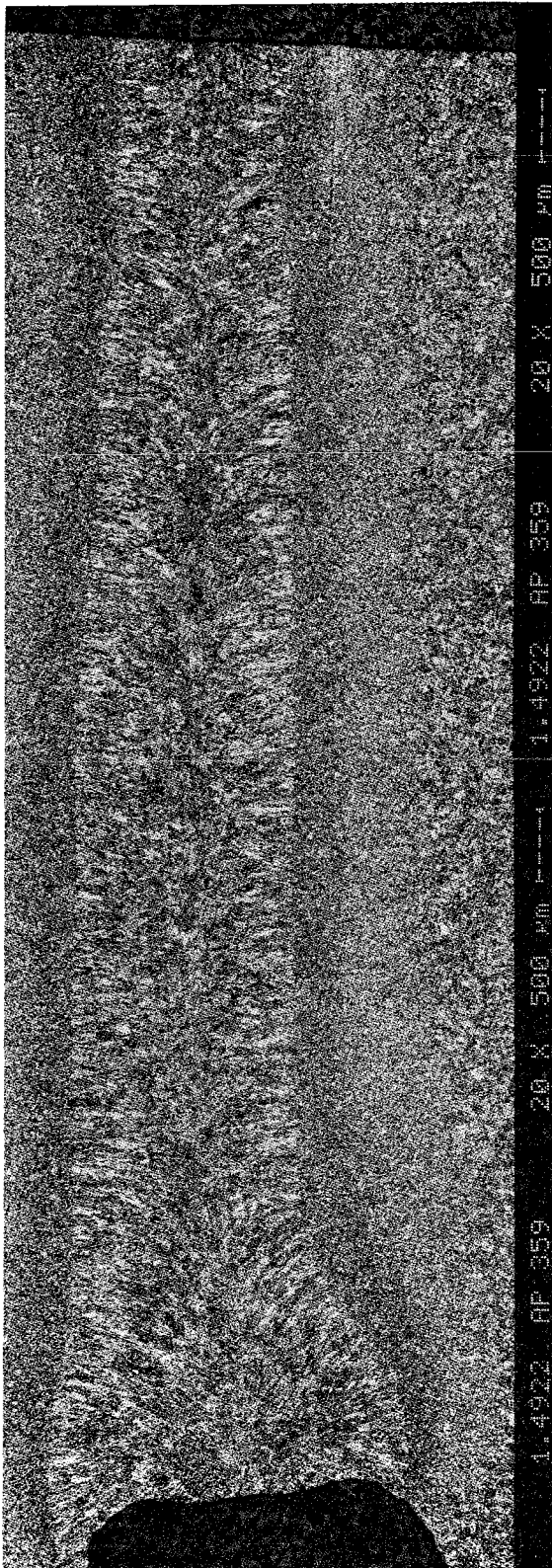


Fig. 3.3-2 Metallographic sections Q1 (left) and Q2 (right)

Q3



Q4

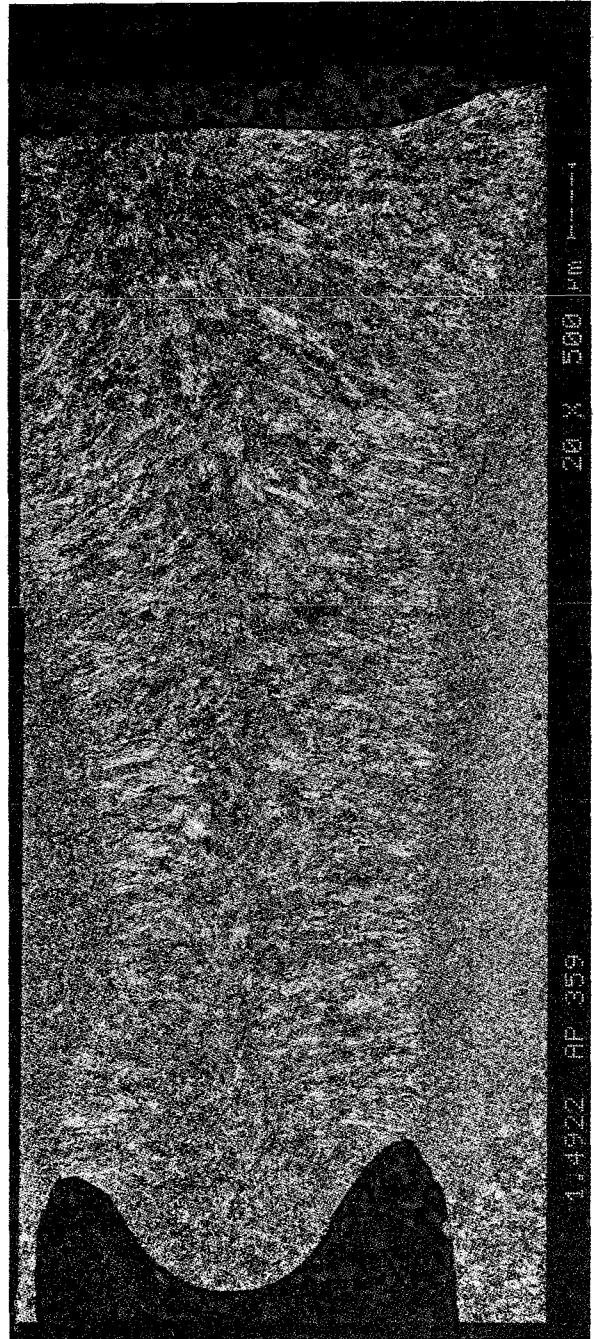


Fig. 3.3-3 Metallographic sections Q3 (left) and Q4 (right), arrow indicates junction of the welded parts

A general conclusion after the EB welding investigations is that manufacturing of the double weld by single pass EB welding is possible. US investigation of the weld is feasible regarding the geometry of the weld and is able to detect gross faults in the weld. Careful demagnetization of the material before welding is essential.

### **3.3.2 Modelling of the EB Welding Process; Reliability Analysis**

Parallel to the experimental investigations, a numerical analysis of the welding procedure was performed [3-5], [3-6]. As a result, time dependent temperature and stress fields were obtained for an assumed heating scenario. Also, residual stresses were calculated and the effect of post-weld heat treatment was considered. Welding and residual stresses may be responsible for the initiation and propagation of cracks in the weld and are therefore essential for a reliability analysis. Temperature fields allow the assessment of the heat affected zone (HAZ) of a weld and give useful hints for the feasibility of geometrical configurations as proposed in the course of blanket design modifications. For the case analyzed, the melt zone extended 2 mm away from the beam, and the HAZ (in which partial austenitisation occurs) about 1 mm farther away.

Future work is aimed at establishing methods for reliability analysis which are based not only on empirical failure rates of characteristic welds but on failure probabilities based on the scatter in the size and detection uncertainties of faults in welds as well as the fracture resistance of the material. A first approach in this direction - at this stage using literature data - has been already performed in Ref. [3-7]. It was possible to establish qualitative criteria for suitable inspection strategies and it is felt that this approach can be very useful in leading to input quantities for a probabilistic system safety analysis.

### **3.4 Insulating Coatings**

#### **3.4.1 Coating Process Options**

Ceramic insulating layers on blanket structural materials have to be compatible with the blanket coolant - the eutectic lead-lithium alloy - which has the capacity to reduce several oxidic compounds due to its content of lithium [3-8]. Surface oxides of austenitic and ferritic steels are only temporarily stable in the range of temperatures of interest (250 to 450°C). Alumina (corundum after removal of humidity by heat treatment at 950°C) was shown to be inert with the liquid alloy up to a temperature of 650°C in a capsule test [3-8]. Thus, alumina was considered as the insulating coating for use in the liquid metal cooled blanket.

The coating of the blanket structure with a thin aluminide layer creates several problems. Coating methods such as chemical or physical deposition or plasma spraying of  $Al_2O_3$  on the inner surfaces of a steel structure do not appear to be applicable for a complicated welded structure, particularly on the inner surfaces of a blanket segment. The equipment available for such procedures is insufficient for such complicated geometric conditions. Thus, aluminization of the steel surfaces and the subsequent oxidation of the intermetallic layer seems to be the most promising way to form such layers [3-9, 3-10].

The aluminizing of MANET steel can be performed by means of the powder-pack cementation (PPC), or the hot-dip aluminizing (HDA) process. The layers produced by these processes are nearly equivalent in their compositions, thickness and properties.

The PPC process uses a pack of solid powders of the activator (halogenide), metal (Al, Fe, Cr, ...) and inert filler material ( $Al_2O_3$ ) to prevent melting of the mixture. The aluminizing is performed at a temperature of  $\approx 900$  °C at which point metal halogenide is transferred through the gas phase to the substrate, where the element is deposited and diffuses into the surface layer. The resulting layer is a diffusively bonded intermetallic layer on the steel. The PPC process is well established in the technology of components at high temperatures in corroding environments. One enormous disadvantage of this method is related to the filling of complex structures with the powder mixture and the completeness of the removal of the reaction products after the filling procedure.

Since the PPC process might be inapplicable for the coating of inner surfaces of the blanket structure, the HDA process was the main subject of these studies. The

HDA process is also applied in industrial scale to aluminize several low alloy steels. However, coating of ferritic-martensitic steel is a new technique.

### 3.4.2 Aluminization tests

Aluminide layers were produced in a laboratory device in small dimensions on sheets of up to 10 x 100 mm. An  $\text{Al}_2\text{O}_3$  crucible containing molten aluminum was placed in a laboratory furnace for melting and maintaining the operation temperature of 700 to 800°C [3-9, 3-10]. The whole procedure was performed in a purified argon atmosphere within a glovebox. The dipping of MANET sheets required a careful purification of their surfaces before coating. Preheating of the sheets to the dipping temperature and stirring during the aluminizing seemed to be advantageous. The time required for the formation of the intermetallic layer was up to ten minutes, depending on temperature.

The aluminide layer was examined by means of metallographic and chemical analytical techniques. The layer has a thickness of about 80  $\mu\text{m}$  with a composition of  $\text{FeAl}_3$ . The layer is well adhesive on the matrix (see Fig. 3.4-1).

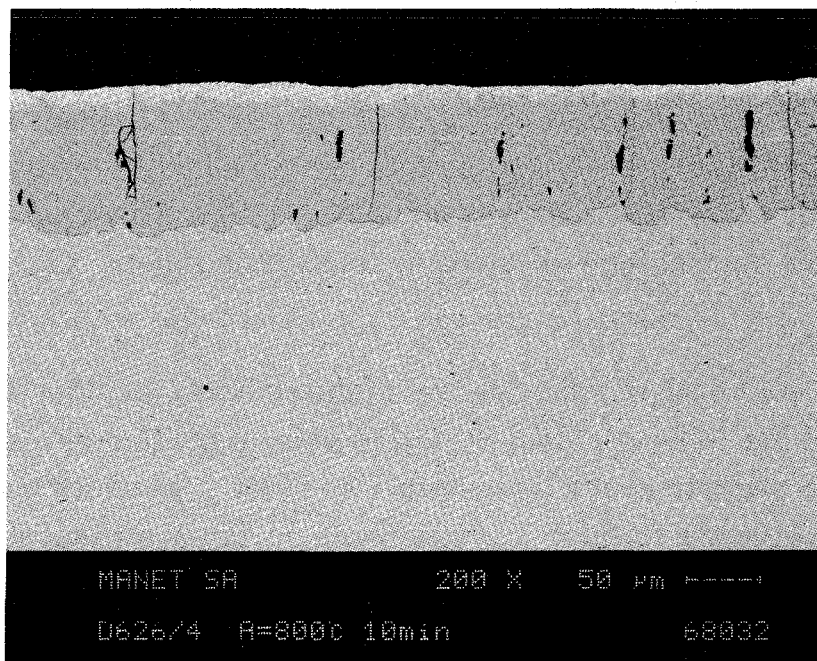


Fig. 3.4-1 Metallographic examination of aluminized MANET specimen

### 3.4.3 Oxidation

The formation of an electrical insulating layer on top of the aluminide layer was tested with two different methods: high temperature and electrochemical oxidation. Electrochemical oxidation of the iron aluminide layer in aqueous acid solution was not successful, since the oxide layers on the anodes suffered breakthrough and a rapid formation of oxides as  $\text{Fe}_2\text{O}_3$ . Thus, gaseous oxidation at high temperatures was applied to form the alumina layers. The gaseous oxidation of aluminum and its alloys requires temperatures of  $\geq 900^\circ\text{C}$  [3-9, 3-10] due to the low diffusion rates through the  $\text{Al}_2\text{O}_3$  phases. The oxidation rates at 900 and 950 °C were found to obey parabolic rate laws. Air or a  $\text{H}_2\text{O}/\text{H}_2$  gas mixture were applied as oxidants.

The high temperature treatment is not only an oxidation but also a diffusion process. Two aluminide layers could be observed on the base material after the heat treatment: the outer one of  $\approx 80 \mu\text{m}$  thickness with a composition of  $\approx 40 \text{ at.}\%$  Al and  $\approx 60 \text{ at.}\%$  Fe, and the inner one of  $\approx 200 \mu\text{m}$  thickness with a gradient of the Al concentration from  $\approx 40 \text{ at.}\%$  to nearly zero at the border of the MANET matrix.

During the oxidation process, Al diffuses to the surface to react with the gaseous oxygen and form the required compound  $\text{Al}_2\text{O}_3$ . Unfortunately, oxygen also diffuses along the grain boundary into the layer to form  $\text{Al}_2\text{O}_3$  internally. This oxidation process influenced the microstructure of the intermetallic layers. Cavities were developed at the boundary between the outer and inner aluminide layers. The surface of the coating became rough, and the oxide layers were not uniform and tight, though their thickness reached the order of 5 - 10  $\mu\text{m}$  (see Fig. 3.4-2).

Analytical examination of the coatings revealed an influence of the purity of the molten aluminum on the quality and the oxidation behaviour of the aluminide. The presence of alloying elements seems to be a contributing factor for the formation of cavities at the border between the outer and inner intermetallic layers. The oxidation behaviour appears also to depend on the composition of the intermetallic layer. Thus, the variation of the aluminum used for coating offers a way to optimize the layers with respect to the uniformity of the insulating oxide. Si or other additives to the aluminum melt are under study.

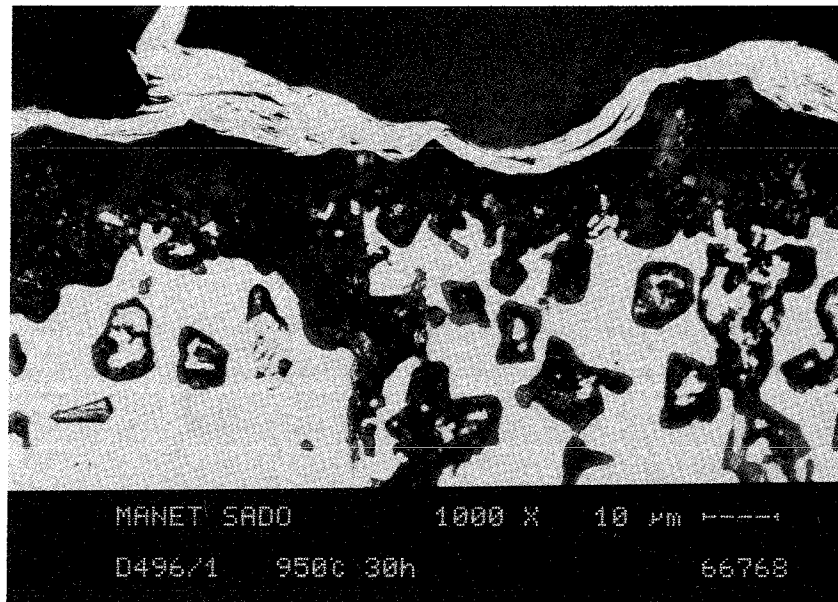


Fig. 3.4-2 Metallographic examination of oxidized surface of aluminized MANET specimen

The temperature and duration of the oxidation process as well as the nature of the oxidizing gas also were found to influence the thickness and uniformity of the oxide layer and the formation of cavities in the intermetallic phase [3-10]. Processes are under development to oxidize the aluminide layer at room temperature or at some moderate temperature.

#### 3.4.4 "Self-healing"

The chemical activity of Al in the outermost intermetallic layer, in which the concentration is of the order of 40 at%, must be high enough to allow its oxidation even in the low oxygen potential in the liquid Pb-Li alloy. The chemical activity in Fe-Al alloys was, therefore, measured in the concentration range up to 45 at% Al at temperatures between 600 and 800°C [3-11]. Preliminary results indicate that the Al potential in the alloy Fe-40Al should be high enough to be oxidized by the oxygen present in the liquid alloy. This provides the thermodynamic basis for "self-healing" of alumina layers on the structure in a liquid metal cooled blanket. The "self-healing" process itself remains to be proven in experiments.

### **3.4.5 Summary and Future Prospects**

The entire process to fabricate the insulating surface layer on the completely welded structure may proceed as follows. The MANET steel is heat treated to its optimized condition first. The whole structure is then heated to the aluminizing temperature (750 - 800°C) and molten aluminum is pumped through the blanket in such a way as to allow all parts of the inner surface to be contacted and wetted. The molten metal may be kept there for some minutes and subsequently drained. The formation of the intermetallic phase is the reason for solidification of the layer at high temperature. The aluminized blanket has to be heated to the oxidation temperature in order to form the  $\text{Al}_2\text{O}_3$  surface oxide layer on top of the intermetallic coating. Finally, a stress relieving heat treatment of two hours at 750°C has to be made in order to recreate the optimized conditions with respect to structure, hardness and creep strength of the MANET steel.

Further work related to the optimization of the properties of the aluminide and the insulating oxide layers is in progress, based on the results which have been gained so far. The parameters under study are the conditions of the dipping procedure, the composition of the molten aluminum and the conditions of the oxidation process. The diffusion processes ruling the oxidation were shown to be influenced by the composition of the aluminide layer.

The attempts to optimize the coating and oxidation processes are accompanied by compatibility tests of the layers with Pb-17Li alloy. The optimization of the iron-aluminide layers may lead to a quality which allows the electrochemical oxidation at low temperature. Thus, also this option is not yet ruled out. It seems that such oxide layers are chemically stable in contact with Pb-17Li at 450°C. But even the high temperature oxidation may be replaced by a technique which allows the formation of  $\text{Al}_2\text{O}_3$  layers at considerably lower temperatures. This might be performed by oxygen exchange between the aluminide layer and a liquid metal containing oxygen at a sufficiently high potential.

## **3.5 Flow Channel Inserts**

### **3.5.1 Objectives**

Another solution to avoid MHD-pressure losses in a liquid metal breeder blanket is the insertion of electrically insulating structures into the flow channels. The design for these flow channel inserts (FCI) is generally a sandwich structure consisting of the three layers metal-insulator-metal. The encapsulation of the

insulating layer into two metallic sheets has two reasons. First, the outer metallic sheet has to provide the structural strength of the FCI, so its thickness should be about 1 mm; the main objective of the inner metallisation however is to act as a barrier against liquid metal corrosion by the Pb-Li, therefore this can show a much lower thickness, about 0.2 mm.

Furthermore the FCI's have to meet the following requirements:

Temperature	:	min ~ 220 °C max ~ 470 °C
Environment	:	Pb17 Li liquid
Liquid metal velocity	:	1.1 m/s
Liquid metal pressure	:	2 MPa min 8 MPa max
Temperature transients	:	10 K/s
Neutron flux	:	$5 \cdot 10^{14}$ n/(cm <sup>2</sup> · s)
Neutron energy	:	< 14 MeV
Material damage	:	~ 70 dpa in steel
Electrical resistivity	:	≥ 25 Ω m
Electrical potential	:	~ 1 V
Time in operation	:	~ 20 000 h
Heat flux density	:	12 W/cm <sup>2</sup>

Detailed descriptions of the FCI-concept are given for example in [3-12, 3-13, 3-14].

### 3.5.2 Material Selection and Layer Morphology

The above mentioned requirements were thought to be fulfilled by a ceramics as insulating material clad by steel liners. The crucial items with respect to the ceramics were a possible degradation of the electrical resistivity due to radiation, the low thermal conductivity and the mismatch of thermal expansion compared with the metallic sheath. The steel liners should be corrosion resistant as well as irradiation resistant. These considerations led to the following material and process selection.

### **Material selection:**

- **Metallic sheath :** Ferritic steel, later MANET (DIN 1.4914).  
As no MANET was available at that time, a ferritic steel, type DIN 1.4021 was taken.
- **Ceramics:** Insulating layers consisting of Al<sub>2</sub>O<sub>3</sub>, Al<sub>2</sub>O<sub>3</sub>/TiO<sub>2</sub> 87/13 and Al<sub>2</sub>O<sub>3</sub>/TiO<sub>2</sub> 60/40 ("Al<sub>2</sub>TiO<sub>5</sub>") were selected.

### **Plasma spraying:**

The base steel sheet was first coated by plasma spray deposition with an adhesive layer of Fe 13 Cr, on which the ceramic layer was sprayed. Finally again a layer of Fe 13 Cr was sprayed on this. The thickness of the ceramic layer was about 200 µm.

The cover steel sheet was only coated by Fe 13 Cr. So, the following bonding process was performed between Fe 13 Cr against Fe 13 Cr.

### **Chemical Vapor Deposition (CVD):**

At first the steel base sheet and the cover sheet were coated by chemical vapour deposition (CVD) with an adhesive layer consisting of Ti(C, N). The insulating layer was then deposited on the adhesive layer of the base sheet. The thickness of the ceramic layer was about 10 µm.

### **3.5.3 Bonding and Testing of the Bonding Strength**

Keeping in mind the application of MANET steel as material for the FCI's, the bonding temperature had to be kept as low as possible and had not to exceed 1050 °C. So, circular sandwich structures with 70 mm diameter were diffusion-bonded by Hot Isostatic Pressing (HIP) using the following conditions:

1050 °C - 200 MPa pressure

950 °C - 200 MPa and 300 MPa

900 °C - 200 MPa and 300 MPa.

### **Adhesion of the ceramic layer:**

Before diffusion bonding, the adhesive strength of the ceramic layers on the steel sheet was tested. Test stripes, 50 mm x 10 mm, were prepared and cyclic tests were performed. The conditions were chosen according to the anticipated thermal load ( $\varepsilon=0.175\%$ ). During bending tests, the ceramic layer was positioned at the bottom side of the test stripes so it met tensile straining. The number of cycles was 100. No delamination of the ceramic layers could be observed.

### **Testing of the sandwich structure:**

Thermal cycling tests were performed in a special thermocycling device. The following conditions could be realized in this device:

Temperature range	: 250 °C - 470 °C
Heatup rate	: 55 °C/min
Cooldown rate	: 64 °C/min
Holding time	: 10 min at 470 °C and 250 °C
No of cycles	: 100.

The sandwich structures were investigated before and after the thermal cycling by high resolution nondestructive ultrasonic examination. After HIP, good bonding quality could be reached for all temperatures and 200 MPa bonding pressure. The samples treated with 300 MPa showed insufficient bonding.

After thermal cycling, homogeneous bonding was apparent in the center region of the samples generally for the plasma sprayed types. Degradation of the bonding quality could be observed in the outer regions. This is due to the fixation of the samples in the thermocycling device.

After nondestructive examinations, test stripes were cut out of the sandwich structures, i.e. out of the center region, which had been strained by thermal cycling. These test stripes again were tested by mechanical cycling, as it had been done before bonding. These tests generally verified the results of the nondestructive examination, especially the samples bonded at 1050 °C showed no delamination, whereas few of the samples failed, which were bonded at lower temperatures.

### 3.5.4 Conclusions

Manufacturing of FCI-structures by plasma-spraying of ceramic layers on steel sheets with subsequent diffusion bonding is possible. The required bonding strength can be met. Nevertheless there should be further detailed investigations with MANET steel and with the original thickness of the steel. These investigations, which were planned for 1994 could not be performed because the FCI-development was interrupted in order to concentrate the effort on the direct coating method (Sect. 3.4) which is considered as the process with the higher potential for large-scale application.

### References

- [3-1] G. Haufler: Diffusionsschweißen von Probepplatten aus MANET 2 für gekühlte Blanketstrukturen. KE-Stuttgart-Bericht, 1-TB-241/94 (1994).
- [3-2] G. Haufler, M. Kopf, D. Kolev: Studie zum Biegen von Platten mit Kühlkanälen. KE-Stuttgart-Bericht 1-TB-242/94 (1994).
- [3-3] K. Ehrlich, M. Schirra: KfK internal report (1989).
- [3-4] H. Breitling: EB-Schweißen und US-Prüfung von Doppelschweißnähten für heliumgekühlte Erste Wand. Arbeitsbericht KWU NT1 BGL/95/002.
- [3-5] L. Cizelj, H. Riesch-Oppermann: An Analysis of Electron Beam Welds in a Dual Coolant Liquid Metal Breeder Blanket. Kernforschungszentrum Karlsruhe, KfK 5360, 1994.
- [3-6] L. Cizelj, H. Riesch-Oppermann: Welding Stresses in the First Wall of a Dual Coolant Liquid Metal Blanket, in: K. Herschbach, W. Maurer, J.E. Vetter (eds.), Fusion Technology (1994), 1213-1216, Proc. SOFT 18, Karlsruhe, 1994, Elsevier Science Publishers, 1995.
- [3-7] S. Zhang, H. Riesch-Oppermann: Probabilistic Analysis of Welded Joints in Blanket Design, in: K. Herschbach, W. Maurer, J.E. Vetter (eds.), Fusion Technology (1994), 1165-1168, Proc. SOFT 18, Karlsruhe, 1994, Elsevier Science Publishers, 1995.
- [3-8] H. Glasbrenner, H.U. Borgstedt, Z. Peric: Compatibility of Insulating Materials in Pb-17Li Alloy. In: Material Behaviour and Physical Chemistry in Liquid Metal Systems II, Karlsruhe, March 16-18, 1993, pp. 95-104.
- [3-9] H. Glasbrenner, H.U. Borgstedt: Preparation and characterization of  $Al_2O_3/Fe_xAl_y$  layers on MANET steel. J. Nucl. Mater. 212-215 (1994) 1561/65.
- [3-10] H.U. Borgstedt, H. Glasbrenner: The development of a direct insulation layer for liquid metal cooled fusion reactor blanket. Fus. Eng. Des. 27 (1995) 659.
- [3-11] H. Kleykamp, H. Glasbrenner, H.U. Borgstedt, to be published.
- [3-12] S. Malang et al.: Das Konzept eines Brutblankets mit der eutektischen Blei-Lithium Legierung Pb-17Li als Brennstoff und Kühlmittel. KfK-Nachrichten 4/89, S. 213 (1989).

- [3-13] L. Barleon, V. Casal, L. Lenhardt, A. Sterl: MHD-Strömung in flüssigmetallgekühlten Blankets. KfK-Nachrichten 4/89, S. 224 (1989).
- [3-14] L. Barleon, V. Casal, L. Lenhardt: MHD flow in liquid metal cooled blankets. Fus. Eng. and Design 14 (1991), S. 401-412.

## 4. Neutronics

### 4.1 Neutronic characteristics of the blanket

The present design of the Dual Coolant blanket has evolved from the concept of a self-cooled liquid metal blanket using the eutectic alloy Pb-17Li as breeder/coolant [4-1]. The layout of the self-cooled liquid metal blanket provides large poloidal flow channels which are needed to minimise the magneto-hydrodynamic (MHD) pressure drop encountered when the liquid metal flows perpendicular to the magnetic field. The large flow channels provide high volume fractions for the liquid metal breeder while the steel fraction is at a low level due to the absence of any cooling tubes. This results in a high tritium breeding potential without the need for a neutronic optimisation with regard to the material arrangement in the blanket. Tritium self-sufficiency can be easily attained for a DEMO reactor using as breeder/coolant both the Pb-17Li alloy with a high  $^6\text{Li}$ -enrichment (typically 90 at%) and liquid lithium with a low  $^6\text{Li}$ -enrichment (typically 30 at%) [4-2].

High flow velocities and, therefore, small flow channels are needed for cooling the first wall with liquid metal. To avoid the resulting excessively large MHD pressure drop in the first wall cooling channel, the solution of a dual coolant blanket has been elaborated combining a liquid metal cooled breeder zone and a helium-cooled first wall [4-3]. In addition, this solution offers improved safety and reliability features over the entirely self-cooled blanket. No major drawback arises with regard to the tritium breeding performance of the blanket, although a liquid metal cooling of the first wall is superior to the helium cooling in this respect.

The main neutronic characteristic of the Dual Coolant blanket is its use of the Pb-17Li alloy as breeding material and the absence of any neutron moderating material in the blanket. The lead neutron multiplier is the major alloy constituent showing a high neutron reflection but a low neutron slowing down power. As a consequence, a sufficiently high blanket coverage and a large breeder zone thickness are required to make full use of the tritium breeding potential of Pb-17Li.

Sufficient space is available for the breeding blanket segments in the DEMO reactor. According to the specifications of the test blanket advisory group (TAG), the radial thickness available to the blanket and shield is 118 and 186 cm, inboard and outboard, respectively, leaving about 86 and 129 cm for the blanket segments. In addition, the divertor region is assumed to be utilised for breeding. Based on the DEMO reactor boundary conditions, the Dual Coolant blanket needs a blanket thickness of 55 and 102 cm for the inboard and outboard blanket seg-

ments, respectively, including the helium manifolds with thicknesses of 14.5 and 21.5 cm, to assure tritium self-sufficiency. This includes safety margins to cover tritium losses, computational and data related uncertainties and the reduced tritium breeding capability due to the presence of radial blanket ports. The total radial thickness of the liquid metal breeder zone amounts to 30 and 68 cm, inboard and outboard, respectively.

The  ${}^6\text{Li}$ -enrichment is kept at the level of 90 at% in the present design. In the divertor breeding region the geometrical configuration of the inboard blanket segment (first wall, breeding zone, manifold region and removable steel shield) is used. For the divertor plates in front of the divertor breeder zone the specifications of the test blanket advisory group are assumed: 5 mm tungsten, 30 mm copper and 40 mm steel at a volume fraction of 50 %. No water is assumed in the divertor.

#### **4.2 Computational procedure and blanket modelling**

Three-dimensional Monte Carlo transport calculations with the MCNP-code [4-4] and nuclear cross-section data from the European Fusion File EFF [4-5] form the basis of the neutronic analysis of the Dual Coolant blanket.

A three-dimensional torus sector model of the DEMO-Reactor has been developed for use in the Monte Carlo transport calculations assuming the boundary conditions that have been specified by the test blanket advisory group. The model has been designed for half a  $22.5^\circ$  torus sector of the DEMO-reactor (1/32 of the torus) including one inboard and one and a half outboard segments. Reflecting boundary conditions were applied at the lateral walls of the modelled torus sector. The sector model includes the vacuum chamber, first wall and blanket segments, the vacuum vessel, top and bottom divertor and the bottom divertor exhaust chamber with a pumping duct entrance. Figure 4-1 shows a radial-poloidal cross-section of the MCNP generated torus sector model. Inside the blanket segment boxes, the heterogeneous array of steel plates, forming the liquid metal ducts, has been explicitly integrated. Note that no material homogenising has been applied in modelling the blanket segments. Figs. 4-2 and 4-3 show horizontal cross-sections of the inboard and outboard blanket segments for illustrating the modelling of the radial-toroidal direction.

In the Monte Carlo calculation the neutron source term is described in a special FORTRAN routine linked to the MCNP-code. The spatial neutron source distribu-

tion is sampled according to the probability distribution of the 14-MeV neutron source density  $s(a)$  [4-6]:

$$s(a) = \left[ 1 - \left( \frac{a}{A} \right)^2 \right]^4 \quad \text{for } 0 \leq a \leq A, \quad A = \text{minor plasma radius}$$

The parameter  $a$  fixes a contour line at constant source density that is described in a parametric representation [4-7].

The following plasma parameters are used for the source description of the DEMO-reactor [4-8]:

Major plasma radius  $R_0 = 630$  cm

Plasma elongation  $E = 2.17$

Minor plasma radius  $A = 182$  cm

Plasma excentricity  $e = 16.2$  cm

Monte Carlo transport calculations were performed for calculating the global tritium breeding ratio, the nuclear power production and density distribution due to neutron and photon interactions with the materials, the shielding efficiency of the blanket with regard to the radiation load to the inboard TF-coil, and for providing the neutron fluxes and spectra needed for performing activation, afterheat and radiation damage calculations. These calculations throughout have been performed using the three-dimensional torus sector model of the DEMO-reactor. Each kind of calculation required, however, a different computational scheme with a corresponding computational effort to ensure a sufficient statistical accuracy for the quantities to be scored. This includes the use and optimisation of spatially dependent sets of particle weights needed for applying the importance sampling technique in shielding calculations.

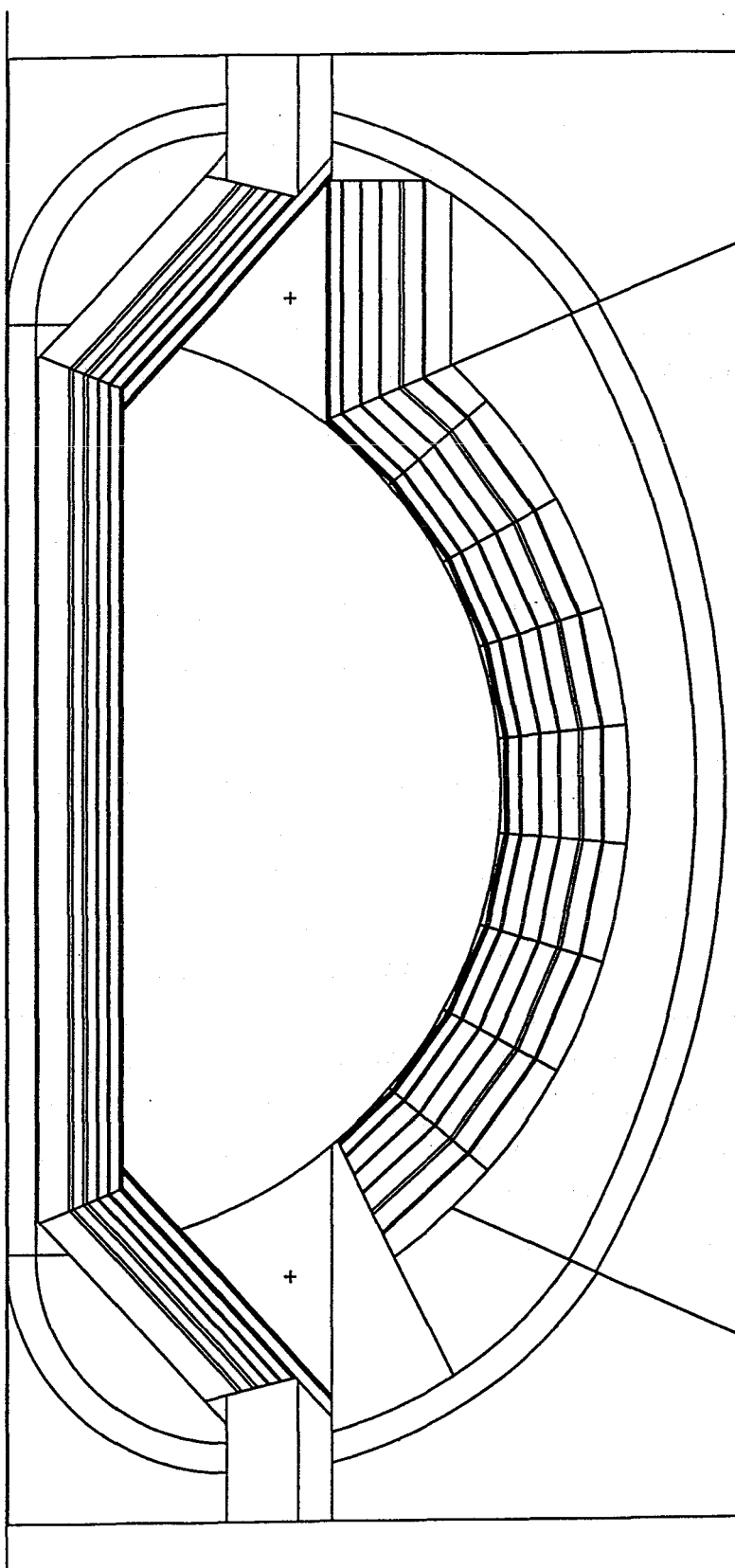


Fig. 4-1: Radial-poloidal cross-section of the torus sector model

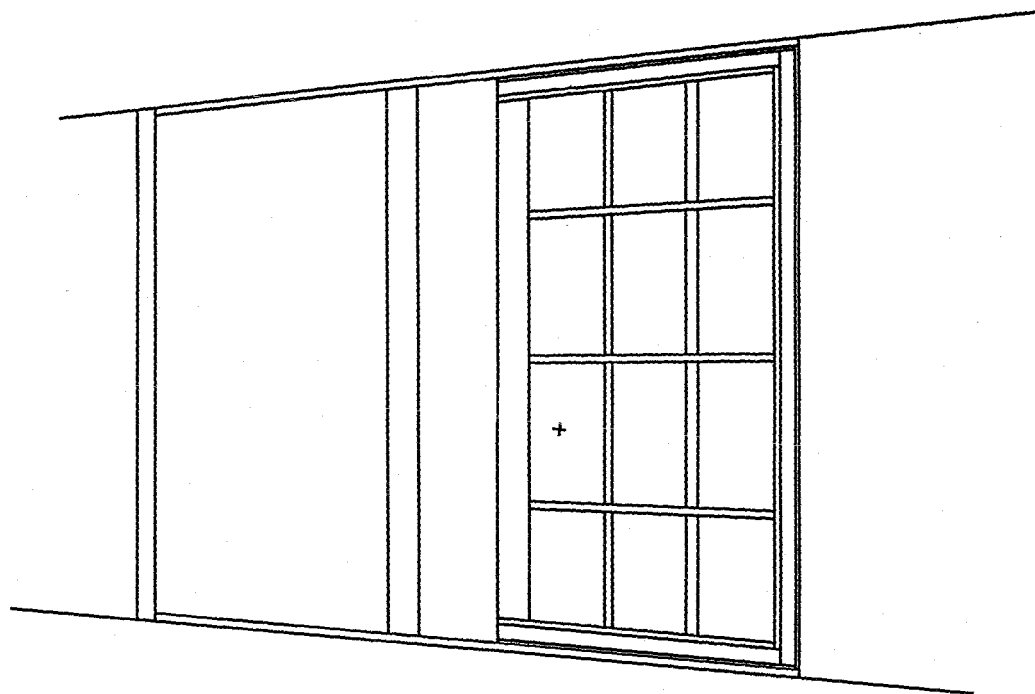


Fig. 4-2: Horizontal cross-section of the inboard segment

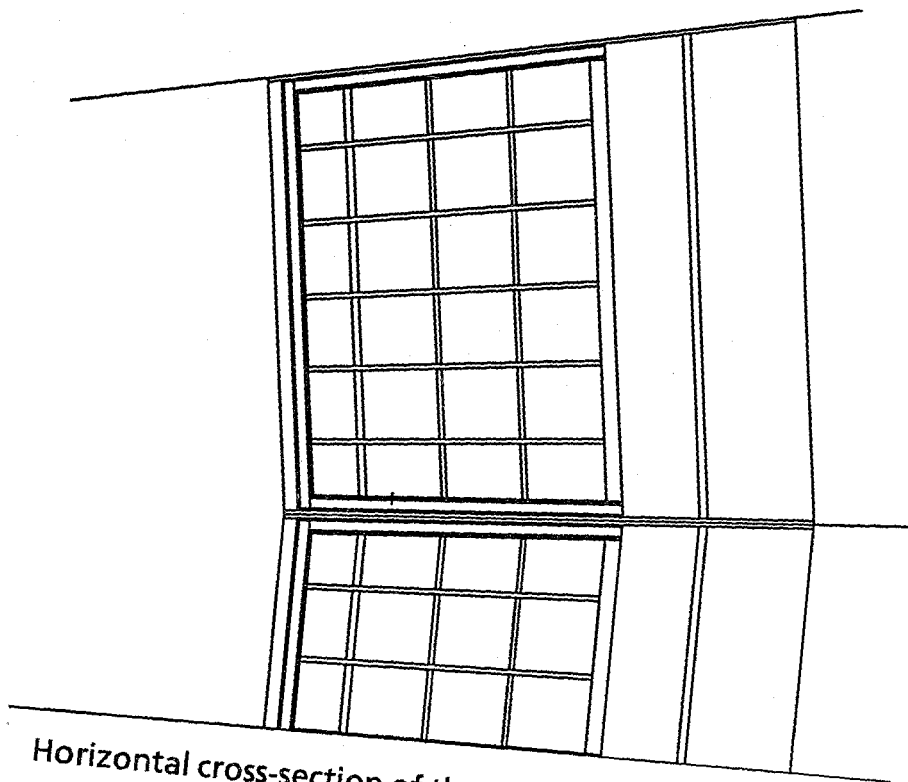


Fig. 4-3: Horizontal cross-section of the outboard segment

### 4.3 Tritium breeding

Three-dimensional Monte Carlo calculations were performed to calculate the global tritium breeding ratio (TBR) for the Dual Coolant blanket in the DEMO reactor. About 110,000 source neutron histories have been typically tracked in the TBR-calculation.

It was attempted not to exceed the level of  $TBR = 1.15$  in order to avoid unnecessary tritium excesses. For the previous version of the Dual Coolant blanket the rather high global tritium breeding ratio of  $TBR = 1.22$  was attained [4-3]. Therefore, the radial thickness of the inboard breeder zone was reduced by about 20 cm to 30 cm in the present design. This offers the advantage of making available more space for shielding material at the inboard side. Alternatively, the high tritium breeding capability of the Dual Coolant blanket would allow operation without using the divertor region for tritium breeding. The final results for the TBR and the neutron multiplication for the present design are shown in Table 4-1. Note that there is much room for enhancing the tritium breeding for the Dual Coolant blanket without technical implications - if there is a need to.

Tritium breeding in the Demo-reactor will be affected by the presence of blanket ports for plasma heating, remote handling, pellet injection, diagnostics etc. According to the TAG-specifications, ten horizontal ports centred at the equatorial plane of the outboard blanket segments are assumed for the Demo-reactor. Each blanket port covers an area of 340 cm height times the full segment width. Actually, the blanket ports are not included in the torus sector model and, therefore, are not taken into account in the TBR-calculation. Their impact on the breeding performance has been previously assessed, however, both for liquid metal and solid breeder blankets in the Demo-reactor [4-9]. Based on these results, a TBR-loss of about 5% is expected and the actual tritium breeding ratio would decrease to  $TBR = 1.07$  in the presence of ten blanket ports in the DEMO-reactor.

Table 4-1 Tritium breeding and neutron multiplication,  
Results of 3D Monte Carlo calculations (no blanket ports)

Neutron multiplication	$1.59 \pm 0.09\%$
Tritium breeding ratio	
Outboard blanket segment	$0.80 \pm 0.3\%$
Inboard blanket segment	$0.23 \pm 0.5\%$
Divertor breeding region	$0.10 \pm 0.8\%$
Total tritium breeding ratio	$1.13 \pm 0.2\%$

#### 4.4 Nuclear power generation

The nuclear power generation has been calculated with coupled neutron-photon Monte Carlo transport calculations. About 690,000 source neutron histories were followed in this calculation. The normalisation was performed for a fusion power of 2200 MW.

Table 4-2 shows the resulting power generated in the inboard and outboard blanket segments. About 75 % of the nuclear power is generated in the front part of the blanket segments (first 30 cm), although the radial power density profiles are comparatively flat for Pb-17Li. The MANET first wall contributes 10% and the liquid metal about 80% to the total nuclear power generation.

If the DEMO-reactor would be equipped with 32 inboard and 48 outboard segments of the Dual Coolant blanket type, a total nuclear power of 2019 MW would be produced. This does not include the power radiated from the plasma. Thus the neutron energy multiplication for the Dual Coolant blanket amounts to 1.15.

Table 4-2 Nuclear power generation [MW] in the blanket segments, results of 3D Monte Carlo calculations (2200 MW fusion power).

Outboard segment (7.5°)		Inboard segment (11.25°)	
Blanket segment	27.6	Central blanket segment	13.5
		Divertor breeding region	3.7
		Divertor plates	4.5
Total outboard	27.6	Total inboard	21.7

Table 4-3 Maximum power densities [W/cm<sup>3</sup>] in the blanket segments at torus midplane, results of 3D Monte Carlo calculations (2200 MW fusion power).

	Inboard segment	Outboard segment
First wall (steel)	20.8	23.4
Pb-17Li	front row (first 3 cm)	19.3
	back row (last 5 cm)	0.61
Rear wall (steel)	0.35	0.14

The radial power density distribution has been calculated for the outboard and inboard blanket segments. A fine radial-poloidal segmentation scheme has been used in the Monte Carlo calculation for this purpose. Figures 4-4 and 4-5 show the radial profiles in the liquid metal and the MANET steel as calculated for the torus mid-plane.

The power density profiles are comparatively flat due to the inherent nuclear properties of the Pb-17Li alloy and the absence of any neutron moderator. As a consequence, the peak power densities in both in the Pb-17Li and the steel structure are rather modest (Table 4-3). For the Pb-17Li the maximum power density at torus mid-plane is not more than 19.3 W/cm<sup>3</sup> (outboard blanket segment, first 3 cm of the first liquid metal row) and for the MANET steel 23.4 W/cm<sup>3</sup> (outboard first wall).

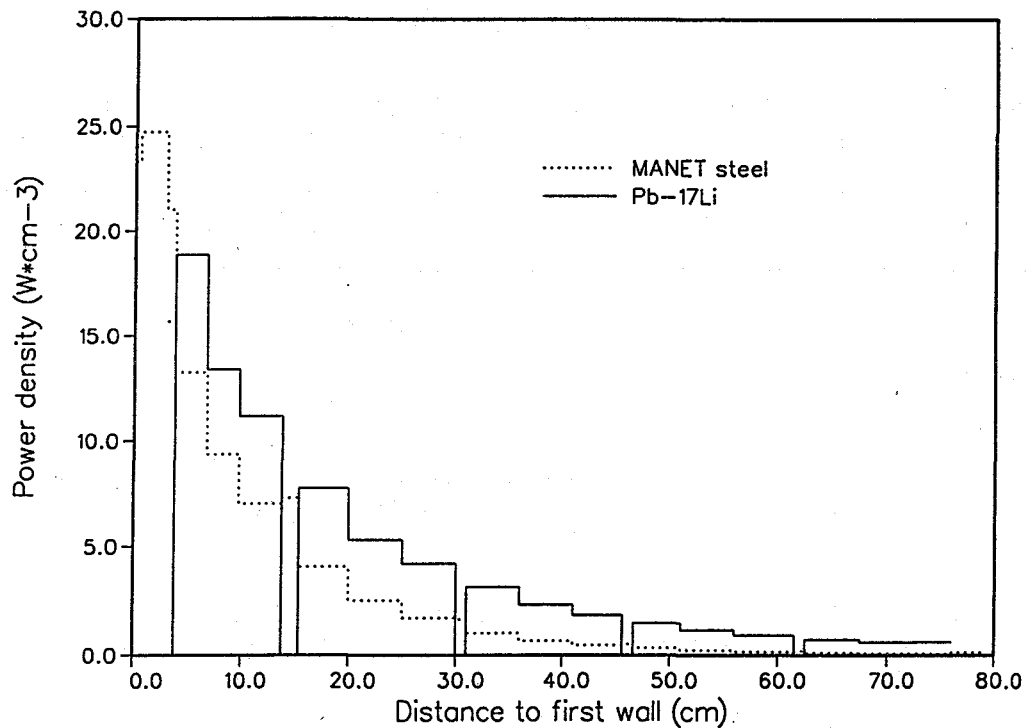


Fig. 4-4: Radial power profiles in the outboard segment

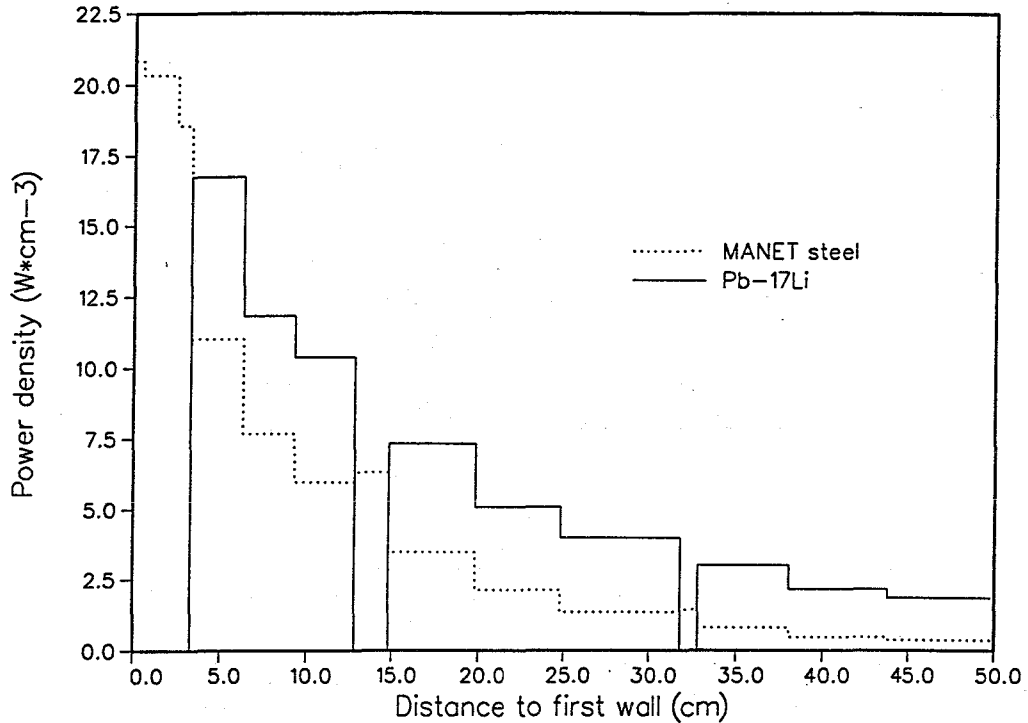


Fig. 4-5: Radial power profiles in the inboard segment

#### 4.5 Activation and afterheat calculations

A reliable assessment of the afterheat generation and the activation inventory in the blanket segments and the other reactor components requires the application of three-dimensional computational procedures. An appropriate code system has been developed that allows three-dimensional activation and afterheat calculations [4-10] by coupling the Monte Carlo transport code MCNP and the inventory code FISPACT [4-11], see Fig. 4-6.

Neutron fluxes and spectra are provided by 3D Monte Carlo calculations performed with the MCNP-code in the torus sector model of the DEMO-reactor. The neutron spectra are calculated in 175 energy groups (VITAMIN-J structure) in the first wall, the breeding zone and the back shield of the blanket segments, at the outboard and the inboard side and in the divertor regions. A fine radial segmentation scheme is applied covering 9 and 12 segments in the inboard and outboard blanket segments, respectively, to properly account for the variations of the neutron spectra and fluxes in the radial direction. The neutron spectra are provided for 5 poloidal segments both at the inboard and outboard side. Typically 1,000,000 source neutron histories are followed in the MCNP-calculation for the neutron spectra to assure a sufficient statistical accuracy.

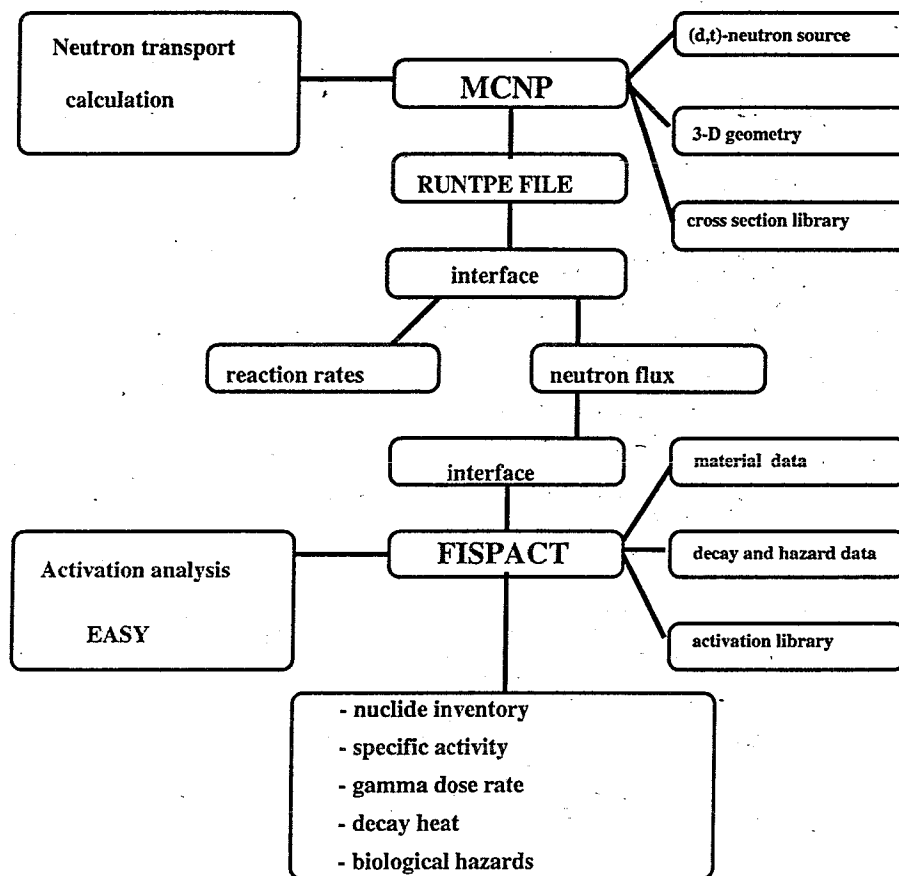


Fig. 4-6: Code system for activation and afterheat calculations

The spectra are routed to the FISPACT-code for performing the inventory calculations in each specified zone. FISPACT collapses the 175 group activation cross-sections of the European Activation File EAF-3 [4-12] to effective one group cross-sections by using the proper neutron spectra of the specified zones. The inventory calculations are performed step by step in running subsequent FISPACT-calculations for each zone and using the proper set of one-group activation cross-sections, neutron fluxes and material data associated to that zone. The individual results of the single zone inventory calculations are merged together to obtain the radial-poloidal distribution of the activation quantities of interest.

For calculating the afterheat generation and the activation product inventory an integral irradiation time of 20,000 hours at a fusion power of 2200 MW is assumed for the DEMO-reactor.

#### 4.5.1 Afterheat generation

The total afterheat power calculated for the individual materials in the blanket segments is given in Table 4-4 at reactor shut down ( $t=0$ ) and various cooling times. At reactor shutdown it typically amounts to 2 - 3 % of the direct power generation. At this time the Pb-17Li liquid metal contributes 60% and 75 % to the afterheat power in the inboard and outboard segments, respectively. The afterheat power of Pb-17Li is decreasing to a low level within a few seconds (Table 4-4) because it mainly originates from a short-lived metastable state ( $T_{1/2} = 0.8$  s) of the lead isotope  $^{207}\text{Pb}$ . After one minute the Pb-17Li contributes of the order of 10% to the total afterheat generation. At this time the dominant nuclides are  $^{204\text{m}}\text{Pb}$  ( $T_{1/2} = 67.2\text{m}$ ) and  $^{203}\text{Pb}$  ( $T_{1/2} = 51.9$  h). After one month the contribution of the Pb-17Li liquid metal to the total afterheat power is negligible.

Table 4-4 Afterheat generation [MW] of the individual materials in the blanket segments, results of 3D - activation calculations (2200 MW fusion power, 20,000h irradiation)

Time after shutdown	MANET steel		Pb-17Li		Total	
	Inboard 11.25° segment	Outboard 7.5° segment	Inboard 11.25° segment	Outboard 7.5° segment	Inboard 11.25° segment	Outboard 7.5° segment
0	1.95	0.187	0.281	0.578	0.476	0.765
1 min	0.191	0.182	1.36E-02	2.61E-02	0.205	0.208
1 h	0.140	0.131	8.25E-03	1.59E-02	0.148	0.147
1 d	1.53E-02	1.78E-02	1.44E-03	2.96E-03	1.67E-02	2.07E-02
1 month	1.13E-02	1.45E-02	4.88E-05	9.00E-05	1.14E-02	1.46E-02
1 y	5.46E-03	6.29E-03	1.01E-05	1.53E-05	5.47E-03	6.30E-03
5 y	1.48E-03	5.88E-04	3.20E-07	5.17E-07	1.48E-03	5.89E-04
10 y	6.89E-03	1.72E-04	1.16E-07	2.00E-07	6.89E-04	1.72E-04

Note that the afterheat share of the liquid metal is considerably larger at the outboard than at the inboard side. This is due to the fact that the Dual Coolant blanket provides large liquid metal volumes in the flow channels at the outboard side, resulting in a comparatively high activation of the liquid metal and a corresponding lower one of the MANET steel. As a consequence, the total afterheat power generation is comparatively low at the outboard side after a few seconds (see Table 4-4).

The decay heat power in MANET is constant over the time period of a few minutes after shutdown. It decreases by one order of magnitude after one day according to the half life of the main contributor  $^{56}\text{Mn}$  ( $T_{1/2} = 2.58$  h). Afterwards it is dominated by  $^{55}\text{Fe}$ ,  $^{54}\text{Mn}$  and  $^{60}\text{Co}$ . These radionuclides are mainly produced by activation reactions on the steel constituents  $^{56}\text{Fe}$ ,  $^{54}\text{Fe}$  and  $^{55}\text{Mn}$ , and  $^{60}\text{Ni}$ , respectively.

Note that the time behaviour is different for the MANET afterheat power at the inboard and outboard side. This is due to the fact that the afterheat generation at the outboard side is mainly in the blanket front region, whereas at the inboard side it originates to a larger extent from the blanket back region because of the smaller liquid metal breeder zone. In the back region the neutron spectrum is softer resulting in enhanced activation reactions of the  $(n,\gamma)$  - type, whereas threshold reactions like  $(n,2n)$  and  $(n,p)$  are dominating in the first wall region. In particular this leads to a significant generation of  $^{60}\text{Co}$  via the  $(n,\gamma)$  - reaction on  $^{59}\text{Co}$  in the back region, whereas in the front region  $^{60}\text{Co}$  is mainly produced by the threshold reaction  $^{60}\text{Ni}(n,p) ^{60}\text{Co}$ . As a consequence,  $^{60}\text{Co}$  ( $T_{1/2} = 5.27$  a) dominates the afterheat power in the MANET of the back region at intermediate term cooling times (about 1 to 10 years). For the MANET in the front region, the afterheat power is dominated by  $^{54}\text{Mn}$  ( $T_{1/2} = 312$  d) and  $^{55}\text{Fe}$  ( $T_{1/2} = 2.7$  a) at these cooling times, mainly originating from the threshold reactions  $^{54}\text{Fe}(n,p) ^{54}\text{Mn}$ ,  $^{55}\text{Mn}(n,2n) ^{54}\text{Mn}$  and  $^{56}\text{Fe}(n,2n) ^{55}\text{Fe}$ , respectively.

The maximum afterheat power densities at the torus mid-plane of the outboard blanket segment amount to 0.84 and 0.66 W/cm<sup>3</sup> for the MANET (first wall) and the Pb-17Li breeder (first 3 cm of the first liquid metal channel row, see Table 4-5) which correspond to 3.6% and 3.4% of the direct heating, respectively.

Table 4-5 Maximum afterheat power densities [W/cm<sup>3</sup>] in the blanket segments at torus mid-plane, results of 3D activation calculations (2200 MW fusion power, 20000 h irradiation)

Time after shutdown	First wall (steel)		Pb-17Li (first 3 cm)	
	Inboard	Outboard	Inboard	Outboard
0	0.742	0.843	0.536	0.664
1 min	0.721	0.819	1.98E-02	2.50E-02
1 h	0.518	0.588	1.23E-02	1.54E-02
1 d	6.98E-02	7.92E-02	2.88E-03	3.60E-03
1 month	5.85E-02	6.64E-02	6.90E-05	8.63E-05
1 y	2.52E-02	2.87E-02	6.32E-06	6.67E-06

#### 4.5.2 Activation product inventories

The activation product inventory accumulating during irradiation in general is strongly dependent on impurities and tramp elements included in the virgin materials. It is essential, therefore, to properly take into account in the activation calculations realistic estimates of the material impurities.

The elemental compositions used in the activation calculations for MANET and the lithium lead alloy are shown in Table 4-6. For the steel, the MANET-I specifications as given by Schirra et al. [4-13] were used. The Pb-17Li data were given by Metaux Speciaux for commercial lithium lead alloy [4-14].

Specific activities and contact  $\gamma$  - dose rates are shown in Figs. 4-7, 4-8 and Table 4-7 for the MANET of the first wall and the Pb-17Li in the front channel row of the outboard blanket segment at torus mid-plane. Note that the materials are exposed to the highest neutron fluence in the DEMO-reactor at these positions. The figures include graphs calculated with and without material impurities to assess this effect on the activation behavior of the MANET steel and the Pb-17Li alloy. The results shown in the tables are with impurities.

Table 4-6 Material compositions including impurities and trap elements [w%] used in the activation calculations

MANET-I [4-13]		Pb-17Li [4-13]	
Fe	86.68	Pb	99.2925
C	0.13	Li	0.7
Si	0.35	Zn	0.001
Mn	1.0	Fe	0.001
P	0.005	Bi	0.0043
S	0.004	Cd	0.0005
Cr	10.5	Ag	0.0005
Ni	0.85	Sn	0.0005
Mo	0.75	Ni	0.0002
V	0.20		
Nb	0.15		
B	0.008		
N	0.03		
Al	0.05		
Co	0.02		
Cu	0.02		
Zr	0.09		

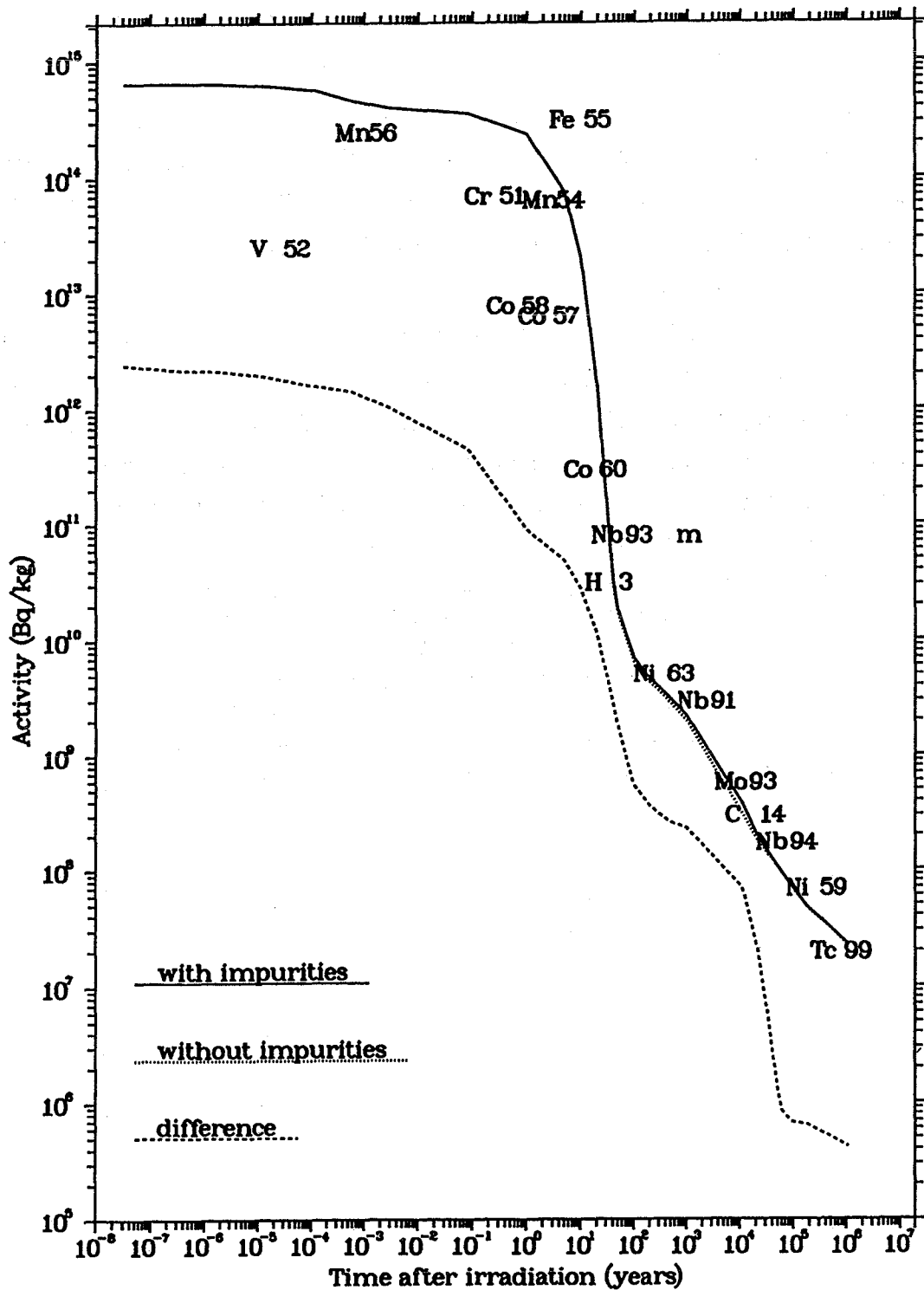


Fig. 4-7a Specific activity versus cooling time for MANET irradiated at the midplane of the outboard blanket FW

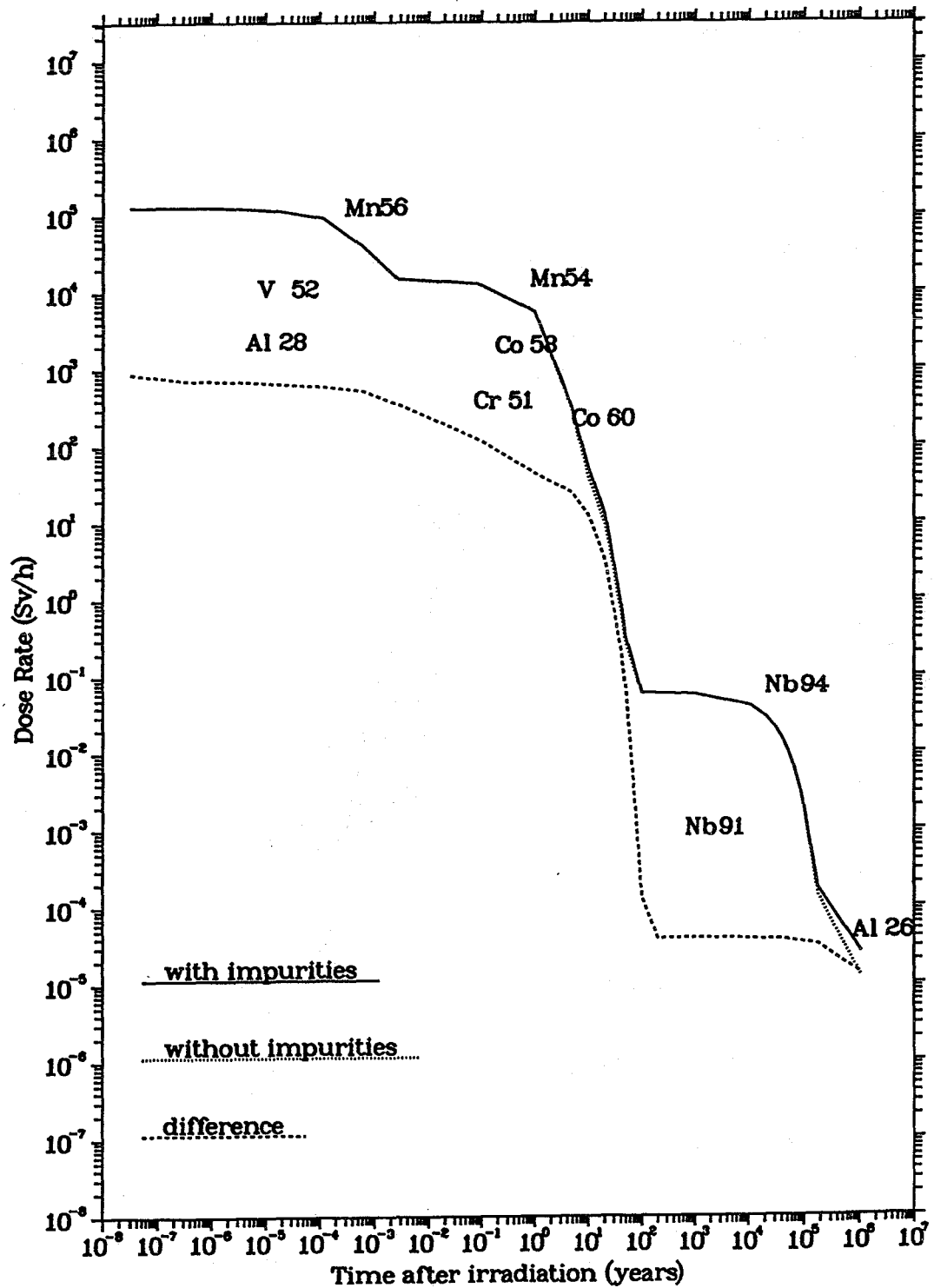


Fig. 4-7b Contact  $\gamma$ -dose rate versus cooling time for MANET irradiated at the midplane of the outboard blanket FW

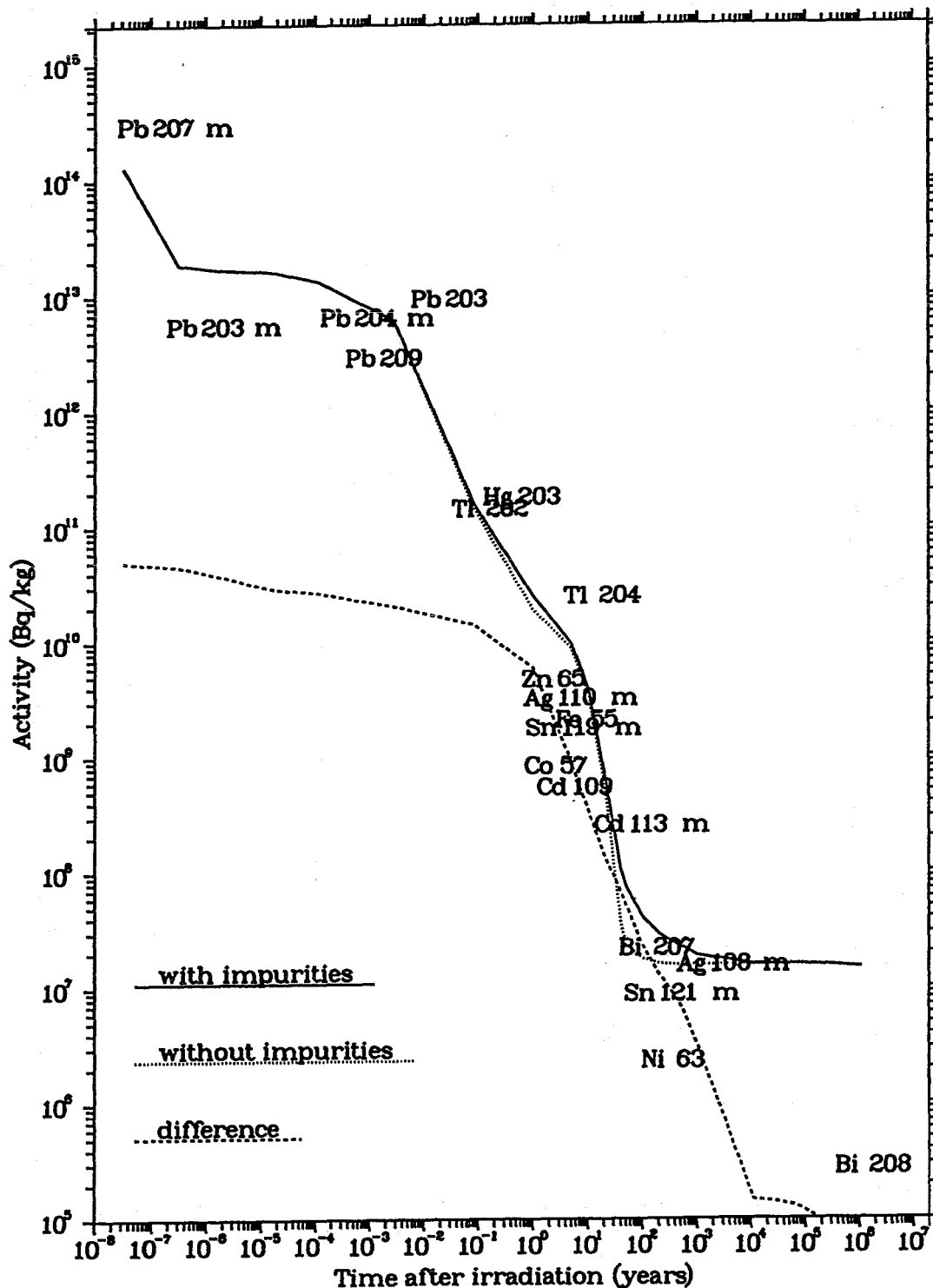


Fig. 4-8a Specific activity versus cooling time for Pb-17Li irradiated at the midplane of the outboard blanket FW

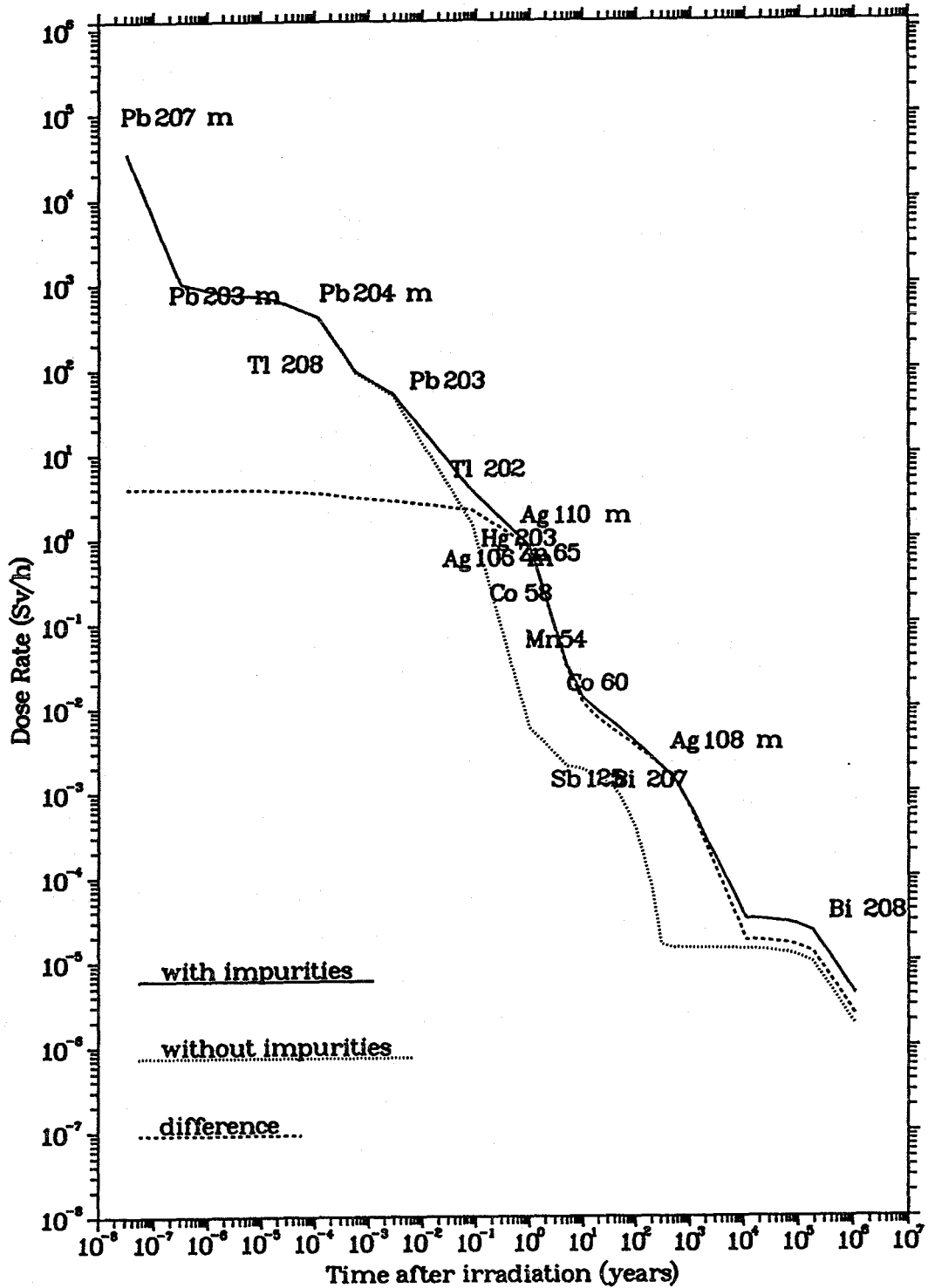


Fig. 4-8b Contact  $\gamma$ -dose rate versus cooling time for Pb-17Li irradiated at the midplane of the outboard blanket FW

**Table 4-7 Maximum specific activities and contact  $\gamma$ -dose rates in the central outboard blanket segment, results of 3D activation calculations (2200 MW fusion power, 20000 h irradiation)**

Time after shutdown	First wall (steel)		Pb-17Li (first 3 cm, without tritium)	
	Specific activity [Bq/kg]	Contact $\gamma$ -dose rate [Sv/h]	Specific activity [Bq/kg]	Contact $\gamma$ -dose rate [Sv/h]
0	6.54E+14	1.30E+05	2.79E+14	8.13E+04
1 min	6.46E+14	1.27E+05	1.72E+13	7.94E+02
1 h	5.69E+14	9.37E+04	1.35E+13	4.20E+02
1 d	4.01E+14	1.50E+04	6.25E+12	5.22E+01
1 month	3.54E+14	1.29E+04	1.60E+11	3.69E+00
1 y	2.34E+14	5.52E+03	2.48E+10	8.08E-01
10 y	2.06E+13	5.22E+01	3.82E+09	1.31E-02
50 y	1.79E+10	3.10E-01	7.37E+09	5.67E-03
100 y	7.01E+09	5.88E-02	4.05E+07	3.83E-03
500 y	3.02E+09	5.74E-02	2.26E+07	1.47E-03

The total activation product inventory (Table 4-8) is largely dominated by the MANET steel. The Pb-17Li breeder contributes significantly to the total activation product inventory solely for short term cooling times (up to a few days after shutdown). The contributing radionuclides are the short-lived lead activation products  $^{207m}\text{Pb}$  ( $T_{1/2} = 0.8$  s),  $^{204m}\text{Pb}$  ( $T_{1/2} = 67.2$  m) and  $^{203}\text{Pb}$  ( $T_{1/2} = 51.9$  h). At intermediate term cooling times (1 to 50 years) the activation inventory of Pb-17Li in terms of Bq/kg is dominated by the tritium generated in that liquid metal breeder. The tritium contribution, however, is not included in the data and figures given for Pb-17Li. At long term cooling times (more than 100 years) the activation inventory of Pb-17Li is dominated by  $^{205}\text{Pb}$  ( $T_{1/2} = 1.5 \cdot 10^7$  a). The activation products of the assumed lead impurities do not significantly contribute to the activity of Pb-17Li in terms of Bq/kg.

For the MANET steel, both the activation inventory, the contact  $\gamma$  - dose rate and the radiological hazard potential are not significantly affected by impurities. Major contributors to the  $\gamma$  - dose rate of MANET are  $^{54}\text{Mn}$  and  $^{56}\text{Mn}$  (activation products mainly of  $^{54}\text{Fe}$  and  $^{56}\text{Fe}$ , respectively, and of  $^{55}\text{Mn}$ , secondly) at short term,  $^{60}\text{Co}$  (activation product mainly of  $^{60}\text{Ni}$ , and of  $^{59}\text{Co}$ , secondly) at medium term

Table 4-8 Total activity inventories [Bq] in the blanket segments, results of 3D activation calculations (2200 MW fusion power, 20000 h irradiation)

Time after shutdown	MANET steel		Pb-17Li		Total	
	Inboard 11.25° segment	Outboard 7.5° segment	Inboard 11.25° segment	Outboard 7.5° segment	Inboard 11.25° segment	Outboard 7.5° segment
0	9.57E+17	1.10E+18	1.12E+18	2.25E+18	2.07E+18	3.35E+18
1 min	9.43E+17	1.08E+18	8.84E+16	1.69E+17	1.03E+18	1.25E+18
1 h	7.78E+17	9.41E+17	6.75E+16	1.30E+17	8.45E+17	1.07E+18
1d	4.54E+17	6.48E+17	2.34E+16	4.82E+16	4.77E+17	6.96E+17
1month	3.64E+17	5.62E+17	6.10E+14	1.23E+15	3.64E+17	5.64E+17
1y	2.31E+17	3.69E+17	1.10E+14	2.09E+14	2.31E+17	3.69E+17
10y	2.16E+16	3.24E+16	1.26E+13	2.64E+13	2.16E+16	3.25E+16
50y	5.56E+13	4.52E+13	5.21E+11	8.99E+11	5.62E+13	4.61E+13
100y	2.69E+13	1.85E+13	3.06E+11	5.17E+11	2.72E+13	1.90E+13
500y	9.78E+12	7.39E+12	1.63E+11	2.78E+11	9.94E+12	7.66E+12

and  $^{94}\text{Nb}$  and  $^{26}\text{Al}$  (activation products of  $^{93}\text{Nb}$  and  $^{27}\text{Al}$ , respectively) at long term cooling times.

At medium and long term cooling times (more than one year after shutdown) both the contact  $\gamma$  - dose rate and the radiological hazard potential of Pb-17Li are dominated by activation products of the assumed material impurities. Major contributors to the  $\gamma$  - dose rate at medium term cooling times are  $^{110}\text{mAg}$  ( $T_{1/2} = 250$  d),  $^{65}\text{Zn}$  ( $T_{1/2} = 244$ d) and  $^{60}\text{Co}$  ( $T_{1/2} = 5.27$ a) and the lead isomer  $^{207}\text{mPb}$  ( $T_{1/2} = 0.8$  s). The formation of  $^{207}\text{mPb}$  at this time scale is by electron capture decay of  $^{207}\text{Bi}$  ( $T_{1/2} = 33.4$  a) being mainly an activation product of the assumed  $^{209}\text{Bi}$ -impurity. At long term cooling times the  $\gamma$  - dose rate is dominated by  $^{108}\text{mAg}$  ( $T_{1/2} = 127$  a), while there is still a significant contribution by  $^{207}\text{mPb}$ .

As a consequence of the assumed material impurities, the Pb-17Li  $\gamma$  - dose rate does not fall below the hands on level limit of  $25 \mu\text{Sv/h}$ . Note that this holds for the highest loaded liquid metal in the first channel row (first 3 cm) of the outboard blanket at torus mid-plane. In the activation calculation it is assumed that the liquid metal is irradiated continuously over the integral operation time of 20,000 hours. Actually, the liquid metal is circulating permanently, inside and outside the radiation field, during reactor operation, and, therefore, the actual fluence to the liquid metal will be considerably smaller. This effect, however, is

not taken into account in the activation calculation resulting in a corresponding overestimation of the calculated  $\gamma$  - dose rate. Likewise, this holds for the calculated specific activity of Pb-17Li, whereas the total activity inventory is not affected in a first approximation.

Special care has been devoted to a reliable assessment of the generation of the radiotoxine  $^{210}\text{Po}$  in the Pb-17Li liquid metal [4-15] because of its high radiological hazard potential.  $^{210}\text{Po}$  ( $T_{1/2} = 138$  d) dominates the short term (up to about 2 year after shutdown) radiological hazard potential of irradiated Pb-17Li. It is formed both as lead activation product through the reaction chain  $^{208}\text{Pb}(n,\gamma)^{209}\text{Pb}(\beta^-, T_{1/2} = 3.5 \text{ h})^{209}\text{gBi}(n,\gamma)^{210}\text{Bi}(\beta^-, T_{1/2} = 5.0 \text{ d})^{210}\text{Po}$  and as activation product of the Bi-impurity contained in the Pb-17Li alloy, starting from  $^{209}\text{Bi}$  in that case. Thus the  $^{210}\text{Po}$  production depends on the Bi-impurity content of the Pb-17Li on one hand, and in a very sensitive way on the irradiation conditions on the other hand.

In checking the involved cross-section data it was recognized that the UKACT1 data library [4-16] contained unphysical cross-sections for the  $^{208}\text{Pb}(n,\gamma)^{209}\text{Pb}$  reaction. The UKACT1 data was most likely the result of simple model calculations performed earlier for the ACTL activation library [4-17]. Both the REAC [4-18] and the UKACT1 activation data libraries made use of these data. The more recent EFF-3 and ENDF/B-VI data libraries provide more reliable  $^{208}\text{Pb}$  cross-section data evaluations that rely on the use of experimental data. The ACTL-based  $^{208}\text{Pb}$  cross-section had led to large overestimations (by a factor of 5 to 10) of the calculated  $^{210}\text{Po}$  inventory in previous assessments when comparing to activation calculations with the more reliable EFF and ENDF/B-VI data

In calculating the  $^{210}\text{Po}$  inventory for the Dual Coolant blanket, it is necessary to take into account the liquid metal circulation. This is due to the  $^{210}\text{Po}$  production pathway involving two sequential  $(n,\gamma)$ -reactions when starting from  $^{208}\text{Pb}$  and, therefore, leading to a quadratic dependence on the neutron flux for the accumulating  $^{210}\text{Po}$  inventory. To cope with this, the following approach has been followed.

In a first step, the internal liquid metal circulation is simulated, i. e. the circulation in the irradiation field inside the blanket segment at power operation. For this purpose the irradiation time is subdivided into a large number of irradiation intervals. At the end of each interval the liquid metal masses are blended according to their actual volume fractions. Irradiation is continued then for the next time interval by using the properly blended liquid metal of the previous irradiation step.

In a second step, the external liquid metal circulation is simulated, too. Essentially, the same blending procedure is applied. In addition, the total liquid metal mass inventory is increased by a factor 3, whereas the irradiation time is reduced to 1/3 of the total one. In this way it is accounted for that 2/3 of the total liquid metal inventory is permanently outside and 1/3 inside the irradiation field.

Table 4-9 shows the resulting  $^{210}\text{Po}$  activity inventories and specific activities for the different blending modes obtained with ENDF/B-VI cross-section data. There is included a static case where the liquid metal is kept stationary during irradiation, i. e. no blending is applied as it is generally assumed for activation calculations. In addition, the effect of varying initial Bi-impurities has been analysed for the different blending modes.

In simulating the internal liquid metal circulation, the calculated  $^{210}\text{Po}$  activity (both the total inventory and the specific activity) is reduced by about 40% with regard to the static case and no initial bismuth present. The reduction is less with higher initial bismuth content, i. e. the more the single  $^{209}\text{Bi}(n,\gamma)^{210}\text{Bi}$  transition contributes to the  $^{210}\text{Po}$  production path. Taking into account the external liquid metal circulation results in a reduction of the specific  $^{210}\text{Po}$  activity by one order of magnitude with regard to the static case (no initial bismuth). The total  $^{210}\text{Po}$  activity inventory is lower only by a factor 3 because of the larger liquid metal mass inventory involved in that case.

Table 4-9 Calculated  $^{210}\text{Po}$  activity inventories and concentrations for different liquid metal blending modes, results of 3D activation calculations using ENDF/B-VI cross-section data (2200 MW fusion power, 20000 h irradiation)

Initial Bi [appm]		Static liquid metal	Internally circulated liquid metal	Externally circulated liquid metal
0	Total activity [Ci]	$8.31 \cdot 10^3$	$5.05 \cdot 10^3$	$2.71 \cdot 10^3$
	Specific activity [Ci/kg Pb]	$1.75 \cdot 10^{-3}$	$1.06 \cdot 10^{-3}$	$1.90 \cdot 10^{-4}$
10	Total activity [Ci]	$1.25 \cdot 10^4$	$9.21 \cdot 10^3$	$1.22 \cdot 10^4$
	Specific activity [Ci/kg Pb]	$2.63 \cdot 10^{-3}$	$1.94 \cdot 10^{-3}$	$8.52 \cdot 10^{-4}$
100	Total activity [Ci]	$5.0 \cdot 10^4$	$4.67 \cdot 10^4$	$9.83 \cdot 10^4$
	Specific activity [Ci/kg Pb]	$1.05 \cdot 10^{-2}$	$9.80 \cdot 10^{-3}$	$6.89 \cdot 10^{-3}$

The effect of initial Bi-impurities on the  $^{210}\text{Po}$  activity inventory is dependent on the blending mode for the liquid metal and the impurity level itself. There is a linear increase of the  $^{210}\text{Po}$  activity inventory by about  $4.2 \cdot 10^3$  Ci per 10 appm Bi both in the internally circulated and the static liquid metal case, and an increase by about  $9.5 \cdot 10^3$  Ci in case of the externally circulated liquid metal. Thus the Bi-impurity effect becomes dominant above 20-30 appm initial bismuth content in the internally circulated and the static liquid metal case, but is dominant at all impurity levels in case of the externally circulated liquid metal.

The increase of the Bi-content in the irradiated Pb-17Li alloy amounts to about 4.4 appm in case of the externally circulated liquid metal, which is the most realistic case for the Dual Coolant blanket. Thus it would be beneficial to keep the bismuth content of the Pb-17Li alloy well below this level. This would require an on-line purification at about 1-2 appm bismuth. In view of the very low polonium release fractions found experimentally for Pb-17Li [4-19], it is questionable, however, if this is really necessary.

For accident scenarios with activation product release from Pb-17Li, the low polonium evaporation fraction results in a nearly negligible contribution of  $^{210}\text{Po}$  to the early dose (see Section 11.4). In contrast, the radiological consequences to the public are governed by the release of the mercury isotope  $^{203}\text{Hg}$  ( $T_{1/2} = 46.6$  d). It is the major contributor to the early dose only due to its high evaporation fraction.  $^{203}\text{Hg}$  is a lead activation product that mainly originates from the  $^{206}\text{Pb}(n,\alpha)^{203}\text{Hg}$  reaction. At short cooling times (several months) it dominates the activity and afterheat of the irradiated Pb-17Li. The  $\gamma$  dose rate and the radiological hazard potential are dominated by  $^{110m}\text{Ag}$ ,  $^{202}\text{Tl}$  and  $^{210}\text{Po}$ , entirely covering the  $^{203}\text{Hg}$  contribution.

#### 4.6 Shielding analysis

The superconducting TF-coils have to be shielded properly against the radiation originating from the fusion plasma to allow a reliable operation of the DEMO-reactor over its lifetime. During the ITER conceptual design activity (CDA) phase, radiation load limits have been elaborated for the dose to the electrical insulator, the displacement damage in the copper stabiliser, the fast neutron fluence to the  $\text{Nb}_3\text{Sn}$  superconductor, the peak nuclear heating in the winding pack and the total nuclear heating in the TF-coil [4-20]. Sufficient shielding needs to be provided to ensure that these limits are not exceeded over the lifetime of the supercon-

ducting magnets which is assumed to be at 10 full power years for the DEMO-reactor.

The shielding efficiency of a breeding blanket in general is poor. In case of the Dual Coolant blanket, the total neutron flux decreases from  $1.5 \cdot 10^{15} \text{ cm}^{-2}\text{s}^{-1}$  at the inboard first wall to  $6.4 \cdot 10^{14} \text{ cm}^{-2}\text{s}^{-1}$  at the blanket back wall, i. e. by not more than a factor 2.3 across the blanket breeding zone with a thickness of 40 cm. Therefore, sufficient shielding has to be provided by shielding materials arranged between the toroidal field (TF) coil and the blanket segments. Actually, the vacuum vessel is assumed - and can be designed - for performing the function of a permanent radiation shield. In addition, the residual space between the vacuum vessel and the breeding zone can be utilised for shielding. According to the DEMO blanket specifications, a removable steel shield attached to the blanket segment, i. e. being an integral part of that, should be assumed for assessing the shielding efficiency of the breeding blankets.

At the inboard side radiation shielding is most crucial due to the restricted space available for the shielding components. According to the DEMO blanket specifications, the total space available to the inboard blanket/shielding system amounts to 115 cm with regard to the radial thickness. The vacuum vessel, acting as major shielding component, is 30 cm thick. Thus a thickness of 85 cm is left for the blanket segment. The Dual Coolant blanket needs 55 cm for the breeder blanket segment including 14.5 cm for the helium manifolds at the back of the blanket. Therefore, 30 cm of the space available for the blanket can be used for providing additional shielding. Table 4-10 shows the radial build and the material compositions used in the shielding calculations.

The shielding calculations were performed for the inboard side of the DEMO-reactor applying the 3D torus sector model developed for the Dual Coolant blanket. Importance sampling techniques available with the MCNP-code - geometry splitting with Russian Roulette and manually optimised particle weights - have been used to direct the neutron and photon radiation through the blanket/shield system. Typically 100,000 source neutron histories have been tracked to attain statistical reliable scorings for the nuclear responses in the TF-coil.

The radiation loads to the TF-coil were obtained by making use of the MCNP surface tally (fast fluence, insulator dose, copper damage, heating rate) and the track length tally estimators (radial distribution of total and fast neutron fluxes). An integral operation time of 10 years was assumed in calculating the radiation doses and fluences.

**Table 4-10: Radial build of the inboard blanket/shield system at torus mid-plane used for the Monte Carlo shielding calculations.**

Radial dimension [cm]	Thickness [cm]	Component	Material	
225.	80.0	TF-coil	TF-coil mixture	
305.	5.0	Magnet casing	SS-316 steel	
	5.0	Gap TF-coil/VV	Void	
315.	11.0	Vacuum vessel	SS-316 steel	
326.	5.0		Borated water	
331.	7.0		SS-316 steel	
338.	2.0		Borated water	
340.	5.0		SS-316 steel	
345.				
	2.4		Gap	Void
374.4	30.9	Removable shield	MANET/ZrH	
378.3				
392.8	14.5	Manifold	64% MANET	
	4.2	Steel wall	MANET	
397.0	33.5	Breeding blanket	Pb-17Li/MANET	
430.5				
433.0	2.5	First wall	MANET/He	

Table 4-11 compares the resulting radiation loads to the inboard TF-coil at torus mid-plane with the allowed limits. For the reference calculation, a simple helium-cooled steel plate is assumed as additional shield. As expected, the required limits of the most crucial radiation loads, i. e. the dose to the electrical insulator and the fast neutron fluence to the Nb<sub>3</sub>Sn superconductor, cannot be met by the simple standard shield configuration.

Table 4-11: Radiation loads to the inboard TF-coil at torus mid-plane, results of three-dimensional Monte Carlo shielding calculations (2200 MW fusion power, 10 full power years operation)

	Radiation load limits [4-20]	3D shielding calculation Dual coolant blanket	
		Reference shield design (steel plate option)	ZrH shield option (50 % ZrH, 50 % steel)
Peak dose to electrical insulator (Epoxy) [rad]	5·10 <sup>9</sup>	3.7·10 <sup>10</sup>	7.5·10 <sup>8</sup>
Peak displacement damage to copper stabiliser [dpa]	6·10 <sup>-3</sup>	5.7·10 <sup>-3</sup>	4.6·10 <sup>-4</sup>
Peak fast neutron fluence (E > 0.1 MeV) to the Nb <sub>3</sub> Sn superconductor [cm <sup>-2</sup> ]	1·10 <sup>19</sup>	1.5·10 <sup>19</sup>	1.0·10 <sup>18</sup>
Peak nuclear heating inwinding pack [mWcm <sup>-3</sup> ]	5.0	3.2	0.04

The shielding efficiency of the total system blanket/shield can be improved by optimising the design of the additional shield and /or the vacuum vessel with regard to the shielding performance. No attempt has been made in this analysis, however, to perform a shielding optimisation. Instead, the efficient solid neutron moderator ZrH<sub>1.7</sub> was integrated into the removable steel shield at high volume fractions (50%). Note that this simple technical measure is sufficient to attain the radiation load limits (Table 4-11) without modifying the vacuum vessel design.

Figures 4-9 and 4-10 show the radial distribution of the fast (E > 0.1 MeV) and the total neutron flux density across the inboard blanket/shielding system at torus mid-plane. It is obvious that there is large room for optimising the shielding efficiency by modifying the vacuum vessel design. In particular, a significant im-

provement can be achieved by integrating an efficient neutron/photon shield (e.g.  $B_4C$  /lead) at the back of the vacuum vessel. The use of an additional neutron moderator thus could be avoided by designing the vacuum vessel as optimal radiation shield.

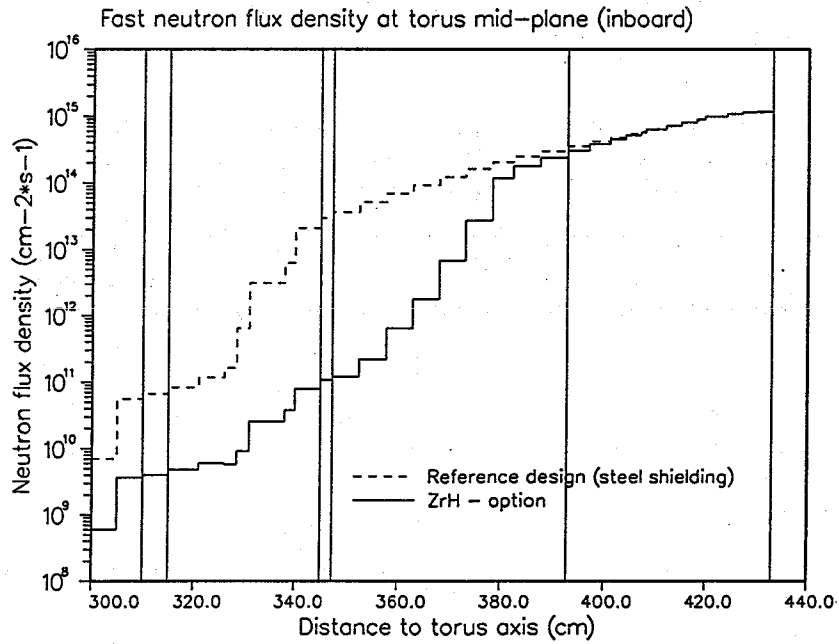


Fig. 4-9: Fast neutron flux ( $E > 0.1$  MeV) at torus mid-plane (inboard)

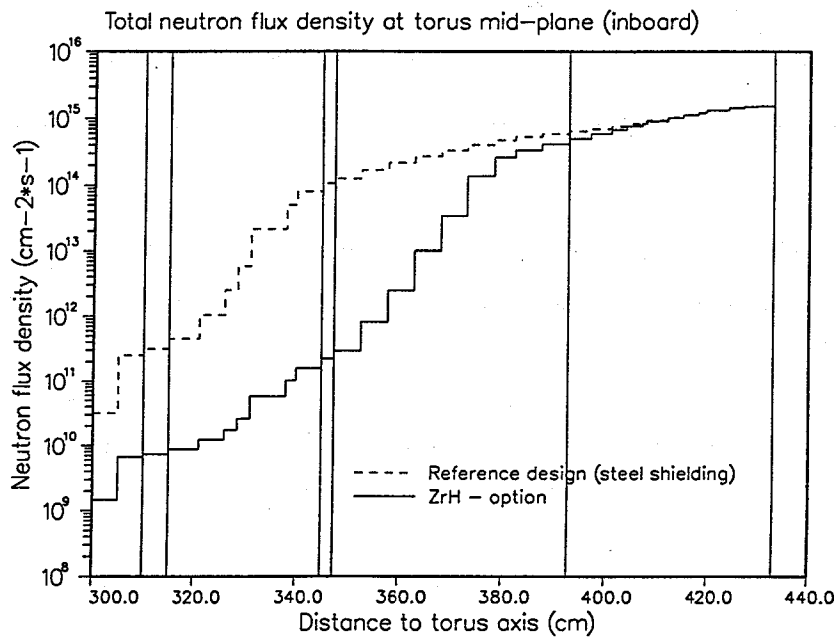


Fig. 4-10: Total neutron flux at torus mid-plane (inboard)

## References

- [4-1] S. Malang et al.: Liquid Metal Cooled Blanket for NET, Proc. 14. Symp. Fusion Technology, 8-12 September 1986, Avignon, France, 1273-1280.
- [4-2] S. Malang, K. Arheidt, U. Fischer.: Test Module in NET for a Self-cooled Liquid Metal Blanket Concept, Proc. 15. Symp. Fusion Technology , 19-23 September 1988, Utrecht, The Netherlands, 1223-1228.
- [4-3] S. Malang et al.: Dual Coolant Liquid Metal Breeder Blanket, Proc. 17. Symp. Fusion Technology , 14-18 September 1992, Rome, Italy, 1424-1428.
- [4-4] J. F. Briesmeister (Ed.): MCNP - A General Monte Carlo Code for Neutron and Photon Transport, Version 3A, Report LA-7396-M, Rev. 2, Sept. 1986
- [4-5] P. Vontobel: A NJOY Generated Neutron Data Library Based on EFF-1 for the Continuous Energy Monte Carlo Code MCNP, PSI-Bericht Nr. 107, September 1991.
- [4-6] K. A. Verschuur: Poloidal Variation of the NET Blanket Nuclear Response Functions, Report ECN-87-011 (1987).
- [4-7] U. Fischer: Qualification of Neutronic Blanket and Shielding Calculations in a One-dimensional Approach to a Tokamak Reactor, Fusion Technology 22 (1992), 251-270.
- [4-8] S. Malang, J. Reimann, H. Sebening (comp.): Status Report KfK Contribution to the Development of Demo-relevant Blankets for NET/ITER, Part 1: Self-cooled Liquid Metal Breeder Blanket, Volumes 1 and 2, KfK- 4907, - 4908, Dezember 1991.
- [4-9] U. Fischer: Impact of Ports on the Breeding Performance of Liquid Metal and Solid Breeder Blankets in the DEMONET Configuration, Fusion Engineering and Design 18 (1991), 323-329.
- [4-10] H. Tsigé-Tamirat, U. Fischer: Three-dimensional Activation and Afterheat Analysis for the Dual Coolant Liquid Metal Breeder Blanket, FZKA-report, to appear.
- [4-11] R. A Forrest, J.-Ch. Sublet: FISPACT3 - User Manual, AEA/FUS/227, April 1993.
- [4-12] J. Kopecky, H. A. J. van der Kamp, H. Gruppelaar, D. Nierop: The European Activation File EAF-3 with Neutron Activation and Transmutation Cross Sections, ECN-C-92-058 , September 1992.
- [4-13] M. Schirra et al.: Untersuchungen zum Vergütungsverhalten, Umwandlungsverhalten und der mechanischen Eigenschaften am martensitischen Stahl 1.4914 (NET-Charge MANET-1), KfK-4561, Juni 1989.
- [4-14] J.-Ch. Sublet: Elemental composition of structural materials including impurities and tramp elements, SEAFP/R-A6/2(93), October 1993.
- [4-15] U. Fischer, E. Wiegner: Production of  $^{210}\text{Po}$  in Pb-17Li: Assessment of Methodological and Data Related Uncertainties, 17. Symposium on Fusion Technology, Rome, Italy, September 14-18, 1992.
- [4-16] R. A. Forrest et al.: The Data Library UKACT1 and the Inventory Code FISPACT, Int. Conf. Nuclear Data for Science and Technology , Mito, Japan, 1988.
- [4-17] M.A. Gardner, R.J. Howeston: ACTL Evaluated Neutron Activation Cross Section Library, UCRL-50400, Vol. 18, Oct. 1978.

- [4-18] F. Mann, et al.: REAC Nuclear Data Libraries, Int. Conf. on Nuclear Data for Basic and Applied Science, Santa Fe, New Mexico, USA, 1985.
- [4-19] H. Feuerstein et al.: Behaviour of Po-210 in molten Pb-17Li, 5. Int. Conf. Fusion Reactor Materials, Clearwater, Florida, USA, November 17-22, 1991.
- [4-20] W. Dänner et al.: Neutron Shielding and its Impact on the ITER Machine Design, Fus. Eng. Design 16 (1991), 183-193.

## **5. Magnetohydrodynamics (MHD) of Liquid Metal Flow**

### **5.1 Introduction**

Perhaps the most important concern for liquid metal blankets is magnetohydrodynamic (MHD) effects and their influence on thermal hydraulics and corrosion. A liquid metal flowing through a high magnetic field experiences an electromagnetic body force which strongly alters the flow behavior. The MHD influence increases the pressure drop through the blanket, resulting in higher stress levels and higher pumping power requirements and could, if countermeasures are not taken, even lead to prohibitively high pressure losses. At most conditions of interest to fusion, MHD effects overwhelm the viscous and inertial effects, resulting in suppression of the normal turbulence and radically altered flow profiles. The altered flow patterns will affect the heat transfer characteristics and possibly the corrosion rates of the insulation layers on the duct walls.

Concerns about MHD effects arise not only due to the limits placed on blanket operating parameters, but also due to potentially large uncertainties. In the 1980's, the level of understanding of MHD phenomena in liquid metal blankets was not sufficient, primarily based on simple empirical correlations and heuristic arguments. While the basic equations for fluid mechanics and electromagnetics have been known for many years, the lack of fundamental understanding of the way the fluid behaves in complex fusion-relevant geometries was a critical issue for this class of blankets. Due to the efforts associated with the work described here, as well as increased efforts on self-cooled liquid metal blankets worldwide, the state of our understanding and predictive capabilities for MHD flow and heat transfer has grown enormously. Data and three-dimensional numerical solutions have been obtained for most of the geometric elements of blankets under laminar flow conditions, including bends, cross-section changes, multiple-duct arrays and manifolds. A general-purpose core flow code has been developed and extensively validated against experimental data, further increasing confidence in our ability to accurately predict thermal-hydraulic behavior of blankets.

The leading designs for self-cooled liquid metal blankets are driven by the need to accommodate MHD-related effects while maintaining the advantages of design simplicity, reliability and extended lifetime [5-1 to 5-5]. The different design options described in Chapter 2 embody different geometric features, and hence varying types and levels of MHD interaction. In the final reference design, with

He-cooling of the first wall and simple poloidal ducts, the interaction of the field with the flow is relatively simple to model. Improved understanding of the MHD behavior of the alternate design provides sound back-up options if the reference dual-coolant design is found to be inadequate for any reason. Hence, through a combination of simplified design approaches and substantially reduced uncertainties in MHD behavior, liquid metal cooled designs have been shown to offer attractive thermal-hydraulic performance.

In this chapter, we summarize the status of research to characterize and provide reliable predictive capabilities for MHD fluid flow and heat transfer. Section 5.2 contains a summary of the governing equations and a simple description of MHD issues and phenomena. Section 5.3 summarizes the numerical solution methods used, and Section 5.4 describes the experimental facilities and diagnostics developed to support research on blanket MHD. Section 5.5 provides detailed results describing an extensive R&D program on liquid metal MHD flow carried out during the past 5 years. Sections 5.6 and 5.7 describe modeling techniques and experiments performed on heat transfer in MHD flow, including consideration of "two-dimensional MHD turbulence", which could significantly improve heat transfer as compared with the normally laminar flow profiles. Finally, in Section 5.8 the tools for MHD and heat transfer are used to analyze the reference Dual-Coolant blanket concept.

## 5.2 Overview of MHD phenomena and solution methods

### 5.2.1 Discussion of MHD design issues

The main issue in designing self-cooled blankets is the cooling of the plasma facing first wall under high heat load. Material properties limit the allowable temperature of the first wall to about 550 °C for ferritic steel and 750°C for vanadium alloys. The maximum temperature at the wall/liquid metal interface has to be maintained approximately 100 °C lower in order to limit corrosion of the structure material by the liquid metal. For effective electricity production, the bulk temperature of the coolant at the blanket outlet should be higher than 400 °C. The coordination of these contrasting requirements form the actual design task. The design limitations can be expressed in terms of an upper and lower limit for the coolant channel pressure drop to ensure structural integrity and sufficient flow rate for heat removal.

Assuming laminar slug flow in the first wall coolant ducts and a developing thermal boundary layer for the whole heated channel length  $L$  and no electrical or heat contact resistances at the fluid/wall interface the following relation can be derived for straight poloidal ducts with thin conducting walls [5-6, 5-7].

$$\frac{4\beta q''^2 L^2}{a \Delta T_w^2 \cdot F_{V,TW}} \frac{\sigma_w t_w}{\pi k_f \rho c_p} B_{\perp}^2 \leq \Delta p. \quad (5.1.1)$$

The pressure drop  $\Delta p$  has to fulfill the relation:

$$\Delta p \leq \frac{t_w \cdot S_{al.}}{a} \quad \text{for circular} \quad (5.1.2)$$

$$\Delta p \leq \frac{t_w^2 \cdot S_{al.}}{3a^2} \quad \text{for rectangular cross-sections} \quad (5.1.3)$$

$\Delta p$  denotes the pressure drop in the duct,  $q''$  the first wall heat flux,  $\Delta T_w$  temperature rise along the first wall of the front cooling channel,  $F_{V,TW}$  a factor tak-

ing into account deviations of the velocity profile from slug flow in thin walled (TW) channels (for slug flow  $F_{V,TW} = 1$ ),  $\beta$  a factor taking into account nonconstant heat flux distribution over the heated wall of the front channel ( $\beta = 1$  for rectangular cross-section),  $\sigma_w$  and  $\sigma$  the electrical conductivities of the duct wall and of the fluid,  $k_f$  the heat conductivity of the fluid,  $\rho$  the density,  $c_p$  the specific heat,  $S_{al}$  the allowable wall stress,  $a$  the half duct width in field direction,  $t_w$  the wall thickness and  $B_{\perp}$  the magnetic induction component perpendicular to the flow.

It is obvious that any design should aim at minimizing the coolant pressure drop and simultaneously achieving the largest possible bulk temperature rise. Guidelines for this procedure can easily be derived from relation (5.1.1). There are two crucial consequences of this relation: As the pressure drop increases linearly with the wall thickness the mechanical stresses in the wall can not be reduced by increasing the wall thickness, because this would increase the pressure drop and thus the overall pressure load in the same way. The minimum required pressure drop to ensure a sufficient coolant flow rate in the first wall coolant channel is controlled by the surface heat flux  $q''$ , the heated channel length  $L$  and the allowed coolant temperature increase  $\Delta T_w$ . Taking into account the limiting conditions of a fusion power blanket, relation (5.1.1) shows clearly that liquid metal cooling of the first wall by simple poloidal conduits without any reduction of the MHD effective wall thickness or any electrical insulation of the duct walls or heat transfer enhancement e.g. by turbulence promotion would either lead to unacceptable high temperatures or to mechanical stresses beyond achievable limits. (Typical values of the parameters used in eq. 5.1.1 are  $\Delta T_w = 100$  °C,  $q'' = 0.25$  MW/m<sup>2</sup>,  $L = 8$  m,  $a = 0.2$  m,  $t_w = 6$  mm,  $B = 5$  T, and  $S_{al} = 100$  MPa). Such a reduction of the MHD effective wall thickness can be achieved by the technique of flow channel inserts (FCI) described in Section 5.5.6.

If the duct walls are electrically insulated the dependence of the pressure drop on the thickness of the duct walls drops out. In this case the following relation holds:

$$\frac{4\beta q''^2 L^2}{a \cdot \Delta T_w^2 \cdot F_{V,Ins.}} \cdot \frac{\sqrt{\sigma \rho v}}{\pi k_f \rho c_p} \cdot B_{\perp} \leq \Delta p \quad (5.1.4)$$

where  $F_{V,Ins.}$  is a factor for the deviations from slug flow in electrically insulated channels ( $F_{V,Ins.} = 1$  for rectangular and  $< 1$  for circular cross section).

It has to be pointed out that in addition to the reduction of the pressure drop by the factor  $C \cdot Ha$ , where  $C = \sigma_w \cdot t_w / \sigma \cdot a$  the wall conduction ratio and  $Ha$  the Hartmann number, the pressure drop in this case scales only linearly with the B-field.

Another hydraulic issue of major importance for direct insulated channels is the flow partitioning into a number of parallel channels. Unequal flow rates in the different channels caused e.g. by defects of the insulating layer in some subchannels may result in a redistribution of the velocity profile in these channels or even in a reduction of the flow leading to local hot spots.

This problem is particularly severe in insulated ducts, because small conducting paths through the structures can easily overwhelm the normally low conductance paths. Some design solutions have been proposed to alleviate this concern. For example, electrical coupling of parallel channels, such as the flow balancing schemes described in [5-8], can serve to maintain equal flow partitioning with only a small increase of the blanket pressure drop.

The cooling circuit for a liquid metal blanket normally consists of more than simple straight ducts; therefore, a more accurate analysis of the blanket operating conditions requires consideration of the various geometric features present. For the purpose of MHD analysis, any blanket concept can be subdivided into basic 2D and 3D hydraulic elements, as shown in Fig. 5.2-1. In Table 5.2-1, these elements are listed together with an elevation in which a ranking is given of the importance of the knowledge about these elements with respect to the feasibility of the three main concepts; toroidally-cooled, helium-cooled, or poloidally-cooled (with turbulence promotion) first wall.

- 0 not relevant
- 1 knowledge not important
- 2 knowledge important
- 3 knowledge decisive for feasibility

A "0" ranking means that no hydraulic element exists from where the corresponding problem could arise, "1" indicates that such a hydraulic element exists but its contribution to the overall pressure drop is negligible, whereas for "2" the

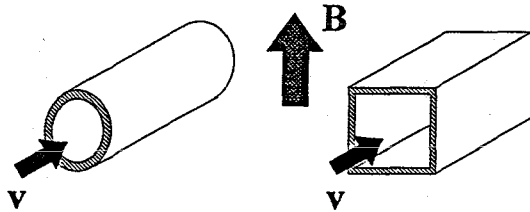
contribution to the pressure drop has an important impact. Finally, "3" demands a deep understanding of the MHD flow of the corresponding element because its contribution to the pressure drop and flow distribution may be decisive for the feasibility of the corresponding concept.

It should be mentioned that the evaluation shows only the relative importance of the different issues. No absolute comparison of the problems involved in the different concepts is possible from this table.

The flow in the straight feeding channel of the self-cooled poloidal-toroidal concept with thin-walled cooling ducts causes a high fraction of the total pressure drop. A further strong contribution to the total pressure drop originates from the 3 D multichannel bends. These 3 D effects have a strong influence on the velocity distribution. Therefore, both, pressure drop and velocity are ranked high. The Dual Coolant concept with fully insulated duct walls reacts very sensitive on uneven velocity distribution over the parallel channels. Therefore, the velocity distribution behind the manifold gets for this concept a high ranking. The same holds for the influence of the inlet and outlet manifold of the self-cooled poloidal flow concept. It is clear that the pressure drop and the flow distribution in the poloidal channels are of the same importance.

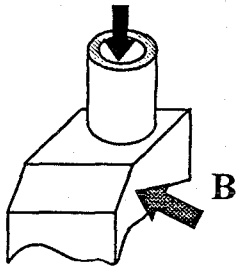
In the remaining sections of this chapter, extensive research into MHD behavior in these geometries is described. This research provides a much more reliable basis for the assessment of the various designs. Before proceeding, a short review of the basic equations and phenomena of MHD is presented.

## 2D-Geometries

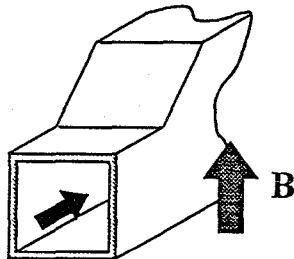


1,2 2D-MHD-flow in circular and rectangular ducts in constant and fringing fields

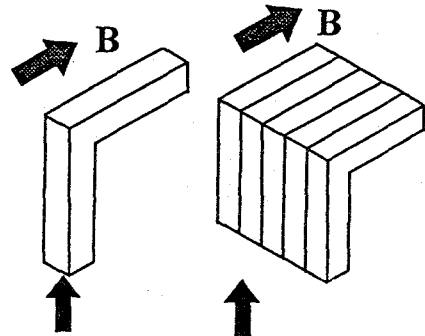
## 3D-Geometries



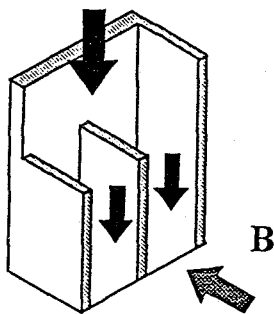
3 Sudden change of cross-section



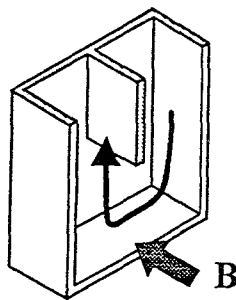
4 Expansions and contractions



5 single- and multi-channel bends



6 Manifolds and Distributors



7 180° U-turn

Fig. 5.2-1 Basic 2D and 3D hydraulic elements of liquid metal cooled blankets

No	problem	feature	field versus velocity	Importance					
				self-cooled Pol.-rad.tor. (thin-walled)		dual coolant (insulated)		self-cooled poloidal (insulated)	
				$\Delta p$	$\frac{v}{Q}$	$\Delta p$	$\frac{v}{Q}$	$\Delta p$	$\frac{v}{Q}$
1	Straight ducts		V $\perp$ B	3	1	1	1	3	3
2	Flow in fringing field		V $\perp$ B	1	2	1	2	1	2
3	Change of geometry		V $\perp$ B	2	2	2	1	2	2
4	Expansions and contractions		V $\perp$ B, VIIB	2	2	2	1	2	2
5	Single and multi-channel bends		V $\perp$ B, VIIB	3	3	0	0	0	0
6	Manifold		V $\perp$ B, VII B	3	3	2	3	2	3
7	180° U-bend		V $\perp$ B	1	1	1	1	1	1

Table 5.2-1 Importance of hydraulic elements to the feasibility of the three blanket concepts

## 5.2.2 Governing equations

The flow of an electrically conducting fluid within the applied strong magnetic field confining the fusion plasma may be described by the following non-dimensional equations accounting for the conservation of

$$\text{momentum} \quad \frac{1}{N} \left[ \frac{\partial v}{\partial t} + (v \cdot \nabla)v \right] = -\nabla p + \frac{1}{Ha^2} \nabla^2 v + j \times B \quad , \quad (5.2.1)$$

$$\text{mass} \quad \nabla \cdot v = 0 \quad , \quad (5.2.2)$$

$$\text{charge} \quad \nabla \cdot j = 0 \quad , \quad (5.2.3)$$

$$\text{and by} \\ \text{Ohm's law} \quad j = -\nabla \phi + v \times B \quad . \quad (5.2.4)$$

The non-dimensional variables  $v, B, j, p$ , and  $\phi$ , denote velocity, magnetic induction, current density, pressure, and electric potential, scaled by the reference values  $v_0, B_0, \sigma v_0 B_0, \sigma L v_0 B_0^2$ , and  $L v_0 B_0$ . The fluid properties like the density  $\rho$ , the viscosity  $\nu$ , and the electric conductivity  $\sigma$  are assumed to be constant.  $v_0$  is the average velocity in a cross section where  $L$  is a characteristic length;  $B_0$  is the magnitude of the applied magnetic field induction.

The relative importance of electromagnetic effects compared to inertia effects is given by the

$$\text{interaction parameter} \quad N = \frac{\sigma L B_0^2}{\rho v_0} \quad (5.2.5)$$

and compared to viscous effects by the square of the

$$\text{Hartmann number} \quad Ha = L B_0 \sqrt{\frac{\sigma}{\rho \nu}} \quad (5.2.6)$$

The ratio of the induced magnetic field to the applied strong field is determined by the

$$\text{magnetic Reynolds number} \quad Re_m = \mu \sigma v_0 L \quad (5.2.7)$$

and the conductance properties of the wall. For fusion applications the induced fields are small compared to the applied strong field (see e.g. [5-9, 5-10]). Thus, the applied field remains unchanged by the fluid motion. This fact justifies the inductionless approximation of equations (5.2.1 to 5.2.4).

The boundary conditions for the flow variables at channel walls are the

$$\text{no-slip condition} \quad v = 0 \quad (5.2.8)$$

and the

$$\text{thin-wall condition} \quad j \cdot n = \nabla_w \cdot (C \nabla_w \phi_w) \quad , \quad (5.2.9)$$

which describes the continuity of currents across the fluid wall interface. The current leaving the fluid region inverse to the direction of the inward wall-normal  $n$  enters the wall and creates there a potential  $\phi_w$ . Here  $\nabla_w$  stands for the components of the gradient vector in the plane of the wall. The

$$\text{wall conductance ratio} \quad C = \frac{\sigma_w \cdot t}{\sigma \cdot L} \quad (5.2.10)$$

characterizes the relative conductance of the wall with the conductivity  $\sigma_w$  and thickness  $t$  compared to the conductance of the fluid domain.

The potential of the wall is related to the fluid potential by

$$j \cdot n = \frac{1}{\kappa} (\phi_w - \phi) \quad , \quad (5.2.11)$$

where  $\kappa$  is the contact resistance or the resistance  $\rho_i \delta_i$  of a thin insulating coating (resistivity  $\rho_i$ , thickness  $\delta_i$ ) scaled by  $L/\sigma$ . For a perfect contact between the fluid and the wall,  $\kappa=0$ , the fluid potential at the wall is equal to the wall potential,  $\phi=\phi_w$ , whereas for a perfect insulation, as  $\kappa \rightarrow \infty$ , the wall normal component of current vanishes.

At the entrance and exit of the fluid domain considered the flow is assumed to be either fully developed or given.

### 5.2.3 MHD Phenomena

The main physical effects described by equations (5.2.1 to 5.2.11) are explained by the following simple considerations. First, the example of fully developed two-dimensional (2D) MHD flow in straight ducts is considered. Figure 5.2-2 shows a sketch of the geometry with boundary layers, velocity, current, and Lorentz force as the main contribution to the pressure drop. Three-dimensional (3D) effects are discussed by heuristic arguments.

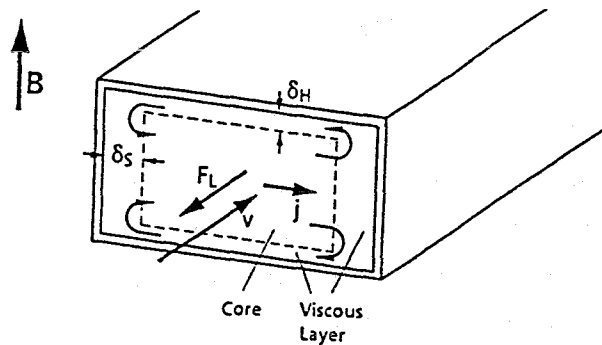


Fig. 5.2-2 Sketch of geometry

**Fully developed flow:** At the fusion relevant values of high Hartmann numbers  $Ha \gg 1$  the flow exhibits an inviscid core surrounded by viscous boundary layers at the walls (see Fig. 5.2-2). In the core the interaction  $v \times B$  of the moving fluid with the magnetic field drives the current of density  $j$  perpendicular to the field and perpendicular to the fluid motion. The interaction of this current with the field causes the Lorentz force  $j \times B$  opposing the fluid motion and thus creates the main part of the high MHD pressure drop. The induced currents complete their circuit in the layers where  $v \times B$  is reduced due to viscous effects. Since these layers are very thin (Hartmann layers of thickness  $\delta_H = 0(Ha^{-1})$  at walls perpendicular to  $B$ , or side layers with  $\delta_S = 0(Ha^{-1/2})$  at walls aligned with  $B$ ) it is obvious that they provide the main electric resistance in the current path and determine the pressure drop in insulated ducts ( $\kappa = \infty$ ).

$$\nabla p = 0(Ha^{-1}) \quad (5.2.12)$$

If the walls are in perfect contact with the fluid ( $\kappa = 0$ ) and more conducting than the viscous layers ( $C \gg Ha^{-1/2}$ ) the main electric resistance is no longer deter-

mined by the layers since almost all the returning current now is flowing inside the wall. The total current is much larger than for the insulating case and results in a pressure gradient

$$\nabla p = O(C) ,$$

if  $C$  is still small. In ducts with highly conducting walls, as  $C \rightarrow \infty$ , the resistance against currents is provided only by the core. This leads to highest currents and to a pressure gradient

$$\nabla p = O(1) . \tag{5.2.13}$$

The results for pressure drop and velocity distribution in ducts of circular and rectangular cross section with thin conducting walls (with and without insulating coatings) are summarized later in Table 5.5-1. The table shows the correlations for the pressure gradient  $\nabla p$  which can be used to obtain easily results with sufficient accuracy for engineering applications.

For the rectangular duct geometry the pressure gradient reaches the value  $\partial_x p_H$  as with pure Hartmann flow if the aspect ratio  $b/a$  or the conductance ratio of the side walls  $C_s$  are large.

**Three-dimensional flows:** 3D effects in MHD flows occur if the induced potential difference between the sides varies in the axial direction. Such variations are possible because of a non-uniform magnetic field at the ends of the magnet, a reduced component of velocity perpendicular to the field (observed in expansions or bends) or because of varying conductance properties of the channel walls (see Fig. 5.2-3). All these effects cause an axial potential gradient which drives additional currents  $j_{3D}$  inside the fluid. In one part of the duct the current density  $j_{3D}$  has the same direction as the 2D currents of the fully developed flow and gives additional contributions to the pressure gradient. Further down stream  $j_{3D}$  is in opposite direction as the 2D currents. Here it creates a Lorentz force acting in the flow direction. This leads to some pressure recovery. In the first part of the duct mechanical energy is transferred into electrical energy (generator effect). Since the transmission to the second part suffers from Ohmic dissipation only a part can be recovered downstream as mechanical energy (pump effect). Therefore, a pressure drop  $\Delta p_{3D}$  remains irreversibly lost. The axial components of  $j_{3D}$  cause Lorentz forces which displace the fluid towards the sides. Finally a flow pattern is

established in the 3D region with a significantly reduced velocity in the center and an increased velocity near the side walls. These simple considerations demonstrate that 3D effects can not be excluded by the use of poorly conducting or insulating channel walls because the currents  $j_{3D}$  take their path inside the fluid itself.

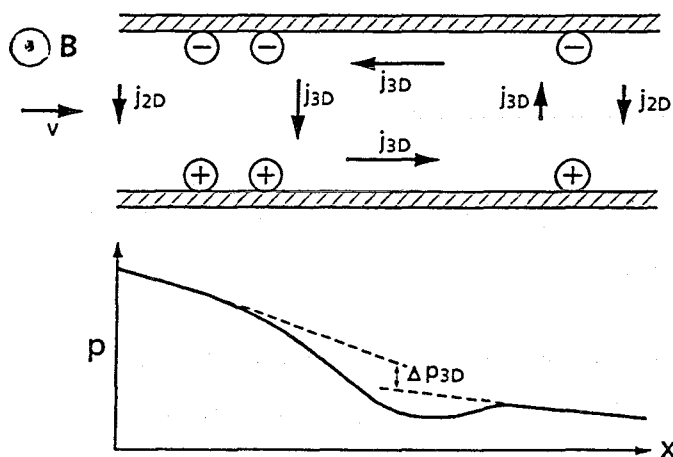


Fig 5.2-3 Sketch of currents and pressure in 3D flows

### 5.3 Solution methods

Analytical solutions to the problem (5.2.1 to 5.2.11) are restricted to very special cases of boundary conditions and only to simple duct geometries in fully developed flows [5-11 to 5-14]. Two methods have been used to determine the unknown flow variables in cases of more general applications. One is the completely numerical approach accounting for all physical effects, but restricted in its applicability to MHD flows in basic rectangular duct geometries at moderate values of  $Ha \leq 100$ . The other approach focuses to the main physical contributions using asymptotic methods.

#### 5.3.1 Direct numerical simulation

Attempts for direct numerical simulation (DNS) of MHD flows on the basis of equations (5.2.1 to 5.2.11) have been made by several authors. The preferred numerical methods are finite difference or finite volume methods [5-15, 5-16]. In the following the method used by [5-17] and later by [5-18] is addressed in some de-

tail. These authors take advantage of the use of fast Poisson solvers for the evaluation of pressure and potential. Starting from a guessed initial flow field they reach the steady state solution of interest in by solving the basic equations in the time dependent form. They are more interested in fast convergence than in a precise modeling of the time dependence.

The iteration procedure starts with a Poisson equation for potential, which results from a combination of equation (5.2.3) and (5.2.4),

$$\Delta\phi = \nabla \cdot (\mathbf{v} \times \mathbf{B}) \quad (5.3.1)$$

ensuring conservation of charge. Once the potential is known the currents can be determined using Ohm's law.

In the proceeding step the artificial "velocity" defined as  $\mathbf{v}^* = \mathbf{v} + \nabla p$  is calculated by the use of equation (5.2.1). The pressure  $p$  is calculated from the Poisson equation

$$\Delta p = \nabla \cdot \mathbf{v}^* \quad (5.3.2)$$

which ensures a solenoidal velocity

$$\mathbf{v} = \mathbf{v}^* - \nabla p \quad (5.3.3)$$

This procedure is repeated until the desired steady state solution is reached with sufficient accuracy. While the case of perfectly insulating or conducting walls can be treated directly by applying the relevant standard boundary condition ( $\partial\phi/\partial n = 0$  or  $\phi = \text{const}$ ) to the Poisson equation (3.3) [5-18] the arbitrary wall conductivity requires in addition the solution of equation (5.2.9) during each iteration step [5-17]. [5-18] introduces domain decomposition techniques for a modeling of more complex geometries by a coupling of basic rectangular subdomains and higher order upwind schemes as an approximation for inertial terms.

For accurate results obtained by DNS, the numerical grid spacing has to be so small that even the thin Hartmann layers are resolved. This fact leads especially for 3D application to an enormous amount of required storage and execution time even on modern vector computers, which finally limits the applicability of DNS to Hartmann numbers  $Ha \leq 100$ , significantly smaller than fusion relevant values of  $Ha = 10^4 - 10^5$ . Nevertheless, one should consider DNS as an appropriate

solution method for fundamental research of elementary MHD problems at moderate Hartmann numbers.

### 5.3.2 Asymptotic solution

Asymptotic methods (AM) have often been used to calculate MHD flows in the range of fusion relevant Hartmann numbers (e.g. [5-19, 5-20, 5-21] etc.) since they have been proposed for 3D applications by [5-22]. The idea is to get a tractable mathematical problem by simplifying the basic equations in such a form that the main physical behavior remains unchanged.

In many fusion applications the interaction parameter  $N$  is high enough that inertial terms can be neglected completely. This leads to a linear system of equations. In a next step the flow is divided into one (ore more) core region(s) in which the viscous effects are unimportant at large Hartmann numbers. The cores are separated from each other or from the walls by thin viscous layers. These assumptions lead to considerable simplifications of the equations governing the flow in the cores (subscript C).

$$\nabla p = j_C \times B, \quad \nabla \cdot v_C = 0, \quad (5.3.4, 5.3.5)$$

$$j_C = -\nabla \phi + v_C \times B, \quad \nabla \cdot j_C = 0 \quad (5.3.6, 5.3.7)$$

From equation (5.3.4) it follows directly that the pressure and the current components perpendicular to  $B$  do not vary in the direction of  $B$ . This fact allows an easy analytical integration of all equations along the field lines. The potential values at the walls are introduced as integration constants.

After the integration the whole 3D problem is reduced to a set of coupled 2D equations governing the pressure in the plane perpendicular to  $B$  and the potential (equation (5.2.9)) at the fluid wall interface.

More detailed considerations which account for viscous effects lead to the result that the pressure and the potential are constant to the main order of approximation across layers in which the normal component of the magnetic field does not vanish. The decay of the velocity and the variation of current towards the wall is exponential.

$$\mathbf{v} = v_c(1 - e^{-\eta}) , \quad (5.3.8)$$

$$\mathbf{j} = \mathbf{j}_c - (\mathbf{j}_c + \nabla_w \phi) e^{-\eta} . \quad (5.3.9)$$

Here  $\eta$  represents the boundary layer coordinate along the inward wall-normal direction  $n$ , stretched with  $Ha(\mathbf{B} \cdot n)$ . At the wall where  $\eta = 0$  the velocity satisfies the no-slip condition and the tangential currents are given by Ohm's law for a media at rest. Far from the walls as  $\eta \rightarrow \infty$  all variables reach the core values. At walls exactly aligned with the magnetic field the modelling is different. For details see [5-23, 5-24].

For the solution of the set of coupled 2D equations two approaches are used. One is iterative with underrelaxation for small values of  $C$  [5-25]. The use of fast Poisson solvers restricts its applicability to ducts, whose surface is composed by rectangular geometries. The solution procedure is relatively fast and allows a high numerical resolution and even the modeling of 3D MHD flows in a number of coupled subchannels.

The other approach [5-24, 5-26] uses boundary-fitted coordinates mapping the arbitrary duct geometry to a standard volume for which the integration and the 2D numerical solution is obtained. The arbitrary coordinate transformation allows non-equidistant grid spacing with high resolution of 3D-regions. The resulting algebraic system is solved by a direct linear solver.

## 5.4 Experimental methods

In order to investigate the key features of liquid metal flows in strong magnetic fields, two main components are needed, a liquid metal loop and magnets of sufficient strength supplying a rather homogeneous magnetic field. In this section, we give an overview and a short description of the liquid metal loop, the magnets and the measuring techniques used in the MEKKA-facility of the Forschungszentrum Karlsruhe in the Institute for Applied Thermo- and Fluidynamics (IATF). A more detailed description of the MEKKA-facility has been given previously by [5-6] or [5-27]. Included are also the main features of some experimental facilities of the collaborating partner institutes like the Argonne National Laboratory (ANL) and the Institute of Physics of the Latvian Academy of Sciences (LAS) in Riga (see Table 5.4.1). The thermophysical values of the liquid metals used in the different facilities may be taken from Table 5.4.2.

Laboratory	ANL <sup>1,2</sup>		Forschungszentrum Karlsruhe <sup>3,4</sup>		LAS <sup>5,6</sup>	
	SCMS2	ALEX	CELLO	MA	MAGDA	-
operating principle super-cond. (s) normal-cond. (n)	s	n	s	n	s	n
magnet type	dipol	dipol	solenoid	dipol	solenoid	dipol
magnet gap shape	conical	rectangle	circular	rectangle	circular	circular
homogeneous test volume [cm] cross section	80-100	20(H) x 76(W)	40	16.5(H) x 48.3(W)	40	40
length [cm]	400	100	45	80	60	40
field strength [Tesla]	6	2.08	3.6	2.1	4.3	1.2
Liquid metal loops liquid metal	Na <sup>22</sup> K <sup>78</sup>		Na <sup>22</sup> K <sup>78</sup> , Ga <sup>68</sup> In <sup>20</sup> Sn <sup>12</sup>		Hg, Ga <sup>68</sup> In <sup>20</sup> Sn <sup>12</sup>	

Table 5.4-1 Experimental facilities used for MHD work related to the Pb17Li blankets [5-28 to 5-33]

Metal	Hg		Ga <sup>68</sup> In <sup>20</sup> Sn <sup>12</sup>		Na <sup>22</sup> K <sup>78</sup>		Na		Li		PbLi <sup>17</sup>	
Melting point [°C]	-38.87		10.5		-11		97.82		179.1		234.85	
Volume change on fusion of solid volume in [%]	3.6		-3.5		2.48		2.5		1.5		3.5	
Density $\rho$ [kg/m <sup>3</sup> ]	20°C	13546.0	20°C	6363.2	20°C	868.2	150°C	915.3	300°C	504.9	300°C	9491.7
A <sub>0</sub>		13595.4		6372		873.55		950.46		535.2		9993.3
A <sub>1</sub>		-2.455		-0.44		-0.258		-0.2307		-0.101		-1.672
A <sub>2</sub>		2.472E-7		0		0		-1.8017E-5		0		0
valid temperature range [°C]	-20°-300°		25°-200°		0°-204°		98°-1370°		200°-600°		235°-400°	
Heat capacity $c_p$ [J/(kg K)]	20°C	139.068	20°C	365.813	20°C	982.1	150°C	1425.65	300°C	4278.7	300°C	189.78
A <sub>0</sub>		139.6		368.01		990.7		1437.08		4530.2		192.51
A <sub>1</sub>		-0.0275		-0.11		-0.5133		-0.5806		0.8382		-9.116E-3
A <sub>2</sub>		4.5E-5		6.67E-6		5.37E-4		4.624E-4		0		0
valid temperature range [°C]	0°-300°		25°-200°		0°-450°		100°-600°		180°-420°		235°-530°	
Kinematic viscosity $\nu$ [m <sup>2</sup> /s 10 <sup>6</sup> ]	20°C	0.1148	20°C	0.34809	20°C	1.05	150°C	0.5916	300°C	0.8911	300°C	0.2209
A <sub>0</sub>		0.1245		0.3853		1.278		0.936775		1.6925		0.6525
A <sub>1</sub>		-4.633E-4		-0.001926		-0.0134		-0.0025806		-0.003515		-0.001943
A <sub>2</sub>		1.136E-6		3.2686E-6		0.0001		2.571E-6		2.9E-6		1.7324E-6
valid temperature range [°C]	-20°-200°		25°-200°		0°-80°		100°-300°		180°-550°		235°-660°	

Table 5.4-2, continued next page

Metal	Hg		Ga <sup>68</sup> In <sup>20</sup> Sn <sup>12</sup>		Na <sup>22</sup> K <sup>78</sup>		Na		Li		PbLi <sup>17</sup>	
Electric conductivity $\sigma$ [A/(V m) 10 <sup>-6</sup> ]	20°C	1.04452	20°C	3.30737	20°C	2.878	150°C	8.6356	300°C	3.3434	300°C	0.78917
A <sub>0</sub>		1.0635		3.4882		2.976		13.1155		4.458		0.876
A <sub>1</sub>		-9.502E-4		-0.00932		-5.05E-3		-0.03344		-0.00438		-3.13562E-4
A <sub>2</sub>		5.95E-8		1.3933E-5		7.188E-6		2.9028485E-5		2.248E-6		8.09524E-8
valid temperature range [°C]	20°-350°		20°-200°		0°-80°		100°-400°		200°-1200°		235°-720°	
Thermal conductivity $\lambda$ [W/(m K)]	20°C	8.7169			20°C	21.8	150°C	84.4	300°C	40.64	300°C	13.184
A <sub>0</sub>		8.214		39		21.38		91.752		34.9275		7.30374
A <sub>1</sub>		0.0257		only available		0.0208		-0.048688		1.903E-2		1.96E-2
A <sub>2</sub>		-2.784E-5		for 100°C		-2.207E-5		-3.03E-7		0		0
valid temperature range [°C]	0°-220°				0°-400°		100°-550°		200°-1100°		235°-400°	

Table 5.4-2

Thermophysical values for different liquid metals. \*1 The temperature dependent values are fitted by polynomial regressions in the form  $A_0 + A_1T + A_2T^2$  with T in °C. The fit formulas for all values have in their range an error of less than 0.5 %. The thermophysical data have been taken from [ 5-1, 5-34 - 5-38].

### 5.4.1 The MEKKA-facility

Two magnets are available in the MEKKA-facility. There is a normal conducting MA dipole magnet providing a transverse magnetic field. Its maximum field strength is 2.1 Tesla. The test volume of constant magnetic field strength amounts to 0.17m x 0.48m x 0.8m. The other magnet is the super-conducting solenoid magnet CELLO with a maximum field strength of 3.6 Tesla. The test volume of constant field strength is 0.4m in diameter and 0.45m in length. An eutectic sodium-potassium alloy ( $\text{Na}_{22}\text{K}_{78}$ ) with a lower density and a higher electrical conductivity compared to a lead-lithium alloy Pb-17Li foreseen in the blanket design is used in the liquid metal loop in order to scale from experimental conditions to fusion blanket relevant conditions. The thermophysical transport properties of the sodium-potassium alloy are given by [5-36] (see also Table 5.4-2). In Fig. 5.4-1 a sketch of the liquid metal loop is shown. A canned motor pump with a maximum pressure head of 0.9MPa at a flow rate of 25m<sup>3</sup>/h circulates the liquid metal at temperatures below 250 C. An additional electromagnetic pump is used for very low flow rates and for high temperature runs. The entire loop can be moved on rails together with the connected test sections along the axis of each magnet. This allows a good access to the instrumented locations of the test sections and variable positioning of the test section within the magnets. Due the technical features of the loop and the magnets the MEKKA facility is capable of attaining Interaction parameters in the range of  $N=10^2$ - $10^5$  at Hartmann numbers up to  $Ha=10^4$ , which are present in liquid-metal cooled fusion blankets.

### 5.4.2 Measuring techniques

#### 5.4.2.1 Integral quantities

The flow rate in the loop is measured by two flow meters, which are integrated in the liquid metal loop and use different measuring principles. The gyrostatic flow meter measures the total mass flow independent of temperature. Its measuring range can be selected from 0-3.84 tons/h up to 25 tons/h. The maximum measuring error in the selected range is 0.3% of the chosen upper limit.

Additionally electromagnetic (EM-) flow meters are used. Due to the small extensions their use is rather flexible without any changes in the piping system. They are, for example, used in multi-channel experiments. To avoid any disturbances of the measuring magnetic field of the flow meters by the scattering field of the 'big' magnets, they are shielded with ferro-magnetic plates. The accuracy of the

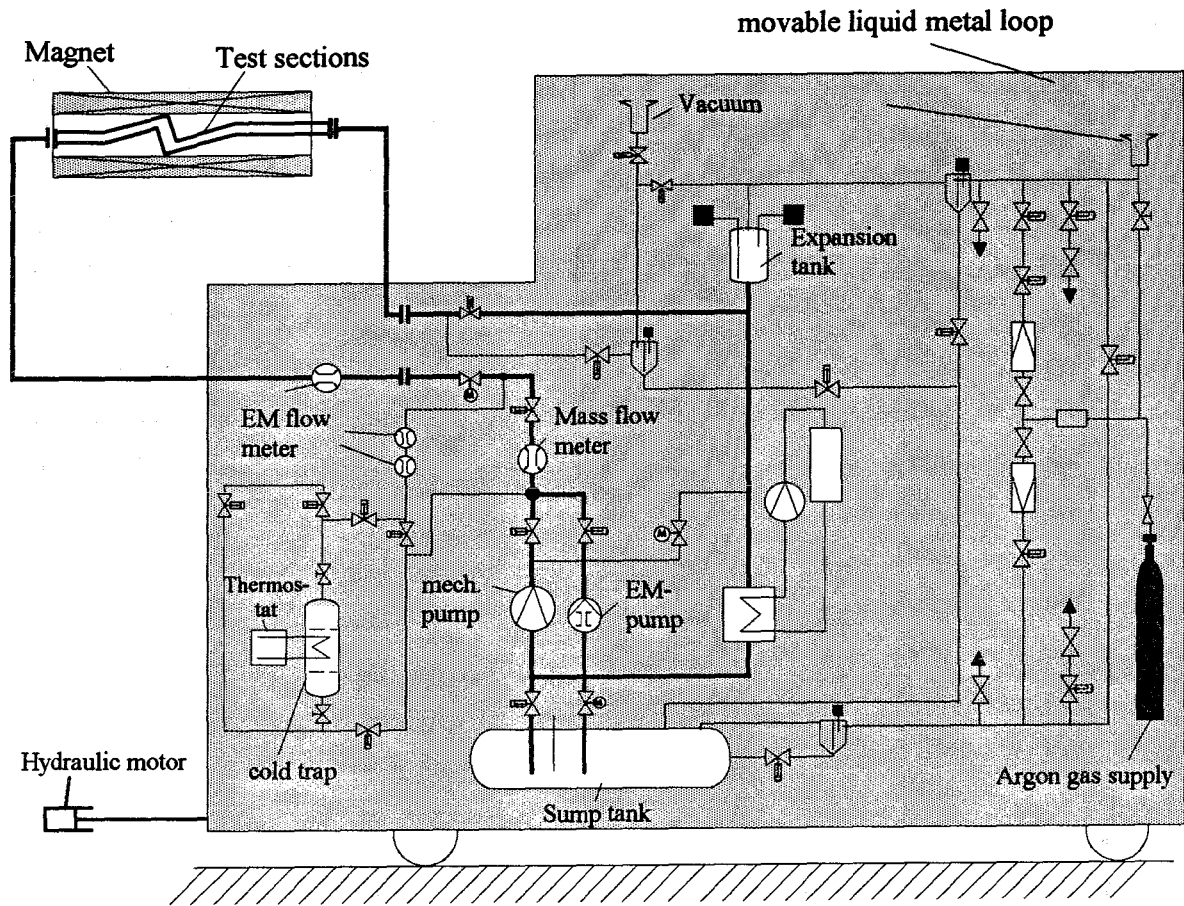


Fig. 5.4-1 The magneto hydrodynamical experimental facility of the Forschungszentrum Karlsruhe (MEKKA)

EM-flow meters is only restricted by the resolution of the data acquisition system. The temperatures determining the physical properties of the fluid are measured in case of isothermal experiments at the inlet and outlet of the loop with Ni-NiCr thermocouples.

#### 5.4.2.2 Local quantities

The MHD-flow at high Hartmann numbers and interaction parameters is determined once the pressure in the duct and the distribution of the electrical potential on the duct surface are known. To measure the pressure differences in the test sections two different systems of pipes are used in which five or three unipolar capacitive pressure transducers of different measuring range are arranged in parallel. To avoid errors in the pressure difference measurement due to non-linearities of the pressure transducers at their upper limitation the measuring ranges were chosen as to overlap. For the pressure difference measurements in MHD-flows some effects completely unknown to ordinary hydrodynamics have

to be taken into account. Electrical currents induced in the duct can short circuit in electrically conducting measuring pipes and as a consequence they may have a feedback through the flow in the duct. Therefore the measuring pipes should be made of insulating materials such as rubber. In three-dimensional MHD-flows even another phenomenon is observed. The directly measured pressure represents not the real pressure at the fluid-wall interface. A virtual pressure difference  $p$  is superimposed to the real pressure at each position, caused by electrical currents flowing in the pressure taps perpendicular to the applied magnetic field (in particular if there is a component of the magnetic field tangential to the wall). This virtual pressure difference can be corrected by measuring the electrical potential at each tap, see Fig. 5.4-2. The pressure correction  $p$  at the tap can be calculated using the relation

$$p = \frac{t_w}{d} (\phi_2 - \phi_1) ,$$

where  $t$  is the wall thickness of the duct,  $d$  the diameter of the pressure tap and  $\phi_1$  and  $\phi_2$  the dimensionless potentials across the tap.

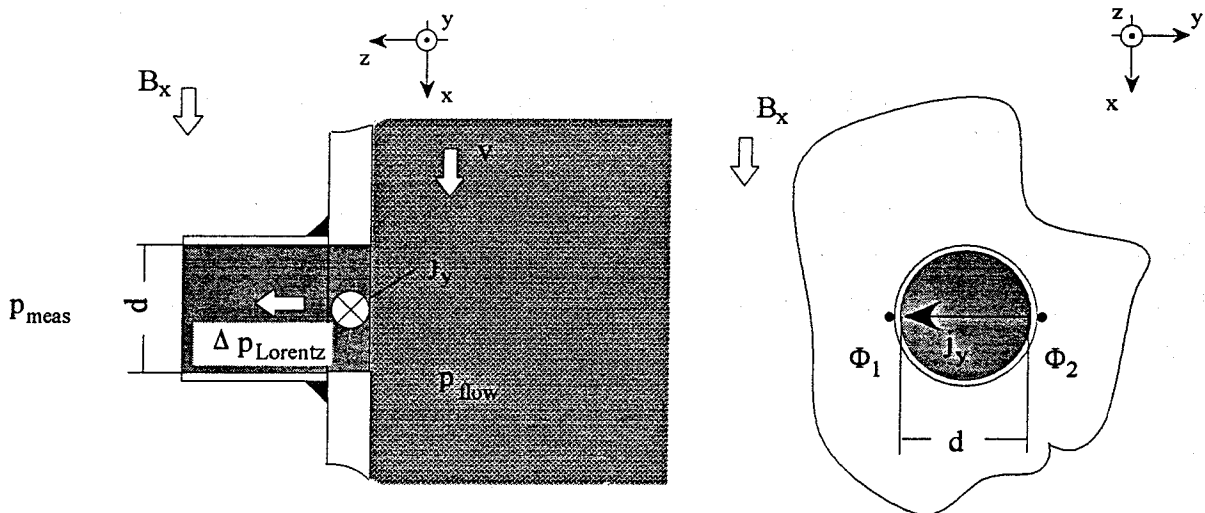


Fig. 5.4-2 Virtual pressure losses related to electrical conducting structure material at a pressure tap

The flow pattern of MHD-flows in electrically almost insulating channels ( $C \ll 1$ ) is depicted as an electrical potential distribution on the wall. Contrary to the pressure difference measurement, the potential measurement on the channel surface has no feedback on the flow. To measure the surface potentials spring loaded needles mounted on fiberglass plates are attached to the test sections. Since the

measurement is currentless the resolution of the potential measurement is only given by the resolution of the data logger.

An instrument to measure the local velocity distribution within the duct is the Liquid-metal Electromagnetic Velocimetry Instrument (LEVI) probe. It is in principle a miniaturized local electromagnetic flowmeter, see e.g. [5-39], which measures local potential gradients. The signal is proportional to the velocity and the applied external magnetic field. The velocity can be calculated according to Ohm's law:

$$\Delta\phi = v \cdot d \cdot B_0$$

where  $\Delta\phi$  is the potential difference,  $v$  is the local velocity perpendicular to the magnetic field,  $d$  is the distance of the two electrodes and  $B_0$  is the applied magnetic field strength.

One can easily see that LEVI-probes are unable to measure velocity components in the magnetic field direction. The LEVI probes can be used either if the currents are known or if they are negligibly small as in almost insulating ducts at high Hartmann numbers. This limits the use of the LEVI-probe to duct flow where the condition  $c \ll 1$  and  $Ha \gg 1$  holds and where no significant three-dimensional currents circulate. In strongly three-dimensional duct flows such as radial-toroidal bends it was shown that LEVI probe signals may give misleading results.

Nevertheless, the LEVI is the most reliable probe, compared to hot-wire anemometers, opto-mechanical probes [5-40] or temperature pulse probes [5-39].

### 5.4.3 Data acquisition system

Data acquisition in the MEKKA facility of the Forschungszentrum Karlsruhe is conducted via two independently operating personal computers which have the following tasks:

1. Control of the data acquisition hardware (Multimeters, data logger, acquisition cards, interfaces, etc.).
2. Data reduction and storage of the obtained experimental data.
3. Control of the facility.

A schematic drawing of the acquisition may be taken from Fig. 5.4-3.

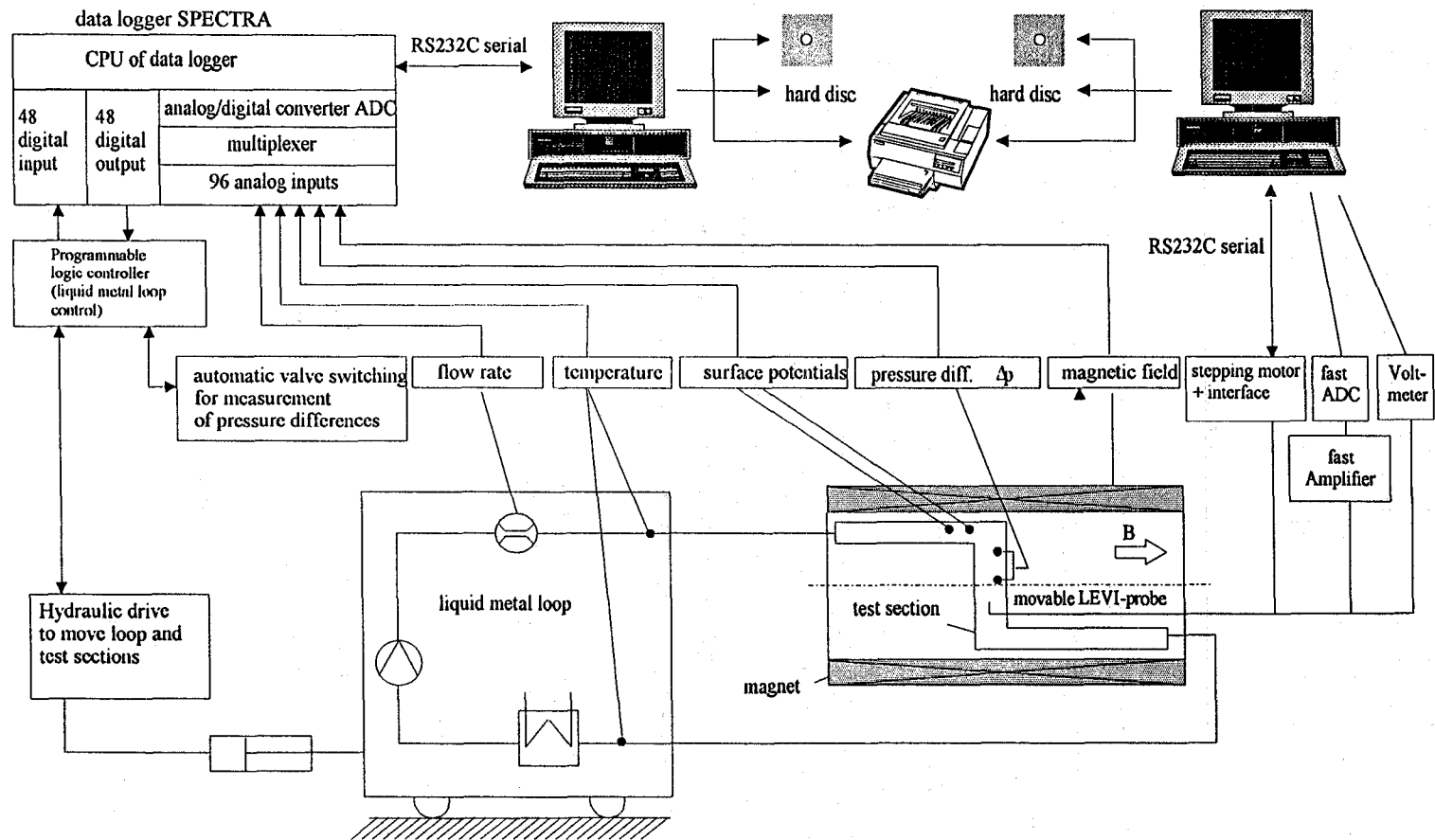


Fig. 5.4-3 Data acquisition system of the MEKKA-facility (Forschungszentrum Karlsruhe).

## 5.5 Results on MHD-flows in hydraulic elements

Any blanket design is based on various basic geometric elements of coolant channels. These are straight ducts of rectangular or circular cross section, expansions, contractions, bends, and manifolds. The importance of these hydraulic elements with regard to the feasibility of a blanket concept has been discussed in the introduction, where a table of weight factors for the different blanket designs has been given. However, the pressure drop caused by MHD flows in such configurations can be minimized by the means of thin conducting walls or by the use of insulating coatings at the wall. Flows for all these possible applications have been investigated by several authors. The main results relevant for fusion applications are summarized in the following chapters. For more detailed information the reader is advised to the original publications named in this report.

### 5.5.1 Flows in single ducts with constant cross section perpendicular to B

The most important duct geometries in engineering applications are straight ducts of circular or rectangular cross section. The flow in straight ducts may be either fully developed (2D) or 3D. The results obtained for the fully developed MHD-flows in fusion element typical geometries for various magnetic field orientations are discussed in Section 5.5.1.1. In very long straight ducts 3D MHD effects occur in regions of a non-uniform magnetic field or in regions of varying conductance properties of the walls, effects which are not observed in pure hydrodynamic flows. A discussion about these phenomena is given in Section 5.5.1.2.

#### 5.5.1.1 Fully developed flows

Although most results for fully developed 2D MHD flows in such geometries are known for quite a long time they are repeated here for getting a complete picture. The results are summarized in Table 5.5-1 for thin conducting ducts and for ducts with perfectly insulating coatings. Table 5.5-1 shows the analytically derived correlations for the pressure gradient which can be used to obtain easily results with sufficient accuracy for engineering applications. For the rectangular duct geometry the pressure gradient reaches the values of the Hartmann flow  $\partial_x p_H$  if the aspect ratio  $b/a$  or the conductance ratio of the side walls  $C_s$  are large.

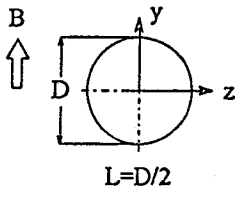
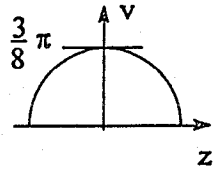
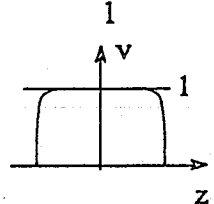
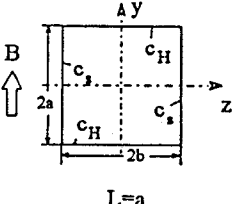
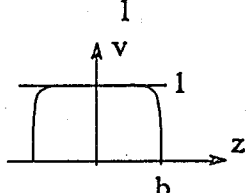
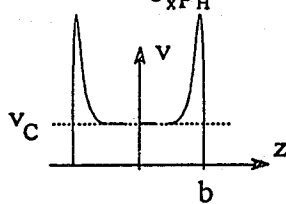
Geometry	conductivity	pressure gradient $\nabla p$	experim. Reference	velocity
 <p style="text-align: center;"><math>L=D/2</math></p>	insulating $\kappa \rightarrow \infty$	$\frac{3\pi}{8Ha}$ a)	e	
	conducting $\kappa \rightarrow 0$	$\frac{c}{1+c}$ , $c \gg \frac{1}{Ha}$ b)	f	
 <p style="text-align: center;"><math>L=a</math></p>	insulating $\kappa \rightarrow \infty$	$\frac{1}{Ha}$ c)	g	
	conducting $\kappa \rightarrow 0$	$\frac{\partial_x p_H}{1 + \frac{a}{3b} \frac{1}{c_s^*} \partial_x p_H}$ <p>where</p> $\partial_x p_H = \frac{c_H + \frac{1}{Ha}}{c_H + 1}$ $c_s^* = c_s + \frac{1}{\sqrt{Ha}}$ <p style="text-align: center;">d</p>	h	$v_c = \frac{\nabla p}{\partial_x p_H}$ 

Table 5.5-1 Pressure drop correlations for fully developed MHD channel flows. For details see a) [5-14, 5-12], b) [5-40], c) [5-13], d) [5-23, 5-41], e) [5-42], f) [5-43], g) [5-74], h) [5-44].

The sketch of velocity profiles corresponds to the position  $y=0$  in the cross section. Along the  $y$ -direction the velocity is constant in the core. The no-slip condition at the wall is reached by a steep exponential decay according to equation (5.3.8). The velocity profile in insulating pipes takes an elliptic shape while in con-

ducting pipes ( $C \gg Ha - 1$ ) the flow pattern is of the slug type. Slug type velocity profiles are also obtained in the cores of rectangular ducts. However, if the duct walls are conducting the core velocity is reduced to  $v_c < 1$ . The volume flux  $4ab(1 - v_c)$  which is now not carried by the core is carried by high-velocity jets along the side wall.

In practical applications of rectangular duct flow one will often find the more general case where the magnetic field is not aligned with any pair of walls. Results for such flows have been obtained [5-17] on the basis of a direct numerical solution or based on asymptotic models by [5-45, 5-46, 5-24]. For inclination angles  $\beta > 0$  the rectangular duct splits into an inner core  $C_i$  and two outer cores  $C_o$  as shown in Fig. 5.5-1. They are separated by two thin internal viscous layers which spread from the inner corner along field lines into the fluid. The inner core exhibits a flat velocity profile while in the outer cores the velocity distribution is linear in the field direction with the highest value at the inner corner. Results for pressure drop and velocity profiles for different inclination angles  $\beta$  and wall conductance ratios are shown in Fig. 5.5-1.

An overview about experimental results in such 2D fully developed MHD-flows for fusion relevant  $Ha$  and  $N$  is given in [5-47]. In general the quality of the derived formulas is quite good. Deviations between experiments and the formulas are approximately  $\pm 10\%$ , which is in the range of the measurement accuracy and should be taken into account in any design calculation.

An also important question is the typical developing length the flow needs to establish a fully developed flow regime. Here only analytical and theoretical calculations are available. But the relations developed in three-dimensional codes by [5-17, 5-18, 5-26] show in comparison with experiments conducted by [5-43 and 5-48] a quite good agreement. In Table 5.5-2 the order of the development length of a MHD single duct flow is given for some characteristic geometries.

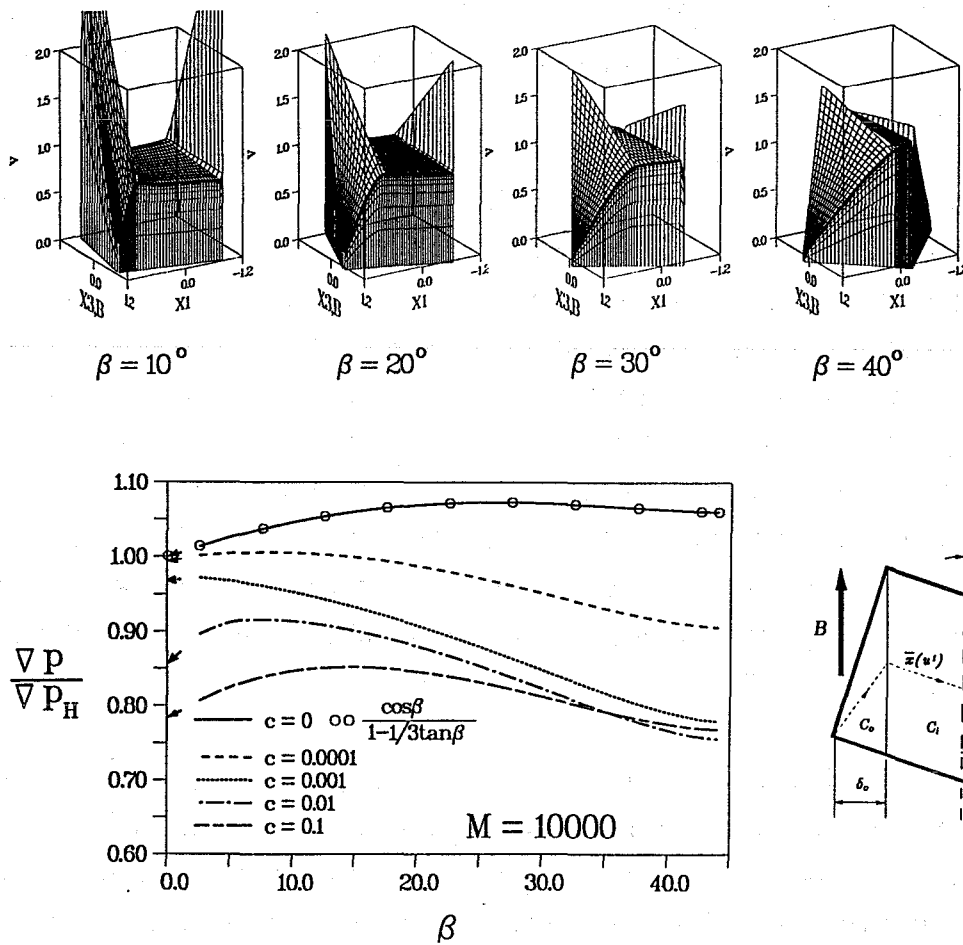


Fig. 5.5-1: MHD flow in inclined rectangular ducts. Numerical results for velocity profiles and pressure drop (compared to the analytically obtained pressure drop  $\nabla p / \nabla p_H = \cos\beta / (1 - 1/3 \tan^2\beta)$  obtained by [5-46] for the case  $C=0$ ).

wall property	insulating		conducting	
	rectangular	circular	rectangular	circular
$l_{dev}$ in characteristic length $a$	$O(1)$	$O(\sqrt{Ha})$	$O(1/\sqrt{C})^*a$	$O(1)$

Table 5.5-2 Developing length of a MHD single duct flow for different geometries.  $*a$  [5-49, 5-50].

### 5.5.1.2 Nonhomogeneous magnetic field

At the inlet and outlet ducts of a blanket penetrating the magnet coil, spatially varying magnetic fields exist. If the magnetic flux density changes along the duct, the electromotive force will also change. This sets up axial potential differences which drive currents in the axial direction. These currents result in electromagnetic body forces which force the fluid out of the core of the flow and into high velocity flow regions near the walls tangent to  $B$ . The flux redistribution is accompanied by a pressure drop higher than it would have been had the flow remained undisturbed and by a transverse pressure varying in the range of the fringing field, as shown in Fig. 5.5-2.

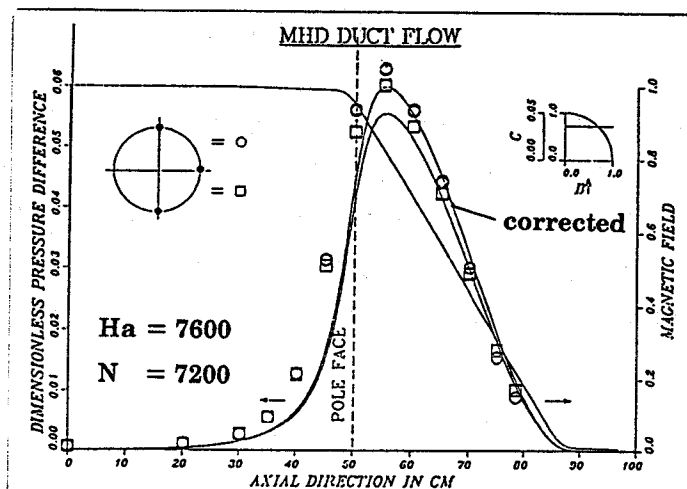


Fig. 5.5-2 Dimensionless transverse pressure difference in a round duct in the range of the fringing field [5-43]

This problem has been investigated theoretically and experimentally for round and rectangular ducts by [5-51] and for round ducts by [5-31] at fusion relevant parameters  $Ha$  and  $N$ . The experimental results agree well with the theory based on the Core Flow assumptions.

## 5.5.2 Single ducts with changing flow direction or cross section in the plane perpendicular to B

No significant additional pressure drops occur for inertialess MHD flows if the cross section or the flow direction changes only in the plane perpendicular to the magnetic field. The reason is that the potential near the sides which is proportional to the product of velocity and duct width remains unchanged by the flow in such geometries for a given flow rate. The driving mechanism for additional currents, namely an axial potential gradient, does not exist for such a type of flow. The total pressure drop of flows in the plane perpendicular to the field can be easily obtained by the integration of the locally fully developed pressure gradient according to Table 5.5-1 along the channel axis.

MHD flow in several geometries has been investigated in which the geometry does not change in the magnetic field direction but perpendicular to it. One example is an expansion from rectangular cross section  $2 \times 2$  to  $2 \times 4$ . The estimation for pressure drop according to the fully developed conditions (dashed line) agrees well with the 3D numerical calculations (solid line), as shown in Fig. 5.5-3.

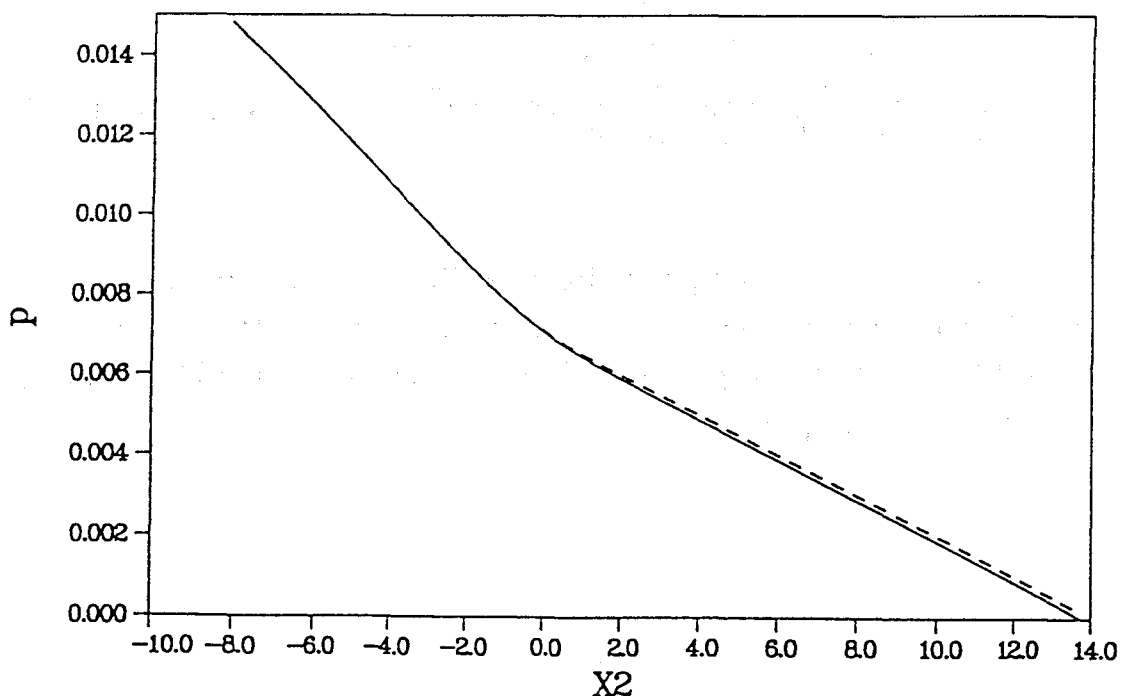


Fig. 5.5-3 Pressure drop along the axis of a rectangular expansion  $Ha = 1000$ ,  $c = 0$ . The dashed line represents the pressure estimation according to locally fully developed conditions. It is compared to the solid line which represents results of a 3D numerical calculation.

Another example is the smooth  $180^\circ$  bend (see Figure 5.5-4 [5-24]). One finds no increase in pressure drop due to 3D effects. In the bend the flow is accelerated along the inner side wall while the flow is reduced at larger distances from the inner radius.

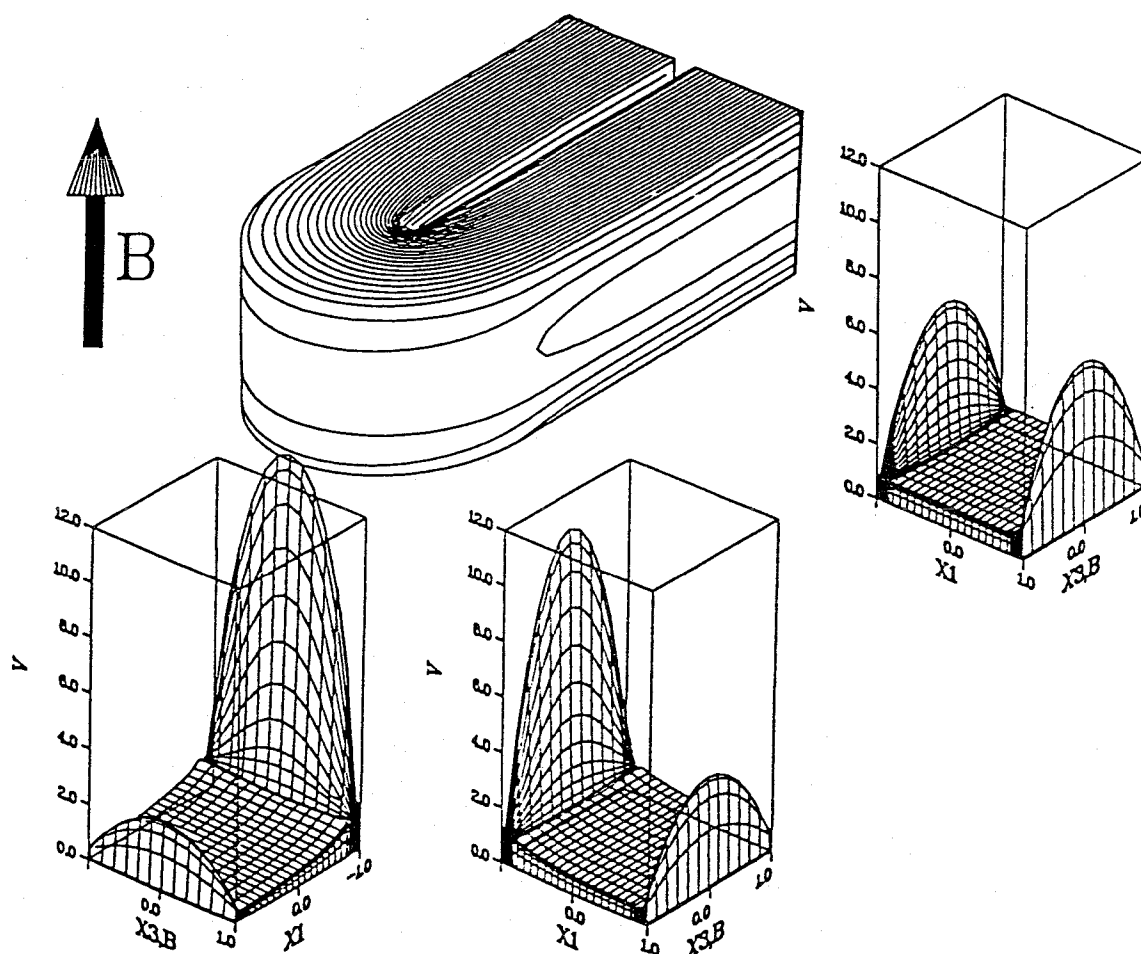


Fig. 5.5-4 Flow in a rounded  $180^\circ$  bend; lines of constant wall potential, velocity profiles at several axial positions.

Similar calculations have been performed for flows in insulating ducts (see Fig. 5.5-5 [5-51]). One finds the same physical effects as already described for flows in conducting thin-wall ducts and no increase of pressure drop due to 3D effects to the leading order of approximation.

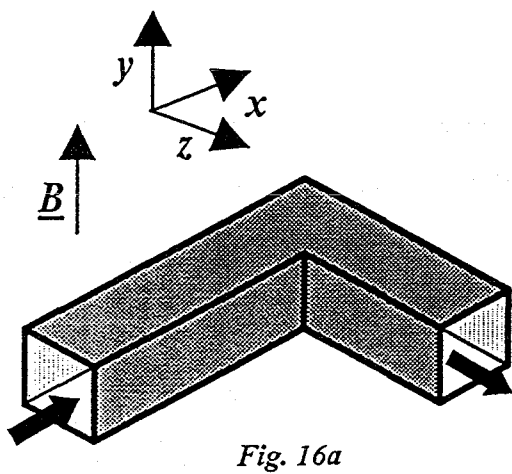


Fig. 16a

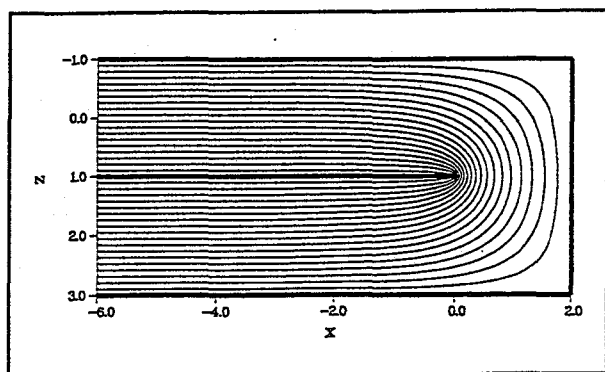
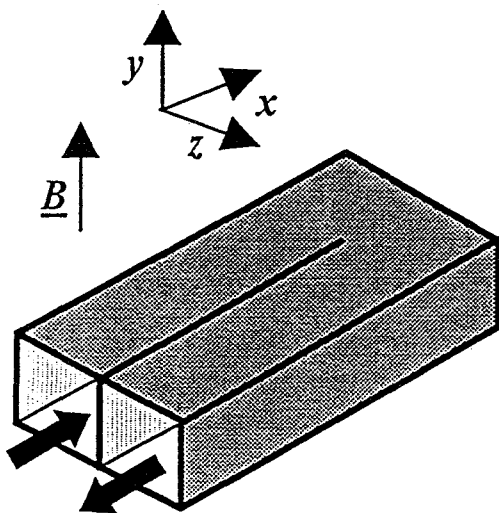
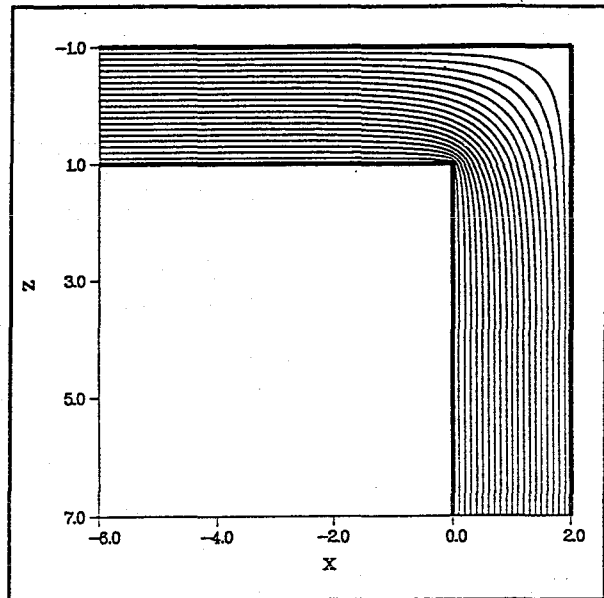


Fig. 5.5-5 MHD flow in a sharp 90° bend and in a sharp 180° bend. Geometry and isolines of wall potential

In order to investigate the lower limits of the MHD parameters where the CFA methods can be applied, pressure drop experiments in a sharp-edged 90° bend were performed [5-33]. The interaction parameter and Hartmann numbers were varied from purely hydrodynamic flow ( $N=Ha=0$ ) to maximum values of  $N=11000$ ,  $Ha=2100$ . Figure 5.5-6 shows the pressure loss coefficient  $\zeta$ , defined by

$$\zeta = \Delta p / (\rho u^2 (1 + N)),$$

where the measured pressure drop  $\Delta p$  is determined by extrapolation of the undisturbed duct pressure gradients upstream and downstream of the bend to the intersection of the duct axis.

For  $N=0$ , the agreement with results from similar hydraulic investigations agree very well. With increasing  $N$  the loss coefficient decreases strongly and becomes constant for  $N \geq 20$ . It is interesting to note that this value is not zero but slightly negative which according to the above definition corresponds to a small pressure increase. This effect, also predicted by 3d CFA calculations, is due to the fact that the average flow path for the flow is shorter than the assumed mean flow path along the duct axis.

These results indicate that the CFA method is well suited to predict the pressure drop in ducts perpendicular to  $B$  even for values of  $Ha$  and  $N$  much lower than relevant for the blanket.

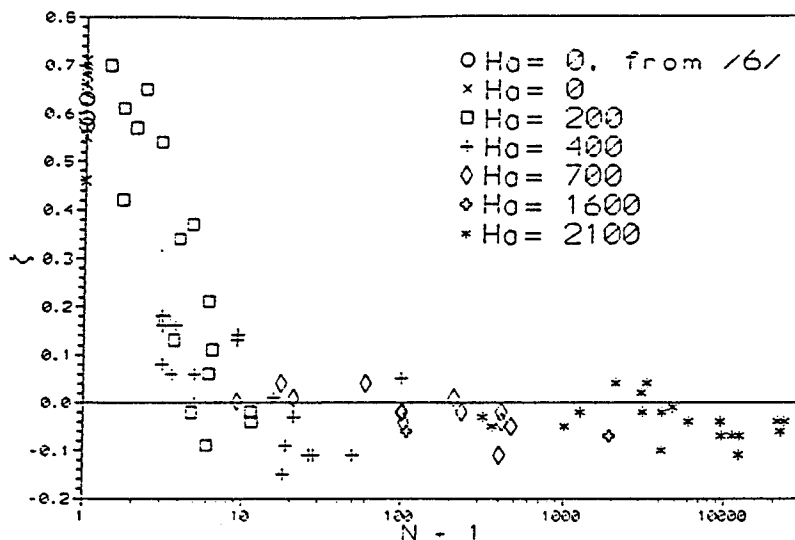


Fig. 5.5-6 Pressure loss coefficients for a 90° bend ( $C=0.05$ ) as a function of Interaction parameter [5-33]

### 5.5.3 Single ducts with changing flow direction or cross section in the plane of B (3D geometries)

#### 5.5.3.1 Expansions and Contractions

Additional pressure drop occurs if the geometry expands or contracts or if the flow turns into the direction of B. Similar effects occur if the magnetic field strength varies in the axial direction, e.g. at the ends of the magnet. For a convenient comparison of results, the additional pressure drop is related to the pressure drop of a fully developed flow in a straight duct over an equivalent length  $L_{3D}$ . The additional pressure drop in a conducting rectangular expansion is shown in Fig. 5.5-7 as a function of the wall conductance ratio. The Hartmann number is  $Ha = 1000$ . The rectangular duct expands from cross section  $2 \times 2$  to  $4 \times 2$ . For highly conducting walls,  $C > 1$ , this additional pressure drop is negligible compared with the high MHD pressure drop of the fully developed flow. If  $C$  decreases the additional pressure drop becomes relatively more important. For the limit  $C \rightarrow 0$   $L_{3D}$  tends to the finite limit  $L_{3D} \approx 14$ . These results are valid only for the case considered. For weaker expansions or smaller expansion ratios lower values for  $L_{3D}$  are expected. Any other expansion ratio or geometry can be treated with the numerical code based on the asymptotic method.

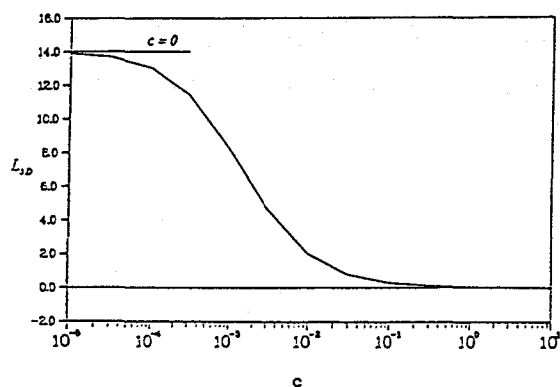


Fig. 5.5-7 Additional pressure drop in a conducting rectangular expansion  $2 \times 2 \rightarrow 4 \times 2$  in the plane of the field compared with the equivalent length  $L_{3D}$  of a fully developed duct flow as a function of  $C$ . ( $Ha = 1000$ ) [5-52]

As a further example, an insulated, circular expansion is considered. The behavior in a round pipe expansion is similar to the rectangular expansion. The geometry changes smoothly from  $r_1 = 1$  for  $x < -2$  to the value  $r_2 = 2$  for  $x > 2$ . Near  $x = 0$  a strong pressure gradient is visible in Fig. 5.5-8. For  $x > 1$  part of the pressure drop is recovered. The velocity profiles in and behind the expansion are shown in sub-

plots. In the expansion the fluid is pushed towards the sides and forms two jets while in the center the flow is almost stagnant or even reversed. Figure 5.5-8 also shows the fact that the development length in insulating circular pipe flow (indicated by deviations from fully developed pressure gradient) becomes very long, i.e.  $10L$  and  $20L$  before and behind the expansion.

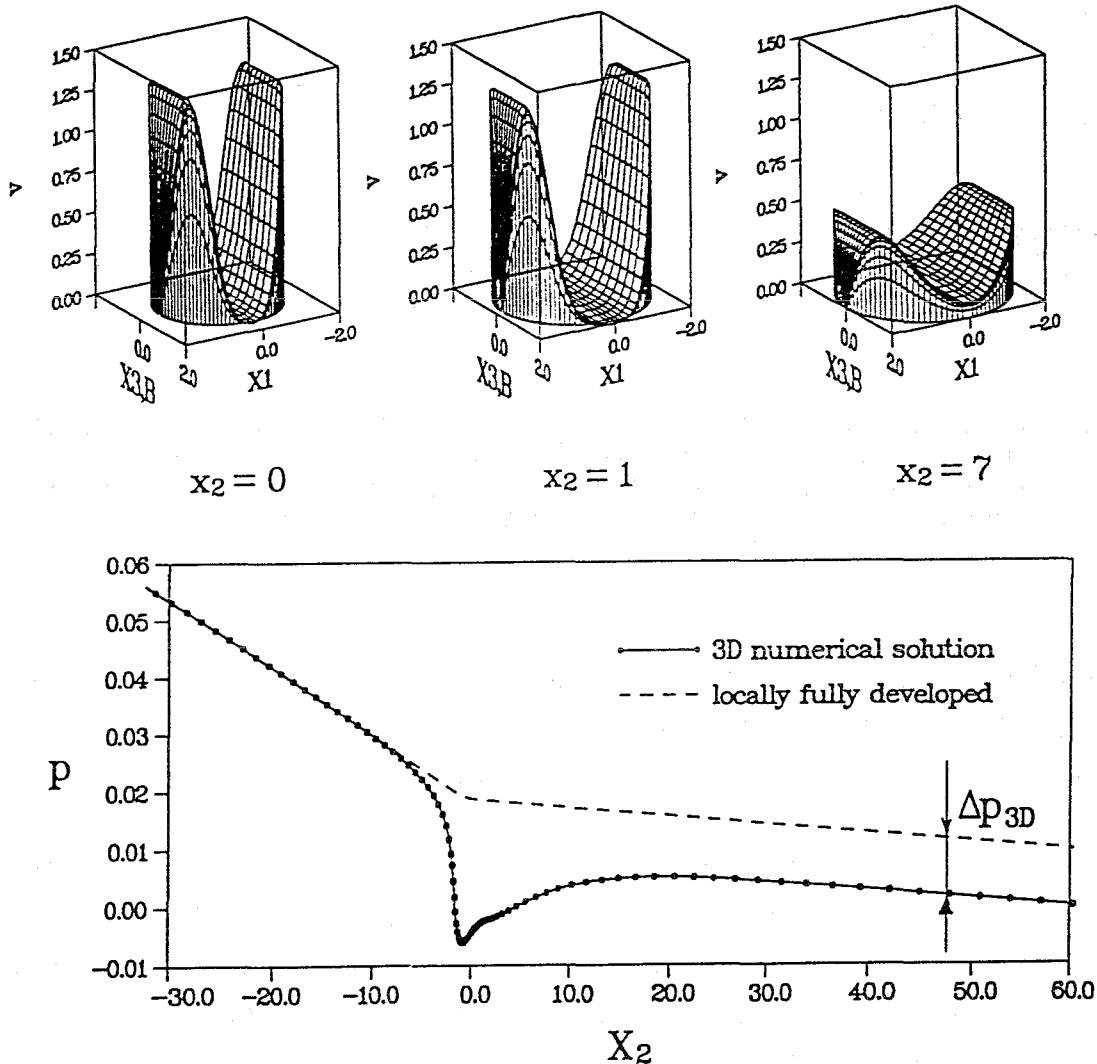


Fig. 5.5-8 MHD flow in an insulated circular expansion at  $Ha = 1000$ .  $r(x_2 < -2) = 1$ ,  $r(x_2 > -2) = 2$ . Flow pattern and pressure distribution along the axis [5-52]

### 5.5.3.2 The $90^\circ$ -bend with one leg parallel to B

In any blanket design bends appear, in which the flow changes the direction with respect to the magnetic field. In the blanket concept described by [5-2], there are two bends forming an U-bend with radial-toroidal-radial orientation. Since in the toroidal part which is perfectly aligned with the magnetic field the main flow direction coincides with the direction of the field the induced potential in this duct is zero. This part of the bend therefore serves as an additional current path and

increases the total current and pressure drop in the radial leg. A schematic of the considered geometry is shown in Fig. 5.5-9.

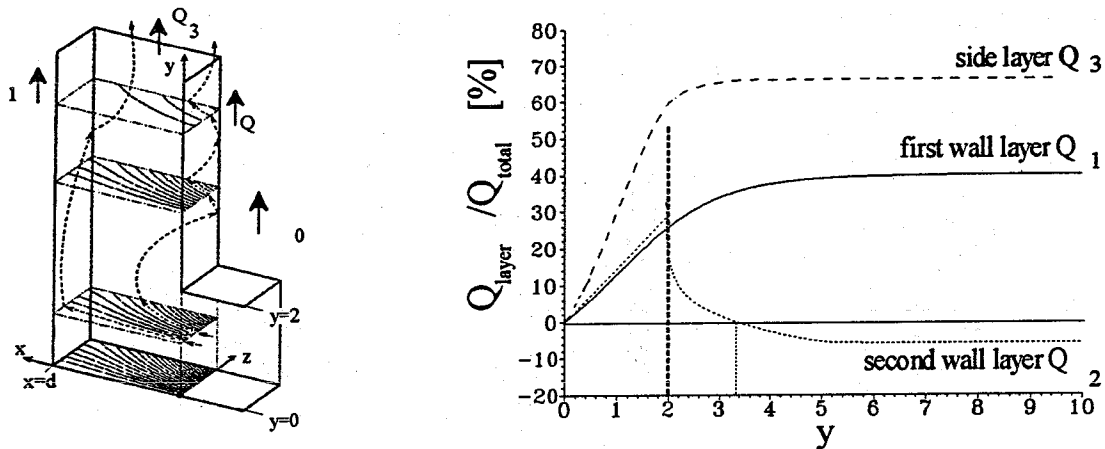


Fig. 5.5-9 a) Isolines of potential at the bottom of the toroidal duct, streamlines in the toroidal core and sketch of flow path in the layers [5-53]  
 b) Flow rates in the wall-adjacent boundary layers in the toroidal duct. Sketch of geometry, orientation of the magnetic field, and coordinates.  $Ha = \infty$ ,  $C = 0.052$  [5-54]

The detailed analysis of this problem based on inertialess, inviscid limit ( $N, Ha \rightarrow \infty$ ) is described by [5-53]. Here only the main results are summarized.

- The core of the toroidal duct has no component of velocity in the main toroidal direction.
- The flow in the toroidal duct is confined to thin boundary layers of the thickness  $\delta \sim Ha^{-1/2}$  at all walls which are aligned with the field and which carry all flow rates  $Q_i$ . Even at the first wall there is a jet which carries a significant rate  $Q_1$  of the total volume flux. In the boundary layer near the second wall the flow may even get reversed. Additionally exists an intensive mass exchange between the layers, which would be favourable for heat transfer purposes.
- The core in the toroidal duct is by no means stagnant. There is an intense exchange of fluid between the four layers which are aligned with the field. This exchange happens because of a direct interaction between neighbouring layers or even along larger distances if the core is involved.
- There is fluid motion in the core only in planes  $y = \text{const}$ , and it does not contribute to an  $O(1)$  volume flux in the toroidal direction. Nevertheless, this motion may lead to improved heat transfer conditions. The intensity of the flow in the core is most pronounced at the Hartmann wall of the toroidal duct and vanishes at the plane of symmetry. The flow behaves qualitatively like the flow analyzed by [5-53].

The flow in the radial-toroidal bend has been investigated experimentally [5-54] and compared with the results of the asymptotic model. Here we summarize only the main results and conclusions:

With the AM the solution of the three-dimensional MHD flow is obtained once the surface potentials and the pressure in the core are known. The experimental results of the electric potentials on the Hartmann walls in the radial and the toroidal duct as well as on the first and the second wall show neither an influence of  $Ha$  and  $N$  in the ranges  $Ha = 2 \cdot 10^3 \rightarrow 8 \cdot 10^3$  and  $N = 2 \cdot 10^2 \rightarrow 3 \cdot 10^4$ . The agreement between the AM and the experiment is quite good. These results demonstrate that the flow in the core behaves like an inviscid, inertialess flow as long as  $Ha$ ,  $N \gg 1$ . At the side walls in the vicinity of the bend, however, an influence of the wall potential on inertia has been detected. The potential there scales proportional to  $N^{-1/3}$ . This indicates that with increasing flow rate the side layers get thicker. Due to the thickening of the side layer these layers are capable of carrying a higher electric current, which is not taken into account in the asymptotic theory. The current can short-circuit within the liquid metal and produces there an inertial part of the pressure drop which is proportional to the thickness of the layer, namely to  $N^{-1/3}$ . The surface potentials on the side walls also showed that for  $N \geq Ha^{3/2}$  the experimental values tend to the calculated ones, as predicted by the theory.

Figure 5.5-10 shows experimental values of the total pressure drop over the whole bend. The calculated asymptotic limit is confirmed almost exactly by the experiment for high values of  $N$ . For  $N < 2 \cdot 10^3$  the total pressure drop shows a significant dependence on  $N$  and  $Ha$ , which may be fitted by the following correlation:

$$\Delta p_{total} = \Delta p_{asymptotic} + 0.406 N^{-0.337} + 0.0939 Ha^{-0.565} .$$

The expression has been obtained by a statistical analysis of the experimental data. The exponents  $-0.337$  and  $-0.565$  are very close to theoretically predicted values  $-1/3$  and  $-1/2$ , respectively. This means that in the inertial flow regime the layers are characterized by inertial-electromagnetic interaction. The asymptotic value  $\Delta p_{asymptotic}$  for high  $Ha$  and  $N$  is that obtained for the inertialess limit for  $N > Ha^{3/2}$  and may be further split in a part of fully developed MHD flow perpendicular to the field and an additional contribution of inertialess 3D effects like:

$$\Delta p_{asymptotic} = \Delta p_{fd} + \Delta p_{3D} ,$$

or

$$\Delta p_{asymptotic} = (l_{rad} + l_{3D}) \left. \frac{\partial p}{\partial x} \right|_{fd}$$

The equivalent length  $l_{3D}$  characterizing the additional pressure drop  $\Delta p_{3D}$  in the considered bend flow is  $l_{3D} = 0.563$ , which is for sure not critical for blanket applications. Since some blanket elements require flows with  $N < 2 \cdot 10^3$ , the above named equation can be used as inertial correction to the theoretically obtained asymptotic solution for pressure drop.

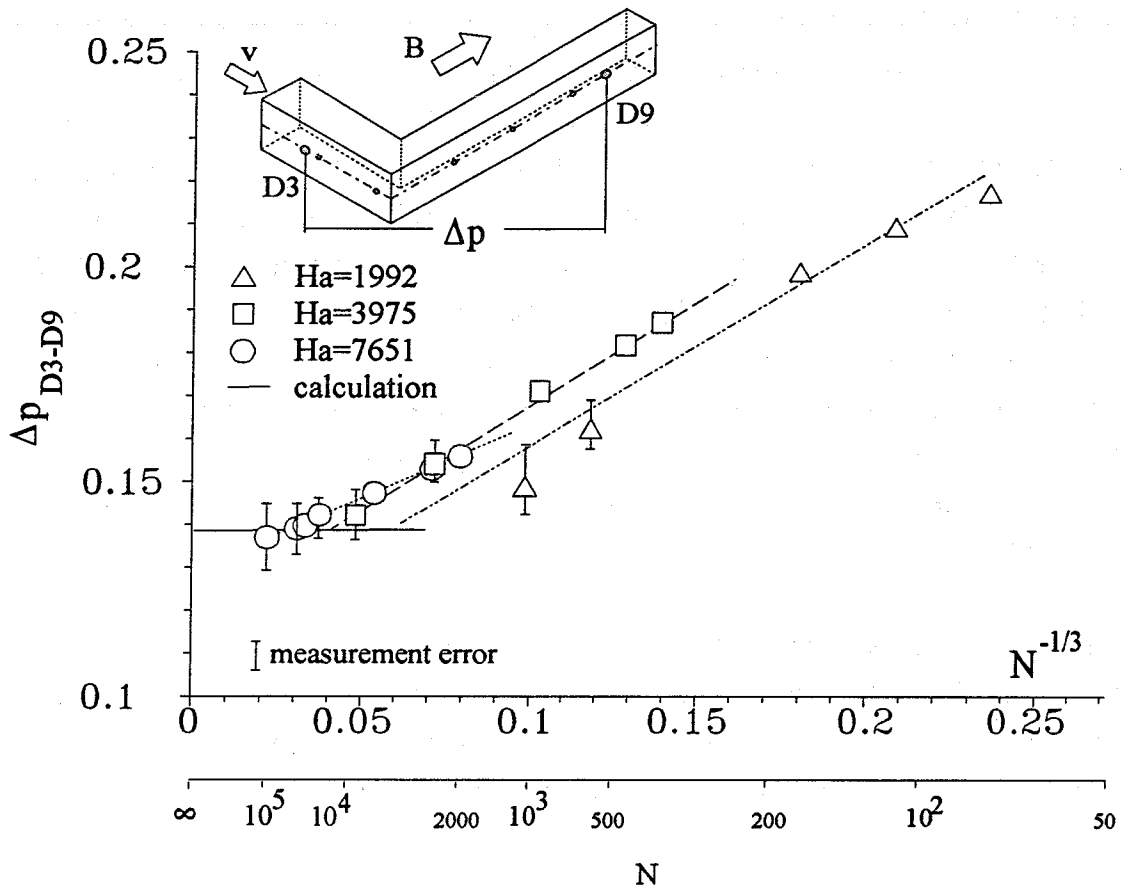


Fig. 5.5-10 Pressure differences between D3-D9 for different values of  $N$  at varying  $Ha$  compared to the asymptotic theory  $N, Ha \rightarrow \infty$  [5-54]

In real engineering applications the desirable perfect alignment of the toroidal duct walls with the magnetic field cannot be achieved. To investigate the effect of small inclinations with respect to the magnetic field direction the test section was turned in the experiment by small angles. The maximum angles of inclination with respect to a rotation around the  $z$ -axis were limited by the test volume of the used magnet to  $-5^\circ < \Theta_z < 15^\circ$ . Figure 5.5-11 shows the total pressure drop for the three angles  $\Theta_z = -5^\circ, 0^\circ, 15^\circ$  as a function of  $N$ . For high values of  $N$  the pressure drop caused by the flow with the three orientations is almost the same.

For small values of  $N$  the pressure drop in bends with  $\Theta_z = -5^\circ$  and  $\Theta_z = 0^\circ$  is still comparable, but significantly different from the case of  $\Theta_z = 15^\circ$ , for which it is about 30% higher. The reason for higher pressure drop in the latter case can be explained by the internal layer, which occurs at the inner corner of the bend along field lines. This layer carries a significant amount of the total flow rate in a thin, high velocity jet from the radial leg to the toroidal one. This high-velocity jet now is responsible for higher inertial sensitivity of the flow. Figure 5.5-11 shows further that for all inclinations the dependence  $\Delta p \sim N^{-1/3}$  remains unchanged.

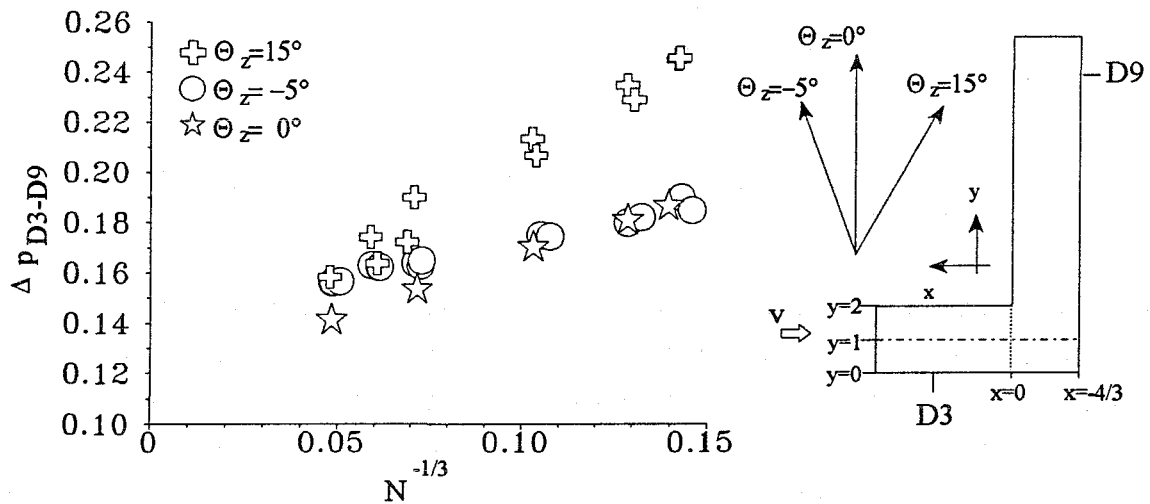


Fig. 5.5-11 Total pressure drop for different values of the inclination angles  $\Theta_z = -5, 0, 15$  as a function of  $N$  at  $Ha = 4175$  [5-54].

### 5.5.3.3 U-bend flows

The U-bend flow-problem represents in principle a coupling between the flow in two  $90^\circ$ -bends. Most of the flow features are similar. In the ducts oriented in the magnetic field direction, a zero potential is induced, whereas in the ducts perpendicular to the field a potential due to  $\mathbf{v} \times \mathbf{B}$  is induced. Therefore, these toroidal ducts act as a shortcut for the electric current, forcing the flow in the radial ducts towards the side walls and moreover producing a 3D pressure drop. If the distance of the two  $90^\circ$ -bends is less than the order  $l \sim \sqrt{Ha}$  an electric current between the two bends can circulate because of an opposite induced potential in the radial ducts (see Fig. 5.5-12). This additional global current leads to an amplified 3D effect compared to a single  $90^\circ$ -bend and as a consequence to a higher 3D-pressure drop in the U-bend compared to two  $90^\circ$ -bends.

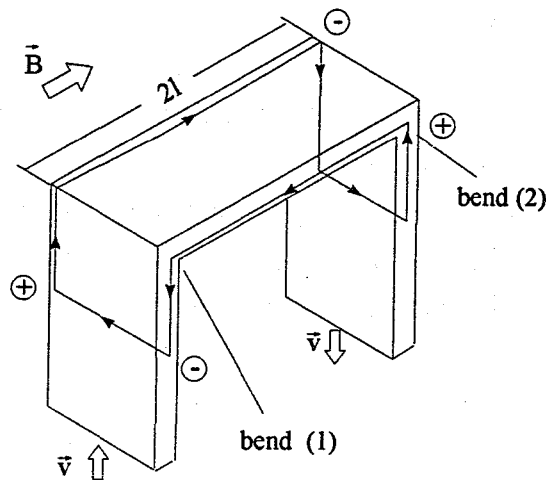


Fig. 5.5-12 Sketch of the additional global current path in a radial-toroidal-radial U-bend

The U-bend flow at high values of Hartmann number and Interaction parameter has been experimentally investigated in the context of the multi-channel U-bend flows by [5-51]. A comparison of the measured wall potentials and the calculated ones shows excellent agreement like in the  $90^\circ$ -bend. The potentials on the Hartmann walls are independent of the interaction parameter in the range  $10^3 \leq N \leq 3.3 \cdot 10^4$  and independent of the Hartmann number in the range  $6 \cdot 10^2 \leq Ha \leq 2.4 \cdot 10^3$ , indicating that the core flow behaves like an inviscid, inertialess flow. Slight deviations in the potential measurements between the calculations and the experiment are confined to the immediate vicinity of the bend. In a distance of four characteristic length after the bend the flow reaches the fully developed flow regime, which is expressed by the pressure gradient of the fully developed MHD-flow in a rectangular duct, see Fig. 5.5-13.

The flow in the U-bend itself is affected by inertial effects. At high interaction parameters, the pressure drop in each of the two  $90^\circ$ -bends is the same but is still 8% higher than that calculated with the inertialess, inviscid asymptotic model, indicating that inertial effects are still present at higher interaction parameters, (see Fig. 5.5-14a). At higher flow velocities (decreasing interaction parameters) discrepancies in the pressure drop between the two  $90^\circ$ -bends appear, which are caused by the different effects of the electric current path due to the formation of recirculation regions in the bends, for detailed discussion see [5-54]. The total pressure drop in a U-bend flow is shown in Fig. 5.5-14b. The additional pressure drop originating by inertial effects  $\Delta p_{3D,N}$  in the U-bend scales like in the  $90^\circ$ -bend with  $\Delta p_{3D,N} \sim N^{-1/3}$ .

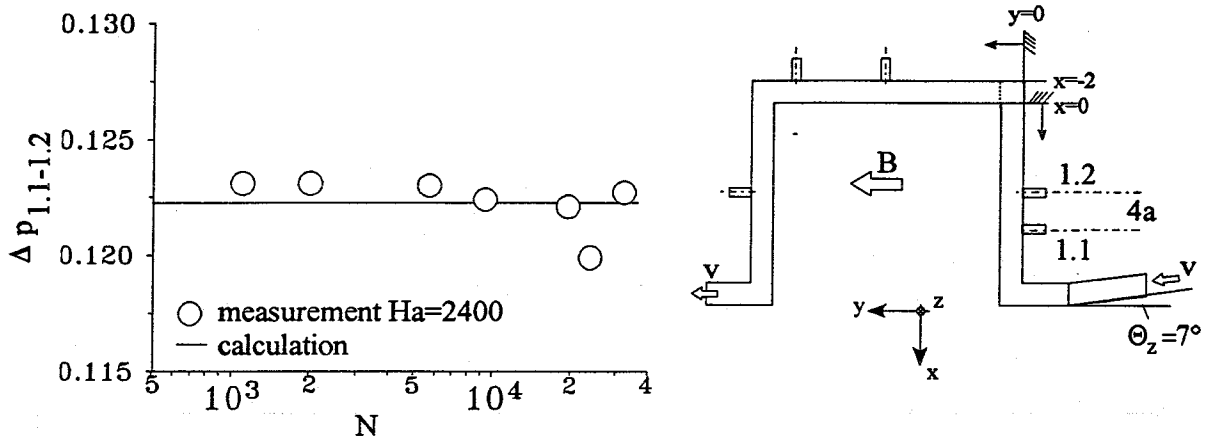


Fig. 5.5-13 Dimensionless pressure difference between the taps 1.1-1.2 in a single U-bend flow for  $Ha=2400$ ,  $C=0.038$  and  $\Theta_z=0^\circ$

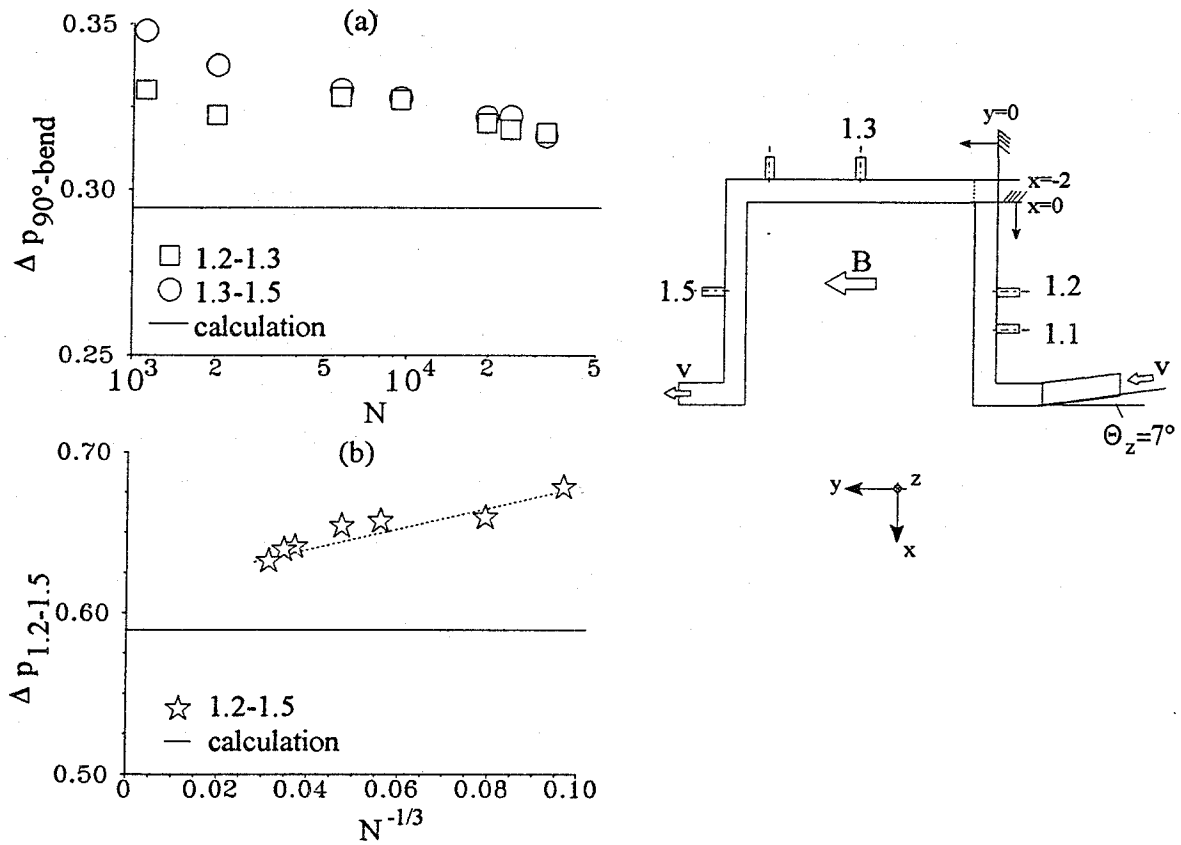


Fig. 5.5-14 a) Dimensionless pressure losses for  $90^\circ$ -bend flows in the radial-toroidal (O) and the toroidal-radial ( $\square$ ) direction for  $Ha=2400$ ,  $C=0.038$  and  $\Theta_z=0^\circ$ .  
 b) Dimensionless pressure drop in a U-bend for  $Ha=2400$ ,  $C=0.038$  and  $\Theta_z=0^\circ$

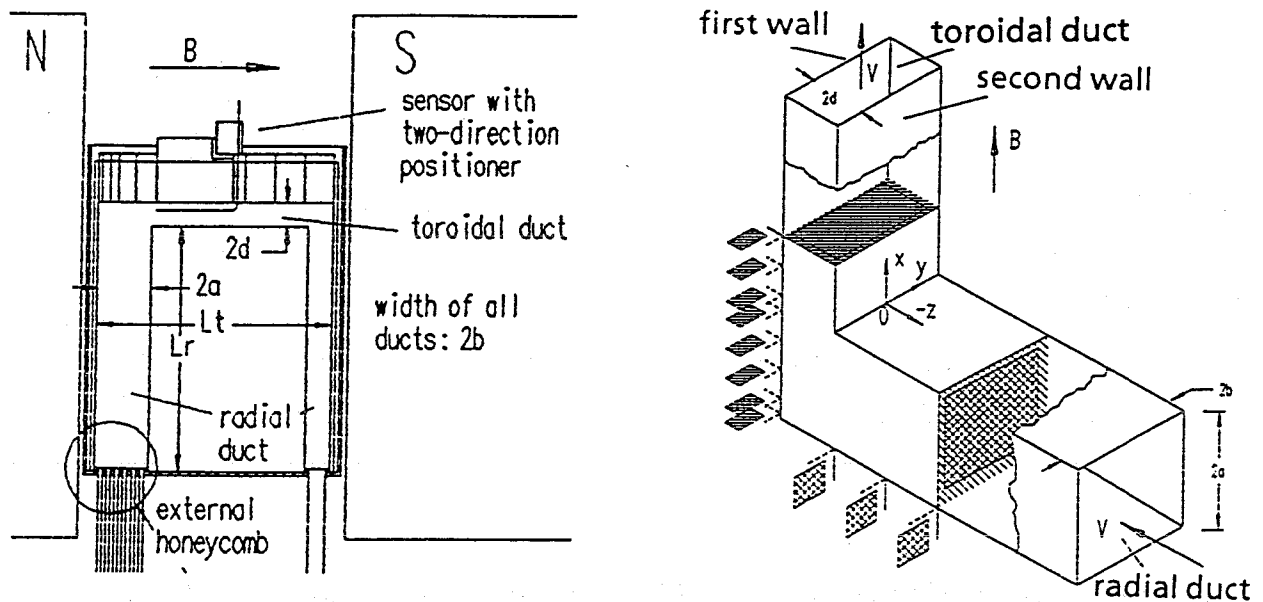


Fig. 5.5-15 Schematical graph of test section and used coordinate system [5-55]

A similar U-bend was also used in mercury experiments in the LAS to investigate the velocity distribution in the radial duct, the bend region and in the toroidal duct [5-55]. These experiments were performed at lower values of  $Ha$  and  $N$  ( $0 \leq Ha \leq 460$ ,  $0 \leq N \leq 150$ ). Figure 5.5-15 shows schematically the test section and the used coordinate system.

Figure 5.5-16 shows corresponding velocity distributions obtained by a hot wire probe for three different values of the interaction parameter. For purely hydrodynamic flow, a characteristic recirculation zone exists downstream of the inner bend corner. With increasing  $N$ , the liquid is pushed towards the side walls, and highest signals are observed close to the first wall as predicted by CFA analyses. For  $N=35$  a recirculation zone no longer exists. Surprisingly, the hot wire signals depict a maximum at  $y=0$  in the bulk of the toroidal duct.

In order to interpret these results, additional measurements with a potential probe were performed.

Figure 5.5-17 shows distributions of the dimensionless velocity components  $v_y$  and  $v_z$  and the absolute velocity  $v_{tr}$  in the plane perpendicular to the  $x$ -axis given by the vectorial sum of  $v_y$  and  $v_z$ . These measurements prove the existence of a pair of vortices with axis parallel to the magnetic field  $B$  which rotate in opposite directions. The sense of rotation is opposite to that sense predicted by the CFA.

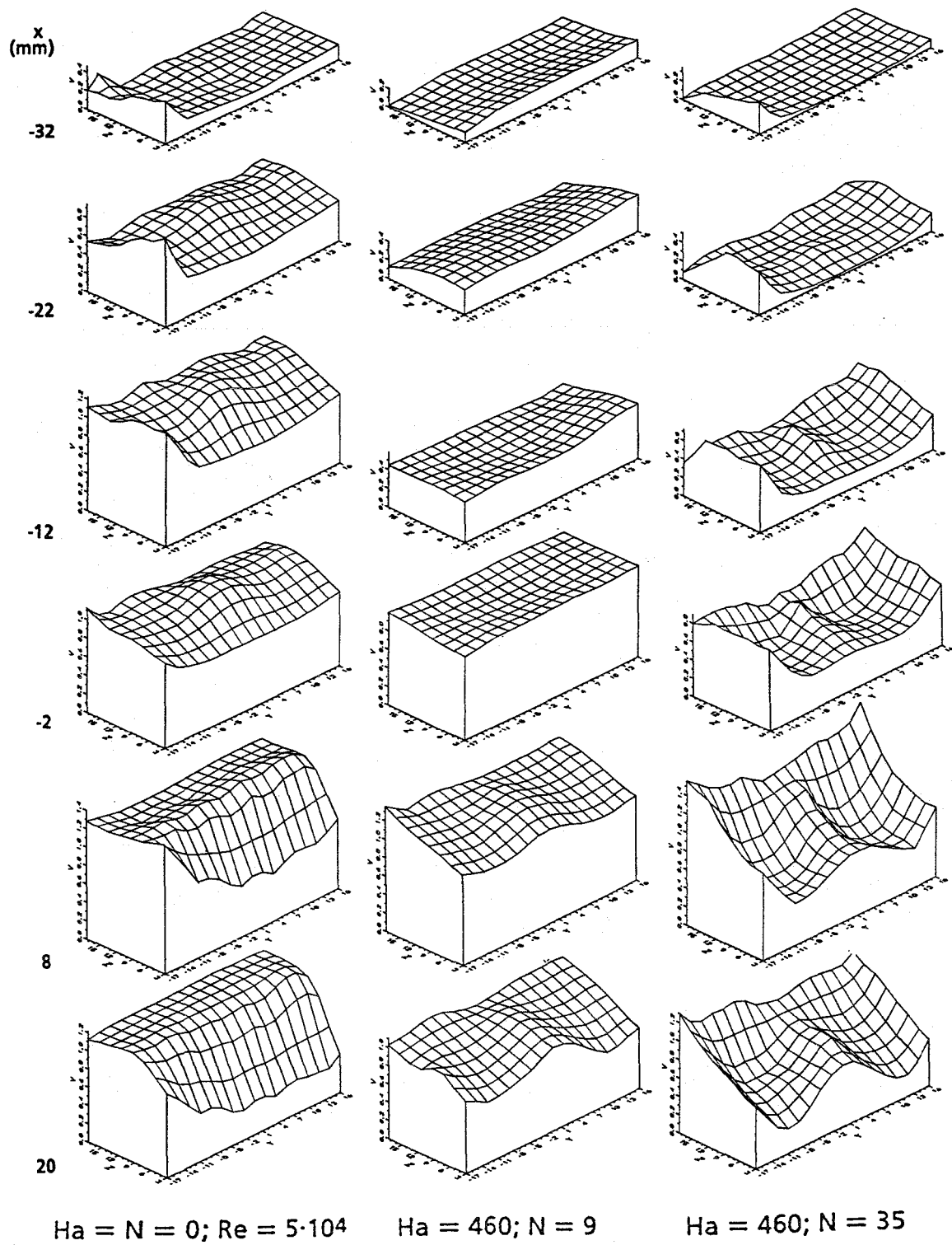


Fig. 5.5-16 Velocity distributions in the toroidal duct ( $C=0.06$ ; Geom. A) [5-55]

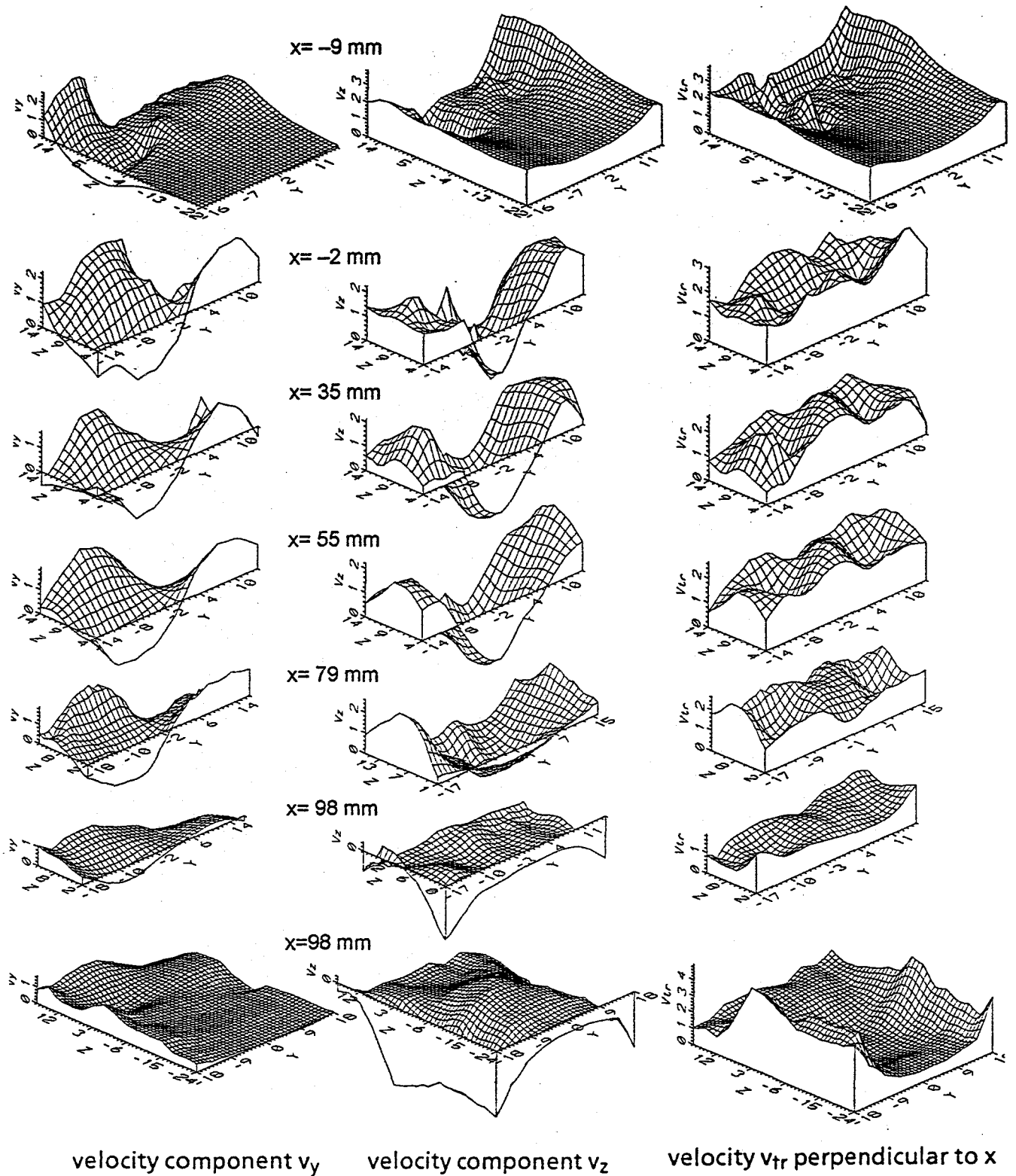


Fig. 5.5-17 Velocity components perpendicular to  $x$  (potential probe) ( $C=0$ ,  $Ha=255$ ,  $N=38$ ) [5-55]

The observed vortices are generated by inertial forces due to the M-shaped velocity profile in the radial duct. With increasing  $N$ , the vortex strength decreased.

Blanket relevant Hartmann numbers and Interaction parameters ( $Ha=8000$ ,  $N\approx 200$ ) are in between the experimentally investigated values and those assumed for the CFA analyses. Therefore, only qualitative conclusions for the blanket geometry can be drawn.

It was observed experimentally, that with increasing  $N$  liquid is increasingly pushed to the first wall as predicted by the CFA analysis. Therefore, the heat transfer from the first wall should be much better than for a slug velocity distribution with laminar flow as assumed in the blanket design [5-56].

The observed occurrence of vortices should be additionally beneficial for heat transfer. The transversal velocities could provide a very effective temperature equilibration in the first wall duct. This could lead to a simplified blanket design. The present knowledge, however, does not allow to judge if these vortices occur at blanket relevant conditions.

#### **5.5.4 Combining and distributing flows in manifolds**

Manifolds which connect a large duct with several sub-channels are required in all blanket designs. In respect to MHD effects it is again differentiated between flow geometries which are in the plane perpendicular to  $B$  and those which include a change of cross section in  $B$  direction (see Section 5.5.4.2)

##### **5.5.4.1 Manifolds in the plane perpendicular to $B$**

For manifolds in the plane perpendicular to  $B$ , again, no significant 3D effects associated with additional pressure drop occur for inertialess flows (compare section 5.5.2). Some examples for insulated duct walls [5-56] are shown in Fig. 5.5-18. The duct geometry in the lower part of the figure is relevant for the combining manifold at the blanket bottom. [5-51] finds negligible pressure drop due to the distribution of flow among the sub-channels for the cases considered. The velocity profiles exhibit constant core velocities along magnetic field lines. Deviations from the slug profile in the transverse direction disappear roughly at distances equivalent to the duct width.

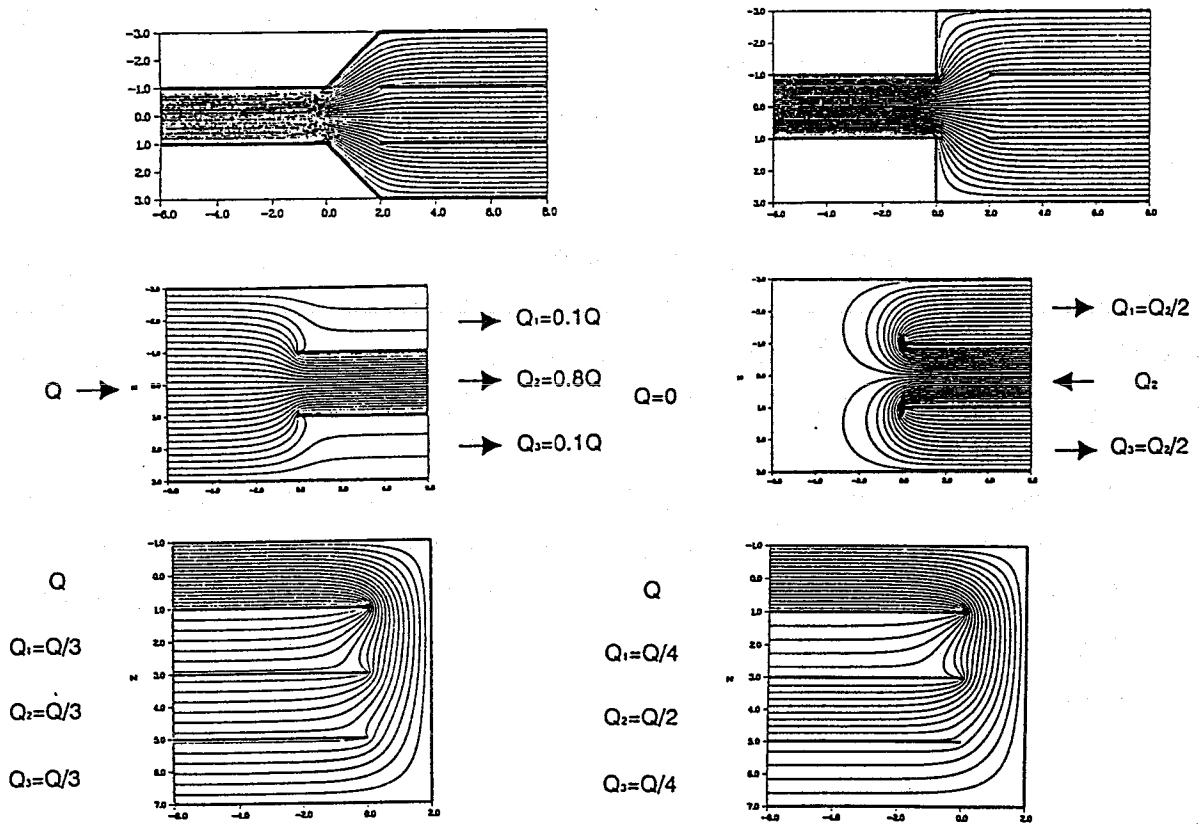


Fig. 5.5-18 Streamlines in the plane perpendicular to the field for some manifolds [5-56]

A T-junction can be considered as a special type of a manifold (see Figure 5.5-19). If all changes of geometry happen in the plane perpendicular to the field, again no significant additional 3D effects due to the flow distribution or recombination are expected for inertialess flow. This was confirmed for conducting walls theoretically using the asymptotic method by [5-24] and [5-51], for conducting and non-conducting walls, respectively.

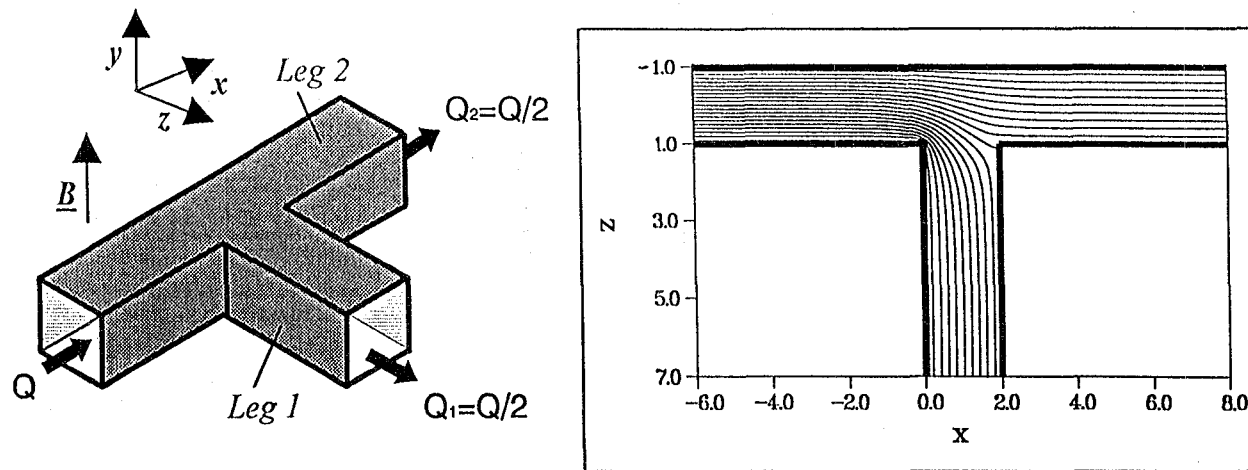


Fig. 5.5-19 Flow in a T-junction for equal flow distribution between legs 1 and 2  
a) Flow geometry; b) Streamlines; c) Development of the core velocity profile

Again, the question arises on the influence of inertial forces. Experiments were performed to investigate the pressure distribution in different types of T-junctions and the blanket bottom manifold [5-33, 5-57]. Figure 5.5-20 shows the test section dimensions, Table 5.5-3 contains characteristic quantities of the experiments performed partly with mercury in the LAS and with NaK at FZK. Test section c) included also the 90° bend discussed in Section 5.5.2.

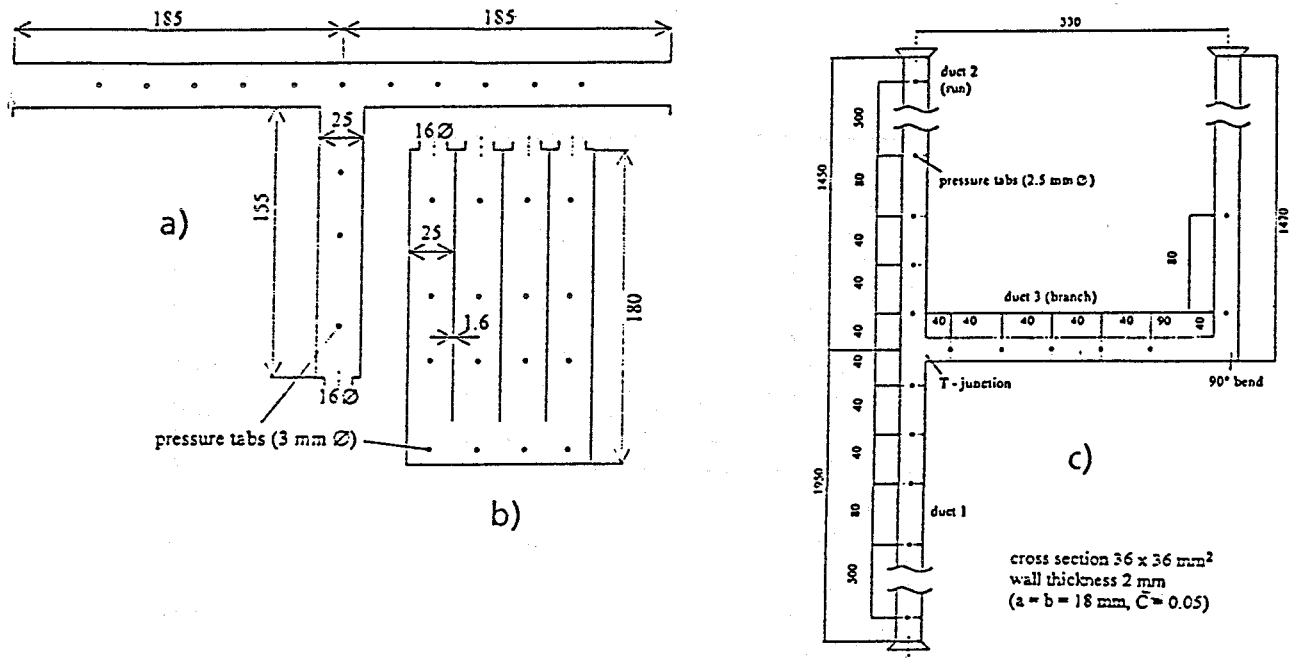


Fig. 5.5-20 Test sections for experiments with T-junction and 90° bend flow [5-57]

Table 5.5-3 Experimental Quantities [5-57]

Test Section	T-junction		90° bend C	blanket geometry b
	C	a		
a(mm)	18	12.5*	18	12.5*
C	0.05	0; 0.047	0.05	0.022; 0.047
Ha	0 - 2100	0 - 360	0 - 2100	0 - 360
N	0 - 11000	0 - 80	0 - 11000	0 - 80

\* for C=0; for other values slightly smaller

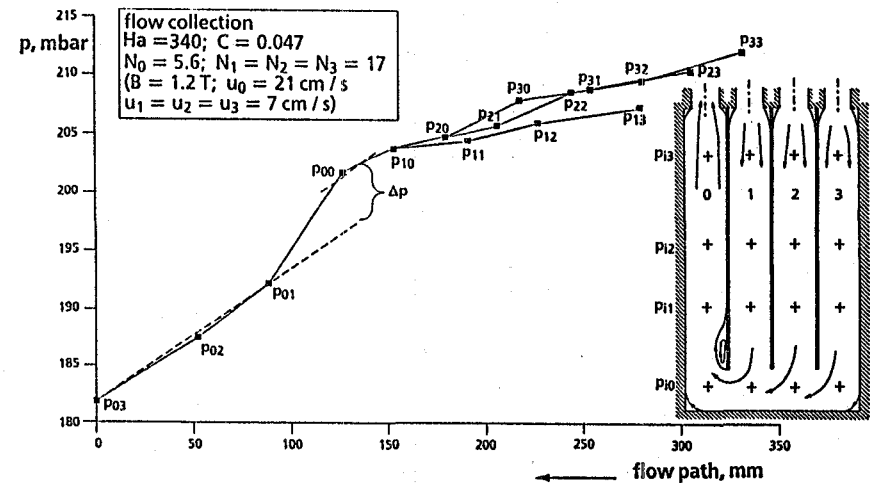
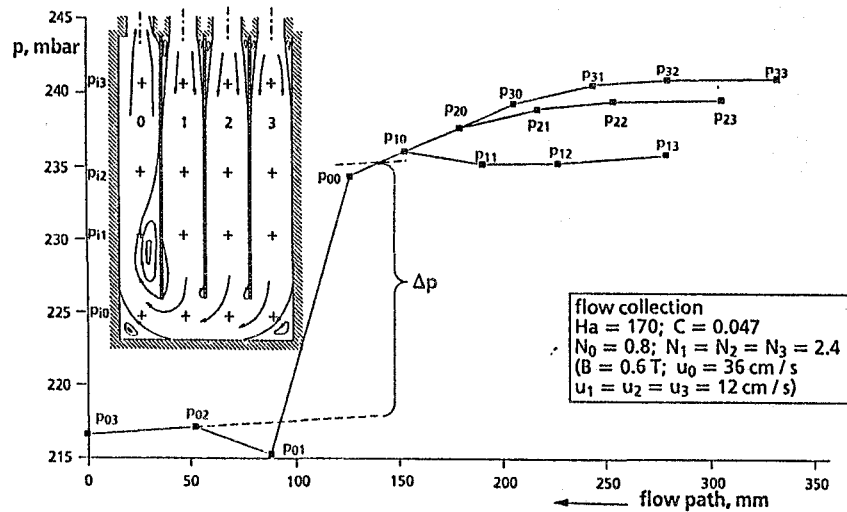
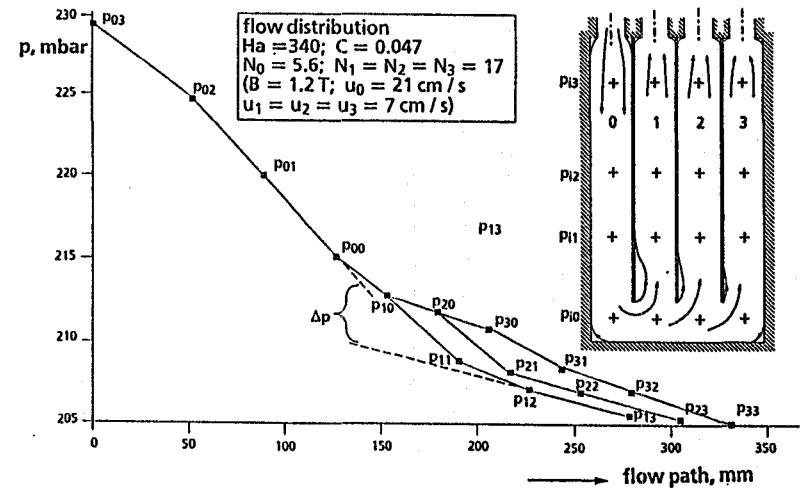
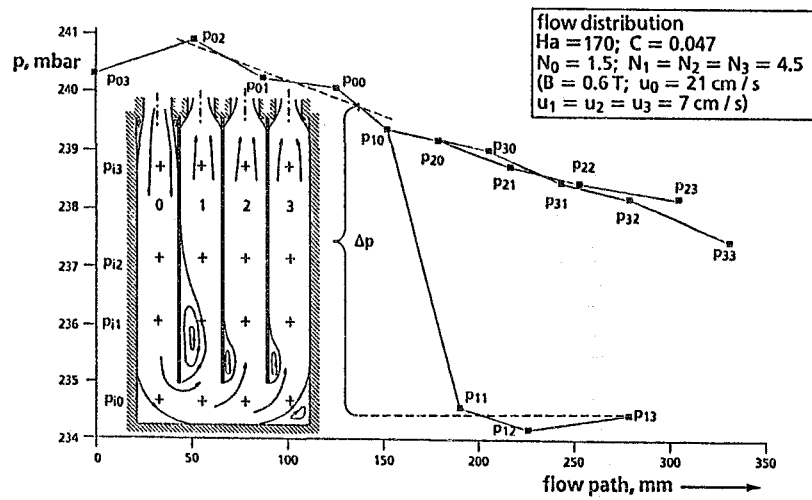


Fig. 5.5-21 Pressure distribution for the flow geometry relevant for the blanket bottom manifold [5-57]

As characteristic results, only pressure distributions for the blanket bottom manifold are shown (Fig. 5.5-21). Significant pressure drops due to strong recirculation zones occur at very small values of  $N$  which disappear at quite moderate values of  $N=20$  as demonstrated in Fig. 5.5-22 which shows the pressure loss coefficient  $\zeta$ , as a function of  $N$ .

All results clearly prove that no significant additional pressure drops due to 3D effects occur at blanket relevant MHD parameters for these quite complex geometries with distributing or collecting flows. This is of large importance for insulating walls where 3D effects easily might dominate the total pressure drop.

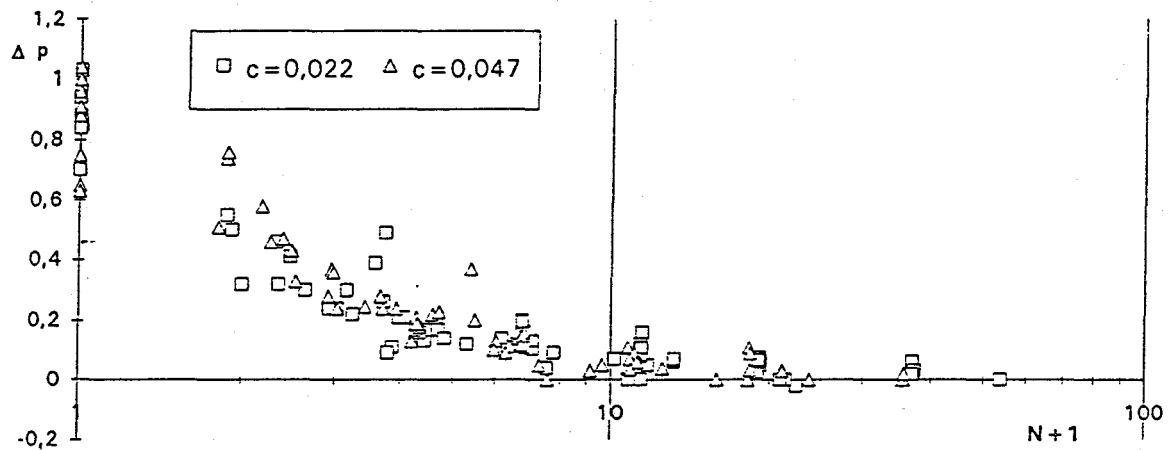


Fig. 5.5-22 Loss coefficient for duct "0" of the blanket bottom manifold ( $0 < Ha < 360$ ,  $C=0.02$ ;  $0.047$ , different flow ratios in ducts 1, 2 and 3) [5-57]

### 5.5.4.2 Manifolds in the plane of B

First theoretical investigations of the pressure drop in a manifold with conducting walls have been performed by [5-9]. The upper half of the manifold is shown in Fig. 5.5-23. In the first part, the flow expands from a flat duct to a larger one before it is distributed. In the expanding part the flow behaves as already discussed in Section 5.5.3.1. According to Hua [5-9], only marginal values of additional pressure drop are found due to the flow distribution to subchannels. A desirable flow distribution among coolant ducts can be achieved with a judicious choice of wall thickness distribution. As a result the MHD effects related to manifolds of this type can be neglected during the blanket conceptual design phase.

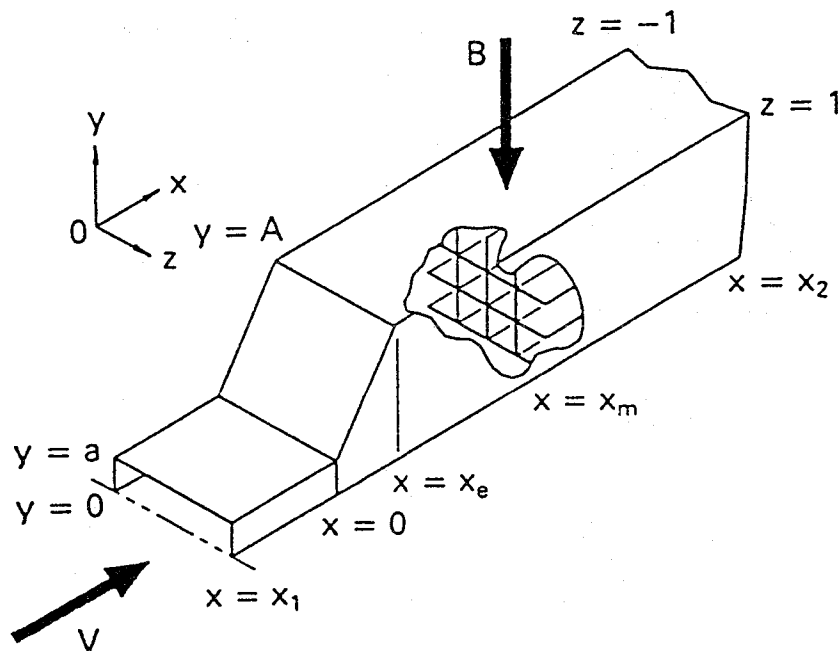


Figure 5.5-23 Geometry of a conducting manifold [5-9]

The geometry considered by [5-9] is only a rough approximation of the real blanket geometry. The flow in the poloidal collector of the Dual Coolant blanket [5-7] has been analyzed in detail using the asymptotic method and boundary fitted coordinates as introduced above. The modelled geometry is shown in Fig. 5.5-24. The duct is considered to have thin conducting walls. The flat rectangular channel has already collected the flow rates from the poloidal subchannels when the fluid enters the expanding region. The fluid flows further through the expansion at the end of which the cross section is almost of square shape. The last rectangular cross section is connected with the circular pipe by a smooth transition zone. All flow variables and non-dimensional parameters are scaled with the pipe radius as the characteristic dimension. The wall-conductance ratio and the Hartmann num-

ber have been chosen to be  $C=0.05$  and  $Ha=10^4$ , respectively. Figure 5.5-24 also shows isolines of wall potential plotted on the surface of the duct. The diagram shows the variation of pressure along the axis.

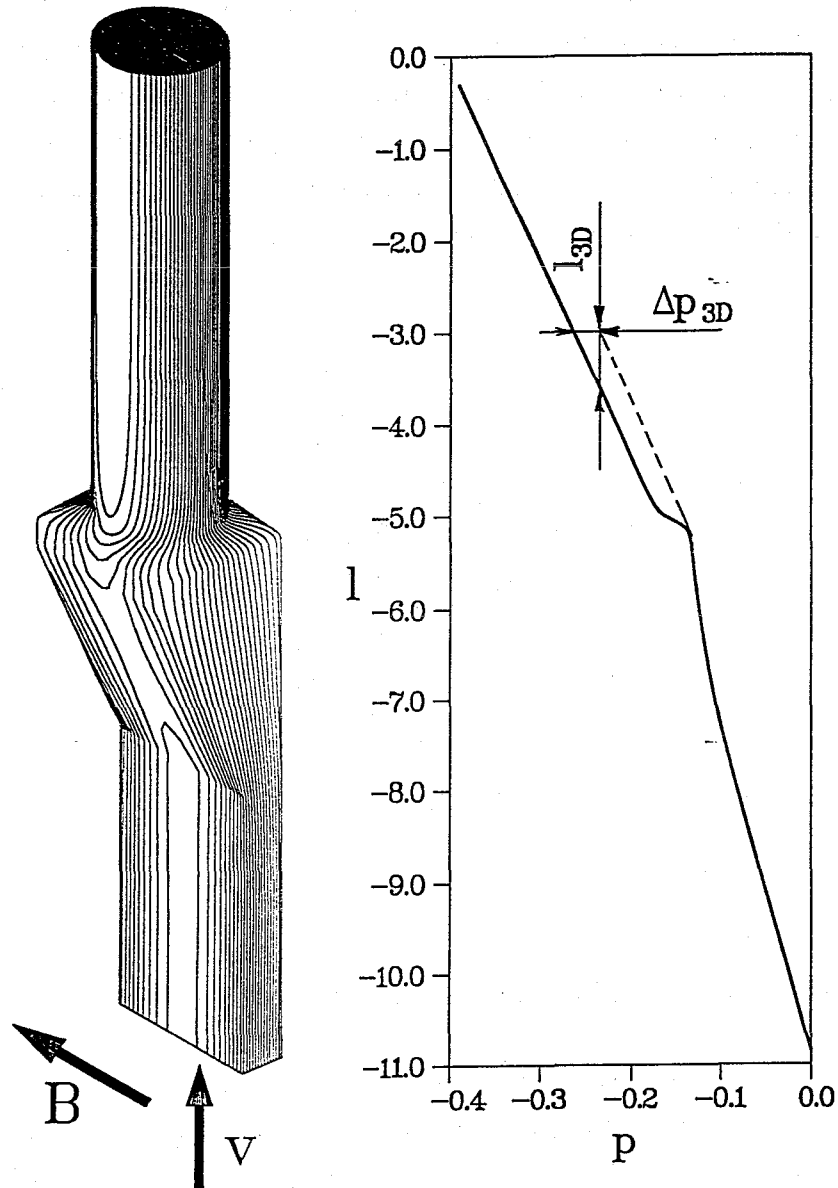


Fig. 5.5-24 MHD flow in a complex element of the Dual Coolant Blanket.  $Ha=10000$ ,  $C=0.05$ . Lines of constant wall potential on the surface of the duct, variation of pressure along the axial coordinate [5-24]

When the fluid passes through the expansion region it is not subjected to significant 3D-effects because the flow expands only in the plane perpendicular to the magnetic field. Due to the reduction of the velocity, the pressure gradient de-

creases in the expanding region. At the junction between the rectangular duct and the circular pipe 3D-effects are unavoidable. They cause there an irreversible pressure drop  $\Delta p_{3D}$ , as indicated in the diagram.  $\Delta p_{3D}$  is equivalent to the pressure drop in the circular pipe, estimated over a length of about  $L_{3D} \approx 0.6$ . A comparison with the total height of the blanket shows that this is a small amount. In the circular pipe the fully-developed pressure gradient of  $\nabla p = -C/(1+C)$  is reached very quickly in a short distance.

For insulated walls  $\Delta p_{3D}$  is assumed to be the same as for thin conducting walls. In order to extrapolate the results to blanket relevant conditions a factor of 2 was used to account for inertia effects. Since the pressure drop for insulated ducts are quite small, the contribution of  $\Delta p_{3D}$  to the total pressure drop becomes larger but is still moderate, compare Table 5.8-1.

Experimental results were obtained for a manifold geometry relevant for the self-cooled Pb-17Li blanket with poloidal-radial-toroidal ducts [5-58], where large "poloidal" ducts are connected with much smaller "radial" ducts. Although all duct axes are perpendicular to B, 3D pressure drops are expected to occur because the duct dimension varies in the direction of B.

Screening tests with mercury were performed in the LAS. Figure 5.5-25 shows schematically the investigated flow duct geometries, Table 5.5-4 contains additional characteristic values. The test section consisted of a poloidal duct with a cross-section of 125 mm x 125 mm, and five perpendicular radial ducts with dimensions 25 mm x 25 mm each. The radial ducts were electrically insulated from each other (simulating the use of FCIs in the blanket). The cross-section of the poloidal duct could be reduced by inserts to an area of 25 mm x 125 mm. Three configurations were investigated as follows:

(a) with insert; B parallel to the small side of the poloidal duct (two-dimensional flow),

(b) with insert; B parallel to the large side of the poloidal duct (three-dimensional flow);

(c) without insert.

Configuration (c) is the most relevant for the blanket; for configuration (b), it was expected that the pressure drops are even larger than for (c) (conservative case); for configuration (a), a negligible pressure drop was expected (and observed).

The pressure distributions were measured both along the axis of the poloidal channel and along the radial channels.

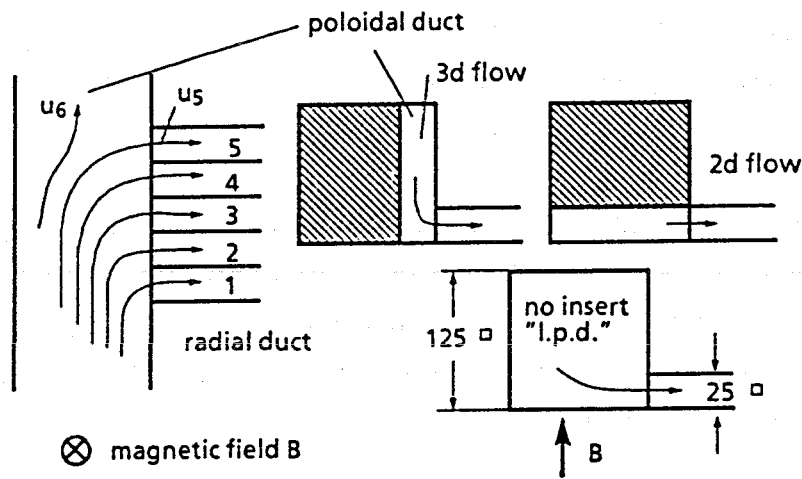


Fig. 5.5-25 Schematic diagram of manifold test sections [5-58]

Table 5.5-4 Characteristic values for the manifolds [5-58]

	poloidal duct	radial duct
<u>blanket</u>		
a (mm)	80	37
M	7600	3900
N	300	200
C	0.01	0.02
k	-	38
<u>experiments</u>		
a (mm)	62.5; 12.5	12.5
$H_{a_{max}}$	1800	360
$N_{max}$	200	40
C	0; 0.004; 0.008	0; 0.025; 0.05
k	-	5

In the following, two characteristic results are presented. Figure 5.5-26 shows the effect of the number of radial channels (k) for configuration (b) with distributing flow (the results for combining flow are very similar). With increasing values of k,

the normalized pressure drop increases. The maximum pressure drop occurs in the middle duct.

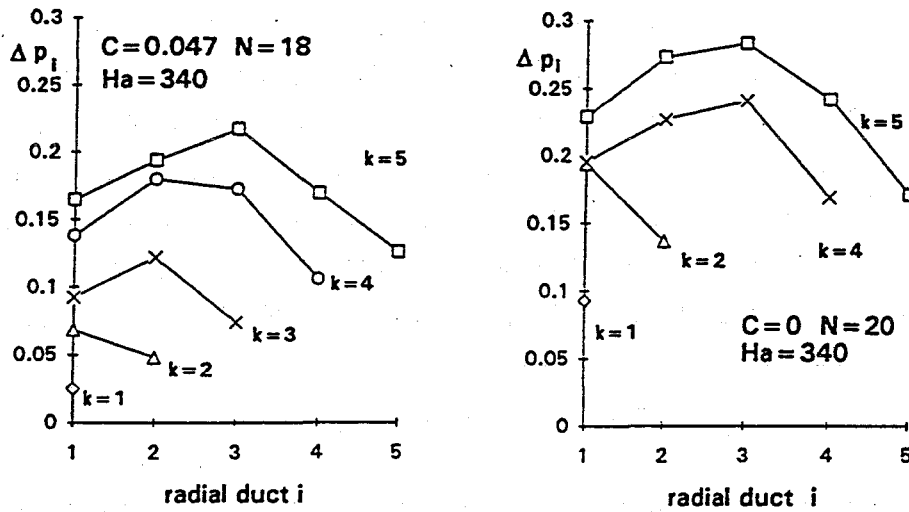


Fig. 5.5-26 Manifold pressure drop (distributing flow): effect of channel number  $k$  for configuration (b) [5-58]

Figure 5.5-27 depicts the dependence on the Interaction parameter  $N$ . A distinct increase is observed for  $N < 5$ . In this range, the first pressure measurement in the radial duct indicated a recirculation zone resulting from inertia effects. The values for configuration (c) are slightly lower than those for configuration (b).

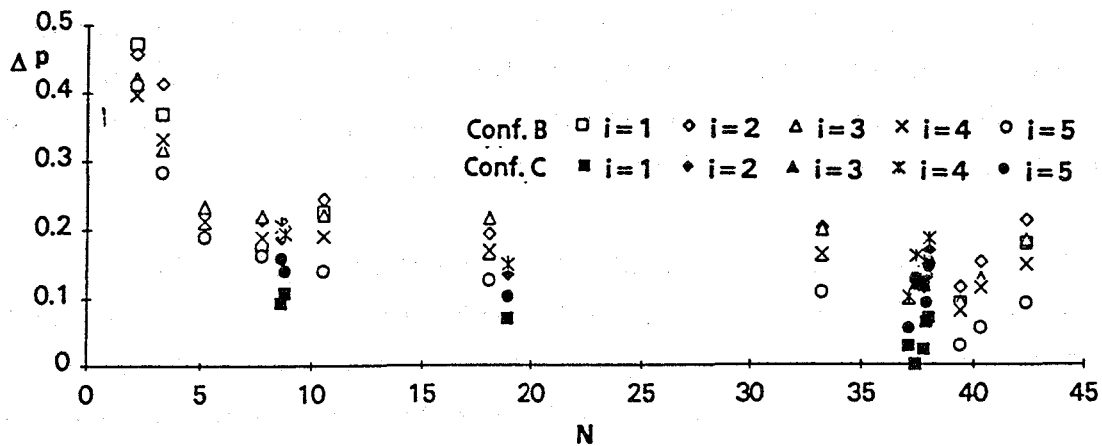


Fig. 5.5-27 Manifold pressure drop (distributing flow): effect of interaction parameter  $N$ :  $C = 0.047$ ;  $k = 5$ ;  $Ha = 180 - 360$  [5-58]

Using very conservative assumptions (e.g. linear increase of  $\Delta p$  with  $k$ ) in order to extrapolate the present results for blanket conditions, a value of 0.78 MPa is obtained which corresponds fairly well to the value estimated previously. With this value there is still a margin of 4 MPa to the maximum tolerable system pressure.

### 5.5.5 Liquid metal flow interaction in multi-channel ducts

Most blanket designs consist of an arrangement of a number of parallel channels. In the case when these channels are electrically insulating, the flow in each sub-channel may be considered to be a completely decoupled single channel flow as discussed before. If there is no insulation at a common conducting wall separating the fluids of two adjacent ducts then, there is electrical coupling between the ducts, which is called the multi channel flow (MCF). In the following two sections MCF in straight ducts (2D) and MCF in U-bends (3D- MCFs) are discussed.

#### 5.5.5.1 Multi-channel flow in straight ducts

MCFs have been considered e.g. by [5-59] for an array of three channels as shown in Fig. 5.5-28a. In this arrangement the potentials along the side wall have almost the same values at the junction of two ducts if the flow rates in the sub-channels are the same. Therefore no significant effects in MCFs are observed. Only for strongly different flow rates in the sub-channels or for different wall conductance ratios an influence due to MCFs is observed. With respect to applications in the radial-toroidal blanket concept [5-2] the arrangement of channels as shown in Figure 5.5-28b is more interesting as it represents the radial duct configuration. Here the potentials at dividing conducting walls can sum up along the whole array of sub-channels. The current can cross the walls and pass via all sub-channels, thus causing a strong electromagnetic coupling. Especially this case is investigated by in the following considerations in more detail.

The MHD flow in an array of sub-channels as shown in Fig. 5.5-28b with conducting dividing walls has been analyzed by Molokov [5-60, 5-61]. In his calculations he used the flow variables velocity and to the induced magnetic field. Since this approach leads to results only for fully developed flow conditions, we do not refer to this formulation in more detail. To keep the notation introduced before using  $v$ ,  $\phi$ , the velocity and the potential, Molokov's basic ideas are expressed using these quantities, which can also serve for calculations in more complex 3D geometries.

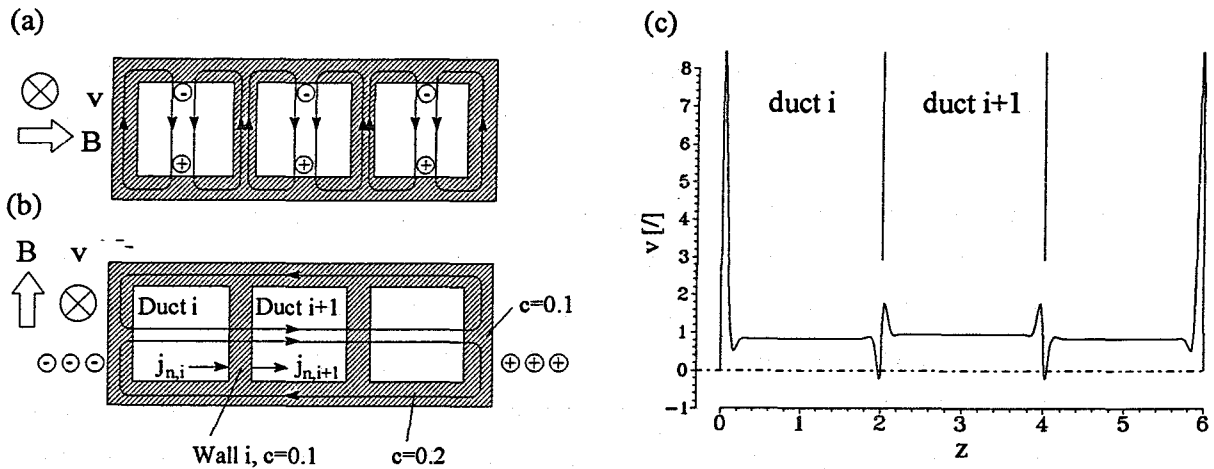


Fig. 5.5-28 Current path in 2D multi-channel duct flows (a, b). c) Velocity distribution of a 2D MHD-flow in the configuration (b) for  $Ha = 800$  [5-61].

The flow in each sub channel is considered to be fully developed. The walls are assumed to be thin and to have perfect contact with the liquid metal so that the thin-wall condition (see Section 5.3) can be directly applied at all the outer walls. At conducting dividing walls this condition needs some modification. Only a part of the current  $j_i$  which enters the wall  $i$  from the duct  $i$  at one side turns in the tangential direction and produces there a distribution of wall potential  $\phi_{w,i}$ . The rest of the current entering the wall at one side may leave it at the other side towards the adjacent sub-channel  $i + 1$  (see Fig. 5.5-28b).

$$j_{n,i} - j_{n,i+1} = c_i \Delta_t \phi_{w,i} .$$

This coupling condition allows the global current path across all sub-channels. The above named equation shows immediately some interesting features.

- If the pressure gradient  $\nabla p = j \times B$  (in the asymptotic limit  $Ha, N \rightarrow \infty$ ) is constant in each sub-channel the currents entering and leaving the side walls have to be equal  $j_{n,i} = j_{n,i+1}$ . There is no net current flux into the wall so that the potential  $\phi_{w,i}$  becomes the same linear function between the two Hartmann walls as for the core potentials  $\phi_{C,i}$ . Flow rates  $Q_{i,R}$  and  $Q_{i,L}$  of  $O(1)$  carried by high-velocity jets along the right and the left side of the wall  $i$  occur only if there exist potential differences between the cores and the walls. For the same pressure gradients in each channel they do exist only at the outer sides but they do not exist along the dividing walls. Thus the MCF in this case is comparable to a single channel flow in a duct with a width of the whole multi channel array.

- More interesting is the case when instead of the pressure gradients the flow rates are equal in all the sub-channels. This case is even more desirable because it should ensure a homogeneous convective heat removal by the array of channels in a technical application. Equal flow rates result mostly not in equal pressure gradients and thus cause different currents at both sides of the dividing walls. The equation leads for this case to a parabolic variation of potential  $\phi_w$  along the dividing wall. Since the potential differences across the right and left side layer at the dividing wall,  $\phi_{w,i} - \phi_{C,i}$ ,  $\phi_{C,i+1} - \phi_{w,i}$ , respectively, are the same but with opposite sign (since  $\phi_{C,i} = \phi_{C,i+1}$ ) the high-velocity jets in the layers have different directions. In one duct the flow rate carried by the layer contributes to the total flow rate while in the adjacent duct it acts in opposite direction.

If the wall conductance ratios of the sub-channels vary and the volumetric flow rate in the sub-channels is identical the velocity profiles may become even more peculiar. There may appear reversed flows and high velocity jets at the side walls, as depicted in Fig. 5.5-28c.

#### 5.5.5.2 Multi-bend flow

In the blanket concept proposed by [5-2] many parallel toroidal ducts are fed by the radial ones. At the opposite toroidal end of the blanket segment the flow direction turns again to the radial direction. Thus, the front part of the blanket is formed by an array of radial-toroidal-radial U-bends. As explained already in the previous section conducting dividing walls lead to an overall current path and a summation of potentials induced in the radial sub-channels where the flow direction is perpendicular to the applied strong magnetic field.

The high resulting voltage may cause now extreme 3D effects leading to high pressure drop near the radial-toroidal junction. There exists in addition the possibility of a current short-cut between one radial leg and the other one via the toroidal ducts. Such a current path becomes possible since the high voltages in both radial legs are induced with opposite sign. That this may lead to severe design problems has been realized already years ago [5-62].

In order to investigate the MHD flow in multichannel U-bends two types of experiments were performed:

- A) Screening Tests (ST) [5-63; 5-64]: Here, the aim was to investigate in a short period of time the influence of the main parameters. The experimental set-up was simple, however, enabled easily the variation of flow geometries. The measurements concentrated on the flow rate and a pressure drop in the individual channels. The experiments were performed in the superconducting MAGDA magnet of the LAS with the liquid metal alloy InGaSn.
- B) Detailed Experiments (DE) [5-48; 5-64; 5-65]: Here, the aim was to provide data for code validation. Detailed measurements of electric potentials at the test section surface and pressure differences at many positions were performed. These experiments were performed in the superconducting CELLO magnet of the FZK using the sodium-potassium alloy NaK as liquid metal.

In both experimental investigations a test section with 5 parallel ducts of square cross section was used. Figure 5.5-29 shows the test section used for the detailed experiments and Fig. 5.5-30 presents characteristic dimensions of the two test sections.

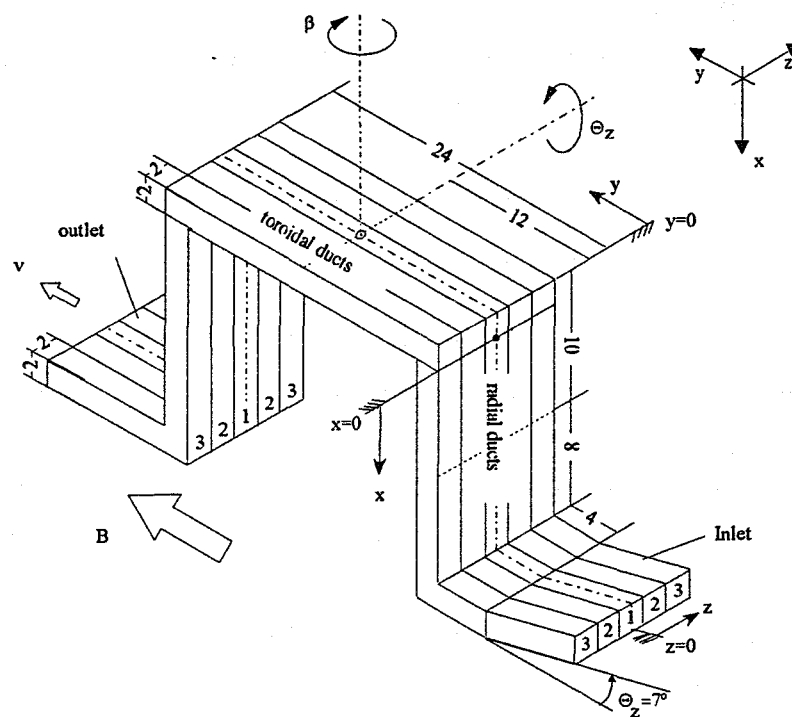
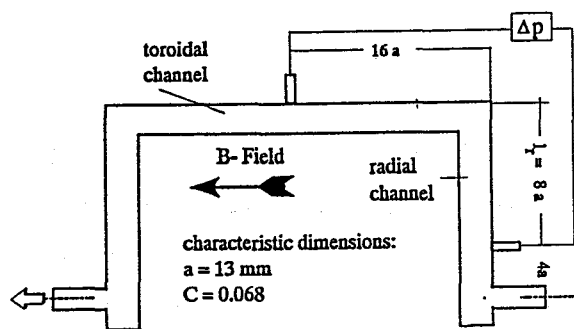


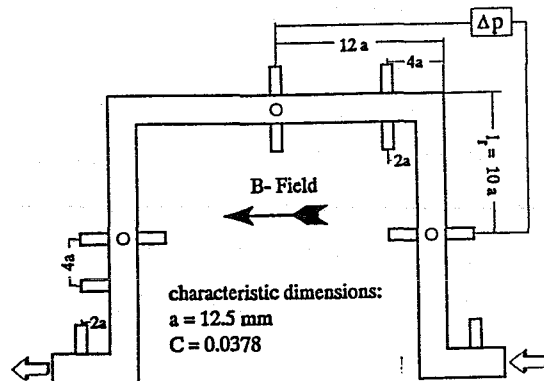
Fig. 5.5-29 Multi-bend test section. Geometry and coordinates [5-48]

### Screening Tests

Four different channel geometries were investigated with various combinations of wall conductances.



a) screening tests



b) detailed experiments

<p><b>Channel Geometry I</b> nonconducting outside walls; conducting dividing walls; number of channels <math>k = 1, 2, 3, 5</math></p>	
<p><b>Channel Geometry II</b> conducting outside walls; conducting dividing walls; number of channels <math>k = 1, 3, 5</math></p>	
<p><b>Channel Geometry III</b> conducting outside walls; nonconducting dividing walls in radial part; conducting dividing walls in toroidal part; number of channels <math>k = 5</math></p>	
<p><b>Channel Geometry IV</b> nonconducting outside walls; conducting dividing walls in first half of test section; nonconducting dividing walls in second half; number of channels <math>k = 5</math></p>	

Fig. 5.5-30 Schematical graph of the test sections

Figure 5.5-31 summarizes characteristic results for the case that the pressure drop in all channels was approximately equal. A strong uneven distribution (denominated with "multichannel effect" = MCE) of the individual flow rates  $Q_i$  normalized by the mean flow rate  $Q$  was observed for  $k \geq 3$ .

The MCE is more pronounced for non-conducting outside walls than for conducting walls because of two effects:

- In the first case more current in the side layers is forced to flow parallel to the magnetic field which results in higher volume flow rates in the side layers of the outer walls.
- The significant pressure drop in the radial duct with thin conducting walls has a damping effect on the redistribution compared to channel geometry II.

The difference between the multichannel U-bend and the multichannel single bend is revealed by comparison of Figs. 5.5-31a and 5.5-31c. The MCE is more expressed for the U-bend because global currents in the toroidal region are enforced due to the reversed flow direction of the electric currents in the second bend.

Figure 5.5-31d shows the results for the blanket relevant channel geometry. No marked maldistribution of the flow rates is observed which indicates that the suggested FCIs are a very effective means to reduce the MCE.

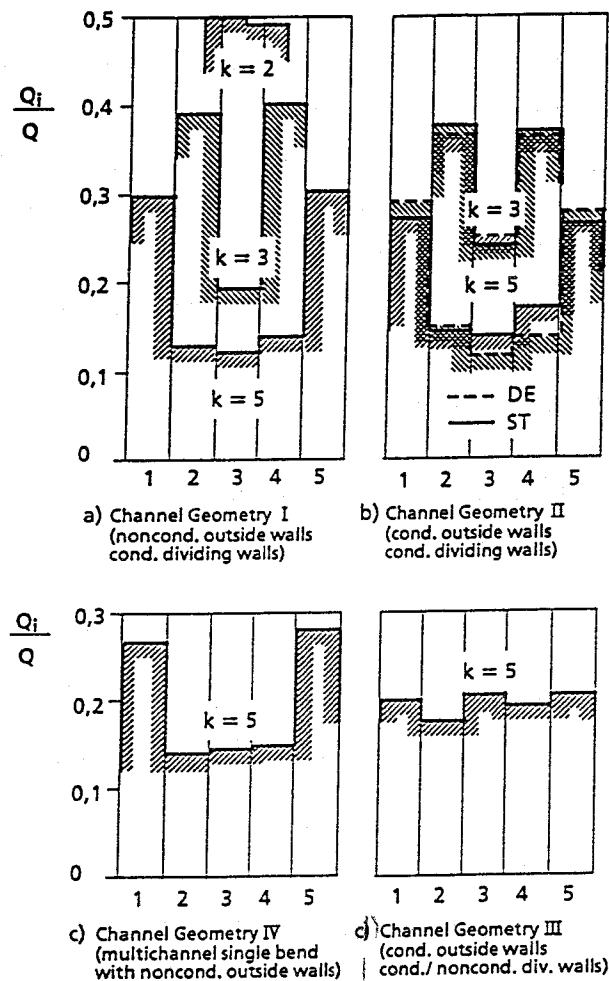


Fig. 5.5-31 Flow rate distribution for high Hartmann numbers and Interaction parameters ( $Ha \approx 1600$ ,  $N = 3000$ ) and  $\Delta p_i = \text{const.}$  [5-64]

### Detailed Experiments

The asymptotic model for the multi-channel flow is similar to the single-bend problem so that the numerical solution is completely given once the potentials on the duct wall and the pressure in the duct are known. The presentation of the experimental data is restricted to the technically important case, where all ducts have the same flow rate. More detailed informations about other flow configurations may be taken from [5-54]. Here only some characteristic positions, which are marked by thick lines in the graphs are presented. All other unmentioned positions show quite the same tendency.

In Fig. 5.5-32 results of the potential measurement for a three-channel U-bend flow are illustrated for different interaction parameters at a fixed Hartmann number of  $Ha = 2431$ .

In a distance of more than four characteristic lengths from the outer bend corner neither on the radial duct walls nor on the toroidal ones any dependence on the interaction parameter can be detected. The measured values agree rather well with the ones numerically obtained indicating that flows at this fusion typical Hartmann number exhibit the asymptotic distribution of wall potential in good agreement with the asymptotic model. This potential distribution is the one of a fully three-dimensional flow, exhibiting that three-dimensional effects persist in multi-channel system over long distances.

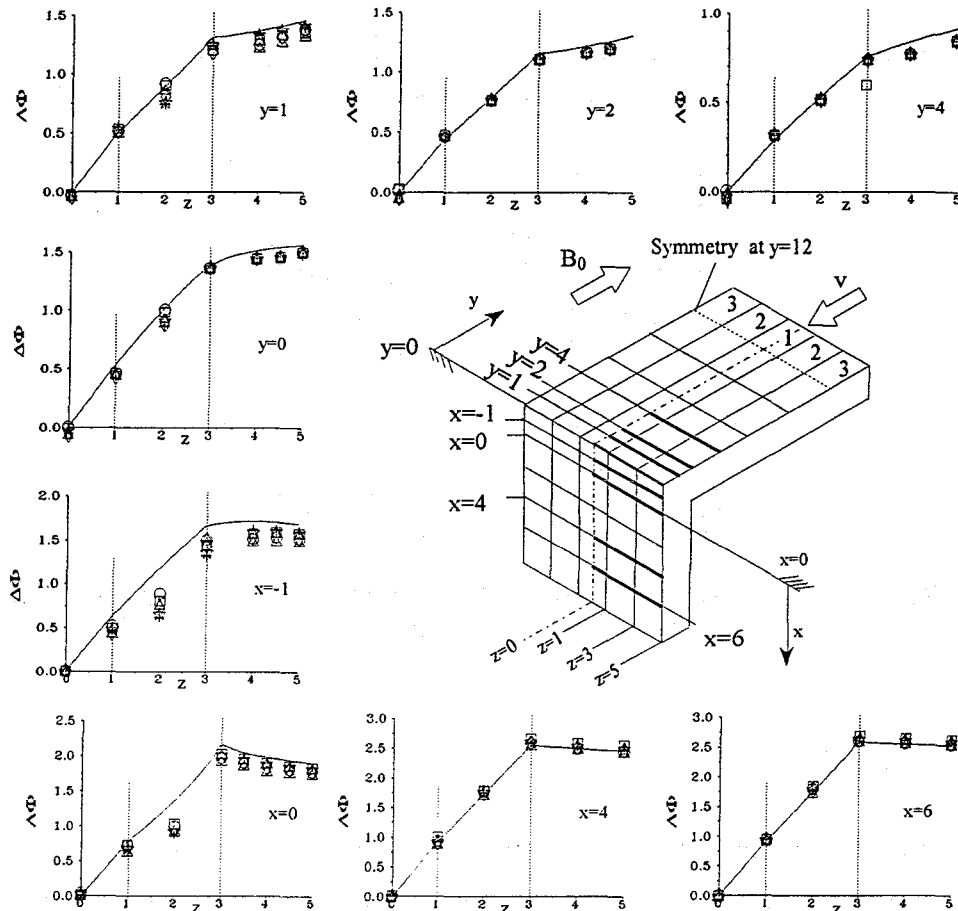


Fig. 5.5-32 Comparison of calculated and measured wall potentials for a three channel flow with equal flow rates in each duct at several positions on the U-bend for  $Ha = 2431$ . The structure material for  $|3| \leq z \leq |5|$  is taken into account in the calculation. ( $\circ$ )  $N = 37436$ , ( $\square$ )  $N = 20355$ , ( $\Delta$ )  $N = 10457$ , ( $\diamond$ )  $N = 4153$ , ( $\circ$ )  $N = 1827$ , ( $+$ )  $N = 1034$ , ( $-$ ) calculation.

In the vicinity of the bend a marked deviation between the model and the measurement has been found, but it is only slightly dependent on the Interaction parameter, also  $N$  is varied by a factor of approximately 40. This effect is most expressed in the duct 2. The measured potential values are lower than the predicted, which may be explained as a stronger depression of the velocity profile at

the dividing walls and an acceleration of the fluid near the outer wall of the duct 2. The same behaviour of the wall potentials was also observed for different Hartmann numbers in the range of  $Ha=634-2431$ , so that these results are not shown here. Since the test section is made of five channels a three-channel flow can only be conducted by empty outer channels. From the potential measurements it can be seen that the potential on the unfilled channels is not constant. As a consequence of the potential gradient an electrical current is driven producing a higher pressure drop in the individual channels. The unfilled channels act like shunts producing a higher pressure drop and, therefore have to be taken into account in an appropriate way in the model. This demonstrates that multi-channel flows are extremely sensitive to the electrical environment.

The dimensionless total pressure difference over a multi-channel U-bend between the positions i.2 and i.5 in a three channel flow in the duct 1 ( $i=1$ ) and the ducts 2 ( $i=2$ ) for different Hartmann numbers and Interaction parameters as a function of  $N^{-1/3}$  is shown in Fig. 5.5-33.

For high interaction parameters an extrapolation of the total pressure loss tends to the value calculated by the asymptotic model both in duct 1 and the ducts 2. The additional pressure loss due to inertial effects scales proportional to  $N^{-1/3}$  like in the single bend experiment, indicating that the inertial part of the pressure drop arises from inertial side layers. However, for extremely low interaction parameters the dependence of the inertial part of the pressure loss with the  $N^{-1/3}$ -powers gets lost in channel 1. The dependency on  $N$  is then weaker. But in order to ensure a conservative estimate in blanket designs still an  $N^{-1/3}$ -dependence of the inertial part of the pressure drop should be considered.

For engineering purposes the dependence of the pressure losses on the number of electrically coupled channels is of main interest. In Fig. 5.5-34 the pressure loss over a U-bend in a central channel 1 is shown as a function of channel number and interaction parameter.

The pressure loss between positions 1.2 and 1.5 in a multi-channel U-bend is significantly higher compared to a single channel U-bend flow of the same aspect ratio and the same average velocity, because in the multi-channel configuration the dividing walls prohibit the flow to establish strong side wall jets. Thus, the fluid is forced to flow perpendicular to the magnetic field and consequently producing a high pressure drop.

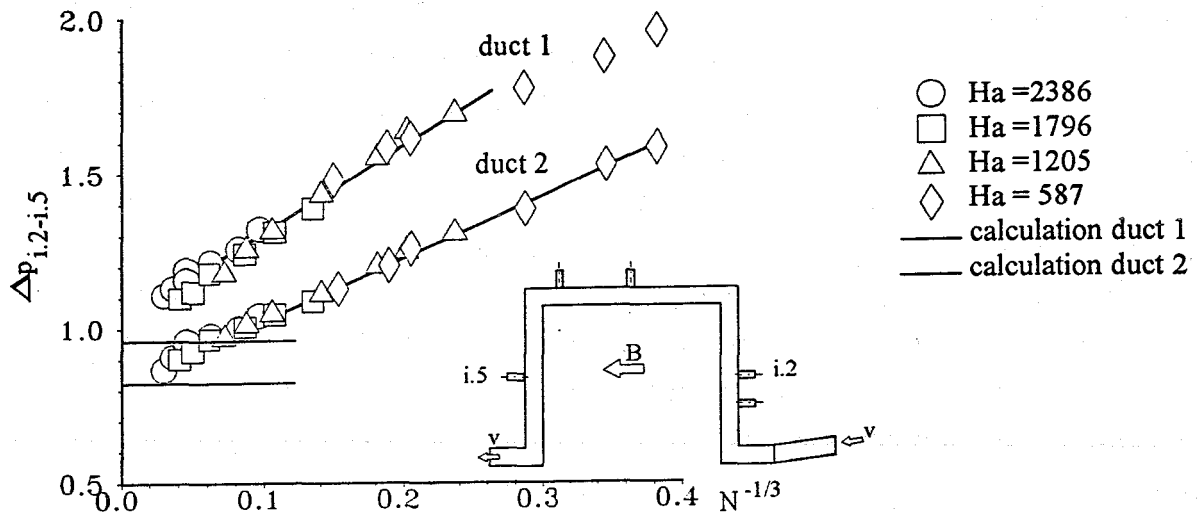


Fig. 5.5-33 Dimensionless pressure drop in duct 1 and duct 2 in a three-channel flow with equal flow rates in each duct between the measuring positions i.2 and i.5 at different Hartmann numbers as a function of  $N^{-1/3}$  from [5-54]

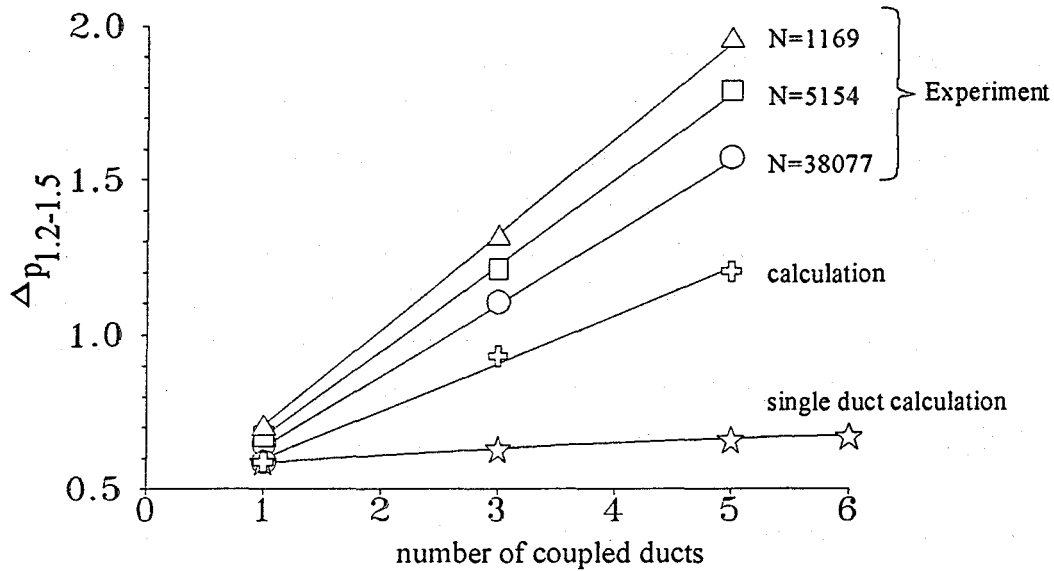


Fig. 5.5-34 Dimensionless pressure drop in duct 1 for a flow mode with equal flow rates in each duct between the measuring positions i.2 and i.5 at a Hartmann number  $Ha = 2400$  for different interaction parameters as a function of the number of coupled channels.

Both in the experiments and the calculations a linear increase of the pressure loss with the number of coupled channels is found. This is unacceptable to any blanket design, without an appropriate separation of the ducts. An upper limitation of the pressure loss cannot be detected. The inertial part of the pressure losses is

increasing with the amount of coupled channels to higher values of  $N$ . The deviations between calculation and measurements may be also explained by the influence of the finite Hartmann number, which is present in the experiment but not taken into account in the asymptotic model.

### 5.5.5.3 Pressure drop reduction in multi-bend flows

A significant reduction of the pressure drop in multi-bend flows can be achieved by an electrical separation of the ducts. Direct insulating coatings at all walls would eliminate MCF completely. In the following chapters it is investigated whether such strong insulating conditions are necessary or if it is possible to get a reduction even by simpler means.

To analyze this problem only the radial part of the bend has been electrically separated at the side walls as shown in Fig. 5.5-35. The dividing radial side walls are split into two conducting sheets separated electrically by a thin layer of insulating material. The ducts are still connected via the conducting Hartmann walls. Such a simple configuration allows a reduction of total pressure drop over the whole range of the interaction parameter of about 30% for the three-bend flow (3BF) and even more for a five-bend flow (5BF) see Figure 5.5-35b. Nevertheless it does not completely avoid 3D effects caused by multi-bend flows. There still persists a linear increase of the pressure drop with increasing number of partly coupled ducts [5-54]. Only if the radial ducts are completely decoupled (e.g. by means of direct insulating coatings or by FCIs, the toroidal ducts are still coupled) that additional pressure drop due to an electrical coupling between the channels does not exist. In this case the pressure drop of multibend flow is the same in each bend and only little higher than in the single bend flow, see [5-63, 5-64, 5-65].

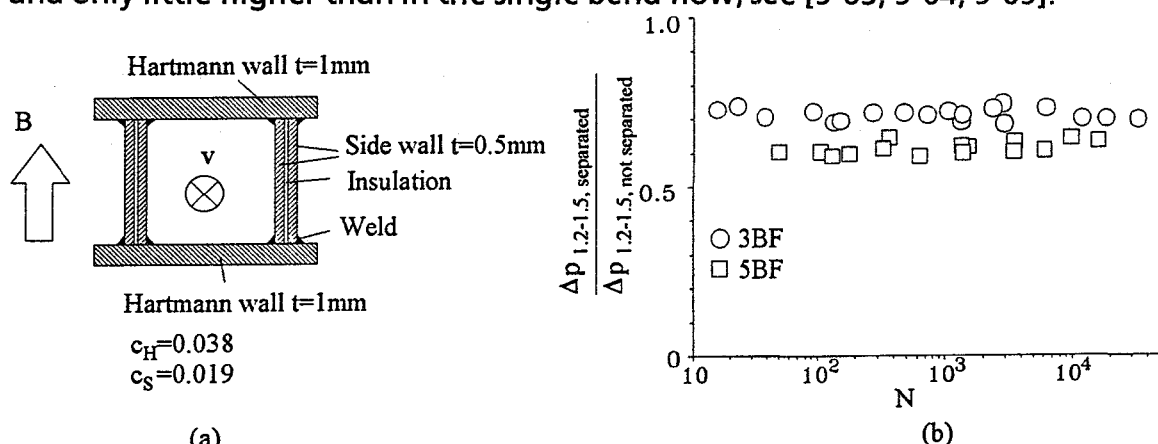


Fig. 5.5-35 (a) Electrically separated dividing side walls of radial ducts. (b) Pressure drop reduction in multi-bend flows. 3BF ( $\circ$ ), 5BF ( $\square$ ) from [5-54]

## 5.5.6 Methods for pressure drop reduction

Table 5.5-1 shows that the pressure drop in conducting ducts depends strongly on the wall conductance ratio  $C$ . The pressure drop may be reduced substantially, if  $C$  becomes very small. Since such walls would be extremely thin they would not withstand the mechanical stresses caused by the liquid metal pressure. To overcome this difficulty, the ducts with thick walls can be supplied with so-called Flow Channel Inserts (FCI) or covered by direct insulating coatings.

### 5.5.6.1 Flow channel inserts

A FCI consists of an insulating ceramic layer which is sandwiched between two thin steel sheets, see Fig. 5.5-36. These sheets are welded together at all edges, so that a direct contact between liquid metal and the ceramic is avoided. The FCI-technique is considered as a backup solution for self-cooled liquid metal fusion blankets, because in contrast to direct insulating coatings the selection of the insulation material does not cause any compatibility problems with the liquid metal. FCIs are fitted loosely into the ducts. Mechanical stresses are negligible because pressure equalization is possible by providing slots between the stagnant fluid in the gap and the flowing liquid metal. The pressure drop in channels equipped with FCIs is considerably reduced and determined by the electric resistance of the inner liner wall. Therefore, this wall should be made as thin as possible.

Experiments carried out by [5-31] demonstrated the viability and the effectiveness of such flow channel inserts. A thickness of 0.5 mm seems sufficient for fabrication and corrosion reasons and is thin enough to reduce MHD-pressure drop to an acceptable value. This reduction of pressure drop can reach values up to 95%. The remaining pressure drop is determined by the ratio of the thickness of the inner conducting sheet and the thickness of the duct wall, see Fig. 5.5-36b.

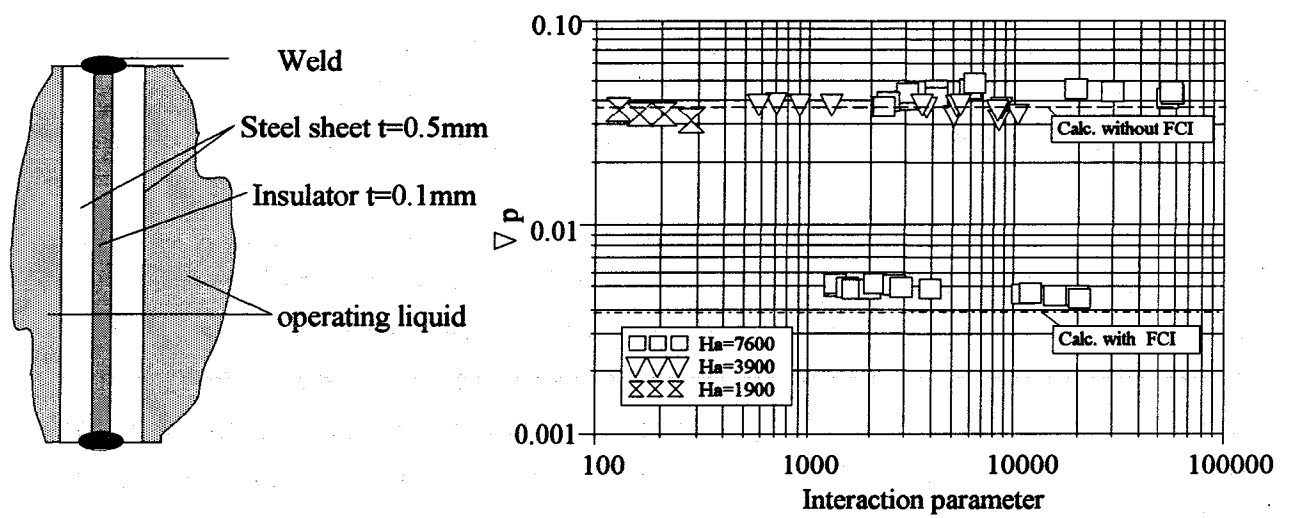


Fig. 5.5-36

a) Flow channel insert to reduce MHD-pressure drop. b) Measured dimensionless pressure gradient in a circular duct without FCI ( $C=0.036$ ) and with FCI ( $C=0.0039$ ) as a function of the Interaction parameter for different Hartmann numbers

## Requirements on the insulating sheet of FCIs

Using flow channel inserts the quality of the electrical insulator is not a so critical issue as for the directly coated duct walls. However, also using FCI's a certain decrease of the insulation quality due to irradiation damage has to be considered.

FCIs consist of a layer of insulating material which is sandwiched between two thin layers of stainless steel in order to protect the insulation material from corrosion processes and to exclude that the liquid metal may penetrate through small cracks into the insulator and thus form a local shortcut. In the past, however, the requirements on the quality of the insulation material or the thickness of the sheet was never specified. This is even more important since the quality may be reduced during operation by irradiation damage, so that a large safety margin must be taken into account.

To answer this question, a detailed analysis has been performed, assuming that the fluid is in perfect contact with the inner sheet of the FCI. The insulation is supposed to have a finite resistance which is characterized non-dimensionally by  $\kappa = (\delta_i \rho_i) \sigma / L$ . The quantities  $\rho_i$  and  $\delta_i$  are the resistivity and the thickness of the insulating sheet. The pressure drop turns out to depend on the wall conductance ratio of the inner sheet, on the value of  $\kappa$ , and on the aspect ratio  $b$  according to the following relation:

$$\frac{\partial p}{\partial x} = - \left[ 1 + \frac{\kappa_S}{b} \left( 1 - \frac{1}{\alpha_H t h \alpha_H b + \alpha_S t h \alpha_S} \right) \right]^{-1},$$

where  $\alpha = (C\kappa)^{-1/2}$  and the subscripts H and S denote values at the Hartmann walls and at the side walls, respectively.

Results for  $C_H = C_S = C$  and  $\kappa_H = \kappa_S = \kappa$  are shown in Fig. 5.5-37. This figure clearly demonstrates that a pressure drop as with perfect FCIs is achieved if  $C\kappa \gg 1$ , i.e. at least one order of magnitude higher. The requirement on the insulation resistance in this case is  $\rho_i \delta_i \gg L^2 / \sigma_w t$ , where  $\sigma_w$  is the conductivity of the inner conducting sheet and  $t$  its thickness.

## Effects at junctions of FCIs

It has been demonstrated that FCIs are an efficient means to reduce the total pressure drop by almost 95% in fully developed flows. However, the fabrication

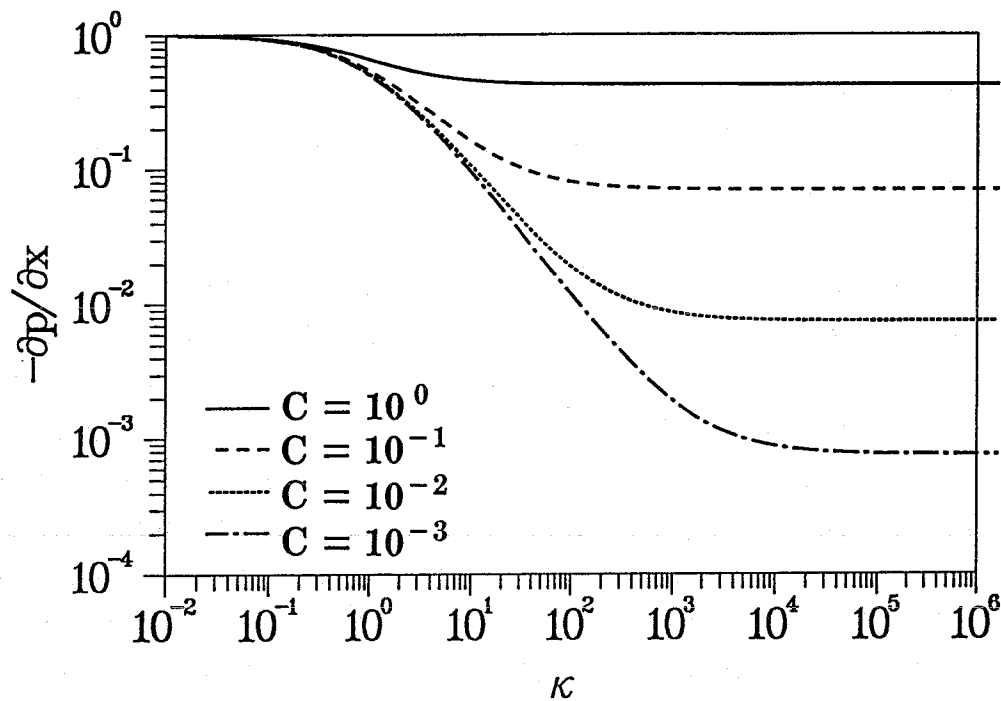


Fig. 5.5-37: Pressure gradient  $\partial p/\partial x$  in highly conducting rectangular ducts supplied with FCIs as a function of the insulation quality.

of FCIs of large size can cause technical problems. It should be mentioned that only FCIs with a finite length (shorter than the channel length) are possible to be produced. In this case one has to put several parts of FCIs into one channel. This can also be necessary for complex geometries. At the seam between two parts of FCIs, the liquid metal is in direct contact with the much better conducting thicker channel walls. The missing insulation in these additional seams results in a higher pressure drop. To improve this situation, an overlapping region should be used, which will reduce the additional pressure drop. A detailed analysis of this problem for a MHD flow in a circular pipe at a fusion typical high Hartmann number  $Ha = 14000$  shows that the additional pressure drop at a junction of overlapping FCIs can be reduced to a value that corresponds to the pressure drop of a fully developed pipe flow (with infinitely long FCI) over a length of about  $3.5L$  [5-68]. In other words, if FCIs can be fabricated with a finite length so that junctions occur at every  $3.5L$ , the total pressure drop would double. In the front channels of the blanket it was foreseen to use FCIs with length of 1 m which corresponds to  $L = 15$ . For this value the additional pressure drop is about 0.4 MPa. There appear to be no-manufacturing problems in using considerably larger FCIs; therefore this value can be significantly reduced.

### 5.5.6.2 Direct insulating coatings

The most efficient pressure drop reduction is obtained if the duct walls are directly covered by insulating coatings. These coatings have to withstand corrosion

processes during the whole operating time of the blanket. Such insulations have been proposed by [5-66, 5-67]. For perfect insulations ( $\kappa = \infty$ ) the pressure drop and flow pattern may be seen from Table 5.5-1.

If direct insulations are extremely thin ( $\delta_i \ll 1$ ) the provided coating resistance  $\kappa = \rho_i \delta_i \sigma / L$  may be not sufficient to establish flow conditions like in perfectly insulating ducts. Reductions of  $\kappa$  may also occur during the operating time of the blanket by impurities in the insulation material, by irradiation damage or by small cracks. The influence of homogeneously reduced insulating properties on pressure drop and flow pattern has been analyzed by [5-56]. Since for highly conducting ducts the reduction of the coating resistance leads to most pronounced influence on the flow this case is considered in some detail. Figure 5.5-38 shows the pressure gradient  $\nabla p = -\kappa$  as a function of the coating resistance. For small values of  $\kappa$  the pressure gradient reaches its highest value  $\nabla p = -1$ . For  $\kappa > 1$  the pressure gradient is essentially reduced. Almost insulating conditions are reached as  $\kappa \gg Ha$ . Values of  $\kappa$  of the order of  $Ha$  or smaller should be avoided in engineering applications even if the resulting pressure drop would be acceptable because flow pattern would establish which are unfavorable for homogeneous convective heat removal.

The influence of cracks in perfectly insulating coatings has been analyzed by [5-69]. The worst case with two small line cracks at both sides of the duct has been analyzed for general cross sections. For the considered example of a circular pipe flow the cracks lead to an increase in pressure drop by a factor of about 13 compared to perfectly insulating conditions. The flow pattern shows a reversed flow near the cracks and increased velocity in the center of the duct. A 3D analysis ( $Ha = 1000$ ) of the flow near uninsulated small spots gives an additional pressure drop comparable to that in a perfectly insulating pipe over a length of about  $25L$ . The pressure and current distribution along the duct is shown in Fig. 5.5-39. The conducting spots are at the sides  $z = \pm 1$  at  $x = 0$ .

These examples demonstrate that the number of uninsulated cracks should not exceed a certain limit. For real applications, however the situation is probably not as critical since there may exist a contact resistance at the crack, because the wall has a finite conductivity, or because of self-healing mechanisms which form a new passive layer at uninsulated parts of the channel wall.

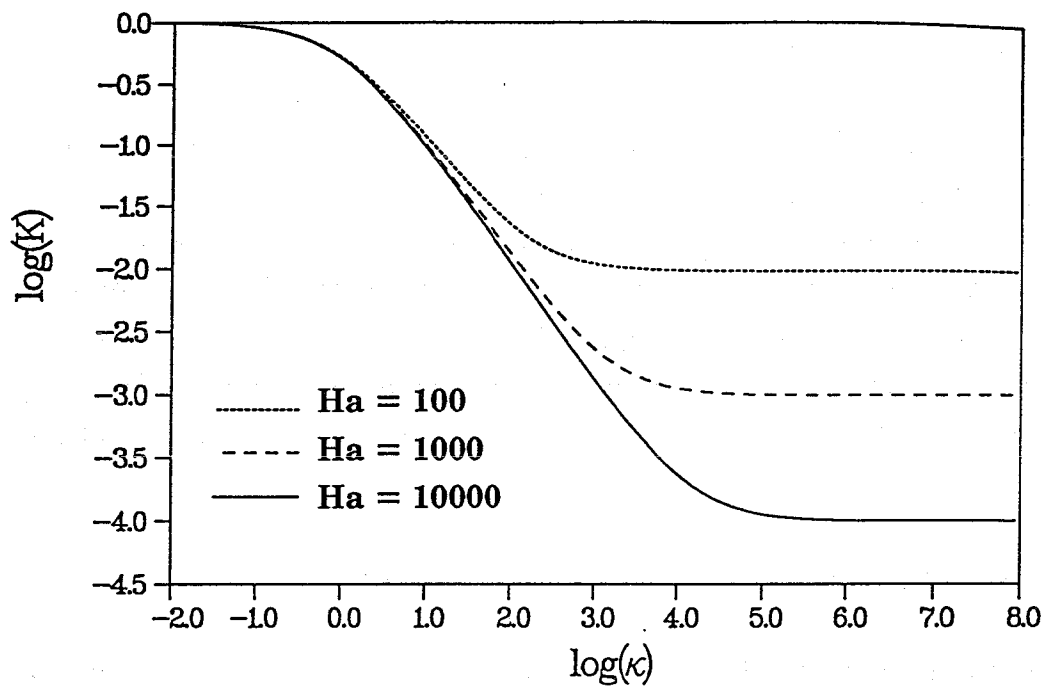


Fig. 5.5-38: Pressure drop  $\nabla p = -\kappa$  in highly conducting rectangular ducts covered with insulating coatings [5-55]

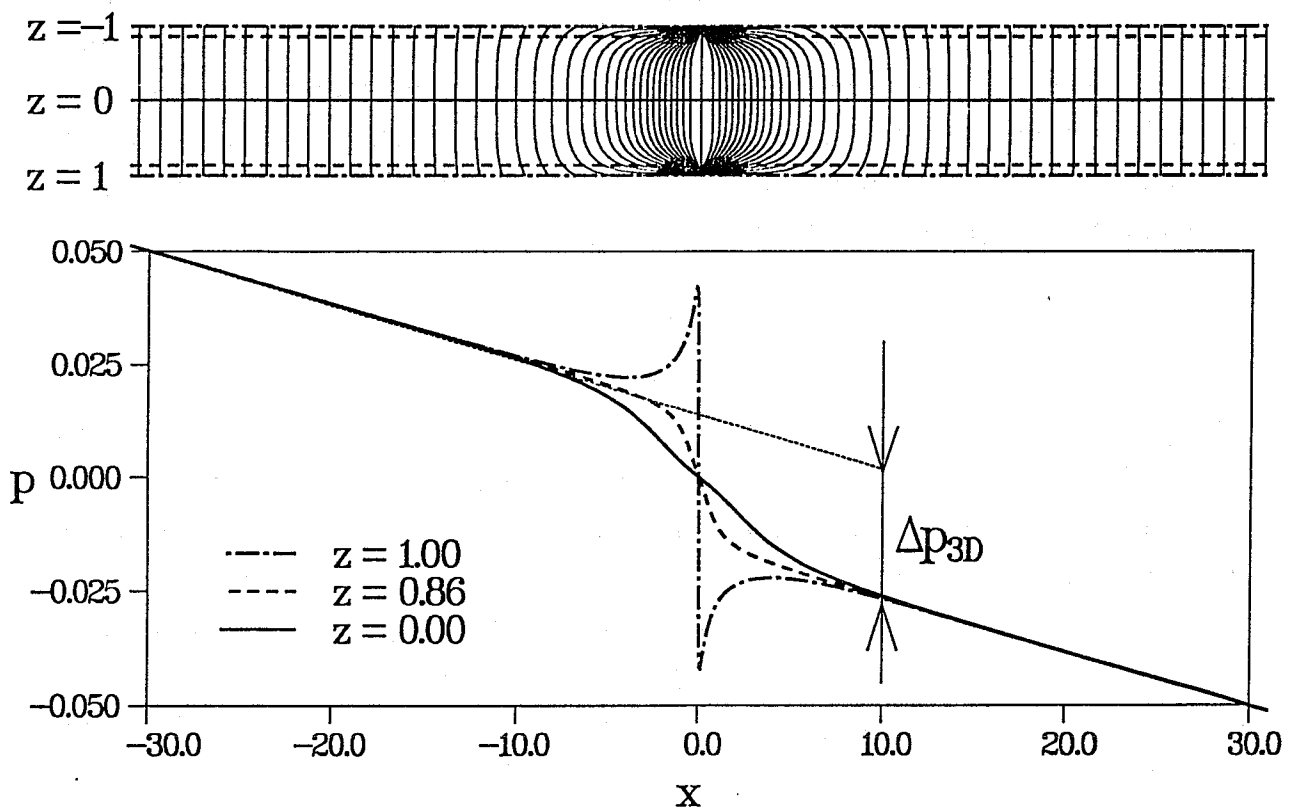


Fig. 5.5-39: Pressure and current distribution along an insulating circular pipe with two small cracks at the sides  $z = \pm 1, x = 0$  [5-69]

## 5.6 Heat transfer for laminar MHD flows

In the following subsections the problem of heat transfer in laminar MHD flows in ducts of arbitrary cross-section is considered. The three-dimensional velocity profiles for heat-transfer calculations are determined using exact solutions whenever possible, or alternatively an asymptotic approach for high values of the Hartmann number. A general code for heat-transfer calculations in ducts with arbitrary geometry, wall conductivity, external magnetic field and thermal conditions has been developed and applied to several test examples. The agreement with known exact solutions is excellent. Finally, heat transfer in a complex blanket element with insulating walls relevant to the Dual Coolant Blanket Concept is presented

### 5.6.1 Governing equations and boundary conditions

Convective heat transfer in MHD flows under fusion relevant conditions is governed by the set of equations describing the conservation of mass, momentum and charge, by Ohm's law, and by the equation for conservation of energy [5-70]. For the very strong magnetic fields present in any fusion application, it is assumed that the electromagnetic forces are dominant compared to inertia or buoyancy effects, which are consequently neglected. Thus the flow problem becomes independent from the temperature (the latter is a passive scalar) and can be solved in a first step. Once the fluid velocity is calculated it is used as input for the evaluations of the non-dimensional energy balance

$$Pe(\mathbf{v} \cdot \nabla)T = -\nabla \cdot \mathbf{q} + Q, \quad (5.6.1)$$

where  $\mathbf{v}=(u,v,w)$  is the velocity vector scaled with the mean velocity  $v_0$ .  $T$  stands for the difference in temperature measured between any position inside the duct and the position with the reference temperature  $T^*_0$ , scaled with a characteristic temperature difference  $\Delta T^*$ ;  $\mathbf{q} = -\nabla T$  represents the diffusive heat flux, and  $Q$  the volumetric heat source due to viscous and Ohm's dissipation or nuclear heating, scaled by  $\Delta T^*/L$ , and  $\lambda \Delta T^*/L^2$ , respectively.  $Pe = \rho c_p v_0 L / \lambda$  is the Peclet number.  $L$  is a characteristic length scale. All fluid properties like the density  $\rho$ , the specific heat  $c_p$  and the heat conductivity  $\lambda$  are assumed to be constant in the range of temperature considered.

The characteristic temperature scale  $\Delta T^*$  is chosen as  $q''L/\lambda$  or  $q'''L^2/\lambda$  if either the surface heat flux  $q''$ , or the volumetric heat generation  $q'''$  gives the major contribution to the total heat input.

The surface heat flux determines the boundary condition for temperature

$$\mathbf{q} \cdot \mathbf{n} = -\partial_n T \quad (5.6.2)$$

### 5.6.2 Heat transfer in fully developed channel flow

The 3D heat transfer problem where the flow enters the heated section with a fully developed laminar velocity profile gets a unique formulation if the non-dimensional axial coordinate is scaled with  $Pe$ .

$$u \partial_\xi T = -\nabla \cdot \mathbf{q}_t + Q \quad (5.6.3)$$

where  $\xi = x/Pe$  is the longitudinal coordinate of Grätz. Using this scale the axial diffusive flux is of the order  $1/Pe$  compared with the fluxes  $q_t$  in the transverse directions and thus neglected for  $Pe \gg 1$ . A code for solving equation (5.6.3) has been used to obtain the results described below [5-71]. The problem considered is the convective transfer from the first wall of a poloidal channel heated by a surface heat flux  $\partial_n T = -1$  at  $z=1$  with  $Q=0$ . Results for the temperature  $T(y=0, z=\pm 1)$  for slug flow and MHD flow ( $Ha = 1000, C = 0.1$ ) are shown in figure 5.6-1. One can distinguish a region where the heat transfer is determined by thermal boundary layers (TBL) where  $T \sim \xi^{1/3}$ , a transition zone (TZ) where the thermal disturbance affects the entire cross section and the region of fully developed thermal conditions (FTC) where  $T \sim \xi$ . Results are compared to those of a slug flow ( $u = 1$ ). First the heat transfer in MHD flows is reduced due to the no-slip condition. Later, however, the high velocity jet at the heated wall aligned with the field improves the heat transfer conditions (smaller temperature at the wall) compared to bulk flow.

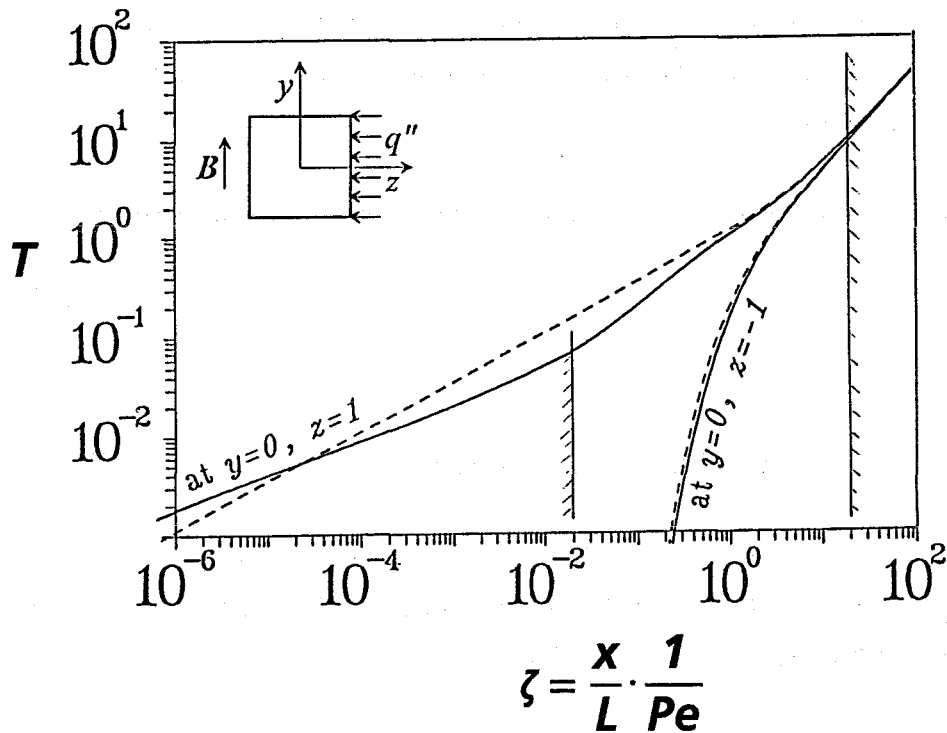


Fig. 5.6-1 Wall temperature along a heated duct.  
 — Ha=1000, C=0.1, ----- slug flow.

### 5.6.3 Heat transfer in ducts of arbitrary geometry

The MHD heat transfer problem in ducts of arbitrary geometry has been solved by using boundary fitted curvilinear coordinates and tensor formulation of the basic equations [5-52]. After the general geometry is mapped to the standard calculation domain the basic equations are discretized and solved numerically. The transverse directions are treated by a fully implicit scheme while (neglecting small axial diffusive fluxes) the axial direction can be treated by an explicit formulation. This saves plenty of storage and ensures the possibility of a high numerical resolution in cross-sectional planes in order to resolve thin thermal boundary layers.

Here, the example of a circular expansion is presented with wall-normal constant heat flux. The geometry and results are shown in Figure 5.6-2. This example is not a typical application in fusion, but clearly demonstrates a wide applicability of the numerical code.

The wall of the considered expansion is relatively poorly conducting ( $C=0.005$  at  $Ha=1000$ ) so that the flow behaves qualitatively as in insulating expansions.

In the entrance region the flow is assumed to be fully developed with respect to both the flow pattern and the temperature field. The core velocity decreases continuously from the highest value at  $z=0$  to zero at  $z=\pm 1$ . Along field lines, in the  $y$ -direction, the core velocity is constant but exhibits a sharp decay across the thin Hartmann layers. Such a flow pattern results in a higher heat transfer near  $z=0$  and consequently in lower wall temperature  $T_1$  at  $z=0$  than  $T_2$  near  $z=\pm 1$ .

Approaching the expansion (Fig. 5.6-2b) the fluid is pushed towards the sides by strong MHD effects. This intensifies the heat transfer near  $z=\pm 1$  with higher density of isotherms. In addition the redistribution of the flow rates leads to a convective transport in the transverse direction, resulting in a stretching of isotherms in  $\pm z$  directions.

In the cross section shown in Fig. 5.6-2c the velocity and thus the heat transfer near  $z=0$  is essentially reduced. This leads to two hot spots at the top and bottom wall in contrast to the fully developed conditions where at the same position the wall temperature is lowest. Inside the cross section two relative temperature minima are observed. The heat which enters the core from the top and bottom has to be carried by conduction to the side regions where the two jets of fluid remove it by efficient convection.

In the downstream part behind the expansion the flow and temperature field is rearranged towards the fully developed conditions.

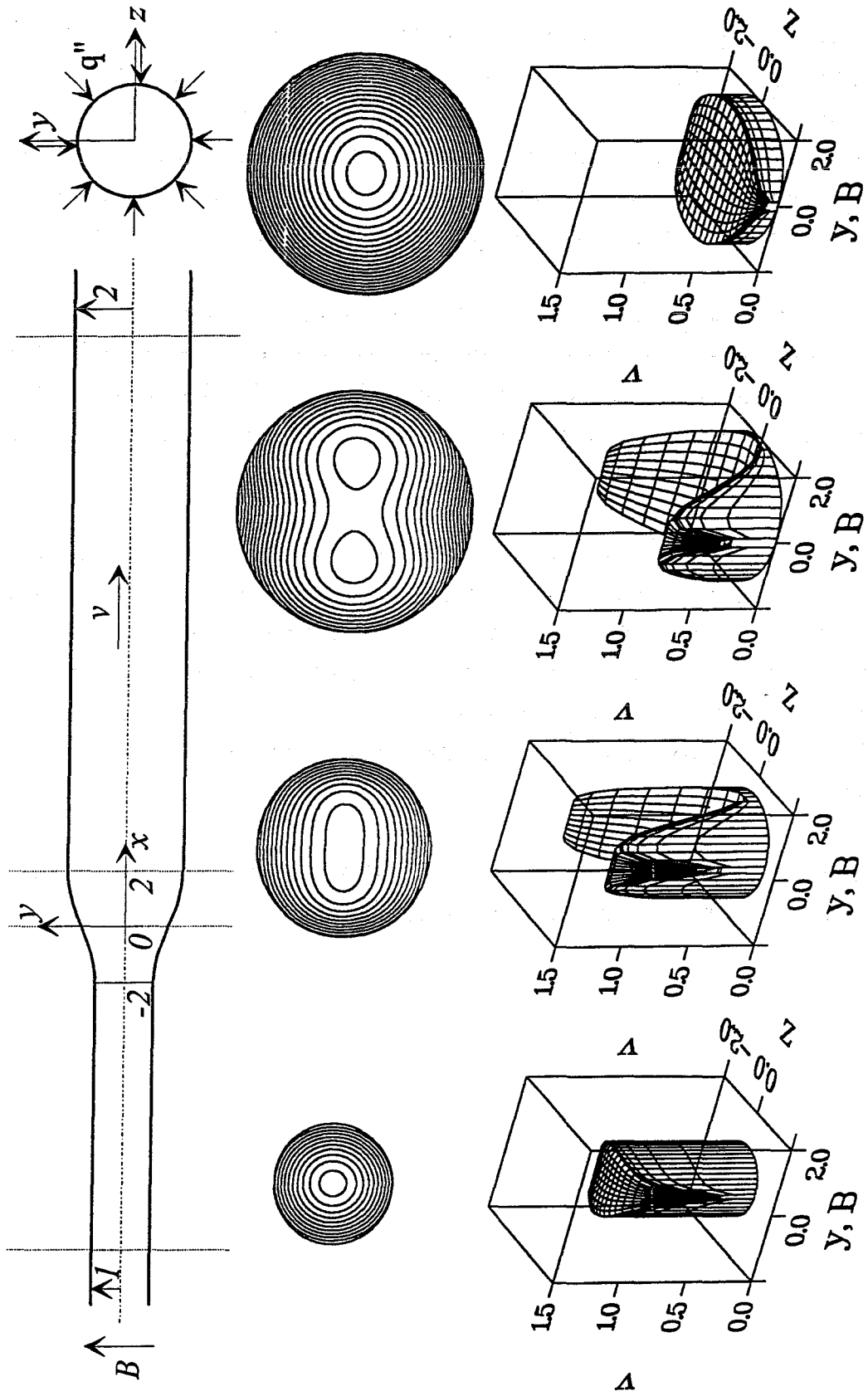


Fig. 5.6-2 MHD flow in a circular expansion with wall heat flux. Isotherms and velocity profiles at different axial positions. a)  $x = -11$ , b)  $x = -0$ , c)  $x = 2$ , d)  $x = 20$ .  $Ha = 1000$ ,  $c = 0.005$ ,  $Pe = 100$ .

#### 5.6.4 Heat transfer in a complex blanket element

Here we consider the flow in a complex element relevant to the Dual Coolant Blanket Concept. The geometry, corresponding to the lower part of the blanket, consists of an array of four rectangular channels. Three of them carry the coolant down at the rear of the blanket, while one duct closer to the plasma carries it up. The duct walls are assumed to be thin, thermally conducting, but electrically insulating. There is no external radiation heat flux at the outer walls so that the entire heating is due to internal sources only.

The velocity profile in such an element is two dimensional in the radial poloidal plane [5-51]. The isotherms for  $Pe=100$ ,  $Q=1/(5-z)$  are shown in Fig. 5.6-3. The average velocities in the rear channels are usually chosen in such a way that the temperature at the blanket bottom is close to being constant. The results show that at the dividing walls thermal boundary layers are formed, which should be taken into account in thermal stress analysis.

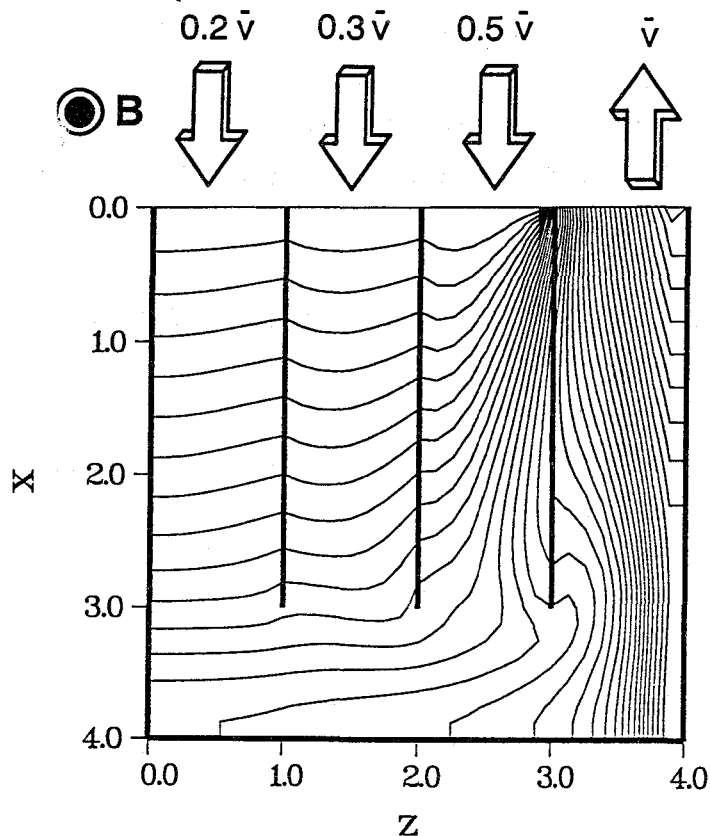


Fig. 5.6-3 Isotherms in the lower part of the blanket

## 5.7 Heat transfer and MHD turbulence experiments

As shown in Chapter 2 the simplest geometry of a self-cooled blanket would be the arrangement of square coolant ducts at the first wall. Calculations show, however, that for channels with thin conducting walls and for realistic boundary conditions (heat flux density, length of the blanket segment, allowable temperatures and stresses) this simple geometry is not feasible if the heat is transported from the wall to the bulk of the flowing liquid metal by conduction only.

Therefore, the potential for heat transfer enhancement by introducing a special kind of turbulence, as proposed in [5-72, 5-73, 5-74], is under investigation at the Forschungszentrum Karlsruhe. An estimate showed that, for the combination lead-lithium and martensitic steel, the effective heat transport from the heated wall to the bulk of the liquid metal has to be enhanced by at least a factor of 2 or 3 in order to allow simple blanket designs.

To explore the potential of such an enhancement two tasks have been started at the Forschungszentrum Karlsruhe in the MEKKA (Magnetohydrodynamic Experiments in Natrium-Kalium-Karlsruhe) facility. In the first experiment the heat transfer is investigated in a duct with electrically insulated walls without and with mechanical turbulence promoters, the second is conducted in a duct of the same size, but with thin conducting walls and with MHD operated turbulence promoters..

### 5.7.1 Flow Measurements of MHD Turbulence in an Electrically Insulated Duct (GALINKA)

In a new facility, GALINKA (Gallium-Indium Experiments in Karlsruhe), different methods for producing turbulence in MHD flow and the effect on heat transfer will be studied systematically under near-fusion conditions [5-75]. This facility is a race track design, where all components of a liquid-metal loop: pump, flow-through meter, heat exchanger, and the test section itself, are housed in a box, which is placed within the magnet. The eutectic alloy indium-gallium-tin is used as the liquid metal. The box is made of electrically insulating material. Two pressure taps are installed at the top Hartmann wall in a distance of 20 a. A traversable potential gradient probe is used to measure the axial and transverse velocity components of the flow at the midplane and near the top Hartmann wall.

By analyzing the signals of the two 3-pole gradient probes (PG probes) installed in the mid of the test section ( $x=0$ ), PG1 at the mid-plane ( $y=0$ ), PG-2 positioned at the coordinates  $x=0, y=0.66$  and  $z=0$  we found the following.

The flow started to oscillate at a rather fixed Reynolds-number around 12000 nearly independent of the Interaction parameter. These oscillations were presumably generated at the upstream bend of the GALINKA channel. Frequencies in the range 15-40 Hz are found depending on the mean velocity. The oscillations of the axial velocity component of probe 1 and 2 are strongly correlated especially for high Hartmann numbers (see Fig. 5.7-1), demonstrating the 2D character of the vortex flow.

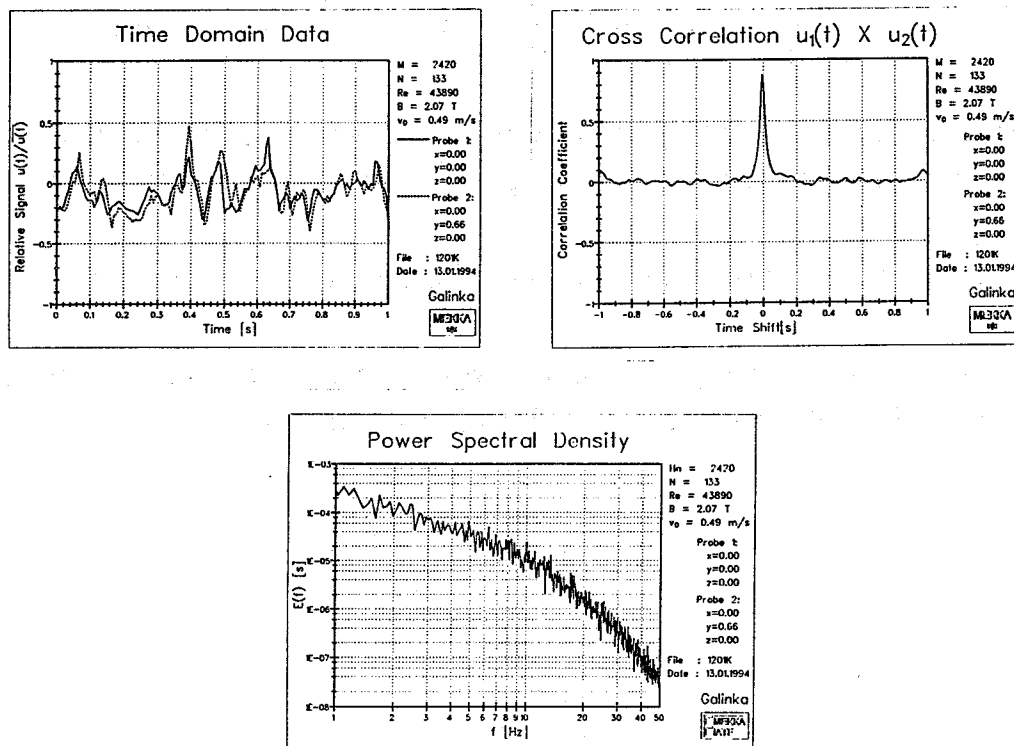


Fig. 5.7-1 Oscillation measurements in GALINKA: (7a) time domain data of the signals of probe 1 and 2, (7b) cross correlation of the two signals, (7c) power spectral density of probe 1, [5-75]

Figure 5.7-2 shows the measured dimensionless pressure drop as a function of  $N$ . We see that the onset of oscillations which occurs nearly independent of the Hartmann number at a Reynolds number of about 13000 has no influence on the pressure drop, leading to the conclusion that only the generation of turbulence results in an increase of the pressure drop and that turbulent flow itself does not affect the pressure drop in MHD flow.

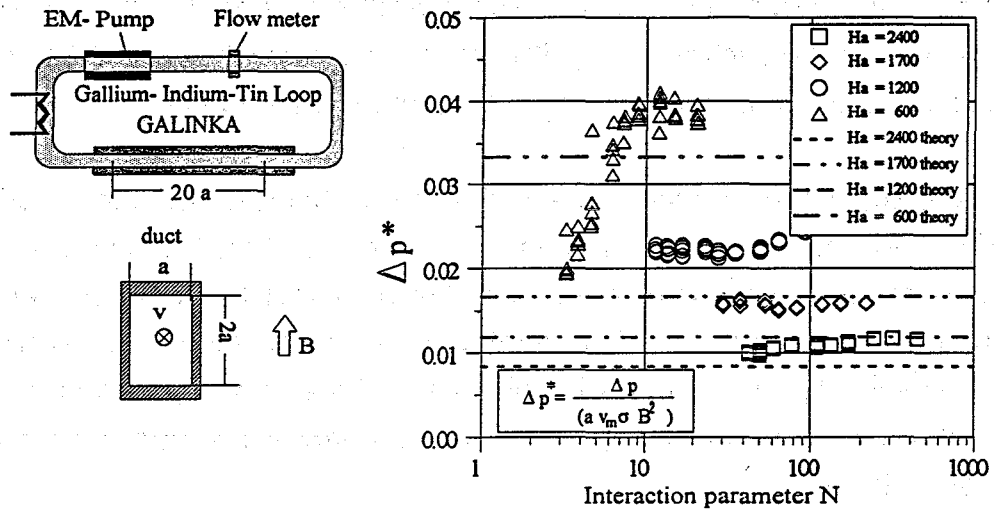


Fig. 5.7-2 Schematic view of GALINKA and the dimensionless pressure drop as a function of the Interaction parameter  $N$ , [5-75].

The measurements in the insulated duct of GALINKA confirmed the predicted low pressure drop. The flow exhibits a very rigid two-dimensional vortex structure.

### 5.7.2 MHD/Heat Transfer in an Electrically Insulated Duct [5-75, 5-76]

The test section is a rectangular channel with an aspect ratio of 2:1, where the longer side  $2a$  ( $a = 40$  mm) is parallel to the applied field (see Fig. 5.7-3).

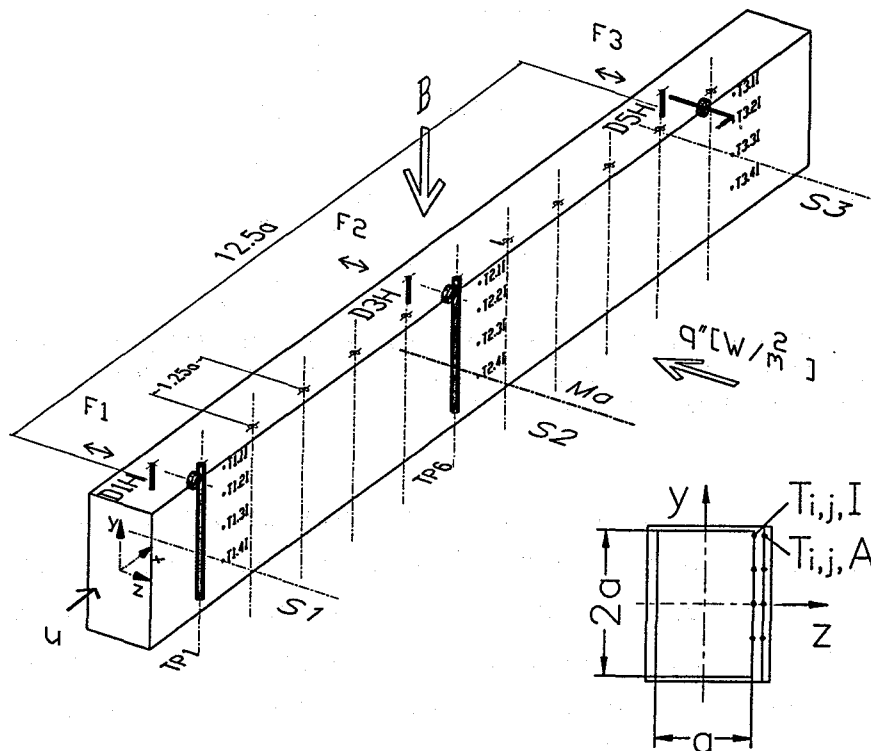


Fig 5.7-3 The MHD/heat transfer test section

The surface of the stainless steel test section contacting the liquid metal is electrically insulated by a temperature resistant painting. A direct contact heater allows a homogeneous heat flux of up to 20 W/cm<sup>2</sup> over a length of 500 mm.

A combined TEMperature and POtential gradient (TEMPO) traversing probe was used to measure the velocity and temperature distribution within the liquid metal in the z-direction.

Two pressure taps installed at the top Hartmann wall, indicated in Fig. 5.7-3 by D1.H, and D5.H, are used to measure the pressure drop over a length of 12.5 a. A detailed description of the test section and the test conditions is given in [5-43, 5-75].

After finishing the experiments with the smooth channel, two mechanical turbulence promoters were inserted in the test section at the positions TP1 and TP6 (Fig. 5.7-3). For this purpose, rods of insulating material 6 mm in diameter were introduced and the experiments repeated.

Profiles of mean velocity and oscillation signal were collected for isothermal conditions as well as for heat transfer conditions using the potential gradient probe without and with turbulence promotion (TPs) at  $x = 12,5 \cdot a$  for  $Ha = 5000$  and  $Pe = 540$ .

The results of the pressure drop experiments are compiled in Fig. 5.7-4 Results for Hartmann numbers higher than 2400 and even for Interaction parameters higher than 2000 - parameters for which asymptotic solutions should be valid - are higher than predicted, revealing that the used painting is not a perfect insulation. This fact was further confirmed by the potential difference measured at the outer surfaces of the channel between the side wall and the mid of the Hartmann wall. Using a simplified electrical circuit model the  $(\rho\delta)_{Ins}$  was determined from the measured potential differences to be

$$(\rho\delta)_{Ins} \approx 2.4 \times 10^{-6} \Omega m^2$$

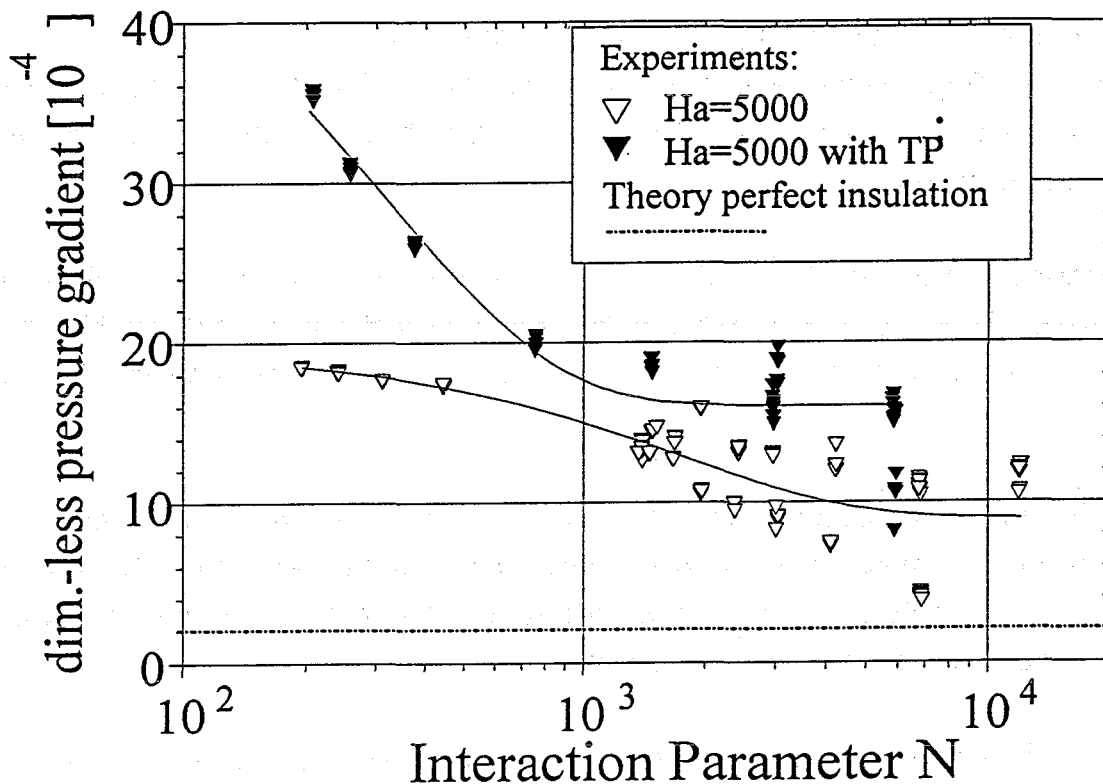


Fig. 5.7-4 Dimensionless pressure gradient

The rather strong scattering of the data may be explained by changes in the wetting behaviour of the NaK on the insulation layer. In the case of perfect insulating walls the degree of wetting has only a small influence on the pressure drop. Therefore, such strong scattering was not observed there (see the results of the pressure drop measurements in GALINKA, Fig. 5.7-2).

The TEMPO probe was used to measure temperature profiles in horizontal planes of the channel at  $y=0$  (the mid-plane) and at the axial position  $x=12.5$  (outlet edge of the heater). All temperatures are non-dimensionalized by  $q'' \cdot a/k_f$ , where  $q''$  is the heat flux and  $k_f$  the thermal conductivity of the fluid.

In Fig. 5.7-5 profiles are shown for  $Ha=0$  and  $5000$  and  $Pe=1100$ . These profiles show the influence of increasing magnetic fields on the heat transfer at constant Peclet number.

In order to see the degree of mixing, an additional curve labeled "Perfect Mixing" is plotted corresponding to the normalized mean outlet temperature.

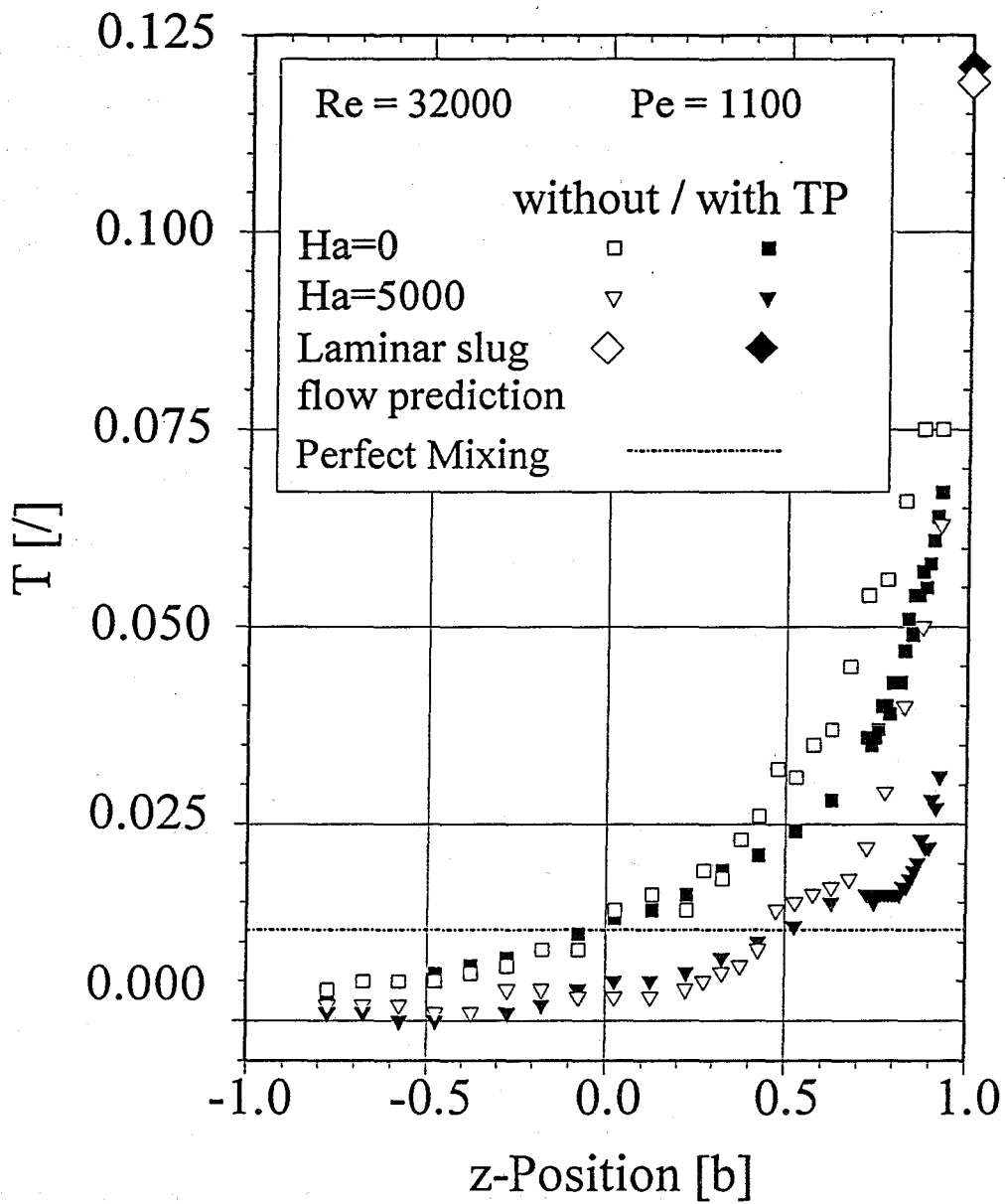


Fig. 5.7-5 Dimensionless temperature profiles

Measured temperature profiles were compared with the results of a simple model for slug flow laminar heat transfer used for most self-cooled liquid metal fusion blanket design calculations [5-31]. According to this model the temperature distribution in z- and x-direction is written as

$$\Theta(z,x) = (2q''/kf) \left\{ (\alpha \cdot x/\eta)^{1/2} \cdot e^{-4\alpha x} - \frac{z}{2} \operatorname{erf} z/(2\sqrt{\alpha x}) \right\}$$

where  $\Theta = T - T_0$  and  $\alpha = k_f / (u \cdot \rho c_p)$

$$\Theta_1(z=0, x) = 2 \cdot q'' \cdot (\pi k_f \mu \rho c_p)^{-1/2} \cdot x^{1/2}$$

$T_0$  corresponds to the mean temperature at the inlet edge of the heater. This model was also used to determine the "effective thermal conductivity"  $k_{f,eff}$  which gives the best fit of the measured curves. Fig. 5.7-6 shows the ratio of  $k_{f,eff}$  divided by the ordinary thermophysical value of the thermal conductivity of NaK as a function of the Peclet number without and with TPs for different Hartmann numbers.

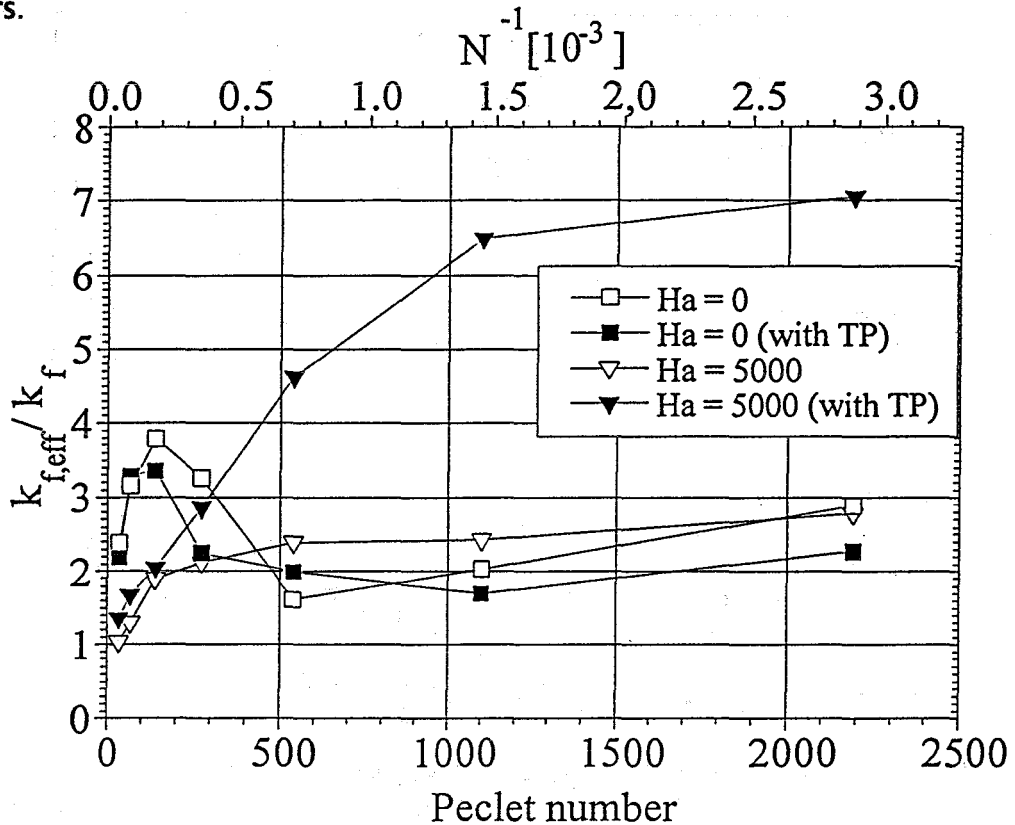


Fig. 5.7-6 Dimensionless effective heat conductivity

The results show that in the smooth (without TP) electrically insulated channel the MHD heat transfer is always better than laminar slug flow heat transfer. The steep increase of the ratio  $k_{f,eff}/k_f$  after installing the TP's is correlated with the onset of MHD turbulence, measured by the TEMPO probe. The increase of  $k_{f,eff}/k_f$  with increasing the Peclet number was very pronounced and reached a value of 7 at  $Pe = 2200$ .

In Fig. 5.7-7 the results of the cost-benefit analysis show that the ratio

$$(k_{f,eff}/k_f) / (\Delta p_{with TP} / \Delta p_{without TP})$$

has a maximum of about 3 at  $Pe \approx 1100$ .

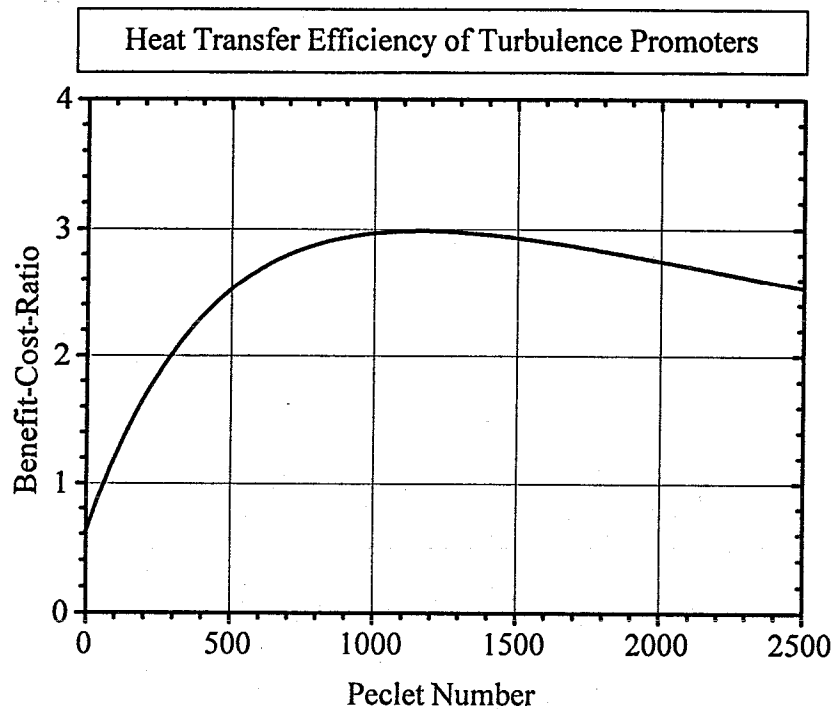


Fig. 5.7-7 Cost-benefit of turbulence promoter

M = 5000

### 5.7.3 MHD/Heat Transfer in a Duct with thin conducting Hartmann Walls

In this experiment the side wall (wall parallel to the magnetic field) of a rectangular test section is heated over a length of 500 mm with a radiation heater (Fig. 5.7-8). The test section, of cross section 80 mm by 40 mm is made of stainless steel, the Hartmann walls (walls perpendicular to the magnetic field) are 1 mm thick, the side walls 6 mm thick.

With the radiation heater a homogeneous heat flux of up to 20 W/cm<sup>2</sup> can be reached. The heater can be moved along the axis of the test section thus enabling the investigation of heat transfer at two positions without removing the test section from the liquid-metal loop. At the first position heat transfer in a simple rectangular channel will be investigated; in the second position, heat transfer in a channel fitted with electric-turbulence promoters will be investigated. The turbulence promoters are copper strips embedded in the Hartmann walls (see Fig. 5.7-9), as proposed first by [5-72] and investigated for thermally fully developed flow by [5-77].

The main aim of this experiment which will start in mid of 1995 is to investigate the influence of dumping the vortices on the thin conducting Hartmann wall and the consequences on the heat transfer improvement.

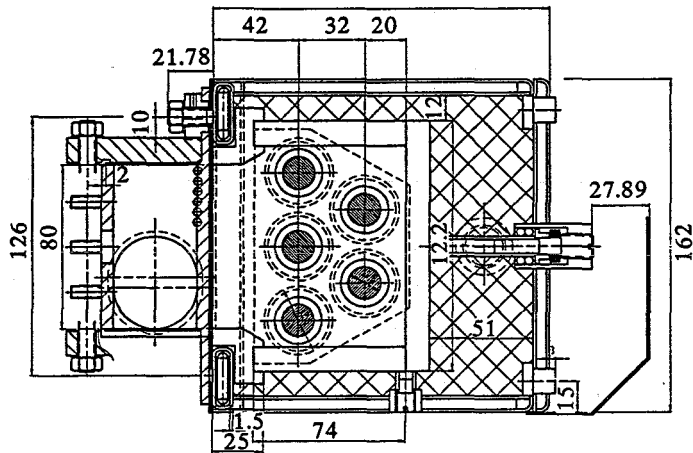
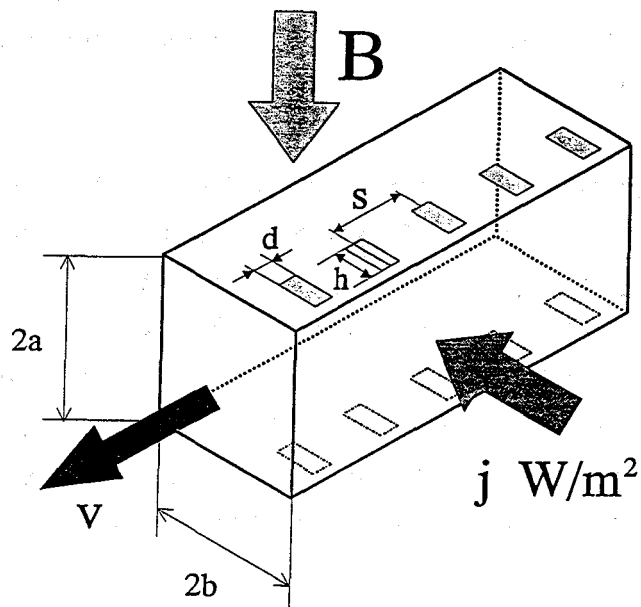


Fig. 5.7-8 Test section for studies of radiation heating of a duct wall. Dimensions in mm.



### MHD-Turbulence and Heat Transfer

Fig. 5.7-9 Test section with turbulence promoters.

## 5.8 Computation of blanket pressure drop

The MHD-analysis is based on the experimental and theoretical work, described in the previous chapters.

The detailed analysis has been restricted to the outboard segment since it has a longer heated length than the inboard blanket and it is exposed to the higher heat load which results in a higher pressure drop although the magnetic field strength is by a factor 1.4 higher at the inboard blanket.

The analysis of the outboard blanket is divided into basic elements (see Fig. 5.8-1) such as circular pipes (I), rectangular poloidal ducts (III) as well as complex three dimensional geometries like the expansion zones from circular pipes to rectangular ducts (II) and the combined 180°-turn with manifold (IV).

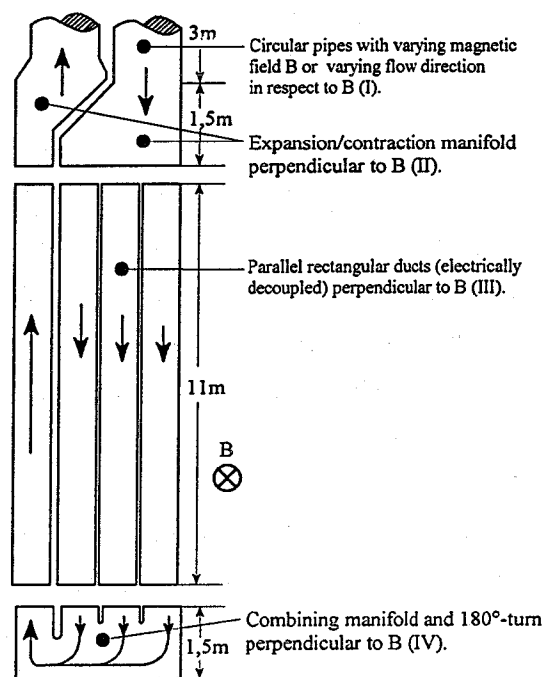


Fig. 5.8-1 Basic elements of the Dual Coolant blanket concept

The MHD flow in the different poloidal channels (III) is assumed to be fully developed and inertialess so that asymptotic solutions can be used. It is analyzed using the well established correlations taken from [5-47].

For 3-dimensional geometries like (IV), 3D pressure drop and pressure drop due to inertia effect are taken into account.

In general the following correlation holds:

$$\Delta p_{tot}^* = \Delta p_{tot} \cdot a \sigma \bar{v} \cdot B^2 \quad (2.81)$$

where

$$\Delta p_{tot} = \Delta p_{asympt} + \Delta p_{inertial} \quad (2.82)$$

and

$$\Delta p_{asympt} = \Delta p_{fd} + \Delta p_{3D} = (l_{pol.} + l_{3D}) \cdot \frac{dp}{dx} |_{fd} \quad (2.83)$$

$$l_{pol.} = \frac{L_{pol}}{a} \quad (2.84)$$

For fully developed poloidal flow the values of  $(dp/dx)_{fd}$  are compiled in Table 5.5-1. The value of  $l_{3D}$  for the poloidal flow in a fringing field is taken from [5-78]. All other geometries are analyzed with the approximation of the Core Flow Solution (CFS) as described in [5-26] and [5-53], neglecting inertia effects. This code provides velocity distribution and pressure drop in ducts of arbitrary shape and thin conducting walls. Thin conducting walls could be realized by using flow channel inserts as described in [5-53].

A better way to reduce MHD pressure drop however, is to apply an electrically insulating coating on the duct walls, as described in Section 5.5.1.6. The minimal resistance of this coating to obtain conditions of MHD flow in electrically insulated channels was investigated by [5-55]. The requirement is that  $C/Ha > 10$ , where  $\kappa = \rho_l \cdot \delta_l \cdot \sigma/a$ , which for typical values of  $Ha = 7000$  and  $a = 0.07$  corresponds to a resistance of  $(\rho \delta)_{ins} > 10^{-2} \Omega m$ . The resistivity of alumina is six orders of magnitude above this requirement.

In the case where  $\Delta p_{inertial}$  is not explicitly known the additional pressure drop caused by inertial effects is taken into account by correcting the results of the calculation with the ratio  $(\Delta p_{tot}/\Delta p_{asympt})$  taken from experimental results of simi-

lar flow geometries. The problem of the MHD flow in the inlet and outlet manifold was analyzed in [5-4], the combined 180 °C-turn with manifold in [5-51]. The lateral blanket module of the DCB uses circular Z-shaped inlet and outlet pipes which results in flow directions partly aligned with and partly perpendicular to the magnetic field. Such bends cause additional pressure drop due to three-dimensional (3d) currents. These Z-shaped in- and outlet pipes are analysed using the theoretical and experimental results of the Z-bend experiment described in Chapter 5.5.3.2. In contrast to the experiment where a duct with rectangular cross section was used the Z-shaped tubes have a circular cross section. Therefore the analysis of the pressure drop in the Z-shaped in- and outlet tubes can be regarded as a very conservative approach.

Calculations of the liquid metal flow in all elements of the blanket segment have been performed assuming a magnetic field of 5 T and for channels with FCI's a thickness of 0.5 mm. The calculation uses the thermophysical and transport properties of the eutectic Pb-17Li compiled in Table 5.4-2. The results of the detailed analysis of the outboard blanket were scaled to the inboard blanket with the magnetic field ( $B^2$ ), the mean velocity in the channels and with the characteristic length.

The results of the calculations are compiled in Table 5.8-1. (The values are 0.6 MPa for the direct coating and 4.1 MPa for the flow channel inserts. These values represent modest or very low pressures which can be accommodated easily.) Comparing the results for insulated channels and channels with FCI's, one should keep in mind that the present design was optimized with respect to perfectly insulated channels. A remarkable reduction of the pressure drop for a design with FCI's could be obtained by changing the flow partitioning between the rear and the front channels.

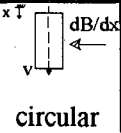
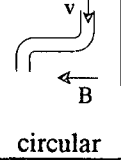
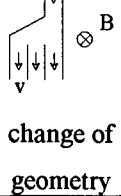
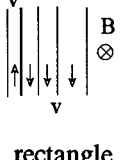
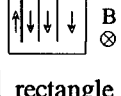
Section	Geometry	a [m]	L [m]	T [°K]	v [m/s]	B [Tesla]	M [/*10 <sup>4</sup> ]	N [/*10 <sup>2</sup> ]	c <sub>FCI</sub>	ΔP <sub>FCI</sub> [MPa]	ΔP <sub>Insulated</sub> [MPa]	
1. Inlet (I) and Outlet (O) in the fringing magnetic field	 circular	0.138	0.84	275 (I) 425 (O)	0.72(I) 0.74(O)	0.5-4.5	1.1-1.4	3.0-3.3	0.0058	0.035 (I) 0.032 (O)	0.0153 (I) 0.0150 (O)	
2. Inlet pipe with bends *1 Outlet pipe with bends *1	 circular	0.138	2.2	275 (I) 425 (O)	0.72 0.74	4.5	1.1-1.4	3.0-3.3	0.0058	0.2824 (I) 0.2727 (O)	0.2028 (I) 0.2000 (O)	
3. Inlet and Outlet manifold Expansion and Distribution in the subchannels	 change of geometry	0.138 -0.066	0.6	275 (I) 425 (O)	0.72→ 0.337	5.0	1.6→0.65 (I) 1.4→0.73 (O)	3.2-3.3 (I) 3.1-3.2(O)	0.0058- 0.0114	0.052 (I) 0.060 (O)	0.052 (I) 0.060 (O)	
4. Poloidal channels *2 Rear Front	 rectangle	0.066	11.0	315 385	0.337 1.020	5.0	0.65 0.73	4.06-4.35 1.33-1.43	0.0118 0.0114	0.7193 2.0420	0.0112 0.0293	
5. Manifold and 180° U-turn	 rectangle	0.068	0.6	350	0.337→ 1.020	5.0	0.69-0.71	4.06→ 1.33	0.0118	0.009*3	0.009*3	
6. FCI-overlapping Rear Front	rectangle	0.066	11.0	350	0.337 1.020	5.0	0.69 0.69	4.04 1.34	0.0118 0.0114	0.1616 0.4068	0	
<b>TOTAL OUTBOARD</b>										<b>ΔP<sub>Total</sub></b>	<b>4.0728</b>	<b>0.5946</b>

Table 5.8-1: MHD-pressure drop in the outboard blanket of the DUAL-COOLANT-BLANKET-CONCEPT

## References

- [5-1] **Smith, D.L. et al. 1984** Blanket comparison and selection study (Final report), Argonne National Laboratory, report ANL/FPP-84.
- [5-2] **Malang, S. et al. 1988** Self-cooled liquid metal blanket concept. *Fusion Technology*, Vol. 14, p.1343.
- [5-3] **Najmabadi, F.; Conn, R.W. et al. 1992** The ARIES-II and ARIES-IV Second Stability Tokamak Reactors; *Fusion Techn.* Vol. 21, May 1992, pp. 1721-1728.
- [5-4] **Malang, S. et al. 1992** Dual coolant liquid metal breeder concept. Proc. of 17th SOFT, Rom, 14th-18th Sept.1992.
- [5-5] **Hua, Th.Q.; Gohar, Y. 1995** MHD Pressure Drop and Thermal Hydraulic Analysis for the ITER Breeding Blanket Design. *Nuclear Technology*, University of California at Los Angeles, June 27-July 1, 1994. *Fusion Eng. and Design* 27(1995) 703.
- [5-6] **Barleon, L., Casal, V., Lenhart, L. 1991** MHD-flow in liquid metal cooled blankets. *Fusion Engineering and Design*, Vol.14, p.401-412.
- [5-7] **Malang, S. et al. 1993** MHD work on self-cooled liquid-metal blankets under development at the Nuclear Research Centre, Karlsruhe. *Perspectives in Energy*, p.303-312.
- [5-8] **Tillack, M.S., Marley, N.B. 1995** Flow balancing in liquid metal blankets, *Fusion Engineering and Design* 27 (1995) 735.
- [5-9] **Hua, T.Q., Picologlou, B. 1990** Magnetohydrodynamic flow in a Manifold and multiple rectangular coolant ducts of self-cooled blankets. *Fusion Technology*, Vol.19, p.102-112.
- [5-10] **Moon, T.J., Walker, J.S. 1990** Liquid-metal flow through a sharp elbow in the plane of a strong magnetic field. *J. Fluid Mech.*; Vol.223, p.397-418.
- [5-11] **Hartmann, I. 1937** Hg-Dynamics I, Theory of the laminar flow of an electrically conductive liquid in a homogeneous magnetic field; Det. Kgl. Danske Videnskabernes Selskab; *Mathematisk-fysiske Meddelelser XV (6)*.
- [5-12] **Shercliff, J.A. 1956** The flow of conducting fluids in circular pipes under transverse magnetic fields: *J. Fluid Mech.*, Vol. 1; S. 644
- [5-13] **Hunt, J.C.R., Stewartson, K. 1965** Magnetohydrodynamic flow in rectangular ducts II. *J. Fluid Mech.*, Vol.23, p.563.
- [5-14] **Gold, R. 1962** Magnetohydrodynamic Pipe flow. Part 1, *J. Fluid Mech.*; Vol.13, p.505-512.
- [5-15] **Aitov, T.N., Kalyutik, A.I., Tananaev, A.V. 1979** Numerical investigations of three-dimensional MHD-flow in a curved channel of rectangular cross section. *Magnetohydrodynamics*, Vol.4, p.82-87.
- [5-16] **Kim, C.N. Hadid, A.H., Abdou, M.A. 1989** Development of a computer method for the full solution of MHD flow in fusion blankets. *Fusion Engineering and Design*, Vol.8, p.265-270.
- [5-17] **Sterl, A. 1990** Numerical simulation of liquid-metal MHD flows in rectangular ducts: *J. Fluid Mech.*; Vol.216, p.161-191.
- [5-18] **Lenhart, L. 1994** MHD Strömungen in Rechteckgeometrien. Dissertation Universität Karlsruhe.

- [5-19] **McCarthy, K.A. 1989** Analysis of liquid metal flow using a core flow approximation with applications to calculating the pressure drop in basic geometric elements of fusion reactor blankets. Dissertation, University of California, Los Angeles.
- [5-20] **Madarame, H., Hagiwara, T. 1989** Computer code for analyzing liquid metal MHD flow in rectangular duct under strong transverse magnetic field. Fusion Engineering and Design, Vol.8, p.167-171.
- [5-21] **Hua, T.Q., Walker, J. 1989** MHD flow in insulating circular ducts for fusion blankets. Fusion Technology, Vol.15, p.699-704.
- [5-22] **Kulikovskii, A.G. 1968** Slow steady flows of a conducting fluid at large Hartmann numbers. Fluid Dynamics, Vol. 3(1), p.1-5.
- [5-23] **Walker, J.S. 1981** Magnetohydrodynamic flows in rectangular ducts with thin conducting walls. Journal de Mécanique, Vol.20, No. 1, p.79-112.
- [5-24] **Bühler, L. 1995** Magnetohydrodynamic flows in arbitrary geometries in strong, non-uniform magnetic fields. A numerical code for the design of fusion reactor blankets. Fusion Technology 27(1995) 3.
- [5-25] **Molokov, S.; Bühler, L., 1994** Liquid metal flow in a U-bend in a strong magnetic field. J. Fluid Mech. 267, 325-352.
- [5-26] **Bühler, L. 1993** Magnetohydrodynamische Strömungen flüssiger Metalle in allgemeinen dreidimensionalen Geometrien unter der Einwirkung starker, lokal variabler Magnetfelder. KfK report, KfK 5095.
- [5-27] **Barleon, L., Bühler, L., Mack, K.-J., Stieglitz, R., Picologlou, B.F., Hua, T.Q., Reed, C.B. 1992** Investigations of liquid metal flow through a right angle bend under fusion relevant conditions; Proceedings of the 17th Symposium on Fusion Technology (SOFT), Rom; Elsevier SCIENCE Publishers B.V., Vol.II, p.1276-1280.
- [5-28] **Meng, J.C.S., Hendricks, P.J.; Hrubec, J.D.; Hensch, C.W. 1994** Experimental studies of a seawater superconducting electromagnetic thruster: A continuing Quest for higher magneto-hydrodynamic propulsive efficiency; 2nd Int. Conf. on Energy Transfer in Magnetohydrodynamic Flows; PAMIR, 26th-30th Sept. 1994; Aussois, France; Vol.2; p.491-500.
- [5-29] **Reed, C.B., Picologlou, B.F., Hua, T.Q., Walker, J.S. 1987** ALEX-results A comparison of measurements from a round and a rectangular duct with 3D-code predictions. 12th Symp. on Fus. Engng. IEEE, Monterey, Ca, Oct. 1987, p.1267-1270.
- [5-30] **Badger, B. et al. 1974** UWMAK-I a Wisconsin toroidal reactor design. University of Wisconsin, report UWFD-68.
- [5-31] **Barleon, L., Casal, V., Mack, K.-J., Kreuzinger, H., Sterl, A., Thomauske, K. 1989** Experimental and theoretical work on MHD at the Kernforschungszentrum Karlsruhe - the MEKKA-program; Liquid Metal Magnetohydrodynamics (Lielpeteris, J.; Moreau, R. editors); Kluwer Academic Publishers, p.55-61.
- [5-32] **Reimann, J., Molokov, S., Platnieks, I. Platācis, E. 1993** MHD flow in multi-channel U-bends: Screening experiments and theoretical analysis. KfK report, KfK-5102.
- [5-33] **Reimann, J.; Bühler, L.; Mack, K.-J.; Platnieks, I.; Stieglitz, R.; Stumpf, F. 1994c** Influence of a magnetic field B on pressure drop of a liquid metal flow through a T-junction perpendicular to B, 2nd Int. Conf. on Energy Transfer in Magnetohydrodynamic Flows; PAMIR, 26th - 30th Sept. 1994; Aussois, France

- [5-34] Lyon, R.N. et al., Liquid-Metals Handbook, Navexos P-733 (Rev.) (1952)
- [5-35] Foust, O.J 1972 Sodium-NaK engineering Handbook; Vol.1; Sodium chemistry and physical properties; Gordon and Breach SCIENCE Publishers; ISBN0677030204.
- [5-36] Addison, C.C. 1984 The chemistry of the liquid alkali metals; John Wiley&Sons Ltd; ISBN0471905089.
- [5-37] Schulz, B. (1986) Thermophysical properties in the system LiPb; KfK-4144.
- [5-38] O'Donnell, J.O., Papanikolaou, P.G., Reed, C.B. 1989 The thermophysical and transport properties of eutectic NaK near room temperature, ANL report ANL/FPP/TM-237.
- [5-39] Reed, C.B.; Picologlou, B.F. 1986 Techniques for measurement of velocity in liquid metal MHD-flows. Fusion Technology, Vol. 10, Nov. 1986, p. 813 - 821.
- [5-40] Boyarevich, A.V. et al. 1990 Measurement of averaged local velocities in magneto-hydrodynamic experiments. Magnetohydrodynamics, Vol.26, p.133.
- [5-41] Tillack, M.S. 1990 MHD flow in rectangular ducts. Report UCLA-FNT-41, University of California Los Angeles.
- [5-42] Miyazaki, K.; Konishi, K.; Gonno, Y. 1991 Reduction of MHD pressure drop of liquid metal flow by insulation; Part II: insulated circular ducts; Fusion Technology; Vol. 19; p.961 ff.
- [5-43] Barleon, L.; Lenhart, L.; Mack, K.J.; Sterl, A.; Thomauske, K. 1989 Investigations on liquid metal MHD in straight ducts at high Hartmann numbers and interaction parameters. Proceedings of Fourth International Topical Meeting on Nuclear Reactor Thermal- Hydraulics NURETH-4, August 22-26, Karlsruhe, Vol.2, p. 857-862.
- [5-44] Miyazaki, K.; Inoue, S.; Yamaoak, N. 1986 Magnetohydrodynamic pressure drop of lithium flow in rectangular ducts; Fusion Technology; Vol. 10; p. 830-836.
- [5-45] Morley, N.B.; Tillack, M.S.; Abdou, M.A. 1991 Development of an analytic core flow approximation for a square duct in an oblique magnetic field. Report UCLA-FNT-46, University of California Los Angeles.
- [5-46] Molokov, S.; Shishko, A. 1993 Fully developed Magnetohydrodynamic flows in rectangular ducts with insulating walls. KfK report, KfK-5247.
- [5-47] Kirillov, I.R.; Reed, C.B.; Barleon, L.; Miyazaki, K. 1995; Present understanding of MHD and heat transfer phenomena for liquid metal blankets; Fusion Eng. and Design 27(1995) 553.
- [5-48] Stieglitz, R.; Molokov, S.; Barleon, L.; Reimann, J.; Mack, K.-J. 1994 MHD-flows in electrically coupled bends; 2nd Int. Conf. on Energy Transfer in Magnetohydrodynamic Flows; PAMIR, 26th-30th Sept. 1994; Aussois, France; Vol. 1; p.403-413.
- [5-49] Holroyd, R.J.; Walker, J.S. 1978 A theoretical study of the effects of wall conductivity, non-uniform magnetic fields and variable area ducts on liquid metal flows at high Hartmann number; J. Fluid Mech.; Vol. 84; part 3; p.471-495.
- [5-50] Grinberg, G.K.; Kaudze, M.Z.; Lielausis, O.E. 1985 Local MHD-resistances on a liquid sodium circuit with a superconducting magnet; Magnetohydrodynamics; No.1; Vol.21; p.99.

- [5-51] **Molokov, S. 1994** Liquid metal flows in manifolds and expansions of insulating rectangular ducts in the plane perpendicular to a strong magnetic field. KfK report, KfK-5272.
- [5-52] **Burr, U.; Bühler, L. 1994** Wärmeübertragung in dreidimensionalen, magnetohydrodynamischen Strömungen. KfK report, KfK5329.
- [5-53] **Molokov, S.; Bühler, L. 1994** Liquid metal flow in a U-bend in a strong magnetic field. J. Fluid Mech., Vol. 267, p.325-352.
- [5-54] **Stieglitz, R. 1994** Magnetohydrodynamische Strömungen in Ein- und Mehrkanalumlenkungen. Dissertation, Universität Karlsruhe.
- [5-55] **Reimann, J.; Buceniaks, Dementev, S.; Flerov, A.; Molokov, S.; Platnieks, I. 1994** MHD-velocity distributions in U-bends partly parallel to the magnetic field. 2nd Int. Conf. on Energy Transfer in Magnetohydro-dynamic Flows; PAMIR, 26th-30th Sept. 1994; Aussois, France, Vol. 1, p. 391-402.
- [5-56] **Bühler, L.; Molokov, S. 1993** Magnetohydrodynamic flows in ducts with insulating coatings. KfK report, KfK5103.
- [5-57] **Reimann, J.; Bühler, L.; Mack, K.-J.; Platnieks, I.; Stieglitz, R.; Stumpf, F. 1994** Influence of a magnetic field B on pressure drop of a liquid metal flow through a T-Junction perpendicular to B. 2nd Int. Conf. on Energy Transfer in Magnetohydro-dynamic Flows; PAMIR, 26th-30th Sept. 1994; Aussois, France, Vol. 1, p. 297-308.
- [5-58] **Reimann, J.; Buceniaks, I.; Flerov, A.; Heller, L.; Platnieks, I. 1994** Experiments on pressure drop of MHD-flows in manifolds; 2nd Int. Conf. on Energy Transfer in Magnetohydrodynamic Flows; PAMIR, 26th-30th Sept. 1994; Aussois, France; Vol.2; p.433-442.
- [5-59] **McCarthy, K.A.; Abdou, M.A. 1991** Analysis of liquid metal MHD flow in multiple adjacent ducts using an iterative method to solve core flow equations. Fusion Engineering and Design, Vol. 13, p.363-380.
- [5-60] **Molokov, S. 1993a** Fully developed liquid metal flow in multiple rectangular ducts in a strong uniform magnetic field; KfK report, KfK5075.
- [5-61] **Molokov, S. 1993b** Fully developed liquid metal flow in multiple rectangular ducts in a strong uniform magnetic field. Eur. J. Mech. B/Fluids, Vol. 12, No.6, p.769-787.
- [5-62] **Madarame, H.; Taghavi, K.; Tillack, M.S. 1984** Analysis of MHD-fluid flow and pressure drop. FINESSE Interim Report, 3, edited by Abdou, M. UCLA-ENG-84-30, 6.9-6.109
- [5-63] **Reimann, J.; Molokov, S.; Platnieks, I. and Platacis, E. 1992** MHD-flow in multichannel U-bends: screening experiments and theoretical analysis, 17th Symposium on Fusion Technology, Roma, September 14-18, Vol. 2, S. 1459-63.
- [5-64] **Reimann, J.; Barleon, L.; Molokov, S.; Platnieks, I.; Platacis, E.; Stieglitz, R. 1993** First Results from Different Investigations on MHD Flow in Multichannel U-Bends, Proceedings of the 7th Beer-Sheva Intern. Sem. on MHD Flows and Turbulence, Jerusalem, Israel, Febr. 14-19, to be published in Magnetohydrodynamics.
- [5-65] **Stieglitz, R.; Barleon, L.; Reimann, J.; Mack, K.-J., 1994**, MHD flows in partially decoupled parallel U-bends at high Hartmann numbers, Proceedings of the 18th Symposium on Fusion Technology (SOFT), Karlsruhe, August 22-26, Vol. 2, p. 1209-1212

- [5-66] **Malang, S. 1991** Development of electrically insulating coatings for Pb-17Li blankets. Presented at the Workshop on requirements, problems and comparison of fusion reactor blanket concepts, St.Petersburg, Oct. 17th-18th, 1991.
- [5-67] **Sze, D.K.; Mattas, R.F.; Hull, A.B.; Picologlou, B.; Smith, D.L. 1992** MHD considerations for a self-cooled liquid lithium blanket. Fusion Technology 21, No.3, Part 2b, p.2099-2106.
- [5-68] **Bühler, L. 1993** Additional magnetohydrodynamic pressure drop at junctions of flow channel inserts. Proc. of the 17th SOFT, Rom, Sept 14-18, 1992, Vol. 2, p.1301-1305.
- [5-69] **Bühler, L. 1995** The influence of small cracks in insulating coatings on flow structure and pressure drop in MHD channel flows. Fusion Eng. and Design 27(1995) 650.
- [5-70] **Blums, E.; Mikhailov, Yu.A.; Ozols, R., 1987** Heat and Mass Transfer in MHD Flows, World Scientific Publishing Co. Pte, Ltd, Singapore.
- [5-71] **Bühler, L., 1993** Convective-diffusive transport in laminar MHD flows, KfK 5241
- [5-72] **Kolesnikov, Yu. B.; Tsinober, A.B. 1972** Magnetohydrodynamic flow in the region of a lump in the conductivity at the wall. Magnetohydrodynamics 1(1972), pp. 61 - 65
- [5-73] **Sommeria, J., Moreau, R., 1982** Why, how and when MHD turbulence becomes two-dimensional. Journal of Fluid Mechanics 118(1982), pp. 597-518.
- [5-74] **Branover, H. 1986** Turbulence and the feasibility of self-cooled liquid metal blankets for fusion reactors. Fusion Technology 10(1986), pp. 822-829.
- [5-75] **Barleon, L.; Mack, K.J.; Kirchner, R.; Stieglitz, R. 1994** Heat Transfer in MHD-Flow at High Hartmann Numbers and Improvement by Turbulence Promotion, 2nd Int. Conf. on Energy Transfer in Magnetohydrodynamic Flows; PAMIR, 26th - 30th Sept. 1994; Aussois, France; Vol. 1, p. 381-390.
- [5-76] **Barleon, L.; Mack, K.-J.; Kirchner, R.; Frank, M.; Stieglitz, R. 1994** MHD Heat transfer and pressure drop in electrically insulated channels at fusion relevant parameters. Proceedings of the 18th Symposium on Fusion Technology (SOFT), Karlsruhe, August 22-26, Vol. 2, p. 1201-1204.
- [5-77] **Andreev, O.V., Kolesnikov, Yu. B. 1993** Possibilities of Heat Transfer Intensification to the MHD Problems of Liquid Metal Fusion Blankets, Proc. 7th Beer-Sheva International Seminar on MHD Flows and Turbulence, Jerusalem, Israel, Febr. 14-18, 1993, to be published in Magnetohydrodynamics.
- [5-78] **Hua, T.Q.; Walker, J. 1988** Three-dimensional flows in rectangular ducts of liquid metal- cooled blankets. Fusion Technology Vol.14, p.1389-1398.



## 6. Thermomechanics

Thermomechanical analysis of the reference Dual Coolant blanket was performed in order to demonstrate that the blanket temperatures and stresses are within allowable limits. More details of the calculations are given in [6-1]. A summary of the main results and design data is presented in Table 6-1.

Steady-state results are reported under normal operating conditions. The primary sources of loading are internal coolant pressure in the He and liquid metal systems, and both volumetric and surface heat loads. Responses to transients (including disruptions) are reported in Chapter 11. The loadings and responses due to ferromagnetism are a complex subject which was not analyzed here in detail.

### 6.1 Cooling system thermal-hydraulics

Heat sources used for the thermal-hydraulics analysis are summarized in Table 6-2. Volumetric heating rates are provided by neutronics analysis. The spatial distributions of power density in the liquid metal (Pb-17Li) and the steel structure (MANET) have been determined using a three-dimensional Monte Carlo calculation (cf. Chapter 4) and are shown in Figs. 4-4 and 4-5. The volumetric heat generation in a single blanket segment caused by the neutron flux results in a heat input of about 26.7 MW and 16.4 MW for the outboard and inboard blanket segments, respectively.

For the plasma facing blanket surface, an average heat flux of 0.4 MW/m<sup>2</sup> and a local maximum value of 0.5 MW/m<sup>2</sup> have been assumed. The maximum surface heat load is expected to occur at the equatorial zone of the torus. Taking into account a mean value for the surface heat flux of 0.4 MW/m<sup>2</sup>, the total heat input amounts to 30 MW and 19.2 MW for the outboard and inboard blanket segments, respectively. The power in the shield is not included in these values. Since the inboard blanket is divided into two halves, the power that has to be removed from each blanket half is 9.6 MW.

The power removed by each coolant system can be determined from the data of the neutronics analysis. With the additional assumption made that the middle of the walls separating the helium and Pb-17Li is an adiabatic limit we obtain the power portions for the helium coolant system and the liquid metal system, as summarized in Table 6-2.

Table 6-1: Summary of Main Results and Design Data

A) Thermohydraulics	outboard segment	inboard segment
First wall heat flux [MW/m <sup>2</sup> ]		
- maximum	0.5	0.5
- average	0.4	0.4
Max. power density [MW/m <sup>3</sup> ]		
- MANET	23.9	20.3
- Pb-17Li	19.4	17.1
Total Power (nuclear-power + surface heat flux) [MW]	30	19.2
Helium cooling:		
- power to be extracted [MW]	6.9	5.8
- pressure [MPa]	8	8
- temperature inlet/outlet [°C]	250/350	250/350
- mass flow rate [kg/s] (total for two systems)	13.2	5.55*
- max. velocity [m/s]	66	63
- pressure drop in segment [MPa]	0.15	0.12
- total pressure drop in the whole helium loop, approx. [MPa]	0.20	0.17
- blower performance, adiabatic ** [MW] (total for the entire reactor: 31.3 MW)	0.443	0.316
Liquid metal cooling:		
- power to be extracted [MW]	23.1	13.4
- temperature inlet/outlet [°C]	275/425	275/425
- mass flow rate [kg/s]	815	237 *
- max. velocity [m/s]	1.1	0.4
- max. interface temperature (struct./breeder) [°C]	443	430
- MHD pressure drop [MPa]		
. with insulating coatings (reference case)	0.4	0.13
. with flow channel inserts (backup solution)	4.3	1.9
- power requirements for LM circulating pump ** [MW] (total for the entire reactor: 2.3 MW)	0.043	0.008

\*) for one blanket half.

\*\*) blower and pump efficiency of 80 % is assumed.

Table 6-1 (continued)

<b>B) Mechanical stresses in the mid-plane of the outboard segment, calculated for average and maximum surface heat flux</b>	
Boundary conditions: - internal pressure [MPa] (in case of large leak between He and LM) - FW surface heat load [MW/m <sup>2</sup> ], average/maximum - temperature of shield [°C] (assumed for average and maximum surface heat flux, respectively)	8 0.4/0.5 285/300*
Max. FW temperature [°C] (external plasma side of FW)	490/527
von Mises stresses [MPa]: - primary membrane (web plate between FW channels) limit given by ASME	161 220
- primary membrane + bending (external plasma side of FW) limit given by ASME	120 176
- primary + secondary (external plasma side of FW) limit given by ASME	402/450* 505/463
max. allowable internal pressure in the segment box during operation (extrapolated) [MPa]	11

\* For the maximum surface heat load of 0.5 MW/m<sup>2</sup> a shield temperature of at least 300°C is required in order not to exceed the ASME limits for the sum of primary and secondary stresses. Therefore, the case of the maximum surface heat load has been analyzed with a shield temperature of 300°C. The higher shield temperature would also lower the stresses in the case of average heat load.

Table 6-2: Summary of heat sources in the inboard and outboard blanket segments (MW)

	Outboard	Inboard
Volumetric heating	26.7	16.4
Surface heating	3.3	2.8
Total power per segment	30.0	19.2
Power removed by He	6.9	5.8
Power removed by PbLi	23.1	13.4
Number of segments	48	32

The total liquid metal mass flow rate is determined by the allowable temperature rise of the liquid-metal flow between the blanket inlet and outlet. This temperature rise is limited by the allowable maximum temperature at the coolant-to-wall interfaces as dictated by corrosion considerations. Table 6-3 summarizes this and other temperature and stress limits imposed on the blanket design. A mean exit bulk temperature of 425 °C has been selected to keep the maximum temperature at the interface of coolant and martensitic steel below 470 °C related to corrosion of the structural material. The minimum inlet temperature of the liquid metal is governed by the melting temperature of the Pb-17Li eutectic alloy which is 235 °C. Therefore, the inlet temperature was set at 275 °C, a temperature which is well above the ductile-brittle-transition temperature (DBTT) for the martensitic steel (MANET) of about 250 °C. This results in an overall temperature rise of 150 K and total mass flow rates of 815 kg/s and 474 kg/s through the outboard and inboard blanket segments, respectively. Since the inboard segment is divided into an upper half and a lower half of equal size, the rate of mass flow through each half is 237 kg/s.

The inlet and outlet temperatures of the helium have been chosen to be 250 °C and 350 °C, respectively, in order to respect the DBTT of MANET and to assure an attractive thermal efficiency of electrical power generation. The helium pressure is set at 8 MPa in order to keep the pressure loss within reasonable limits. The helium mass flow rate calculated from the energy balance is 13.2 kg/s and 11.1 kg/s for the outboard and inboard blanket segments, respectively. Since the inboard segment is divided into two halves, the helium mass flow rate for each half is 5.55 kg/s. Furthermore, the helium cooling gas is carried in two separate coolant systems. This guarantees emergency cooling in case of failure of one cooling system.

The helium of the two cooling systems flows in opposite directions through the First Wall and the channels belong alternately to one of the two systems. This reduces the temperature differences within the First Wall and thus minimizes the thermal stresses. Table 6-1 summarizes the mass flows of all coolant systems.

There is an additional constraint which influences the thermal-hydraulics layout: To assure a sufficiently large material strength and to leave a margin for temperature rises during transients, it was estimated that the First Wall temperature should not exceed 550 °C under steady state conditions. For a given thermal loading this temperature limit is generally controlled by the helium temperature and the heat transfer coefficient in the First Wall channels.

Table 6-3: Maximum values obtained from the 3D temperature and stress analyses of the outboard blanket and maximum allowable values

Temperature Analysis	Maximum Temperature [°C]	Location	Design Basis Limit [°C]
- First Wall . at $q=0.4 \text{ MW/m}^2$ . at $q=0.5 \text{ MW/m}^2$ 1)	505 527	top end of blanket blanket mid-plane	550 550
- PbLi/steel interface	443	top end of blanket	470

1) assuming helium flow distribution according to mean surface heat flux

Stress Analysis (p=80 bar)	Maximum von Mises Stress [MPa]	Location	Admissible Stress [MPa]
a) Primary stress First Wall . external plasma side (T=527 °C) . web plate (T=330 °C) . side wall (T=300 °C)	120 161 178	blanket mid-plane	176 220 227
b) Primary plus secondary stresses ( $q=0,4 \text{ MW/m}^2$ , $T_{\text{shield}}=285 \text{ °C}$ ) . First Wall - external plasma side (T=490 °C) - inside wall (T=388 °C) - side wall (T=300 °C)	402 441 184	blanket mid-plane	505 610 681
c) Primary plus secondary stresses ( $q=0,5 \text{ MW/m}^2$ , $T_{\text{shield}}=285/300 \text{ °C}$ ) . First Wall: - external plasma side (T=527 °C) - inside wall (T=404 °C) . side wall (T=300 °C)	470/450 517/494 173/162	blanket mid-plane	463 596 681

The helium gas enters the blanket at the top and flows downward through the main supply channels. After diversion at the bottom end of the blanket to the manifolds, it is carried into the parallel toroidal channels of the First Wall.

Since the helium gas on its way upwards from the bottom to the top of the blanket is carried up to five times consecutively through the segment walls on a meander-shaped path (Fig. 6-1), its temperature reaches finally 350 °C at the top of the blanket.



The resulting maximum First Wall temperature of about 600 °C would exceed the admissible value. To overcome this problem, an artificial roughness is applied at the plasma facing channel wall in order to achieve an increase by a factor 2 in the heat transfer coefficient [6-1]. The roughness ribs with a depth 0.25 mm are arranged transverse to the helium flow direction (see Fig. 6-2). Moreover the helium passages are arranged in such a manner that the helium velocity increases from bottom to the top of the blanket in order to achieve larger heat transfer coefficients at the blanket top. According to the results of a temperature calculation with the FE code ABAQUS [6-2], the maximum First Wall temperature is reduced to 530 °C which is well below the admissible limit. In these calculations the local peak value for the surface heat flux of 0,5 MW/m<sup>2</sup> is considered for all helium passages.

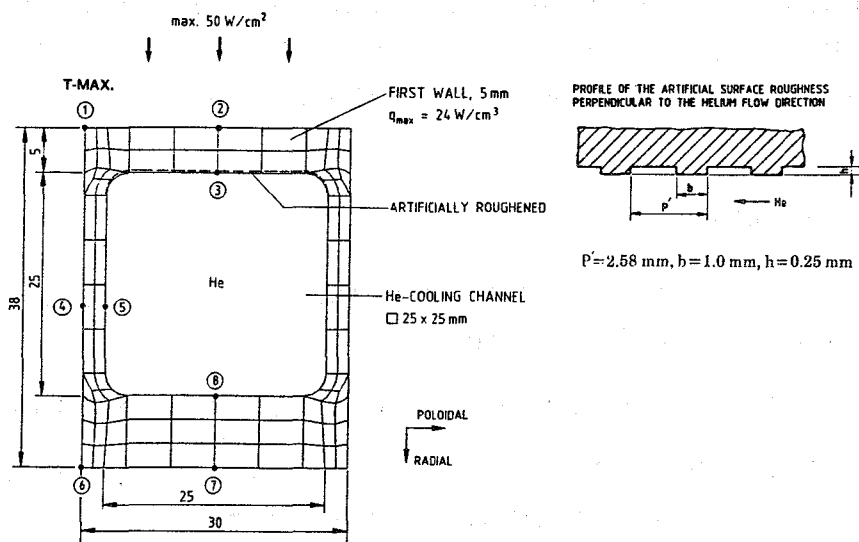


Fig. 6-2: Cross-section of the artificially roughened First Wall cooling channels

After definition of the cooling systems the pressure drop of the helium flow was calculated on the basis of Ref. [6-3]. The total helium pressure drop between the blanket inlet and outlet, including all bend and flow resistances, amounts to 0.15 MPa and 0.12 MPa for the outboard and inboard blanket segments, respectively. About two thirds of the total pressure drop occur in the First Wall channels. The increase in pressure drop due to artificial roughness is about 0.022 MPa. This value is rather small because the artificial roughness is applied at only one surface of the cooling channels.

The pressure drop in the liquid metal is dominated by MHD effects. Assuming fully-insulated electrical conditions in the poloidal ducts, the pressure drop on the

outboard and inboard segments will be 0.4 MPa and 0.13 MPa, respectively (see Chapter 5 and [6-4]).

The power required for the helium blowers and liquid metal pumps was determined; it amounts to 31.3 MW and 2.3 MW, respectively, for the whole reactor assuming 0.5 bar additional helium pressure losses in the heat exchanger and other components and an efficiency of the helium blowers and liquid metal pumps of 80 %.

## **6.2 Thermal and Stress Analysis**

After definition of all thermohydraulics data detailed three-dimensional temperature and stress calculations were performed. The analysis was carried out for a radial/toroidal section of the outboard blanket with a poloidal height of one helium channel pitch (see Fig. 6-3). The three-dimensional FE mesh was generated using the CAD system BRAVO3/GRAFEM [6-5, 6-6].

### **6.2.1 Thermal Analysis**

For the computation of the temperature distribution in the liquid metal, the following assumptions have been made:

- The liquid metal flow is uniform (slug flow) as a result of the MHD effects.
- Axial heat conduction in the direction of flow is neglected; perpendicular to the flow direction, heat is transported by conduction only.
- The liquid metal temperature at the inlet of the respective coolant channel is distributed homogeneously.
- Thermal barriers between the First Wall and the liquid metal flow due to insulating coatings or flow channel inserts are neglected.

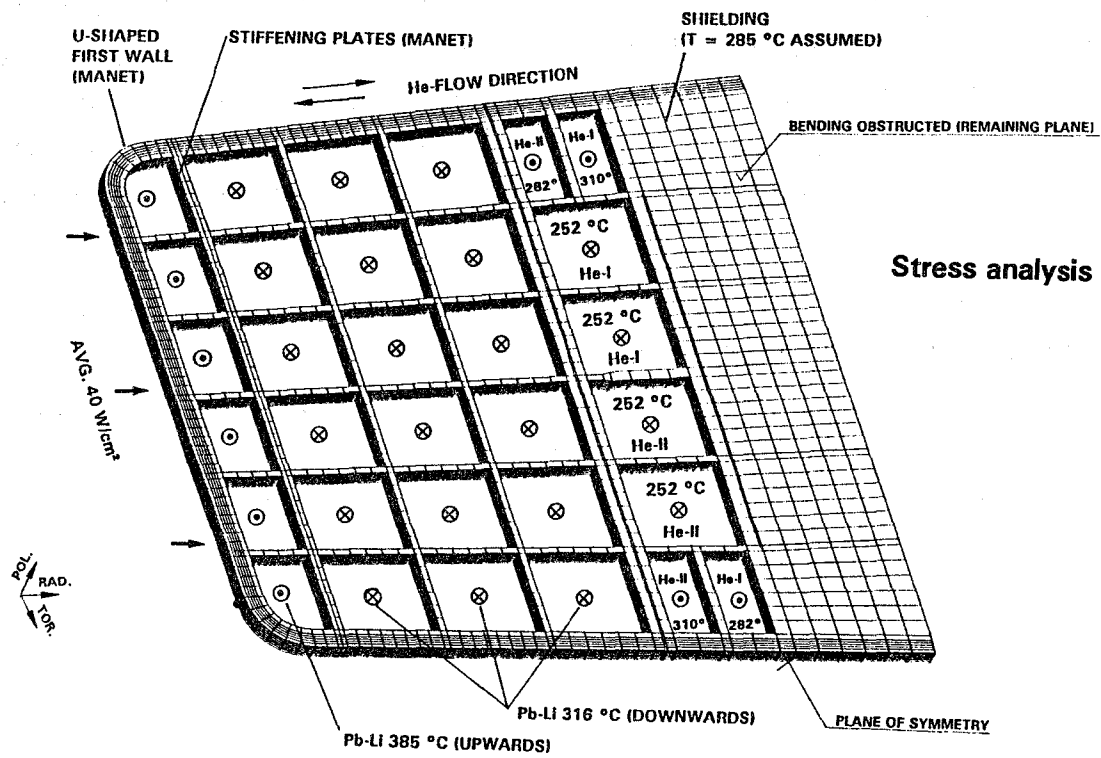
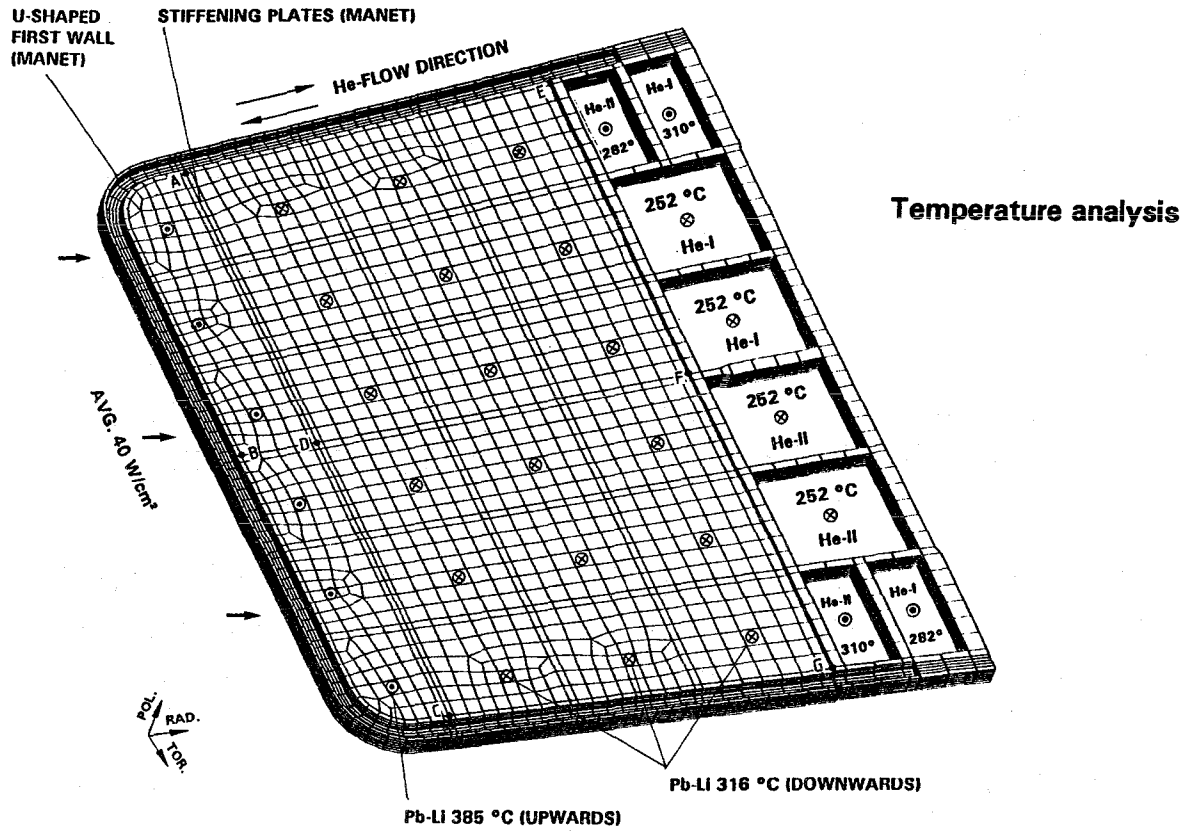


Fig. 6-3: Finite Element models for temperature and stress computations

Because of the lack of more sophisticated computer programs for the coupled application to solids and fluids, the method of a moving coordinate system has been utilized in the computation. Quasi-time-dependent calculations were carried out within the calculated residence time of the fluid in the poloidal coolant channels and setting zero the specific heat of the solid materials. The different flow directions require in addition that the temperatures of some sub-regions are computed separately in an initial step. For nodes at the intersecting lines, the resulting temperatures have to be averaged and serve as input for a rerun. The same method has to be applied to the connection with the First Wall and the rear part of the blanket segment containing the poloidal coolant inlet channels.

For the computation of the temperature field, both the mean surface heat flux of  $0.4 \text{ MW/m}^2$  and the maximum local surface heat flux of  $0.5 \text{ MW/m}^2$  have been taken into account. The material data of lead-lithium and MANET steel are from Ref. [6-7], [6-8], and [6-9].

The radial distribution of the material dependent power density has been provided by neutronics calculations. The heat generation in the steel structure decreases with the radial distance from the First Wall. In the First Wall, the volumetric heat generation amounts to  $23.9 \text{ MW/m}^3$ . The power density in the liquid metal takes a maximum value of  $19.4 \text{ MW/m}^3$  in the front channel. In the poloidal direction the power density decreases with the poloidal distance from the equatorial plane to the top and bottom ends of the blanket as well. At both ends of the blanket it takes about 70 % of the maximum value of the equatorial plane.

Figure 6-4 shows the result of the 3D temperature calculation. The maximum First Wall temperature at the blanket mid-plane is  $490 \text{ }^\circ\text{C}$  and  $527 \text{ }^\circ\text{C}$  using the mean and maximum surface heat fluxes, respectively. At the blanket top a value of  $505 \text{ }^\circ\text{C}$  is reached using the mean surface heat flux. The maximum liquid metal-to-wall interface temperature is  $443 \text{ }^\circ\text{C}$  at the blanket top end and is well below the limit of  $470 \text{ }^\circ\text{C}$ . The results of the 3D calculations agree well with the 2D results mentioned above.

### 6.2.2 Stress Analysis

After the temperature calculations, stress calculations were performed for a part of the outboard blanket at the equatorial plane of the torus where the maximum thermal loading is expected to occur. In the stress calculations, a quasi-plane strain condition was applied to the poloidal surfaces of the model which means that these planes remain plane and parallel. For the breeder zone (Pb-17Li) the same pressure of 8 MPa was assumed as for the helium system. This is a conservative upper limit of the internal load which is reached only in case of a large leak between the helium and the Pb-17Li systems. The temperature fields for average and maximum surface heat fluxes were used, as shown in Figure 6-4.

The resulting stresses have been evaluated using the ASME code [6-10], assuming no degradation of mechanical properties due to neutron irradiation.

For the shield at the blanket back side a constant temperature of 285 °C was assumed in the first calculation. The results of this calculation have shown that in the case of the maximum surface heat load the average shield temperature has to be slightly increased to 300 °C in order to keep the thermal stresses below the admissible limit. In the First Wall, the calculated primary von Mises stress amounts to 120 MPa. This value is below the limits for yield, rupture and 20000 h creep stresses allowed for MANET at 527 °C according to ASME ( $1.5 \times S_{m,t} = 176$  MPa in the case of membrane plus bending stresses).

With respect to the total von Mises stress assessment it has to be emphasized that the assumption of an internal pressure of 80 bar in the liquid metal is very conservative. Since this load is present only for a limited period of time in the case of a leak between the First Wall and the breeding zone, the 20000 h creep stress limit has not been taken into account in assessing the combination of primary and secondary stresses.

The total von Mises stress distribution is shown in Fig. 6-5. The maximum primary plus secondary stresses occur at the location of the temperature maximum and amount to 402 MPa and 450 MPa for average and maximum surface heat loads, respectively. These values are well below the limits for rupture and yield stress of 505 MPa and 463 MPa at the temperature of 490 °C (average surface heat load) and 527 °C (maximum surface heat load), respectively. A maximum allowable internal pressure of the blanket for a short period of time was extrapolated to 11 MPa. The calculated maximum temperatures and stresses are summarized in Table 6-3.



Further FE-calculations have been performed to analyse the global deformation behaviour of the blanket, caused by gravity induced loading, internal pressure, and thermal loading with different types of support [6-11]. The influence exerted by the temperature in the rear shielding structure on deformation and stress is studied. The 2D calculation, which describes the radial/poloidal section, shows that the influence of the helium pressure and the gravity load on the global displacements is negligible. The maximum thermal stress and the stress distribution in the First Wall depend strongly on the support conditions of the segment and the temperature of the rear shield plate. A relatively cool shield plate increases the bending of the free hanging blanket. This causes a reduction of the thermal stresses. If bending is restricted by an additional support, e.g. by connecting the shield plates of the segments to a rigid toroidal shell, a hot shield causes an increased poloidal strain and also a reduction of the secondary stresses. The quasi plane strain conditions assumed in the three-dimensional calculations for the radial/torodial section were confirmed to be reasonable in the case that bending of the segment is suppressed. By optimizing the boundary conditions a reduction of the main compressive stresses can be achieved.

The shield temperatures assumed in the two-dimensional calculations were in all cases lower than the mean value of the minimum and maximum temperature of the blanket structure. This allows the conclusion that also under operational power variations, assuming full coolant flow and constant inlet temperature are maintained, the temperature difference between the shield and the structure, and consequently also the thermal stresses will not be larger than under the steady state conditions described above.

The 2D and 3D models describe large sections of the blanket; therefore the FE-mesh at the FW is not sufficiently fine to calculate accurate stresses. Hence, additional 3 D computation should be carried out for a locally limited segment applying the previously determined strains as displacement boundary conditions.

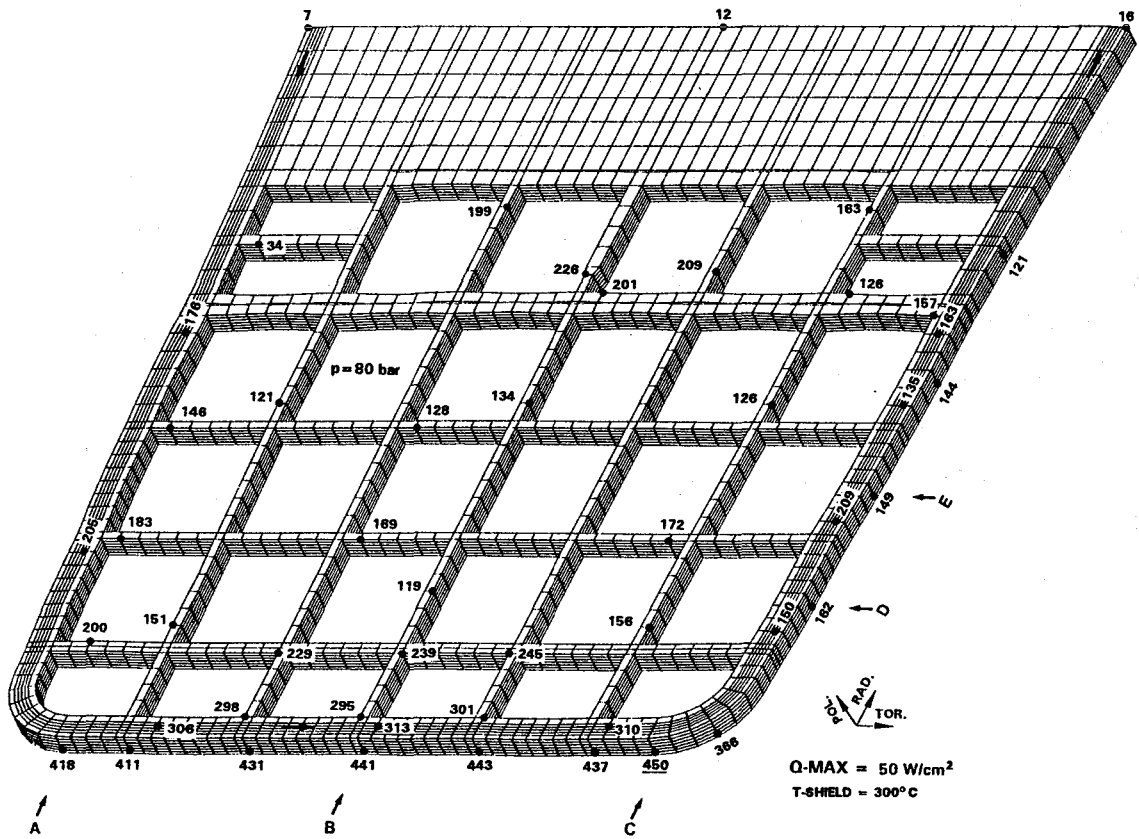
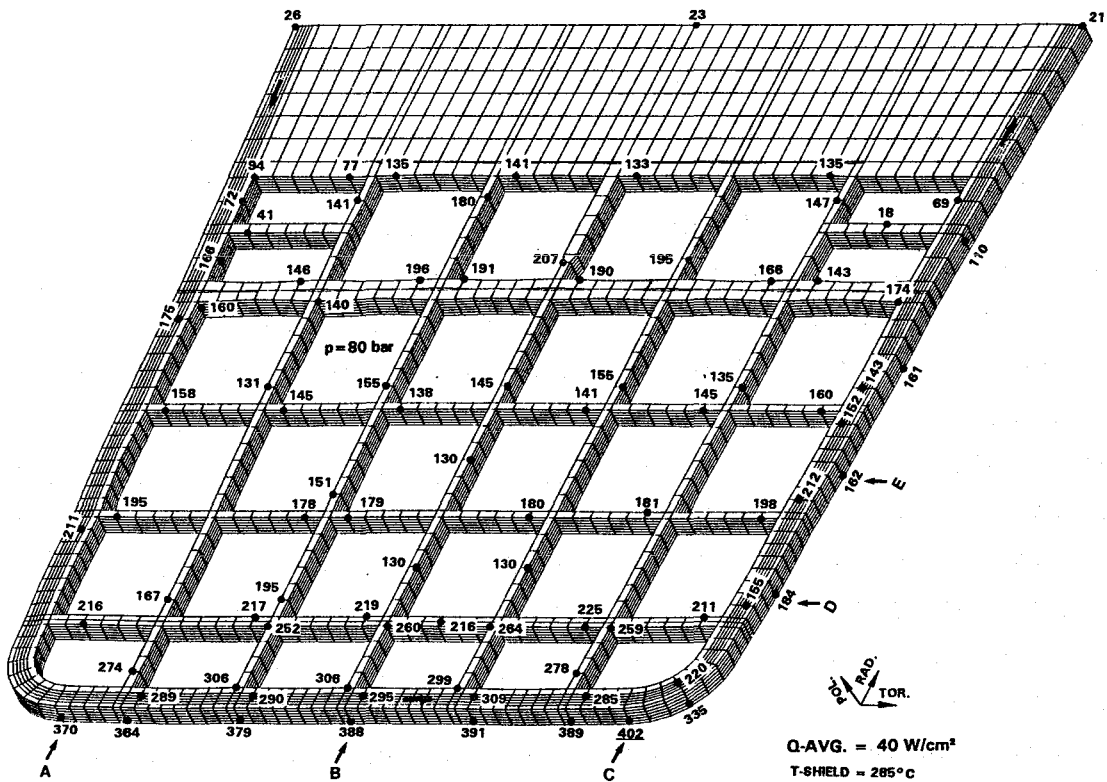


Fig. 6-5: Von Mises primary plus secondary stresses in the blanket structure at torus midplane of the outboard segment for average and maximum local heat fluxes

## References

- [6-1] P. Norajitra  
Thermohydraulics Design and Thermomechanics Analysis of Two European Breeder Blanket Concepts for DEMO  
FZKA 5580, Forschungszentrum Karlsruhe (1995).
- [6-2] Hibbit, Karlsson Sorensen  
ABAQUS User's Manual Version 4.9, Providence, R.I., USA.
- [6-3] W. Kalide  
Einführung in die technische Strömungslehre  
Carl Hansen Verlag, München, 1971.
- [6-4] S. Malang, E. Bojarsky, L. Bühler, H. Deckers, U. Fischer, P. Norajitra, H. Reiser, Dual-coolant liquid metal blanket, 17th SOFT, Rome, Italy, Fusion Technology, 1424-1428, 1992.
- [6-5] BRAVO3 GRAFEM User's Guide  
Document No. A-22240-003  
Applicon/Schlumberger, May 1984.
- [6-6] BRAVO3 GRAFEM Command Reference Guide  
Document No. 23718-006, Revision A, October 1989  
Schlumberger CAD/CAM, Michigan, USA.
- [6-7] U. Jauch, V. Karcher, B. Schulz  
Thermophysical Properties in the System Li-Pb  
KfK 4144, September 1986
- [6-8] K. Ehrlich  
Internal KfK report, May 1986, unpublished.
- [6-9] M. Küchle (compiled by)  
Material Data Base for the NET Test Blanket Design Studies,  
Test Blanket Advisory Group, KfK, February 1990.
- [6-10] ASME Code III, edition 1986.
- [6-11] H. Gerhardt  
FZK internal-report, May 1995, unpublished.



## **7. TRITIUM EXTRACTION AND RECOVERY**

The requirements on the blanket tritium removal and recovery system are to keep tritium inventory low in the total blanket system and to limit the tritium loss through the steam generator into the water to an acceptable value (assumed: 20Ci/d for all blankets). The latter requirement is the crucial one for a Pb-17Li blanket due to the low tritium solubility of Pb-17Li which results in a high tritium partial pressure (the driving force for permeation) for a given concentration.

The reference tritium removal concept is described in detail in Section 7.1. This concept is based on the use of a double-walled heat exchanger with a NaK filled gap between the Pb-17Li side and the water-steam side. In Section 7.2 an alternative method is described based on the use of solid getters in direct contact with the Pb-17Li.

### **7.1 Tritium Extraction with NaK Cold Trap**

#### **7.1.1 Principal Considerations**

The reference technique for tritium removal and recovery includes the following steps:

- a) tritium permeation from Pb-17Li into the NaK-filled gap of the double-walled steam generator
- b) tritium removal from NaK by precipitation as tritide in a cold trap
- c) tritium recovery by thermal decomposition of the tritide at elevated temperatures.

In order to keep the tritium inventory low in the tritium extraction system (TES), four removal/recovery cycles per day are anticipated. Figure 7-1 shows schematically the flow sheet and the investigations described in the next sections. Some comments are given in respect to the individual steps:

To a): Here, advantage is taken from the high tritium partial pressure in Pb-17Li which results in relatively low tritium inventories in the Pb-17Li and structural materials as long as no permeation barriers at the Pb-17Li/steel interface and steel/NaK interfaces occur.

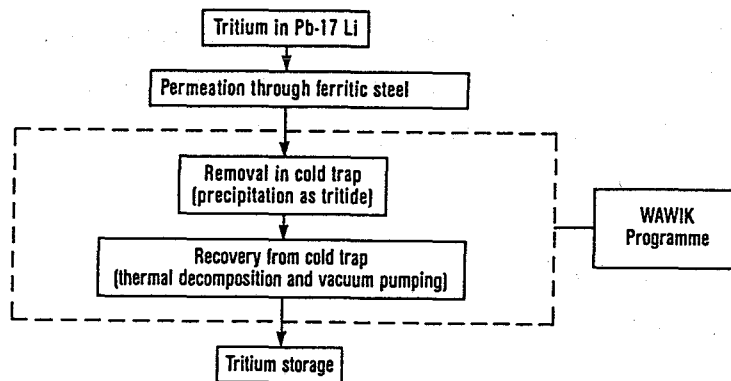
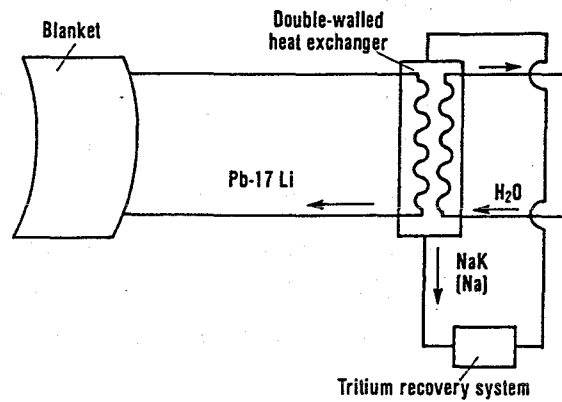


Fig. 7-1 Schematic flow sheet and specific investigations

The build-up of oxide surface layers (which reduce drastically permeation) is not expected. Corrosion experiments in both Pb-17Li and NaK had shown that the chemical activity of the liquid metals towards oxygen is higher than that of the ferritic steel wall and initial oxide layers are dissolved. If, for MHD reasons, electrically insulating direct coatings are used in the blanket it must be proven that no constituents of this coating are transported into the steam generator and give rise to a permeation barrier. Using an  $Al_2O_3$  layer as coating grown on an Al rich sublayer, the only possibility could be the dissolution of Al in cracks or flakes of damaged  $Al_2O_3$  coatings. For MHD reasons only very small sizes of these defects can be tolerated (some  $cm^2$  for a total blanket segment, compare Chapter 5.5) and additionally a fast formation of a new  $Al_2O_3$  coating due to the oxygen present in the Pb-17Li must occur (self-healing of coatings, compare Chapter 3.4). Therefore, the transport of Al and deposition in the steam generator is expected to be so small that it can not impede permeation significantly.

As a consequence, the permeation step was not considered as an important design issue and no R&D was performed yet.

To b): Tritium must be removed at significantly lower concentration levels than those existing in sodium loops where cold trapping is general practice. In order to base a TES on this process step, it must be proven that the efficiency of cold traps is favourable for fusion-relevant concentration levels and loading periods (which are much shorter than for conventional cold trap operations).

To c): Cold trap regeneration is not standard practice in conventional applications, and again no relevant results existed in respect to required temperatures and recovery time periods.

Therefore, specific investigations in respect to b) and c) were performed in the frame of the WAWIK programme (WAWIK = Wasserstoff-Abscheidung und Wiedergewinnung in Kaltfallen).

### 7.1.2 Overview of Hydrogen Removal by Cold Trapping

For the further understanding, some fundamental aspects of cold trapping are briefly summarized. For more details see [7-1, 7-2].

Upstream of the cold trap a nonsaturated solution of hydrogen in the liquid metal exists (temperature  $T_i$ , concentration  $c_i$ , see Fig. 7-2), where the concentration is proportional to the square root of the partial pressure  $p$  ( $c = Kp^{0.5}$ , where  $K$  is the Sieverts constant).

In the cold trap the liquid metal is cooled down; hydride crystals start to form below the corresponding saturation temperature  $T'$ . With decreasing temperature, the saturation concentrations  $c_{\text{sat}}$  decreases. Ideally, the liquid metal leaves the cold trap with the concentration  $c_{\text{osat}}$ , corresponding to the saturation concentration for the lowest temperature in the cold trap, designated with cold trap temperature  $T_0$ . In practice, this equilibrium is not reached due to nonideal precipitation kinetics.

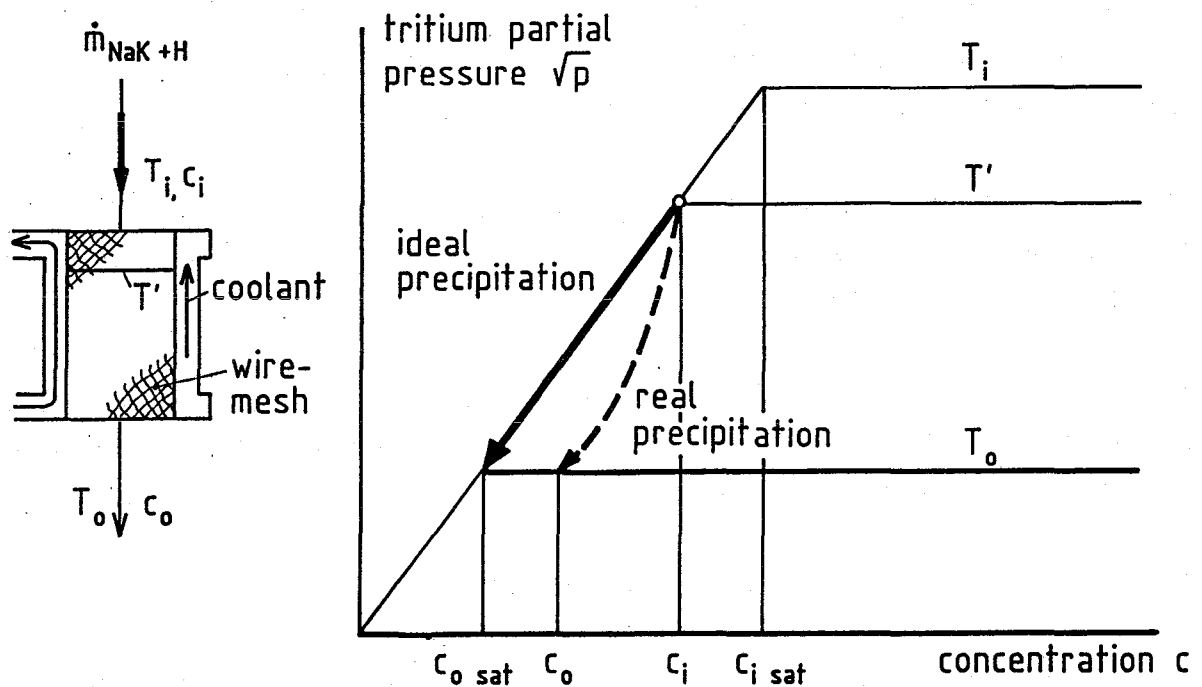


Fig. 7-2 Principle of hydrogen removal by cold trapping

Figure 7-3 (see also Table 7-1 in Section 7.1.7) shows characteristic solubility data for different liquid metal-hydrogen systems. The term hydrogen is generally used if it is not differentiated between the different isotopic species. If concentrations are defined with atomic fractions then the Sieverts constants  $K$  and saturation concentrations  $c_{\text{sat}}$  are approximately equal for all isotopes. In order to keep the permeation losses to the steam-water system small the Sieverts constant should be large and the minimum saturation concentration should be small. Figure 7-3 shows that NaK is more favourable than Pb-17Li in respect to both requirements: the Sieverts constant is higher by more than three orders of magnitude and the minimum saturation concentration (close to the melting point of  $T_m = -12^\circ\text{C}$ ) is lower by six orders of magnitudes.

However, the concentrations  $c_o$  reached in practice at the cold trap temperature  $T_o$  might be considerably larger than the equilibrium values given in Fig. 7-3. This difference  $(c_o - c_{o\text{sat}})$  is of prime importance for the characterisation of cold trap behaviour.

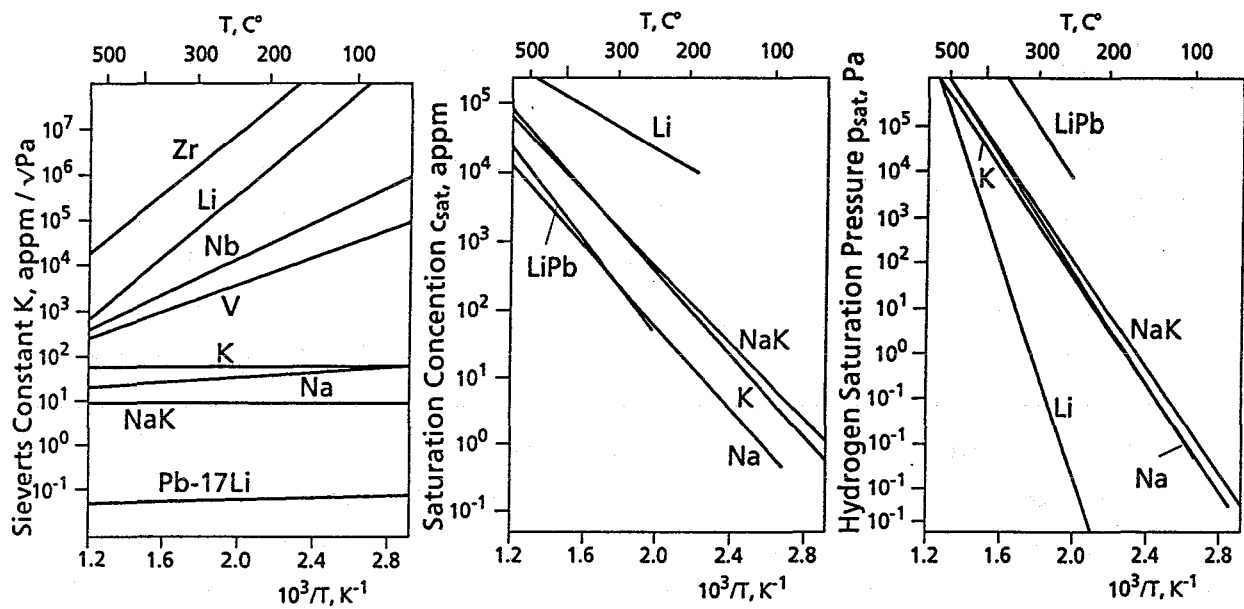


Fig. 7-3 Hydrogen solubility characteristics for different liquid metals

The local hydride precipitation rate is generally described by the sum of two deposition mechanisms: At first, crystal nuclei must be provided. At a later stage, the precipitation rate is governed by crystal growth. For cold traps with large internal surfaces crystal nucleation is expected to occur at the solid surfaces (heterogeneous nucleation).

Contradictory statements are found in the literature concerning the importance of the nucleation process on the total precipitation process. For hydrogen precipitation in Na it is often assumed (see e.g. [7-3]) that the nucleation process is very fast and can be neglected in modeling the precipitation kinetics. In other experiments [7-4] it was found that nucleation determines the location of crystals and, therefore, cannot be neglected.

For crystal growth the local mass transfer rate  $\dot{m}$  is expressed by

$$\dot{m} = k A (c - c_{\text{sat}})^n, \quad (7.1)$$

where  $k$  is the mass transfer coefficient,  $A$  is the surface relevant for crystal growth,  $c$  is the local concentration, and  $n$  is the order of reaction. Again, there are two groups of opinions: The growth rate is either diffusion controlled ( $n=1$ )

(see e.g. [7-3]) or controlled by the integration of the hydride molecule into the crystal lattice ( $n > 1$ , see e.g. [7-4]). Unfortunately, the publication [7-4] does not contain sufficient information in order to use quantitatively the results.

In the following, some characteristic features of cold traps as used in sodium-cooled fission reactors are outlined, for details see [7-1]. For practical applications, mostly mesh-packed cold traps were used providing a large internal surface for crystallization. Besides obtaining a high efficiency the design goal of these cold traps is to reach a high loading before plugging. In practice, often a premature plugging in the cold trap occurred due to improper design (high local supersaturation concentrations) or changing operational conditions (e.g. during initial loop purification or after an impurity increase due to leaks). Some design recommendations from [7-4] are taken into account in the schematical view of a cold trap shown in Fig. 7-4. The liquid metal flows downward in the annular gap which is countercurrently cooled from the outside and the inner tube (regenerative heat exchanger). The precipitation should occur in the wire mesh located in the annular gap having a large cross section in order to obtain small local supersaturation concentrations. A noncooled mesh-packed zone is recommended to decrease further the local supersaturation before heating up the liquid in the inner

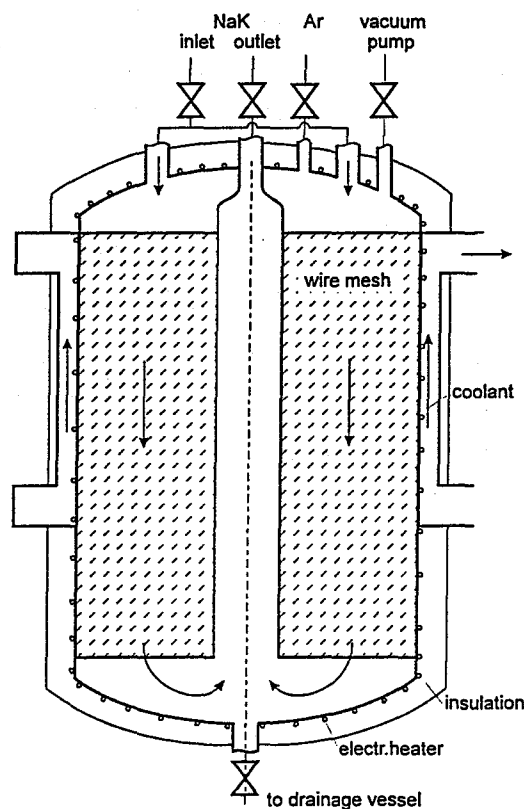


Fig. 7-4 Mesh-packed cold trap

tube. This heating-up reduces the cooling power and also ensures that the hydrogen concentration at the cold trap outlet is far below saturation concentration which presents plugging in the downstream piping.

The problem of premature plugging is not relevant to the fusion blanket cold trap because no large hydride quantities can accumulate due to the short removal/recovering cycles. Therefore, a higher wire mesh density can be selected which improves the cold trap efficiency. On the other hand, the nucleation process might play a more significant role because of the short hydrogen removal periods (about 6 hours).

Meshless cold traps were also investigated, see e.g. [7-5], especially for the use in changing operational conditions. Such cold traps are supposed to be less sensitive to premature plugging, however, the efficiency is considerably smaller due to the small specific surface. A novel approach [7-6] where an enhanced mass transfer should compensate the reduced specific surface is shown in Fig. 7-5a. The annular duct is alternatively equipped with two types of concentric rings of metal sheet (or wire mesh) resulting in a meander-shaped flow. A rotational flow is superimposed, generated by the rotating electromagnetic field of the stator of an electric motor. Characteristic of such a rotational flow are boundary layers (Ekman

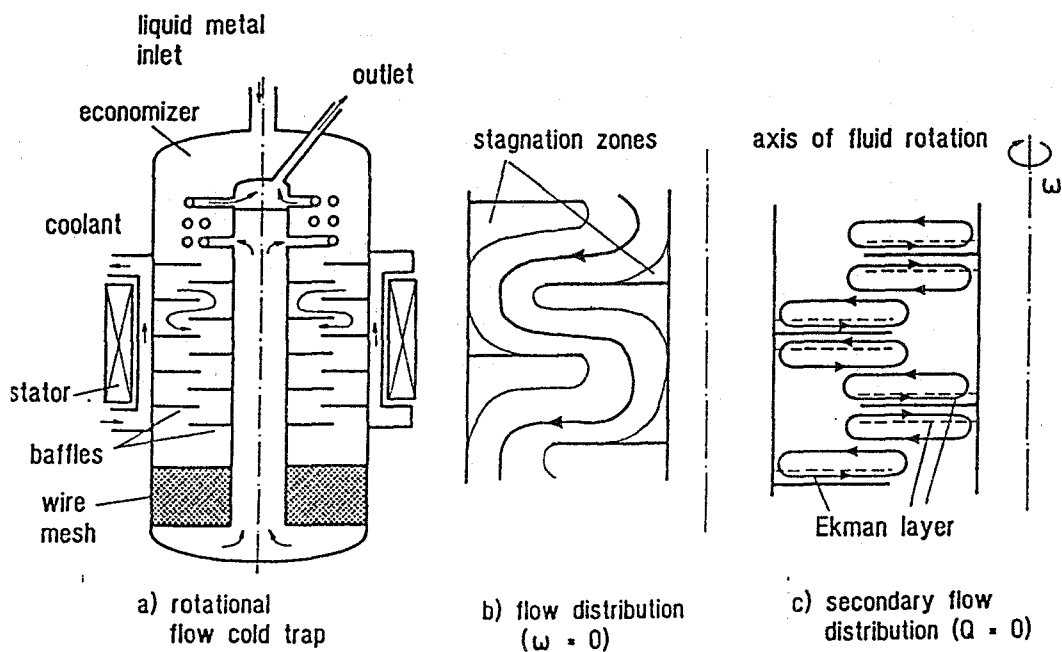


Fig. 7-5 Meshless cold trap with rotational flow

layers) where the fluid has a velocity component towards the rotational axis as shown schematically in Fig. 7-5b for the case of no cold trap throughput ( $Q = 0$ ). This superimposed rotational flow is supposed to enhance mass transfer by two effects:

- thin boundary layers exist which shorten hydrogen diffusion lengths
- no flow separation zones occur (which would be very expressed if no fluid rotation exists)

Results of first experiments with such a rotational cold trap will be also included in Section 7.1.5.

### 7.1.3 Experimental Investigations

Tritium was simulated by protium  $^1\text{H}$ . Therefore, the term hydrogen refers always to  $^1\text{H}$ . The experiments were performed in the WAWIK facility shown in Fig. 7-6. Hydrogen was permeated into the NaK through a coiled nickel tube (diameter 3 mm, wall thickness 0.3 mm, length 20 m, permeation temperature  $400\text{ }^\circ\text{C}$ ) and precipitated in one of two parallel experimental cold traps (ECT). Hydrogen concentrations were measured at the cold trap inlets and outlets by means of a hydrogen meter of the nickel membrane diffusion type (operating temperature  $450\text{ }^\circ\text{C}$ ).

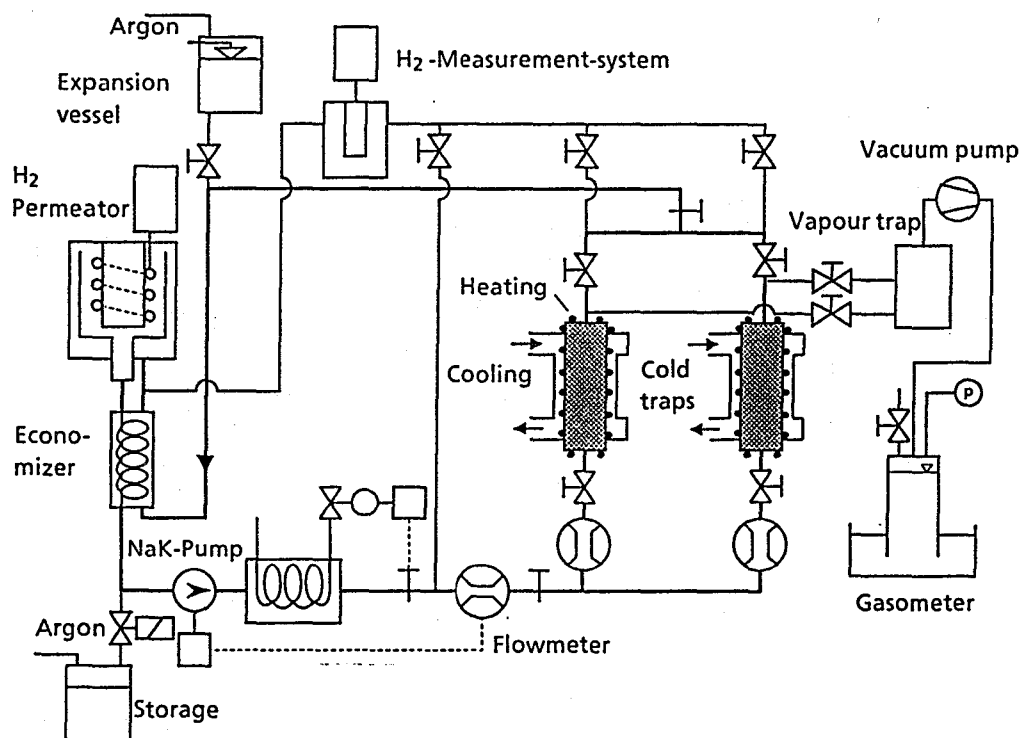


Fig. 7-6 WAWIK facility for hydrogen removal and recovery

For hydrogen recovery experiments [7-7] either complete drained ECTs or individual wire mesh packings were electrically heated up and the hydrogen flow rate was pumped off and measured with a gasometer. More details are given in Section 7.1.6.

Figure 7-7 shows different ECTs used in the course of the investigations: There is

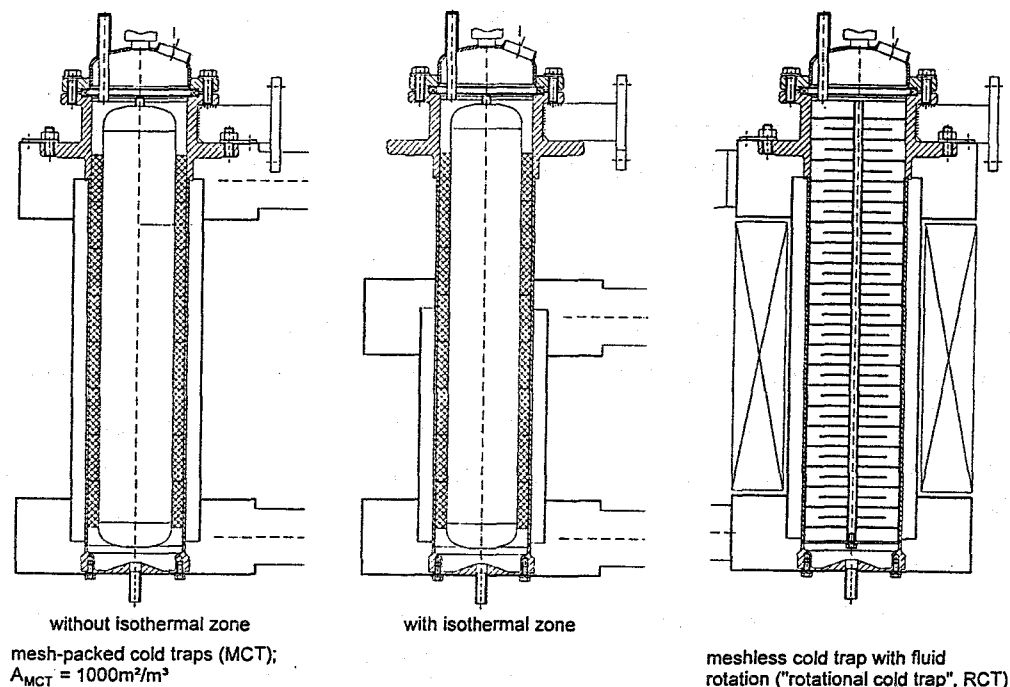


Fig. 7-7 Experimental cold traps (ECTs)

no internal countercurrent liquid metal flow in order to have better defined temperature and velocity distributions. The lowest cold trap temperature occurs at the cold trap outlet. The ECTs had an inner diameter of 102 mm and a height of 500 mm.

The experiments concentrated on wire mesh-packed cold traps (wire diameter  $d_w = 0.3$  mm, individual packing height  $H_p = 50$  mm, (total height 400 mm) specific surface  $A_{spec} = 500$  or  $1000$   $m^2/m^3$ ). The end of the 8th packing agreed fairly well with the beginning of the cooling zone. If 9 packings were used, the last packing was located in the isothermal zone.

The ECTs were equipped with about 38 thermocouples arranged at different axial, radial and azimuthal positions. First, ECTs with a circular cross-section (Fig. 7-4.a) were investigated. However, it showed that azimuthal and radial temperature differences occurred which were unfavourable for using the results for com-

parisons with model calculations. Therefore, a cold trap with an annular flow cross-section was later investigated using a gas-filled displacement body. Temperature differences in a cross-section were at most 2 °C.

With both types of cold traps, two types of experiments were performed:

- 1) Short-time loadings ( $t_{\text{load}} \approx 5$  hours). Here, the aim was to measure the local supersaturation ( $c_o - c_{\text{osat}}$ ) at the cold trap outlet as a function of time for the following parameters:
  - cold trap temperature  $T_0$
  - temperature difference between inlet and outlet ( $T_i - T_o$ )
  - NaK velocity  $v_{\text{NaK}}$
  - number of removal/recovery cycles

After each loading experiment the hydrogen was recovered. For short-time loading experiments cold traps with eight packings were better suited than a cold trap with an isothermal zone because the cold trap outlet concentration difference ( $c_o - c_{\text{osat}}$ ) is larger and, hence, reacts more sensitively on the investigated parameters.

- 2) Long-time loadings ( $t_{\text{load}}$ : 100 - 200 hours). Here, the aim was to determine the hydride mass distribution in the cold trap. These experiments were both time- and cost-consuming (the preparation and performance of the hydrogen recovery experiments with the individual packings required some months; new cold trap internals were needed for each experiment). Therefore, only a few experiments of this type were performed.

### 7.1.4 Theoretical Work

In order to predict the hydrogen removal in cold traps, relationships for the local mass transfer and the velocity and temperature distribution in the total cold trap must be known. For circular flow cross-sections radial temperatures in the NaK are no longer negligible (although the Prandtl number is small,  $Pr = 0.1$ ). For low NaK velocities, buoyancy might be of significant effect on the velocity profiles.

A computer code was developed [7-8] where in order to determine the precipitation distribution, first the code solves the two-dimensional (2D) incompressible continuity, momentum and energy equations in axisymmetric coordinates. The fluid properties were assumed to be constant except for the Boussinesq approximation, that density is a linear function of temperature in the buoyancy term.

Then, for local mass transfer, relationships according to Eq (7.1) were used; as long as no detailed experimental results existed, a correlation for diffusion-dominated mass transfer taken from literature was used [7-9].

Fig. 7-8 shows the flow geometry and the boundary conditions: constant fluid

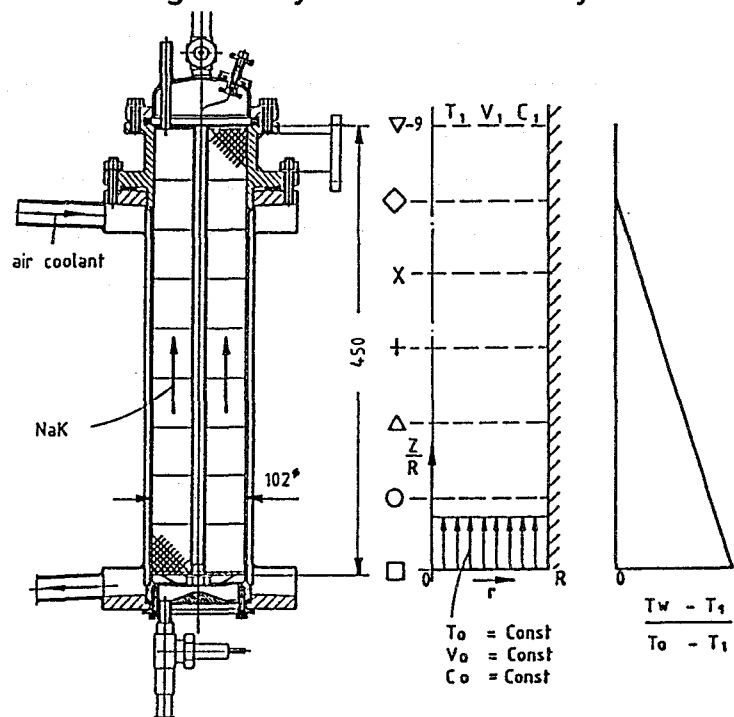


Fig. 7-8 Geometry and boundary conditions for 2 D modeling

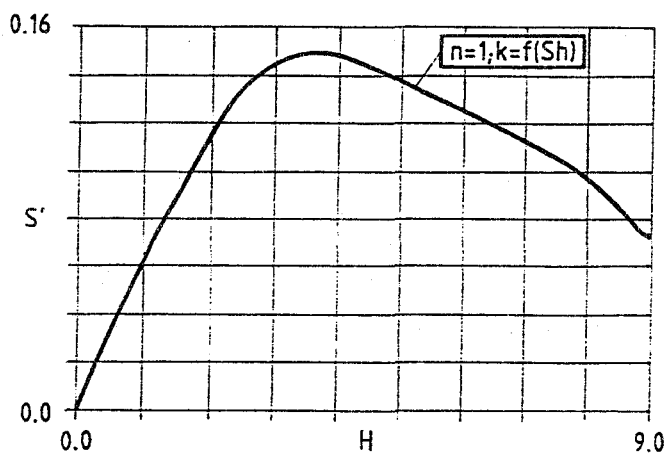
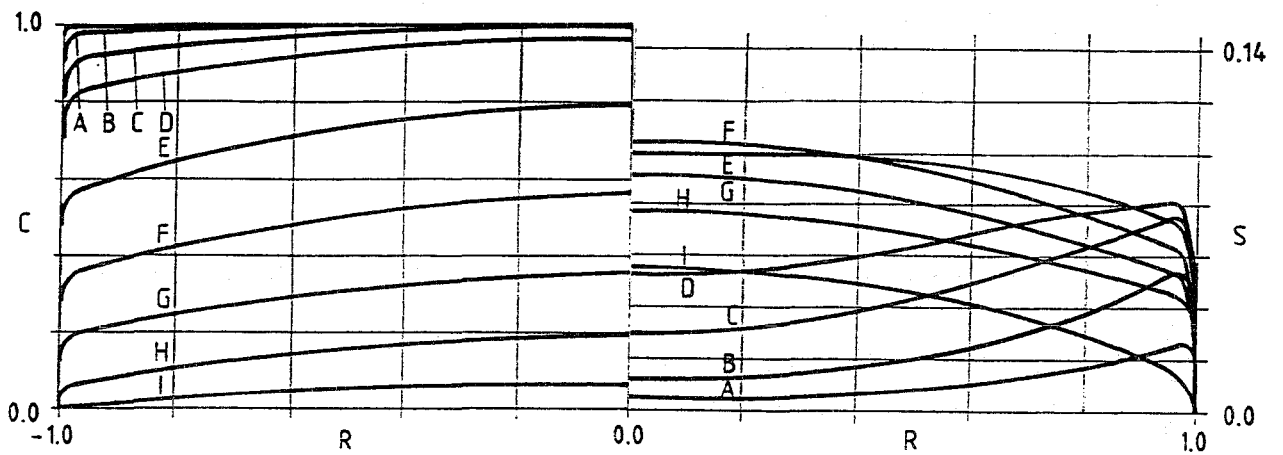
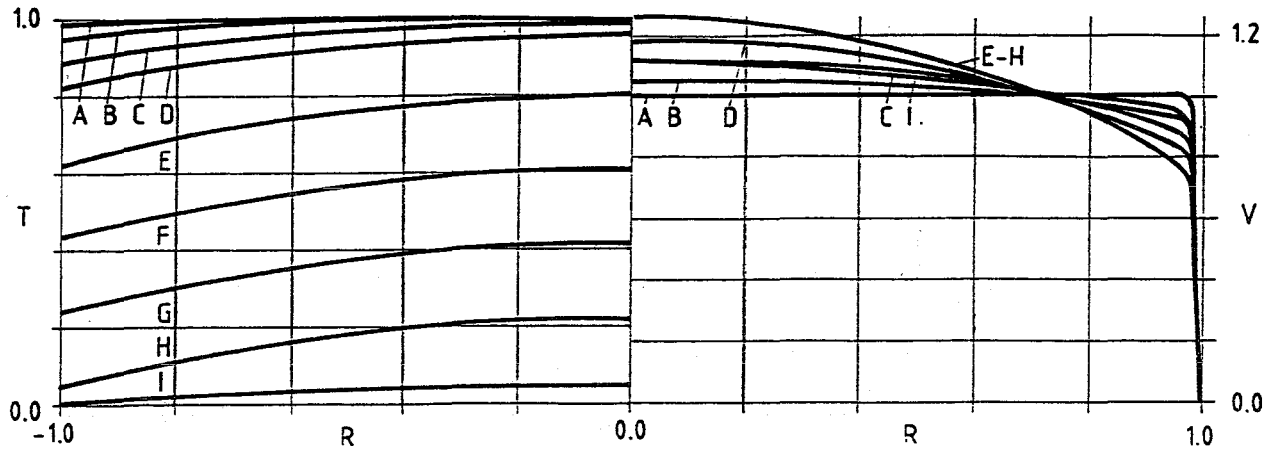
quantities are assumed at the cold trap inlet; a linear decrease of the wall temperature until the end of the 8th packing and a constant wall temperature for the 9th packing, for details see [7-8, 7-10].

Fig. 7-9 contains characteristic radial distributions of the normalized temperature (T), velocity (v), concentration (c), and deposition rate (s) for different values of the dimensionless axial coordinate  $x/R$ .

Without natural convection (results not shown), the internal friction due to the packing forces a nearly constant radial velocity distribution except close to the cylinder walls. With natural convection (Grashof number  $Gr = 6 \cdot 10^7$ ) the profiles differ significantly: the wall gradients become smaller for upward flow and a velocity maximum develops at the center line.

A temperature maximum at the center line develops with increasing flow length which is reduced at the cold trap end due to the constant wall temperature. The local concentration and with this the local deposition rate show also a distinct radial dependency. These results indicate that for a detailed cold trap design a 2 D code should be used.

For the cold trap with the circular cross-section, the temperature was not constant in the azimuthal direction due to asymmetrical cooling conditions. Therefore, the 2 D code could not be applied. For the cold trap with the annular gap the cooling conditions were improved and temperature differences were small both in the azimuthal and radial directions. Therefore, a one-dimensional (1 D) model could be used which considers a change of quantities only in the axial flow direction. It proved that the axial temperature profile influences sensitively the local mass distribution. This is demonstrated in Fig. 7-10, showing the axial mass distribution for a measured temperature distribution and an assumed linear distribution.



curve	height H
I	9.0
H	7.5
G	6.0
F	4.5
E	3.0
D	1.5
C	1.0
B	0.5
A	0.0

Fig. 7-9 Radial distributions of T, v, c and s

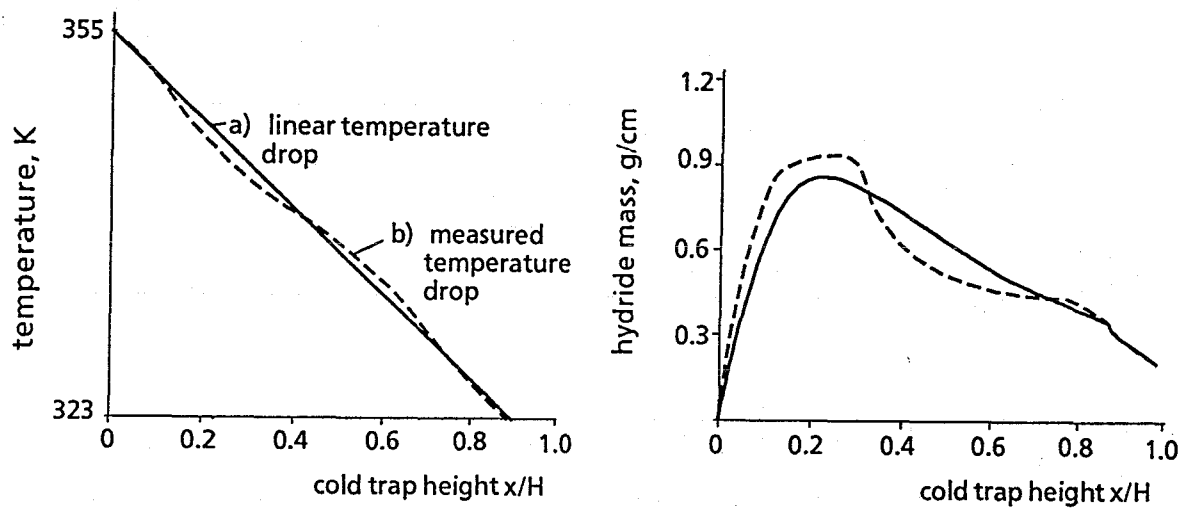


Fig. 7-10 Sensitivity of axial temperature distribution on axial mass distribution

## 7.1.5 Results for Hydrogen Removal

### 7.1.5.1 Mesh-packed Cold Traps

Figures 7-11 and 7-12 show results for the ECT with the circular cross-section [7-9]. Figure 7-11 summarizes the results for short-time loading experiments; the supersaturation at the cold trap outlet is represented as a function of the cold trap outlet temperature  $T_o$ . Different packing numbers  $N$  and wire mesh densities were investigated. The experiments were performed for a constant temperature between inlet and outlet of  $T_i - T_o = 40^\circ\text{C}$ .

The first number behind the measurement symbol denotes the NaK velocity  $v$  (mm/s); the second number denotes the total loading time at the end of the measurement. The supersaturation is lowest for ECT A with an extended isothermal zone. The supersaturation increases, as expected, with decreasing  $A_{\text{spec}}$ .

The most important result of these experiments is that the supersaturation decreases with decreasing outlet temperatures  $T_o$  and no change of this tendency is observed for the lowest investigated values. This is important because it was supposed, at least for the H-Na system [7-11], that nucleation requires a distinct val-

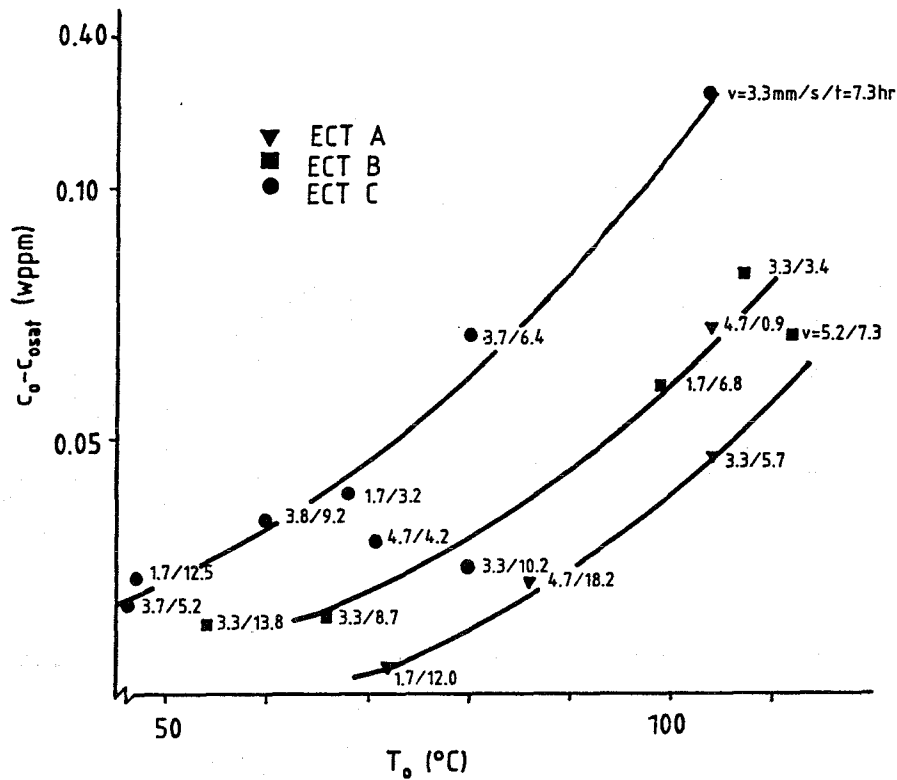


Fig. 7-11 Supersaturation at cold trap outlet (mesh-packed ECT with circular cross-section)

ue of the supersaturation concentration which might be no longer achieved at very low cold trap temperatures.

From these experiments it is difficult to determine the influence of the NaK velocity. Concerning the loading times there is the tendency that  $(c_o - c_{osat})$  decreases with  $t_{load}$ . The influence of  $v_{NaK}$  and  $t_{load}$  will be more clearly shown below.

Figure 7-12 shows measurements of the axial hydrogen distribution in the cold trap together with the result from a 2 D calculation assuming diffusion-controlled mass transfer [7-9]. The agreement is satisfactory.

The following results refer to mesh-packed ECTs with an annular cross-section, eight packings, and  $A_{spec} = 1000 \text{ m}^2/\text{m}^3$ . With these cold traps most of the experiments were performed.

Figure 7-13 (from [7-12]) shows results for experiments with different outlet temperatures  $T_o$  and  $(T_i - T_o) = \text{const} = 40 \text{ }^\circ\text{C}$ . The values are valid for a loading time of about 5 hours. Again  $(c_o - c_{osat})$  decreases with  $T_o$ . The supersaturation difference  $(c_o - c_{osat})$  increases slightly but distinctively with increasing NaK velocity.

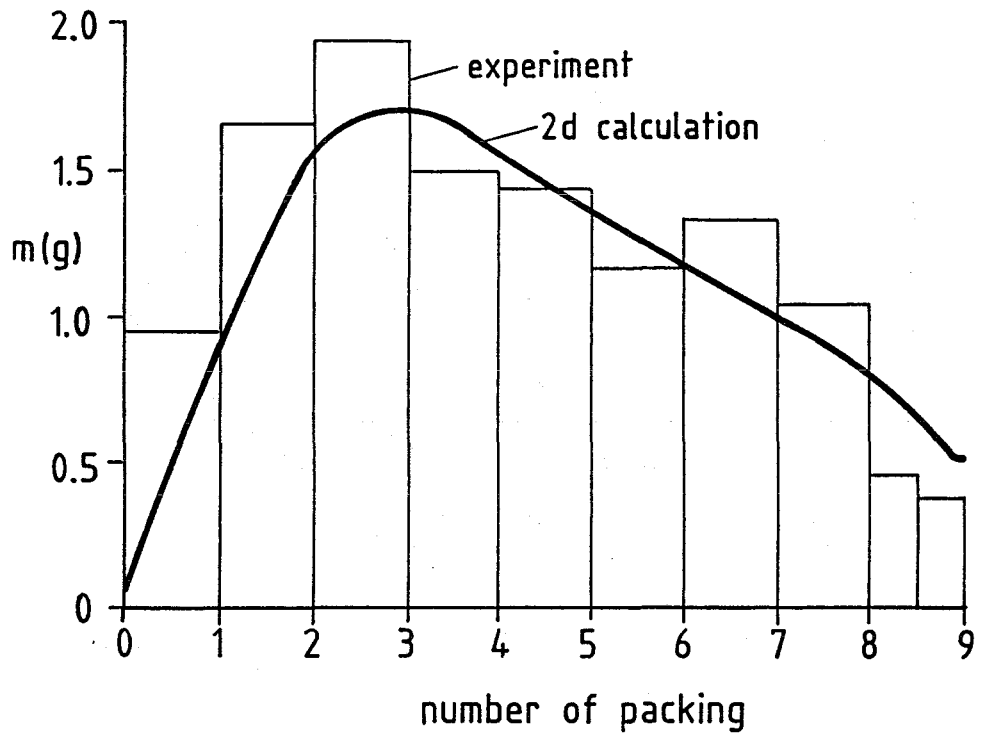


Fig. 7-12 Measured and calculated axial hydrogen mass distribution (mesh-packed ECT with circular cross-section)

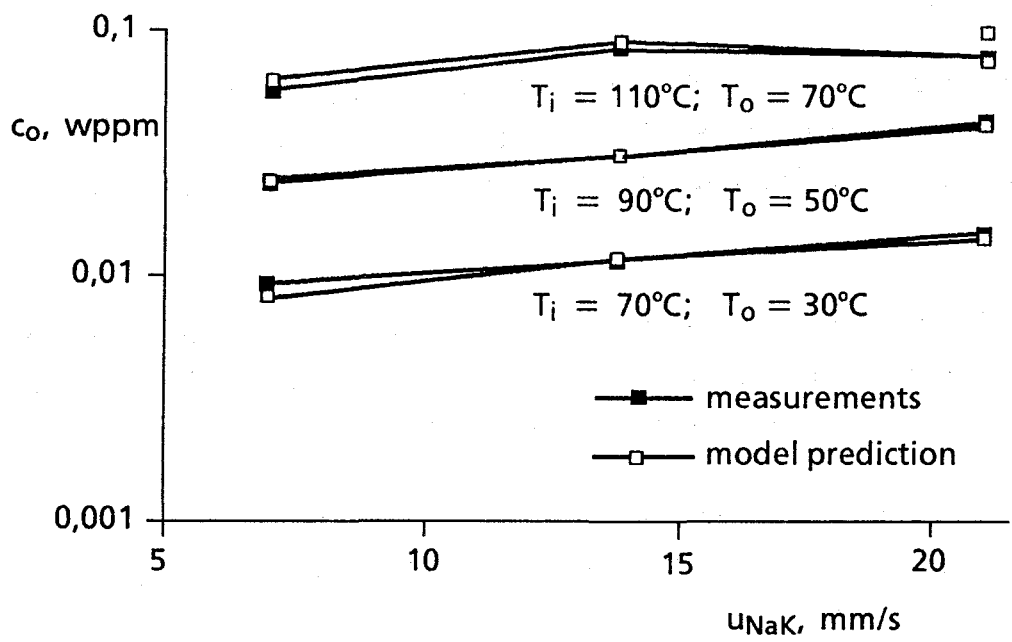


Fig. 7-13 Supersaturation at cold trap outlet (mesh-packed ECT with annular gap,  $A_{spec} = 1000 \text{ m}^2/\text{m}^3$ , 8 packings,  $t_{load} \approx 5$  hours)

The experimental results are well described by a diffusion-dominated mass transfer model, described in detail below.

Figure 7-14 shows the corresponding cold trap efficiency  $\eta$  as a function of loading time where  $\eta$  is defined by

$$\eta = (c_i - c_o) / (c_i - c_{osat}) = \left( 1 + (c_o - c_{osat}) / (c_i - c_o) \right)^{-1} \quad (7.2)$$

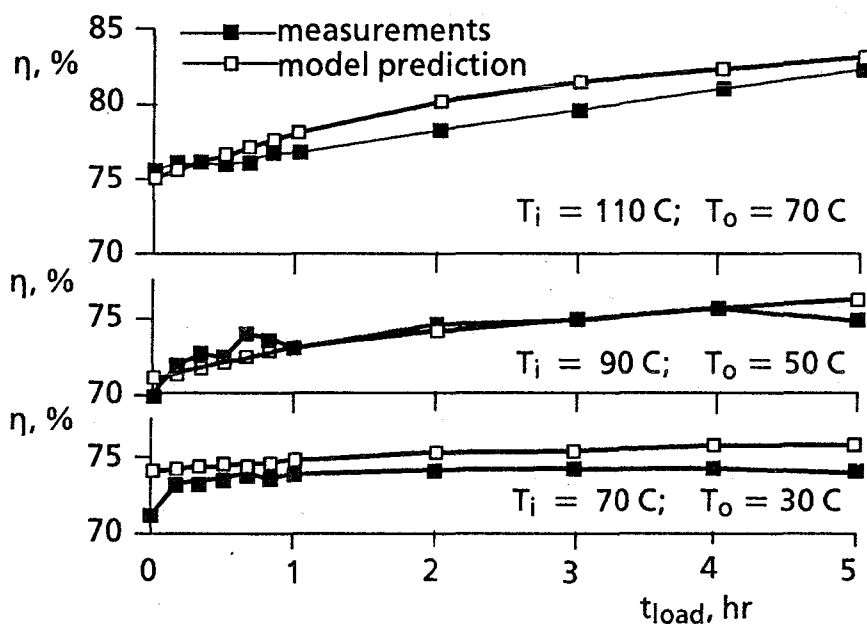


Fig. 7-14 Cold trap efficiency (mesh-packed ECT with annular gap,  $A_{spec} = 1000 \text{ m}^2/\text{m}^3$ , 8 packings)

The efficiencies are surprisingly high even for the lowest temperature level (having in mind that for  $N = 8$  the efficiencies are lower than for cold traps with an isothermal zone). The small increase with increasing  $t_{load}$  is caused by the increasing surface available for crystal growth. At the beginning of the loading period no significant deterioration of the cold trap behavior exists. Therefore, the nucleation phase is not governing the precipitation process even in the lowest concentration range.

These results are characteristic of cold traps which were subjected to at least one recovery cycle previously. During the first loading of a new cold trap a stronger decrease of  $\eta$  occurred. (For blanket tritium recovery this would mean that prior

to tritium loading some removal/recovery cycles with protium should be run). With increasing cycle number no deterioration of cold trapping is expected (rather an improvement). This might be caused by "roughening" the wire surface by minor amounts of other impurities (e.g. oxides) which are not removed during the hydrogen recovery process.

Figure 7-15 shows cold trap efficiencies for long-time-loadings. The efficiency increases during the total loading period due to the increasing surface available for precipitation. The model, compare Section 7.1.6, describes fairly well this long-time behaviour.

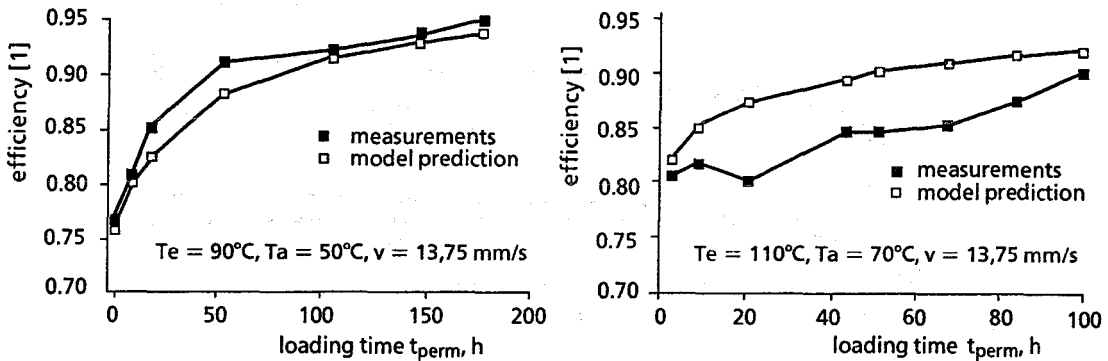


Fig. 7-15 Cold trap efficiencies for long-time loading experiments (mesh-packed ECT with annular gap,  $A_{spec} = 1000 \text{ m}^2/\text{m}^3$ )

Figure 7-16 shows the measured axial hydrogen mass distributions. A maximum is observed in the first third. Again the agreements between model predictions and experiments are fairly good. For the experiment with  $T_i = 90^\circ C$ ,  $T_o = 50^\circ C$  an ECT with nine packings was used. In order to determine more sensitively the axial mass distribution, the 9th packing was split into two parts for hydrogen recovery. A distinct precipitation still occurs in this 9th packing which decreases further the outlet concentration and, hence, increases the efficiency compared to a cold trap without an isothermal zone. An efficiency improvement of more than 5 % is observed (and calculated), compare the corresponding curve in Fig. 7-14.

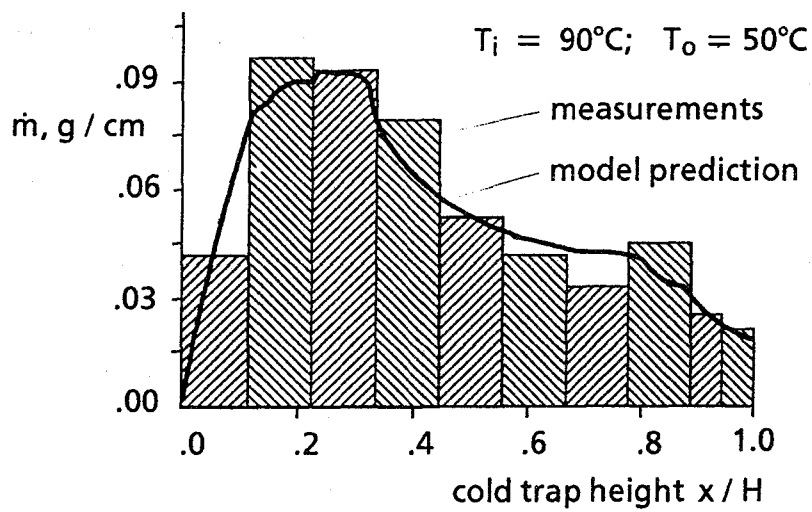
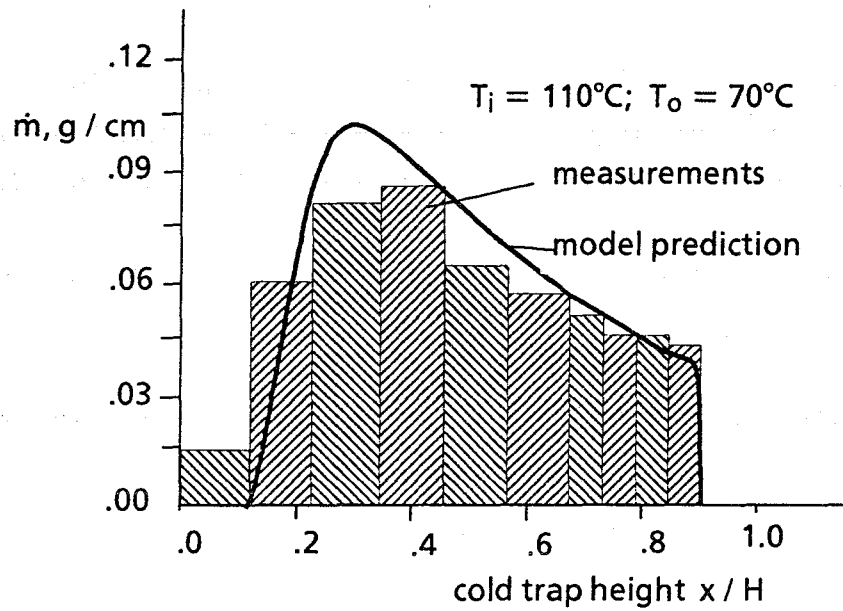


Fig. 7-16 Hydrogen mass distribution in cold trap (mesh-packed ECT with annular gap,  $A_{\text{spec}} = 1000 \text{ m}^2/\text{m}^3$ )

In order to model the cold trapping the surface available for crystal growth must be described. Figures 7-17 and 7-18 show hydride crystals, characteristic of large cold trap loadings (experiment in the high concentration range, see Fig. 7-12). Crystals of the octahedral type with maximum sizes of several tenths of a millimeter were observed. No significant differences with respect to size were found for the different packings. Some residual liquid metal is seen between the crystals due to incomplete draining.

The EDAX (Energy Dissipative X-Ray Analysis) method proved that all crystals in the total cold trap consist of pure potassium hydride. The occurrence of KH is suspected due to the higher chemical activity of potassium compared to sodium.

In the following the proposed model for hydrogen removal from cold trapping from NaK is summarized:

A diffusion-dominated crystal growth process is assumed (nucleation phase neglected) with

$$\dot{m} = \rho A k(c - c_{\text{sat}}), \quad (7.3)$$

where  $\rho$  is the liquid metal density,  $A$  ( $\text{m}^2/\text{m}^3$ ) the specific surface available for crystal growth normalized with the cold trap volume  $V$ ,  $k$  is the mass transfer coefficient and  $(c - c_{\text{sat}})$  is the local difference between concentration and saturation concentration.

NaK properties are evaluated for mean cold trap temperatures according to relationships given by [7-13], see Table 7-1. The temperature-dependent saturation concentration is determined according to [7-14], see also Table 7-1.

For the mass transfer coefficient  $k$ , the following relationship was found:

$$\text{Sh} = (0.21\text{Re}^{0.5} + 0.0008 \text{Re})\text{Sc}^{0.4}, \quad (7.4)$$

where the Sherwood, Reynolds and Schmidt numbers are defined by

$$\text{Sh} = kd_w / D, \quad \text{Re} = vd_w / \nu, \quad \text{Sc} = \nu / D,$$

where  $d_w$  is the wire diameter,  $D$  the hydrogen diffusivity in the liquid metal,  $v$  and  $\nu$  are the liquid metal velocity and kinematic viscosity.

Equation (7.4) differs from the correlation given in [7-9] by a factor of 0.4. The diffusivity  $D$  is determined using the Stokes-Einstein relationship and property data [7-14] to

$$D(\text{m}^2/\text{s}) = 6 \cdot 10^{-10} (803 - 0.258 T)^{-1/3} \cdot T \cdot \exp(1 - 3005/T). \quad (7.5)$$

The effective specific surface  $A$  during cold trap loading is expressed as the sum of two terms, the surface of the bare wires and an increase due to the crystals:

$$A(\text{m}^2/\text{m}^3) = \left( (\pi d_w L_w)^2 + 4 \pi f L_w m_{\text{hyd}} / \rho_{\text{hyd}} \right)^{0.5} / V, \quad (7.6)$$

where  $L_w$  is the total wire length of the packings,  $\rho_{\text{hyd}}$  is the hydride density ( $\rho_{\text{hyd}} = 1.1 \text{ g/cm}^3$ ),  $m_{\text{hyd}}$  is the time-dependent locally precipitated hydride mass, and  $f$  is a roughness factor, assumed to be  $f = 100$ .

Equations (7.3 - 7.6) can be combined with 1d or 2d calculations of the velocity, temperature and concentration distributions. As shown in the previous figures, the 1d model proved to be well suited to describe the experiments in the ECT with the annular gap.

#### 7.1.5.2 Rotational Cold Trap (RTC)

The development of the meshless RTC can be considered as a "spin-off" of our work on cold traps and MHD (Chapter 5). As mentioned earlier this type of cold trap is of no prime interest for fusion blanket conditions but for impurity removal from liquid metal loops with high (or undefined) concentration levels; e.g. to be used for impurity removal for the start-up phase.

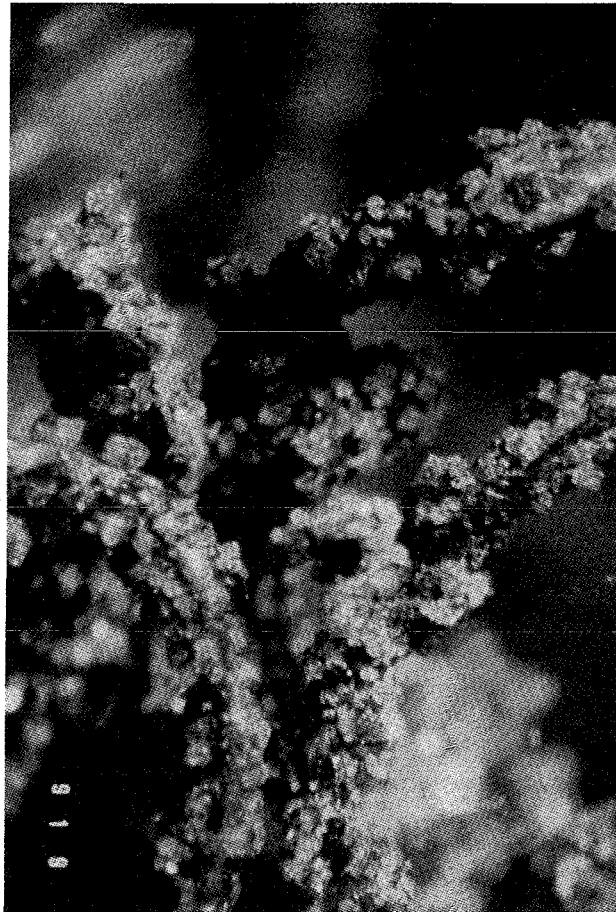


Fig. 7-17 Wire mesh with hydride crystals (optical microscopy)

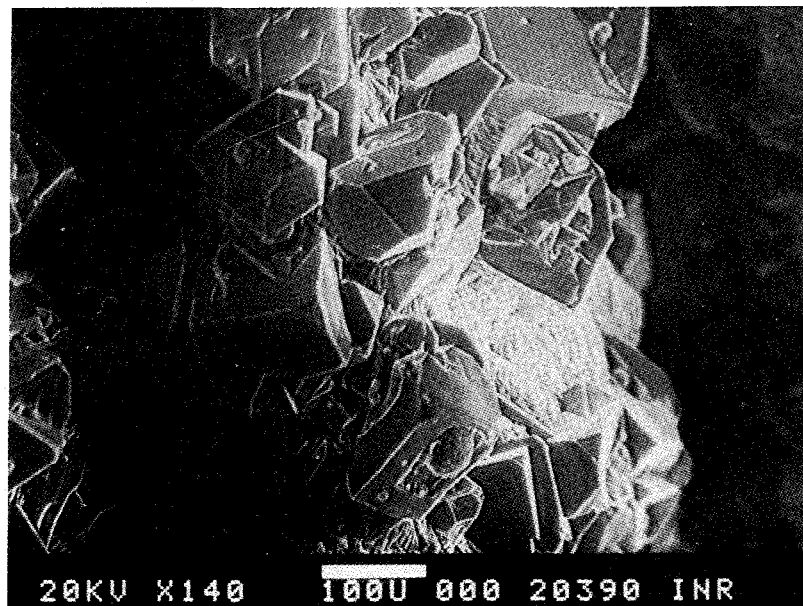


Fig. 7-18 Hydride crystals (scanning electron microscopy)

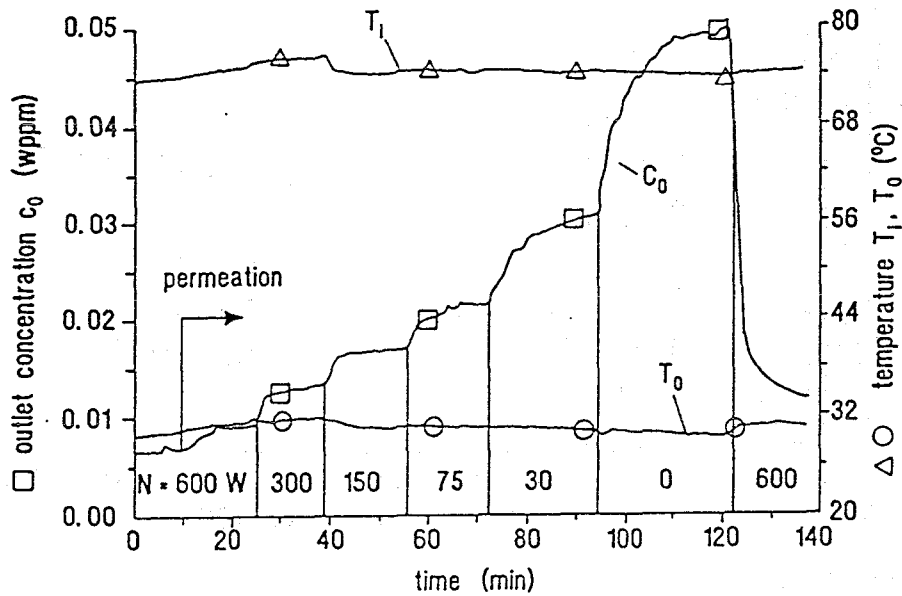


Fig. 7-19 Outlet concentration of rotational cold trap (RCT)

Up to now only a few experiments were performed with the RCT. Figure 7-19 shows a characteristic experiment: Before starting the hydrogen permeation (at about  $t = 0$ ), the loop was operated for about 10 hours with constant inlet and outlet temperatures and with an electrical stator power of about 600 W in order to obtain a concentration close to the saturation concentration  $c_{0sat}$  at the cold trap outlet. About nine minutes after the onset of permeation, the hydrogen front has travelled through the cold trap and a small bypass flow has reached the hydrogen meter. The outlet concentration  $c_0$  increases; however, reaches a fairly constant value after some minutes. Then, the stator power is stepwise reduced down to zero which results in always higher levels of the outlet concentration.

For the case of no flow rotation, the outlet concentration became so large that the hydride started very quickly to plug probably at the cold trap outlet. Therefore, the stator power was again increased to 600 W and nearly instantaneously the outlet concentration dropped close to that value which existed previously.

Figure 7-20 shows the cold trap efficiency for these different stator powers. This curve demonstrates clearly the improvement of mass transfer due to rotation.

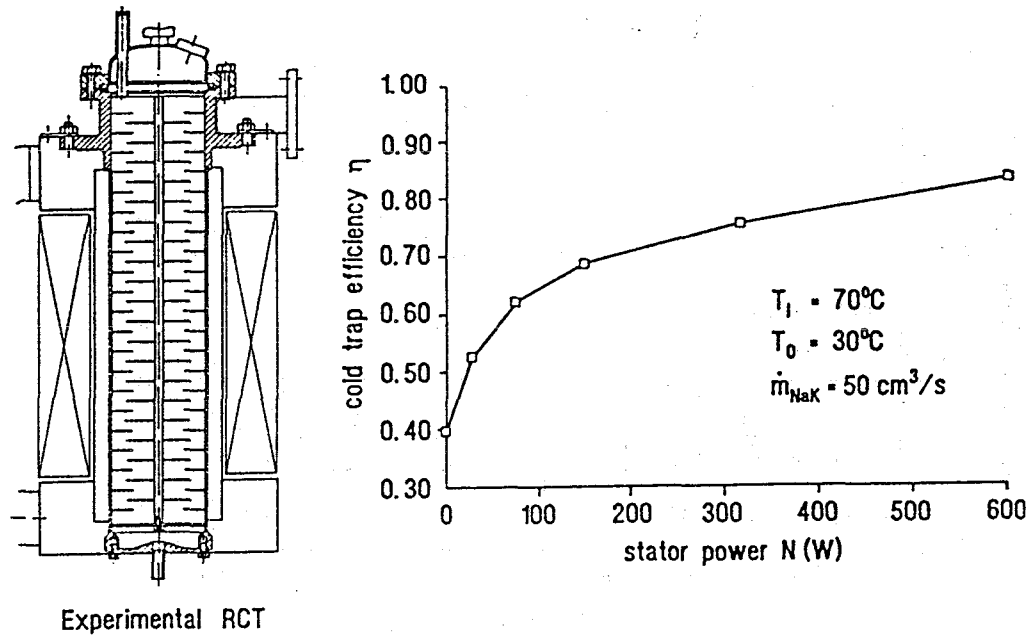


Fig. 7-20 Efficiency of RCT

Some comments should be given on the stator power measured as the product of current and voltage on the primary side of the transformer. This electric power consists of about 95 % of "apparent power". Therefore, only about 5 % of this value are transferred to the liquid metal. If the power is increased from zero to 600 W, a temperature rise and a reduction of the flow rate due to the increased pressure drop can be merely detected. (There is a small influence on the temperature distribution but this is attributed to the changed heat transfer characteristics).

The comparison between the mesh-packed cold traps (MCTs) and the RCT is difficult due to several reasons:

- i) The RCT experiment was performed with loading periods of less than one hour which results in lower efficiencies compared to the results given for the MCTs.
- ii) The results are compared with MCTs using a specific surface of  $A_{\text{spec}} = 1000 \text{ m}^2/\text{m}^3$  which is much higher than the value currently used in MCTs for high capacity. For a more characteristic value of  $A_{\text{spec}} = 300 \text{ m}^2/\text{m}^3$ , the cold trap efficiencies are considerably smaller.

- iii) The fluid rotation is most pronounced in the area covered by the stator, compare Fig. 7-7. In the zone close to the cold trap outlet, the fluid rotation and with this the mass transfer improvement is apparently not very significant. In this zone, the specific surface area of the investigated RCT is small which is unfavourable for achieving high efficiencies. For practical applications it is, therefore, recommended to use a wire mesh packing at the cold trap outlet, as indicated in Fig. 7-4. Then, the largest portion of the hydride would precipitate in the zone which is characterized by large ducts which are insensitive to premature plugging and only a very small hydride mass would precipitate at the cold trap end which would not result in premature plugging.

To summarize, one can conclude that this novel cold trap design is of special interest for impurity removal from liquid metal systems with high concentration levels.

#### 7.1.6 Results for Hydrogen Recovery

As mentioned in Section 7.1.2, hydrogen was recovered either from complete cold traps or from individual wire mesh packings. In the former case the hydrogen loading was quite small (short-time loading experiments) in contrast to the much larger loading of the individual packings.

Hydrogen recovery from the complete ECTs was performed without removing the cold trap from the loop. In the other case the ECTs were transferred to a glove box, dismantled and the individual packings were positioned in the middle of a small vessel, see Fig. 7-21.

Figure 7-22 (from [7-7]) contains a typical time-dependent graph of the hydrogen mass flow rate  $\dot{m}$ , the temperatures of two thermocouples inside the mesh packing and the recovery rate coefficient  $k_{rec}$  assuming a first-order reaction.

$$\dot{m} = -k_{rec} m, \quad (7.7)$$

where  $m$  is the actual hydrogen mass of the hydride crystals

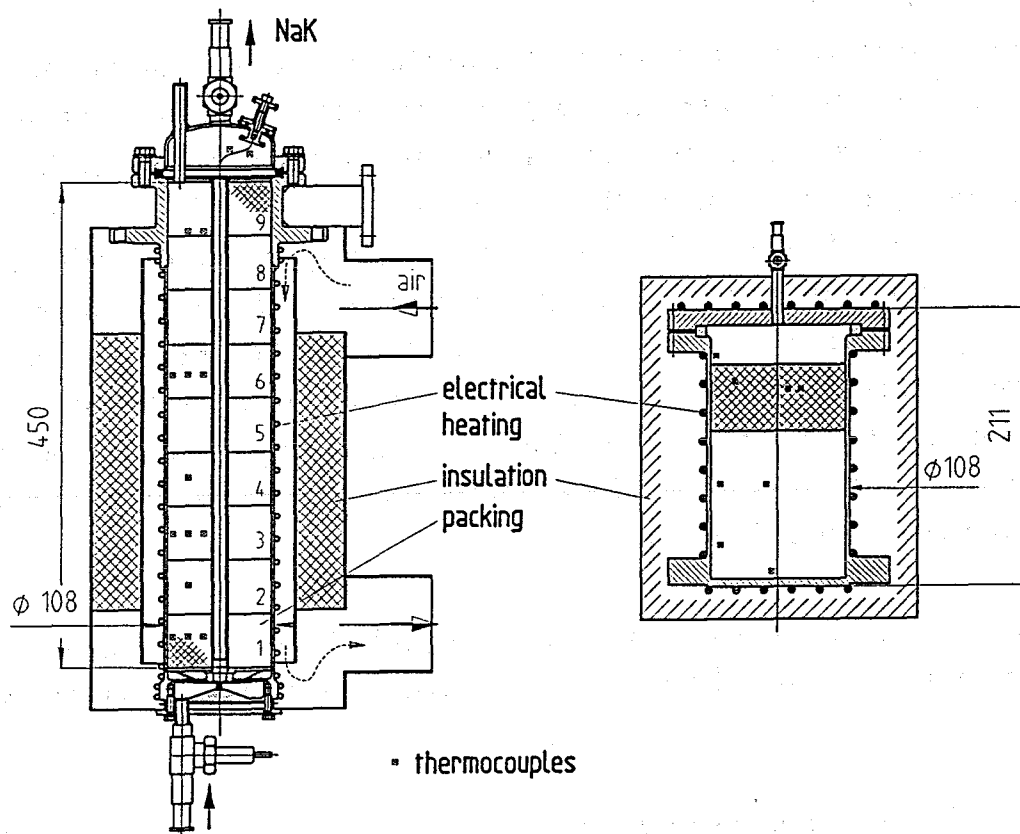


Fig. 7-21 Cold trap and small vessel for hydrogen recovery

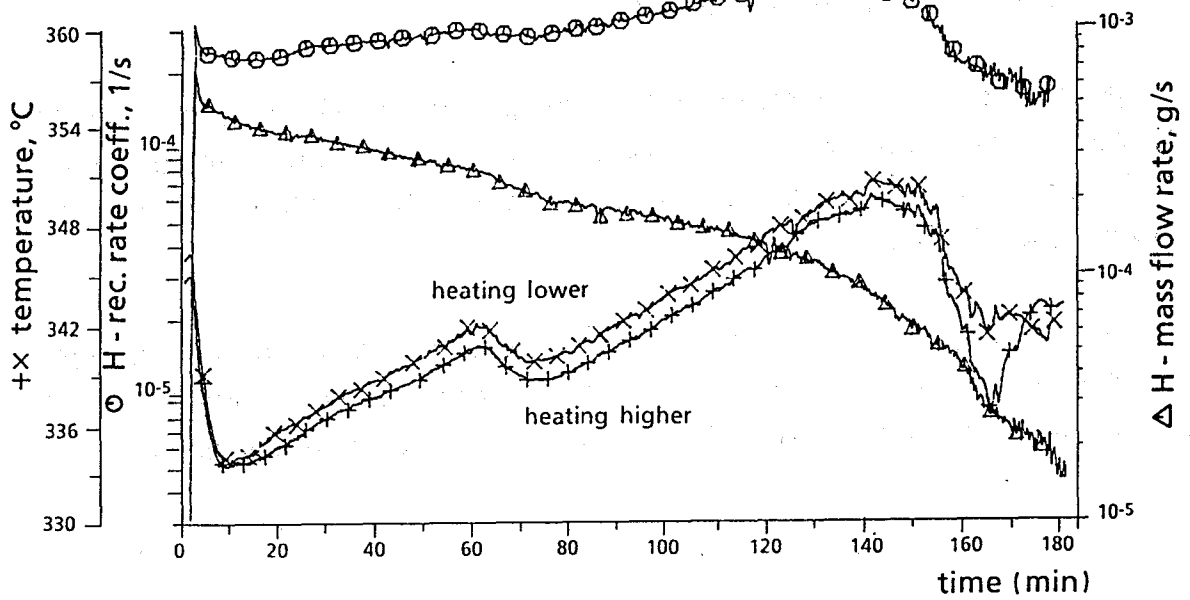


Fig. 7-22 Characteristic hydrogen recovery experiment

In both sets of experiments, the evacuated vessels were heated up uniformly to a given temperature. After opening the valve to the gas collecting system (compare Fig. 7-6) the temperature inside the packing fell due to the endothermic decomposition of KH (60 kJ/mol) and due to the changed heat transfer conditions. This period was followed by a gradual rise in temperature due to the heating at the vessel walls. For about 140 minutes the recovery rate coefficient  $k$  is fairly constant. The slight increase of  $k_{\text{rec}}$  is attributed to the slight increase of temperature.

At the end of the decomposition process (about 140 min. in Fig. 7-22) the mass flow rate starts to decrease strongly (in a semilog plot) and with this, the recovery coefficient  $k$  decreases. This process is accompanied by a characteristic temperature drop which is explained by the fact that for negligible hydrogen generation rates the partial pressure in the vessel becomes so small that heat conduction in the gas to the thermocouples becomes negligible.

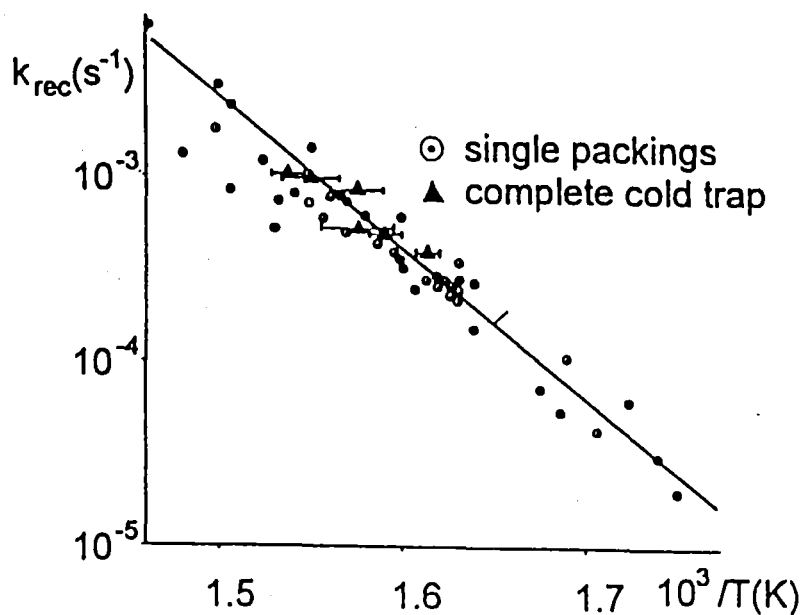


Fig. 7-23 Hydrogen recovery coefficients

Figure 7-23 (from [7-7]) shows the recovery rate coefficient in a plot of  $\log k$  as a function of the inverse temperature. There is no distinct dependence between the experiments with low or high loadings. The results are fitted by the following correlation:

$$\log k_{\text{rec}} (\text{s}^{-1}) = 9.63 - 81.3 / T(\text{K}). \quad (7.8)$$

With these results, 99 % of the hydrogen is released at a temperature of 400 °C in about three hours. For the fusion blanket system this would mean that four regeneration cycles per day would be feasible which results in a quite low tritium inventory in the total blanket system, see Section 7.1.7.

### 7.1.7 Layout of the Tritium Extraction System (TES) for PbLi

The critical design value for the TES is the tritium permeation loss into the steam generators (SG) of 20 Ci/d for the total blanket system. About 75 % of the heating power is transferred by the Pb-17Li SGs, therefore a tritium loss of  $\dot{m}_{\text{T, SG}} = 15 \text{ Ci/d}$  is tolerated for this system.

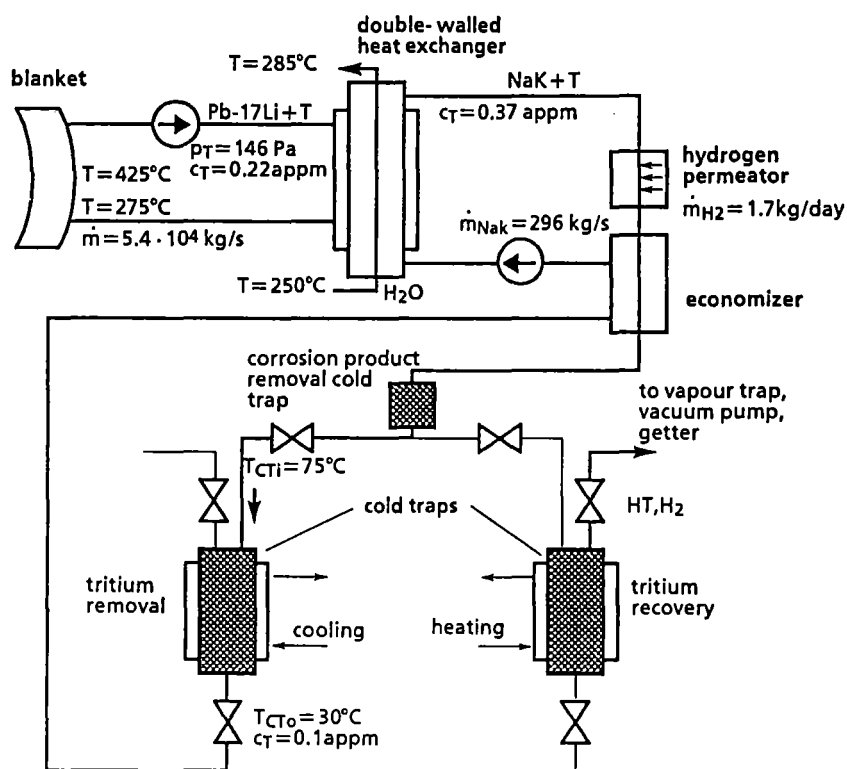


Fig. 7-24 Tritium flow sheet for a DEMO reactor

Figure 7-24 shows the flow sheet and characteristic values for the total reactor with a tritium production rate of  $\dot{m}_{\text{T}} = 400 \text{ g/d}$  and assuming a tritium permeation barrier factor of  $B = 50$  on the steam-water side. This value is supposed to

be reached with an adequate steel pretreatment and water chemistry without requiring additional development efforts.

The required tritium partial pressure  $p_T$  in the NaK is determined by Richardson's Law, modified by including the permeation barrier factor B

$$\dot{m}_{T, \text{loss}} = \phi A p_T^{0.5} / (s \cdot B), \quad (7.9)$$

where  $\dot{m}_{T, \text{loss}}$  is the tolerable tritium loss ( $\dot{m}_{T, \text{loss}} = 2.5 \cdot 10^{-13}$  kg/s corresponding to 15 Ci/d),  $\phi$  is the permeability, A the steam generator (SG) surface, and s the tube thickness.

A ferritic steel is assumed as SG material (whose permeability is characteristically one order of magnitude larger than that for austenitic steels). Since the permeability among ferritic steels is very similar, the data for MANET are taken, see Table 7-1.

Table 7-1: Characteristic properties (Properties related to solubility characteristics defined for tritium. For protium use a factor  $(1/3)^{0.5}$  for permeability and diffusivity and a factor  $(1/3)$  for Sieverts Constant, and sat. concentration)

Quantities	Correlations	Ref.
<u>Na-68K</u>		
density	$\rho \text{ (kg/m}^3\text{)} = 803 - 0.258 T$	[7.13]
dynamic viscosity	$\mu \text{ (kg/ms)} = 8.2 \cdot 10^{-6} \rho^{1/3} \exp(0.979 \rho/T)$	[7.13]
Sieverts constant	$K \text{ (w.fr./Pa}^{0.5}\text{)} = 1.29 \cdot 10^{-6} \exp(576/T)$	[7.14]
diffusivity	$D \text{ (m}^2\text{/s)} = 3.81 \cdot 10^{-15} T/\mu$	[7.14]
saturation concentration	$c_{\text{sat}} \text{ (w.fr.)} = 10.4 \exp(-6286/T)$	[7.14]
<u>MANET</u>		
Sieverts constant	$K \text{ (w.fr./Pa}^{0.5}\text{)} = 3.13 \cdot 10^{-7} \exp(-3562/T)$	[7.15]
permeability	$\phi \text{ (kg/(smPa}^{0.5}\text{))} = 1.01 \cdot 10^{-10} \exp(-5184/T)$	[7.15]
<u>Pb-17Li</u>		
Sieverts constant	$K \text{ (w.fr./Pa}^{0.5}\text{)} = 4.02 \cdot 10^{-10} \exp(-162.4/T)$	[7.16]
diffusivity	$D \text{ (m}^2\text{/s)} = 4.03 \cdot 10^{-8} \exp(-2346/T)$	[7.16]
density	$\rho \text{ (kg/m}^3\text{)} = 1.06 \cdot 10^4 (1 - 1.22 \cdot 10^{-4} T)$	[7.17]
kinematic viscosity	$\nu \text{ (m}^2\text{/s)} = 1.9 \cdot 10^{-8} \exp(1406/T)$	[7.17]

A total SG surface of A about 20.000 m<sup>2</sup> is obtained for the water and PbLi inlet and outlet temperatures shown in Fig. 7-24 and a feed water temperature of T<sub>FW</sub> = 150 °C.

Combining the temperature distribution in the SG (taken from heat transfer calculations) with the temperature dependent permeability of the SG material (Table 7-1), the mean tritium partial pressure in the NaK filled gap of the SG becomes  $p_{T,SG} = 4.57 \cdot 10^{-6}$  Pa. With Sieverts Law

$$c_{T,SG} = K_{NaK} p_{T,SG}^{0.5} \quad (7.10)$$

and evaluating the Sieverts constant  $K_{NaK}$  (Table 7-1) for a mean NaK temperature of 663 K, the mean concentration becomes  $c_{T,SG} = 7.35 \cdot 10^{-8}$  at fr.

The cold trap inlet and outlet concentrations are related by

$$c_{T,SG} = 0.5 (c_{Ti} + c_{To}) \quad (7.11)$$

$$\dot{m}_T = \dot{m}_{NaK} (c_{Ti} - c_{To}) \quad (7.12)$$

where  $\dot{m}_{NaK}$  is the NaK mass flow rate to the cold trap.

If tritium is the only hydrogen isotope in the system, the resulting concentrations are so low that no efficient cold trap operation is expected. In order to shift the hydrogen concentration into a range which has been experimentally verified protium is purposely added (method of isotope swamping). The basic idea of this method is that hydrogen removal by cold trapping is equal for each hydrogen isotope. Isotope swamping, therefore, requires a subsequent isotope separation process. The isotope separation column of the fuel clean-up system could be used.

In order to use experimentally verified data the following values are assumed: cold trap inlet and outlet temperatures  $T_{CTi} = 75^\circ\text{C}$  and  $T_{CTo} = 30^\circ\text{C}$  and a cold trap efficiency of  $\eta_{CT} = 0.80$ . With these values the following hydrogen concentrations are calculated:  $c_{CTi} = c_{sat} = 1.673 \cdot 10^{-6}$  at fr,  $c_{CTo} = 5.26 \cdot 10^{-6}$  at fr.

The mean concentration is then  $c = 1.05 \cdot 10^{-6}$  at fr. which is higher by a factor of about 14 than the mean tritium concentration. This means that about 13 mol hydrogen per mol tritium must be added, a value which is very small compared to values of 100 or 500 proposed for tritium removal from ceramic breeders [7-19].

The required NaK mass flow rate to the processing units then becomes

$$\dot{m}_{\text{NaK}} = 14.2 \cdot \dot{m}_{\text{T}} / (c_{\text{Ti}} - c_{\text{CTO}}) = 8787 \text{ mol/s} = 296 \text{ kg/s} \quad (7.13)$$

For a NaK velocity in the cold trap of  $v = 3 \text{ cm/s}$  and a specific wire mesh surface of  $1000 \text{ m}^2/\text{m}^3$  a total cold trap volume of  $13.86 \text{ m}^3$  for a height of  $1 \text{ m}$  is obtained.

For 4 parallel loops for the inboard segments (140 MW each) and 6 loops for the outboard segments (280 MW each) 2 cold traps with a diameter of  $0.8 \text{ m}$  are required in each inboard loop and 3 cold traps in each outboard loop. Due to the batchwise operation twice the number of cold traps is required for tritium removal and recovery.

The total cold trap volume appears to be quite favourable although significant conservative assumptions were made.

An important feature of the proposed system is that no corrosion or radioactive products from the Pb-Li loop are transported into the tritium extraction system. The only impurities in the NaK-system are corrosion products generated in the steam generator. These corrosion products are precipitated in a special cold trap upstream of the hydrogen cold trap operated at a temperature somewhat above the hydrogen saturation concentration.

No additional carrier fluid is required for tritium processing, therefore, only small volume flow rates have to be processed and a small number of process components is required. The separation of tritium from protium can be carried out in the hydrogen separation column of the fuel clean-up system.

The clean-up system in the helium coolant loop for tritium permeating from the plasma and Pb-17Li into the helium has not been considered in detail because tritium separation from helium is investigated in detail for helium-cooled ceramic breeder blankets.

An important feature of the blanket is the tritium inventory and most important the tritium inventory in the large Pb-17Li system. In order to determine the tritium concentration in the Pb-17Li both the concentration differences required for permeation and diffusion through boundary layers in the liquid metal are considered.

Figure 7-25 shows schematically the concentration distribution, for simplicity the quantities in the Pb-17 Li system, the structural material, and the NaK system are characterized by the indices 1, W, 2.

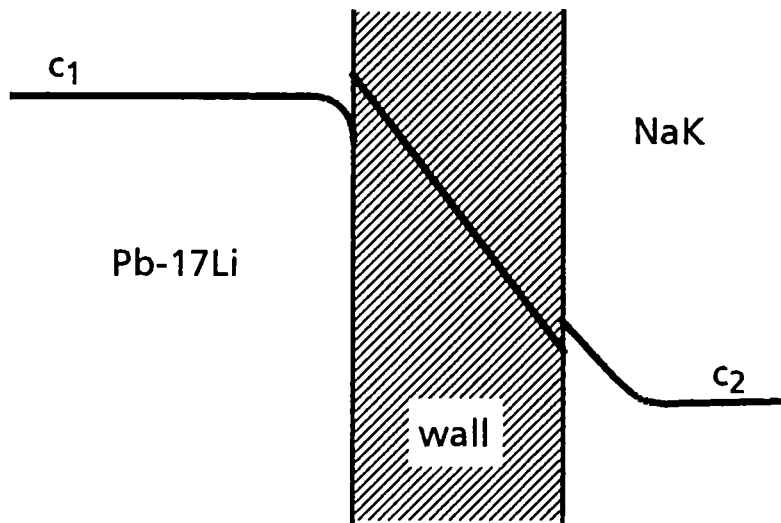


Fig. 7-25 Concentration distribution

For the tritium transport from the bulk of the Pb-17Li into the bulk of the NaK holds (assuming no permeation impediment at the interfaces):

$$\dot{m}_T = \rho_1 h_1 A(c_1 - c_{1W}) = \frac{\phi A}{s}(c_{W1} - c_{W2}) = \rho_2 h_2 A(c_{2W} - c_2), \quad (7.14)$$

where  $h_1$  and  $h_2$  are the mass transfer coefficients in the liquid metals.

With equal chemical activity at the boundaries

$$\frac{c_{1W}}{K_1} = \frac{c_{W1}}{K_W}, \quad \frac{c_{W2}}{K_W} = \frac{c_{2W}}{K_2}, \quad (7.15)$$

finally follows

$$\dot{m}_T = A \left( \frac{s}{\phi} + \frac{1}{\rho_1 K_1 h_1} = \frac{1}{\rho_2 K_2 h_2} \right)^{-1} \cdot \left( \frac{c_1}{K_1} - \frac{c_2}{K_2} \right) \quad (7.16)$$

The mass transfer coefficients are determined with a Sherwood number correlation valid for turbulent flow:

$$Sh = 0.923 Re^{0.8} Sc^{0.33} = h D_p/D \quad (7.17)$$

where the Reynolds number is defined with the hydraulic pipe diameter  $D_p$

Using properties (see Table 7-1) at  $T = 663$  K which is the mean permeation temperature, the following values are obtained

$$\dot{m}_T = A (4.9 \cdot 10^{10} + 0.653 \cdot 10^{10} + 0.003 \cdot 10^{10})^{-1} (\rho_{PbLi}^{0.5} - \rho_{NaK}^{0.5}) \quad (7.18)$$

It is seen that the diffusion through the PbLi boundary layer contributes about 13 % to the total mass transfer resistance whereas the mass transfer resistance in the NaK is negligible.

For  $\dot{m}_T = 400$  g/d and  $A = 2 \cdot 10^4$  m<sup>2</sup> the partial pressure in the PbLi becomes  $p_T = 146.7$  Pa. For a total PbLi mass of  $1.53 \cdot 10^7$  kg and assuming that one half is at the blanket inlet temperature and the rest at the outlet temperature, the total tritium inventory in the PbLi becomes  $\dot{m}_{T,PbLi} = 57.2$  g. The total tritium inventory in the NaK ( $m_{NaK} = 4.1 \cdot 10^4$  kg) is about 0.38 g and in the steel (blanket, piping, SG:  $\dot{m}_{steel} = 3.6 \cdot 10^6$  kg) is about 12 g.

The inboard liquid metal loops are connected for reasons of redundancy as well as 3 outboard loops. Therefore, three totally independent loop systems exist with about one third of the inventory each (this should not imply that in case of a coolant accident one third of the Pb-Li can flow out). Concerning the NaK system and cold trap each SG has an independent system, therefore, the maximum tritium inventory (occurring in an outboard SG) is about 0.04 g in the NaK and 15 g in the cold traps.

## 7.2 Tritium Extraction from Pb-17Li with Solid Getters

The use of a solid getter metal in direct contact with the eutectic Pb-17Li is an alternative method for tritium extraction. This method could be more advantageous than the reference method if the tritium partial pressure in the PbLi could be maintained at such a low level that no additional intermediate NaK system (and with this a double-walled steam generator) would be required.

Four main requirements have to be satisfied for using getter metals for tritium extraction from Pb-17Li:

1. The metal must be stable in the eutectic for a long time.
2. The Sieverts constant for the metal must be much higher than that of Pb-17Li.
3. The rate of tritium uptake must be high enough.
4. Easy tritium recovery must be possible.

These items were investigated in an experimental program [7-19 through 7-22].

### **7.2.1 Possible getter materials**

Compatibility tests are described in Chapter 8.2 of this report. It is not possible to use typical hydrogen getter metals as Y, U, Ti, Zr, or alloys of these metals. All of them react with lead from the eutectic. The metals get dissolved or destroyed. However, vanadium was found very stable up to high temperatures. The Sieverts constant of V is four to five orders of magnitude higher than those of Pb-17Li, see Fig. 7-3. Therefore, vanadium was investigated in detail and proposed as a possible getter for tritium [7-20].

### **7.2.2 Experiments**

To study the behavior of hydrogen in Pb-17Li systems and the possibility of its extraction, mainly thermal convection loops (TCL) were used. The results were verified in the TRITEX facility [7-23], originally built for these investigations, see Chapter 8.3. TCLs proved to be more flexible. Most of the experiments were done with deuterium. Because of a hydrogen (protium) background, also hydrogen was investigated. Furthermore, results were obtained with tracer amounts of tritium. In this Section, "hydrogen" means always deuterium, if not otherwise stated.

Table 7-2 lists the main parameter of TCL-4; Fig. 7-26 shows the loop.

Table 7-2: Main parameters of thermal convection loop TCL-4

Structure material	austenitic steel 1.4571
Main pipe inner diameter	10 mm
Covergas	Ar-6.0 (in special experiments He, Ne, Kr, Xe)
Total inventory of Pb-17Li	5.5 kg
Circulating Pb-17Li	4.6 kg
Total wetted surface	800 cm <sup>2</sup>
Temperature	280°C to 700°C
Flow rate at a temperature gradient of 150°C	0.24 l/min
Surface of permeation membran	100 cm <sup>2</sup>
sweep gas	Ar-6.0

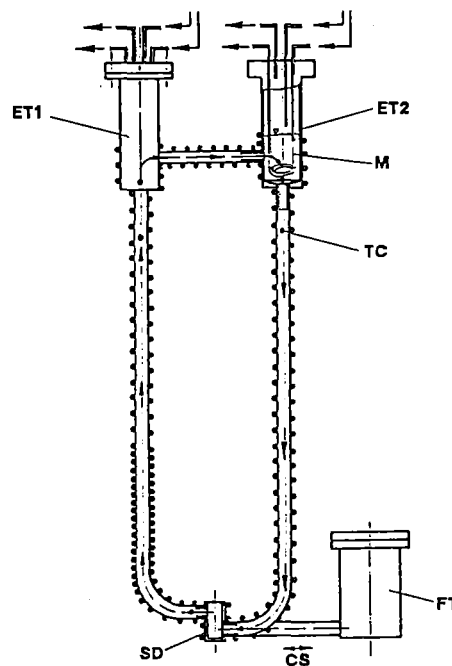


Fig. 7-26: Thermal convection loop 4. ET = expansion volumes. M = permeation membranes, TC = thermo couples, FT = filling tank, CS = area of the cold spot, SD = special device for measurements of the flow rate.

Permeation membranes from pure iron with 0.3 mm wall were installed in two expansion volumes. The following effects were studied:

- Dissolution of hydrogen from a gas phase through the gas-liquid interface in flowing Pb-17Li.
- The reverse effect, desorption of hydrogen into the gas phase.
- Permeation of hydrogen through an iron membrane into the liquid metal.
- The reverse effect, desorption through a membrane.
- Transport of hydrogen circulating in a loop system.
- Extraction of hydrogen by inserting a sample of getter metal in one expansion volume.
- Recovery of hydrogen from the getter metal.
- Behaviour of He, Ne, Ar, Kr and Xe.

Measurement of the hydrogen dissolution and desorption characteristics were performed between 280 and 700 °C. Deuterium partial pressures ranged from 0.05 to 1000 mbar. With the Sieverts constants from ref. [7-24], the equilibrium partial pressures for degassing correspond to 0.05 to 0.9 appm in Pb-17Li, values which are discussed for Pb-17Li blankets.

### 7.2.3 Results

Sieverts law was verified over the whole investigated pressure range. All dissolution, desorption and permeation rates were proportional to the square root of the partial pressure [7-22]. Fig. 7-27 shows the rate of hydrogen uptake by the vanadium getter. It is not much different from the transport through the gas-liquid interface. This was also found for the iron membranes. This rate is given by

$$\ln(R) = -14.0 - 2167/T$$

R in (mol D<sub>2</sub>/m<sup>2</sup> · s · mbar<sup>0.5</sup>).

Clearly, the rate determining step was diffusion in a liquid metal boundary layer at the getter surface. Diffusion in vanadium was faster than in this layer, certainly because concentrations in vanadium were far away from saturation.

These results show, that tritium can be removed from Pb-17Li by gettering with vanadium at blanket temperatures and that low partial pressures (concentrations) can be reached.

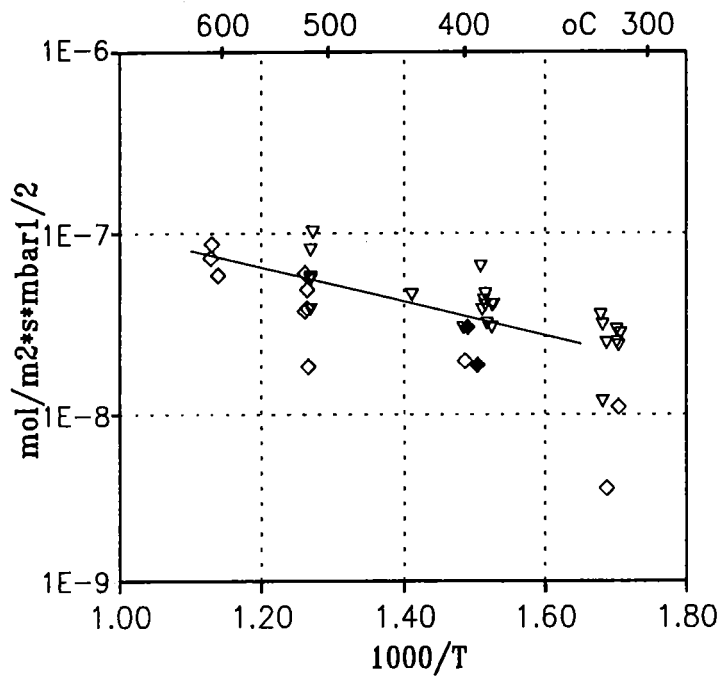


Fig. 7-27: Uptake of deuterium by vanadium getter from Pb-17Li.

After removing the sample from the loop ("drain"), recovery of tritium (hydrogen) was done by heating the metal in flowing argon. An typical experiment is shown in Fig. 7-28.

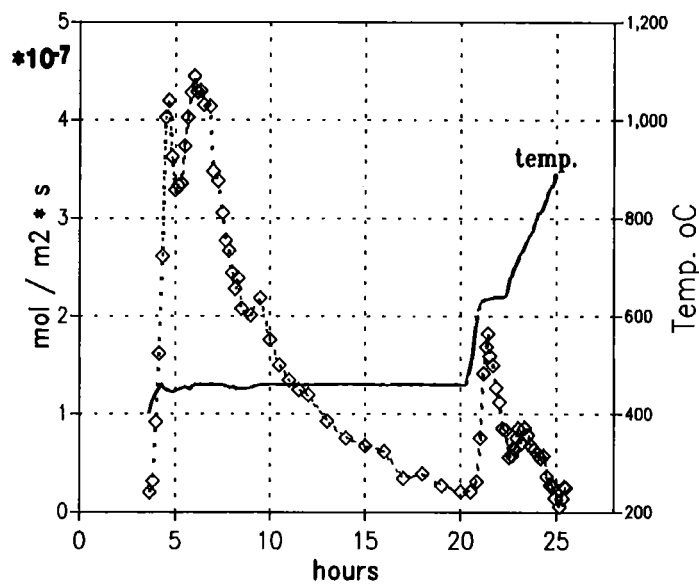


Fig. 7-28: Recovery of deuterium from a vanadium foil with flowing Ar-6.0. The foil in this experiment was loaded in Pb-17Li for 76 hours at 315°C

Recovery can be done at the same temperature as loading; however, higher temperatures are more favourable. Within 10 hours, more than 90% of the dissolved hydrogen is released at 460°C.

#### **7.2.4 Other observations**

Getter metals for hydrogen are usually also getters for nonmetallic impurities. However, the solubilities of oxygen and nitrogen in the eutectic are extremely low [7-25]. Vanadium samples, exposed to flowing Pb-17Li in TRITEX for more than 5000 hours at 450°C showed neither a corrosion effect nor substantial up-take of impurities.

There was no delay when inserting vanadium into the liquid metal [7-20]. That means the metal needed no activation process.

Always at the end of operation of a TCL, the liquid metal in the expansion volumes was oxidized by air. This oxidation had no influence on hydrogen transport or gettering.

Helium is formed in a blanket with the same rate as tritium. It is not removed by a getter metal and will be transported to cover gas areas. We found helium solubilities about 5 orders of magnitude lower than for hydrogen [7-22]. That means, formation of gas bubbles has to be considered. These bubbles may transport some tritium to the cover gas. In some experiments, such an effect was observed (e.g. [7-26]). This effects needs to be investigated, but is expected to be of minor importance for the blanket with its low tritium concentration.

Helium is formed also by decay of tritium. It will accumulate in the getter metal. Assuming an average of 1000 appm tritium in vanadium, about 100 appm He will be formed during a blanket lifetime. This concentration is low enough to avoid embrittlement.

#### **7.2.5 Evaluation of the getter process**

An evaluation of the use of vanadium getters for tritium extraction from self-cooled blankets was performed [7-21]. The process was compared to the reference technique described in Section 7.1. It was found that for very high values of the permeation factors (e.g.  $B = 5000$ ) on the steam generator surface the getter

technique alone will be sufficient for tritium extraction. For low values ( $B \approx 50$ ) the required vanadium volumes would be too large for practical use. However, a combined method, consisting of gettering in PbLi and cold trapping in NaK, could be attractive for low values of B because it could result in low tritium inventories and small dimensions of the extraction components.

### 7.2.6 Summary

The use of solid getter metals for tritium extraction from Pb-17Li was investigated as an alternative technique to a separate NaK circuit. Vanadium can be used as the getter metal. It is stable in Pb-17Li and allows tritium extraction to the required low concentrations. An efficient recovery of tritium from vanadium can be performed at moderate temperatures.

For tritium extraction from the Pb-17Li of the Dual Coolant Blanket the combined process V getters in Pb-17Li and cold trapping in NaK exhibits several advantages and should be studied in more detail. The use of the proposed gettering technique could be also very promising for the Water-cooled Blanket.

## References

- [7-1] J. Reimann and S. Malang, A study of tritium separation from LiPb by permeation into Na or NaK and cold trapping, Kernforschungszentrum Karlsruhe, KfK-4105 (Oct. 1986).
- [7-2] H. John, S. Malang, H. Sebening (ed.), Status report, KfK contribution to the development of DEMO-relevant test blankets for NET/ITER, Part 1: Self-cooled liquid metal breeder, Vol. 2: Detailed version, KfK 4908 (Dec. 1991).
- [7-3] C. McPheeters and D. Raue, Cold trap modeling experiments and NaH precipitation, BNES, London (1984).
- [7-4] C. Saint-Martin et al., Mechanisms and kinetics of crystallization of sodium hydride in cold traps, Forth Int. Conf. Liquid Metal Eng. and Techn., Avignon, France, Oct. 17-21, Vol. 3 (1988), 617/1-10.
- [7-5] Eichelberger, Testing of a meshless cold trap for hydrogen removal from sodium, Sec. Int. Conf. Liquid Metal Techn. in Energy Production, Richland, USA, CONF-800401-A2(1980),20/33-20/38.
- [7-6] J. Reimann et al., Hydrogen removal from NaK with mesh-packed and meshless cold traps, Proc. Liquid Metal Systems, March 16-18, 1993, Karlsruhe.
- [7-7] J. Reimann, R. Kirchner, and D. Rackel, Tritium recovery from NaK cold traps. Investigation of hydrogen release kinetics, Fusion Engineering and Design 18(1991), pp. 67-72.
- [7-8] L. Bühler and J. Reimann, Mass transfer at mixed convection in vertical cylinders, VII Symp. Heat & Mass Transfer, Jadwison, Poland, Oct. 23-26 (1989), 57-69.
- [7-9] H. Brauer, Stoffaustausch einschließlich chemischer Reaktionen, Verlag Sauerländer, Hanau und Frankfurt (Main) (1971), p. 343.
- [7-10] J. Reimann, R. Kirchner, M. Pfeff, and D. Rackel, Tritium removal from NaK cold traps: First results on hydride precipitation kinetics, Fusion Technology, Vol. 21, March (1992), pp. 872-877.
- [7-11] C. Saint-Martin, C. Latge, P. Michaille, and C. Laguerie, Etude experimentale de la cristallisation de l'hydrure de sodium dans un piege froid garni, Journ. of Nucl. Mat. 151(1988)112-119.
- [7-12] J. Reimann, R. Kirchner, M. Pfeff and D. Rackel, Tritium removal technique for a self-cooled Pb-17Li blanket, 18th Symp. Fusion Technology, SOFT, Karlsruhe, 22-26 Aug. (1994).
- [7-13] H. Bomelburg, C. Smith, Chapter 1: Physical properties, Sodium-NaK Engineering Handbook, Vol. 1, Ed. O.J. Foust, Gordon and Breach (1972), pp. 1-107.
- [7-14] P. Hubberstey, Solutions of hydrogen in alkali metals, in: Handbook of thermodynamic and transport properties of alkali metals, ed. R.W. Ohse (Blackwell Scientific Publications, 1984).
- [7-15] K. S. Forcey et al., Hydrogen transport and solubility in 316L and 1.4914 steels for fusion reactor applications, J. Nucl. Mater. 160 (1988) pp. 117-124.
- [7-16] F. Reiter, J. Camposilvan, G. Gervasini and R. Rota, Interaction of hydrogen isotopes with the liquid eutectic alloy 17Li83Pb, Proc. 14th SOFT, Avignon (1986), pp. 1185-1190.

- [7-17] B. Schulz, Thermophysikalische Eigenschaftsmessungen am  $\text{Li}_{17}\text{Pb}_{83}$  Eutektikum, Ergebnisbericht über Forschungs- und Entwicklungsarbeiten 1984 des Projektes Kernfusion, KfK 3879, Februar 1985.
- [7-18] M. Dalle Donne (Ed), European DEMO BOT Solid Breeder Blanket, KfK 5429, November 1994.
- [7-19] H. Feuerstein, H. Gräbner, S. Horn and J. Oschinski, Transport of Deuterium and Rare Gases by Flowing Molten Pb-17Li, J. of Nucl. Materials 179-181 (1991) 882-885.
- [7-20] H. Feuerstein, H. Gräbner and S. Horn, Extraction of Tritium from Molten Pb-17Li by Use of Solid Getters, Fusion Technology 1990, 646-649.
- [7-21] J. Reimann and H. Feuerstein, Gettering and/or Cold Trapping for Tritium from a Self Cooled Pb-17Li Blanket, Fusion Technology 1990, 752-756.
- [7-22] H. Feuerstein, H. Gräbner, S. Horn and J. Oschinski, Behavior of Deuterium and Rare Gases in Thermal Convection Loops with Molten Pb-17Li, Fusion Engineering and Design 14 (1991) 261-271.
- [7-23] H. Feuerstein, H. Gräbner and G. Kieser, TRITEX, a Forced Convection Loop with Pb-17Li, J. Nucl. Mater. 155-157 (1988) 520-523.
- [7-24] F. Reiter, Solubility and Diffusivity of Hydrogen Isotopes in Liquid Pb-17Li Fusion Engineering and Design (1991) 207-211.
- [7-25] H.U. Borgstedt, Chemische Eigenschaften des flüssigen Blanketstoffs Pb-17Li, KfK4620, 1989.
- [7-26] V.G. Vasilyev, Tritium Release from Neutron Irradiated  $\text{Li}_7\text{P}_2$  and  $\text{Li}_{17}\text{Pb}_{83}$  Proc. 14th SOFT Conf. Avignon, September 8-12, 1986, p. 1505-1509.



## 8. Pb-17Li Physical Chemistry

The eutectic Pb-17Li is a unique alloy system proposed specifically for fusion applications. Many of its properties were poorly known when the concept was proposed, leading to speculations of several serious issues involving corrosion of the structural alloy, transport of corrosion and activation products, impurity control, and segregation and replenishment of the eutectic. These issues all have been addressed through a program of analysis and experiments described below.

Corrosion experiments indicate that Pb-17Li is compatible with MANET up to  $\approx 470^\circ\text{C}$ . The primary corrosion mechanism is dissolution rather than internal depletion of constituents; the bulk properties of the structural material appears insensitive to the presence of the molten alloy. With insulating layers between the steel and Pb-17Li, the corrosion rate was drastically reduced below the limit of detection.

In experiments, most of the corrosion products were transported by buoyancy to become crusts at the cover gas interface, indicating a promising technique for impurity removal. Many of the remaining corrosion products were trapped by the electromagnetic pump rather than the cold trap.

Some of the more exciting new results involve the chemistry of Po and Bi. Po is a highly radio toxic isotope ( $\alpha$ -emitter) produced by neutron adsorption in Bi. Bi is a normal impurity in Pb, and is also produced by neutron capture in Pb. New experimental evidence suggests that Po forms the compound PbPo, which has an evaporation rate orders of magnitude lower than pure Po, thereby dramatically reducing its potential release rate. Bi is found to form the compound  $\text{Li}_3\text{Bi}$ , which can be cold trapped. This, together with observations of Bi transporting to cover gas interfaces (as with corrosion products) suggests that low impurity levels (below 10 wppm) may be obtained in the coolant.

Finally, observations of both thermal gradient and gravitational segregation have been made. Using cold traps, thermal gradient segregation can be used for effective self-adjustment of the Li concentration in the eutectic. An effective technique for Li replenishment due to burnup was demonstrated by dissolving  $\text{Li}_3\text{Pb}$  in the eutectic.

## 8.1 Corrosion of the Structural Material in Flowing Pb-17Li

Corrosion tests of MANET steel in liquid Pb-17Li alloy have been performed for long periods of time (several thousand hours) in the pumped loop PICOLO, the hot leg of which was constructed of ferritic steel [8-1]. Cylindrical bars of MANET steel were exposed in the flowing eutectic melt at 450 to 550°C. The flow velocity at the surfaces of specimens was 0.3 m/s ( $Re = 21000$ ), thus, turbulent flow conditions were maintained. The lowest temperature in the loop was 310°C. A magnetic trap was installed in the region of lowest temperatures. Magnetic corrosion products were precipitated in the cooling device and collected within the magnetic trap. The appearance of the deposited crystals indicated, that crystal growth may also contribute to the corrosion product collection in this trapping device. The corrosion tests were interrupted for determinations of material losses; kinetic data were gained in this way. The MANET specimens were examined by means of metallographic and chemical methods.

The evaluation of long-term corrosion tests of MANET steel in flowing liquid Pb-17Li eutectic alloy at 450 to 550°C in the PICOLO loop showed that the material did not suffer internal corrosion effects as the formation of element depleted zones. Mass losses of MANET steel due to corrosion in flowing Pb-17Li eutectic at 550°C were comparable to mass losses of 316L(N) steel at 500°C. However, contrary to the uniform dissolution of martensitic steel, a highly porous layer is formed on austenitic steels in addition to the material loss. The corrosion was temporarily reduced during the initial period of contact with the liquid alloy [8-2]. The results of corrosion tests indicate that the reduced corrosion during the initial period of up to 2500 h might be related to the removal of the passivation layers of the steel.

These material losses were analysed on the basis of a hydraulic model of dissolution and diffusion processes in the turbulent flowing liquid metal. The results showed that the corrosion in flowing Pb-17Li is due to a material dissolution mechanism [8-3]. The material losses under the conditions in the PICOLO facility are shown in Fig. 8.1-1.

The corrosion  $dr$  as loss of wall thickness can be expressed by the equation valid for the parameters in the test section, i.e. turbulent flow of the liquid alloy at 30 cm/s:

$$\log dr = 13.28 - 10960/T$$

where  $dr$  is the corrosion rate expressed in mm/a and  $T$  is in Kelvins. This equation results in conservative values of the material losses, since it is valid for a downstream position near zero, the position of highest material losses. The annual material loss at 450°C and a flow velocity of 0.3 m/s is in the order of a layer of 13  $\mu\text{m}$  thickness as calculated from the equation. The mass losses are not proportional to the flow velocity; in turbulent flow without magnetic field they depend on the Reynolds number at less than linearity.

The influence of typical parameters of the fusion reactor blanket, the strong magnetic field and the irradiation with high energy neutrons has to be considered. Since the magnetic field may suppress the turbulence of the flow of the liquid alloy, corrosion may be less than in the experimental facility. Irradiation may enhance the diffusion rates in the solid material, faster diffusion may lead to higher corrosion rates. However, the system MANET steel/liquid alloy is not characterized by solid state diffusion, the corrosion is mainly a process of the solid/liquid interface. It can, therefore, be expected that the irradiation does not significantly increase the liquid metal corrosion of MANET steel. The irradiation causes the formation of activation products, thus the liquid alloy dissolves certain amounts of activated material which may be precipitated in peripheral parts of the cooling system.

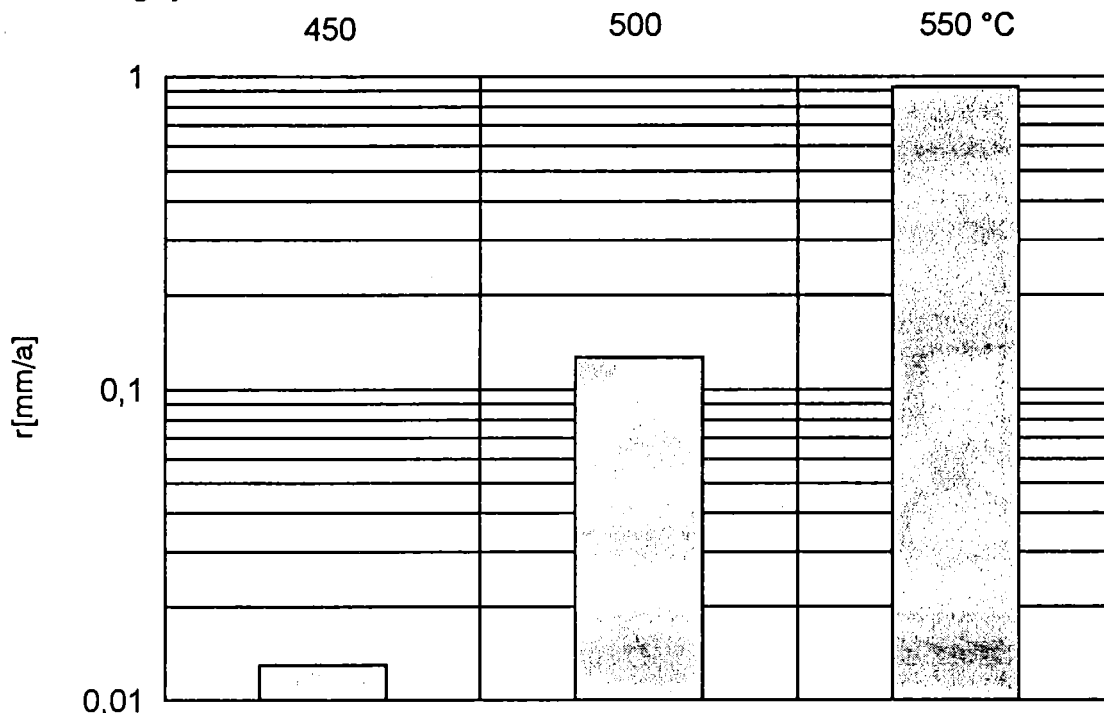


Fig. 8.1-1 Material loss of MANET steel in the test section of PICOLO as a function of reciprocal temperature

The creep-rupture properties of MANET steel at temperatures up to 600°C were not influenced by the presence of the eutectic Pb-17Li alloy [8-4]. The bulk properties of the martensitic steel are not sensitive to the action of the molten alloy. However, the material loss due to corrosion has an influence on the creep data and must be considered in the design rules.

The compatibility of MANET steel with the liquid alloy does not reduce the functionality, feasibility and reliability of blanket components which are in contact with the flowing liquid alloy.

The necessity to coat the steel with an insulating surface layer reduces further the corrosion problem in the self-cooled liquid metal blanket. Since such a coating has a protective effect against liquid metal corrosion, the corrosion rate was drastically reduced to below the detection limit [8-5]. The coating provides such a protection just at positions with most severe conditions, i.e. the highest temperature and the highest flow velocity.

## **8.2 Compatibility of metals and alloys in static Pb-17Li**

Typical corrosion experiments are done usually with more or less complicated loop systems. With these, the number of tests is limited. Also, corrosion rates may be influenced by a usually very large surface of the facility compared to small sample surfaces. Static tests were used, therefore, to determine relative compatibilities for metals and alloys over a wide range of conditions. From the tests, also solubilities, and in some cases diffusion coefficients could be obtained.

More than 300 tests were performed for 25 metals and alloys. The temperature range was from 300 to 700°C and exposure time up to 6000 hours. The results were published recently [8-6].

Fig. 8.2-1 shows the inner part of a capsule. Up to 6 crucibles with different samples in Pb-17Li were heated together under argon. After the exposure time the whole eutectic was dissolved by a special extraction technique in nitric acid, and the solution analyzed. Metal samples were investigated by metallography, and in some cases by SEM and microprobe. The results can be summarized as follows.

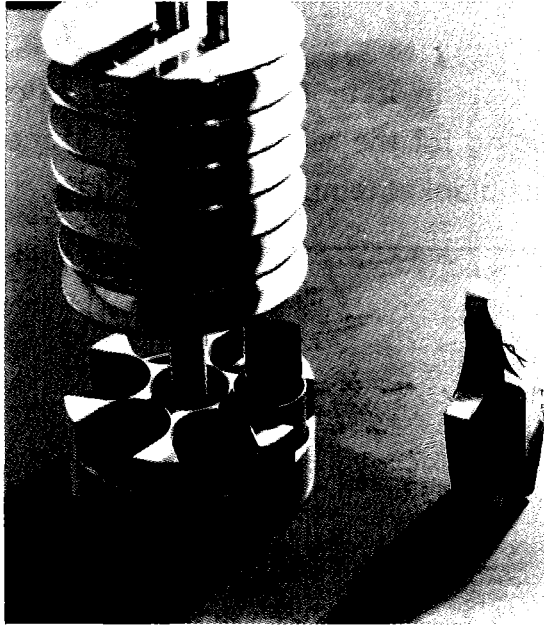


Fig. 8.2-1: Arrangement of samples in a capsule

### Solubilities

Fig. 8.2-2 shows solubility functions for 8 metals, most of them not reported before. In addition to the functions, single values were obtained for Y, Nb and Ta.

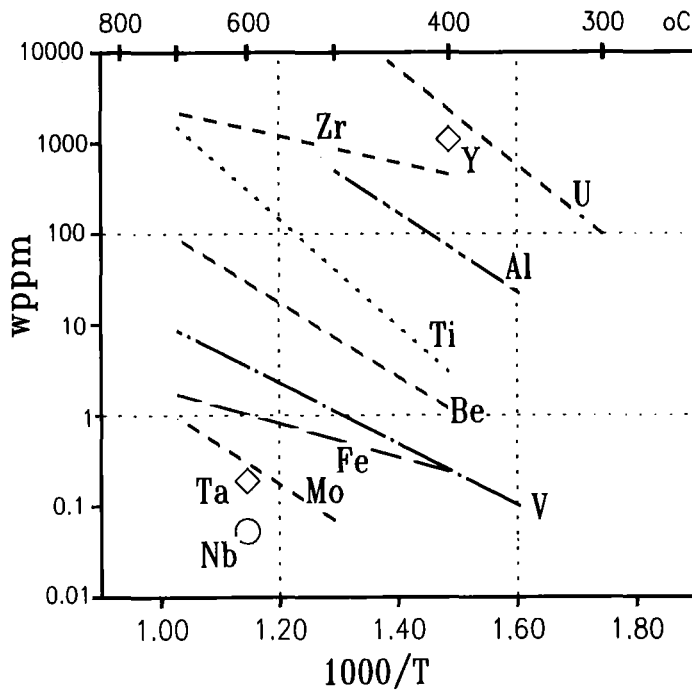


Fig. 8.2-2: Solubility of metals in Pb-17Li

## Dissolution rates

Even if dissolution rates from tests in static Pb-17Li cannot be compared with corrosion rates, they give a feeling for the relative stability of metals. Fig. 8.2-3 compares dissolution rates at the blanket temperature of 450°C.

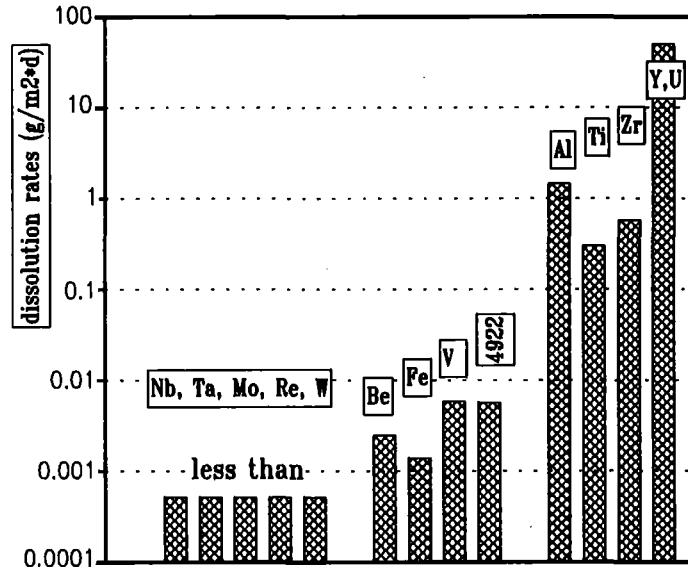


Fig. 8.2-3: Dissolution rates of metals in Pb-17Li at 450°C

## Diffusion coefficients

Diffusion coefficients in Pb-17Li could be determined for the metals, Be, Fe and V. From 500 to 600°C, values are between 1.E-10 (Fe and V) and 1.E-11 (Be). As expected, there is nearly no temperature dependence of the diffusion coefficients.

## Intermetallic compounds

Y, U, Ti and Zr, as well as alloys with Ti and Zr, form intermetallic compounds with lead. These metals cannot be used in contact with the eutectic. Some compounds were never reported before. Especially, the compound  $Ti_3Pb_2$  was investigated in detail [8-7]. In this compound, titanium can be replaced partly by Zr, Mo, Sn and V, lead by Al.

## **Beryllium**

Beryllium should be mentioned separately, because it was considered for liquid metal blankets. Be has low solubilities and dissolution rates, but it is strongly attacked by intercrystalline corrosion.

## **Alloys, Coatings**

From the investigated alloys, Mo-Re and ferritic steels are most stable. Mo coatings on Ti, Ti alloys and Zr were protective only for a short time at lower temperature.

## **Summary**

The figures show clearly, that metals like Y, U, Ti and Zr, and its alloys, cannot be used in contact with Pb-17Li. Also, Be cannot be used because of strong intercrystalline corrosion. On the other hand, Fe, Mo, Nb, Ta, V, W and Re are very stable, as well as ferritic steels.

### **8.3 Removal of corrosion products**

The main impurities in a Pb-17Li blanket are corrosion products. With steel MANET, the corrosion function from Borgstedt (Section 8.1), and estimating temperatures vs. surfaces, 150 kg of corrosion products may be formed in the blanket in one year of operation, or 2 kg in one blanket module.\* The solubilities of steel elements at blanket temperatures are below 1 wppm. Most corrosion products, therefore, will deposit in the form of solid particles. It is evident, that kg-amounts of solid particles can easily block narrow channels, especially if caught by magnetic fields. Corrosion products must be removed from the flowing eutectic.

#### **8.3.1 Formation of corrosion products**

The steel MANET dissolves mainly from high temperature surfaces. There is nearly no leaching [8-6] of elements (Section 8.1). Near the dissolving surface, the

\*The surface area of the interface Pb-17Li/structure in a segment is  $\approx 150 \text{ m}^2$ . The temperature at this interface is between 275 °C and 443°C. A corrosion rate of 2 kg/a for each segment corresponds to an average temperature of 430 °C for one third of the area or 410 °C for the total area.

concentration of elements in the eutectic is proportional to their chemical activity in the steel. The maximum possible concentration is the saturation concentration. Saturation concentrations are lower in cooler parts of the system. Here, dissolved elements should deposit. Therefore, cold traps were installed in many facilities. So far, however, efficiencies of these cold traps for corrosion product removal from Pb-17Li were not reported.

The deposition starts with nucleation - the formation of micro-particles, then particles will grow. This nucleation may be delayed by super-saturation. Then nucleation may occur at positions with higher than the minimum temperature of a system.

The deposition and subsequent growth of particles may be anywhere. In addition, particles will be transported by flowing eutectic to other parts of the system.

For non-isothermal systems, models were developed to describe mass transfer of corrosion products. The main part of such codes considers the hydraulic behavior of the liquid and particles. Usually, chemical reactions are not included. But there is chemistry involved. Barbier describes the formation of MnNi in austenitic loops, always found at the lowest temperature. We too found this compound in thermal convection loops [8-9]. Tortorelli [8-10] reports particles with different Cr concentrations at different temperatures in austenitic steel loops. We found in the ferritic loop TRITEX (below) particles with Cr concentrations between 2 and 80 wt.% [8-11].

### **8.3.2 Experiments**

The facility TRITEX [8-12] is used for the experiments. TRITEX was built in 1985 to 1987 to study tritium extraction from Pb-17Li with solid getter metals. Now, TRITEX is used mainly for the development of purification methods.

Table 8.3-1 shows the main parameters of TRITEX and Fig. 8.3-1 a flow sheet of loop 5. TRITEX is a pumped system with circulating Pb-17Li. The possible temperature range is 250 to 550°C and the maximum flow rate 2.5 l/min (or 25 cm/s in main pipes). With the exception of magnetic traps, flow meters (vanadium), and a molybdenum liner in the EMP, the loop is fabricated from ferritic steel 1.4922. The composition of this steel is similar to MANET. Therefore

the same kind of corrosion products are expected as in a blanket. TRITEX is equipped with magnetic traps and cold traps to study purification techniques. These devices are removed after an experimental phase and investigated in detail. New and modified systems are installed for the next phase. Furthermore, liquid metal-covergas interface areas are investigated. TRITEX has operated so far in 6 experimental phases for 11000 hours.

**Table 8.3-1: Main parameters of TRITEX**

Structure material	ferritic steel 1.4922 12 % Cr, 0,5 %, 0,5 % Ni, 1 % Mo, 0,3 % V
Main pipe inner diameter	15 mm
Circulating metal	Pb-17Li
Covergas	Ar-6.0
Total inventory of Pb-17Li	120 kg
Circulating Pb-17L	80 kg
Total wetted surface	1.2 m <sup>2</sup>
Temperature	250 to 550 °C
Flow rate main loop	0.1 to 2.5 l/min
Flow rate cold trap	ajustable

### 8.3.3 Results

Except for a first report at a European workshop in 1993 [8-9] all results in this chapter were unpublished.

They should be considered as preliminary results. Most of the results were obtained after phase 5. The loop was not drained and all parts could be analyzed for Pb-17Li composition, impurity concentrations and deposited particles.

#### Distribution of corrosion products

Including phase 5, TRITEX had operated for 6000 hours between 400 and 450 °C, always with the cold trap in bypass mode below 260 °C. The main pipes are the largest source for corrosion products. The flow velocity there was mainly around 15 cm/s. With Borgstedt's function (Section 8.1), about 70 to 80 grams of corrosion products are expected.

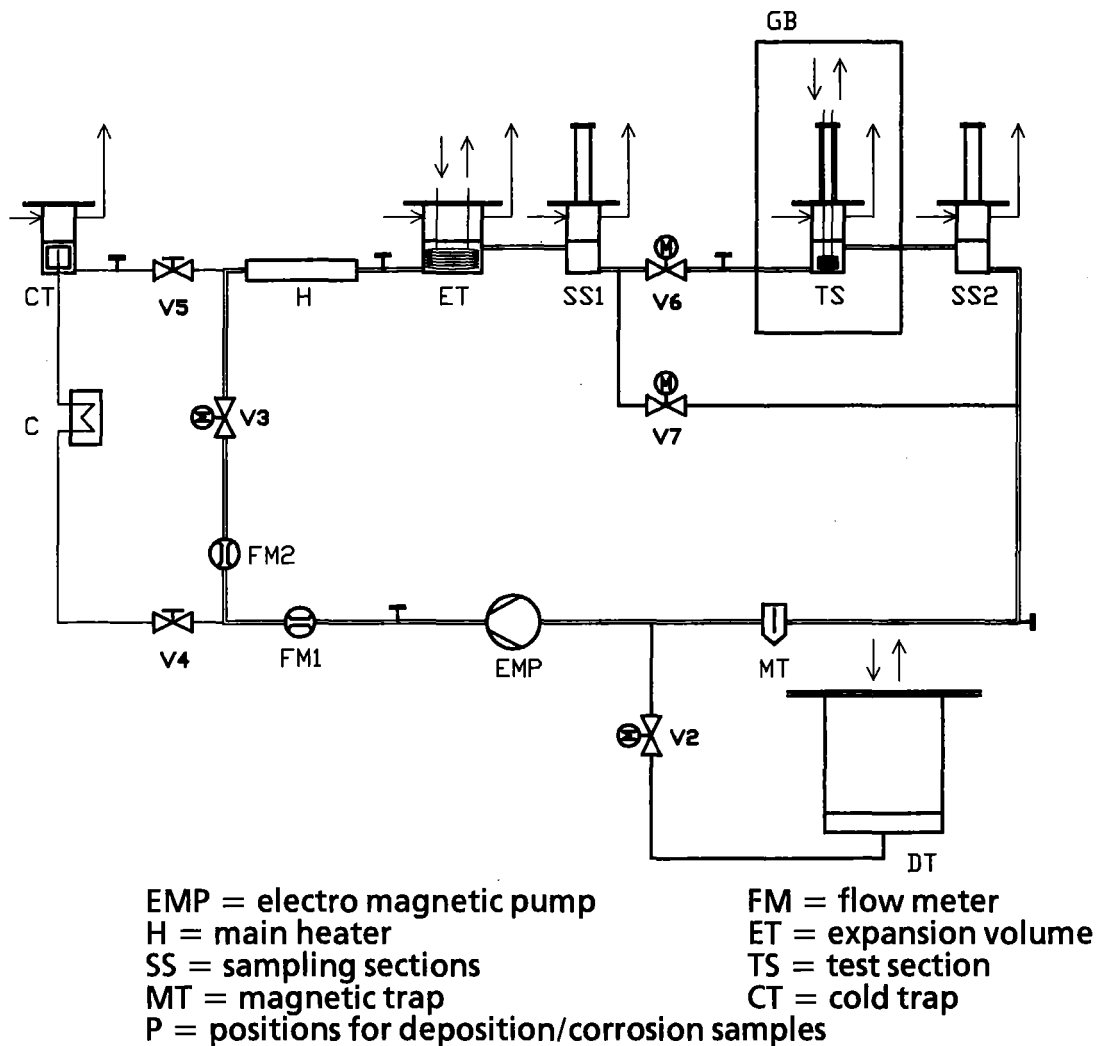


Fig. 8.3-1: Flow diagram of the loop TRITEX-5.

Altogether, 110 grams of corrosion products were found. Remarkable is the fact that the largest fraction of particles was found in crusts at liquid metal-covergas interfaces. The buoyancy of particles in the eutectic will be responsible for this effect: particles are floating up to these interfaces. Because the loop was drained at least 10 times before the end of phase 5, crusts in the drain tank contained 45% of all corrosion products. Crust at other smaller interfaces of the loop contained another 11% of the particles. That means, more than half of the corrosion products were in crusts. Fig. 8.3-2 shows a crust deposit on the stem of valve 4. Often, crusts contained up to 10 wt.% particles from steel components.

The magnetic trap was upstream of the electromagnetic pump (EMP). While the trap was nearly empty (only 20 mg particles), the EMP contained another 25% of the corrosion products. Nearly all particles were magnetic, the EMP acted as an effective magnetic trap! (Such an effect was reported also from other loop facilities with EMP's).

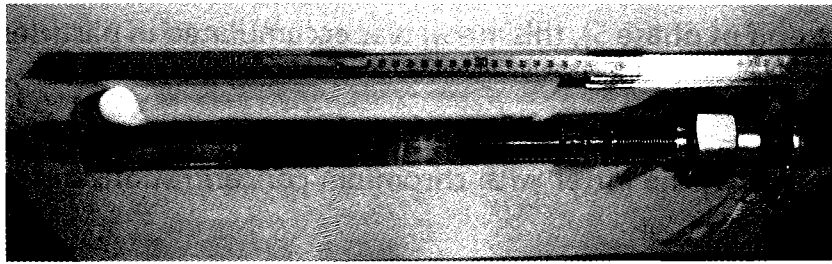


Fig. 8.3-2: Deposited crusts at the liquid metal-covergas interface. Stem of valve 4.

The amount dissolved in Pb-17Li was 10 grams (9%). This amount may still contain some particles. It is an average of a large number of samples from all parts of the loop, some taken during operation. It corresponds to a concentration of 100 wppm for (Fe+Cr+Ni+Mn), too high to be dissolved.

The remaining 11 % of particles were found in the cooler and cold trap, a fraction of this again in crust in the cold trap. The analysis of this cooler-cold trap system is still under way. Table 8.3-2 summarizes the distribution of corrosion products found in the loop.

Table 8.3-2: Corrosion product inventory (weight fractions)

drain tank crusts	45 %
crusts at smaller interfaces	11 %
EM pump trapping	24 %
dissolved in the Pb-17Li	9 %
cooler and cold trap, including crusts	11 %

### Composition of particles

The investigation of different particles is a difficult task. After dissolving adhering Pb-17Li with very mild acids, different mixtures of acids were used to dissolve different particles. The many results need further studies to understand all of the effects.

More than 95% of particles from the EMP were magnetic. They contained 10 to 30 wt.% Cr and up to 0.4 wt.% Ni. In spite of the low concentration of Ni in Pb-17Li (11 wppm at the end of phase 5), this metal was accumulated in particles.

Particles from other parts of the loop have different fractions of magnetic and non-magnetic particles, the latter with chromium concentrations between 2 and 80 wt%.

## Discussion

The total amount of corrosion products is in the expected range, using the wetted surface and Borgstedt's function.

The cold traps of loop 1 to 5 were not very effective for the removal of corrosion products. This may be an effect of bypass flow, or a feature of the design. Trapping of magnetic particles with magnetic traps is possible, as seen by the effectiveness of the EMP. However, the buoyancy of particles was not considered so far for particles removal. (This effect is not known from sodium systems because of the low density of Na compared to the density of particles).

Particles of many different compositions were found, with chromium concentrations between 2 and 80 wt.%. So far it is not possible to give composition/position or temperature patterns for particles. Instead, with the exception of the EMP, particles of all compositions were found in all positions. This is in agreement with the description of corrosion product plate out, described above in Section 8.3.1.

After phase 5, the loop was completely cleaned. Derived from results as given before, a new cold trap system was installed for phase 6, and operated always in the main flow. It consists of several parts. The first part is a "cooler-crystallizer". Seven volumes, each 40 cm<sup>3</sup> and filled with ferritic steel wire, allows the analysis of deposits as a function of temperature. This part is followed by an isothermal section with low linear flow velocity and a large ferritic steel wire mesh surface for deposition. As a third part, a magnetic trap is installed before the main loop. Fig. 8.3-3 shows this arrangement. TRITEX has furthermore a new designed magnetic trap before the EMP.

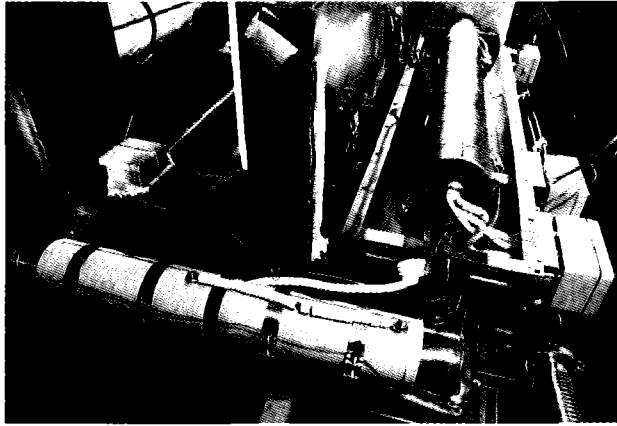


**Fig. 8.3-3: Arrangement of cold traps for experimental phase 6**

Experimental phase 6 is finished. The investigation of the cold trap system has just started. No results are available.

### **Summary**

Through Phase 5, the TRITEX loop has been operated for 6000 hours with forced convection of Pb-17Li in a ferritic steel loop. Analysis of the distribution of corrosion products indicated a new trapping mechanism for particles: more than 50 % were in crust deposits at interfaces to cover gas. The buoyancy of particles in the high-density eutectic is responsible for this effect. Whether such an effect can be used to remove particles from a blanket system needs further investigation.

In the Phase 5 experiments, effective magnetic trapping was observed in the EMP. Magnetic trapping is of special interest, because the blanket itself could act as a huge magnetic trap. However, deposition in magnetic traps depends on both the magnetic susceptibility of suspended particles and significant magnetic field gradients; therefore the piping in and out of the main magnetic field are the most endangered. If the generation of suspended particles can be avoided by heterogeneous nucleation in a more effective cold trap, then homogeneous nucleation in the bulk coolant may be avoided, and subsequently magnetic trapping reduced.

A new cold trap system was installed following analysis of Phase 5 results. This new system utilizes a much larger surface area in the cold traps. The investigation of this new purification system following experimental Phase 6 is expected to help design better purification systems for corrosion product removal.

## 8.4 Aerosols and activation products

Besides corrosion products, non-radioactive as well as radioactive impurities have to be considered. Some impurities will be formed by neutron transmutation of lead. For example, Po-210 is formed from Bi-209 by neutron capture. Bi-209 is formed from lead with a rate of 2 to 10 appm Bi per year [8-13]. That means, even with a "Bi-free" eutectic mixture at the beginning, Bi will build up during operation, and with this also Po-210. Other important nuclides are Hg-203 and Tl-204, both formed from lead. All three nuclides - Po-210, Hg-203 and Tl-204 - are of special concern because of their assumed high volatility from the eutectic in case of accidents [8-14]. It was calculated that the highest body dose results from Hg-203, and the highest lung dose from Po-210 [8-14]. The goal, therefore, must be to remove Bi, Po-210, Hg-203 and Tl-204 from the system. At first, chemical activities in the eutectic, evaporation behavior and aerosol formation were studied. Aerosols may transport radionuclides to cover gas areas. The investigation of Hg-203 and Tl-204 has just started with basic consideration. Experiments for bismuth and Po-210 are nearly completed.

### 8.4.1 Experiments

In all experimental facilities (Chapters 7.2/8.2/8.3), deposits of evaporated Pb and Li were found. Therefore, Langmuir-type evaporation experiments were performed [8-15]. Langmuir evaporation takes place from free surfaces into vacuum or an inert gas. Results are comparable to conditions in loop experiments or in a blanket.

Evaporation rates in vacuum can be calculated by a modified Knudsen function:

$$ER = 1.60 \cdot 10^6 \cdot \alpha \cdot p \cdot \sqrt{M/T}$$

ER in  $\text{g/m}^2 \cdot \text{h}$ ,  $M$  = the molecular weight of the formed gas,  $p$  = vapor pressure of the evaporating metal (mbar),  $\alpha$  = an experimental factor (accommodation coefficient).

The vapor pressure for an evaporating metal in a solution is given by:

$$p = p_s \cdot x \cdot \gamma$$

$p_s$  = vapor pressure of the pure metal (mbar),  $x$  = mole fraction of the metal, and  $\gamma$  = coefficient of chemical activity.

Accommodation coefficients  $\alpha$  for the experimental arrangement were determined from evaporation rates of pure metals [8-16]. Chemical activities, specifically activity coefficients, were then calculated from evaporation rates of metals from mixtures.

Fig. 8.4-1 shows the used facility. 140 grams Pb-17Li in a Mo crucible were heated in vacuum or flowing inert gas. Evaporated metals condensed in cooler parts and were analyzed.

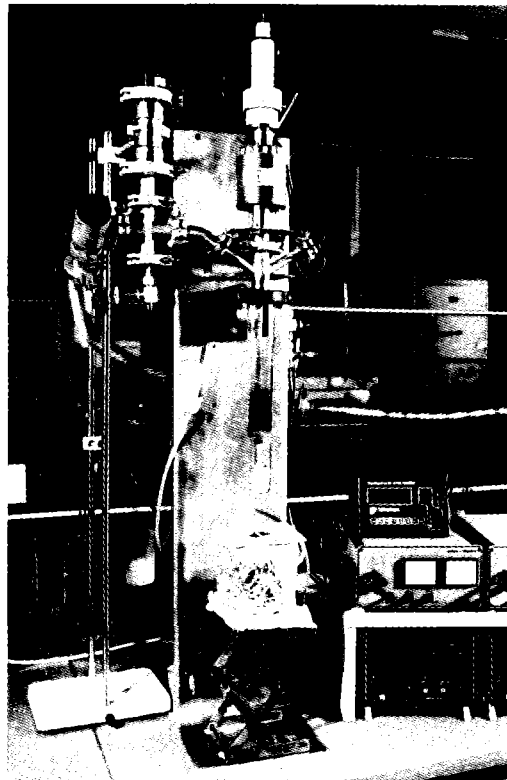


Fig. 8.4-1 Facility for determination of evaporation rates

#### 8.4.2 Evaporation of lithium + lead, aerosols

Fig. 8.4-2 shows evaporation rates for Pb (approximately Li + Pb) in vacuum, He and Ar.

Vacuum: The temperature dependence is given by

$$\ln ER = 23.7 - 17900/T,$$

where the heat of evaporation is -149 kJ/mol. For example, at 450°C, 0.34 g eutectic mixtures evaporate in 1 hour from 1 m<sup>2</sup>.

Li and Pb evaporate proportional to their chemical activities in the eutectic. The chemical activity of Li, derived from evaporation rates, was found in agreement with the literature [8-16].

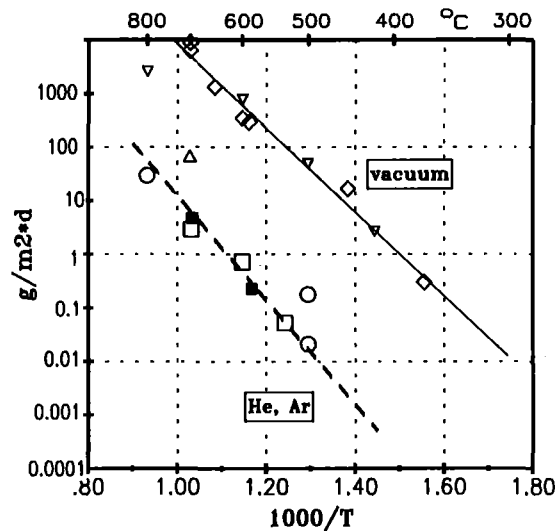


Fig. 8.4-2 Evaporation of (Pb + Li) in vacuum and inert gas

Inert gas: Much lower evaporation rates were measured for evaporation in an inert gas at 1 bar. The temperature dependence is given by:

$$\ln ER = 20.1 - 21030/T.$$

The heat of evaporation is -175 KJ/mol, very near to the literature value for lead of -176 kJ/mol. At 450°C, only 0.0001 g eutectic mixture evaporate in 1 hour from 1 m<sup>2</sup>.

Evaporation of Li and Pb together in an inert gas can also be expressed by the simple relation:

$$ER = 48 \cdot p.$$

$p$  = vapor pressure of pure lead [8-17] in mbar, multiplied by 0.83 to compensate for the chemical activity in the eutectic.

**Aerosols:** It is evident from evaporation rates, that aerosol concentrations in gases will be low. In a typical experiment, the argon flow was 50 cm<sup>3</sup>/min and the evaporating surface 5 cm<sup>2</sup>. At 450°C, the aerosol concentration was only  $2 \cdot 10^{-5}$  g/m<sup>3</sup> near the Pb-17Li surface.

Sometimes, the eutectic mixture is compared with sodium coolant of LMFBRs. A similar relation for the evaporation of sodium from a pool was found by Schütz [8-18]. Na aerosol concentrations up to 70 g/m<sup>3</sup> were reported at the outlet of vessels. This is caused by a 3 to 5 orders of magnitude higher vapor pressure for sodium, compared with the eutectic.

## Discussion

From low evaporation rates it is evident that no aerosol problems will occur with the eutectic during normal operation of a blanket. That means, also radioactivity transport by aerosols is negligible. However, evaporation rates are not zero, and deposits were found in covergas areas of all experimental facilities. Evaporation must especially be considered for the process of tritium extraction by gas bubblers or spray towers (work of JRC Ispra), because the evaporating surface is large.

### 8.4.3 Behavior of Po-210

As mentioned earlier, Po-210 was considered as one of the most serious potential hazards in case of an accident. Therefore, experiments and analyses were performed to characterize the evaporation rates into inert gas and vacuum environments. The experiments and results are described in more detail in Ref. [8-16].

## Experimental Measurements

There is no stable isotope of Po; experiments had to be done with radioactive Po-210. The chemistry of Po in the eutectic is always tracer chemistry. Up to  $6 \cdot 10^4$  Bq Po-210/g, eutectics in the blanket are expected [8-13], corresponding to only 0.3 appb. In our experiments, up to 100 Bq/g were used, 1000 times lower than expected for the blanket. The results, however, will be valid for the higher concentrations, as reported for evaporation of Po from bismuth [8-19].

Evaporation rates for Po-210 in vacuum can be calculated by

$$ER_{Po} = 9.51 \cdot 10^{29} \cdot p \cdot X \cdot \gamma \cdot \alpha \cdot \sqrt{\frac{1}{M \cdot T}}$$

$ER_{Po}$  = atoms/m<sup>2</sup> · h;  $p$  = vapor pressure of Po (mbar) from Ref. [8-20];  $X$  = mole fractions of Po in the mixture,  $\gamma$  = chemical activity coefficient;  $\alpha$  = accommodation coefficients of the experiment,  $M = 210$  (Po-210).

As found by Moyer [8-19] for bismuth, relative evaporation rates are independent of concentrations. Therefore, relative evaporation rates were calculated.

$$ER_{Po,rel} = 2.75 \cdot 10^4 \cdot p \cdot \gamma \cdot \alpha \cdot \frac{1}{m} \cdot \sqrt{\frac{1}{M \cdot T}}$$

$ER_{Po,rel}$  = fractions of inventory, released from 1 cm<sup>2</sup> surface in 1 hour;  $m$  = mass of used Pb-17Li (g); others as before.

## Results

Fig. 8.4-3 shows measured relative evaporation rates of Po-210 from vacuum experiments, together with the calculated function for  $\gamma = 1$ . Measured rates are 1000 times smaller than calculated ones. That means, the activity coefficient of Po is 0.001. It shows only a weak temperature dependence:

$$\ln \gamma = -4.77 - \frac{1329}{T}$$

The activation energy is -11 kJ/mol.

The low activity coefficient points to a chemical compound. Abakumov [8-21] has determined the vapor pressure of lead polonide, PbPo. The extrapolated functions are included in Fig. 8.4-3. The agreement with our experimental results is good. That means, PbPo instead of Po metal is dissolved in the eutectic. Except for a spill into the vacuum chamber, evaporation into the cover gas helium, argon, or in air has to be considered. Fig. 8.4-4 compares the release in vacuum and helium

or argon at 1 bar pressure. As expected, release in a gas is orders of magnitude smaller than release in vacuum.

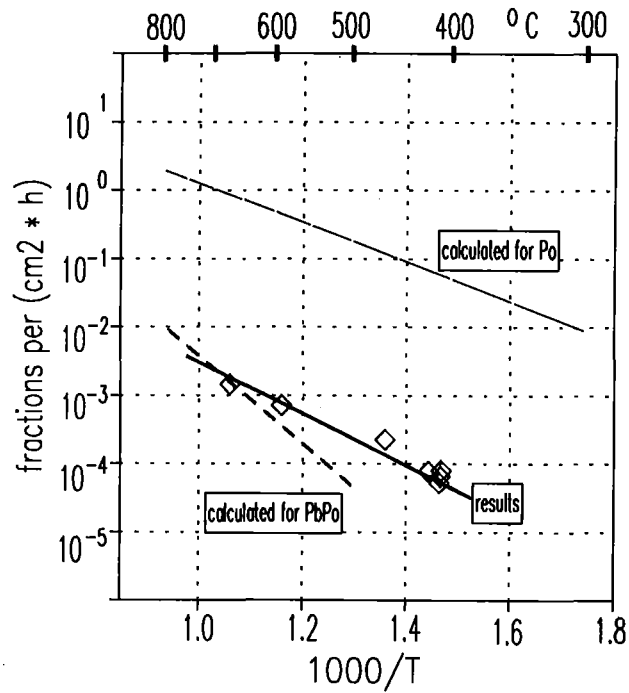


Fig. 8.4-3 Evaporation fractions of Po-210 in vacuum experiments  
Dashed line = calculated for PbPo

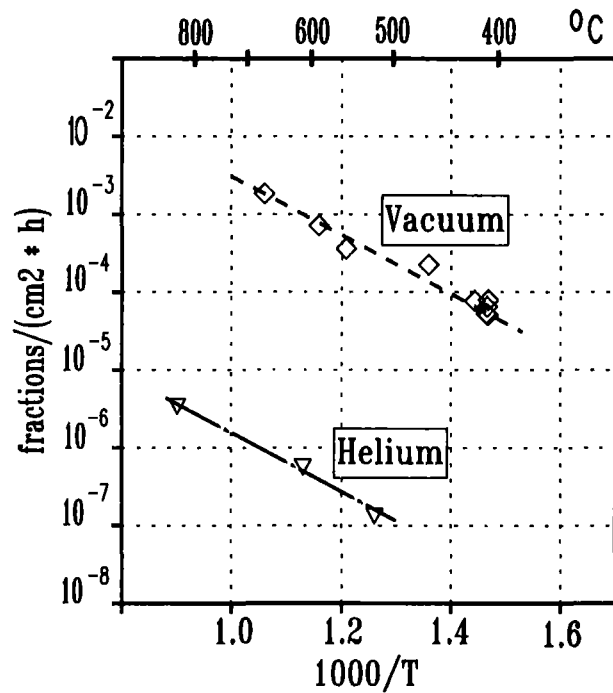


Fig. 8.4-4 Evaporation fractions of Po-210 in vacuum and helium experiments

## Discussion

All previous calculations of polonium release from Pb-17Li did not consider the formation of PbPo, evaporation rates were assumed too high. Even for the case of a spill into the vacuum chamber, release of Po-210 is a factor 1000 lower. Mostly, however, we have to consider a spill in an inert gas or air. In this case, evaporation rates will be  $10^6$  times lower than assumed without PbPo formation. Release of Po-210, therefore, will not be a problem in case of a Pb-17Li spill.

### 8.4.4 Behavior of bismuth

Only some preliminary results will be reported in this section [8-22].

There was an early requirement to keep the concentration in the blanket below 10 appm [8-23]. We found concentrations between 5 and 30 appm in thermal convection loops (TCLs, Chapter 7.2) and in the pumped loop TRITEX (Chapter 8.3). The initial concentration in these facilities was 30 to 50 appm. Furthermore, Bi was added to one TCL, equivalent to 400 appm. The concentration decreased within a few days to the low values. In thermal gradient capsules [8-24], values as low as 0.5 appm were found.

In all these facilities, the eutectic was in thermal gradients with a solid Pb-17Li phase. Bi forms the very stable intermetallic compound  $\text{Li}_3\text{Bi}$  [8-25]. This compound is migrating into the solid to low temperatures. In these "diffusion-type cold traps" of facilities, enrichments have been found up to 10 wt%. Sometimes,  $\text{Li}_3\text{Bi}$  was also found floating at covergas interfaces because of its low density of  $5 \text{ g/cm}^3$ , compared to Pb-17Li with 9.5. Fig. 8.4-5 shows the Bi distribution in a thermal gradient capsule [8-24].

In the meantime, first solubility functions for Bi in Pb-17Li were determined. The results confirm the observations from loop facilities. That means it will be possible to maintain less than 10 appm Bi in the eutectic with simple devices.

### 8.4.5 Summary

In agreement with theoretical considerations, evaporation rates of Pb-17Li are low. Very low concentrations of aerosols are formed in a transporting gas. Only for some special cases, aerosol formation should be considered.

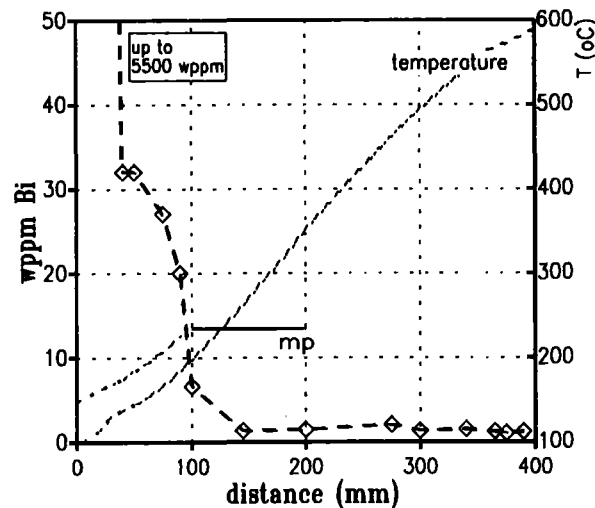


Fig. 8.4-5: Distribution of Bi in a thermal gradient

Po-210 does not cause any problems in case of an accident. Because of the formation of PbPo, the release rate is three to six orders of magnitude lower than previously anticipated.

Bi can be removed from Pb-17Li systems to below the required 10 appm by simple diffusion type cold traps.

### 8.5 Behavior of lithium replenishment

The name Pb-17Li stands for a mixture of 17 at. % Li with 83 at. % Pb. (Actually, LiPb is dissolved in lead and not Li). Often, however, Li concentrations in experimental facilities were lower. An assessment by Hubberstey [8-26], supported by its own measurements, showed, that the eutectic mixture contains only 15.7 at. % Li. This was confirmed by our measurements [8-24]. Even if the new eutectic composition is 15.7 at % Li, the writing Pb-17Li will be used in this report.

We found also, that the Li content of a presumably homogeneous solid sample was scattered over a wide range of concentrations. In some cases this was clearly an effect of gravitational segregation. But thermal gradients have also an influence on Li distribution. The second item in connection with an operating Pb-17Li blanket is replenishment of Li during operation. Li is consumed by burn-up, and lost mainly by oxidation [8-27]. Lithium has to be added to have a constant tritium breeding rate, and to keep the solidification point at 234°C.

In an experimental program, the effect of Pb-Li segregation, and the way to add lithium to a system, were investigated.

### 8.5.1 Gravitational segregation

Fig. 8.5-1 shows the Li distribution in a 10 kg bar Pb-17Li from Metaux Speciaux. While the average concentration was as specified 17 at.%, concentrations between 15.5 and 20.7 at.% were found in different parts. Clearly, the effect of gravitational segregation can be seen. The lowest values at the bottom are near Hubberstey's 15.7 at.%, highest values are found at the top. During cooling "excess" LiPb is crystallizing and floating up because of the higher density of the eutectic. "Excess" means more than required to have a solidification at the eutectic temperature 234°C.



Fig. 8.5-1: Distribution of Li in a 10 kg bar Pb-17Li from Metaux Soeciaux [8-24]

This shows, that sampling for analysis has to be done with great care, otherwise results are not representative for a system. We recommend grab-samples from molten stirred Pb-17Li and to dissolve the whole sample for analysis [8-24].

## 8.5.2 Thermal gradient segregation

Thermal gradient segregation occurs, if the Li concentration is not exactly eutectic. In this case, LiPb (Li-excess) or Pb (Li-deficiency) will plate out at temperatures corresponding to the solidus curve of the phase diagram.

Thermal gradient capsules were used to study the effect in detail. They were filled with different initial Li concentrations in the Pb-Li mixture. Especially horizontally heated capsules show dramatic effects. Fig. 8.5-2 shows the arrangement of a capsule in a furnace, Fig. 8.5-3 results from two capsules. The initial concentration in capsule 8 was just below the eutectic, a lead phase is found at low temperatures. The initial concentration in capsule 9 was higher than the eutectic, a LiPb phase is formed at low temperature. Remarkable is the fact, that in both capsules the new eutectic concentration was found over the whole range of molten Pb-17Li [8-24].

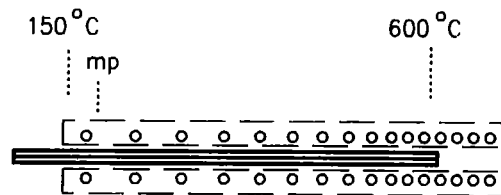


Fig. 8.5-2: Thermal gradient capsule

Thermal gradients can always be found in loop systems. Such parts are in thermal convection loops (Chapter 7.2), as well as in TRITEX (Chapter 8.3) in form of freeze valves, they act as diffusion type cold traps with a solid phase. In all facilities, the Li concentration in the circulating eutectic was around the new eutectic value. "Excess" lithium from the original 17 at.% was found in cold spots.

Thermal segregation will cause a kind of "self adjustment" of the Li concentration. This could be favorable for a system. All which is needed is a sufficient large diffusion type cold trap with a solid phase in Pb-17Li systems. But, if this effect can be used for a blanket needs further analysis.

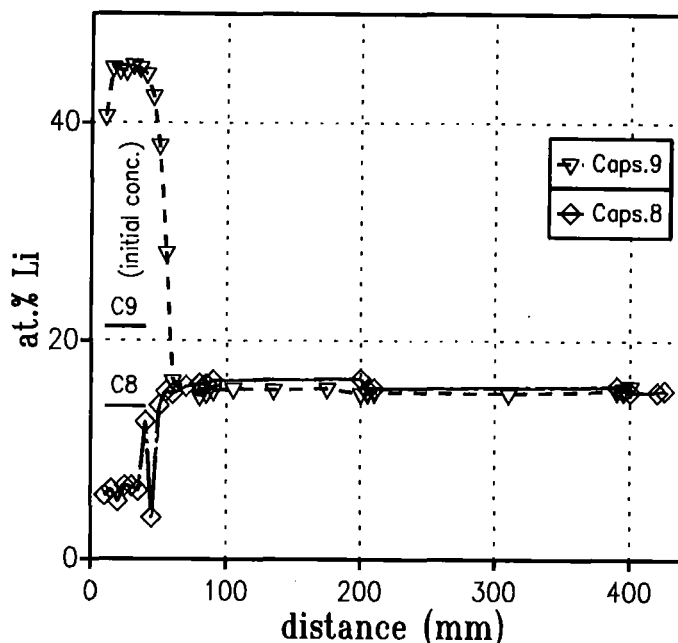


Fig. 8.5-3: Distribution of Li in two capsules heated for 760 hours horizontally in a thermal gradient

### 8.5.3 Replenishment of lithium

During blanket operation, Li is consumed by burn-up and oxidation. It has to be added to have a constant tritium breeding rate. Lithium metal cannot be used because of two reasons. The very large density difference between Li ( $0.5 \text{ g/cm}^3$ ) and Pb-17Li ( $9.5 \text{ g/cm}^3$ ) causes quickly floating-up to upper parts of the system. On the other hand, Li metal may be covered by high melting Li-Pb compounds after dipping in the eutectic. Particles can be formed, circulating around with the risk for blocking narrow channels.

Usually only smaller amounts of Li have to be added. The mentioned intermetallic compounds can be used for this.  $\text{Li}_3\text{Pb}$  was fabricated by melting the elements together in an argon filled glove box. Its melting point is  $658^\circ\text{C}$ . Cooling curves of a whole batch can be used as a simple thermal analysis for characterization (Fig. 8.5-4). Never any segregation between Li and Pb was seen in samples after solidification. This compound dissolves in near eutectic mixtures at  $330^\circ\text{C}$  with a constant rate of  $0.14 \text{ g/cm}^2\text{-h}$ , slowly enough for the purpose of adjustment.

The adjustment was demonstrated with a thermal convection loop [8-28]. It operated originally with pure lead and was converted into a Pb-Li loop by adding  $\text{Li}_3\text{Pb}$  (Fig. 8.5-5).

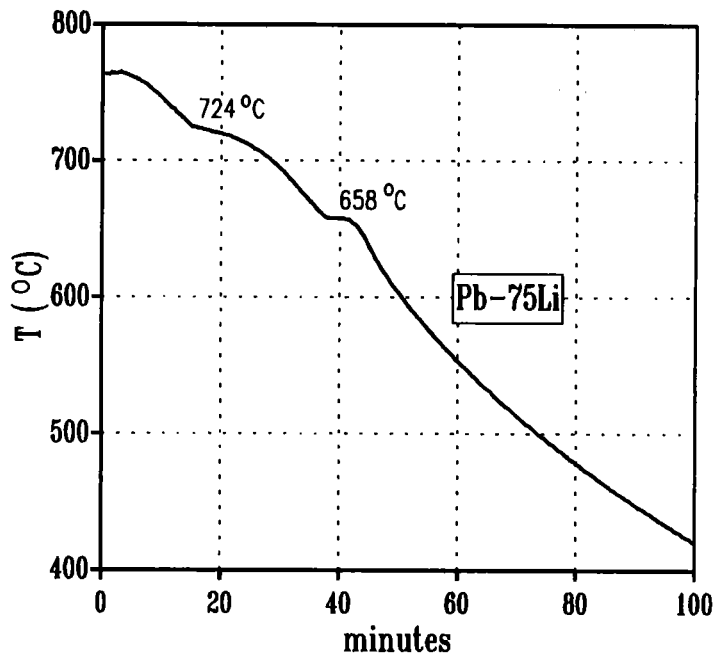


Fig. 8.5-4: Cooling curve of a 500 g batch of  $\text{Li}_3\text{Pb}$

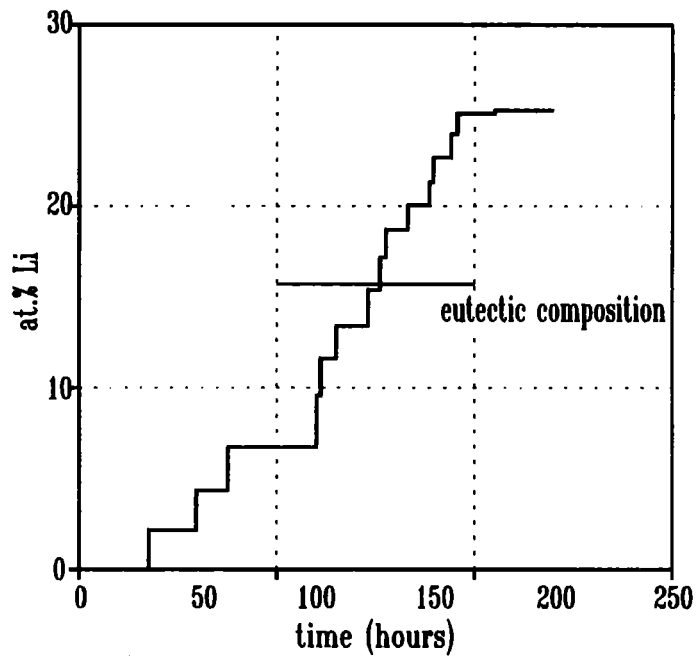


Fig. 8.5-5: Addition of  $\text{Li}_3\text{Pb}$  to a thermal convection loop

#### 8.5.4 Summary

When analyzing samples from Pb-Li systems, gravitational as well as thermal gradient segregation of Li and Pb was found.

The first effect is especially of importance for sampling. It is recommended to dissolve always a whole grab sample for analysis.

The effect of thermal gradient segregation may be used for self-adjustment of Li in all kinds of Pb-Li systems. All which is needed is a sufficient large diffusion type cold trap with a solid phase.

Li replenishment can be done by dissolving  $\text{Li}_3\text{Pb}$ . This compound is easy to fabricate. The replenishment was demonstrated with a thermal convection loop. It operated originally with pure lead and was converted into a Pb-Li system.

#### References

- [8-1] G. Frees, G. Drechsler and Z. Peric, "Dynamische Korrosionsuntersuchungen in der eutektischen Blei-Lithium-Schmelze Pb-17Li", *Werkstoffe und Korrosion* 40 (1989) 593.
- [8-2] H.U. Borgstedt, G. Frees, and Z. Peric, "Material compatibility tests with flowing Pb-17Li eutectic", *Fusion Engng. and Design* 17 (1991) 179 - 183.
- [8-3] H.U. Borgstedt, and D. Röhrig, "Recent Results on corrosion behaviour of MANET structural steel in flowing Pb-17Li eutectic", *J. Nucl. Mater.* 179-181 (1991) 596 - 598.
- [8-4] H.U. Borgstedt, G. Frees, M. Grundmann, and Z. Peric, "Corrosion and mechanical properties of the martensitic steel X18CrMoVNb 12 1 in flowing Pb-17Li", *Fusion Engng. and Design* 14 (1991) 329 - 334.
- [8-5] H.U. Borgstedt, H. Glasbrenner and Z. Peric, "Corrosion of insulating layers on MANET steel in flowing Pb-17Li", *J. Nucl. Mater.* 212 - 215 (1994) 1501 - 03.
- [8-6] H. Feuerstein et. al., Compatibilities of 25 metals and alloys with static Pb-17Li, FZKA-5596 (1995).
- [8-7] H. Gräbner et al., Behavior of titanium and its alloys in molten lead and molten Pb-17Li, p. 524-1 to 524-10, Proc. 4th Intern. Conf. on Liquid Metal Engineering and Technology, Avignon, 17-21 Oct. 1988.
- [8-8] F. Barbier et.al., Influence of manganese on the nickel concentration in solution in the Pb17Li alloy, paper PA-196, 18th SOFT conference, Aug. 22-26, 1994, Karlsruhe, Germany.
- [8-9] H. Feuerstein, Contribution to European Workshop on Lithium and Lithium-Lead Corrosion and Chemistry, Nottingham, GB, 1990.

- [8-10] P.F. Tortorelli et.al., Corrosion and mass transfer of ferrous alloys in Pb-17Li, page 528-1 to 528-10, Proc. 4th Intern. Conf. on Liquid Metal Engineering and Technology, Oct. 17-21, 1988, Avignon, France.
- [8-11] H. Feuerstein, Contribution to European Workshop on Lithium and Lithium-Lead Corrosion and Chemistry, Fonteney-aux-Roses, France, Oct. 1993.
- [8-12] H. Feuerstein et.al., TRITEX, a forced convection loop with Pb-17Li, J. of Nucl. Materials 155-157 (1988)520-523.
- [8-13] U. Fischer and E. Wiegner, Production of Po-210 in Pb-17Li, an Assessment, Fusion Technology 1992, p. 1719-1723.
- [8-14] G. Casini et. al., Radioactivity effects of Pb-17Li in fusion power reactors, Fusion Engineering and Design 17 (1991) 351-357.
- [8-15] H. Feuerstein et.al., Evaporation of lead and lithium from molten Pb-17Li-Transport of aerosols, Fusion Engineering and Design 17 (1991)203-207.
- [8-16] H. Feuerstein et. al., Behavior of Po-210 in molten Pb-17Li, J. of Nucl. Materials 191-194 (1992)288-291.
- [8-17] O. Kubaschewski et.al., Metallurgical Thermochemistry, Pergamon Press, Oxford 1967.
- [8-18] W. Schütz and H. Sauter, Experimental determination of sodium evaporation rates, Nucl. Sci. Engineering 80 (1982)667-672.
- [8-19] H.V. Moyer et.al., TID-5221 (1956).
- [8-20] L.S. Brooks, J. Am. Chem. Society 77(1955)3211.
- [8-21] A.S. Abakumov et.al., Sov. Radiochem. 16(1974)396; Radiokhimiya 16(1974)397.
- [8-22] H. Feuerstein, contribution to European Workshop on Lithium and Lithium-Lead Corrosion and Chemistry, Karlsruhe 1994.
- [8-23] H. John, et.al., DEMO relevant test blankets for NET/ITER, KfK 4908 (1991).
- [8-24] H. Feuerstein et.al., Behavior of lithium in Pb-17Li systems, Proc. of the Intern. Conf. on Liquid Metal Systems, March 16-18, 1993, Karlsruhe, to be published, Plenum Press 1995.
- [8-25] P. Hubberstey and T.Sample, Thermodynamics of Pb-17Li-bismuth solutions, J. Nucl. Materials 212-215 (1994) 1021-1025.
- [8-26] P. Hubberstey et.al., is Pb-17Li really the eutectic alloy ? J. of Nucl. Materials 191-194 (1992)283-287.
- [8-27] H. Feuerstein et. al., Oxidation of Pb-17Li in air between 25 and 650 °C - Comparison with Lead, KfK 4927 (1992).
- [8-28] H. Feuerstein et.al., Eutectic mixture Pb-17Li - In-situ production and Li adjustment, Fusion Technology 1994, Proc. 18th, SOFT Conference, Karlsruhe, August 22-26, 1994.



## **9. Ancillary Loop System**

For each of the two coolants - Pb-17 Li and helium - a completely different system is required for heat and tritium extraction. All methods and components of the helium system are very similar to those designed for helium-cooled solid breeder blankets and are described for example in [9-1].

In the lead lithium loops both heat and the tritium are transported to the steam generators (SG) for extraction. Double walled tubes are used in these heat exchangers where the liquid metal flows around the outer tube, the water in the inner tube and a secondary liquid metal (NaK) in the concentric gap between the tubes. Tritium diffuses through the outer tube wall into the NaK and is removed by batchwise cold trapping of this liquid metal. This tritium removal method is described in Chapter 7.1. The main reasons for selecting this steam generator design are

- a) The large surface area required in the SG`s for heat extraction can be used at the same time as a permeation window to remove the tritium bred in the blanket from the Pb-17Li.
- b) Cold trapping of NaK is an attractive method to recover tritium.
- c) The high solubility of tritium in NaK results in a very low tritium partial pressure, minimizing permeation losses to the water.

### **9.1 Steam generator design**

The basic design of such SG`s are described in [1-6]. Straight tubes are used and the design is similar to the one successfully operated in the Experimental Breeder Reactor (EBR-II) [9-2]. In the case of the EBR-II, the gap between the concentric SG tubes is filled with stagnant helium, connected to a plenum at one end of the tubes for leak detection. In the fusion reactor, however, NaK is flowing slowly through the gap. This requires a NaK plenum at both ends but the same design and fabrication technology as used for EBR-II can be employed.

Large emphasis has been placed on design measures to avoid damage propagation in case of a water leak into the NaK. Wastage protection sleeves are arranged in the region of the plena (see [1-6]). An extensive study [9-3] showed that the potential for liquid metal-water reactions is much smaller than in a single wall fast breeder SG and that no failure propagation (i.e. no connection between water and lead lithium) has to be anticipated.

## 9.2 Circulation pump

A single stage radial centrifugal pump is proposed to circulate the Pb-17Li coolant. It is arranged in the cold leg of the Pb-17Li primary loop and has a free surface with an inert cover gas. There is a hydrostatic bearing with Pb-17Li as working fluid at the bottom of the vertical pump shaft. Similar pumps are used in fast breeder reactors but the high density of Pb-17Li allows to achieve a head up to 4 MPa with a single stage. Such pumps are already in use for similar fluids like lead and bismuth.

## 9.3 Power conversion system

A system designed for an entirely self-cooled lead-lithium blanket is described in [1-6]. In that case, the Pb-17Li temperatures at SG inlet/outlet were 400°/275 °C. Processes with two candidate steam conditions had been assessed:

- a) saturated steam at 70 bar
- b) superheated steam at 350 °C and 50 bar

It was shown that a slightly higher overall efficiency could be achieved with superheated steam but the small difference probably does not justify the additional complexity. For the same reason a system based on the use of saturated steam is proposed for the Dual Coolant Blanket. The conditions in this system are nearly the same as in a Pressurized Water Reactor (PWR) and result in about the same thermal efficiency ( $\approx 34.5\%$ ). The use of two different coolants makes the power conversion system more complex in any case.

The boundary conditions for the power conversion system are listed in Table 9-1.

All listed values of mass flux rates and thermal power are valid for the entire system.

**Table 9-1 Boundary conditions for the power conversion system**

**a) Parameter of the cooling loops**

	Helium	Pb-17Li
Total power to be extracted, MW	510	1530
- inboard blanket segments, MW	180	420
- outboard blanket segments, MW	330	1110
Temperature inlet, SG, °C	350	425
Temperature outlet SG, °C	250	275
System pressure (max)MPa	8	2
Mass flux rate Kg/s	990	54300

**b) Parameter of the steam system**

Steam pressure	7 MPa
Saturation temperature	286 °C
Feed water temperature	150 °C
Total thermal power	2040 MW
Power required for preheating	603 MW
Power required for evaporation	1437 MW
Water flow rate (feed water, steam)	956 kg/s

Helium loops cooling the first wall as well as the circulating Pb-17Li cooling the breeder zone have to deliver the heat to the same steam cycle.

A comparison of the heat delivered by helium with the power required to heat the feed water up to the boiling point indicates that the helium system could be used for preheating. In this case, however, the liquid metal temperature would be too low for a positive temperature difference at the pinch point in the Pb-17Li SG. A split of the feed water flow rate to the helium and Pb-17Li systems in the same ratio as the thermal power would lead to a negative temperature difference at the pinch point in the helium SG.

The given temperatures as listed in Table 9-1 require an overproportional water flow rate to the helium SG leading to an overproportional steam generation rate in the Pb-17 Li SG. This distribution of the flow rates can be seen in Fig. 9-1.

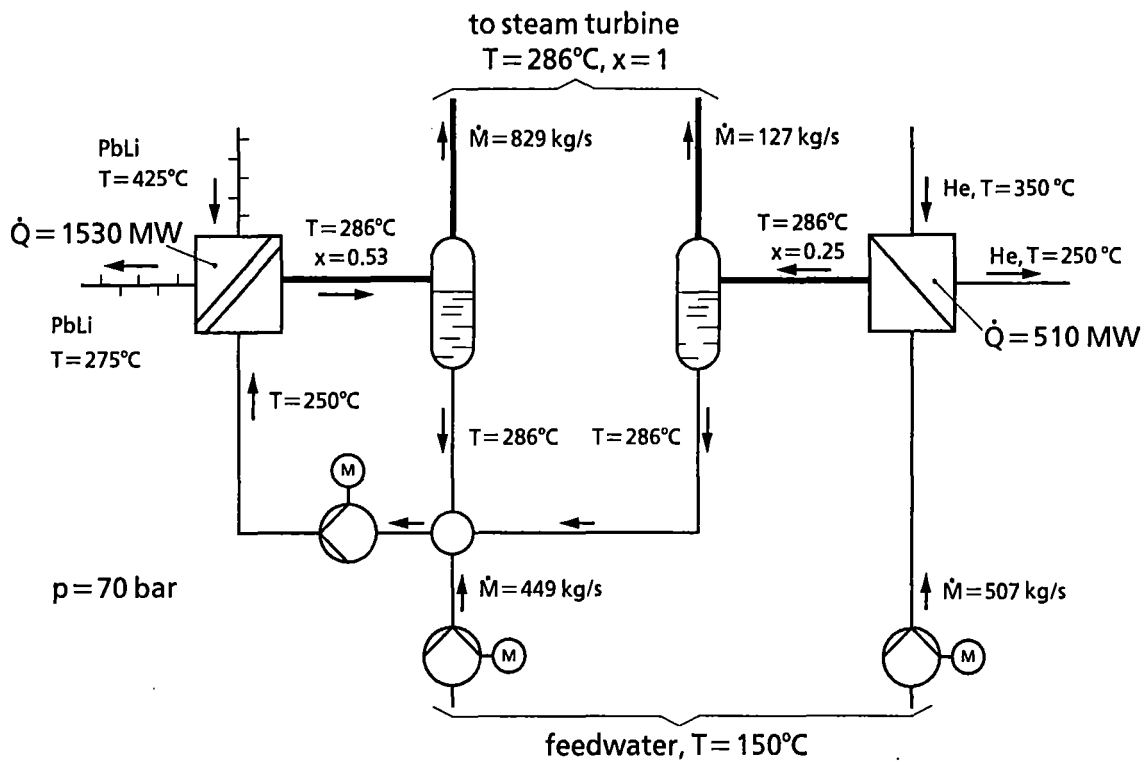


Fig. 9-1 Flow rates in the steam generating system

The selected flow distribution results in a steam quality at the exit of the helium and Pb-17Li SG of  $x_{\text{He}} = 0.25$  and  $x_{\text{LM}} = 0.53$  respectively. Figure 9.2 shows the temperature - thermal power diagram for both steam generators.

The temperature differences at the pinch point are 27 K (helium) and 17 K (Pb-17 Li). This leads to a total heat transfer surface area in the helium and Pb-17 Li SG's of 15.000 m<sup>2</sup> and 21.000 m<sup>2</sup> respectively. The surface area in the Pb-17Li SG is in the optimum range required for tritium extraction. However, it would be desirable to reduce the size of the helium SG in order to reduce tritium permeation. This would be possible if either the helium or the Pb-17Li temperature at the SG exit could be increased by 10 to 30 K.

An important point in the thermal design is the water inlet temperature at the Pb-17 Li SG. A value of 250 °C has been chosen in order to avoid freezing of the Pb-17Li (melting point 235 °C). This temperature can be controlled by adjusting the recirculation rate and consequently the steam quality at the exit of the Pb-17Li SG.

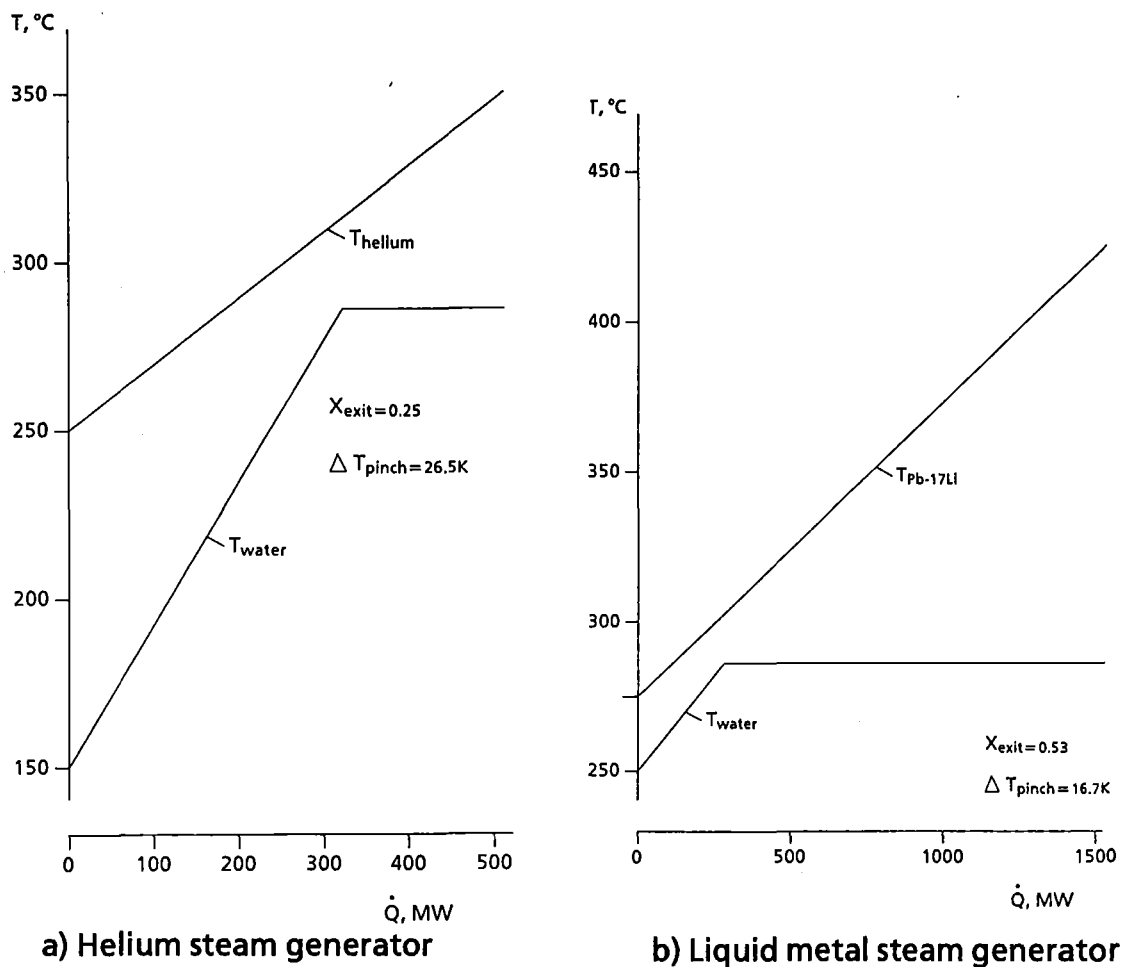


Fig. 9-2 Temperature-thermal power diagram for the steam generators

#### 9.4 Subdivision of the primary systems

Separated cooling systems are proposed for the inboard and outboard blanket segments since the pressure drop is different in the two regions. Additionally, the helium cooling is subdivided into two completely separated systems in order to provide high redundancy for afterheat removal. For safety reasons the Pb-17Li cooling system of the outboard region is subdivided, too, into two independent systems in order to reduce the mass of activated liquid metal in one system. There are at least 2 parallel loops in each of the seven independent cooling systems for redundancy and maintenance reasons. This subdivision of the primary loop system is listed in Table 9-2.

The result of this redundancy in all primary systems is a decisive increase of the availability. However, it requires a considerable increase in costs by both the rather large number of loops and the overcapacity installed in the cooling system. The

**Table 9.2 Subdivision of the primary loop systems**

	inboard blankets	outboard blankets
Helium:		
– number of independent systems	2	2
– number of parallel loops in each system	2	3
– design value for each parallel loop	90 MW	90 MW
Pb-17 Li:		
– number of independent systems	1	2
– number of parallel loops in each system	4	3
– design value for each parallel loop	140 MW	280 MW

total installed cooling capacity of the helium system is 76 % higher than the power to be extracted. For the Pb-17Li loops the overcapacity amounts to 46 %.

#### References

- [9-1] M. Dalle Donne (ed.), DEMO-relevant Test Blanket for NET/ITER , Part 2: BOT Helium Cooled Solid Breeder Blanket, Vol. 1 and 2, KfK 4928 and 4929 (1991).
- [9-2] C.C. Stone et al., Experience with Liquid Metal Fast Breeder Reactor Steam Generators - U.S. Design, Fusion Technol., 14 (Oct. 1981) p. 60-87.
- [9-3] Siemens AG, internal report (July 1992).

## 10. Testing of Electrical Insulators

In the Dual Coolant blanket concept the electrical insulators on the steel walls (see Chapter 3.5) serve to reduce the MHD pressure drops, which are related to the interaction of the flowing liquid alloy with the magnetic field of the torus. They have to insulate the liquid metal against the solid walls of the blanket during its whole life time. Therefore, they have to withstand liquid metal corrosion as well as the influence of irradiation for long periods of time. Tests of the corrosion resistance of the alumina layers on aluminized MANET steel and of the electrical resistance in contact with the liquid alloy at temperatures around 450 °C have been performed and are described in Section 10.1, the results of irradiation tests with alumina in the dual beam facility are reported under 10.2, and the work to prepare the irradiation tests of alumina in the HFR reactor at Petten under 10.3.

### 10.1 Tests in Pb-17Li

Cylindrical specimens of MANET steel were coated with an aluminum containing intermetallic layer by means of the hot-dip process, and this layer was covered with an oxide layer of about 5 µm thickness. High temperature oxidation at 950 °C was used to produce this alumina layer. The coated specimens were finally heat treated at 750 °C in order to condition the MANET steel. The specimens were inserted into the PICOLO loop for corrosion tests in flowing Pb-17Li alloy at 450 °C.

The specimens were placed in the central position in the test section of PICOLO, five of them were mounted in series. Thus, the liquid alloy passed the specimens in the annular shaped channel of 4 mm width. The flow velocity in this channel was maintained at 0.3 m/s ( $Re = 21000$ ), the temperature difference between the test section (450 °C) and the coldest point of the circuit (magnetic trap, 300 °C) was 150 K [10-1].

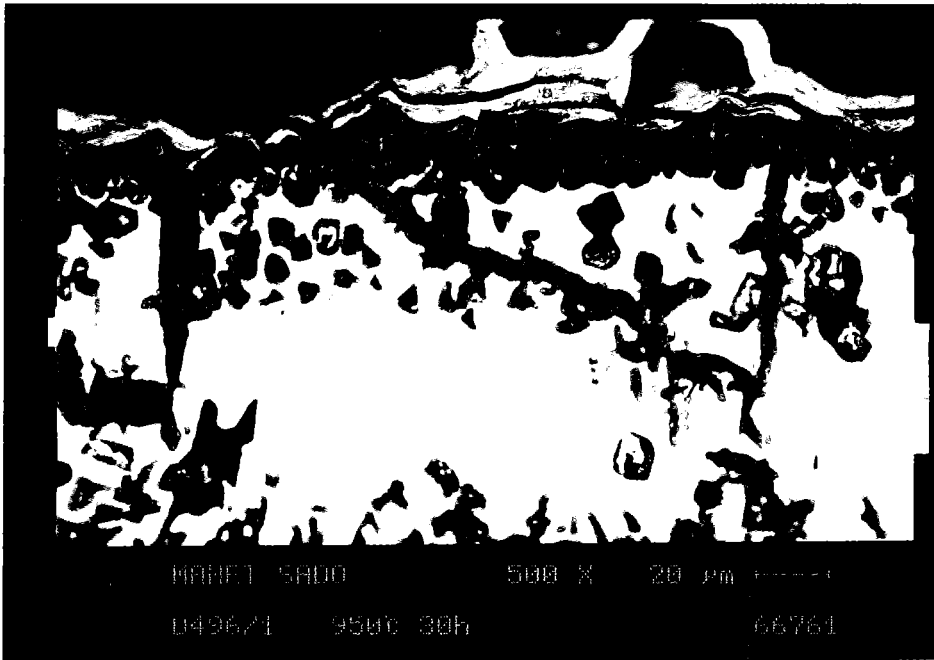
Specimens of the coated MANET steel were exposed in the flowing liquid alloy for between 1000 and 10000 hours. Interruptions of the tests allowed specimens to be extracted in a way that the materials were in contact with the environment for 1000, 2000, 3000,... and 10000 hours.

The specimens were wetted by the liquid Pb-Li alloy, which froze on their surfaces when the specimens were taken out of the test section (under Ar atmosphere). Before the examinations of the material the adhering alloy must be removed. This was performed by washing in an aqueous solution of acetic acid and hydrogen peroxide, subsequent neutralization, washing in water and drying.

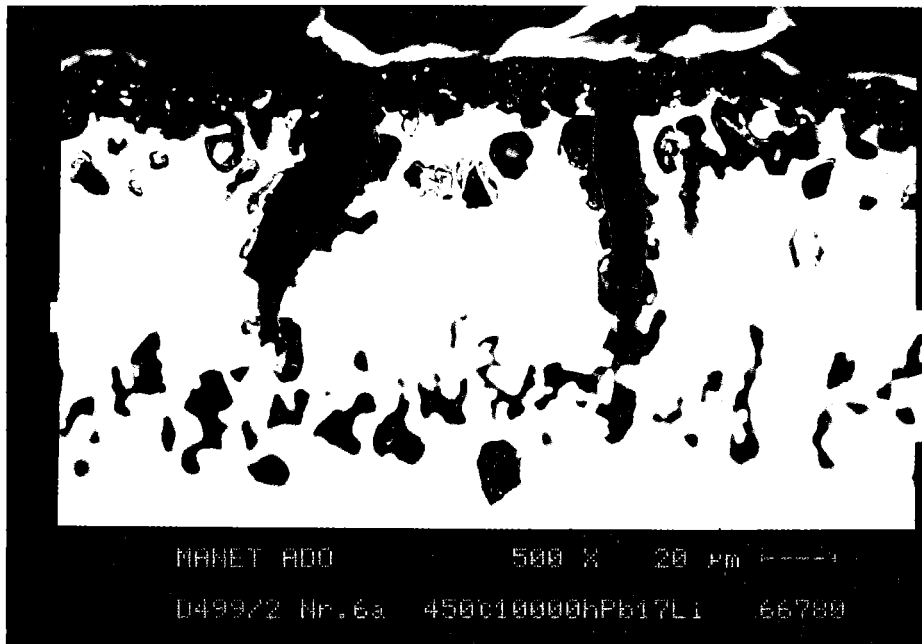
The corrosion effects were evaluated by means of microscopic examinations. Weighing was not sensitive enough to detect the very small changes of the mass of the specimens. Metallographic cross sections allowed very exact measurements of the diameters of the cylindrical bars and of the thicknesses of the layers before and after exposure to the liquid alloy. Scanning electron microscope was additionally applied for the detection of geometrical changes. Energy dispersive X-ray analysis (EDX) and Auger electron spectroscopy (AES) were used to look for changes of the compositions.

The examination of the exposed specimens resulted in encouraging data. The appearance of the surfaces did not indicate any attack of the liquid alloy on the coatings, this finding was supported by the cross-sectional views which showed unchanged thicknesses of the oxides layers of corroded specimens in comparison to unexposed ones [10-1] as is obvious from the micrographs in Fig. 10.1-1. This stability against corrosion was consistent with earlier findings concerning the chemical stability of  $\text{Al}_2\text{O}_3$  in Pb-17Li melt at temperatures up to 600 °C [10-2].

The thickness and the chemical composition of the intermetallic layer remained unchanged in the corrosion tests at 450 °C even after 10000 hours of exposure. The results of EDX measurements in cross sections of the specimens are shown in Fig. 10.1-2. The composition of the intermetallic layers is characterised by the Al content of 40 at% which showed some scatter but not a trend with the exposure time. The thickness of the aluminide layer is also not affected by diffusion of Al due to the thermal or chemical conditions. This indicates that the MANET steel should not suffer any changes due to the ingress of Al into the structure [10-3].

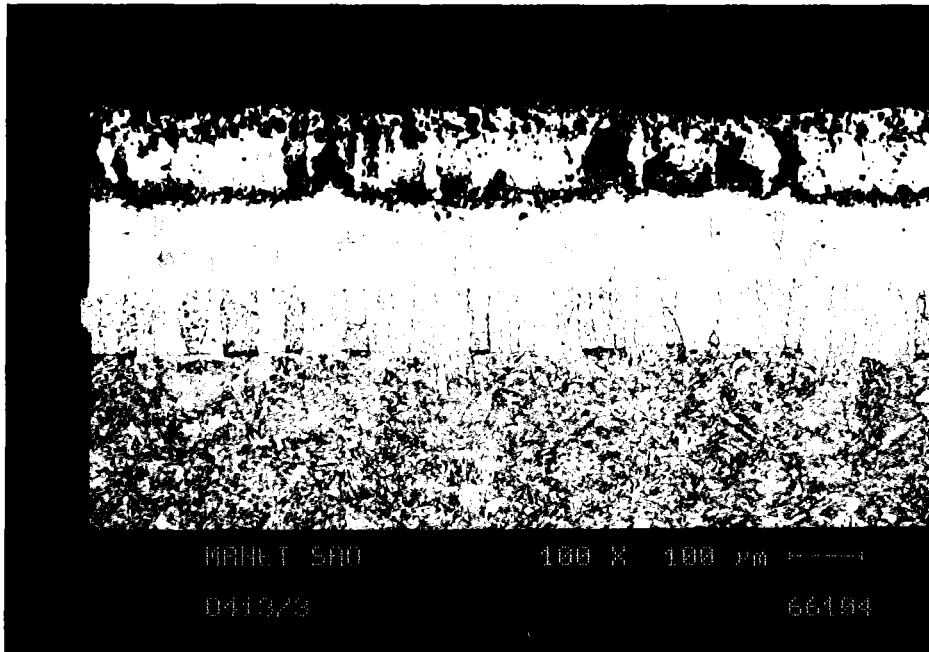


a) after fabrication

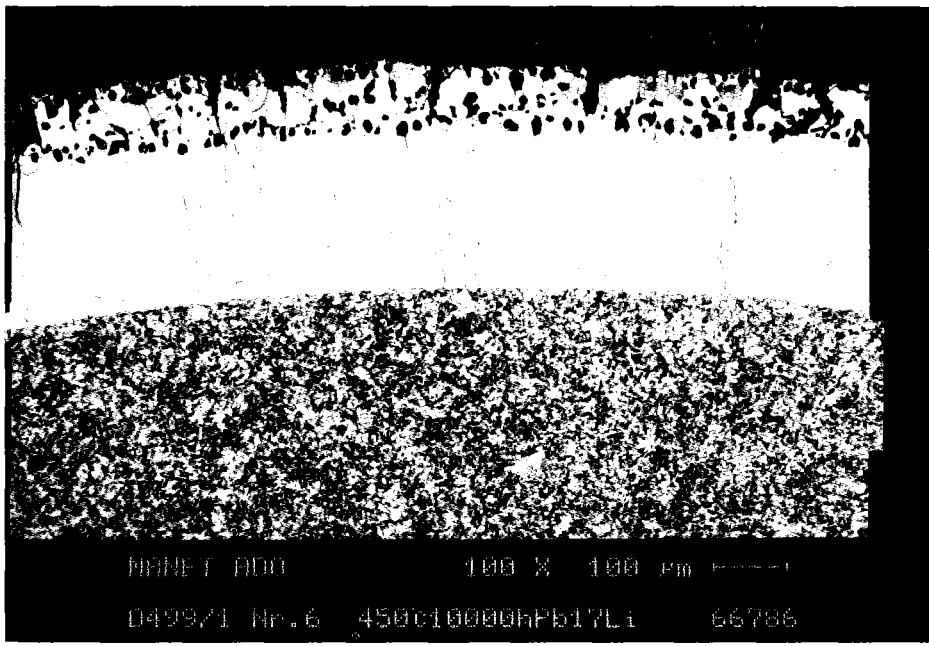


b) after 10000 hours exposure to Pb-17Li at 450 °C

Fig. 10.1-1 Micrographs showing the Al<sub>2</sub>O<sub>3</sub> layers on the aluminide



a) before exposure to Pb-17Li



b) after exposure in Pb-17Li at 450 °C

Fig. 10.1-2 Composition and thickness of aluminide layers on MANET steel

A simple experimental set-up to measure the electrical resistance of a limited coated surface in contact with molten Pb-17Li at elevated temperature was established inside a pure argon glove box. The principle of this set-up is shown in Fig. 10.1-3.

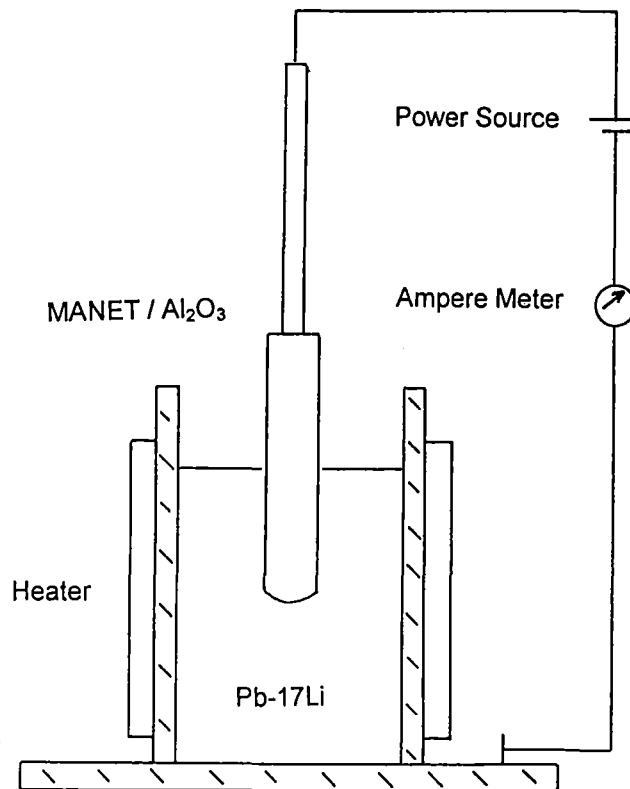


Fig. 10.1-3: Experimental set-up to measure the resistance of Al<sub>2</sub>O<sub>3</sub>-aluminide coating on steel in argon atmosphere

The set-up allows the measurement of the electrical current passing through the insulating layer on the MANET steel specimen at a voltage in the order of 1 - 2 V. The apparatus is already proved, it is ready for studies of the quality of layers and the healing of layers in contact with the liquid alloy.

## 10.2 Results of Irradiation Tests with Alumina in the FZK Cyclotron Facility

Well known in the literature is the radiation induced conductivity (RIC), which is due to the excitation of electrons from the valence into the conduction band by x- and γ-rays or charged particles. RIC has often been found to be in a wide range proportional to the density of this energetic ionizing particles and immediately disappears when the particle current is turned off. Even under intense neutron irradiation where the ionizing dose rates usually are much smaller compared to charged particle

irradiations, RIC is orders of magnitude above the thermal induced conductivity at elevated temperatures. Recently, E. Hodgson discovered an additional considerable increase in the conductivity, called radiation induced electrical degradation (RIED), during electron irradiation when an electric field is applied. In contrast to RIC, RIED has found to be of permanent character. The prime objectives of the present investigations were to produce data on the in-situ and postirradiation conductivities  $\sigma$  and  $\sigma_0$  under fusion relevant loading conditions.

Ceramic specimens have been cut from plates made of polycrystalline  $\text{Al}_2\text{O}_3$  (99.9%, Vitox) and  $\text{Al}_2\text{O}_3$  (99.2 %, Wesgo). The main impurities analysed with chemical methods are: MgO (0.09%), CaO (0.03%),  $\text{Na}_2\text{O}$  (0.03%) and  $\text{Fe}_2\text{O}_3$  (0.03%) in Vitox-alumina, as well as MgO (0.31%), CaO (0.095%),  $\text{Na}_2\text{O}$  (0.027%) and  $\text{Fe}_2\text{O}_3$  (0.076%) in Wesgo-alumina. All numbers are given in weight-%. To ensure well defined measurements of the volume conductivity, a guarded circuit design with three electrodes was used (Fig. 10.2-1). The substrate consisted of a hollow fatigue specimen with a square cross section developed for in-beam creep-fatigue experiments and was made of the European ferritic/martensitic reference steel MANET.

The setup shown in Fig. 10.2-1 served several vital function: (i) The solid state bonding between ceramic and MANET-steel removes effectively the heat deposition of the  $\alpha$ -particle beam and minimizes thermal gradients. Even in the alumina samples with its very low thermal coefficient of linear expansion the calculated temperature gradient amounted to less than 3 K during these irradiations. (ii) The solid state bonded leads guaranteed constant and small ( $< 1\Omega$ ) contact resistance. (iii) An isolated, calibrated tiny thermocouple brazed between ceramic and MANET substrate allowed to measure directly the temperature in the centre of the beam spot.

All irradiations were performed using the high energy Dual Beam Facility of the Forschungszentrum Karlsruhe, where  $\alpha$ -particles ( $\geq 104$  MeV) and protons ( $\leq 30$  MeV) can be focused onto a common target (see Table 10.2-1). For these investigations, however, only the  $\alpha$ -particle beam has been used.

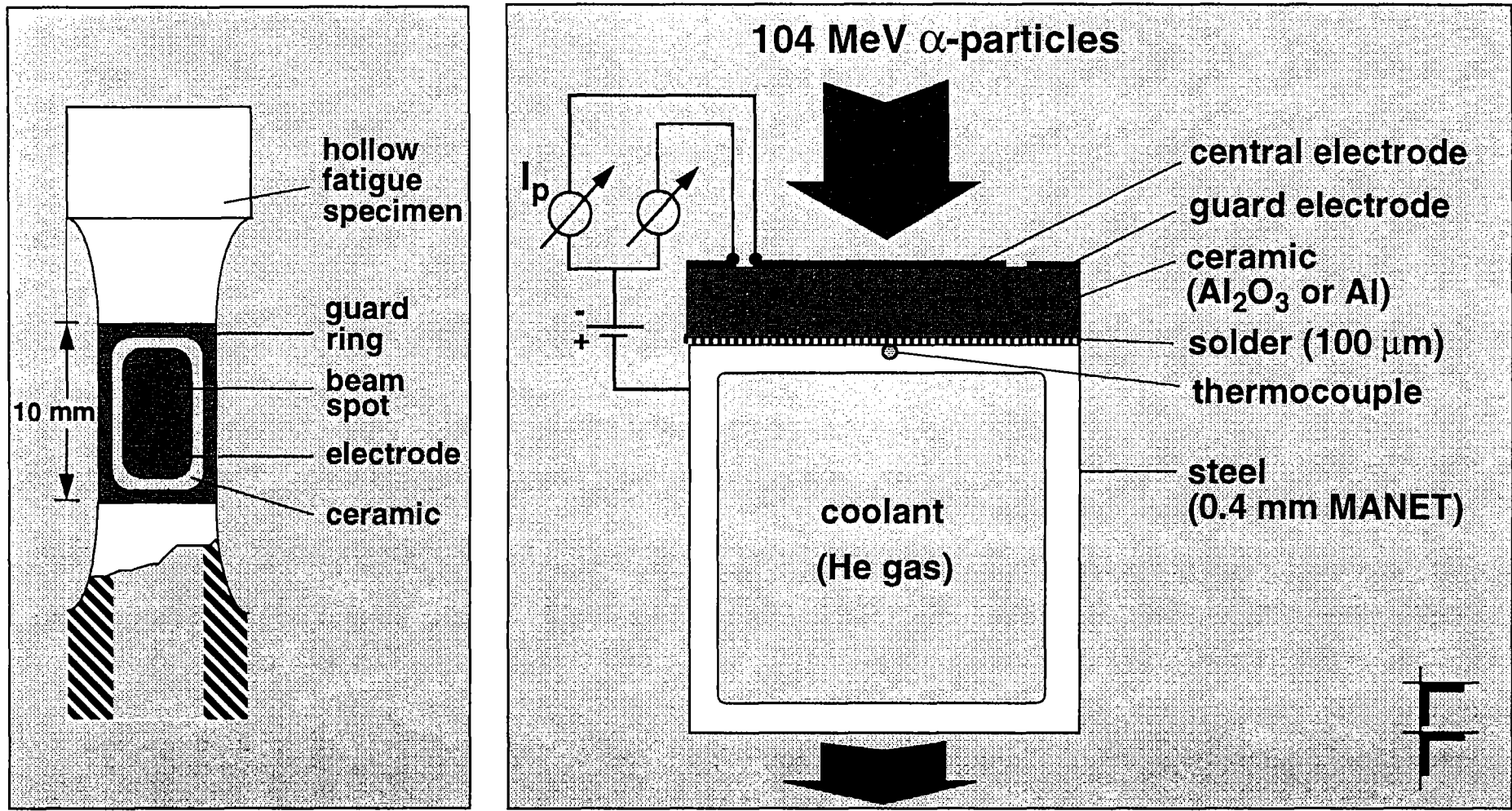


Fig. 10.2-1: Experimental set-up of the electrical conductivity measurements. A guarded circuit design was used to detect and rule out any leakage currents due to surface contaminations during irradiation.

Table 10.2-1 Irradiation conditions under which the conductivity measurements were performed

Ceramic thickness	(0.25 - 0.47) mm
E-.field (DC)	100 kV/m
$\alpha$ -particle energy	104 MeV
Displacement rate (total)	$(1.2-2.5)\times 10^{-7}$ dpa/s
Ionizing dose rate	$<(0.9-2.0)\times 10^6$ Gy/s
Irradiation temperature	250, 350, 450, 550 °C
Beam size	$\varnothing = 4$ mm
$\alpha$ -particle beam current	$(0.9-2.0)$ $\mu$ A/beam area
Vacuum (total pressure)	$(5 \pm 4)\times 10^{-6}$ mbar

Standard methods have been used to measure the DC resistance or conductivity of the ceramic specimens. Of special importance for elevated temperature irradiations under an electric field is the avoidance of significant errors due to carbon layers which may grow during the extended measuring periods at the specimen surface leading to short-circuiting currents. Therefore, the gap resistivity  $R_g$  between central and guard electrode has to be far above the volume resistivity of interest  $R_p = U_p/I_p$ , where  $U_p = (25-47)$  V is the applied voltage and  $I_p$  the measured current through the central electrode.

In the high purity *Vitox-alumina* the electrical conductivities  $\sigma$  and  $\sigma_0$  show at 450°C the highest irradiation induced electrical breakdown ever observed (Fig. 10.2-2). The  $\sigma_0$  measurements were always taken three minutes after turning off the  $\alpha$ -particle beam. Because the resistivity between the central electrode and the guard ring kept a high value of  $R_g = (6 \pm 2)\times 10^{11}$   $\Omega$  during the 115 hours of irradiation, any surface layers formed during irradiation and leading to short-circuit currents can unambiguously be ruled out. Therefore,  $\sigma$  and  $\sigma_0$  represent volume conductivity, that is, significant RIED occurs.

After irradiation  $\sigma_0$  still shows and Ohmic behaviour in *Vitox-alumina* and in contrast to unirradiated ceramics almost no temperature dependency (Fig. 10.2-3). The irreversible nature of RIED is confirmed. It is important to note, that the saturation level near  $4\times 10^{-2}$  ( $\Omega\text{m}$ )<sup>-1</sup>, reached already after 0.054 dpa, is above the critical value of about  $10^{-3}$  ( $\Omega\text{m}$ )<sup>-1</sup> necessary to avoid MHD pressure drop with 10  $\mu\text{m}$

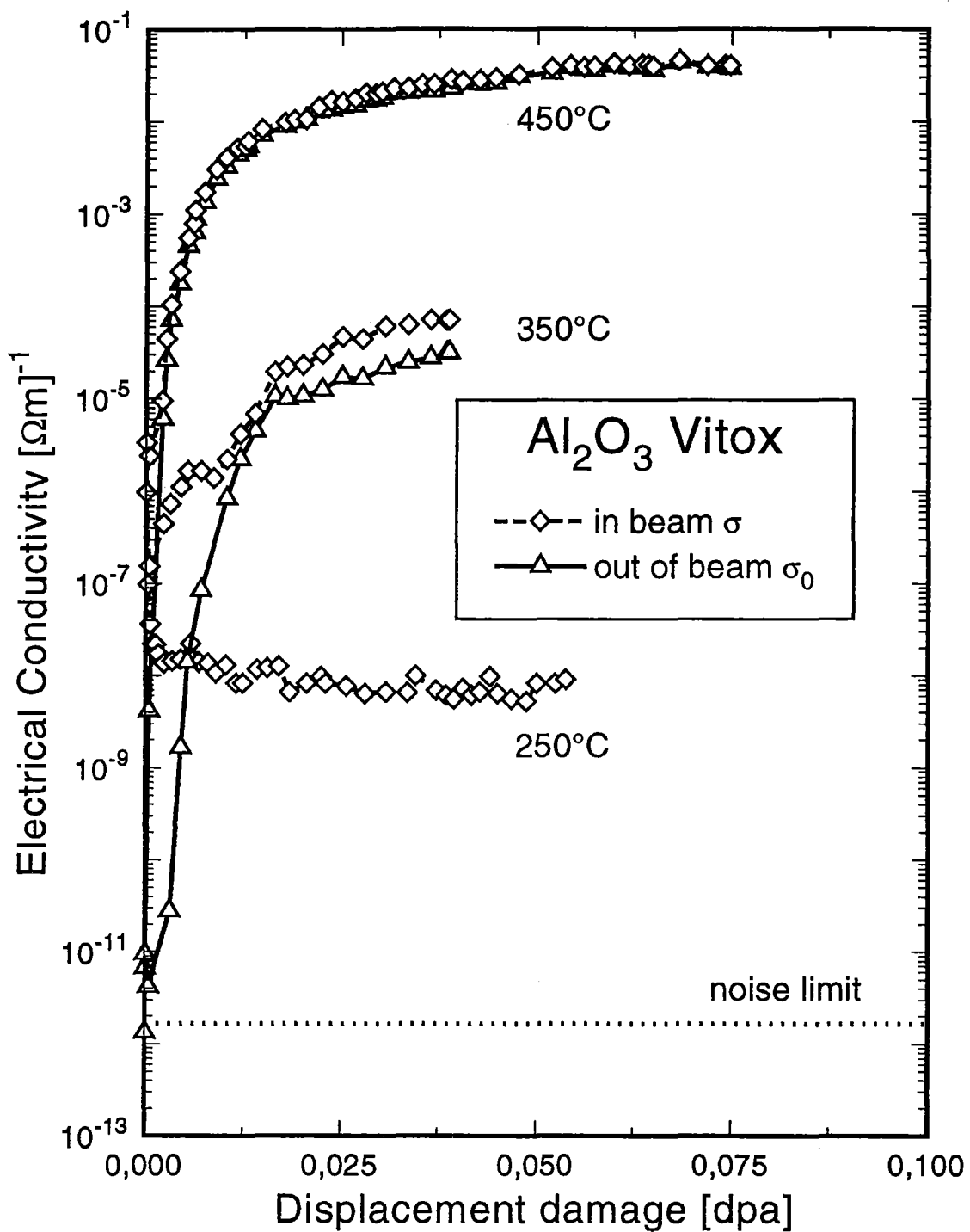


Fig. 10.2-2 Temperature dependency of the electrical volume conductivity during ( $\sigma_0$ ) irradiation in Vitox-alumina (99.9 wt%)

coatings in flowing liquid metal coolants. While at 350°C the electrical degradation is still pretty high, practically no RIED was observed at 250°C (Figs. 10.2-2 and 10.2-3). At 250°C  $\sigma$  is governed by RIC, that is by the particle beam current, and the out-of-beam conductivity  $\sigma_0$  always was below the limit of resolution of about  $10^{-12} (\Omega\text{m})^{-1}$ .

In contrast to Vitox-alumina no RIED at all has been observed up to damage levels of about 0.05 dpa in *Wesgo-alumina* (Fig. 10.2-4) at 450°C [10-9] and AlN [10-5]. The initial  $\sigma_0$  values even decrease during the early stage of irradiation. Consequently, these grades reveal a much higher resistance to damage accumulation.

At a given temperature, the difference between the in-situ conductivity  $\sigma$  and the out-of-beam conductivity  $\sigma_0$  is due to RIC. In general, RIC is strongly correlated with the Gy-production and in our experiments ranges typically from  $10^{-6}$  to  $10^{-7} (\Omega\text{m})^{-1}$ . Therefore, the total conductivity  $\sigma_0$  during irradiation can be either governed by RIC (e.g. in *Wesgo-alumina*) or by RIED (e.g. in Vitox-alumina).

The general consensus of the present data, that RIED sensitivity is at least greatly retarded in  $\text{Al}_2\text{O}_3$  grades with higher amounts of impurities, is a promising result for coating developments, but has to be confirmed also at much higher dpa-doses on suitable coatings.

### 10.3 Irradiation in the HFR-Petten

Since 1989, when Hodgson discovered the so called "radiation induced electrical degradation (RIED)" effect [10-6], many irradiation experiments have been done [10-7 - 10-13] with electrons, protons, alpha's and neutrons and  $\text{Al}_2\text{O}_3$  as isolator material. During most of these tests, the electrical conductivity did not exceed  $1 \cdot 10^{-3} \Omega^{-1}\text{m}^{-1}$  and often showed a saturation effect. Only two experiments yielded values up to  $4 \cdot 10^{-2} \Omega^{-1}\text{m}^{-1}$  but at higher ionizing to displacive ratio of at least  $1.6 \cdot 10^{12}$  Gy/dpa [10-12] or a temperature of 590 °C [10-13]. On the other hand, in none of the experiments a displacement dose of 1 dpa was exceeded.

To investigate the behaviour of  $\text{Al}_2\text{O}_3$  under fusion relevant conditions, experiments will be carried out in the HFR Petten. With the assumption that the thickness of such insulators is about 10  $\mu\text{m}$ , the insulator conductivity must not exceed  $10^{-3} \Omega^{-1}\text{m}^{-1}$ . The operating conditions in the blanket are: coolant temperature up to 450 °C, applied electrical field 1 kV (DC)/cm, neutron flux ( $E_n > 0.1$  MeV)  $8 \cdot 10^{14} \text{n}/(\text{cm}^2 \cdot \text{s})$ , which equals a displacement rate of  $5 \cdot 10^{-7}$  dpa/s,

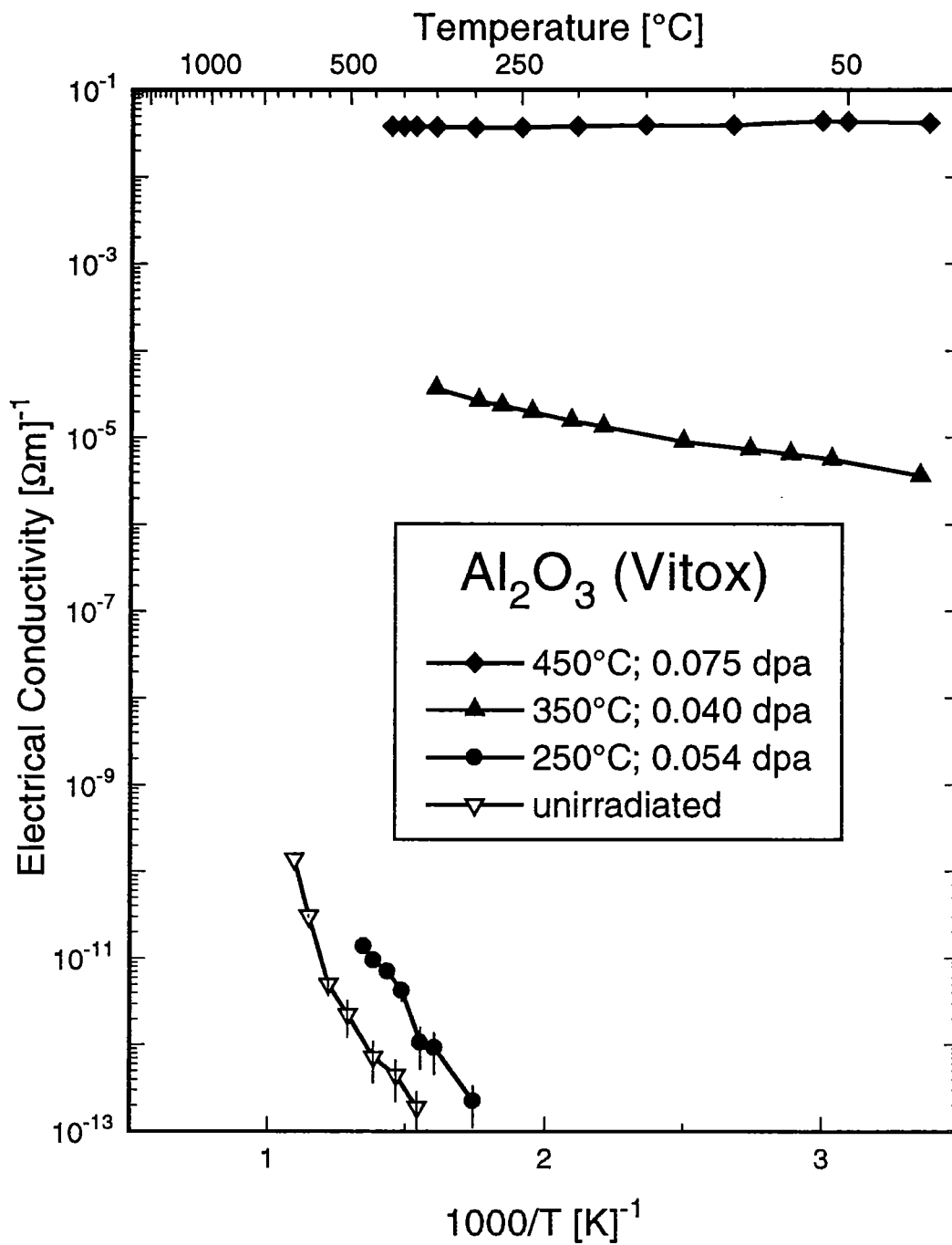


Fig. 10.2-3: Temperature dependency of the conductivity ( $\sigma_0$ ) before and after irradiation. All measurements were performed in high vacuum.

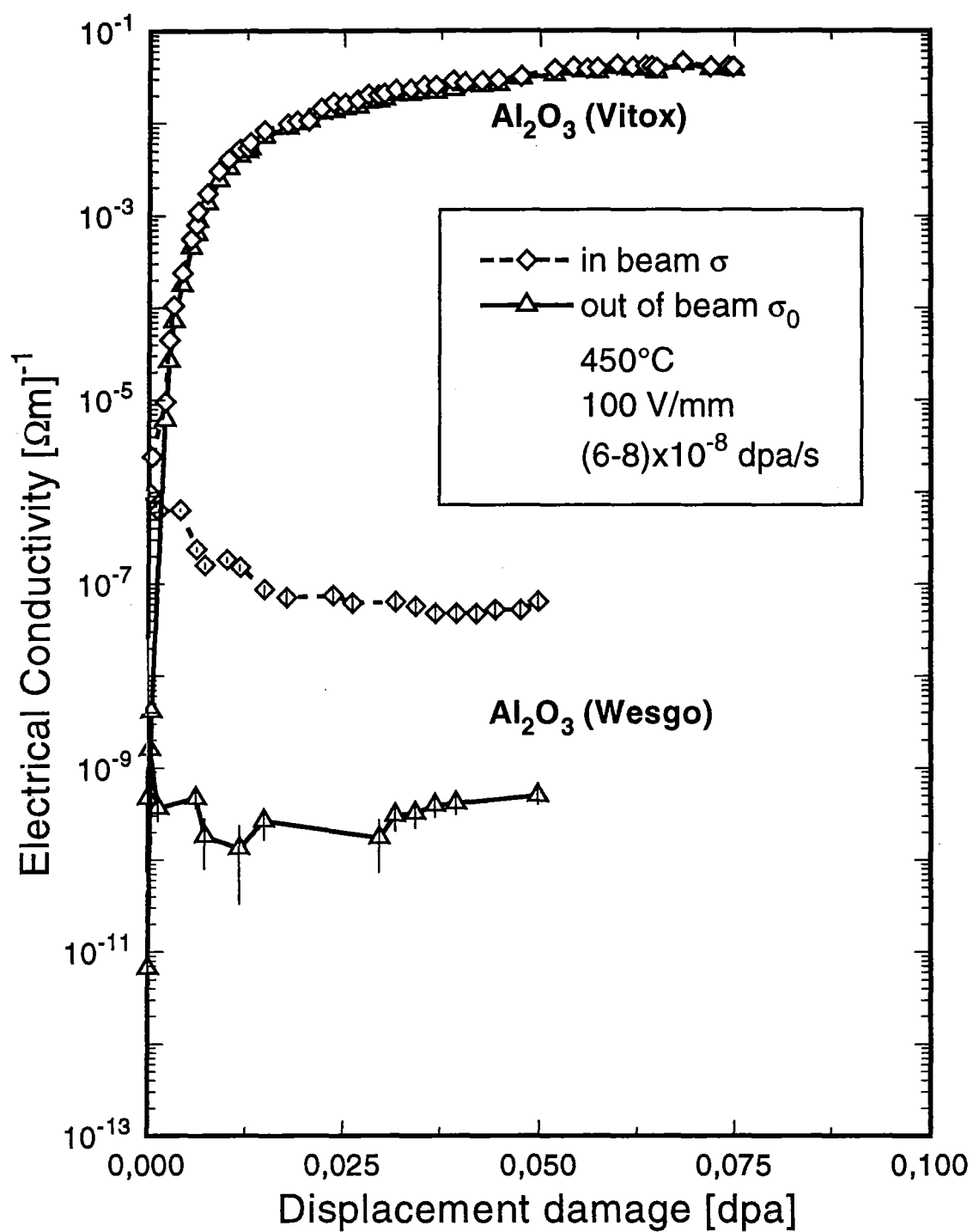


Fig. 10.2-4: Electrical volume conductivity during ( $\sigma$ ) and after ( $\sigma_0$ ) irradiation in Vitox-alumina (99.9wt%) and Wesgo-alumina (99.2 wt%) at 450°C.

and a gamma dose rate of  $1 \cdot 10^3$  Gy/s. The resulting ionizing to displacive ratio is  $2 \cdot 10^9$  Gy/dpa. The expected blanket segment lifetime is 20000 hours of full power operation, corresponding to a displacement dose in  $Al_2O_3$  of 36 dpa, which is the goal fluence of the experiments.

In the first test series, four highly pure (99,8 %) bulk plates of 14 mm diameter and 0.5 mm thickness will be used. They are on both sides covered with vapor-deposited metal electrodes to be connected with the electrical leads for voltage, guard and current. The probes are separately placed inside inner capsules, which are evacuated. These inner capsules are placed inside outer capsules, which are cooled by reactor water. By changing the gas-mixture inside the gaps between inner and outer capsules the temperatures of the inner capsules can be controlled. The outer capsules will be inserted in a special rig of the type TRIO-131, which will be placed into one of the experimental in-core positions of the HFR Petten. The actual capsule design of the irradiation device is shown by Fig. 10.3-1. The irradiation will start at the end of 1995.

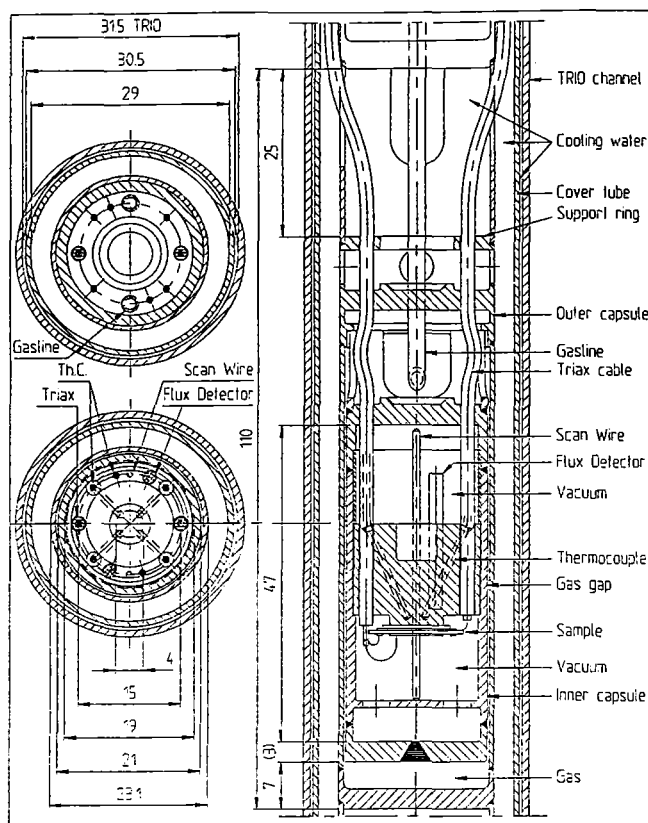


Fig. 10.3-1 Capsule for n-irradiation of  $Al_2O_3$  in HFR Petten

## References

- [10-1] H.U. Borgstedt, H. Glasbrenner, Z. Peric "Corrosion of insulating layers on MANET steel in flowing Pb-17Li" 6th Internat. Conf. on Fusion Reactor Mater., Stresa, Sept.27-Oct.1, 1993; J. Nucl. Mater. 212-215 (1994) 1501-03
- [10-2] H. Glasbrenner, H.U. Borgstedt, Z. Peric "Compatibility of Insulating Materials in Pb-17Li Alloy" in "Material Behaviour and Physical Chemistry in Liquid Metal Systems II", Karlsruhe, March 16-18,1993, 95-104.
- [10-3] H.U. Borgstedt, H. Glasbrenner "The development of a direct insulation layer for liquid metal cooled fusion reactor blanket", Fusion Eng. and Design 27(1995) 659.
- [10-4] A. Möslang, E. Daum and R. Lindau "Irradiation-induced electrical conductivities of AlN and Al<sub>2</sub>O<sub>3</sub> at 450°C", 18th SOFT, Karlsruhe, 22-26 Aug., 1994.
- [10-5] R. Lindau and A. Möslang "Electrical conductivity of the ceramic AlN under irradiation" to be presented at the Internat. Conf. on Fusion Reactor Materials (ICFRM-7), Obninsk, 25-29 Sept. 1995.
- [10-6] E.R. Hodgson; Cryst. Latt. Def. Amorph. Mater 18 (1989) 169.
- [10-7] Y. Chen, B.D. Evans, R. Gonzalez and C.H. Sellers; Phys. Rev. B 49, No. 0, (1994).
- [10-8] G.P. Pells; J. Nucl. Mater 184 (1991) 177.
- [10-9] G.P. Pells; J. Nucl. Mater 184 (1991) 183.
- [10-10] T. Shikama, M. Narui, Y. Endo, T. Sagawa and H. Kayano; J. Nucl. Mater. 191-194 (1992) 575.
- [10-11] K. Noda, T. Nakazawa, Y. Oyama and H. Maekawa; ISFNT-3, Los Angeles, June 26-July 1, 1994; to be accepted in Fusion Engineering and Design.
- [10-12] A. Möslang, E. Dam, R. Lindau; Irradiation-induced electrical conductivities of AlN and Al<sub>2</sub>O<sub>3</sub> at 450 °C, 18th SOFT, Karlsruhe, 22-26 Aug., 1994.
- [10-13] F. Clinard, E.H. Farnum, J.C. Kennedy, T. Shikama, W.P. Sommer; "LASREF 1992 neutron irradiation in-situ ac measurements" in "Dynamic Effects of Irradiation in Ceramics", a US/Japan Workshop, Santa Fe, New Mexico November 11-14, 1992.

## 11.0 Safety and Environmental Impact

This section summarises the safety considerations performed for the Dual Coolant blanket (Section 2.2) in the frame of the blanket concept selection exercise as briefly described in [11-1] in five chapters: (1) blanket materials and toxic materials inventory, (2) energy sources for mobilization, (3) fault tolerance, (4) tritium and activation products release, and (5) waste generation and management. The assessment is based (in contrast to [11-1]) on the latest cooling system design, comprising 10 Pb-17Li circuits and 10 helium circuits for the first wall cooling. The results are highlighted below:

### Blanket and loop material inventories

The total blanket volume (all inboard and outboard segments, full toroidal coverage) amounts to 1020  $m^3$  with fractions of 40/41/16/3 percent for steel/Pb-17Li/helium/void, respectively. The loop arrangements account for redundancies, leading to an overpower capacity of 50 % from nominal. Considering this fact, the total Pb-17Li inventory amounts to  $14.8 \times 10^6$  kg and the total helium inventory amounts to 6300 kg (970  $m^3$ ) with 53-60 % of the inventory being in the piping.

### Toxic material inventories

The tritium inventories in fluids are small, i.e., 57 g in Pb-17Li, <6.3 g in helium, and  $\approx 0.4$  g in NaK. The major part (100 g) is in the cold traps. Activation products inventory in MANET decays slowly, reaching hands-on levels only after very long times (10<sup>5</sup> years). The Al contained in the insulation layer contributes to less than 1 %.

### Energy sources for mobilization

The main energy sources for mobilization result from decay heat and work potential of helium. The chemical energy potential of lithium is also high but the extent of reaction is very limited. The decay heat would cause adiabatic temperature rises in isolated parts of the blanket of about 0.15 K/s in the first wall, 15 K/day in the shield and in the Pb-17Li, and 50 K/h in the mixed material of the outboard blanket. The helium inventory from one outboard cooling subsystem would pressurise the vacuum vessel in the case of a LOCA to 0.45 MPa which is below the expected design pressure. The release times are short (few seconds) and the momentum forces of a double-ended major pipe break are high (2000 kN). Chemical

reactions between Pb-17Li and water, air, nitrogen, and concrete have been reviewed and found to be moderate.

### **Fault tolerance**

Induced peak stresses caused by disruptions are predicted to be moderate (73 MPa), but the modelling needs refinement. Short term LOCA temperature excursions in the blanket structure of the order of 100 K above steady state levels for the assumed cases do not threaten the blanket integrity.

### **Tritium and activation product release**

The early and chronic dose for overly conservative tritium release scenarios from Pb-17Li, helium, and NaK are close to, or beyond, dose limits presently discussed. An activation products release scenario from a major Pb-17Li spill yields a moderate early dose of 10 mSv. Hg-203 is by far the dominating nuclide contributing with 98.9 % followed by Po-210 and tritium.

### **Waste generation**

The total amount of structural material from one complete set of blanket segments (without demountable and permanent shield) to be disposed of amounts to 1400 tons ( $180 \text{ m}^3$ ) with decay heats one year after shutdown ranging from  $1.6 \times 10^4 \text{ W/m}^3$  for first wall material down to  $2.6 \times 10^2 \text{ W/m}^3$  for the removable shield.

## **11.1 Blanket Materials and Toxic Materials Inventory**

### **11.1.1 Volumes and Volume Fractions in the Blanket Segment**

The total volume in different parts of the Dual Coolant blanket and the volume fractions of steel, Pb-17Li, helium and void have been calculated for the inboard blanket and for the outboard blanket. The basis for the calculations is the vertical cross section for the DEMO reactor and the midplane cross sections of inboard and outboard blanket segments as shown in [11-1]. The main dimensions used in the calculations are tabulated in Table 11-1.

Table 11-1 MAIN DIMENSIONS OF BLANKET

Item	Length (cm)
<b>Outboard Blanket</b>	
Major radius to first wall at midplane	827.4
Radius of curvature of first wall (poloidally)	475
Poloidal angle of circular section relative to midplane (deg.)	-52 to + 48 <sup>1)</sup>
Radius of first wall upper section	650
Length of upper section	240
<b>Inboard Blanket</b>	
Radius of first wall at midplane	430
Length of vertical section	800
Length of upper divertor section (45 degrees inclined)	250
Length of lower divertor section (-45 degrees inclined)	250

1) Note that this is not identical to the assumption  $\varnothing = \pm 45^\circ$  made in the neutronics analysis of Chapter 4.

The computed volumes for the blanket sections (outboard central part with upper extension, and inboard central part with top and bottom extensions behind the divertors) are listed in Table 11-2. The total blanket volume amounts to about 1020 m<sup>3</sup> with volume fractions of 40/41/16/3 percent for steel/Pb-17Li/He/void, respectively.

Table 11-2 VOLUME OF DUAL COOLANT BLANKET (in m<sup>3</sup>)

Blanket Part	Steel	Pb-17Li	Helium	Void
Outboard center	199	269	112	13
Outboard top	44	59	24	4
<b>Outboard total</b>	<b>243</b>	<b>328</b>	<b>136</b>	<b>17</b>
Inboard center	90	52	16	8
inboard top	36	20	6	3
inboard bottom	36	20	6	3
<b>Inboard total</b>	<b>162</b>	<b>92</b>	<b>28</b>	<b>14</b>
<b>Outboard + Inboard total</b>	<b>405</b>	<b>420</b>	<b>164</b>	<b>31</b>
<b>Total blanket volume</b>	<b>1020</b>			

In the outboard blanket most of the steel is located in the back of the blanket with only 3 % of the total steel volume being in the first wall region. The Pb-17Li volume contained in the first channel row (next to the first wall with upward flow) amounts to about 16 % of the total Pb-17Li volume in the blanket segment. In the inboard, the fraction of steel in the first wall is also about 3 % of the total steel volume. The fraction of Pb-17Li in the first channel row is here 34 %. A more detailed list of the steel volume in the first wall and of the Pb-17Li volume in the first channel row for the different blanket parts is given in Table 11-3.

**Table 11-3 VOLUME FRACTIONS OF STEEL AND Pb-17Li IN DIFFERENT BLANKET PARTS**  
 Volumes are given in  $m^3$  and in percent of the total material volume in the respective blanket part

Blanket Part	Steel volume in first wall		PB-17Li volume in first channel row	
	( $m^3$ )	(%)	( $m^3$ )	(%)
Outboard center	5.89	2.96	41.7	15.5
Outboard top	1.51	3.4	9.6	16.2
Outboard total	7.4	3.04	51.3	15.6
Inboard center	2.88	3.18	17.6	33.8
inboard top	1.09	3.0	6.7	33.4
inboard bottom	1.09	3.0	6.7	33.4
Inboard total	5.05	3.1	31.0	33.6
Outboard + Inboard total	12.452	3.06	82.3	19.6

### 11.1.2 Coolant Inventories

Coolant inventories in the primary cooling circuits of the dual coolant blanket have been calculated for the piping system along with estimates for other components like steam generators, pumps, purification systems, and expansion vessels.

The loop arrangements and thermal power per loop have been taken as described in Chapter 12, accounting for redundancies. This leads to larger power capacities as compared to the nominal power to be removed from the blanket segments. Hence, the loops (except for the feeders between the ring collectors and the blanket segments) become substantially larger than would be required for the nominal power capacity. Table 11-4 gives an overview of the nominal thermal power to be removed by Pb-17Li and helium from the inboard and outboard blanket segments. It also shows the redundancy factors foreseen and the required power capacities in the external loops, which results from equation 11.1. As a consequence of this layout the feeders have to be dimensioned for their share of the nominal power, whereas the external loops (including the ring collectors and the components) have to be dimensioned for the case that one circuit of the subsystem has failed (Table 11-4).

**Table 11-4 THERMAL POWER AND REDUNDANCY FACTORS FOR PRIMARY COOLING CIRCUITS**

<b>Blanket Region and Coolant</b>	<b>Thermal power per segment (MW)</b>	<b>No. of blanket segments</b>	<b>No. of primary circuits</b>	<b>Redundancy factor</b>	<b>Power capacity per circuit or total (MW) (nominal power in brackets)</b>
Outboard blanket (Pb-17Li)	23.1	48	2 x 3	1.5	277 (185)
Inboard blanket (Pb-17Li)	13.8	32	1 x 4	1.33	147 (110)
Total blanket (Pb-17Li) (48 Outboard + 32 Inboard Segments)	1550	80	10		2250 (1550)
Outboard blanket (helium)	6.9	48	2 x 3	1.5	83 (55)
Inboard blanket (helium)	5.8	32	2 x 2	2	93 (46)
Total blanket (helium) (48 Outboard + 32 Inboard Segments)	517	80	10		870 (517)
Total blanket (Pb-17Li + helium)	2067	80	20		3120 (2067)

**Note:** The redundancy factor is expressed in the same terms as the unavailability assessment (Chapter 12). All subsystems consisting of  $n$  circuits ( $n=2,3$ , or  $4$ ) are designed in a 2-out-of- $n$  redundancy, meaning that two systems must fail for the plant to be unavailable, For instance, for a 2-out-of-3 subsystem to be unavailable, 2 circuits must fail. Hence, it is available, if 1 circuit fails, in which case the remaining circuits have to take 1.5 times the nominal power. In the same way the redundancy factor of 2 corresponds to a 2-out-of-2 subsystem, and the redundancy factor of 1.33 corresponds to a 2-out-of-4 subsystem.

The required power capacity per circuit (in the event that one circuit of a subsystem had failed) has been calculated by use of the following equation. Note that due to the redundancy the overall power capacity of the cooling systems (3120 MW) is 51 % larger than the nominal power to be removed from the blanket (2067 MW).

$$\text{Required power capacity per circuit} = \frac{P_{\text{segment}} n_{\text{segment}}}{n_{\text{circuit}}} f_{\text{redundancy}} \quad (11.1)$$

where

- $P_{\text{segment}}$  = thermal power per segment
- $n_{\text{segment}}$  = number of blanket segments
- $n_{\text{circuit}}$  = number of primary circuits
- $f_{\text{redundancy}}$  = redundancy factor (see Table 11-4)

### 11.1.2.1 Inventories in Piping

For the Pb-17Li circulation in the outboard blanket six circuits with steam generators, pumps, purification stations, and expansion vessels are foreseen as outlined in [11-2], serving the 48 outboard segments. Each three of such circuits are joined at the ring collectors to form two 2-out-of-3 Pb-17Li subsystems, each of which supplies the coolant for one 180 degree sector of the torus. If all circuits are intact, one circuit per subsystem is in stand-by or, alternatively, all three circuits per subsystem are operated at reduced power.

Likewise, for the Pb-17Li circulation in the inboard blanket four circuits with steam generators, pumps, purification stations, and expansion vessels are foreseen, serving the 32 inboard segments. They are joined at the ring collectors to form one 2-out-of-4 redundancy. If all circuits are intact, one circuit is in stand-by or, alternatively, all four circuits are operated at reduced power.

Pipe lengths for the hot leg, cold leg, ring collectors, and feeders have been estimated to be on the order of 116 m per outboard loop (130 m per inboard loop), not accounting for parallel branches. Pipe diameters result from the flow rates necessary to remove 277 MW thermal power for the outboard circuits and 147 MW for the inboard circuits, respectively, with inlet/outlet temperatures of 275/425 °C and an assumed flow velocity of the Pb-17Li of 1 m/s. Typical pipe dimensions for the outboard/inboard circuits are 1.15m/0.83m for the main loop, 0.94m/0.72m for the ring collector, and 0.33m/0.25m for the feeders.

Concerning the helium loops for the outboard first wall cooling the loop arrangement is similar to that of the Pb-17Li system. Again, six main circuits with steam generators, circulators and clean-up systems serve the 48 outboard first wall segments. For redundancy purposes each three of such circuits are joined at the collectors to form two 2-out-of-3 helium cooling subsystems for the outboard first walls. In contrast to the Pb-17Li system each of the first wall cooling subsystems serves the full 360 degree sector of the torus in two parallel streams, requiring two inlet and two outlet helium feeders per segment. If all circuits are intact, one circuit per subsystem is in stand-by, or alternatively, all three circuits are operated at reduced power. Pipe lengths are assumed to be similar as for the helium cooled solid breeder blanket, i.e., 172 m per outboard loop, not accounting for parallel branches. Pipe diameters in the different pipe sections result from the flow rates necessary to remove 83 MW per circuit, given inlet/outlet temperatures of 250/350 °C and a system pressure of 8 MPA with an assumed flow velocity of 60 m/s. Typical pipe diameters are 0.76 m for the hot leg, 0.7 m for the cold leg, 0.6 m for the ring collectors, and 0.15 m for the feeders.

Finally, the helium loops for the inboard first wall cooling are also arranged similar to those of the Pb-17Li system. Four main circuits are foreseen, serving the 32 first wall segments. For redundancy purposes each two of such circuits are joined at the collectors to form two 2-out-of-2 helium cooling subsystems. As for the outboard each of the two first wall cooling subsystems serves the full 360 degree sector of the torus in two parallel streams. If all circuits are intact, one circuit per subsystem is in stand-by, or, alternatively, the two circuits are operated at reduced power. Pipe lengths are assumed to be similar as for the outboard except for the ring collector length and feeder lengths, resulting in a total length of 220 m per inboard loop, not accounting for parallel branches. Typical pipe diameters are 0.8 m for the hot leg, 0.73 m for the cold leg, 0.55 m for the ring collectors, and 0.14 m for the feeders.

### 11.1.2.2 Inventories in Components

The assumed coolant inventories in the circuit components are rough estimates. The dominating components are the steam generators, for which a first layout has been performed (see Chapter 12). Based on the dimensions reported, the Pb-17Li inventories result to approximately 22.5 and 11.3  $m^3$  for the 277 and 147 MW steam generators in the outboard and inboard circuits, respectively. The helium inventory in the 83 MW steam generator for the outboard first wall cooling circuit would be approximately 9.4  $m^3$  and in the 93 MW steam generator for the inboard first wall cooling circuit would be approximately 10.5  $m^3$ . Helium and Pb-17Li inventories in the blanket segments are evaluated in 11.1.1.

### 11.1.2.3 Summary of Coolant Inventories

Coolant inventories in primary cooling circuits (excluding ancillaries, such as storage tanks) are summarized in Table 11-5 for the Pb-17Li and helium circuits. The total Pb-17Li inventory amounts to  $14.8 \times 10^6$  kg (1571  $m^3$ ) and the total helium inventory amounts to 6293 kg (969  $m^3$ ). Also given in the table are the data for the subsystems. This is important in assessing leak rates in case of pipe rupture, without the capability to isolate the failed circuit in time. Thus, one Pb-17Li outboard cooling subsystem with three circuits contains 569  $m^3$  of Pb-17Li. The inboard cooling subsystem with four circuits contains 433  $m^3$  of Pb-17Li. Only part of this can be drained by gravity in case of a pipe rupture or blanket segment failure. The respective first wall cooling subsystems carry 298  $m^3$  (1934 kg) of helium to the outboard and 187  $m^3$  (1213 kg) to the inboard. Most of the coolant inventory is in the piping (53-60 %), only 18-22 % being in the blanket proper.

### 11.1.3 Toxic Inventories

Radioactive inventories in the different regions of the blanket (first wall, breeding zone and shield) as well as in the cooling systems have been assessed in two categories, i.e., tritium and other activation products. No intentional chemical toxins, like beryllium, are foreseen in the dual coolant blanket concept. Inventories are discussed for the whole blanket system, if not otherwise stated.

Table 11-5 COOLANT INVENTORIES IN PRIMARY CIRCUITS (SUMMARY)

Circuit or System	Pb-17Li		Helium	
	Volume ( $m^3$ )	Mass (kg)	Volume ( $m^3$ )	Mass (kg)
Outboard cooling circuit	190	$1.8 \times 10^6$	99.4	645
Inboard cooling circuit	108	$1.03 \times 10^6$	93	606
Outboard cooling subsystem (3 circuits)	569	$5.49 \times 10^6$	298	1934
Inboard cooling subsystem (4 circuits for Pb-17Li, 2 for helium)	433	$4.1 \times 10^6$	187	1213
All outboard cooling circuits (% in blanket/piping/ components)	1138	$10.8 \times 10^6$ (29/53/18)	596	3868 (23/55/22)
All inboard cooling circuits (% in blanket/piping/ components)	433	$4.1 \times 10^6$ (21/60/18)	373	2425 (8/68/24)
<b>Total cooling circuits (not including ancillaries)</b>	<b>1571</b>	<b><math>14.8 \times 10^6</math></b>	<b>969</b>	<b>6293</b>

### 11.1.3.1 Tritium Inventory

The tritium inventory in the breeder (Pb-17Li) is determined by the recovery process (permeation through the outer wall of the steam generator tubes into the NaK circuit) as outlined Chapter 7.1. Given an equilibrium partial pressure of 147 Pa and a Pb-17Li mass of  $15 \times 10^6$  kg (see Section 11.1.2.3), the total tritium inventory in the breeder (excluding the recovery system) amounts to 57 g. In one coolant subsystem for the outboard consisting of 3 circuits the tritium inventory is 21 g. In the subsystem for the inboard consisting of four circuits the tritium inventory is 16 g.

A considerable amount of tritium ( $\approx 4 \text{ g/d}$ ) will permeate into the helium coolant passing the first wall channels, if no credit is taken of any permeation barrier, e.g. the  $\text{Al}_2\text{O}_3$  electrical insulation at the steel/Pb-17Li interface. This tritium is assumed to be permanently removed in a tritium extraction plant, so that the tritium concentration in the helium can be kept low, say  $< 1 \text{ wppm}$  [11-3], corresponding to a total tritium inventory of  $< 6.3 \text{ g}$  in  $6300 \text{ kg}$  of helium. This is partitioned into four subsystems as outlined in section 11.1.2.1.

The tritium inventory in the NaK circuits has been derived in Chapter 7 to be  $0.38 \text{ g}$  in a total of  $4.1 \times 10^4 \text{ kg}$  of NaK. Each steam generator has an independent NaK system with cold traps. Therefore, the maximum tritium inventory occurring in a single NaK subsystem for the outboard is about  $0.04 \text{ g}$ . This is small compared to the tritium trapped in the cold traps (see below).

Control of the tritium losses to the steam circuit is a common critical issue, requiring permeation barriers, a low tritium partial pressure in the NaK circuits (or in the first wall helium coolant, respectively) and control of the water/steam circuit chemistry. Estimates revealed for the NaK/water tubes in the steam generators a tritium permeation rate of  $0.12 \text{ g/d}$  ( $1200 \text{ Ci/d}$ ) for ferritic steel (for 10 steam generators) without any permeation barrier. Thus, barrier factors on the order of 120 need to be achieved in order to reduce the losses to  $10 \text{ Ci/d}$ . The first wall helium cooling system has to cope with similar problems. A tritium loss of another  $10 \text{ Ci/d}$  seems to be feasible [11-4]. The total tritium losses of  $20 \text{ Ci/d}$  ( $0.002 \text{ g/d}$ ) would accumulate to  $1.7 \text{ g}$  of tritium in the entire water/steam system after  $20000 \text{ h}$  of operation. This is considered to be acceptable (compare [11-2], [11-4]).

The tritium inventory in the recovery system is dominated by the inventory in the cold traps and amounts to about  $15 \text{ g}$  for the cold traps in one NaK circuit for an outboard steam generator (see Chapter 7.1) and approximately  $100 \text{ g}$  for all cold traps.

The tritium build-up in the structural material after  $20000 \text{ h}$  has been evaluated for the outboard blanket. The poloidally averaged concentration as a function of radius falls off linearly in a semi-logarithmic scale by four orders of magnitude, i.e., from  $3 \times 10^{-5} \text{ g}$  per kg of MANET in the first wall to  $3 \times 10^{-9} \text{ g}$  per kg of MANET in the back plate ( $20 \text{ cm}$  shield). The tritium profile weighted with the corresponding mass distribution of steel results in a total tritium inventory of  $2.2 \text{ g}$  in the central part of the outboard blanket (excluding the upper cylindrical part),

that is about 1.3 g in the first wall, 0.9 g in the steel of the breeding zone, and only 0.003 g in the back plate.

For the upper part of the outboard blanket as well as for the inboard blanket the tritium inventory has not been elaborated. Due to the small amount it is assumed that this is of the same order as the inventory in the central part of the outboard, leading to a total tritium inventory in the whole blanket structure of  $\approx 4.4$  g ( $\approx 2.6$  g in the first wall, 1.8 g in the breeding zone, and 0.006 g in the back plates). However, this does not account for the tritium implanted in the first wall from the plasma. This may be much higher and is currently assumed to range between 3 g and 300 g. It should also be noted that the solubility of tritium in MANET at a partial pressure equal to that in the Pb-17Li ( $\approx 150$  Pa) is on the order of  $10^{-5}$  g per kg of MANET at 350 °C. This is in the same range as the build-up in the first wall discussed above but is much higher than in the breeding zone and back plate. Nevertheless, a substantial take-up of tritium from the Pb-17Li will be impaired by the electrical insulation layer.

An overview of the mass and tritium inventories in the breeder material, coolants and in the major radial zones of the structural material is given in Table 11-6.

Table 11-6 RADIOACTIVE INVENTORIES IN BLANKET AND RELATED SYSTEMS

Blanket region or system	Total mass inventory (kg)	Tritium (g)
Breeder material (Pb-17Li)	$1.5 \times 10^6$	57
Primary first wall coolant (helium)	6300	<6.3
Tritium removal fluid (NaK)	41,000	0.38
Steam system	not assessed	<1.7
Tritium recovery system	mainly in cold traps	$\approx 100$
Structural material		
First wall	$10^5$	2.6
Breeding zone	$1.3 \times 10^6$	1,8
Shield	$1.8 \times 10^6$	0.006

### 11.1.3.2 Activation Products Inventory

**Activation of Pb-17Li:** The specific activity in Pb-17Li has been assessed in Chapter 4. For example, the specific activity in the outboard blanket (averaged over the liquid metal in the central plus the upper blanket part) after decay times of 0 s, 1 d, and 1 year amounts to  $3.3 \times 10^{13}$ ,  $7.0 \times 10^{11}$ , and  $3.0 \times 10^9$  Bq/kg, respectively. Corresponding values obtained for the inboard are almost the same. It is to be noted that the specific activity shortly after shutdown is dominated by the short-lived Pb isotopes, in particular Pb-207, so that after a few seconds the initial values are already reduced by one order of magnitude, and after about 1 day by another.

In the neutronics calculations performed for this analysis it was assumed that the Pb-17Li remained stationary in the blanket for the 20000 hours of operation. Given the liquid metal inventories in the blanket proper (excluding external circuits) of about 900,000 kg inboard and 3,100,000 kg outboard would result in a total activity in the Pb-17Li after decay times of 0 s, 1 d, 1 y of  $1.3 \times 10^{20}$ ,  $2.8 \times 10^{18}$ , and  $1.2 \times 10^{16}$  Bq, respectively.

Due to the circulation the specific activity will be altered. As a first approach it is assumed here that the specific activity is diluted by the ratio of the total Pb-17Li inventory in the cooling circuits to the inventory in the blanket itself. This ratio (and hence the dilution factor) is 3.5 for the outboard cooling system and 4.7 for the inboard cooling system. The total radioactive inventory is assumed to be unchanged. Table 11-7 summarises the specific and total activity in Pb-17Li in the inboard and outboard for various decay times.

**Activation of Structural Material:** The specific activity of the structural blanket material (MANET) has been assessed in Chapter 4 but has been reformatted here with view to safety aspects. Average values are deduced for major blanket regions (inboard, outboard), radial zones (first wall, breeding, shielding), and various decay times (0 s, 1 d, 1 y, 10 y, 500 y).

For instance, the specific activity in the "first wall region midplane average outboard" after decay times of 0 s, 1 d, 1 y, and 10 years is, respectively,  $6.6 \times 10^{14}$ ,  $4.0 \times 10^{14}$ ,  $2.4 \times 10^{14}$ , and  $2.0 \times 10^{13}$  Bq/kg. It is the highest specific activity in the blanket. Corresponding numbers at the inboard are about 10 % lower. In contrast to the activity in Pb-17Li the decay in MANET is very slow, i.e., only by a factor of three within the first year. In the radial direction the decrease is about one order of magnitude from the first wall to the breeding zone, and another order of mag-

nitude from the breeding zone to the removable shield. Typical radial profiles and decay curves are given in Chapter 4.

**Table 11-7 SPECIFIC AND TOTAL ACTIVITY IN Pb-17Li AFTER VARIOUS DECAY TIMES (including dilution factors of 3.5 for the outboard and 4.7 for the inboard due to circulation)**

<b>Blanket Region Inboard or Outboard</b>	<b>0 s</b>	<b>1 d</b>	<b>1 y</b>	<b>10 y</b>	<b>500 y</b>
Specific Activity Inboard (Bq/kg)	7.0E12	1.5E11	6.9E08	7.9E07	1.0E06
Specific Activity Outboard (Bq/kg)	9.3E12	2.0E11	8.5E08	1.1E08	1.1E06
Total Activity Inboard (Bq)	2.0E19	6.0E17	2.8E15	3.2E14	4.2E12
Total Activity Outboard (Bq)	1.0E20	2.2E18	9.2E15	1.2E15	1.2E13
Total Activity Inboard plus Outboard (Bq)	1.3E20	2.8E18	1.2E16	1.5E15	1.6E13

Looking at the poloidally averaged values of the specific activity in the same radial zones which combine the respective radial zones in the central and top part of the outboard, and in the central and divertor parts of the inboard one observes a reduction relative to the midplane values by typically a factor of 0.7 in the outboard and 0.4 in the inboard.

The poloidally averaged values have been used to compute the total activity in the corresponding blanket regions by weighting them with the mass inventory of MANET. Summing up over all blanket regions results in a total activity after 0 s, 1 d, 1 y, and 10 years of  $7.5 \times 10^{19}$ ,  $4.0 \times 10^{19}$ ,  $2.2 \times 10^{19}$ , and  $1.8 \times 10^{18}$  Bq, respectively, in a total steel mass of  $3.2 \times 10^6$  kg.

To summarise the activity in MANET, Table 11-8 lists the total activities after a 10 year decay period in the first wall, breeding zone, and removable shield (each one for inboard and outboard) and the corresponding steel masses. This division is of interest for waste purposes.

Table 11-8 TOTAL AND MIXED MEAN SPECIFIC ACTIVITY IN DIFFERENT REGIONS OF THE BLANKET STRUCTURE

Blanket Region Inboard or Outboard	Steel Inventory (10 <sup>3</sup> kg)	Total Activity after 10 y (Bq)	Mixed mean Specific Activity after 10 y (Bq/kg)
First wall region inboard	39	1.5E17	3.8E12
First wall region outboard	58	8.0E17	1.4E13
Breeding region inboard	454	8.8E16	1.9E11
Breeding region outboard	793	6.2E17	7.9E11
Shield region inboard	759	7.5E16	9.9E10
Shield region outboard	1019	4.1E16	4.1E10

**Activation of Insulating Layers:** The activation of the insulating layer (Al plus Al<sub>2</sub>O<sub>3</sub>) has not been elucidated but an estimation based on the effect of 500 wppm Al impurities in MANET is presented below.

If all the channel walls in contact with Pb-17Li would be covered with a 10 μm thick insulation layer consisting mainly of pure aluminum, this would result in a total Al mass in the blanket of 360 kg. The Al blended with the steel contained in the first wall and in the breeding region would correspond to an extra Al concentration in MANET of 175 wppm and 300 wppm, respectively, i.e., less than the original Al impurity of 500 wppm. The contribution of the 500 wppm of Al in MANET to the total specific activity in MANET results from activation calculations described in Chapter 4 and is only 0.005 at shutdown (mainly from Al-28) and falls off sharply to the order of 10<sup>-10</sup> after one month. At very long decay times (10<sup>5</sup> years) it comes back to the order of 10<sup>-3</sup> due to the long-lived Al-26 isotope. A similar behavior is found for the γ-dose rate. Here the contribution of the 500 wppm of Al in MANET amounts to a fraction of 0.015 at shutdown, falls off to the order of 10<sup>-8</sup> after 1 year and comes back to 0.03 after 10<sup>5</sup> years. Consequently, the contribution of a 10 μm insulation layer equivalent to an extra Al content of 200-300 wppm is below the 1 % range in terms of specific activity and γ-dose rate. Even a 50 μm thick layer would be uncritical.

A different problem may arise in the Pb-17Li dose rate due to sputtering and corrosion products carried by the liquid metal. This has not been assessed and is to be seen in the context of on-line purification (Chapter 8).

## 11.2 Energy Sources for Mobilisation

Energy sources in upset or accidental conditions are seen in (a) plasma disruptions, (b) delayed plasma shutdown after cooling disturbances, (c) decay heat, (d) work potential for pressurised coolants, and (e) exothermic chemical reactions. This section summarises the energy sources for the dual coolant blanket based on the inventories described in 11.1. An overview of the energy sources (a) to (e) is given in Table 11-9.

Table 11-9 ENERGY SOURCES FOR MOBILISATION

Energy source	Value (GJ)
Plasma disruptions (localised)	≈ 1
Delayed plasma shutdown (reference scenario)	11
Decay heat integrated over:	
1 minute	1.2
1 hour	50
1 day	550
1 month	3200
Work potential of helium coolant	9.1
Chemical energy potential	
Li/water reaction	2300
Li/oxygen reaction	3900

### 11.2.1 Energy Liberated during Plasma Disruptions

Plasma disruptions can cause local evaporation of first wall material or mobilisation of adhesive dust. This is a common and unresolved problem of first wall protection and dust processing and is not considered here. The energy source is essentially the stored energy in the plasma which is typically of the order of 1 GJ and, hence, is small compared to other energy sources discussed in the following subsections.

### 11.2.2 Energy due to Delayed Plasma Shutdown

Delayed plasma shutdown after a sudden cooling disturbance will bring any first wall to melt within seconds. The energy source is simply the time integral of fusion power from the cooling disturbance to complete shutdown. For instance, for the reference plasma shutdown scenario (plasma is shutdown 1 s after cooling disturbance; at that time the internal heat source disappears instantaneously and the first wall surface heat flux decreases linearly down to zero in 20 s) the energy transmitted to the first wall is 4.2 GJ and to the blanket 0.8 GJ per GW of fusion power (ignoring that a large fraction of the 4.2 GJ goes to the divertor). This scales up to 9.2 GJ to the first wall and 1.8 GJ into the blanket for a 2.2 GW reactor.

### 11.2.3 Decay Heat

The decay heat is the governing feature in managing the cooling disturbances like LOCA, LOFA (Section 11.3) and, in particular, loss of site power or loss of heat sink. The decay heat in the entire blanket amounts to 52 MW after shutdown and declines to 11.8 MW after 1 h, 1.53 MW after 1 d, 1.07 MW after 1 month, and 0.48 MW after 1 year. The accumulated decay heat at several times after shutdown is listed in Table 11-9, ranging from 1.2 GJ for the first minute period to 3200 GJ during the first month.

The decay heat source has to be seen in connection with the thermal inertia of the blanket and related cooling systems. High thermal inertia limits temperature transients and amplitudes in upset or faulted conditions and, thereby, contributes inherently to minimise potential consequences for a primary initiating event and eases plant control. A measure for the thermal inertia is the adiabatic temperature rise of the isolated blanket or of parts of the blanket, like the first wall, the breeding zone, or the shielding (that is the removable back plate). These temperature vs. time curves are plotted in Figure 11-1 and it can be seen that the transient for the isolated first wall is very steep, reaching a temperature rise of 300 K after about 40 minutes. In contrast, the isolated shield warms up very slowly (about 10 K per day), and likewise the Pb-17Li alone. For a mixture of the whole blanket structure (first wall, breeding zone plus shield) including the liquid metal the temperature rise amounts to approximately 280 K within the first day. So in general, the adiabatic transients (except in the first wall) are moderate, leaving sufficient time for afterheat removal measures, including establishing a natural circulation heat transport. Temperature transients in the first wall are discussed in 11.3.

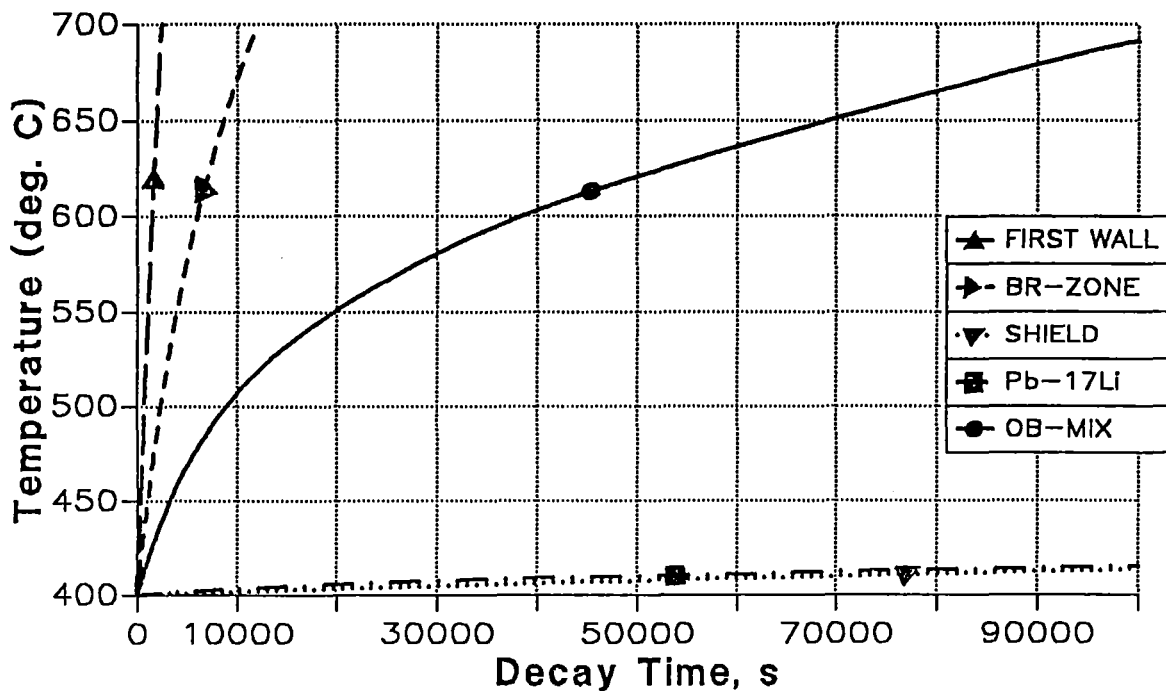


Figure 11-1 ADIABATIC TEMPERATURE RISE OF BLANKET MATERIALS DUE TO DECAY HEAT. Curves relate to isolated materials in the first wall, (MANET), breeding region (MANET or Pb-17Li), and shield region (MANET), and to a mixture of all materials in the entire outboard blanket.

#### 11.2.4 Work Potential of Helium Coolant

The first wall cooling system contains 6300 kg of helium at 8 MPa and inlet/outlet temperature of 250/350 °C, i.e., a mean temperature of  $\approx 300$  °C. The work potential relative to ambient conditions for the total helium inventory is 9.1 GJ. A more realistic scenario is the adiabatic expansion of the helium inventory from one outboard cooling subsystem, comprising three primary loops with an inventory of about 2000 kg (see Table 11-5). The corresponding work potential would be 2.9 GJ. Upon release this helium would pressurise the vacuum vessel (assuming a free volume of 5000  $m^3$ ) in the event of an in-vessel pipe rupture to 0.45 MPa. This is probably below the expected design pressure and, hence, would not require an extra expansion volume. In case a high pressure resistance of the vacuum vessel could not be achieved, the required expansion volume would be 14000  $m^3$ , when assuming 0.2 MPa as absolute end pressure.

The release times for the helium of one of the two independent outboard cooling subsystems ( $300\text{ m}^3$ ) in case of a double-ended pipe break of different cooling pipes in the primary loop were investigated. Analytical computations assuming reversible adiabatic expansion of the pressurised helium yielded draining times of 1.8/2.9/46 s for inner pipe diameters of 760/600/150 mm which belong to the hot leg, ring collector, and feeders, respectively.

To obtain an estimate of the effects of wall friction and heat transfer from the pipe walls to the helium during outflow, a simple RELAP model was established. The simulated pipe lengths were 100/100/30 m for the diameters 760/600/150 mm mentioned above. Computations with this model resulted in draining times of 2.5/4.3/72 s for the respective diameters. The longer release times are due to dissipation of kinetic energy by friction and due to decreasing density of the outflowing gas stream by heat supply from the pipe walls. Figure 11-2 shows the depressurisation of one of the two outboard first wall cooling subsystems after a double-ended break in either the hot leg, ring collector, or in one feeder.

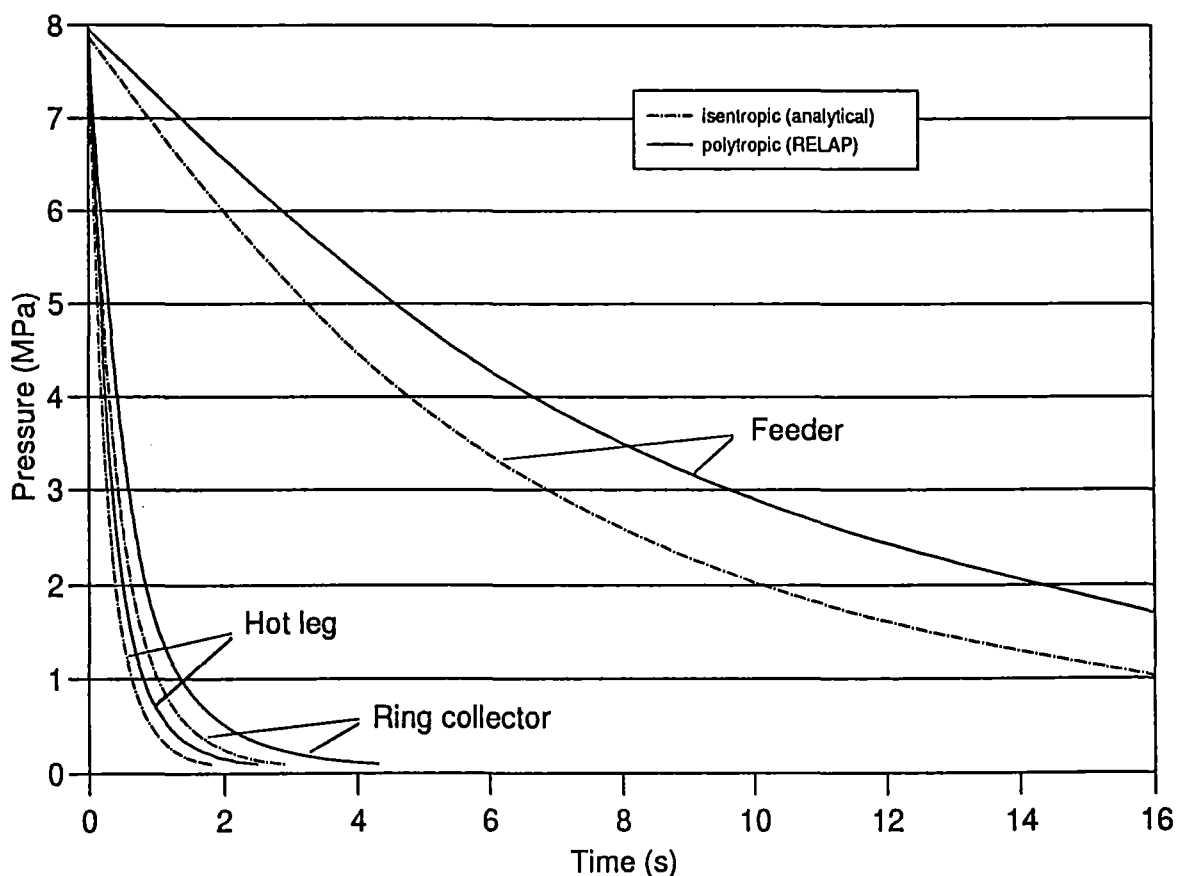


Figure 11-2 DEPRESSURIZATION OF ONE OUT OF TWO OUTBOARD COOLING SUBSYSTEMS. Curves refer to a double-ended pipe break in either the hot leg (760 mm), ring collector (600 mm), or in the feeder (150 mm).

The momentum forces of the gas stream immediately at beginning of discharge were calculated according to the mass flows and velocities obtained with the RELAP model to 2000/1100/54 kN per side for the pipe diameters of 760/600/150 mm.

The minimum release time for the helium in case of a double-ended break of a cooling channel in the first wall (cross sectional area 25 mm x 25 mm, reversible adiabatic expansion) was estimated to 22 minutes. This long time span is due to the small cross sectional area of a first wall cooling channel, which limits the outstreaming mass flow to some kilograms per second.

It should be noted that there exists a potential for the release of the helium of both cooling subsystems at the same time into the vacuum vessel in case of a crack in a segment box extending over adjacent cooling channels, each one pertaining to one cooling subsystem. Then the end pressure and, if necessary, the expansion volume discussed above would be doubled if the failure occurred in an outboard first wall. A similar occurrence in the inboard first wall would have less consequences because of the smaller helium inventory.

### 11.2.5 Exothermic Chemical Reactions

Chemical reactions may occur between Pb-17Li and water, air, nitrogen if used as inert gas in rooms, and concrete in various accident scenarios. These processes have been reviewed in [11-5] and found to be moderate. A summary of the experimental evidence from a literature review is given below.

#### 11.2.5.1 Pb-17Li-Water Reactions

In contrast to pure lithium the reaction of Pb-17Li with water in an open pool has been found to be modest or mild in a wide range of melt temperature (up to 600 °C) [11-6][11-7]. Water addition to excess alloy melt at 600 °C led to an increase in the temperature to 652 °C. The amount of hydrogen released during the reaction was 0.22 mol H<sub>2</sub>/mol H<sub>2</sub>O.

Small scale reaction kinetics studies have shown low reactivity of Pb-17Li with water compared with other alloys with higher lithium concentration and lithium [11-8]. For instance, the reaction rate of lithium with steam was found to be two

orders of magnitude higher than that of Pb-17Li at 400 °C. Measured mean reaction rates were 0.05 mol/(m<sup>2</sup>s) and 4.0 mol/(m<sup>2</sup>s) for Pb-17Li and Li, respectively.

On the other hand, an intermediate scale Pb-17Li alloy-steam reaction test [11-9] identified areas of concern to be pressurization of containment and generation of hydrogen, aerosols, moderately high temperatures and corrosive reaction products. In this test, steam at 335 °C was injected into 200 kg of Pb-17Li at 500 °C at a rate of 5 g/s for 325 s. Practically all of the lithium in the alloy reacted to form Li<sub>2</sub>O and LiOH. The amount of hydrogen generated was 0.56 molH<sub>2</sub>/molH<sub>2</sub>O. The lead in the alloy did not react with steam at this temperatures. The bulk Pb-17Li temperature rose to 870 °C. Aerosols produced from steam reactions of lithium amounted to 0.25 mg per kg alloy. The maximum suspended mass concentration of lead and lithium was 3.9 and 8.4 mg/m<sup>3</sup>, respectively.

At Westinghouse, 500 g of water were injected into 200 kg of alloy at 532 °C [11-10]. One mole of hydrogen was formed for each mole of water reacted, and aerosols were released.

More recently, a cooperative CEC-DOE fusion safety test was conducted by injecting 1.2 kg of water into 475 kg of lithium-lead alloy at 500 °C [11-11]. 99.8 % of the water reacted and 0.57 mol of hydrogen was released per mol of water reacted. The water injection was self limiting. The maximum pressure attained in the reaction module was limited to that of the water supply pressure. Aerosol products identified were mainly lead and lead oxide.

Simulation of water leakages into liquid alloy with the BLAST facility (Ispra) has shown that mixing is the governing factor in the Pb-17Li-water interaction process [11-8][11-12]. It was found that the pressurization in the reaction vessel depends strongly on the hydraulic constraints of the Pb-17Li pool. With a low flow resistance between the reaction vessel and the expansion vessel the pressurization in the reaction vessel did not exceed the water injection pressure. However, with a large flow resistance pressure pulses in excess of the injection pressure were observed [11-12]. With view to the vapour explosion hazards it has been concluded in [11-12] that the BLAST experiments indicated that the chemical reaction is self-limiting and, due to the hydrogen generation and production of solid LiOH and Li<sub>2</sub>O, the melt is partially isolated from the water so that energetic vapour explosions appear unlikely under the mixing conditions tested. Reservations have been made to this statement for small leakage.

### **11.2.5.2 Pb-17Li-Air Reactions**

The reaction of an eutectic lithium-lead pool with air (humidity less than 70 %) is negligible. Even at 900 °C no violent reaction could be observed [11-13].

Low reaction rates (weight gain) at temperatures up to 500°C have also been reported in [8-27] to range between 0.5 (mg/cm<sup>2</sup>)/h at 300°C and < 100 (mg/cm<sup>2</sup>)/h at 500°C in "room air" and 1 - 2 orders of magnitude less in dry air. Unlike the oxidation of molten lead which is diffusion-controlled, the mechanism of oxidation of molten Pb-17Li has been found to be complex.

Fusion safety tests with Pb-17Li alloy breeder material have been conducted by Westinghouse Hanford Company in cooperation with CEC in Ispra. HEDL tests in air with up to 200 kg of Pb-17Li and spill temperatures of 714 °C show no temperature increase [11-10]. At 450 °C no aerosol formation and no containment pressurization was observed, only a thin oxide layer was formed on the surface. At 700 °C, some lithium aerosols and lead aerosols were released.

Similarly, JRC-Ispra tests have confirmed that no ignition occurred in 700-800 g of Pb-17Li tests up to 1050 °C [11-13]. But, in heating the alloy to 1050 °C in an open crucible, oxide layers were formed and removed during heat-up.

An alloy spray in air reaction test (HEDL) indicated that there was no significant containment pressurization or temperature increase due to chemical reactions. Pb-17Li at 720 °C was sprayed into air producing lithium and lead aerosols [11-10].

According to Piet et al. [11-14], the low severity of the Pb-17Li-air reaction comes from (a) the lower amount of lithium in Pb-17Li (0.68 % by mass), (b) the ability of the lead to act as heat sink, and (c) lithium becoming depleted near the Pb-17Li surface. Furthermore, the chemical activity of lithium is relatively low even in the liquid alloy [11-15].

### **11.2.5.3 Pb-17Li-Nitrogen Reactions**

A lithium-lead alloy pool reaction test with nitrogen showed that nitrogen is the least reactive of atmosphere gases. The alloy-nitrogen reaction up to 500 °C produced no aerosols, very little heat and no combustible gas [11-15].

#### 11.2.5.4 Pb-17Li-Concrete Reactions

A medium scale Pb-17Li-concrete reaction test was performed at HEDL [11-10]. 200 kg of lithium-lead alloy at 600 °C were poured on top of a basalt concrete test article. The reaction was quite mild. In fact, heaters had to be turned on to keep the test at 600 °C. Hydrogen gas was released, about  $0.45 \text{ molH}_2/\text{molLi}$ , close to the maximum of  $0.5 \text{ molH}_2/\text{molLi}$ . Thus, the Pb-17Li did react with water of the concrete. However, there was no reaction with solid concrete constituents.

### 11.3 Fault Tolerance

The following analyses of electromagnetic forces and temperature transients have been performed in order to show whether this blanket system is tolerant against transients and accidental conditions.

#### 11.3.1 Behavior during Electromagnetic Transients

Electromagnetic forces and induced stresses caused by disruptions have been analyzed with the CARIDDI code. The 3D eddy current code has been improved in several aspects, so that it is possible now to take into account toroidally conducting structures and to model a dynamic plasma behavior. Additionally, an interface to the FEM structural program ABAQUS has been developed.

With the latest version of CARIDDI which is now running on UNIX workstations further computations for the Dual Coolant blanket concept were conducted. For example, the loading of the blanket subjected to a so-called design plasma disruption (20 MA decaying linearly within 20 ms) was determined. The maximum von-Mises stress of 73 MPa occurs in the internal radial wall next to the side wall (see Figure 11-3). Because of the assumed rigid fixing at the back side the eddy current damping of the structural parts is small (Figure 11-4) and may be neglected.

With the aid of the new features of CARIDDI and with a simple model for the blanket the influence of the electrically conducting first wall was investigated. In contrary to earlier investigations the time function of the plasma current was not prescribed any more. Instead, the plasma could evolve freely. Nevertheless, the results proved the former expectation that a toroidally conducting first wall will reduce the induced currents and forces. Although the magnetic induction in-

creases decisively in the domain of the blanket, the former will be reduced by a factor of 3 to 5. This is caused by the increased time constant of the resistive-inductive system built up of the plasma, the first wall, and the blankets. This increased time constant is linked to smaller time gradients of the magnetic induction.

An important effect neglected up to now is the large toroidal current (some MAs), which together with the magnetic field of the poloidal field coils will produce extra forces. They will try to bend the first wall around the toroidal axis. Further computations are needed in this area.

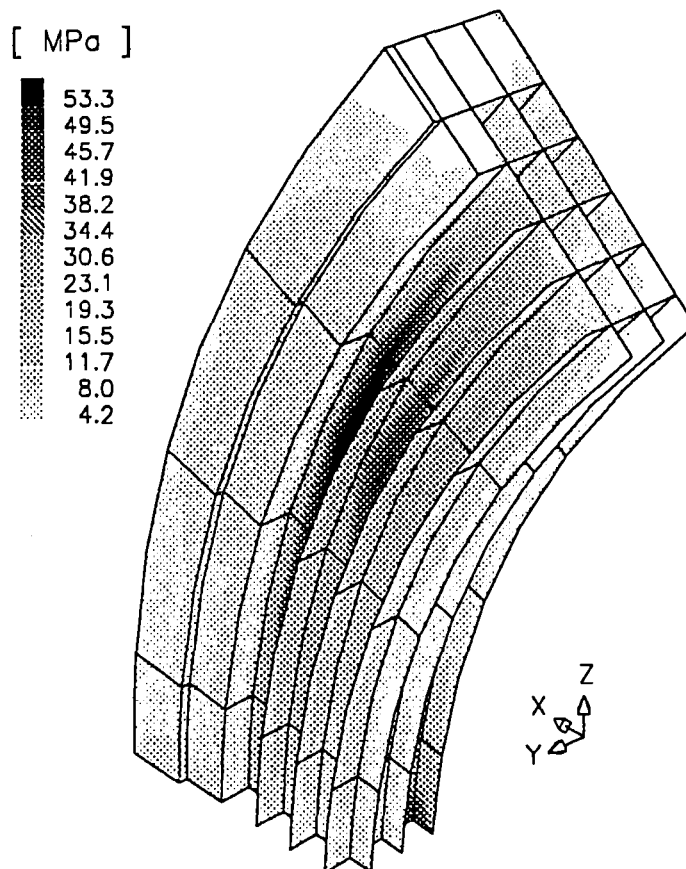


Figure 11-3 DISTRIBUTION OF VON-MISES STRESSES WITH FIXED BACK PLATE.  
(one quarter model, assuming symmetry in the  $y=0$  plane and in the  $z=0$  plane)

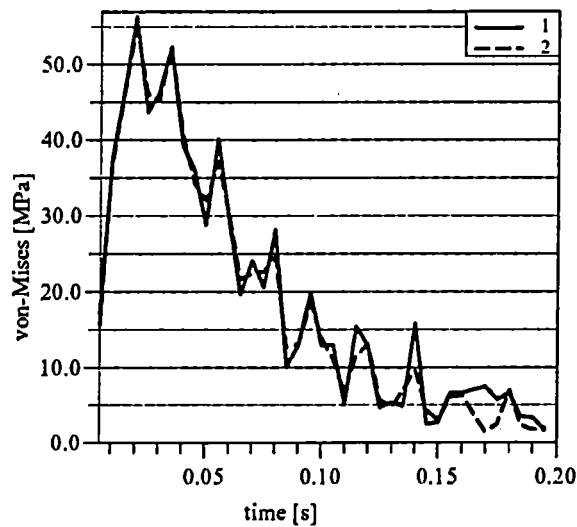


Figure 11-4 MAXIMUM VON-MISES STRESS WITH FIXED BACK PLATE  
(1=without, 2=with current damping)

### 11.3.2 LOCA Temperature Transients

Temperature transients have been studied for instantaneous loss-of-coolant scenarios with leaks in one of the three primary coolant subsystems attached to one blanket segment (2 helium subsystems for the first wall and one Pb-17Li subsystem for the breeding zone), and in the NaK circuit.

#### 11.3.2.1 LOCA in a First Wall Helium Subsystem

The analysis has been performed with the FIDAP code for a reference loss of coolant accident scenario as already defined in 11.2.2. Since the cooling of the first wall is done in multiple passes, a representative 3D model containing a half-channel of both cooling systems was generated for each pass. The helium inlet temperature of a pass is determined by the outlet temperature of the preceding pass. It was assumed that there is no heat exchange between the first wall and the breeding zone. The calculations were carried out with the average value for the surface heat flux of  $0.4 \text{ MW/m}^2$  to determine the transient helium temperature. For the calculations of the temperature distribution in the structure, carried out in a second step with a finer 2D mesh, the peak value of  $0.5 \text{ MW/m}^2$  was

used. The value of the internal heat sources depends on the poloidal and radial position and is taken from neutronics calculations.

The maximum steady state temperatures obtained are 515 °C in the equatorial midplane and 521 °C at the blanket top. This is in good agreement with the calculations carried out with ABAQUS. The maximum transient temperature, reached about 13 s after LOCA occurrence, were obtained at the toroidal side of a blanket segment, where the hotter coolant channels belonged to the cooling system that failed. They are 615 °C in the equatorial midplane and 620 °C at the blanket top (Figure 11-5). The temperature increase from 521 °C to 620 °C causes a reduction of the allowable primary stress according to the ASME code from 234 to 166 MPa which is still larger than the actual primary stresses caused by the coolant pressure. Therefore, a failure of the structure is not expected. However, a thermal stress analysis with computed transient temperature distributions has still to be carried out. A more detailed description of the results and the calculational method is given in [11-16].

#### 11.3.2.2 LOCA in the Pb-17Li Circuit

A LOCA in the Pb-17Li circuit can cause (a) loss of liquid metal flow in the blanket in case of an ex-vessel leak or (b) a drainage of the Pb-17Li from a blanket segment in case of a major in-vessel leak. For (a) the decay heat in the structure plus Pb-17Li per outboard segment would be about 0.77 MW at shutdown (2.8 % of the normal power), leading to a hypothetical adiabatic temperature increase of 0.4 K/s in the Pb-17Li in the front channel row next to the first wall. This temperature would stabilize at  $T_{Pb-17Li} < T_{He} + 160$  °C if the first wall cooling remained intact ( $T_{He}$  = helium coolant temperature) and ignoring in a conservative way the heat dissipated to the rear part of the blanket segment. For case (b) with all Pb-17Li removed but with the first wall cooling systems operating an estimation revealed a maximum structure temperature  $T_{structure} < T_{He} + 100$  °C. At  $T_{He} = 350$  °C this is slightly above the normal operating temperature. These transients do not threaten the integrity of the structure.

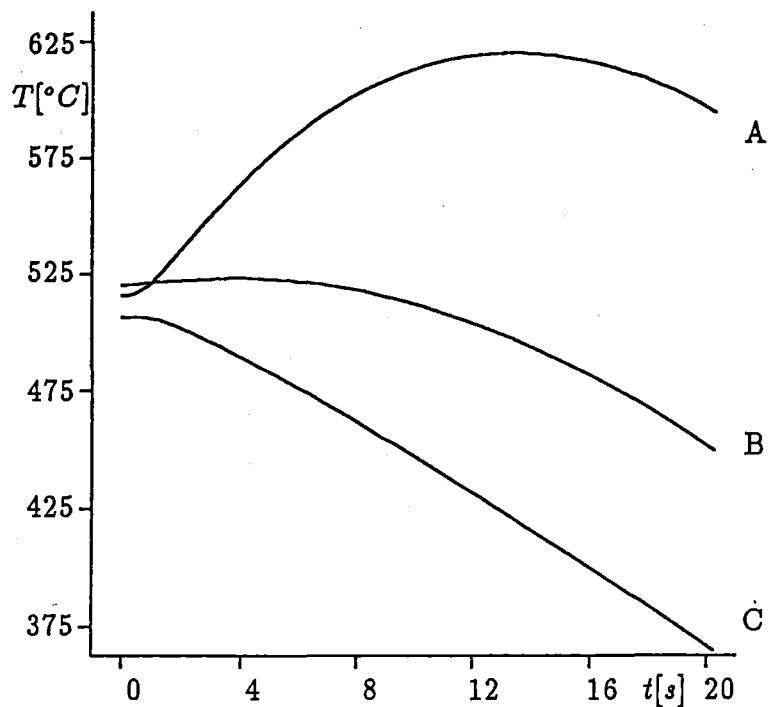


Figure 11-5 TEMPERATURE HISTORY AT THE TOROIDAL SIDE AT SELECTED POINTS (Curves A, B, and C refer to points at the first wall plasma facing surface with A=at the failed channel, B=at the rib, and C=at the intact channel).

### 11.3.2.3 LOCA in the NaK Circuit

A LOCA in the NaK circuit with the consequence of substituting the NaK in the steam generator tube gaps by the cover gas, e.g., argon, would impede the heat transfer coefficient in the steam generator by 1 to 2 orders of magnitude, leading to a strong temperature increase of Pb-17Li at the steam generator outlet. This transient arrives with a delay of  $\approx 30$  s at the blanket inlet and after a further 75 s at the blanket outlet. Therefore, in order to avoid excessive temperatures in the blanket the plasma has to be shutdown within approximately 60 s after drainage of the NaK. The afterheat of less than 3 % of the normal power generation can then be dissipated by the failed steam generator in combination with the first wall cooling circuits. The scenario does not present a safety concern, but the temperature transients need further attention with regard to design limits.

## **11.4 Tritium and Activation Products Release**

### **11.4.1 Release during Normal Operation**

In normal operation the total release of tritium and activation products to the environment should not exceed 1 TBq/d as a guide line. The release is expected to be dominated by the liquid tritium effluents arising from the cooling loops via permeation in the steam generators into the secondary water/steam cycle. For these discharges an upper limit of 20 Ci/d (0.74 TBq/d) is assumed to be achievable (see 11.1.3.1). This leaves little margin for other effluents, for instance originating from primary coolant leakages (into the containment and from there via the plant air detritiation system into the environment) and from other fuel cycle equipment. Those have not been assessed here but conservative estimates performed in the frame of the safety and environmental assessment of fusion power (SEAFP) indicate that they may also range up to close to 1 TBq/d, so that the total releases would exceed the 1 TBq/d guideline. Further assessment is needed in this area.

### **11.4.2 Tritium Release in Accidental Situations**

For a first judgement on the radiological hazard potential an assessment has been made on the early dose and chronic dose to the most exposed individual at a distance of 1 km from the point of release caused by the tritium inventory escaping into the vacuum vessel or containment in the case of a LOCA, and from there into the environment. In this chapter the tritium release from the various coolants and the radiological consequences are discussed.

The accidental tritium release into the vacuum vessel or into the containment in the case of a LOCA is summarised in Table 11-10 along with the radiological consequences to the most exposed individual. The scenario starts from the total tritium inventory in the various coolants (Pb-17Li, helium, and NaK as intermediate fluid in steam generators) from which a certain fraction can escape into the vacuum vessel or some other compartment of the containment upon a LOCA. The envisaged escape fractions are assumed to be a proportion of the escaping fluids and are as follows:

For the breeder material one half of one outboard Pb-17Li subsystem (15 % of the total inventory) is assumed to drain by gravity. The other half will remain in the blanket segments not affected, in the piping, and components located below

the ring headers (which connect the main circuits with the individual blanket segments at some elevated level). If the LOCA occurred ex-vessel the escape fraction would probably be even smaller than 15 %. These assumptions do not take any credit from isolation valves which would likely reduce the escape fraction to a few percent. For the primary first wall helium LOCA the whole inventory from one subsystem would escape either into the vacuum vessel or into another compartment. The largest subsystem (for the outboard) comprises 31 % of the total helium inventory (Table 11-5). The NaK system for tritium removal is divided into 10 subsystems (one subsystem per steam generator) with one of the outboard subsystems containing about 12 % of the total NaK. This can be released into the containment but not into the VV.

Table 11-10 EARLY AND CHRONIC DOSE FOR ACCIDENTAL TRITIUM RELEASE FROM FLUIDS  
(Estimates for in-vessel and ex-vessel LOCAs without retention)

Type of fluid	Total tritium inventory (g)	Fraction escaping into		Source term (g)	Early dose (mSv)	Chronic dose (mSv)
		Vacuum vessel	Containment			
Breeder Material (Pb-17Li)	57	≈0.15	<0.15	≈10	2.2	13.7
Primary first wall coolant (helium)	6.3	0.31	0.31	≈2	0.51	3.1
Tritium removal fluid (NaK)	0.38	0	0.12	0.04	0.012	0.07

For the mechanisms that follow the fluid escape into the vacuum vessel or containment, i.e., tritium mobilization (predominantly in elemental form), oxidation, transportation within the containment, and finally release into the environment, it is assumed in a conservative way that no retention occurs in either of these mechanisms. In that case all the tritium contained in the escaped fluid is released to the environment in the form of HTO (the more dose effective form compared to HT). To compute the early dose (7 days exposure plus 50 years integration, no ingestion) from the tritium source term a conversion factor of 0.26 mSv/g-T, and for the chronic dose (EDE, 50 years exposure plus 50 years integration, with inges-

tion) a factor of 1.6 mSv/g-T has been used [11-17]. These factors vary with release scenarios by about 3 orders of magnitude as investigated in [11-18] and the chosen values range close to the upper bound (of 1 mSv/g-T for the early dose and 4 mSv/g-T for the chronic dose).

Thus, the predicted early dose and the chronic dose, respectively, to the most exposed individual resulting from tritium release range from very low values for a NaK spill (0.01 and 0.07 mSv), and still low values for primary helium blowdown (0.5 and 3.1 mSv) to considerable values for Pb-17Li spills (2.2 and 13.7 mSv) when applying this conservative scenario. The tolerable dose limits on the other hand are still under discussion and the spectrum of national regulations is rather wide. Recent recommendations discussed in ITER for various classes of event sequences range from 0.1 mSv/a for likely sequences ( $f > 10^{-2}/a$ ) over 5 mSv/event for unlikely sequences ( $10^{-2}/a > f > 10^{-4}/a$ ) to 5-50 mSv/event for extremely unlikely sequences ( $10^{-4}/a > f > 10^{-6}/a$ ), where  $f$  is the rate of occurrence. In SEAFP a value of 100 mSv/event is suggested as a yardstick with the understanding that doses of this level trigger the consideration of evacuation but do not yet mandate it.

Hence, depending on the classification of the events regarded in Table 11-10 and on the established dose limits the early and chronic doses obtained for the tritium releases for in-vessel and ex-vessel LOCAs will probably comply with the dose limits. If a conflict should arise a less conservative assessment would have to be undertaken that could bring down the doses by at least two orders of magnitude, for instance in the areas of mobilization, chemical form of the liberated tritium, and confinement retention (for the latter compare the example in 11.4.3).

### 11.4.3 Activation Products Release for a Pb-17Li LOCA

As an example for the potential activation products release from the liquid metal breeder to the environment and its radiological consequences to the public a major spill of Pb-17Li into the vacuum vessel is discussed in terms of activation products inventory, liberation of liquid metal (LM) into the vacuum vessel, mobilization of radionuclides from the spill, retention by the containment, release to the environment, and the radiological impact to the most exposed individual. The assessment is made on a nuclide-by-nuclide basis revealing the Hg-203 isotope as the major contributor to the early dose.

The underlying scenario for the in-vessel LOCA in a Pb-17Li subsystem (similar to the one discussed in 11.4.2) is as follows:

- The plant has operated for 20000 hours at full power, radioactive nuclides generated are taken from FISPACT calculations for the outboard front channels at midplane, which are assumed to be diluted by radial and poloidal averaging and by circulation in loops (dilution factor  $f_D$ )
- Major break in the Pb-17Li confining walls of the outboard segment
- Drainage of one half of one Pb-17Li subsystems inventory into the vacuum vessel ( $2.1 \times 10^6$  kg), postulating that isolation valves fail to close
- Collection of spilled Pb-17Li mass at the bottom of vacuum vessel without break of vacuum (non-oxidizing atmosphere) rendering a spill height of 2 m, a spill surface of  $200$  m<sup>2</sup>, and a mixed mean temperature of 350 °C
- Evaporation of radionuclides into VV at low pressure (vacuum) for a time period of 7 days after which the melt is assumed to be solidified, no condensation within the VV.
- Break of vacuum in the VV and release of 100 % of evaporated nuclides into the second containment (instantaneously)
- Release of fraction,  $f_R$ , of the nuclides from the containment into the atmosphere within 1 hour (usual release scenario), where  $f_R$  = containment retention factor
- Dispersion of released source term and 7 day early exposure to the most exposed individual at 1 km distance (without ingestion).

Then the 7 day early dose, ED, is computed by equation 11.2.

$$ED = M \sum_i \hat{a}_i f_{D_i} f_{M_i} f_{R_i} d_i \quad (11.2)$$

where

- $\hat{a}_i$  peak specific activity of nuclide i in 1 kg of Pb-17Li irradiated in outboard front channels at midplane (stationary) after 20000 h,
- $f_{D_i}$  dilution factor for peak specific activity due to radial and poloidal averaging and due to circulation in loops for nuclide i,

- $f_{M_i}$  evaporation fraction of nuclide  $i$  (mobilization factor) from spilled Pb-17Li with free surface of 200  $m^2$  during given time period,
- $f_{R_i}$  containment retention factor as a result of plate-out at cold walls and/or vent/filter system for nuclide  $i$ ,
- $M$  spill mass of Pb-17Li at bottom of VV,
- $d_i$  specific early dose of radionuclide  $i$  per unit source term (1E9 Becquerel) released at the containment boundary.

Table 11-11 lists all these factors for the twelve leading nuclides out of 73 nuclides that have been traced, and their contribution to the early dose to the most exposed individual. The following comments refer to the choice of parameters in addition to the definitions given to equation 11.2:

Table 11-11 THE TWELVE LARGEST CONTRIBUTORS TO THE EARLY DOSE OF Pb-17Li SPILL (Spill of  $2.1 \times 10^6$  kg of Pb-17Li rendering 200  $m^2$  of free surface)

Nuclide	Peak specific activity (Bq/kg-LM)	Dilution factor	Evaporation fraction	Containment retention factor	Specific early dose (Sv/1E9Bq)	Early dose (Sv)
Hg-203	1.43E+11	0.033	1.00E+00	1.00E-02	1.10E-07	1.09E-02
Po-210	1.08E+09	0.11	5.00E-04	1.00E-02	6.44E-05	8.03E-05
HTO	1.41E+09	1	1	0.01	7.03E-10	2.07E-05
Zn-65	3.74E+09	0.033	1.00E-04	1.00E+00	3.38E-07	8.76E-06
Cd-113m	1.96E+08	0.033	1.00E-04	1.00E+00	2.93E-06	3.98E-06
Cd-109	4.02E+08	0.033	1.00E-04	1.00E+00	3.26E-07	9.08E-07
Bi-210	1.26E+09	0.11	1.00E-06	1.00E+00	1.46E-06	4.25E-07
Ag-110m	2.67E+09	0.033	1.00E-06	1.00E+00	1.47E-06	2.72E-07
Tl-202	8.80E+10	0.033	5.00E-06	1.00E-02	1.08E-07	3.29E-08
Co-58	8.24E+08	0.033	1.00E-06	1.00E+00	3.93E-07	2.24E-08
Pb-203	6.82E+12	0.033	1.30E-07	1.00E-02	3.28E-08	2.02E-08
Zn-69m	1.12E+08	0.033	1.00E-04	1.00E+00	2.18E-08	1.69E-08
Total early dose						1.10E-02

The specific activity for the nuclides (except for tritium in HTO form) is taken from activation analyses [11-19]. The activity for HTO of  $1.41 \times 10^9$  Bq/kg-LM corresponds to the tritium inventory of 57 g in  $15 \times 10^6$  kg of Pb-17Li (Table 11-6).

The dilution factor accounting for the radial and poloidal averaging of the specific activity and for circulation in external loops has generally been assumed to be 1/30 (with 1/3.5 for circulation multiplied by 1/8.6 for averaging). This assumption seems appropriate for long-lived isotopes resulting from simple reactions in the neutron and gamma field, like Hg-203, Zn-65, Cd-113m, Cd-113, Ag-110m. The Po-210 build-up does not follow this simple rule and an approximate dilution factor of 0.11 has been deduced from investigations performed by Fischer et al. [11-20]. The same factor has arbitrarily been assumed for Bi-210 (although in this case of no importance). Finally, the tritium activity in Pb-17Li is not diluted in the circuit, since it is determined by the extraction process for which 57 g tritium in  $15 \times 10^6$  kg of Pb-17Li have been predicted.

Evaporation fractions (mobilization data) from a Pb-17Li spill are reported in [11-21] for a number of elements, like Po, Bi, Pb, Tl, Hg, and Li. They have been adapted for a spill temperature of 350 °C and a free surface of 200  $m^2$  in vacuum for the elements mentioned. For the other elements, where no such data are available, mobilization data collected in the SEAFP study are adopted which, however, include already the containment retention factor (see below).

The containment retention factor was generally set to 0.01, presuming that 99 % of the airborne nuclides will condense at containment walls and/or will be retained in the containment air detritiation system. For those elements where only combined mobilization fractions (including evaporation and retention as mentioned above) are available, the containment retention factor was set to 1.

The specific early dose per unit source term released into the environment was used from dose calculations performed by Raskob [11-17] [11-18]. They hold for a seven day exposure in 1 km distance without ingestion, release height of 10 m, a release duration of 1 h, (weather condition data set 4826).

The result of this conservative LOCA scenario for a spill of one half of the Pb-17Li inventory contained in one subsystem show that the total early dose resulting from 73 nuclides amounts to 11 mSv, a moderate value when compared to the dose limits already discussed in 11.4.2. It must be noted that 98.9 % of the early dose arises from a single nuclide, Hg-203, due to the extremely high vapour pressure of mercury, leading to a complete release of Hg-203 from the spill. This will

be a matter of further investigation [11-21]. The contribution of Po-210 and tritium to the early dose are only 0.7 % and 0.2 %, respectively. (Note that in this scenario the containment retention factor for HTO was set to 0.01 instead of 1 as used in 11.4.2.).

## 11.5 Waste Generation and Management

Only the decommissioning waste (no operational waste) is considered here. The masses, volumes, radioactivities, and afterheat are summarized in Table 11-12. The total amount of radioactivity in the blanket structure (MANET) sums up to  $7.5 \times 10^7$  TBq at shutdown for all inboard and outboard segments according to 11.1.3.2, one half of which being in the small volume of the first wall and only  $\approx 5$  % being in the large volume of the removable shield. The contribution of each radionuclide has been calculated as described in Chapter 4 for different cooling times. The dominating nuclides vary with time and activation parameter (specific activity,  $\gamma$ -dose rate, ingestion dose rate, inhalation dose rate). For example, Fe-55 and Mn-54 dominate the specific activity at a cooling time of 1 year, and Nb-91, Ni-63, Nb-93 dominate after 100 years. The contact  $\gamma$ -dose rate in the first wall ranges up to  $1.1 \times 10^5$  Sv/h, declining slowly. The IAEA low level waste (LLW) limit of  $2 \times 10^{-3}$  Sv/h is reached after about  $10^5$  years, and the hands-on limit of  $2.5 \times 10^{-5}$  Sv/h is met not sooner than  $3 \times 10^5$  years.

The total amount of radioactivity in Pb-17Li is  $1.3 \times 10^8$  TBq at shutdown, decaying by seven orders of magnitude within 100 years. (The numbers quoted in Table 11-12 for Pb-17Li have been derived from radially and poloidally averaged values for the different blanket parts and account for a dilution factor due to external circulation of 3.5 for the outboard and 4.7 for the inboard.) The following nuclides dominate the specific activity by more than 65 % at various times: Pb-207 (after 0 s), Pb-203 and Pb-204 (after 1 h), Pb-203 (after 1 d), Hg-203 (after 1 month), Tl-204 (after 1 year), Pb-205 and Ag-108 (after 100 years). The contact  $\gamma$ -dose rate of Pb-17Li reaches the LLW limit without any purification after 300 years, the hands-on limit after a few 1000 years. In view of the high lithium enrichment needed (90 atom-% Li-6) the liquid metal breeder is envisaged to be used for several blanket life times or even for more than one reactor life time, since the burnt amount of lithium can be replaced easily.

Table 11-12 RADIOACTIVE WASTE OF THE BLANKET SYSTEM  
(after 20000 hours of full power operation)

Blanket region or system	Total mass (kg)	Total volume (m <sup>3</sup> )	Total radioactivity in Bq after			Decay heat after 1 y (W/m <sup>3</sup> )
			1 y	10 y	500 y	
Breeder Material (Pb-17Li)	15 x 10 <sup>6</sup>	1600	1.2x10 <sup>16</sup>	1.5x10 <sup>15</sup>	1.6x10 <sup>13</sup>	0.57
Structural material (total)	3.2x10 <sup>6</sup>	407	2.2x10 <sup>19</sup>	1.8x10 <sup>18</sup>	7.9x10 <sup>14</sup>	see below
First wall	1x10 <sup>5</sup>	13	1.2x10 <sup>19</sup>	9.4x10 <sup>17</sup>	1.8x10 <sup>14</sup>	1.6x10 <sup>4</sup>
Breeding zone	1.3x10 <sup>6</sup>	162	8.5x10 <sup>18</sup>	7.1x10 <sup>17</sup>	4.7x10 <sup>14</sup>	1.1x10 <sup>3</sup>
Shield	1.8x10 <sup>6</sup>	231	8.9x10 <sup>17</sup>	1.2x10 <sup>17</sup>	1.4x10 <sup>14</sup>	2.6x10 <sup>2</sup>
Insulating layers	360	0.13	7x10 <sup>9</sup>	7x10 <sup>9</sup>	7x10 <sup>9</sup>	3x10 <sup>-2</sup>

## 11.6 References

- [11-1] S. Malang, K. Schlesiak (ed.): Dual coolant blanket concept, KfK 5424, November 1994.
- [11-2] S. Malang et al.: DEMO-relevant Test Blankets for NET/ITER, Part 1: Self-cooled Liquid Metal Breeder Blanket, KfK 4908, (1991).
- [11-3] J. Wagner et al.: SEAFP internal report (Febr. 1994).
- [11-4] M.A. Fütterer, X. Raepsaet, E. Proust: Tritium permeation through helium-heated steam generators of ceramic breeder blankets for DEMO, Proc. ISFNT-3, Los Angeles, Ca., June 27-July 1, 1994, 225-232.
- [11-5] K. Kleefeldt et al.: KfK internal report (Aug. 1993).
- [11-6] D.W. Jeppson, L.D. Muhlestein, R.F. Keough, S. Cohen: Fusion Reactor Blanket Material Safety-Compatibility Studies, HEDL-SA-2747, AIChE Fall 1982 Annual Meeting, Los Angeles, November 1982.
- [11-7] G. Kuhlbörsch, H. Dietz, D. Droste: The Chemical Behavior of Eutectic Lithium-Lead Alloy  $Li_{17}Pb_{83}$  in Comparison with Pure Lithium, Commission of the European Community, JRC, Ispra, (October 1983).
- [11-8] H. Kottowski, O. Kranert, C. Savatteri, C. Wu, M. Corradini: Studies with Respect to the Estimation of Liquid Metal Blanket Safety, Fus. Eng. Des. 14 (1991) 445-458.
- [11-9] D.W. Jeppson, L.D. Muhlestein: Safety considerations of lithium alloy as a fusion reactor breeding material, Fus. Tech. 8 (1985), 1385-1391.

- [11-10] M. Corradini, D.W. Jeppson: Lithium Alloy Chemical Reactivity with Reactor Materials: Current State of Knowledge, *Fus. Eng. Des.* 14 (1991) 273-288
- [11-11] D.W. Jeppson, C. Savatteri: Consequences of Water Injection into High-Temperature  $Li_{17}Pb_{83}$  Alloy Breeder Material, *Fusion Technology* Vol. 19, May 1991, 1403-1408.
- [11-12] C. Savatteri, A. Gemelli: Lithium-lead/water interaction. Large break experiments, ISFNT-2, Karlsruhe, FRG, June 2-6, *Fusion Eng. Des.* 17 (1991) 343-349.
- [11-13] G. Kuhlbörsch, F. Reiter: Physical properties and chemical reaction behavior of  $Li_{17}Pb_{83}$  related to its use of a fusion reactor blanket material, *Nucl. Eng. Des./Fus.* 1 (1984), 195-203.
- [11-14] S.J. Piet, D.W. Jeppson, L.D. Muhlestein, M.S. Kazimi, M.L. Corradini: Liquid Metal Chemical Reaction Safety in Fusion Facilities, *Fusion Eng. Des.* 5, (1987), 273-298.
- [11-15] H.U. Borgstedt: Chemische Eigenschaften des flüssigen Blanketstoffs Pb-17Li, KfK 4620, 1989.
- [11-16] F. Dammel, KfK internal report (1994).
- [11-17] W. Raskob: Unit release of nuclides in COSYMA, private communication, June 1995.
- [11-18] W. Raskob: Dose assessment for releases of tritium and activation products into the atmosphere performed in the frame of two fusion related studies: ITER-EDA and SEAFP, *Fusion Technology 1994, Proceedings of the 18th SOFT, Karlsruhe, Germany, 22-26 August 1994*, 1473-1476.
- [11-19] H. Tsige-Tamirat, KfK internal note, June 16, 1994.
- [11-20] U. Fischer, E. Wiegner: Production of Po210 in Pb-17Li: Assessment of Methodological and Data Related Uncertainties, *Proc. 17th. Symp. on fus. Tech., Rome, Italy 14-18 Sept. 1992*, 1719-1723.
- [11-21] H. Feuerstein, FZK internal report, Mai 1995.



## **12. Reliability and Availability**

### **12.1 Introduction**

The reliability of the blanket segments and associated cooling circuits determines the availability of the entire blanket system and, hence, affects the availability of the whole plant. The blanket segments are particularly important because no redundancy is possible; i.e., all segments must be operable at the same time. In case of a defect, the affected blanket segment must be exchanged. The time needed for this procedure - the mean time to repair (MTTR) - is also a decisive factor for the overall blanket system availability.

The system availability of the Dual Coolant blanket has been analyzed in order to obtain preliminary quantitative estimates. To accomplish this, the system was divided into two subsystems: the blanket segments and the external systems. Since the external cooling circuits are composed primarily of components using established technology, the component failure rates can be estimated relatively easily. However, no experience is available for the blanket segments, in which case the failure rates have been determined "synthetically".

Basic events which may lead to segment failure have been defined and their causes broken down into tractable "reliability indicators" such as number and length of welds, number and dimensions of bends, etc. Data for these reliability indicators are obtained by transfer from other technologies, combined with assumptions based on expert opinion to establish a common reliability data base. In this way, failure rates can be determined for the basic design elements and the net system availability can be calculated. The results of the evaluation are useful for comparative evaluations; they do not provide a reliable absolute quantification. They are also useful for identifying the main contributors to unavailability, and thus the most important areas of research and development which could lead to higher availability.

The methodology and the basic failure rate data are consistent with the analyses performed on the three other DEMO blankets. Therefore, a quantitative comparison of the availabilities of the alternative blanket design candidates is possible. A preliminary comparison is given here; more extensive comparisons have been performed as a part of the blanket comparison and selection exercise (BCSE).

Prior to evaluating the availabilities, Section 12.2 presents a summary of the methodology and data used in the evaluation. Section 12.3 then presents the results for the blanket segments and external systems, and Section 12.4 summarizes the important conclusions.

## 12.2 Methodology

The quantitative evaluation of reliability and unavailability is performed using standard methods of fault tree analysis [12-1, 12-2, 12-3]. Failure rates and MTTR's are determined based on published data [12-4, 12-5, 12-11], with some adjustments which were agreed upon with EU partners within the BCSE. The analysis assumes only OR connections (no AND connections) in the fault tree, which significantly simplifies the solution. To evaluate new design elements, for which data were not available, the failure rates were estimated by defining basic events which lead to failure and the characteristic reliability indicators which contribute to those failure modes.

A basic difference arises between calculations of operational unavailabilities as compared with safety analyses. In the safety area, unavailability values are normally  $\ll 1$ , such that the last term in the OR connection relation:

$$U_{OR} = U_1 + U_2 - U_1 \cdot U_2$$

can be neglected. In the area of operational unavailability, with values of  $U_{OR}$  closer to 1, all terms in the equation must be kept.

### 12.2.1 Basic events

In fault tree analysis, basic events are failures of the essential components which lead to failure and the need to replace a segment (an OR condition). A problem arises because any highly reliable complex technology simply does not produce enough failures over a reasonable period of time to produce confidence in the failure rate data. On the one hand, the number of components is small, and on the other hand the operating time needed to get reliable data is extremely large. This is not only a question of time, but also a financial problem.

By dividing the system into smaller parts, such as welds, bends, tubes, etc., useful conclusions about reliability/availability can be produced. Therefore, the basic

events are characterized by a set of "characteristic reliability indicators" which are design features that have a controlling influence on the basic events. The specific failure rates for these reliability indicators can be estimated from existing literature. Additional input is needed to characterize the tolerance of the segments to certain types of failures and admissible types of defects (e.g., tolerance of a single failure in a double weld, or of small leaks in the case of double containment).

The quantitative results obtained from this method are only relative. Use of the same data base in comparing design options will eliminate inconsistencies, but the absolute level of the availability may be too high or too low. Improvements in the absolute values of the results will be obtained ultimately through R&D and operating experience.

### **12.2.2 Failure rates and repair times**

Common failure rate and MTTR assumptions were obtained by consensus within the BCSE, and are provided in Table 12-1. The assumed time to replace a complete blanket segment is 3 months, or 2160 hours.

A special problem exists in the analysis of the liquid metal double wall steam generator (SG), which has a unique design. An internal industrial study was performed by Siemens, considering all of the data available internally by the industrial partners, and the results are published in [12-6]. They are in reasonable agreement with the values in Table 12-1 which were obtained by the completely independent FZK assessment.

## **12.3 Evaluation results**

### **12.3.1 External cooling system evaluation**

Redundancy is provided in all of the coolant systems such that a single circuit can fail completely with no influence on the availability. The definition of redundancy used here is the number of components or circuits which must be inoperable in order to cause system unavailability as compared with the total number of components or circuits in the system. Most of the systems used for the Dual Coolant blanket employ "2-out-of-n" redundancy, meaning that 2 circuits must fail to create unavailability with a total of n circuits.

Table 12-1 Agreed values of failure rates and MTTR for the different EU blanket concepts

FAILURE MODES EXTERNAL CIRCUITS		Common agreement Failure rate [l7h]	MTTR [h]
Pipe failure	(He)	$3.0 \cdot 10^{-9}$	100
Pipe failure	(LiPb)	$3.0 \cdot 10^{-9}$	200
Pipe failure	(H <sub>2</sub> O)	$3.0 \cdot 10^{-9}$	100
SG failure 140 MW	(LiPb)	$2.0 \cdot 10^{-5}$	1200
SG failure 280 MW	(LiPb)	$4.0 \cdot 10^{-5}$	1200
SG failure 90 MW	(He)	$7.4 \cdot 10^{-6}$	1000
SG failure 180 MW	(He)	$1.2 \cdot 10^{-5}$	1000
SG failure 467.5 MW	(H <sub>2</sub> O)	$2.3 \cdot 10^{-5}$	1000
SG failure 300 MW	(H <sub>2</sub> O)	$1.5 \cdot 10^{-5}$	1000
SG failure 322.4 MW	(He)	$7.9 \cdot 10^{-6}$	1000
SG failure 115.7 MW	(He)	$4.4 \cdot 10^{-5}$	1000
Valve failure	(H <sub>2</sub> O)	$1.0 \cdot 10^{-6}$	100
Valve failure	(He)	$1.0 \cdot 10^{-6}$	100
Valve failure	(LiPb)	$3.0 \cdot 10^{-6}$	200
Pump failure	(LiPb)	$5.6 \cdot 10^{-6}$	200
Pump failure	(H <sub>2</sub> O)	$1.0 \cdot 10^{-6}$	100
Blower failure	(He)	$1.0 \cdot 10^{-5}$	100
Collector failure	(H <sub>2</sub> O)	$1.0 \cdot 10^{-8}$	100
Collector failure	(He)	$1.0 \cdot 10^{-8}$	100
<b>BLANKET SEGMENT</b>			
EB weld	[l/m]	$1.0 \cdot 10^{-9}$	
Diffusion weld	[l/m]	$1.0 \cdot 10^{-8}$	
Longitudinal weld	[l/m]	$1.0 \cdot 10^{-9}$	
Butt weld	[l/weld]	$1.0 \cdot 10^{-9}$	2160*
Pipe bend (180°)		$1.0 \cdot 10^{-8}$	
Pipe bend (90°) (assumed 1/2 180°)		$5.0 \cdot 10^{-9}$	
Straight pipe	[l/m]	$1.0 \cdot 10^{-10}$	
Breeder rod	[l/rod]	$1.0 \cdot 10^{-9}$	

\* MTTR for the exchange of a complete segment

The liquid metal cooling system consists of inboard and outboard parts. The inboard part is composed of a single system with 4 circuits using the "2-out-of-4" principle. The outboard part is composed of 6 circuits subdivided into 2 systems, each using the "2-out-of-3" principle. Each circuit removes 140 MW for the inboard and 280 MW for the outboard cooling system.

The principle is shown in Fig. 12-1. The simplified drawing shows only one of the redundancy groups for the outboard liquid metal system. The inlet and outlet collectors are displayed in a simplified manner. The connections between the blanket segments and the collectors are likewise simplified and not completely displayed in the figure.

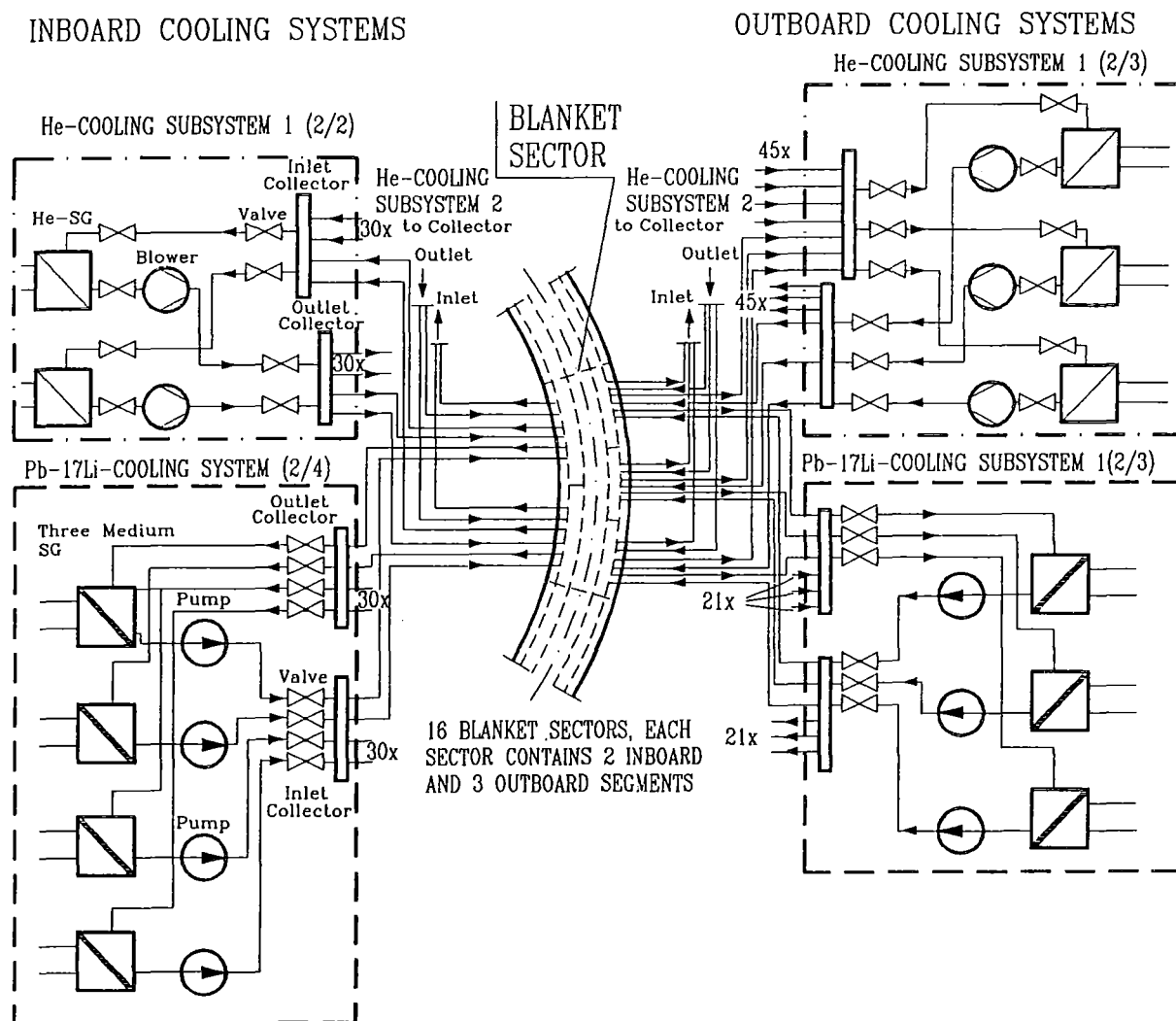


Fig. 12-1 Flow diagram of the external cooling systems for the Dual Coolant blanket concept

Table 12-2 Pb-17Li and He steam-generator (SG) data

Location	Inboard	Outboard	In-/Outboard
Design power per unit [MWth]	140	280	90
Primary medium (Pm)	Pb-17Li		He
No. of SG`s	4	6	4      6
Redundancy in cycles	2v4	2v3	2v2      2v3
$t_{P_m \text{ in}}$ [°C]	425		350
$t_{P_m \text{ out}}$ [°C]	275		250
$p_{P_m \text{ in}}$ [bar]	2		80
$t_{H_2O \text{ in}}$ [°C]	250		150
$t_{H_2O \text{ out}}$ [°C]	286		286
$p_{H_2O \text{ out}}$ [bar]	70		70
Tube OD/ID      [mm]	24/20-30/26		23/19
Bundle type	Straight tube		Helical coil
Bundle height      [m]	24.9	23.4	4.3
Bundle OD      [m]	1.04	1.51	2.42
Heat transfer area      [m <sup>2</sup> ]	1323	2646	1516
$\Delta p_{P_m}$ [bar]	0.89	0.78	0.32
$\Delta p_{H_2O}$ [bar]	1.3	1.2	1.52
Failure rate      [10 <sup>-5</sup> /h]	2.0	4.0	0.74

There are two independent systems for the inboard FW He system according to the "2-out-of-2" principle and two independent cooling systems for the outboard FW according to the "2-out-of-3" principle. Corresponding data are listed in Table 12-2. The Q-T diagrams are shown in Fig. 12-2 for the 140 MW liquid metal SG's and in Fig. 12-3 for the 90 MW He SG's. The Q-T diagram for the 280 MW liquid metal SG's is equivalent to Fig. 12-2 when the abscissa is linearly compressed according to the larger power.

A previous version of the cooling system was based on the assumption that the liquid metal cooling consisted of 80 circuits: the outboard blanket has 48 circuits arranged in 16 2-out-of-3 systems and the inboard blanket has 32 circuits arranged in 16 2-out-of-2 systems. The SG design calculation data for the previous version are given in Table 12-3.

Tab. 12-3 Pb-17Li and He-steam generator (SG) data for previous version

Location		Inboard	Outboard	In-/Outboard
Design power per unit	[MWth]	30	35	80
Primary medium (Pm)		Pb-17Li		He
No. of SG's		32	48	4      6
Redundancy per sector		2v3	2v3	2v2      2v3
t <sub>Pm in</sub>	[°C]	425		350
t <sub>Pm out</sub>	[°C]	275		260 *)
p <sub>Pm in</sub>	[bar]	2		80
t <sub>H<sub>2</sub>O in</sub>	[°C]	250		170
t <sub>H<sub>2</sub>O out</sub>	[°C]	286		286
p <sub>H<sub>2</sub>O out</sub>	[bar]	70		70
Tube OD/ID	[mm]	24/20-30/26		23/19
Bundle type		Straight tube		Helical coil
Bundle height	[m]	11.0	11.0	7.0
Bundle OD	[m]	0.82	0.90	2.60
Heat transfer area	[m <sup>2</sup> ]	426	497	2275
Δp <sub>Pm</sub>	[bar]	0.13	0.13	0.16
Δp <sub>H<sub>2</sub>O</sub>	[bar]	1.1	1.1	2.4
Failure rate	[10 <sup>-5</sup> /h]	0.58	0.68	1.1

\*) Input for lay-out calculation

The Q-T diagrams are shown in Figs. 12-4 and 12-5. The FW He cooling circuits are arranged in two 2-out-of-2 redundancies for the inboard part and two 2-out-of-3 redundancies for the outboard part.

The external cooling circuits are composed of components with established technology; therefore, failure rate data is generally available. One exception is the novel three-fluid steam generator. In this case, failure rates were calculated by the method described in Section 12.2 [12-6, 12-12]. The result of the fault tree calculation is presented in the form of a block diagram, as introduced in [12-3]. The block diagram shows the influence and interconnections of very extended fault trees in a clear and simple way, and also indicates at which points the design is adequate and at which points improvements could be obtained. Each horizontal path in the diagram is equal to an undesired event, which in this case means a plant shutdown.

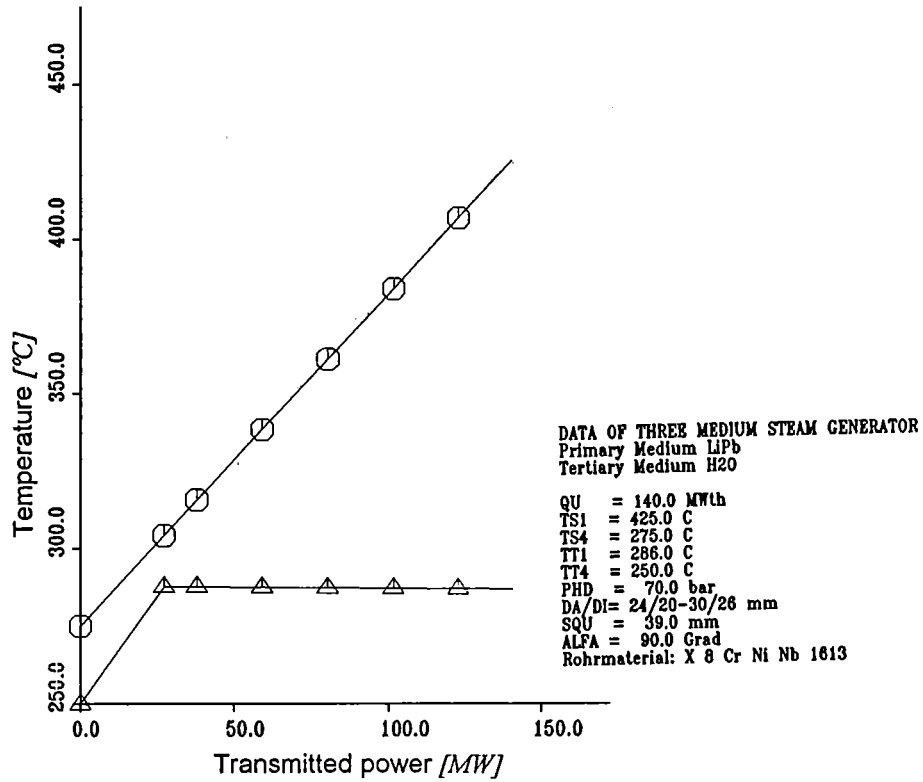


Fig. 12-2 Q-T-Diagram for the 140 MW liquid metal double wall steam generator

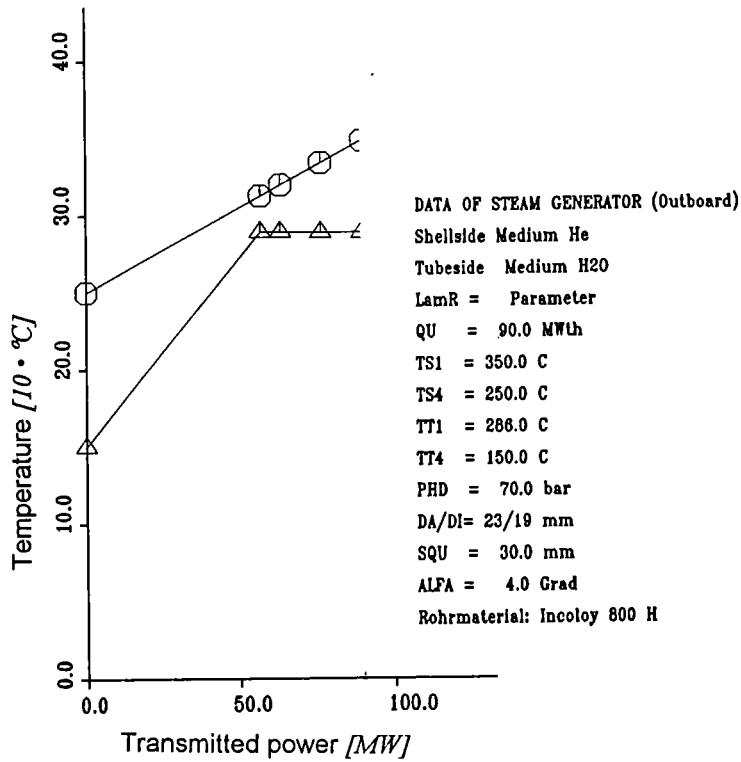


Fig. 12-3 Q-T-Diagram for the 90 MW He steam generator

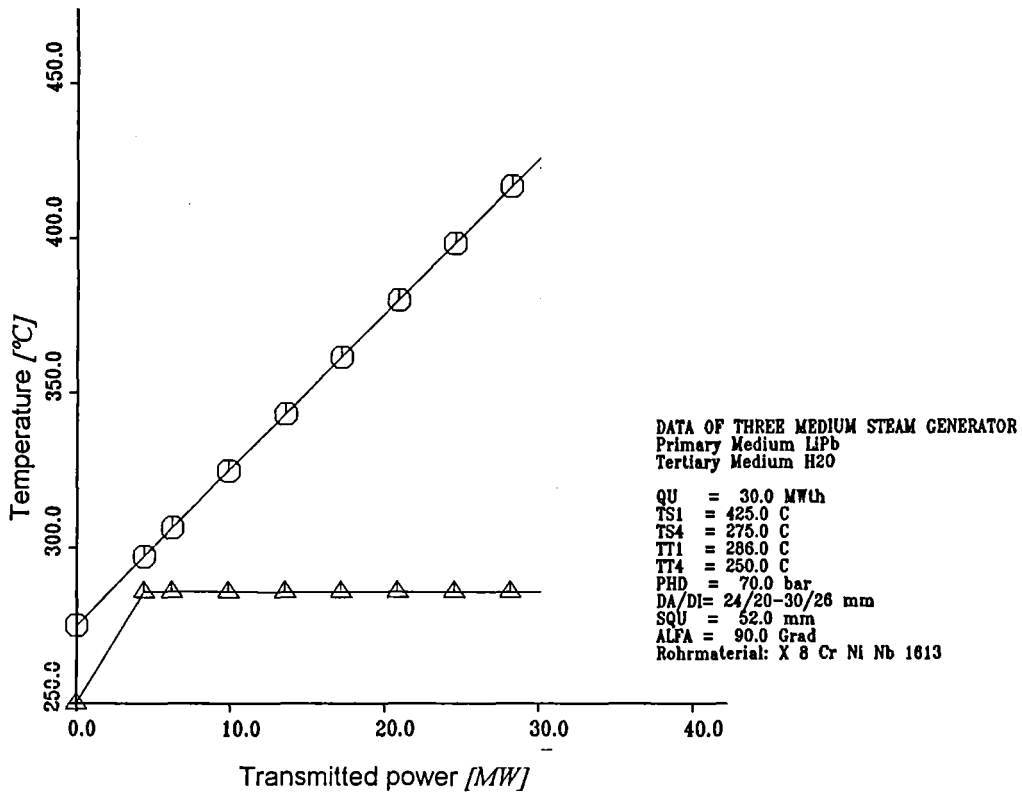


Fig. 12-4 Q-T-Diagram for the 30 MW liquid metal double wall steam generator

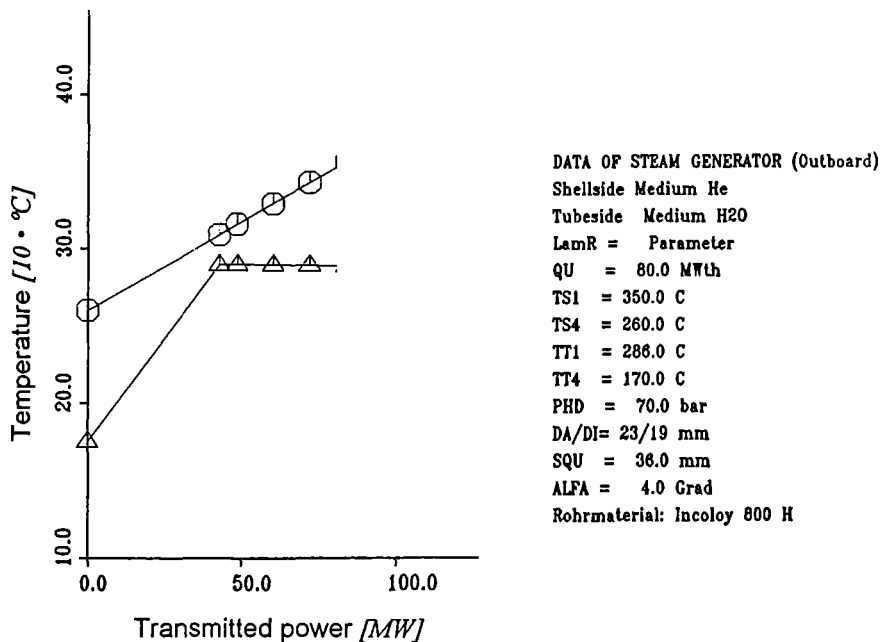


Fig. 12-5 Q-T-Diagram for the 80 MW He steam generator

The block diagram for the external cooling cycles is related to the failure modes given in Table 12-1. The block diagram shown in Fig. 12-6 contains the 7 completely independent systems (4 He and 3 liquid metal).

Fig. 12-7 contains the expected values of unavailability for the 7 individual systems according to Fig. 12-6. The largest part comes from the outboard liquid metal cooling system - nearly 95%. The overall unavailability becomes 1.46%, which represents an availability of 98.5%.

The previous lay-out of the cooling system, consisting of 80 Pb-17Li 30 or 35 MW each) and 10 He circuits (80 MW each) as shown in Table 12-3 resulted in an availability of 99.2 %.

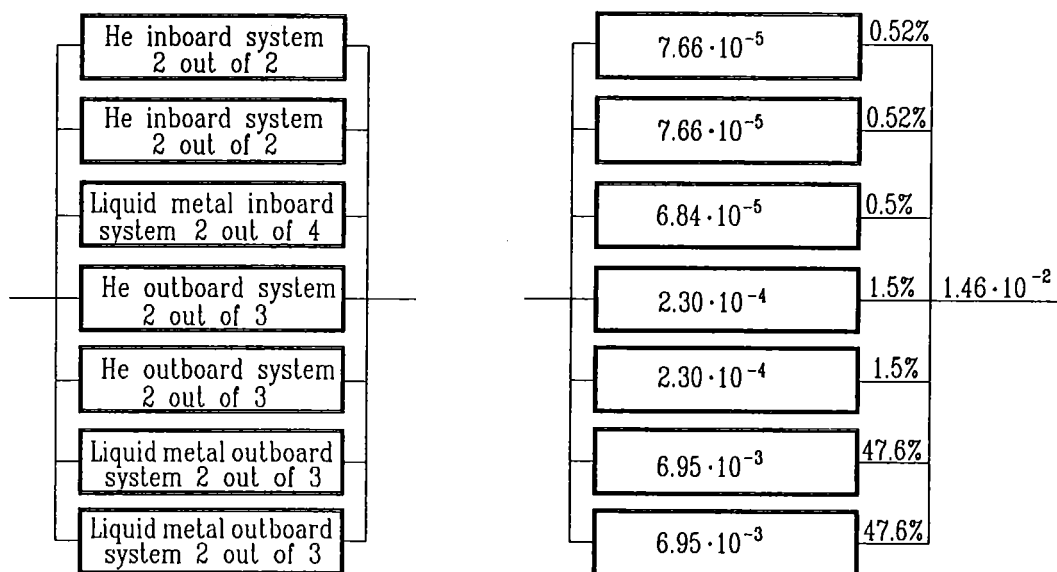


Fig. 12-6 Block diagram for the cooling system of the Dual Coolant blanket

Fig. 12-7 Expected unavailabilities for the cooling system of the Dual Coolant blanket concept

The system according to Figs. 12-1, 12-6 and 12-7 was also considered for a higher degree of redundancy in the outboard liquid metal system by connecting the two 2-out-of-3 redundancy groups, which would yield a 3-out-of-6 redundancy. The overall availability for the external systems in this case increases from 98.5% to >99.9%. This parameter variation shows that there is ample room for improvement with no changes in the size of the SG's and circuits, in case the value of 98.5% is judged to be too low.

### 12.3.2 Blanket segment evaluation

The basic events to be considered for the blanket, together with their reliability indicators, are given in Table 12-4a.

The first events -  $FDD_{o,i}$  and  $DWD_{o,i}$  (the index o stands for outboard and i stands for inboard) - describe the behavior of the first wall. During the BSE all EU blanket options have used an equal value for the unavailability of the FW, thereby making the relative rankings independent of the FW analysis. For simplicity, these events are combined into the basic event  $FWS_{o,i}$ .

The considered events include one or multiple diffusion weld failures. This event occurs only if the FW is damaged in such a way that the coolant (He or Pb-17Li) leaks into the vacuum chamber. This is also possible by failure of an e-beam double weld. The two welds of a double weld could be considered as completely independent. For conservatism, a mean value between completely independent (an AND connection) and completely dependent (an OR connection) is assumed. The mean value of the failure rate is calculated by the relation:

$$U_1 = U_2 = \lambda \cdot \text{MTTR (independent single weld failure)}$$

$$U_{\text{OR}} = U_1 + U_2 - U_1 \cdot U_2$$

and for  $U_1 = U_2 \gg U_1 \cdot U_2$

$$U_{\text{OR}} = U_1 + U_2 = 2 U$$

$$U_{\text{AND}} = U_1 \cdot U_2$$

$$\bar{U} = \sqrt{2U^3}$$

$$\lambda = \bar{U} / \text{MTTR}$$

The basic events  $FCD_{o,i}$  in Table 12-4a describe the connections between the FW and the vertical plates of the stiffening grid which are connected by a weld. A weld failure here is not necessarily associated with a plant shutdown. Multiple weld failures are tolerable. Only a failure in the FW structure itself represents an event leading to shutdown.

$FLD_{o,i}$  describes the flow supply system from the blanket segment box, which is bounded by the first wall and the manifolds on the side opposite of the plasma, and leads to the external cooling system. The key values for determining the fail-

ure rates are the calculated failure rates as listed in Table 12-4b. These values are based on the values of the reliability indicators also given in the table.

The block diagram for the failure analysis of the blanket segment is given in Fig. 12-8. The limit here is the connection to the external cooling system. Fig. 12-9 contains the expected values of unavailability for the basic events in this special case. The values inside the blocks (inside the boxes) are related only to one segment. In other words, the basic events for the outboard part are multiplied by 48 and for the inboard part by 32. The values outside the boxes represent the expected unavailability values for the whole system: 8.9% for the outboard blanket and 3.78% for the inboard blanket. The overall unavailability is 12.3%, or the availability is 87.7%.

The unavailability contribution of the FW is 9.4%. This results in a failure rate of  $4.4 \times 10^{-5}$ /hr, taking into consideration the MTTR of 2160 hours. The overall blanket availability without the FW increases to 96.8%. The contributions to the availability from the various events are:

	<b>inboard</b>	<b>outboard</b>
FDD	70.0%	76.5%
DWD	0.05%	0.07%
FCD	3.6%	3.0%
LDD	11.7%	7.0%
FLD	14.7%	14.0%

This means that more than 70% of the overall availability of the blanket is determined by the diffusion welds in the FW.

Table 12-4a Main basic events for the Dual Coolant blanket concept

Basic event	Description	Basis	Characteristic reliability indicators	Characteristic basic assumption for data generation	Remarks
<b>FDD<sub>n</sub></b> n=0=out-board n=1=in-board	Damage of the FW structure. Leakage of He, Pb-17Li or both into the vacuum chamber.	Diffusion welds (DW) besides the EB-welds	Length of DW neighbouring the EB-double-welds	Failure rate according DW	This assumption includes a safety potential. One or more failures of the DW are tolerable. Only in connection with a FW-structure failure an undesirable event occurs.
<b>DWD<sub>n</sub></b>	Damage of the FW structure cause by EB-double-weld damage. Leakage of Pb-17Li into the vacuum chamber.	Length of the EB-welds	Length of the welds	Failure rate according EB-weld	Consideration as two independent single welds. Only if both welds fail at the same time the undesired event occurs. Conservatively assumed mean value between complete independent and dependency.
<b>FCD<sub>n</sub></b>	Damage of the FW structure caused by a damage of the connection between the FW and the vertical flow leading plates.	Length of the longitudinal welds fixing the flow leading plates at the FW structure	Length of the welds in contact with the FW.	Failure rate 0.1 of the longitudinal weld	One or more weld failures are tolerable. Only in combination with a FW structure failure an undesired event is supposed. Taken into account of the basis of a longitudinal weld failure
<b>LDD<sub>n</sub></b>	Leak detection in the back of the segment box	Length of longitudinal welds	Length of welds	Failure rate of the longitudinal weld	A single failure is considered as an undesired event.
<b>FLD<sub>n</sub></b>	Damage of the flow leading system outside the blanket main structure.	Tubes, bends, welds and collectors outside the blanket segments until the border to the external cooling systems.	Length of the tubes, number of bends, length of welds.	Failure rates according to the noncorrected source.	A single failure is considered as an undesired event.

Between the He and the Dual Coolant Concept there are by the similarities in design many similarities in the basic events. Leakages inside the blanket segments are tolerable. Only if the coolability is remarkably disturbed than the undesired event occurs. At the present time it is possible to define the leak size. Answering the question about the critical size of the leakage must be part of future R&D work.

Table 12-4b Dimensions of the reliability indicators and the calculated failure rates for the main basic events for the Dual Coolant Blanket concept

Basic event	Figures of reliability indicators [m]	Calculated-failure rate $\lambda$ [1/h]	Remarks
FDD <sub>o</sub>	68.8	$6.88 \cdot 10^{-7}$	
DWD <sub>o</sub>	43.2	$5.90 \cdot 10^{-10}$	$\bar{U} = \sqrt{2} \cdot U^3$ $U = \lambda \cdot \text{MTTR}$ $\lambda = \bar{h} / \text{MTTR}$
FCD <sub>o</sub>	264	$2.64 \cdot 10^{-8}$	
LDD <sub>o</sub>	60	$6.0 \cdot 10^{-8}$	
FLD <sub>o</sub>	<u>He:</u> Length of tubes: 21.6 m No. of 90°: bends 12 Length of welds 20.4 m <u>Pb-17Li:</u> Length of tubes: 7.0 m No. of 90°: bends 4 Length of welds 21.2 m	$1.24 \cdot 10^{-7}$	
FDD <sub>i</sub>	39.4	$3.94 \cdot 10^{-7}$	
DWD <sub>i</sub>	26.8	$2.88 \cdot 10^{-10}$	$\bar{U} = \sqrt{2} \cdot U^3$ $U = \lambda \cdot \text{MTTR}$ $\lambda = \bar{U} / \text{MTTR}$
FCD <sub>i</sub>	198	$1.98 \cdot 10^{-8}$	
LDD <sub>i</sub>	60	$6.0 \cdot 10^{-8}$	
FLD <sub>i</sub>	<u>He:</u> Length of tubes: 32.0 m No. of bends 90°: 8 Length of welds 10.6 m <u>Pb-17Li:</u> Length of tubes: 16 m No. of bends 90°: 4 Length of welds 7.5 m	$8.29 \cdot 10^{-8}$	

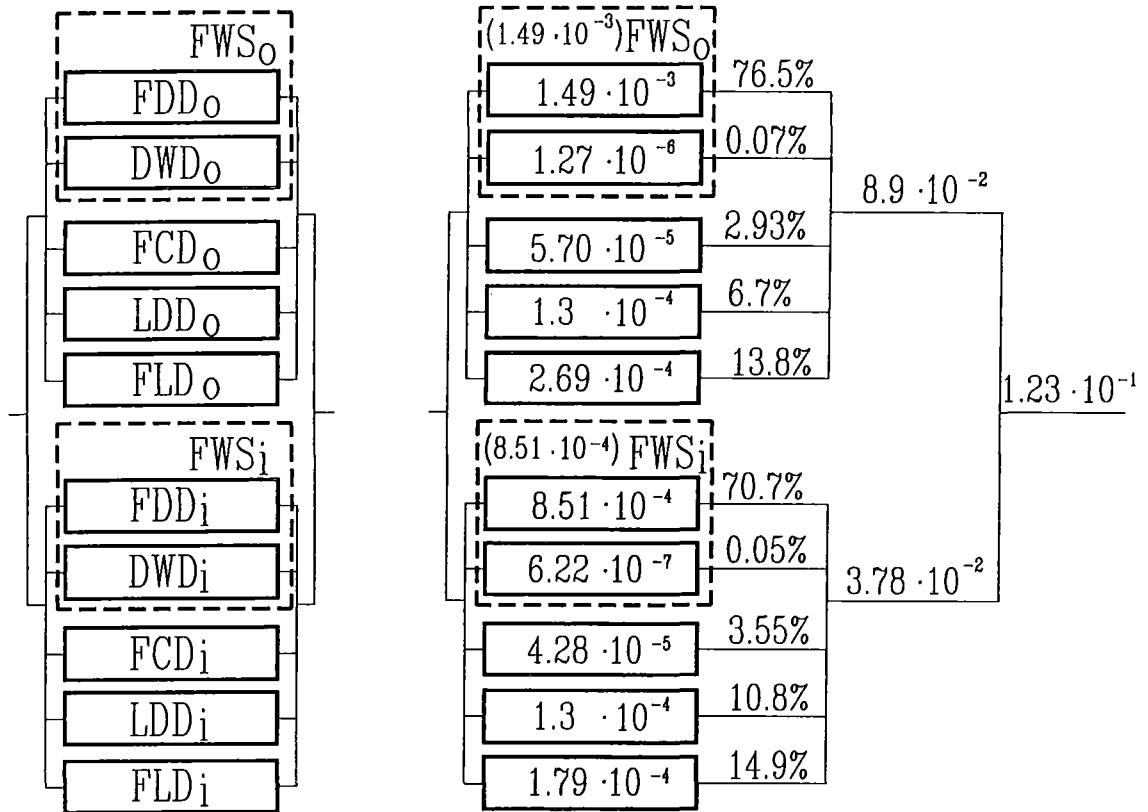


Fig. 12-8 Block diagram for the blanket segments of the Dual Coolant concept

Fig. 12-9 Expected unavailabilities for the blanket segments of the Dual Coolant concept

### 12.4 Conclusions

The preliminary analysis of the Dual Coolant (DC) blanket indicates that the overall availability is ~86.4%. This value seems to be satisfactory, but improvements are desirable, and also attainable.

The overall availability is dominated mainly by the segment failure rate, which itself is dominated by the diffusion welds in the first wall. The failure rate data used in the analysis are considered to be conservative. Confirmation and further improvements in the reliability of the blanket segments are expected from present and future R&D work. Improvements of the external systems are also possible, which would raise their availability from 98.5% to 99.5% or more.

There are several sources of uncertainties in these analyses. First of all, there are significant uncertainties in the basis failure rate and MTTR data base. The "syn-

thetic" technique depends on assumptions and engineering judgements. Nevertheless, the results are sufficient to perform a relative assessment between the DC blanket and the other EU DEMO blankets. Relative application of the failure analysis is expected to be more accurate than the absolute values themselves.

For the comparison, basic events and failure rate data for the reliability indicators were agreed upon amongst the different parties involved in the BCSE. Furthermore, the first wall failure rate calculated for the DC blanket was assumed for all concepts. This eliminates differences due to the leading source of unavailability.

All four blanket concepts have been analysed using basic failure rates and Mean Time To Repair (or Replace) as listed in Table 12-1. The fact that double walled tubes are used in the segments of the WC concept has been taken into account by assuming one order of magnitude lower failure rate compared to a single tube/single weld case. The results are listed in Table 12-5 for both the blanket segments and the external cooling systems.

For the blanket segments the DC concept has the highest reliability due to the relative simplicity of the design but the differences between the concepts are small. It should be mentioned that the impact of coating failures has not been assessed because there is no data base available.

For the external systems it is obvious that the availability depends mainly on the degree of redundancy. Rather extensive redundancies are proposed for DC and BOT, resulting in an availability of the cooling system of 99.4 % and 98.5 % respectively. No redundancy is proposed for the WC concept and the calculated availability of the cooling system is 87.8 %. It is not clear if the layout of the BIT-external cooling systems allows full power operation in case of a SG or a blower failure. A value of 61.3 % has been calculated without any redundancy. If full power operation is possible in case of a SG failure, the availability of the cooling system would be 93.4 %.

In principle the same availability of the cooling systems could be achieved for all four concepts by providing adequate redundancy. There is a trade off between availability and the costs of the cooling system.

Table 12-5 Comparison of the availabilities of the different concepts

	BOT	Dual Coolant	BIT	Water Cooled
FW availability	90.6% (U=9.4%)			
Availability of the blanket without the FW part	93.0/95.3% <i>(7.0/4.7 %)</i>	96.8% <i>(3.2 %)</i>	93.3% <i>(6.7%)</i>	95.4% <i>(4.6%)</i>
Availability of the blanket including FW part	84.3/86.3% *) <i>(15.7/13.7%)</i>	87.7% <i>(12.3%)</i>	84.4% <i>(15.6%)</i>	86.3% <i>(13.7%)</i>
Availability of the external cooling system	99.4% <i>(0.6%)</i>	98.5% <i>(1.5%)</i>	61.3% <i>(38.7%)</i>	87.8% <i>(12.2%)</i>
Overall availability	83.8/85.8% *) <i>(16.2/14.2%)</i>	86.4% <i>(13.6%)</i>	51.7% <i>(48.3%)</i>	75.8% <i>(24.2%)</i>

Values in italic are the unavailabilities  $U = 1 - V$  ( $U = \text{Unavailability}$ ,  $V = \text{Availability}$ )

\*) Reference design (with bends)/modified design (without bends)

#### References:

- [12-1] DIN 25 424, Teil 2, Fehlerbaumanalyse, Beuth Verlag GmbH; Berlin 1990.
- [12-2] Reactor Safety Study, WASH 1400, NUREG 75/014, PB-24 3203/204, Oct. 1975.
- [12-3] L. Caldarola, A. Wickenhäuser; The Boolean Algebra with Restricted Variables as a Tool for Fault Tree Modularization, Kernforschungszentrum Karlsruhe, KfK 3190, Aug. 1981 (EUR 7056e).
- [12-4] R. Bünde, S. Fabritsiev, V. Rybin; Reliability of welds and brazed joints in blankets and its influence on availability; Fusion Engineering and Design 16(1991) 59-72, North Holland.
- [12-5] L. C. Cadwallader, S.J. Piet; 1988 Failure rate screening data for fusion reliability and risk analysis, EGG-FSP-7922, January 1988, Idaho National Engineering Laboratory.
- [12-6] H. John, H. Schnauder, E. Bogusch, J. Wehling; Reliability investigations and improvements of the cooling system of a self-cooled liquid metal breeder blanket; Fusion Technology 2(1992) 1399-1403.
- [12-7] S. Malang, K. Schlesiak, et al.; Dual Coolant Concept, Kernforschungszentrum Karlsruhe KfK 5424, Nov. 1994.
- [12-8] M. Dalle Donne, et al.; European DEMO BOT Solid Breeder Blanket, Kernforschungszentrum Karlsruhe KfK 5429, Nov. 1994.

- [12-9] L. Giancarli, et al.; Water-cooled Pb-17Li DEMO blanket line EU reference conceptual design and performance presentation; DMT 94/538 (SERMA/LCA/1678, CEA October 1994).
- [12-10] M. Eid, et al.; Helium-cooled ceramic breeder-in-tube blanket line, CEA Report DMT 95/576 Sernal/1682, ENEA Report RI-RCT 94/2, November 1994.
- [12-11] R. Bünde; Reliability, availability, and quality assurance considerations for fusion concepts, Fusion Engineering and Design 29(1995)262-285.
- [12-12] R.A. Müller, H. Schnauder; The evolution of heat-Exchanger design for sodium-cooled reactors, Atomic Energy Review, Vol. 13, No. 2, 215-223 (1975).

### 13. Conclusions

This report summarizes the R&D work of liquid metal breeder blankets for fusion reactors carried out in the years 1992 to 1995 in the frame of the European Fusion Technology Program. The main objective of the work was the development of blankets for a future DEMO reactor. However, also a liquid metal blanket for ITER was studied. Several design options have been studied ranging from full self-cooling to full helium cooling. Pb-17Li was used as breeder/multiplier material. In general, the results obtained confirm that liquid metal blankets are attractive options for experimental and power reactors.

A reactor with relatively conservative features (neutron wall load 2.2 MW/m<sup>2</sup>, thermal efficiency > 30 %, martensitic steel (MANET) as structural material and blanket life-time 20 000 h) had been specified as a common basis for the European DEMO blanket development.

The design studies described in this report together with the accompanying R&D show that the requirement of the specified DEMO reactor can be met with self-cooled blanket concepts. A Dual Coolant Blanket Concept has been selected as reference solution where the First Wall (FW) is cooled by helium and the breeder zone by circulating the Pb-17Li breeder to external heat exchangers. The main results are:

- Self-cooled liquid metal breeder blanket are in principle the most simple concepts since no separate coolant requiring large internal heat transfer surfaces is needed.
- Cooling of the FW with helium leads to the potential for high safety and reliability due to a leak tolerant design, a real double containment of the liquid metal breeder, redundant cooling systems, large margins for internal pressure and additional loads, e.g. caused by plasma disruptions. There are three independent cooling systems, each of them sufficient for after heat removal below normal operating temperatures. A LOCA with delayed plasma shutdown results in a temperature increase of less than 100 K for a few seconds only.
- The radiological hazard from accidental release of Pb-17Li is very low and mainly determined by <sup>203</sup>Hg. The release of <sup>210</sup>Po is no longer a feasibility issue since both the generation and the release rate of this isotope are orders of magnitude lower compared to previous investigations.

- An availability of 87.7% has been calculated for all blanket segments, assuming a mean time to replace a blanket segment of 3 months. About 70 % of this 12.3% unavailability are caused by failures of the FW. The unavailability of the external cooling systems has been reduced to 1.5 % by providing redundancy of these systems. This leads to an overall availability of 86.4 %.
- Large progress has been made in theoretical and experimental investigations of MHD issues. This allows the conclusions that MHD pressure drop is no longer an important issue if the feasibility of insulating coatings or flow channel inserts can be proven. Velocity profiles and turbulent motions are no important issues for a concept with helium cooled FW. However, more knowledge in these field is required before the feasibility of more advanced blanket concepts based on liquid metal cooled FW can be judged.
- Detailed neutronics calculations have shown that tritium self-sufficiency can be easily achieved with self-cooled Pb-17Li blankets. The shielding efficiency of such blankets is rather poor but can be increased by using a neutron moderator either in the outer part of the blanket/shield or in the vacuum-vessel.
- The feasibility of the proposed tritium extraction method from Pb-17Li, based on diffusion through the steam generator tubes into a secondary liquid metal (NaK) where is removed from by cold trapping, has been proven experimentally. Sufficiently low tritium permeation losses can be achieved and the regeneration time of the cold traps allows for a cycling time of less than one day for the batchwise tritium recovery.
- The performance of the blankets in terms of allowable power density and achievable thermal efficiency is limited by the temperature of the FW determining the limits for mechanical stresses. This limit is reached a long time before corrosion of the structural material by the liquid metal could become a problem. Corrosion is further reduced by electrically insulation alumina coatings.
- The remaining feasibility issue is the fabrication of insulating coatings and their performance under long-time neutron irradiation. This development requires an ongoing effort over the next three years including new fabrication technologies and testing in fission reactors.
- However, self-cooled liquid metal breeder blankets must not be judged on the basis of development risk only. The development potential should become an at least as important criteria as the development risk. Self-

cooled blankets have the potential to become attractive concepts for commercial power reactors since their performance can be improved decisively by design modifications and by employing the attractive features of more advanced materials (e.g. vanadium alloys, lithium).